PHYSICS OF POROUS MEDIA

EDITED BY: Dick Bedeaux, Eirik G. Flekkøy, Alex Hansen, Signe Kjelstrup, Knut Jørgen Måløy and Ole Torsaeter

PUBLISHED IN: Frontiers in Physics

frontiers Research Topics

frontiers

ISSN 1664-8714
ISBN 978-2-88963-535-1
DOI 10.3389/978-2-88963-535-1

About Frontiers

Frontiers is more than just an open-access publisher of scholarly articles: it is a pioneering approach to the world of academia, radically improving the way scholarly research is managed. The grand vision of Frontiers is a world where all people have an equal opportunity to seek, share and generate knowledge. Frontiers provides immediate and permanent online open access to all its publications, but this alone is not enough to realize our grand goals.

Frontiers Journal Series

The Frontiers Journal Series is a multi-tier and interdisciplinary set of open-access, online journals, promising a paradigm shift from the current review, selection and dissemination processes in academic publishing. All Frontiers journals are driven by researchers for researchers; therefore, they constitute a service to the scholarly community. At the same time, the Frontiers Journal Series operates on a revolutionary invention, the tiered publishing system, initially addressing specific communities of scholars, and gradually climbing up to broader public understanding, thus serving the interests of the lay society, too.

Dedication to Quality

Each Frontiers article is a landmark of the highest quality, thanks to genuinely collaborative interactions between authors and review editors, who include some of the world's best academicians. Research must be certified by peers before entering a stream of knowledge that may eventually reach the public - and shape society; therefore, Frontiers only applies the most rigorous and unbiased reviews.
Frontiers revolutionizes research publishing by freely delivering the most outstanding research, evaluated with no bias from both the academic and social point of view. By applying the most advanced information technologies, Frontiers is catapulting scholarly publishing into a new generation.

What are Frontiers Research Topics?

Frontiers Research Topics are very popular trademarks of the Frontiers Journals Series: they are collections of at least ten articles, all centered on a particular subject. With their unique mix of varied contributions from Original Research to Review Articles, Frontiers Research Topics unify the most influential researchers, the latest key findings and historical advances in a hot research area! Find out more on how to host your own Frontiers Research Topic or contribute to one as an author by contacting the Frontiers Editorial Office: researchtopics@frontiersin.org

PHYSICS OF POROUS MEDIA

Topic Editors:
Dick Bedeaux, Norwegian University of Science and Technology, Norway
Eirik G. Flekkøy, University of Oslo, Norway
Alex Hansen, Norwegian University of Science and Technology, Norway
Signe Kjelstrup, Norwegian University of Science and Technology, Norway
Knut Jørgen Måløy, University of Oslo, Norway
Ole Torsaeter, Norwegian University of Science and Technology, Norway

Citation: Bedeaux, D., Flekkøy, E. G., Hansen, A., Kjelstrup, S., Måløy, K. J., Torsaeter, O., eds. (2020). Physics of Porous Media. Lausanne: Frontiers Media SA. doi: 10.3389/978-2-88963-535-1

Table of Contents

frontiers in Physics

EDITORIAL
published: 28 January 2020
doi: 10.3389/fphy.2020.00003

Editorial: Physics of Porous Media

Dick Bedeaux[1], *Eirik G. Flekkøy*[2], *Alex Hansen*[3]*, *Knut Jørgen Måløy*[2], *Signe Kjelstrup*[1] *and Ole Torsæter*[4]

[1] PoreLab and Department of Chemistry, Norwegian University of Science and Technology, Trondheim, Norway, [2] PoreLab and Department of Physics, University of Oslo, Oslo, Norway, [3] PoreLab and Department of Physics, Norwegian University of Science and Technology, Trondheim, Norway, [4] PoreLab and Department of Geosciences and Petroleum, Norwegian University of Science and Technology, Trondheim, Norway

Keywords: flow in porous media, two-phase flow in porous media, non-Newtonian fluids, reactive fluids, electrohydrodynamics (EHD), capillary fiber bundle model, soil mechanics, thermodynamics of small systems

Editorial on the Research Topic

Physics of Porous Media

The physics of porous media is, when taking a broad view, the physics of multinary mixtures of immiscible solid and fluid constituents. Its relevance to society echoes in numerous engineering disciplines such as chemical engineering, soil mechanics, petroleum engineering, groundwater engineering, geothermics, and fuel cell technology. It is also at the core of many scientific disciplines ranging from hydrogeology to pulmonology.

Perhaps one may affix a starting point for the study of porous media as the year 1794 when Reinhard Woltman introduced the concept of volume fractions when trying to understand mud [1]. In 1856, Henry Darcy published his findings on the flow of water through sand packed columns and the first constitutive relation was born [2]. Wyckoff and Botset proposed in 1936 a generalization of the Darcy approach to deal with several immiscible fluids flowing simultaneously in a rigid matrix [3]. This effective medium theory assigns to each fluid a relative permeability, i.e., a constitutive law for each fluid species. It remains to this day the standard framework for handling the motion of two or more immiscible fluids in a rigid porous matrix even though there have been many attempts at moving beyond it.

When the solid constituent is not rigid, forces in the fluids and the solid phase influence each other. von Terzaghi realized the importance of capillary forces in such systems in the thirties [4]. An effective medium theory of poroelasticity was subsequently developed by Biot in the mid fifties [5]. Biot theory remains to date the state-of-the art for handling matrix-fluid interactions when the deformations of the solid phase remain small. For large deformations, e.g., when the solid phase is unconsolidated, no effective medium theory exists.

The situation today in porous media research is a patchwork of domains, some of which are advancing at high speed, whereas other domains remain where they have been for decades. For example, pore scale visualization techniques together with advances in numerical techniques and hardware have today reached a level of refinement that makes it possible numerically to reproduce the motion of immiscible fluids and their interfaces in complete detail at the pore level. On the other hand, to derive effective equations at the large-scale continuum level based on what happens at the pore scale the upscaling problem remains a rather stagnant endeavor as proven by the popularity of the 80-year old relative permeability theory of Wyckoff and Botset.

It is the aim of any physical theory to join experimental observations into a common framework reducing the field to solving mathematical problems. Here is an example. The flow of Newtonian fluids remained a catalog over experimental observations until the advent of the Navier-Stokes equations. Afterwards, the problem became solving these equations with the proper boundary

OPEN ACCESS

Edited and reviewed by:
Ferenc Kun,
University of Debrecen, Hungary

***Correspondence:**
Alex Hansen
Alex.Hansen@ntnu.no

Specialty section:
This article was submitted to Interdisciplinary Physics, a section of the journal Frontiers in Physics

Received: *06 December 2019*
Accepted: *06 January 2020*
Published: *28 January 2020*

Citation:
Bedeaux D, Flekkøy EG, Hansen A, Måløy KJ, Kjelstrup S and Torsæter O (2020) Editorial: Physics of Porous Media. Front. Phys. 8:3. doi: 10.3389/fphy.2020.00003

conditions. The fact that it is extremely difficult to solve these equations in the majority of instances is a different story. The science of porous media is still at the catalog stage with no general theory of porous media flow in existence nor in sight.

This Research Topic attempts to present a snapshot of the state-of-the-art in some of the domains that constitute the physics of porous media. The physics of porous media is of course far too wide to make it possible to give a comprehensive picture of the field. Interdisciplinarity is a key word.

The paper by Xu et al. studies the dissolution of plaster by water in a two-dimensional Hele-Shaw cell. The water is drained from the center of the cell which has a radial geometry. This causes fingers to grow inwards from the surface of the plaster. There has been a number of numerical studies of similar phenomena, but the experimental work is sparse—in spite of the importance of this process in geological settings.

In another experimental and numerical study, Xu et al. inject a reactive fluid into an open fracture with the result that the fracture surface is modified locally by creating a ramified structure around the injection point. A tracer is then injected and the influence of the modified fracture surface on stability of dispersion front is studied.

Roy et al. consider theoretically and numerically two-phase flow in the capillary fiber bundle model. This is a model that can be solved analytically. At high flow rates, the authors find a linear relation between flow rate and pressure drop across the model, i.e., a standard Darcy law. However, at smaller pressure drops, there is a crossover to a non-linear regime where the flow rate is a power law in the pressure drop. This is precisely what is seen in experiments (see references in the paper), but the exponent of the power law depends on the disorder in the model. This is a surprising result.

In Eberhard et al., the flow of non-Newtonian fluids in porous media is addressed. The authors propose a generalization of the Darcy law to describe the flow of a certain class of non-Newtonian fluids, the Carreau fluid, based on theoretical, numerical, and experimental work.

Another work focused on the flow of non-Newtonian fluids in porous media is that of Talon and Hansen. They focus on bi-linear fluids that have one viscosity up to a given shear rate and then switch abruptly to another viscosity above this shear rate. Through analytical and numerical arguments, the authors demonstrate that there is a critical point with a diverging correlation length characterizing this transition.

Wettability alteration due to adsorbtion of nanoparticles is the topic of the experimental paper by Li et al. This is a very promising approach to mobilizing stuck liquid clusters and droplets in porous media through flooding—an important process in many industrial applications such as EOR (Enhanced Oil Recovery).

Sinha et al. pose the question: when two immiscible fluids flow simultaneously in a porous medium at high enough speeds so that capillary forces are negligible compared to the viscous forces, what would be the effective viscosity that goes into the Darcy law describing the flow? It turns out not to be so simple: The authors propose a formula that contains a parameter that is determined by the pore structure of the porous medium.

There are many very different approaches to numerical modeling of immiscible two-phase flow in porous media. Network models constitute one class of such models, and a subgroup within this class consists of models that track the motion of the fluid interfaces inside the porous medium. Gjennestad et al. present here a way to stabilize such models numerically at very low capillary numbers, i.e., at very low flow rates. This leads to a vast improvement in range of capillary number over which these models may be used.

In two papers, Kjelstrup et al. and Kjelstrup et al., present a new way to coarse grain the thermodynamic variables at the pore level to the continuum level based on the Euler theorem for homogeneous functions and classical non-equilibrium thermodynamics. This way of coarse graining the system avoids the explosion of variables and complexity seen in other approaches to this problem. It leads also to a generalization of Darcy's law, including for instance contributions from thermal forces.

What is the pressure inside a nano-porous medium containing a single fluid? This is the question that Galteland et al. pose. Based on Hill's thermodynamics for small systems (see references in paper), the authors find that there are in fact *two* pressures necessary: an integral and a differential pressure. The authors support their findings by molecular dynamics simulations.

Grimstad et al. build a bridge between porous media physics and the classical concepts in soil mechanics/geotechnical engineering. The languages used by the practitioners of these two approaches to the *same problem* are quite different. Such bridges are therefore very important if multidisciplinary is to have any meaning. Physicists, read and learn!

"Bernaise" they call it, the beautiful computational framework that Linga et al. present for dealing with immiscible two-phase electrohydrodynamic flow in complex geometries such as porous media. The flow of immiscible electrolytes is important in many geological contexts, but little is so far known about how these electrical phenomena affect the hydrodynamics. Now, we have a good tool to explore this. Expect much more to come.

Kirichek et al. present a model for the dielectric response of porous sandstone saturated with NaCl which they proceed to verify experimentally using a two-electrode setup.

AUTHOR CONTRIBUTIONS

All authors listed have made a substantial, direct and intellectual contribution to the work, and approved it for publication.

FUNDING

This work was supported by the Research Council of Norway through its Centres of Excellence funding scheme, project number 262644.

REFERENCES

1. Woltman R. *Hydraulischen Architectur*. Göttingen: Johann Christian Dieterich (1794).
2. Darcy HPG. *Les Fontaines publiques de la ville de Dijon. Exposition et application des principes à suivre et des formules à employer dans les questions de distribution d'eau*. Paris: Victor Dalamont (1856).
3. Wyckoff RD, Botset HG. The flow of gas-liquid mixtures through unconsolidated sands. *Physics*. (1936) **7**:325–45. doi: 10.1063/1.1745402
4. von Terzaghi K. Auftrieb und Kapillardruck an betonierten Talsperren. *Die Wasserwirtschaft*. (1933) **26**:397–9.
5. Biot MA. Theory of deformation of a porous viscoelastic anisotropic solid. *J Appl Phys*. (1956) **27**: 459–67. doi: 10.1063/1.1722402

Conflict of Interest: The authors declare that the research was conducted in the absence of any commercial or financial relationships that could be construed as a potential conflict of interest.

frontiers in Physics

ORIGINAL RESEARCH
published: 16 April 2018
doi: 10.3389/fphy.2018.00029

Dispersion in Fractures With Ramified Dissolution Patterns

Le Xu[1]*, *Benjy Marks*[1,2], *Renaud Toussaint*[1,3], *Eirik G. Flekkøy*[1] and *Knut J. Måløy*[1]

[1] PoreLab, Department of Physics, University of Oslo, Oslo, Norway, [2] The University of Sydney, Sydney, NSW, Australia, [3] Centre National de la Recherche Scientifique, Université de Strasbourg, IPGS UMR 7516, Strasbourg, France

The injection of a reactive fluid into an open fracture may modify the fracture surface locally and create a ramified structure around the injection point. This structure will have a significant impact on the dispersion of the injected fluid due to increased permeability, which will introduce large velocity fluctuations into the fluid. Here, we have injected a fluorescent tracer fluid into a transparent artificial fracture with such a ramified structure. The transparency of the model makes it possible to follow the detailed dispersion of the tracer concentration. The experiments have been compared to two dimensional (2D) computer simulations which include both convective motion and molecular diffusion. A comparison was also performed between the dispersion from an initially ramified dissolution structure and the dispersion from an initially circular region. A significant difference was seen both at small and large length scales. At large length scales, the persistence of the anisotropy of the concentration distribution far from the ramified structure is discussed with reference to some theoretical considerations and comparison with simulations.

Keywords: dispersion, fracture, convection-diffusion, fractal-like, Hele-Shaw cell, fluorescein tracer

OPEN ACCESS

Edited by:
José S. Andrade Jr.,
Federal University of Ceará, Brazil

Reviewed by:
Eric Josef Ribeiro Parteli,
Universität zu Köln, Germany
Ramon Castañeda-Priego,
Universidad de Guanajuato, Mexico

***Correspondence:**
Le Xu
le.xu@fys.uio.no

Specialty section:
This article was submitted to Interdisciplinary Physics, a section of the journal Frontiers in Physics

Received: *29 January 2018*
Accepted: *23 March 2018*
Published: *16 April 2018*

Citation:
Xu L, Marks B, Toussaint R, Flekkøy EG and Måløy KJ (2018) Dispersion in Fractures With Ramified Dissolution Patterns. Front. Phys. 6:29. doi: 10.3389/fphy.2018.00029

1. INTRODUCTION

In both geological systems and industrial fields, fractures are known to be important pathways for fluid transport. Typically, the permeability of fractures is significantly higher than the porous matrix, so in many systems fractures play an important role in the fluid transport processes. The flow of tracer particles in a fracture is influenced by both convection and diffusion processes, and the combined effect of these two processes leads to Taylor dispersion. This effect was first studied by Taylor [1] for solvent flowing slowly through a tube. Afterwards it has been applied to various situations, for example, in single and parallel fractures [2, 3], in rough fractures [4], particle dispersion in narrow channels [5], and in a radial flow geometry [6, 7]. Some previous works consider geometric anisotropy, using self-organized percolation model to study flow through disordered porous media [8–10].

In most previous studies a flat open fracture with a constant aperture is considered, leading to a smooth and uniform front [11–15]. However in geological systems or industrial fields, such ideal initial states are rare. For example, when injecting a reactive fluid into an oil field, the injected fluid will react with the porous media which is stimulated by engineers trying to maximize the permeability around wells. A ramified dissolution pattern [16–18] will be formed around such an inlet. Those ramified features of the inlet will alter the fluid flow transport path in the rocks significantly. The flow transport problems in the fractures encountered in nature and in industry typically have irregular initial fronts, which is significantly different from the flat fronts obtained by injection into an open flat fracture. Considering a pollution leak problem for instance, if we

suppose that the localized pollution source presents an initially uniform front in a homogeneous porous medium or aperture, we expect that the contamination spreads with radial symmetry, which deviates considerably from the actual situation because of the irregular initial front state. In this paper, we present experimental and numerical results demonstrating that with a ramified dissolution initial front state, in some directions the tracer will transport much faster than what we expect for an initially uniform front while in other directions there is no tracer transport at relatively long times.

In order to study these more realistic situations, a ramified dissolution pattern has been produced in a plaster sample, which is then used as the injection geometry. A fluid with a fluorescein tracer is injected into the cavity between this plaster sample and a flat plate, which together represent an open fracture. The injected fluid with tracer first fills the dissolved part and then starts flowing through the open fracture from the tips of dissolution fingers. The fluorescein tracer allows tracking of the flow radiating from this structure. We describe our experiments in section 2. In section 3, the simulation methods are illustrated. In section 4, the characteristics of the ramified dissolution patterns are studied. The experimental results are compared with results from numerical modeling in section 5. The conclusions follow in the last section.

2. DESCRIPTION OF EXPERIMENTS

The experimental setup is illustrated in **Figure 1**. The experiments were performed in a Hele Shaw cell which consists of two circular and parallel flat glass plates. The bottom glass plate (Diameter $d_1 = 36.0$ cm) is larger than the upper one (Diameter $d_2 = 25.0$ cm) and has an external rim. An inlet is located at the center of the lower glass plate, and the two glass plates are separated by aluminum spacers of thickness $b = 1.00$ mm and held together by clamps.

2.1. Sample Preparation

In the experiments we study the dispersion phenomena in an open fracture with an initial state representing a ramified dissolution pattern. We therefore first created a dissolution pattern in the sample, and later performed the tracer dispersion experiment. The plaster sample with a dissolution pattern on the top surface was prepared by the following steps:

A plaster saturated water solution was first injected into the Hele Shaw cell. Water and plaster powder (Alabaster plaster, Panduro) was then mixed with the ratio 2:3 by weight respectively to form the plaster paste. Next, this paste was injected from the center of the Hele Shaw cell displacing the plaster saturated water forming a circular plate of radius $R \approx 8.0$ cm. The circular plaster paste was then kept in the cell surrounded by saturated water for hydration which was completed in approximately 1 h. During the plaster hydration process, a form of segregation called bleeding takes place, where some of the water in the plaster tends to rise to the top surface of the plaster plate [19]. This process gives an aperture of $h \approx 50$ μm above the surface of the plaster. The next step was to inject pure water into the center of the Hele Shaw cell using a syringe pump. The plaster dissolved slightly into this pure water and a dissolution pattern on the surface of the plaster sample was formed after several days. This process is known as wormhole formation [16, 20–22]. After the plaster sample with dissolution pattern was prepared, we changed the injected fluid from pure water to the tracer fluid (water with fluorescein) ready to start the dispersion experiment.

2.2. Dispersion Experiment

The tracer fluid was prepared by mixing water and fluorescein sodium salt powder. The solubility of fluorescein powder is 1.0 mg/mL and the solution was diluted at a ratio of 1:10. The concentration of the injected tracer fluid was $C_0 = 0.27$ mmol/L. The viscosity of the tracer fluid $\mu = 0.965 \pm 0.004$ mPa·s, is slightly larger than the water viscosity at room temperature of 23.5°C. The molecular diffusion coefficient of fluorescein in water is $D_m = 4.25 \cdot 10^{-6}$ cm^2/s [23].

The water with fluorescein was injected into the open fracture by a syringe pump from the central inlet with an injection rate of $Q = 6.00$ mL/h. Dissolution of the plaster can be neglected due to the short time scale of the dispersion experiment (50 min). The aperture (thickness $h = 50.0$ μm) is defined as the distance between the upper glass plate and the upper surface of the plaster sample. The permeability of this aperture is calculated as $\kappa = h^2/12 = 2.1 \cdot 10^{-10}$ m^2 and the permeability of the plaster sample itself is $6.0 \cdot 10^{-14}$ m^2. Because of the large permeability contrast between the aperture and the plaster, almost all injected fluid will flow through the aperture instead of the porous matrix. An ultraviolet light bulb was used to illuminate the system from underneath, and a digital camera was placed 1 m above the Hele Shaw cell to capture images of the dispersion experiment.

2.3. Image Processing

In our experiments, the plaster plate not only provides the complex injection boundary of a fractal-like dissolution pattern, but also plays a role as a light diffuser so that the UV light will stimulate the fluorescent fluid uniformly. We want to establish a relation between the image intensity $I(\mathbf{r}, t)$ and the tracer concentration $C(\mathbf{r}, t)$. The intensity of the light measured by the CCD camera is proportional to the intensity of the emitted light from the fluorescein molecules stimulated by the UV light. The brightness of image captured by CCD camera is directly linked to the light intensity. The image brightness field is linearly related to the fluid concentration field in the fracture if the fluorescein concentration is low enough [24]. The relation between the image intensity and the flow tracer concentration has been measured experimentally as shown in Figure S1 in the Supplemental Data. The calibration shows as expected a linear relation between the gray scale levels and the concentration C when $C \leq 100$ mg/L. Applying this linear relationship, we obtain the normalized fluorescein concentration field from the experimental images by $C_n(\mathbf{r}) = I(\mathbf{r})/I_{max}$ where $I(\mathbf{r})$ is the intensity of the gray-scale image at position $\mathbf{r}$ and I_{max} is the maximum intensity observed in the area with highest fluorescein tracer concentration, located at the injection inlet where the concentration was kept fixed at $C_0 = 0.27$ mmol/L.

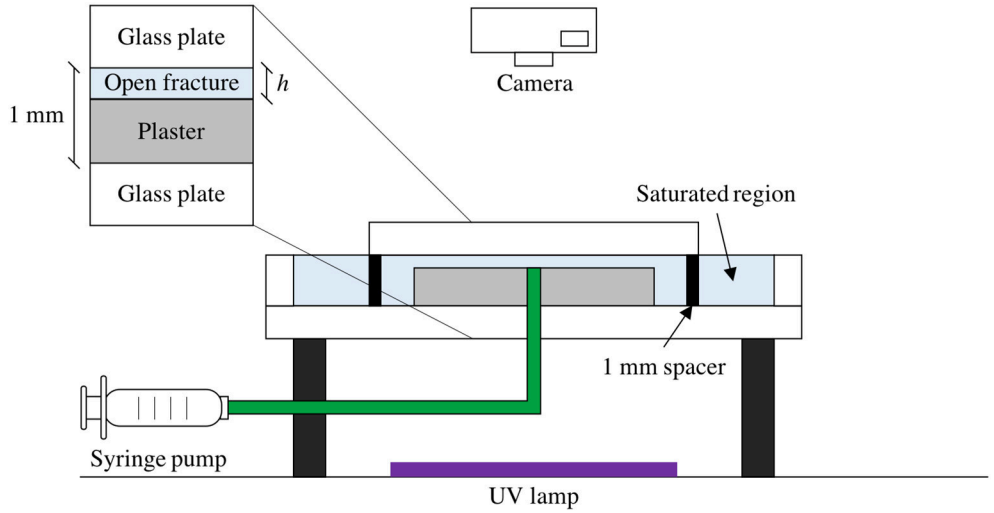

FIGURE 1 | Schematic diagram of experimental setup. A circular Hele Shaw cell (spacing 1 mm) contains a saturated plaster plate with a small gap ($h = 50.0$ μm) above the plaster. A tracer fluid is injected by a syringe pump into the center of the Hele Shaw cell, where it flows radially outwards. The model is illuminated from below by an ultraviolet light source. The plaster plate has a fixed dissolution pattern around the injection point, formed by distilled water injection before the tracer injection experiment.

The concentration C is linked to the normalized concentration C_n as $C(\mathbf{r}, t) = C_0 C_n(\mathbf{r}, t)$.

3. NUMERICAL METHODS

3.1. Molecular Diffusion Model

In the Molecular Diffusion Model, we assume that the flow velocity and fluorescein concentration is uniform in the vertical direction, and the problem can be modeled in two spatial dimensions. For this 2D model we only consider convection and molecular diffusion, i.e., the dispersion effect combining the coupling of diffusion and convection is not included. Because of the contrast between the permeability of the dissolved part and the undissolved part, as an approximation, we assume that the pressure in the dissolution pattern is uniform, equal to a pressure P_0. The pressure outside the plaster sample, defined by the external boundary, is equal to the atmospheric pressure $P_{out} = 1atm$, and we choose $P_0 > P_{out}$. We assume that the flow in the open fracture between the plaster sample and the glass plate follows Darcy's law, as

$$\mathbf{u} = -\frac{\kappa}{\mu}\nabla P\,, \tag{1}$$

where $\mathbf{u}$ is average flow velocity across the fracture, κ is the permeability for the flow in the fracture (estimated assuming Poiseuille flow as $\kappa = h^2/12$) and μ is the viscosity of the fluid. We assume that the fluid is incompressible which implies that $\nabla \cdot \mathbf{u} = 0$. We thus obtain the Laplace equation for the pressure field in the fracture as

$$\Delta P = 0\,. \tag{2}$$

By numerically solving for the pressure field, assuming the boundary pressures as defined above, we can apply Darcy's law to obtain the velocity field in the fracture. Combining the flow field with the Convection-Diffusion Equation gives

$$\frac{\partial C}{\partial t} = \nabla \cdot (D_m \nabla C) - \nabla \cdot (C\mathbf{u})\,, \tag{3}$$

where C is the concentration of fluorescein in water, and this concentration field can be solved for and compared with experimental results. We also consider the Taylor dispersion effect by simply replacing the diffusion coefficient D_m by the dispersion coefficient $D_\parallel$ [25, 26]

$$D_\parallel = \frac{h^2 u_0^2}{210 D_m} + D_m = D_m\left(1 + \frac{h^2 u_0^2}{210 D_m^2}\right)\,. \tag{4}$$

In this way, we assume that the transversal dispersion coefficient $D_\perp$ is the same as $D_\parallel$ which will give a larger dispersion in the transversal direction. In section 5, We compare the simulation results with experimental images, and don't find significant differences between the molecular diffusion model and the Taylor dispersion model. For this reason, we will first present our 2D model with molecular diffusion.

3.2. Simulation Implementation

The dissolution pattern is measured via thresholding of an experimentally obtained image, and the boundary of this pattern is used as an internal boundary for the simulation. The external boundary is defined to coincide with the outer edge of the plaster. At the external boundary, the pressure is set to atmospheric pressure. At the internal boundary, an inverse analysis is performed, where the internal pressure within the dissolved area is iteratively varied until the volumetric flow rate matches the

experimentally observed value. For the internal boundary we set the concentration constant equal to C_0 corresponding to the injected tracer concentration everywhere inside the dissolved part. We set concentration outside of the plaster disk to 0. For the initial condition, we set the concentration to 0 everywhere except in the dissolved structure. Flow rates are calculated assuming incompressibility and Darcy flow, as explained above, and an explicit finite difference algorithm is implemented to solve the Laplace equation. Once the velocity field is known, the convection-diffusion equation is solved using a finite volume method that accurately preserves discontinuities [27]. This is implemented on a regular grid of 800 × 800 cells, which covers the experimental domain.

4. CHARACTERISTICS OF THE RAMIFIED DISSOLUTION PATTERN

At early stages, the fluid fills the ramified dissolution pattern and the pattern is "fractal-like." We call it "fractal-like" because it looks similar to fractal structures and these dissolution patterns were considered as fractal in earlier studies [16]. We will show in this section that our dissolution pattern presents significant differences relative to typical fractal patterns such as viscous fingering [28] or DLA [29] structures. Fractal structures are commonly described by a fractal dimension. The fractal dimension can be estimated by many methods [30–32]. Here we will use the mass within radius method and the box-counting method to analyze the structures. In fact, we will see that our dissolution pattern is an example where the box counting method and mass within radius method yield quite different results. The total mass $m(r)$ within a radius r is calculated by counting the number of points (pixels) within this circle as seen in **Figure 2B**. For a fractal structure the mass within the radius will follow a power law $m(r) \propto r^{D_m}$ where D_m is the mass fractal dimension. In the box-counting method, we draw a grid on the structure that consists of squares of size $\delta \times \delta$ each. If the structure is fractal, the number of squares N needed to cover the structure will follow the scaling relation $N \propto \delta^{-D_b}$ where D_b is the box-counting fractal dimension.

From **Figure 2**, we observe that the Mass Method and the Box-counting Method give very different results. The r^2 scaling seen in the mass method close to the injection point ($r = 0$) is caused by the compact structure in this region which goes up to about 0.5 cm from the injection point. Above this length scale the curved green line is due to the decrease in thickness of the fingers but also to the crossover associated to the finite size of the system. The data in **Figure 2C**, was fitted to a straight line using linear regression with a slope of 1.5 which gives an estimate of a box counting dimension as $D_b = 1.5$. Notice that there is a small systematic deviation from a linear curve. For the mass within a radius method **Figure 2B** shows a linear behavior with slope of 2.0 for the region within the red circle in **Figure 2A**. However in the local zone between the red circle and the green circle in **Figure 2A** (the green region in **Figure 2B**), the slope gradually decreases from 2 to 0 and it is not possible to find a unique mass fractal dimension. The black solid line in this region with slope 1 is a reference to the eye. Notice that in the dissolution pattern, the fingers get thinner from the center to the tips. This specific feature of finger width variation found in the dissolution pattern is not found for instance for fractal viscous fingering [28] or DLA structures [29].

5. EXPERIMENTAL RESULTS COMPARED WITH SIMULATIONS

5.1. Qualitative Comparison

Pictures of the dynamic process of dispersion were taken every 30 s from the beginning of injection until the tracer fluid reached the edge of the sample. The whole process takes 50 min in total, which corresponds to 100 digital images. The experiments are reproducible and the repeated experiments give similar results. Here we present one set of experimental results and data analysis. Results from another experiment is shown in the supplemental data. In **Figure 3**, four pairs of images corresponding to different time periods are compared between the simulations and the experiment.

A visual overview of the concentration pattern evolution over time is illustrated in **Figure 4**. It is constructed by firstly thresholding each grayscale image at $I/I_{max} > 0.2$, next computing the incremental difference by subtracting successive thresholded images, and subsequently compositing each of the incremental changes together, leading to **Figure 4**. This spatiotemporal diagram allows for a more detailed comparison of the dynamic process between simulation and experiment. In the Supplemental Data, Figure S2 shows a similar diagram for another experiment. The simulation and the experimental images look qualitatively very similar to each other.

5.2. Overlap Ratio

To compare quantitatively the experiments and the simulations we have calculated the overlap between two corresponding images with the same size and spatial resolution. We have only considered the overlap within the area of interest, which is the area $\mathcal{A}_D$ defined as the union of area between the experimental and simulations images with a detectable fluorescein concentration. To calculate the overlap we will introduce the overlap ratio (γ_{OL}) defined as:

$$\gamma_{OL} = 1 - \frac{\sum_{(i,j)\in\mathcal{A}_D} \|E(i,j) - S(i,j)\|}{\sum_{(i,j)\in\mathcal{A}_D} max(E(i,j), S(i,j))} \tag{5}$$

where E and S are respectively the experimental and the simulation image (i.e., grayscale fields) which have been normalized (i.e., from 0 to 1), and $max(E(i,j), S(i,j))$ gives the maximum value of $E(i,j)$ and $S(i,j)$. In the case where E and S are binarized (black and white images), this calculation of the overlap ratio leads to the measure of the ratio of the area of intersection between E and S divided by the area of union between E and S (i.e., $A(E \cap S)/A(E \cup S)$), which we call the structure overlap ratio γ_{SOL}. This computation can also be performed on the gray-scaled images of E and S to obtain the intensity overlap ratio γ_{IOL}.

In **Figure 5**, we show a pair of images, E and S, from one experiment and simulation, and the subtracted image

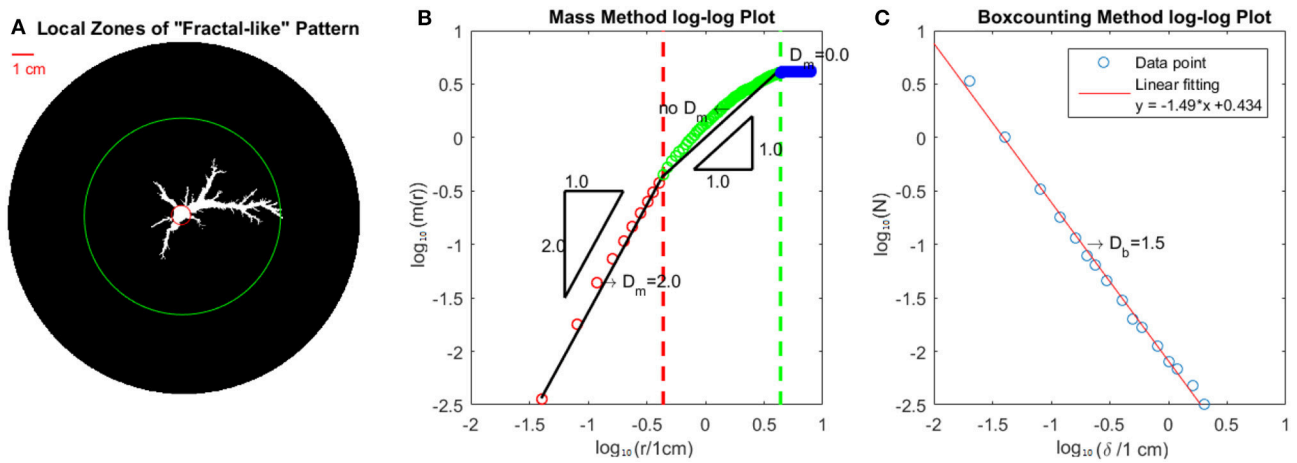

FIGURE 2 | Measurement of fractal dimension from experimentally derived images. **(A,B)** Show the mass fractal dimension estimation method. In **(A)**, we divide the pattern into 3 zones. The part within the red circle is completely dissolved. Between the red and green circles, "fractal-like" fingers expand in different directions. Outside of the green circle lies an entirely undissolved zone. **(B)** Shows a log-log plot of mass $m(r)$ vs. radius r, with the colors corresponding to the relevant zones in **(A)**. The black linear solid lines act as a guide for the eye. The slopes of the black lines are illustrated with the triangles. For the red and blue parts, the fractal dimension by mass method D_m is indicated. For the green part, there is no clear linear part, i.e., no well defined mass fractal dimension D_m. In **(C)** we use the Box-counting Method to obtain the box-counting fractal dimension $D_b = 1.5$.

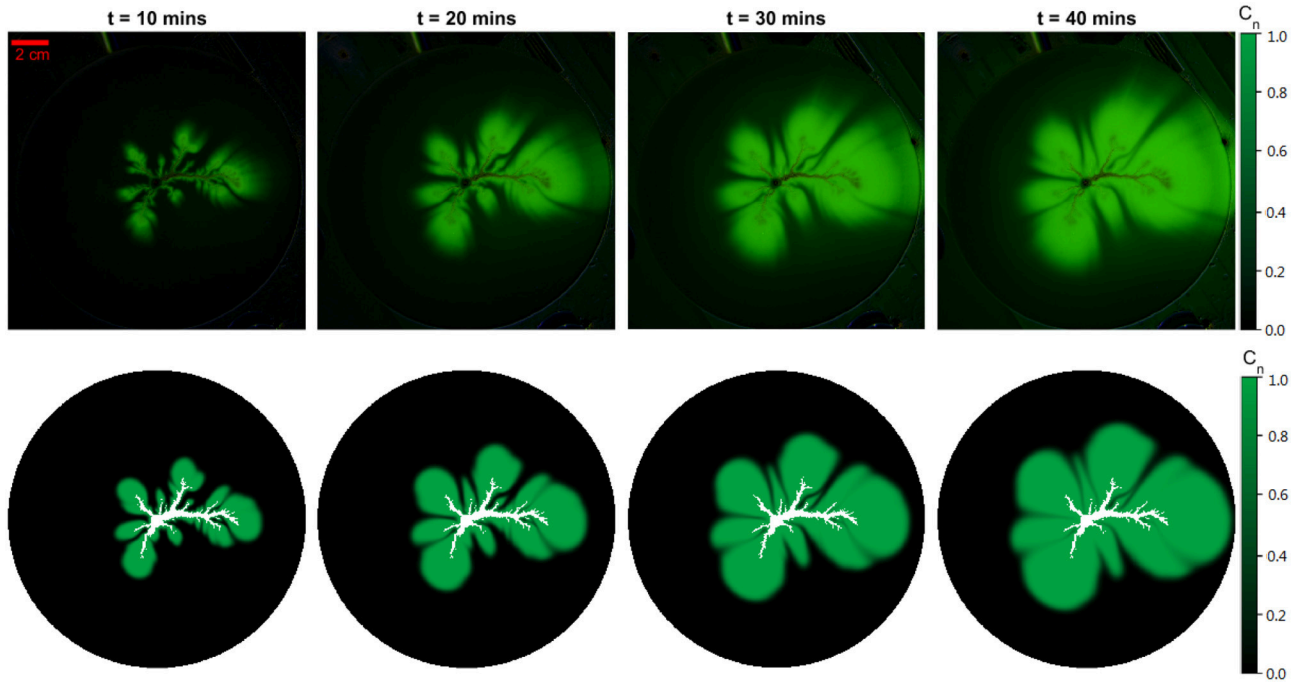

FIGURE 3 | Experimental results compared with simulation images. **(Top)** Experimental images subtracted by the initial state image. **(Bottom)** Simulation output of the dissolution pattern. The boundary conditions are extracted from the experimental image before fluid flow begins. The green intensity represents the normalized tracer concentration C_n in the simulation. The vertical pairs of images show comparison after an injection lasting respectively 10/20/30/40 min, which gives a qualitative description of the similarity between the experiments and simulations.

$\|E(i,j) - S(i,j)\|$. The overlap ratio, indicated in the figure, demonstrates a good similarity between experiment and simulation. From **Figure 5**, we further observe that the fan-shaped dispersion fingers in the simulation grow somewhat more uniformly than in the experiments. On the other hand the experiment presents longer fingers, but with a more gradual change in the concentration toward the tips. One reason for this difference is that in the simulations the dissolution patterns

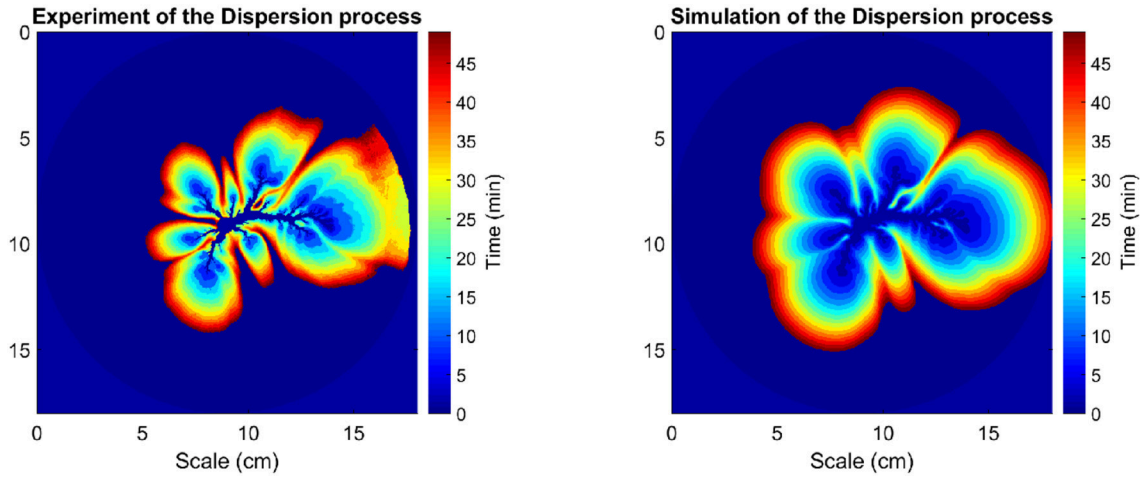

FIGURE 4 | Dynamic process of dispersion with time evolution, time duration 50 min. **(Left)** Data derived from experimental images; **(Right)** Equivalent data obtained from numerical simulation.

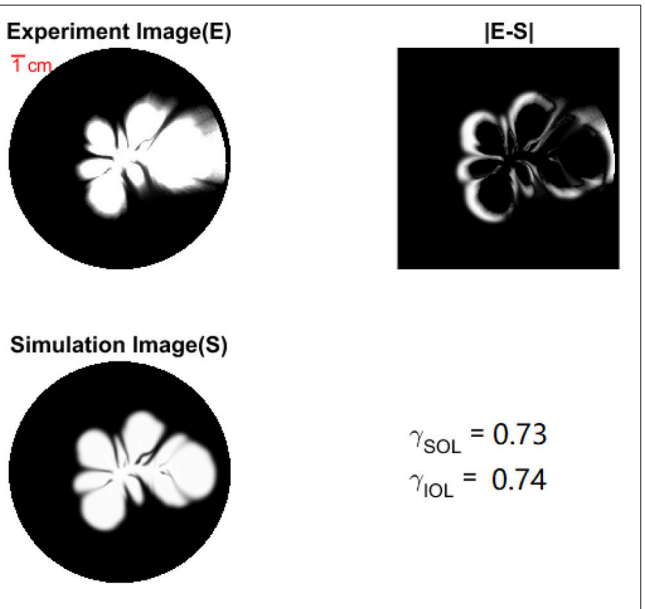

FIGURE 5 | Experimental image (E) and simulation image (S) are resized gray-scaled images from original RGB images. $|E - S|$ displays the intensity difference between experiment and simulation. γ_{SOL} is the structure overlap ratio which compares the black-white images of E and S. γ_{IOL} is the intensity overlap ratio comparing E and S which are gray-scaled images.

are taken to be completely dissolved while in the experiments the plaster sample is gradually dissolved. Therefore in the experiments there is a change in the thickness in the dissolved part which we don't consider in the simulations. For a similar reason the assumed undissolved part in the simulations might have some dissolved fingers that we are not able to see in the experiments due to limited resolution. These slightly dissolved fingers will give finer scale structures in the dissolution patterns. Another difference between the experiments and the simulations is that experimentally, a very small fraction of fluid infiltrates into the porous matrix instead of flowing in the open fracture. Flow in the porous medium is however not included in the simulations. Eventually, because the Hele Shaw cell is three dimensional, we expect a concentration distribution in the vertical direction and a gradient in the measured average concentration (averaged in vertical direction). However our simulation is 2D and a gradient in the average concentration due to the 3D velocity field is not considered.

Figure 6 shows the time dependence of the overlap ratio both for the structure (black-white images) γ_{SOL} and for the intensity (gray-scaled images) γ_{IOL}. The overlap ratio increases with time and gets almost stable with an overlap of about 0.7 after injection of 20 min but decreases slightly toward the end, certainly because of the boundary effect in the experiments different from those in the simulations, the experimental plaster sample is not a perfectly circular disk. We implement 3 different simulations to compare with the experimental results, one simulation without diffusion, one with molecular diffusion and one with Taylor dispersion. The figures presented here demonstrate that the simulation with only a convection term is able to roughly simulate what we have observed in the experiments. However, the simulation with diffusion terms (molecular or Taylor dispersion) is more consistent with the experiments than without diffusion terms. The simulations with pure molecular diffusion and Taylor dispersion show almost no significant difference, then the simulation results in the remainder of this paper use 2D model with molecular diffusion.

5.3. Concentration Distribution

From the dispersion pictures of both the experiments and the simulations, we clearly observe that the tracer flow acts very differently from what we expect from a point injection or injection from a circular region. These differences are expected on small length scales but are less obvious on large length and time scales. Such differences might be important to bear in mind

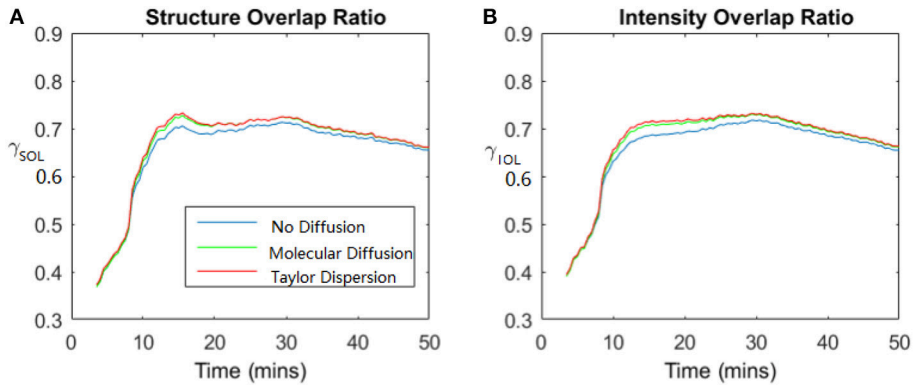

FIGURE 6 | Dynamic process of dispersion: the value of the overlap ratio evolves with time. Total time duration is 50 mins. **(A)** Shows the structure overlap ratio (derived from black and white images) evolution with time and **(B)** shows the intensity overlap ratio (derived from grayscale images) evolution with time. Blue lines show the comparison between experimental results and simulation with no diffusion, green lines with molecular diffusion and red lines with Taylor dispersion.

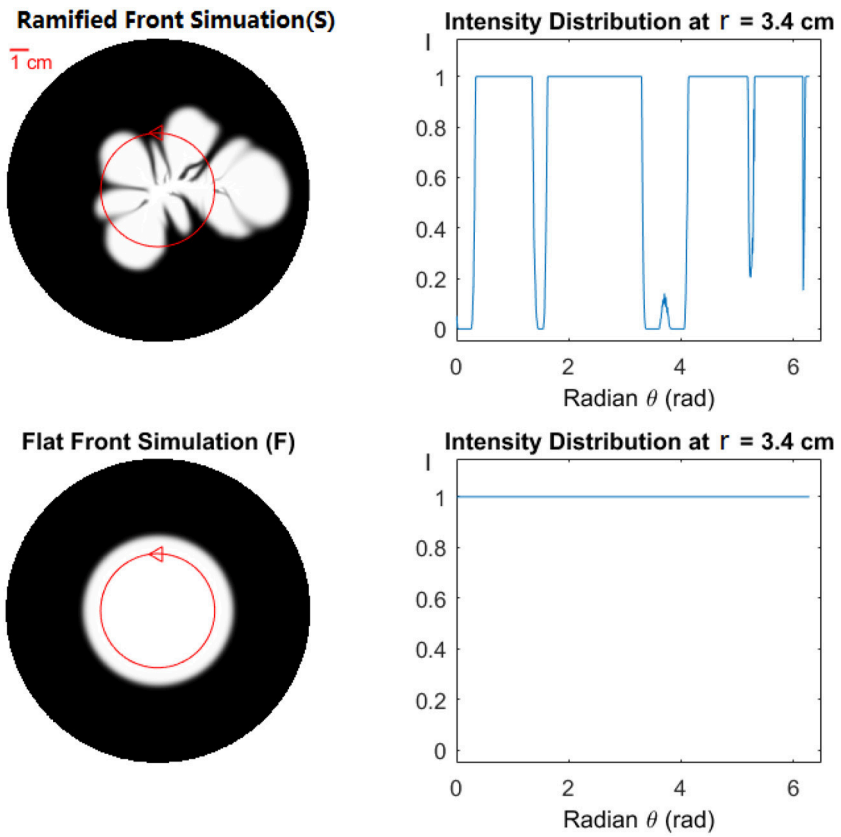

FIGURE 7 | Effect of front geometry. **(Top)** Ramified Front Simulation (S) shows the result of simulation with the ramified front (dissolution pattern). **(Bottom)** Flat Front Simulation (F). The normalized intensity distribution at $r = 3.4$ cm, marked with a red circle on the left, is shown as a function of angle on the right. The distribution begins at the marked triangle, and continues counter-clockwise.

and evaluate when simple model geometries are used to model transport around wells in large-scale applications. In this section we will compare experimentally and by computer simulations the dispersion in an open fracture with an initial state of a ramified dissolution pattern with simulations with an initial stage of circular injection. We will choose a radius of the circular disk injection $R_d = \sqrt{A/\pi}$ where A is the area of the initial ramified dissolution pattern.

5.3.1. Concentration Distribution Width

A quantitative comparison between the dispersion with a ramified and a circular initial structure was performed by comparing the mean value and standard deviation of the tracer concentration on circles of different radii r. **Figure 7** illustrates the difference in the tracer concentration distribution on a circle of a certain radius (here r = 3.4 cm) between the initial circular front and the ramified front. The mean value of the normalized tracer concentration on a circle is defined as

$$< C_n(\mathbf{r}) >= \sum_{i=1}^{N} C_n(\mathbf{r_i})/N(r) \,, \tag{6}$$

where $N(r)$ is the number of pixels along the circle with radius r and $C_n(\mathbf{r_i})$ is the normalized tracer concentration at position $\mathbf{r_i}$. Let $\sigma(r)$ be the standard deviation of $C_n(\mathbf{r})$ on the circle for a fixed value of r. **Figure 8** shows the mean value $< C_n(\mathbf{r}) >$ and the standard deviation $\sigma(r)$ at different radii r among experimental images and simulations with circular and ramified initial fronts. The **Figure 8** clearly demonstrates that the simulation with a ramified initial front fits the experiment much better than the simulation with a flat circular initial front. In the standard deviation **Figure 8B**, a small peak is observed in the circular front simulation (green line) which is not expected from the analytical results. This peak is caused by pixel-size deviations due to a finite pixel resolution describing the circle.

We will define the width $\Delta r(t)$ of the normalized mean concentration distribution as the difference in radius between $< C_n(\mathbf{r}) >= 0.8$ and $< C_n(\mathbf{r}) >= 0.2$ as illustrated in **Figure 9A**. For the circular initial front simulation (yellow line in **Figure 9C**) , $\Delta r(t)$ stays stable at a low level, and the fluctuation in the curve is due to few data points. While the circular initial front simulation is completely different from the experimental curve, the simulation with the ramified initial front is much closer to the experimental results. The width of the mean concentration distribution $\Delta r(t)$ in both the experiments and the simulation with ramified initial front increases to a peak and then decreases to a stable value.

From **Figures 9A,B**, we observe a noticeable change of the concentration distribution from a wider distribution at a time $t =$ 10–15 min to a more localized front at later times $t > 20$ min. In the Supplemental Data Figure S3, another experiment reproduces a similar mean concentration distribution. At short times the angle average concentration curves $< C_n(\mathbf{r}) >$ are dominated by the ramified fractal-like initial structure, but they change to a very different behavior at large scales, to get dominated by the complex velocity field generated by the same ramified dissolution structure and diffusion. On average $< C_n(\mathbf{r}) >$ has a well defined width at large times, but it is much wider than what one would expect from a circular initial front, 5 times wider for simulation and 7 times wider for experiment. For a constant radius r there are large fluctuations in the local values of $C_n(\mathbf{r})$ at different directions. These fluctuations in the concentration are due to velocity fluctuations in the initial ramified structure (see **Figure 7**). An interesting and open question is if these fluctuations will be reduced or disappear for a sufficient large systems and times. Will the model with a circular initial state describe the system at large length scales and times? In the next section, we will propose a theoretical calculation to address this question.

5.3.2. Concentration Distribution Shape

A key question is whether the anisotropy of the concentration profiles will survive over arbitrarily large distances from the dissolution structure. In order to address this question we first pose the same question for the flow field $\mathbf{u}$: Will $\mathbf{u}$ remain anisotropic indefinitely? One way to answer this is to consider a group of two point sources of equal pressure and extent rather than the complex dissolution structure. In this way the distance over which an anisotropic flow field becomes isotropic or not may be explored. Taking the two sources to be located at $\pm\mathbf{r}_1$ where r_1 is the characteristic radius of the dissolution structure, we may work out the pressure field and by Darcy's law, the flow field.

We will take the pressure, or rather the overpressure relative to the atmospheric pressure, to satisfy the 2D Laplace equation, take on the value P_0 inside a radius a around $\pm\mathbf{r}_1$ and vanish at some large distance R. This pressure may to a good approximation be written as

$$P(r) = P_0 \frac{\ln(|\mathbf{r} - \mathbf{r}_1|/R) + \ln(|\mathbf{r} + \mathbf{r}_1|/R)}{\ln(a/R)}. \tag{7}$$

The approximation consists in the fact that the point where the pressure vanishes is shifted a small distance of the order r_1. Darcy's law now gives the Darcy velocity

$$\mathbf{u} = -\kappa \frac{\nabla P}{\mu} = \frac{2\kappa P_0}{\mu \ln(R/a) r} \mathbf{e}_r \left(1 + O\left(\frac{r_1}{r}\right)^2\right), \tag{8}$$

where the unit vector $\mathbf{e}_r = \mathbf{r}/r$ and the higher order term depends on products like $\mathbf{e}_r \cdot \mathbf{r}_1$. This result shows that the flow velocity field becomes isotropic over a distance of the order r_1. We define this distance of the order r_1 for our experimental geometry as r_0, which in our experiments, r_0 is the length of the longest dissolution finger. The argument is that the the two point sources must create a flow field that is at least as anisotropic as the real field, or worse. Since the model field decays to the isotropic field as $(r_1/r)^2$, we conclude that the real field decays as quickly, or quicker.

Now, the fact that the velocity becomes isotropic does not imply that the concentration field does, as this field is governed by an anisotropic source. We calculate the skin-depth to go as the diffusion length $l_D = \sqrt{2D_\perp t}$ where $D_\perp$ is a transverse dispersion constant. This constant characterizes the porous media. In this case, since this medium is just a gap of width h, we may take $D_\perp \approx D_m$. Close to the injection point anyhow, once it is at a point within a few skin-depths of the injection points, it should have reached a concentration which is equal to the imposed central concentration, at least due to diffusion if this did not happen in the first place by convection because the point considered was along a fast transporting finger. So we expect a zone growing like $\sqrt{D_\perp t}$ where the concentration is homogeneous and naturally isotropic but outside of this zone, possible anisotropy is discussed by calculating the convection

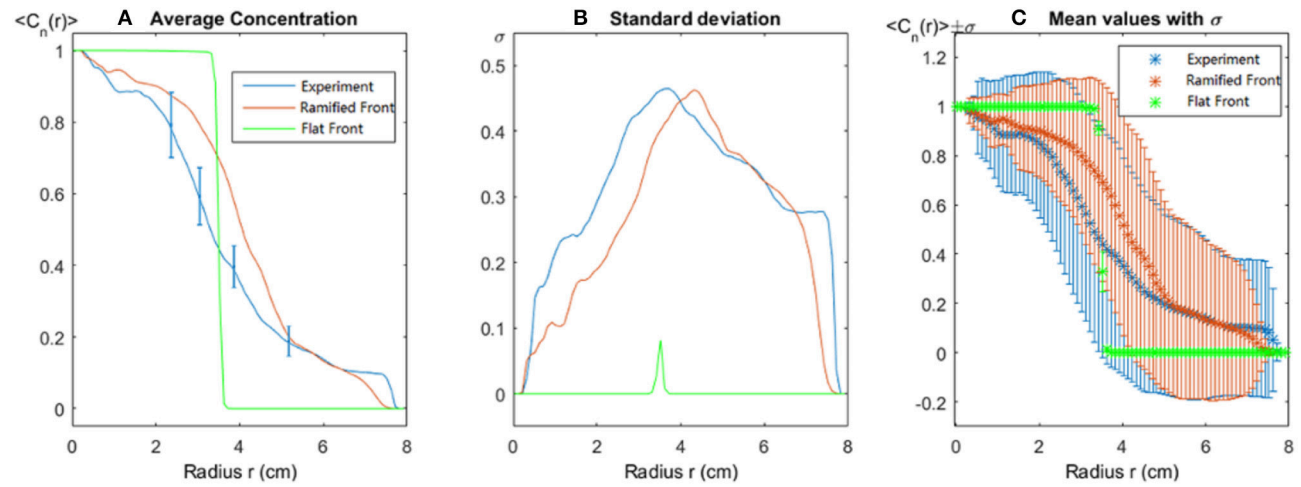

FIGURE 8 | Spatial dependence of structure as function of the circle radius. **(A)** The normalized average concentration, the error bar comes from experimental measurement for fluid tracer concentration according to the calibration performed in Supplemental Data. **(B)** Its standard deviation and **(C)** mean values with error bars at one standard deviation. In all cases, the blue line is the experimental result, the red line corresponds to the simulation with an injection ramified front corresponding to the dissolution pattern present in this experiment, and the green line represents the simulation result with an internal flat (circular) front of similar area.

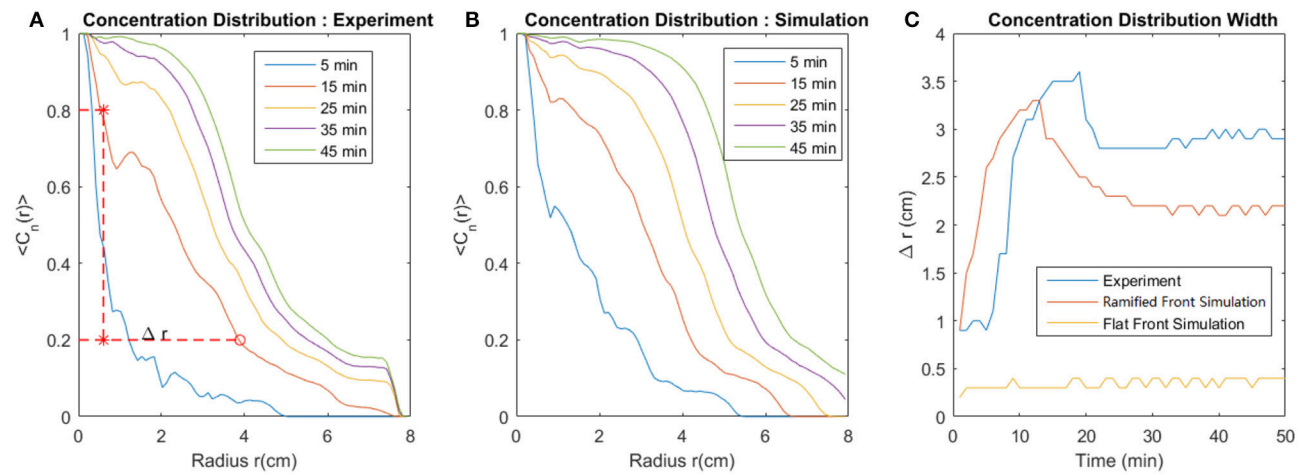

FIGURE 9 | Evolution of the average concentration distribution at different times. **(A)** Experimental data. **(B)** Simulation data. The red dotted line in **(A)** shows how we get the width of concentration distribution at 15 min ($\Delta r(t = 25min)$) which is the distance between the red circle (20% of reference concentration) and red asterisk (80% of reference concentration). **(C)** Displays the width of concentration distribution evolution with time, the blue line is the experimental result, the red line is the simulation with an injection ramified front identical to the dissolution pattern present in this experiment, and the yellow one is the simulation result with a flat circular front of similar area.

length l_C. The convection length is defined as the concentration profile convection length outside the circle of r_0, $l_C = \int udt$ so that

$$\frac{dl_c}{dt} = u(l_C) = \frac{Q}{2\pi l_C h}, \tag{9}$$

or $dl_c^2 = \frac{Q}{\pi h} dt$, which immediately gives

$$l_c = \sqrt{\frac{Qt}{\pi h}}. \tag{10}$$

Here the time t starts from t_D where t_D is the time it takes for molecular diffusion alone to homogenize the immediate neighborhood of the dissolved cluster. Now we take the maximum convection length l_{max} and the minimum convection length l_{min} into account, the maximum convection length l_{max} starts growing outside of the circle of r_0 while the minimum convection length l_{min} starts growing after t_D. So the ratio of these two convection lengths is:

$$\frac{l_{min}}{l_{max}} = \sqrt{\frac{t - t_D}{t}} = \sqrt{1 - \frac{t_D}{t}} \approx 1 - \frac{t_D}{2t} \tag{11}$$

The length difference of l_{max} and l_{min} is:

$$\begin{aligned} l_{max} - l_{min} &= \sqrt{\frac{Q}{\pi h}}(\sqrt{t} - \sqrt{t - t_D}) \\ &= \sqrt{\frac{Q}{\pi h}} \cdot \sqrt{t}(1 - (1 - \frac{t_D}{t})^{1/2}) \\ &\approx \sqrt{\frac{Q}{\pi h}} \cdot \frac{t_D}{2\sqrt{t}} \end{aligned} \tag{12}$$

From the calculations above, we conclude that the ratio between the maximum and the minimum convection length tends to 1 and the length difference between two decreases as $t^{-1/2}$ and tends to 0. It implies that the anisotropy of the concentration profiles will vanish after an enough long time. To see an isotropic behavior, a theoretical criterion for a length scale can be calculated from Equations (10, 11) requiring t_D/t less than a small number. For instance, $t_D/t < 0.1$ and $\sqrt{2D_m t_D} = d_D$ where d_D is a distance between dispersion fans that could be estimated from **Figure 3** as $d_D = 0.5\,cm$. Consequently, the length scale $l = \sqrt{10}\sqrt{\frac{Qt_D}{\pi h}} = \sqrt{\frac{5Q}{\pi D_m h}} \cdot d_D$ to see an isotropic behavior will be of the order of 1 m. These theoretical conclusions are also verified by the simulation results. The simulation is implemented with the same system of initial dissolution pattern but expanding by scale of 8 times so that we can observe the concentration profile after a long time, see **Figure 10**.

The convection lengths are obtained by calculation of the distance between the points at the boundary of the dispersion pattern and the center of the circular system from the simulation data. We analyze the maximum and minimum convection length evolution with time, the ratio and the difference between the two lengths. The results are shown in **Figure 11**.

From the simulation results shown in **Figure 12**, we make a log-log plot of the data curve and compare it with theoretical calculations. The convection length follows the relation $l_c \propto t^{1/2}$. The ratio of lengths tends to 1 and the difference between lengths has a decreasing trend. The fluctuations of the simulation data is because the boundary line of concentration profile is not a prefect line numerically and also the center is not a prefect point.

For the initial state which is close to the inlet with ramified dissolution pattern, the velocity field is not radial flow. For the late stage which is close to the finite edge of system, the boundary effect will influence the concentration profile close to the rim. The deviations between the simulation results and theoretical calculation under these two limiting conditions are expected as we observe in **Figure 12**.

Using a similar development, in the case of injection in a three dimensional porous medium from a ramified structure, without large scale correlations in the permeability, one expects at large scale, the flow velocity in a radial field $u(l_c) = Q/(4\pi l_c^2)$ and the convection length $l_c = (3Qt/(4\pi))^{1/3}$. A concentration field converging at large times to the point source solution, with a ratio of minimum convection length over the maximum one,

$$\frac{l_{min}}{l_{max}} = (\frac{t - t_D}{t})^{1/3} \approx 1 - \frac{t_D}{3t}, \tag{13}$$

and a difference

$$\begin{aligned} l_{max} - l_{min} &= (\frac{3Q}{4\pi})^{1/3} \cdot (t^{1/3} - (t - t_D)^{1/3}) \\ &= (\frac{3Q}{4\pi})^{1/3} \cdot t^{1/3} \cdot (1 - (1 - \frac{t_D}{t})^{1/3}) \\ &\approx (\frac{3Q}{4\pi})^{1/3} \cdot \frac{t_D}{3t^{2/3}}. \end{aligned} \tag{14}$$

In this 3D case, we predict that the anisotropic concentration patterns would eventually always go away, the maximum and minimum convection length ratio and difference would follow the power law as a function of t as shown in the calculation above.

6. CONCLUSION

We have performed experiments and computer simulations of dispersion in an open fracture with an initial state emerging from a ramified dissolution pattern. A fluorescent technique was used to measure the tracer concentration in a transparent Hele Shaw cell. We implemented a 2D simulation which in addition to convective motion can include both molecular diffusion and

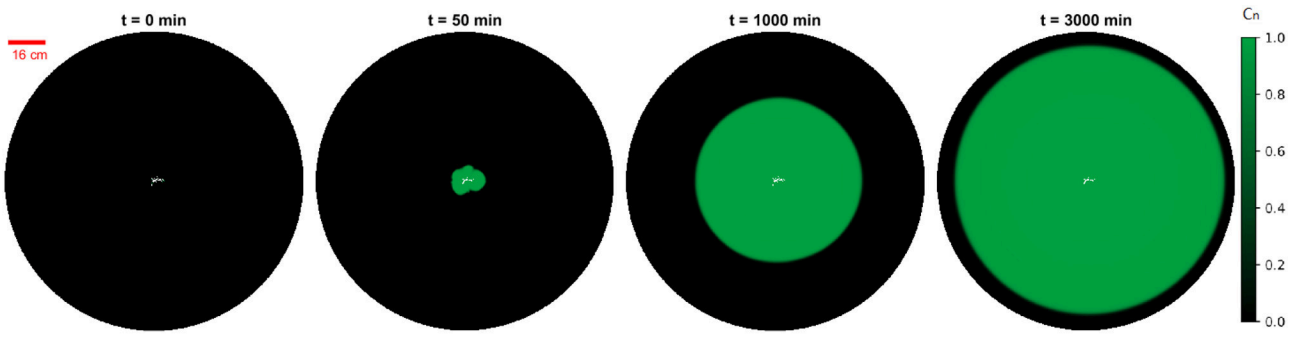

FIGURE 10 | Example of persistence of anisotropy at larger length scales. The simulation images are obtained from the molecular diffusion model, with the same dissolution pattern as before but the whole system is expanded by scale of 8 times. The green intensity represents the normalized tracer concentration C_n in the simulation. The images show the concentration profile after an injection lasting respectively 0/50/1, 000/3, 000 *min*. We observe that the anisotropy of the concentration profile vanishes gradually with time.

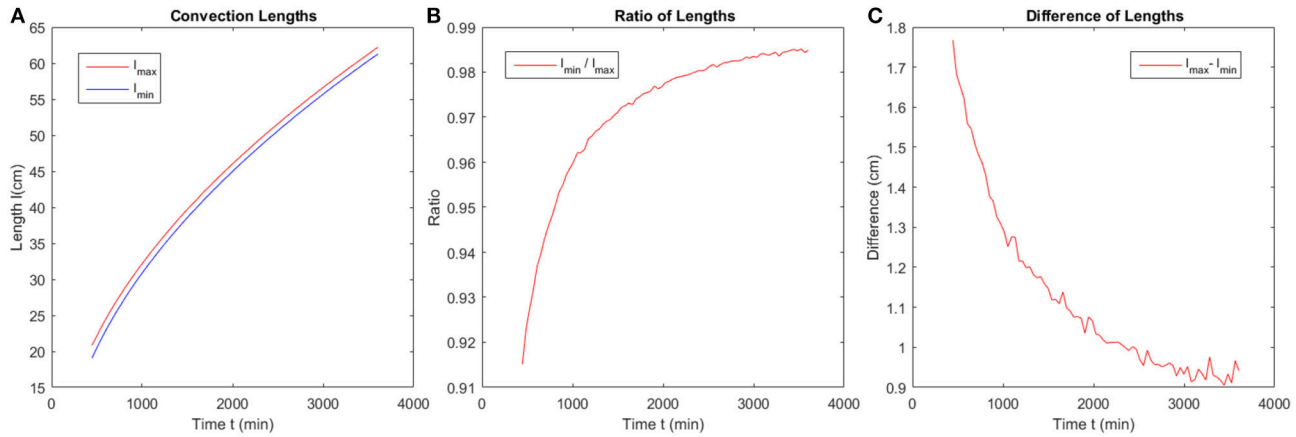

FIGURE 11 | Evolution of characteristic length scales in the system with time. **(A)** The maximum and minimum convection length evolution with time. **(B)** The ratio of the two lengths shown in **(A)**, which approaches unity at long times. **(C)** The difference of the two lengths shown in **(A)**, which approaches zero at long times.

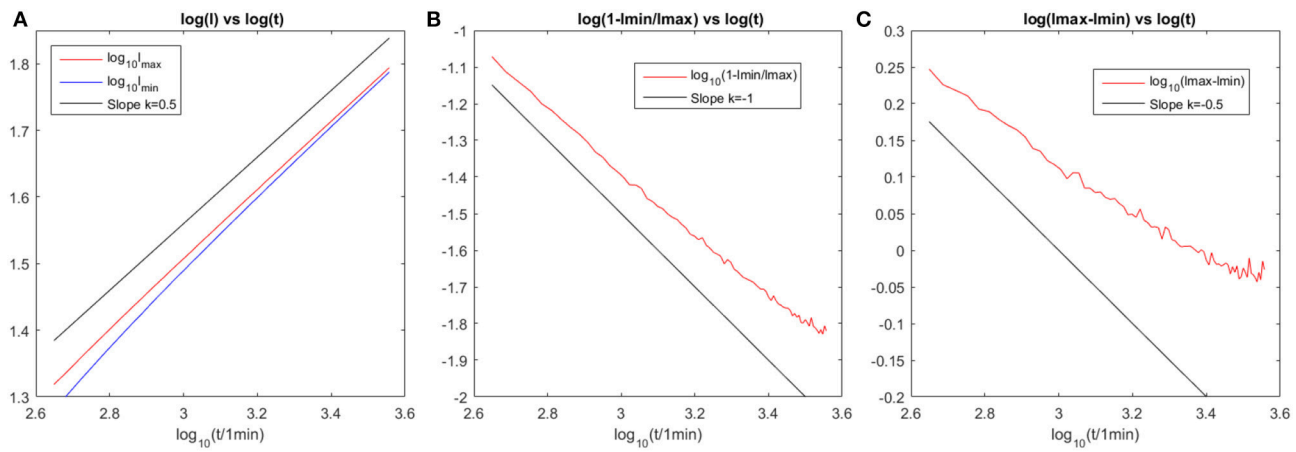

FIGURE 12 | Evolution of characteristic length scales in the system with time. The corresponding log-log plot for **Figure 11** is shown. **(A)** Logarithmic plot of the maximum and minimum convection length evolution with time, where the black line gives a reference slope of $k = 0.5$ which implies that the curves tend to follow the power law of $\sqrt{t}$. **(B)** One minus the ratio of the two lengths evolution with time follows the power law of $1/t$ with a reference slope $k = -1$. **(C)** The difference of the two lengths evolution with time follows the power law of $1/\sqrt{t}$ with a reference slope $k = -0.5$.

Taylor diffusion. For the investigated patterns, simulations with molecular diffusion and Taylor diffusion have no significant difference. The ramified dissolution structures have a significant effect on the local concentration $C_n(\mathbf{r})$ and the concentration averaged over angles $< C_n(\mathbf{r}) >$ both for small and large length and time scales. The shape of the concentration distributions far from the dissolution structure is discussed with some theoretical calculations. The convergence in open systems of structures injected from ramified patterns to the point-like (or circular) injection solution is not obvious: When molecular diffusion presents a skin depth $\sqrt{2Dt}$ exceeding largely the central zone size R_d, the concentration gradients in the central zone are expected to reduce, and the concentration field should be smoother there. Nonetheless, the strong anisotropy of the permeability in the central region leads to clear fingering outside this region. Whether the influence of these fingers is felt only up to a finite range is questionable, in particular in this radial geometry, since the center of the different emerging fingers diverges with time. We make some theoretical calculations and simulations to conclude that the anisotropy of the concentration distribution in the system will vanish at sufficiently large length and time scales. The experimental verification of isotropy of the tracer concentration at large scales is an interesting question for further experimental work. From the theoretical calculation and our simulation result we estimate that we need an experimental model of the order of $1m$ to reach this isotropy. At the expected 3D structure, we predict that the shape of concentration distribution far from the dissolution structure will eventually experience a slowly vanishing anisotropy, in future work it would certainly be nice to explore these 3D structures both experimentally and numerically to see how they correspond to these predictions.

AUTHOR CONTRIBUTIONS

LX and KM designed the experiment. LX performed the experiments, analyzed the data and authored the paper. BM conducted the simulations. EF contributed to the idea for the simulations and performed some theoretical calculations together with RT and KM. RT, EF, and KM assisted with the interpretation and data analysis, and editing of the manuscript.

ACKNOWLEDGMENTS

This project has received funding from the European Union's Seventh Framework Programme for research, technological development and demonstration under grant agreement no 316889. We acknowledge the support of the University of Oslo and the support by the Research Council of Norway through its Centres of Excellence funding scheme, project number 262644, and the INSU ALEAS program. We thank Mihailo Jankov for technical support and Marcel Moura, Fredrik K. Eriksen, Monem Ayaz, and Guillaume Dumazer for useful discussions.

SUPPLEMENTARY MATERIAL

The Supplementary Material for this article can be found online at: https://www.frontiersin.org/articles/10.3389/fphy.2018.00029/full#supplementary-material

REFERENCES

1. Taylor G. Dispersion of soluble matter in solvent flowing slowly through a tube. *Proc R Soc Lond A Math Phys Eng Sci.* (1953) **219**:186–203. doi: 10.1098/rspa.1953.0139
2. Tang D, Frind E, Sudicky EA. Contaminant transport in fractured porous media: analytical solution for a single fracture. *Water Resour Res.* (1981) **17**:555–64. doi: 10.1029/WR017i003p00555
3. Sudicky E, Frind E. Contaminant transport in fractured porous media: analytical solutions for a system of parallel fractures. *Water Resour Res.* (1982) **18**:1634–42. doi: 10.1029/WR018i006p01634
4. Boschan A, Auradou H, Ippolito I, Chertcoff R, Hulin JP. Miscible displacement fronts of shear thinning fluids inside rough fractures. *Water Resour Res.* (2007) **43**:W03438. doi: 10.1029/2006WR005324
5. Sané J, Padding JT, Louis AA. Taylor dispersion of colloidal particles in narrow channels. *Mol Phys.* (2015) **113**:2538–45. doi: 10.1080/00268976.2015.1035768
6. Måloy KJ, Feder J, Boger F, Jossang T. Fractal structure of hydrodynamic dispersion in porous media. *Phys Rev Lett.* (1988) **61**:2925. doi: 10.1103/PhysRevLett.61.2925
7. Ippolito I, Hinch E, Daccord G, Hulin J. Tracer dispersion in 2-d fractures with flat and rough walls in a radial flow geometry. *Phys Fluids A Fluid Dyn.* (1993) **5**:1952–62. doi: 10.1063/1.858822
8. Alencar AM, Andrade JS, Lucena LS. Self-organized percolation. *Phys Rev E* (1997) **56**:R2379. doi: 10.1103/PhysRevE.56.R2379
9. Andrade JS Jr, Costa UMS, Almeida MP, Makse HA, Stanley HE. Inertial effects on fluid flow through disordered porous media. *Phys Rev Lett.* (1999) **82**:5249. doi: 10.1103/PhysRevLett.82.5249
10. Parteli EJR, da Silva LR, Andrade JS Jr. Self-organized percolation in multi-layered structures. *J Stat Mech Theory Exp.* (2010) **2010**:P03026. doi: 10.1088/1742-5468/2010/03/p03026
11. Bodin J, Delay F, De Marsily G. Solute transport in a single fracture with negligible matrix permeability: 1. Fundamental mechanisms. *Hydrogeol J.* (2003) **11**:418–33. doi: 10.1007/s10040-003-0268-2
12. Qian J, Zhan H, Zhao W, Sun F. Experimental study of turbulent unconfined groundwater flow in a single fracture. *J Hydrol.* (2005) **311**:134–42. doi: 10.1016/j.jhydrol.2005.01.013
13. Koyama T, Neretnieks I, Jing L. A numerical study on differences in using navier–stokes and reynolds equations for modeling the fluid flow and particle transport in single rock fractures with shear. *Int J Rock Mech Mining Sci.* (2008) **45**:1082–101. doi: 10.1016/j.ijrmms.2007.11.006
14. Bauget F, Fourar M. Non-fickian dispersion in a single fracture. *J Cont Hydrol.* (2008) **100**:137–48. doi: 10.1016/j.jconhyd.2008.06.005
15. Rastiello G, Boulay C, Dal Pont S, Tailhan JL, Rossi P. Real-time water permeability evolution of a localized crack in concrete under loading. *Cement Concrete Res.* (2014) **56**:20–8. doi: 10.1016/j.cemconres.2013.09.010
16. Daccord G, Lenormand R. Fractal patterns from chemical dissolution. *Nature* (1987) **325**:41–3. doi: 10.1038/325041a0
17. Fredd CN, Fogler HS. Influence of transport and reaction on wormhole formation in porous media. *AIChE J.* (1998) **44**:1933–49. doi: 10.1002/aic.690440902
18. Szymczak P, Ladd AJC. Instabilities in the dissolution of a porous matrix. *Geophys Res Lett.* (2011) **38**:L07403. doi: 10.1029/2011GL046720
19. Powers TC. *The Properties of Fresh Concrete*. New York, NY: John Wiley & Sons. (1969).
20. Szymczak P, Ladd AJC. Wormhole formation in dissolving fractures. *J Geophys Res Solid Earth* (2009) **114**:B0620. doi: 10.1029/2008JB006122
21. Daccord G. Chemical dissolution of a porous medium by a reactive fluid. *Phys Rev Lett.* (1987) **58**:479. doi: 10.1103/PhysRevLett.58.479
22. Wang H, Bernabé Y, Mok U, Evans B. Localized reactive flow in carbonate rocks: core-flood experiments and network simulations. *J Geophys Res Solid Earth* (2016) **121**:7965–83. doi: 10.1002/2016JB013304
23. Culbertson CT, Jacobson SC, Ramsey JM. Diffusion coefficient measurements in microfluidic devices. *Talanta* (2002) **56**:365–73. doi: 10.1016/S0039-9140(01)00602-6
24. Walker D. A fluorescence technique for measurement of concentration in mixing liquids. *J Phys E Sci Instrum.* (1987) **20**:217. doi: 10.1088/0022-3735/20/2/019
25. Aris R. On the dispersion of a solute in a fluid flowing through a tube. *Proc R Soc Lond A Math Phys Eng Sci.* (1956) **235**:67–77.
26. Boschan A, Charette V, Gabbanelli S, Ippolito I, Chertcoff R. Tracer dispersion of non-newtonian fluids in a hele–shaw cell. *Phys A Stat Mech Appl.* (2003) **327**:49–53. doi: 10.1016/S0378-4371(03)00437-0
27. Kurganov A, Tadmor E. New high-resolution central schemes for nonlinear conservation laws and convection–diffusion equations. *J Comput Phys.* (2000) **160**:241–82. doi: 10.1006/jcph.2000.6459
28. Måløy KJ, Feder J, Jøssang T. Viscous fingering fractals in porous media. *Phys Rev Lett.* (1985) **55**:2688. doi: 10.1103/PhysRevLett.55.2688
29. Witten TA, Sander LM. Diffusion-limited aggregation. *Phys Rev B* (1983) **27**:5686. doi: 10.1103/PhysRevB.27.5686
30. Barabási AL, Stanley HE. *Fractal Concepts in Surface Growth*. Cambridge: University Press (1995).
31. Feder J. *Fractals*. Springer Science & Business Media (2013). doi: 10.1007/978-1-4899-2124-6
32. Eriksen FK, Toussaint R, Måløy KJ, Flekkøy EG. Invasion patterns during two-phase flow in deformable porous media. *Front Phys.* (2015) **3**:81. doi: 10.3389/fphy.2015.00081

Conflict of Interest Statement: The authors declare that the research was conducted in the absence of any commercial or financial relationships that could be construed as a potential conflict of interest.

frontiers in Physics

ORIGINAL RESEARCH
published: 13 June 2018
doi: 10.3389/fphy.2018.00056

Stable and Efficient Time Integration of a Dynamic Pore Network Model for Two-Phase Flow in Porous Media

Magnus Aa. Gjennestad[1]*, *Morten Vassvik*[1], *Signe Kjelstrup*[2] and *Alex Hansen*[1]

[1] PoreLab, Department of Physics, Norwegian University of Science and Technology, Trondheim, Norway, [2] PoreLab, Department of Chemistry, Norwegian University of Science and Technology, Trondheim, Norway

We study three different time integration methods for a dynamic pore network model for immiscible two-phase flow in porous media. Considered are two explicit methods, the forward Euler and midpoint methods, and a new semi-implicit method developed herein. The explicit methods are known to suffer from numerical instabilities at low capillary numbers. A new time-step criterion is suggested in order to stabilize them. Numerical experiments, including a Haines jump case, are performed and these demonstrate that stabilization is achieved. Further, the results from the Haines jump case are consistent with experimental observations. A performance analysis reveals that the semi-implicit method is able to perform stable simulations with much less computational effort than the explicit methods at low capillary numbers. The relative benefit of using the semi-implicit method increases with decreasing capillary number Ca, and at Ca $\sim 10^{-8}$ the computational time needed is reduced by three orders of magnitude. This increased efficiency enables simulations in the low-capillary number regime that are unfeasible with explicit methods and the range of capillary numbers for which the pore network model is a tractable modeling alternative is thus greatly extended by the semi-implicit method.

Keywords: porous media, two-phase flow, pore network model, numerical methods, time integration, stability, low capillary number

OPEN ACCESS

Edited by:
Romain Teyssier,
Universität Zürich, Switzerland

Reviewed by:
Daniele Chiappini,
Università degli Studi Niccolò Cusano, Italy
Christian F. Klingenberg,
Universität Würzburg, Germany

***Correspondence:**
Magnus Aa. Gjennestad
magnus@aashammer.net

Specialty section:
This article was submitted to Computational Physics, a section of the journal Frontiers in Physics

Received: *19 January 2018*
Accepted: *17 May 2018*
Published: *13 June 2018*

Citation:
Gjennestad MA, Vassvik M, Kjelstrup S and Hansen A (2018) Stable and Efficient Time Integration of a Dynamic Pore Network Model for Two-Phase Flow in Porous Media. Front. Phys. 6:56. doi: 10.3389/fphy.2018.00056

1. INTRODUCTION

Different modeling approaches have been applied in order to increase understanding of immiscible two-phase flow in porous media. On the pore scale, direct numerical simulation approaches using e.g. the volume of fluid method [1] or the level-set method [2, 3] to keep track of the fluid interface locations, have been used. The lattice-Boltzmann method is another popular choice, see e.g. Ramstad et al. [4]. These methods can provide detailed information on the flow in each pore. They are, however, computationally intensive and this restricts their use to relatively small systems.

Pore network models have proven to be useful in order to reduce the computational cost [5], or enable the study of larger systems, while still retaining some pore-level detail. In these models, the pore space is partitioned into volume elements that are typically the size of a single pore or throat. The average flow properties in these elements are then considered, without taking into account the variation in flow properties within each element.

Pore network models are typically classified as either quasi-static or dynamic. The quasi-static models are intended for situations where flow rates are low, and viscous pressure drops are

neglected on the grounds that capillary forces are assumed to dominate at all times. In the quasi-static models by Lenormand et al. [6], Willemsen [7], and Blunt [8], the displacement of one fluid by the other proceeds by the filling of one pore at the time, and the sequence of pore filling is determined by the capillary entry pressure alone.

The dynamic models, on the other hand, account for the viscous pressure drops and thus capture the interaction between viscous and capillary forces. As three examples of such models, we mention those by Hammond and Unsal [5], Joekar-Niasar et al. [9], and Aker et al. [10]. A thorough review of dynamic pore network models was performed by Joekar-Niasar and Hassanizadeh [11].

The pore network model we consider here is of the dynamic type that was first presented by Aker et al. [10]. Since the first model was introduced, it has been improved upon several times. Notably, it was extended to include film and corner flow by Tørå et al. [12]. The model considered here does not contain this extension. This class of models, which we call the Aker-type models, is different from the majority of other pore network models [5, 9] in that both the pore body and pore throat volumes are assigned to the links, and no volume is assigned to the nodes. Fluid interface locations are tracked explicitly as they move continuously through the pore space. This is in contrast to the model by Hammond and Unsal [5], where interfaces are moved through whole volume elements at each time step, and to the model of Joekar-Niasar et al. [9], where interface locations are only implicitly available through the volume element saturation. One of the advantages of the Aker-type model is that a detailed picture of the fluid configuration is provided at any time during a simulation. Dynamic phenomena, such as the retraction of the invasion front after a Haines jump [13–16], are thus easily resolved.

Since 1985, numerical instabilities at low capillary numbers have been known to occur for various types of dynamic pore network models [17]. A whole section is devoted to the topic in the review by Joekar-Niasar and Hassanizadeh [11]. It is important to address such stability problems rigorously, as many of the practical applications of two-phase porous media flow are in the low capillary number regime. Examples include most parts of the reservoir rock during CO_2 sequestration, flow of liquid water in fuel cell gas diffusion layers and studies of Haines jump dynamics, see e.g. Armstrong and Berg [15].

When Aker-type pore network models are used, the numerical instabilities are observed as oscillations in the positions of the fluid interfaces. Some efforts to avoid these oscillations have been made by introduction of modifications to the model. Medici and Allen [18] used a scheme where water was allowed to flow in the forward direction only in order to study water invasion in fuel cell gas diffusion layers. While this approach led to interesting results, it has some downsides. First, the interface movement is artificially restricted, and certain dynamic effects can not be resolved. This includes e.g. invasion front retraction after a Haines jump. Second, the method can only be used in cases with transient invasion. Studies of steady-state flow, such as those performed by Knudsen et al. [21] and Savani et al. [19], are not possible.

Because the oscillations originate in the numerical methods, rigorous attempts to remove them should focus on these methods rather than the models themselves. Joekar-Niasar et al. [9] followed this avenue and achieved stabilization using a linearized semi-implicit method. Their work, however, concerned a different type of pore network model than that considered here.

In this work, we present three numerical methods that can be utilized to perform stable simulations of two-phase flow in porous media with pore network models of the Aker type. The stability problems previously observed are thus solved without the need to resort to model modifications that restrict interface movement or preclude steady-state flow simulations. Two explicit methods are discussed, the forward Euler method and the midpoint method. These are stabilized by a new time step criterion derived herein. The third method is a new semi-implicit method. Thorough verifications of all methods are performed, confirming correct convergence properties and stability. Finally, we compare the methods in terms of performance.

The rest of this paper is structured as follows. Section 2 contains background information on the pore network model. Section 3 presents briefly the nomenclature, used in subsequent sections to describe the time integration methods. In section 4, we recapitulate how the forward Euler method is used to integrate the model and we present a new time step criterion that stabilizes both forward Euler and the midpoint method at low capillary numbers. We briefly review the midpoint method in section 5. The new semi-implicit method is described in detail in section 6. Some remarks about the numerical implementation are made in section 7. Section 8 contains a description of the cases simulated. Numerical experiments, including a Haines jump case, that show convergence and stability are given in section 9 and a comparison of the method performances are made in section 10. Section 11 summarizes and concludes the paper.

2. PORE NETWORK MODEL

We consider incompressible flow of two immiscible fluids in a porous medium, where one fluid is more wetting toward the pore walls than the other. We call the less wetting fluid non-wetting (n) and the more wetting fluid we call wetting (w). The porous medium is represented in the model by a network of N nodes connected by M links. Each node is given an index $i \in [0, N-1]$, and each link is identified by the indices of the two nodes it connects. An example pore network is shown in **Figure 1**. The nodes are points that have no volume and, consequently, all fluid is contained in the links. The links therefore represent both the pore and the throat volumes of the physical porous medium. In this respect, the pore network model studied here differ from most other pore network models [11]. Each fluid is assumed to fill

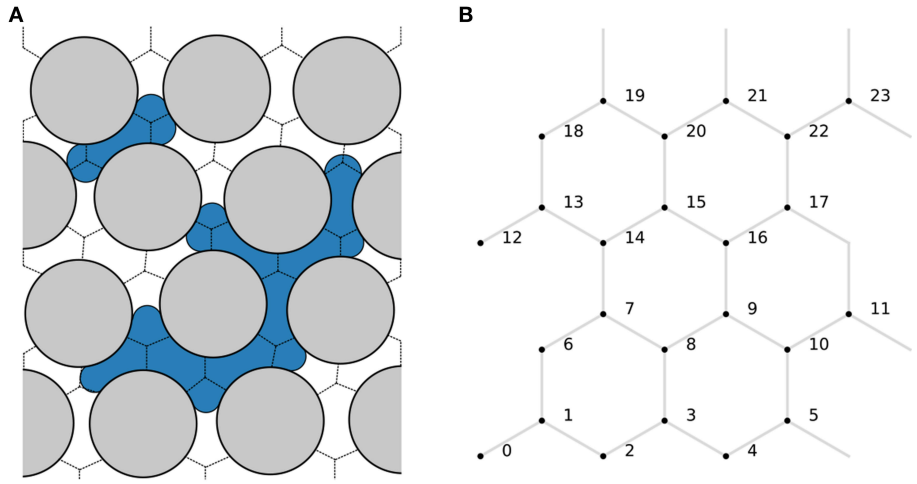

FIGURE 1 | Illustration of **(A)** a physical pore network with wetting (white) and non-wetting fluid (blue) and **(B)** its representation in the pore network model. The void space volumes separated by dashed lines in **(A)** are each represented as one link in **(B)**. The node points in the model representation **(B)** is assumed to be located at the intersection points of the dashed lines in **(A)**. Each fluid is assumed to fill the entire link cross section. The interface positions are therefore each represented in the model by a single number, giving its location along the link length.

the entire link cross section. The interface positions are therefore each represented in the model by a single number, giving its location along the link length.

The flow in each link is treated in a one-dimensional manner, where the flow is averaged over the link cross section. As we consider flow in relatively small cross sections only, we neglect any inertial effects and the volume flow rate ($m^3\ s^{-1}$) from node j to node i through the link connecting then is given by Washburn [20]

$$q_{ij} = -g_{ij}\left(\mathbf{z}_{ij}\right)\left\{p_i - p_j - c_{ij}\left(\mathbf{z}_{ij}\right)\right\}. \tag{1}$$

Herein, p_i (Pa) is the pressure in node i, g_{ij} ($m^3\ s^{-1}\ Pa^{-1}$) is the link mobility, c_{ij} (Pa) is the link capillary pressure and $\mathbf{z}_{ij}$ (m) is a vector containing the positions of any fluid interfaces present in the link. Both the link mobility and the capillary pressure depend on the fluid interface positions in the link. If two nodes i and j are *not* connected by a link, then $g_{ij} = 0$. Due to mass conservation, the net flow rate into every node i is zero

$$\sum_j q_{ij} = 0. \tag{2}$$

While the mobilities are symmetric with respect to permutation of the indices, the capillary pressures are anti-symmetric,

$$g_{ij} = g_{ji}, \tag{3}$$
$$c_{ij} = -c_{ji}. \tag{4}$$

Introducing this into Equation (1), we obtain the immediately intuitive result

$$q_{ij} = -q_{ji}. \tag{5}$$

The cross-sectional area of link ij is denoted a_{ij} (m^2). Interface positions are advected with the flow according to

$$\frac{\mathrm{d}}{\mathrm{d}t}\mathbf{z}_{ij} = \frac{q_{ij}}{a_{ij}}, \tag{6}$$

when they are sufficiently far away from the nodes. Near the nodes, however, the interfaces are subject to additional modeling to account for interface interactions in the pores. This is discussed further in section 2.3.

The form of the expressions for the mobilities and capillary pressures depends on the shape of the links, and many different choices and modeling approaches are possible. Here, we will use models similar to those previously presented and used by e.g. Knudsen et al. [21] and Aker et al. [10]. However, the treated time integration methods are more general and can be applied to other models as well.

2.1. Link Mobility Model

We apply a cylindrical link model when computing the mobilities, so that

$$g_{ij}(\mathbf{z}_{ij}) = \frac{\pi r_{ij}^4}{8 L_{ij}\mu_{ij}\left(\mathbf{z}_{ij}\right)}. \tag{7}$$

Here, r_{ij} (m) is the link radius and L_{ij} (m) is the link length. The viscosity μ_{ij} (Pa s) is the volume-weighted average of the fluid viscosities and can be computed from the wetting and non-wetting fluid viscosities μ_w and μ_n and the wetting fluid saturation s_{ij},

$$\mu_{ij}\left(\mathbf{z}_{ij}\right) = \mu_w s_{ij}\left(\mathbf{z}_{ij}\right) + \mu_n\left\{1 - s_{ij}\left(\mathbf{z}_{ij}\right)\right\}. \tag{8}$$

2.2. Capillary Pressure Model

In each link ij, there may be zero, one or more interfaces present. These are located at the positions specified in $\mathbf{z}_{ij}$. As the interfaces may be curved, there may be a discontinuity in pressure at these interface locations. The capillary pressure c_{ij} is the sum of interfacial pressure discontinuities in the link ij. When computing the capillary pressures, we assume that the links are wide near each end, and therefore that interfaces located near a link end have negligible curvature and no pressure discontinuity, while the links have narrow throats in the middle. The link capillary pressures are thus modeled as

$$c_{ij}\left(\mathbf{z}_{ij}\right) = \frac{2\sigma_{\mathrm{wn}}}{r_{ij}} \sum_{z \in \mathbf{z}_{ij}} (\pm 1) \left\{1 - \cos\left(2\pi\, \chi_{ij}\left(z\right)\right)\right\}. \tag{9}$$

The interfacial tension between the fluids is denoted σ_{wn} (N m^{-1}) and

$$\chi_{ij}\left(z\right) = \begin{cases} 0 & z < \alpha r_{ij}, \\ \frac{z - \alpha r_{ij}}{L_{ij} - 2\alpha r_{ij}} & \alpha r_{ij} < z < L_{ij} - \alpha r_{ij}, \\ 1 & z > L_{ij} - \alpha r_{ij}. \end{cases} \tag{10}$$

The χ_{ij}-function ensures zones of length αr_{ij} at both ends of each link with zero capillary pressure across any interface located there. Choosing $\alpha = 0$ is equivalent to replacing χ_{ij} with z/L_{ij} in (9).

2.3. Fluid Interface Interaction Models

The equations discussed so far in this section describe how the fluids and the fluid interfaces move through the links. In addition, we rely on models for how they behave close to the nodes. The purpose of these are to emulate interface interactions in the pore spaces.

The following is assumed about the fluid behavior near the nodes and is accounted for by the fluid interface interaction models.

- The mass of each fluid is conserved at every node. This means that at all times, all wetting and non-wetting fluid flowing into a node from one subset of its neighboring links must flow out into another disjoint subset of its neighboring links.
- The network nodes in the model have no volume. However, due to the finite size of the physical pore void spaces, wetting fluid flowing into a pore space must be able to flow freely past any non-wetting fluid occupying the node point if the non-wetting fluid does not extend far enough into the pore void space cut the wetting fluid off. An example is illustrated in **Figure 2**. We consider a link ij to be cut off from free outflow of wetting fluid if the non-wetting fluid continuously extends a length at least αr_{ij} into the link. Non-wetting fluid may freely flow past wetting fluid, or not, the same manner.
- In each link ij, interfacial tension will prevent droplets with length smaller than αr_{ij} from forming by separation from larger droplets. An example is illustrated in **Figure 3**.

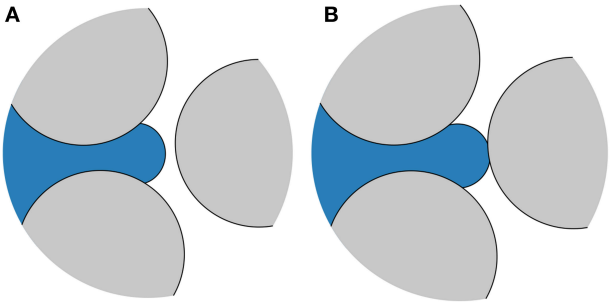

FIGURE 2 | Network node connected to three links. The node point, located near the middle of the pore space, is occupied by non-wetting fluid (blue). **(A)** The non-wetting fluid extends only a short distance into the links containing wetting fluid (white). The wetting fluid therefore remains connected and may flow freely through the pore space. **(B)** Non-wetting fluid protrudes far enough into all links to block the pore space for wetting fluid. The wetting fluid must now displace the non-wetting fluid in order to flow through.

2.4. Boundary Conditions

We consider only networks where the nodes and links can be laid out in the two-dimensional x-y plane. These networks will be periodic in both the x- and y-direction. However, the model is also applicable to networks that extend in three dimensions [22], and the presented numerical methods are also compatible both with networks in three dimensions and with other, non-periodic boundary conditions [23].

We will here apply two types of boundary conditions to the flow. With the first type, a specified pressure difference ΔP (Pa) will be applied across the network in the y-direction. This pressure difference will be equal to the sum of all link pressure differences in any path spanning the network once in the y-direction, ending up in the same node as it started. With the other type of boundary condition, we specify a total flow rate Q (m^3 s^{-1}) across the network. This flow rate will be equal to the sum of link flow rates flowing through any plane drawn through the network normal to the y-axis.

3. TEMPORAL DISCRETIZATION

In the following three sections, we describe the different time integration methods considered. These methods are applied to Equation (6), where evaluation of the right hand side involves simultaneously solving the mass conservation equation (2) and the constitutive equation (1) to obtain all unknown link flow rates and node pressures.

The discretized times (s) are denoted with a superscript where n is the time step number,

$$t^{(n)} = t^{(0)} + \sum_{i=0}^{n-1} \Delta t^{(i)}. \tag{11}$$

The time step $\Delta t^{(i)}$ is the difference between $t^{(i+1)}$ and $t^{(i)}$ and the time $t^{(0)}$ is the initial time in a simulation. Similarly,

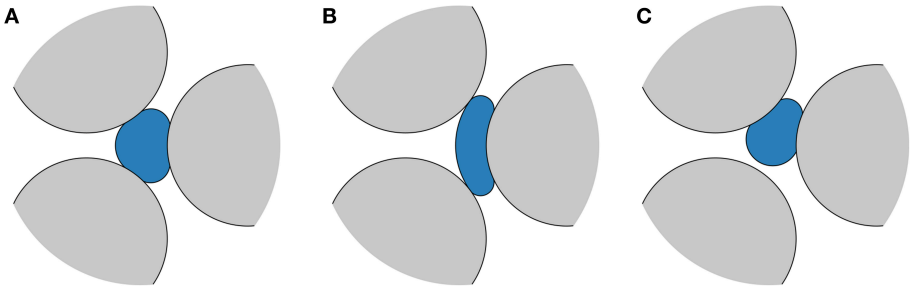

FIGURE 3 | (A) Small non-wetting bubble (blue) whose volume is small compared to the link volumes and is prevented from splitting by interfacial tension. This limits the minimum size of non-wetting bubbles, which will either **(B)** be stuck or **(C)** move through one of the links without splitting.

quantities evaluated at the discrete times are denoted with time step superscripts, e.g.

$$q_{ij}^{(n)} = q_{ij}\left(t^{(n)}\right). \tag{12}$$

Mobilities and capillary pressures with superscripts are evaluated using the interface positions at the indicated time step,

$$g_{ij}^{(n)} = g_{ij}\left(\mathbf{z}_{ij}^{(n)}\right), \tag{13}$$

$$c_{ij}^{(n)} = c_{ij}\left(\mathbf{z}_{ij}^{(n)}\right). \tag{14}$$

4. FORWARD EULER METHOD

The forward Euler method is the simplest of the time integration methods considered here and is the one used most frequently in previous works, see e.g. Knudsen et al. [21] and Sinha and Hansen [24]. We include its description here for completeness and to provide context for the proposed new capillary time step criterion that is introduced to stabilize the method at low capillary numbers.

The ordinary differential equation (ODE) (6) is discretized in a straightforward manner for each link ij using forward Euler,

$$\mathbf{z}_{ij}^{(n+1)} = \mathbf{z}_{ij}^{(n)} + \Delta t^{(n)} \frac{q_{ij}^{(n)}}{a_{ij}}. \tag{15}$$

The flow rates are calculated by inserting Equation (1), evaluated with the current known interface positions,

$$q_{ij}^{(n)} = -g_{ij}^{(n)}\left\{p_i^{(n)} - p_j^{(n)} - c_{ij}^{(n)}\right\}, \tag{16}$$

into the mass conservation equation (2). This results in the a system of linear equations consisting of one equation,

$$\sum_j g_{ij}^{(n)} p_j^{(n)} - p_i^{(n)} \sum_j g_{ij}^{(n)} = -\sum_j g_{ij}^{(n)} c_{ij}^{(n)}, \tag{17}$$

for each node i with unknown pressure. This linear system can be cast into matrix form,

$$\mathbf{A} \cdot \mathbf{x} = \mathbf{b}, \tag{18}$$

where the vector $\mathbf{x}$ contains the unknown node pressures, e.g.

$$\mathbf{x} = \begin{bmatrix} p_0^{(n)} \\ p_1^{(n)} \\ \vdots \\ p_{N-1}^{(n)} \end{bmatrix}. \tag{19}$$

The matrix elements are

$$A_{ij} = \left\{1 - \delta_{ij}\right\} g_{ij}^{(n)} - \delta_{ij} \sum_k g_{ik}^{(n)}, \tag{20}$$

and the elements of the constant vector are

$$b_i = -\sum_k g_{ik}^{(n)} c_{ik}^{(n)}. \tag{21}$$

The node pressures are obtained by solving this linear equation system. The flow rates are subsequently evaluated using Equation (16) and the interface positions are then updated using Equation (15) and the interface interaction models.

4.1. Time Step Restrictions

In previous works [10, 21], the time step length was chosen from a purely advective criterion,

$$\Delta t_{\mathrm{a}}^{(n)} = C_{\mathrm{a}} \min_{ij}\left(\frac{a_{ij} L_{ij}}{q_{ij}^{(n)}}\right). \tag{22}$$

The parameter C_{a} corresponds to the maximum fraction of a link length any fluid interface is allowed to move in a single forward Euler time step. The value of C_{a} must be chosen based on the level of accuracy desired from the simulation.

However, selecting the time step based on the advective criterion only, often results in numerical instabilities at low capillary numbers, where viscous forces are small relative to the capillary forces. This is demonstrated in section 9.2. The origins of the numerical instabilities can be identified by performing analysis on a linearized version of the governing equations. This is done in Appendix A. This analysis also leads to a new time step criterion, whereby the time step length is restricted by the

sensitivity of the capillary forces to perturbations in the current interface positions,

$$\Delta t_{\mathrm{c}}^{(n)} = C_{\mathrm{c}} \min_{ij} \left(\frac{2a_{ij}}{g_{ij}^{(n)} \left| \sum_{z \in \mathbf{z}_{ij}^{(n)}} \frac{\partial c_{ij}}{\partial z} \right|} \right). \tag{23}$$

For the particular choice of capillary pressure model given by (9), we obtain

$$\Delta t_{\mathrm{c}}^{(n)} = C_{\mathrm{c}} \min_{ij} \left(\frac{a_{ij} r_{ij} L_{ij}}{2\pi g_{ij}^{(n)} \sigma_{\mathrm{wn}} \left| \sum_{z \in \mathbf{z}_{ij}^{(n)}} (\pm 1) \sin\left(2\pi \chi_{ij}(z)\right) \frac{\mathrm{d}\chi_{ij}}{\mathrm{d}z} \right|} \right). \tag{24}$$

According to the linear analysis, numerical instabilities are avoided if the parameter C_{c} is chosen such that $0 < C_{\mathrm{c}} < 1$. However, we must regard (23) as an approximation when we apply it to the full non-linear model in simulations and, consequently, we may have to chose C_{c} conservatively to ensure stability for all cases.

At each step in the simulation, the time step used is then taken as

$$\Delta t^{(n)} = \min\left(\Delta t_{\mathrm{c}}^{(n)}, \Delta t_{\mathrm{a}}^{(n)}\right), \tag{25}$$

to comply with both the advective and the capillary time step criteria. The capillary time step restriction (23) is independent of flow rate. It therefore becomes quite severe, demanding relatively fine time steps, when flow rates are low.

4.2. Boundary Conditions

The periodic boundary conditions, specifying a total pressure difference ΔP across the network, can be incorporated directly into the linear equation system (18). For each node i, a term $g_{ij}^{(n)} \Delta P$ is added to or subtracted from b_i for any link ij that crosses the periodic boundary.

With the specified ΔP condition implemented, we can use it to obtain the node pressures and link flow rates corresponding to a specified total flow rate Q. Due to the linear nature of the model, the total flow rate is linear in ΔP [10], so that

$$Q = C_1 \Delta P + C_2, \tag{26}$$

for some unknown coefficients C_1 and C_2, that are particular to the current fluid configuration.

We choose two different, but otherwise arbitrary, pressure drop values ΔP_1 and ΔP_2 and, using the above procedure, we solve the network model once for each pressure difference and calculate the corresponding total flow rates Q_1 and Q_2. The coefficients C_1 and C_2 are then determined by,

$$C_1 = \frac{Q_2 - Q_1}{\Delta P_2 - \Delta P_1}, \tag{27}$$

$$C_2 = \frac{Q_2 \Delta P_1 - Q_1 \Delta P_2}{\Delta P_1 - \Delta P_2}. \tag{28}$$

The pressure difference ΔP required to obtain the specified flow rate Q is determined by solving Equation (26) for ΔP. Subsequently, the network model is solved a third time with pressure drop ΔP to obtain the desired node pressures and link flow rates.

5. MIDPOINT METHOD

The forward Euler method is first-order accurate in time. To obtain smaller numerical errors, methods of higher order are desirable. We therefore include in our discussion the second-order midpoint method. This method is identical to that used by Aker et al. [10], except with respect to choice of time step length.

The ODE (6) is discretized as

$$\mathbf{z}_{ij}^{(n+1)} = \mathbf{z}_{ij}^{(n)} + \Delta t^{(n)} \frac{q_{ij}^{(n+1/2)}}{a_{ij}}, \tag{29}$$

where $q_{ij}^{(n+1/2)}$ is the flow rate at the midpoint in time between point n and $n+1$. This flow rate is calculated in the same manner as described in section 4. The interface positions at $n + 1/2$ are obtained by taking a forward Euler step with half the length of the whole time step,

$$\mathbf{z}_{ij}^{(n+1/2)} = \mathbf{z}_{ij}^{(n)} + \frac{1}{2} \Delta t^{(n)} \frac{q_{ij}^{(n)}}{a_{ij}}. \tag{30}$$

5.1. Time Step Restrictions

Since the forward Euler stability region is contained within the stability region for the midpoint method, we use the same time step restrictions for the midpoint method as for forward Euler, see section 4.1.

5.2. Boundary Conditions

Both the specified ΔP and the specified Q boundary conditions are incorporated into the midpoint method by applying the procedures described in section 4.2 for each evaluation of the right hand side of Equation (6).

6. SEMI-IMPLICIT METHOD

To avoid both the numerical instabilities and the time step restriction (23), which becomes quite severe at low flow rates, we here develop a new semi-implicit time stepping method. Simulation results indicate that this method is stable with time steps determined by the advective criterion (22) only, and much longer time steps are therefore possible than with the forward Euler and midpoint methods at low capillary numbers.

The ODE (6) is now discretized according to

$$\mathbf{z}_{ij}^{(n+1)} = \mathbf{z}_{ij}^{(n)} + \Delta t^{(n)} \frac{q_{ij}^{(n+1)}}{a_{ij}}. \tag{31}$$

The semi-implicit nature of this discretization comes from the flow rate used,

$$q_{ij}^{(n+1)} = -g_{ij}^{(n)} \left\{ p_i^{(n+1)} - p_j^{(n+1)} - c_{ij}^{(n+1)} \right\}. \tag{32}$$

Herein, the link mobility is evaluated at time step n, while the node pressures and the capillary pressure are evaluated time step $n+1$.

The link mobilities could of course also have been evaluated at time step $n+1$, thus creating a fully implicit backward Euler scheme. As is shown in Appendix A, we may expect backward Euler to be stable with any positive $\Delta t^{(n)}$. The backward Euler scheme may therefore seem like a natural choice for performing stable simulations with long time steps. However, to evaluate the mobilities at time step $n+1$ complicates the integration procedure and was found to be unnecessary in practice. A semi-implicit alternative is therefore preferred.

To obtain the node pressures, we solve the mass conservation equations,

$$F_i = \sum_k q_{ik}^{(n+1)} = 0. \tag{33}$$

Again, we have one equation for each node i with unknown pressure. However, because the capillary pressures now depend on the flow rates,

$$c_{ij}^{(n+1)} = c_{ij}\left(\mathbf{z}_{ij}^{(n)} + \Delta t^{(n)}\frac{q_{ij}^{(n+1)}}{a_{ij}}\right), \tag{34}$$

the mass conservation equations are now a system of non-linear equations, rather than a system of linear equations. This system can be cast in the form

$$\mathbf{F}(\mathbf{x}) = \mathbf{0}, \tag{35}$$

where $\mathbf{x}$ contains the unknown pressures, e.g.

$$\mathbf{x} = \begin{bmatrix} p_0^{(n+1)} \\ p_1^{(n+1)} \\ \vdots \\ p_{N-1}^{(n+1)} \end{bmatrix}. \tag{36}$$

In order to solve Equation (35) using the numerical method described in section 7, it is necessary to have the Jacobian matrix of $\mathbf{F}$. Details on how the Jacobian matrix is calculated are given in Appendix B.

The calculation of link flow rates from node pressures, and thus every evaluation of $\mathbf{F}$ and its Jacobian, involves solving one non-linear equation for each link flow rate,

$$G_{ij}\left(q_{ij}^{(n+1)}\right) = q_{ij}^{(n+1)} + g_{ij}^{(n)}\left\{p_i^{(n+1)} - p_j^{(n+1)} - c_{ij}^{(n+1)}\right\} = 0. \tag{37}$$

The derivative of G_{ij} with respect to $q_{ij}^{(n+1)}$ is

$$\frac{\mathrm{d}G_{ij}}{\mathrm{d}q_{ij}^{(n+1)}} = 1 - g_{ij}^{(n)}\frac{\mathrm{d}c_{ij}^{(n+1)}}{\mathrm{d}q_{ij}^{(n+1)}}. \tag{38}$$

The procedure for updating the interface positions with the semi-implicit method may be summarized as follows. The non-linear equation system (35) is solved to obtain the unknown node pressures. In every iteration of the solution procedure, the flow rates are evaluated by solving Equation (37) for each link. When a solution to Equation (35) is obtained, the interface positions are updated using Equation (31) and the interface interaction models.

6.1. Time Step Restrictions

We aim to select the time steps such that

$$\Delta t^{(n)} = \Delta t_{\mathrm{a}}^{(n+1)}. \tag{39}$$

However, to solve the non-linear system (35) is challenging in practice and requires initial guess values for the link flow rates and node pressures that lie sufficiently close to the solution. For this purpose, we here use values from the previous time step. This turns out to be a sufficiently good choice for most time steps, but our numerical solution procedure does not always succeed. As the link flow rates and node pressures at two consecutive points in time become increasingly similar as the time interval between them is reduced, we may expect the guess values to lie closer to the solution if we reduce the time step. Thus, if our solution procedure is unable to succeed, our remedy is to shorten $\Delta t^{(n)}$. This will sometimes lead to time steps shorter than $\Delta t_{\mathrm{a}}^{(n+1)}$. If, for a given time step, $\Delta t^{(n)}$ must be reduced to less than twice the time step length allowed by the explicit methods, we revert to forward Euler for that particular step. As we demonstrate in section 10, however, this does not prevent the semi-implicit method from being much more efficient than the explicit methods at low capillary numbers.

6.2. Boundary Conditions

As with the explicit methods, the specified ΔP boundary condition can be incorporated directly into the mass balance equation system, in this case Equation (35). This is done by adding to or subtracting from the right hand sides of Equation (32) and Equation (37) a term $g_{ij}^{(n)}\Delta P$ for each link ij crossing the periodic boundary.

The specified flow rate boundary condition is incorporated by including ΔP as an additional unknown and adding an additional equation

$$F_m = \left\{\sum_{ij\in\Omega} q_{ij}^{(n+1)}\right\} - Q = 0, \tag{40}$$

to the non-linear equation system (35). Herein, Ω is the set of links crossing the periodic boundary, with i being the node on the downstream side and j being the node on the upstream side. Thus, Equation (40) is satisfied when the total flow rate through the network is equal to Q.

7. IMPLEMENTATION

The non-linear equation system (35) is solved using a Newton-type solution method that guarantees convergence to a local

minimum of $\mathbf{F} \cdot \mathbf{F}$, see Press et al. [25, p. 477]. However, a local minimum of $\mathbf{F} \cdot \mathbf{F}$ is not necessarily a solution to Equation (35), and good initial guess values for the node pressures and link flow rates are therefore crucial. For this purpose, we use the values from the previous time step and reduce the length of the current time step if the solution method fails, as discussed in section 6.1.

Solving Equation (37) is done using a standard Newton solver [26]. For robustness, a bisection solver [26] is used if the Newton solver fails.

The Newton-type solver for non-linear systems and the explicit time integration methods require methods for solving linear systems of equations. We use the conjugate gradient method in combination with the LU preconditioner implemented in the PETSc library, see Balay et al. [27]. An introduction to solving systems of Kirchhoff-type equations numerically can be found in Batrouni and Hansen [28].

8. CASE DESCRIPTIONS

In this section, we describe the two simulated cases. One is a test case where a single bubble is contained in a network consisting of links connected in series, while the other is designed to capture a single Haines jump in a small network where fluids flow at a specified rate.

8.1. Links-in-Series Test Case

The verification will include comparison of results from the various numerical methods applied to a test case. The test case is chosen such that it can be set up as a single ODE with a closed expression for the right-hand side. An accurate reference solution can thus be easily obtained using a high-order Runge–Kutta method. As our test case, we consider a network consisting of $M = 3$ identical links connected in series. The network contains a single bubble of length ℓ (m) with center position z (m). In the capillary pressure model, we choose $\alpha = 0$. The ODE (6) can then be restated as an equivalent equation for the bubble position,

$$\frac{\mathrm{d}z}{\mathrm{d}t} = \frac{Q}{a}, \tag{41}$$

where Q is the flow through the network and a is the link cross-sectional area. The model equations can be reduced to the following expression for flow rate.

$$Q = -\frac{g}{M}\left\{\Delta P + \frac{4\sigma_{\mathrm{wn}}}{r}\sin\left(\frac{\pi\ell}{L}\right)\sin\left(\frac{2\pi z}{L}\right)\right\} \tag{42}$$

Here, g is the mobility of a single link, $L = 1.0 \cdot 10^{-3}$ m is the length of a single link and $r = 1.0 \cdot 10^{-4}$ m is the link radius. The bubble has length $\ell = 4.8 \cdot 10^{-4}$ m and is initially located at $z = 2.4 \cdot 10^{-4}$ m. The fluid parameters used in all simulations are given in **Table 1**. The pressure difference ΔP will be stated for each simulation.

8.2. Haines Jump Case

The Haines jump was first reported almost 90 years ago [13]. It refers to the sudden drops in driving pressure observed in drainage experiments when non-wetting fluid breaks through a throat and invades new pores. This process was studied experimentally and numerically by Måløy et al. [16] and, more recently, it was imaged directly and analyzed in detail by Armstrong and Berg [15] for flow in a micromodel and by Berg et al. [14] for flow in a sample of Berea sandstone. The Haines jump case simulated here captures one such break-through and subsequent pressure drop.

TABLE 1 | Fluid properties corresponding to water (w) and decane (n) at atmospheric pressure and 298 K.

Parameter	Value	Unit	References
μ_{w}	$8.9 \cdot 10^{-4}$	Pa s	[29]
μ_{n}	$8.5 \cdot 10^{-4}$	Pa s	[29]
σ_{wn}	$5.2 \cdot 10^{-2}$	$\mathrm{N\,m^{-1}}$	[30]

Among the findings in the study by Måløy et al. [16] was that pore drainage is a non-local event, meaning that as one pore is drained, imbibition occurs in nearby neck regions. This was also observed by Armstrong and Berg [15], and was explained as follows. When the imposed flow rates are low, the non-wetting fluid that fills the newly invaded pores needs to be supplied from nearby locations rather than the external feed. Armstrong and Berg [15] also found, for their range of investigated parameters, that pore drainage occurred on the same time-scale, regardless of the externally imposed flow rate.

We consider a hexagonal network consisting $N = 24$ nodes and $M = 36$ links. All links have length $1.0 \cdot 10^{-3}$ m, while the link radii are drawn randomly from a uniform distribution between 0.1 and 0.4 link lengths. In the capillary pressure model, we choose $\alpha = 1$. The fluid parameters μ_{w}, μ_{n} and σ_{wn} are the same as in the links-in-series test case, see **Table 1**. With these fluid parameters and network length scales, the case mimics the flow of water (w) and decane (n) in a Hele-Shaw cell filled with glass beads similar to those used in e.g. Måløy et al. [16, 31] and Tallakstad et al. [32]. The linear dimensions are ~ 10 times bigger in this network compared to the micromodel of Armstrong and Berg [15]. Initially, the fluids are distributed in the network as shown in **Figure 4**, with the non-wetting fluid in a single connected ganglion.

Simulations are run at different specified flow rates Q until a net fluid volume equivalent to 5% of the total pore volume has flowed through the network. The flow dynamics will, of course, depend upon the specified flow rate. At low flow rates, however, the flow will exhibit some relatively fast fluid redistribution events and one relatively slow pressure build-up and subsequent Haines jump event. The Haines jump will occur as the non-wetting fluid breaks through the link connecting nodes 9 and 16 and invades node 16, see **Figure 4**.

It was mentioned by Armstrong and Berg [15] that the large local flow velocities that they observed as a pore was filled with non-wetting fluid during a Haines jump has implications for how such processes must be numerically simulated. Specifically, the time resolution of the simulation needs to be fine enough during these events to capture them. This poses a challenge when externally applied flow rates are low and there is thus a large difference in the large time

scale that governs the overall flow of the system and the small time scale than governs the local flow during Haines jumps.

9. VERIFICATION

In this section, we verify that the time integration methods presented correctly solve the pore network model equations and that the time step criteria presented give stable solutions.

9.1. Convergence Tests

All time integration methods presented should, of course, give the same solution for vanishingly small time steps. Furthermore, the difference between the solution obtained with a given finite time step and the fully converged solution should decrease as the time steps are refined, and should do so at a rate that is consistent with the order of the method. In this section, we verify that all three time integration methods give solutions that converge to the reference solution for the links-in-series test case and thus that the methods correctly solve the model equations for this case.

We choose the pressure difference to be $\Delta P = -3200\,\text{Pa}$. This value is large enough to overcome the capillary forces and push the non-wetting bubble through the links. We therefore expect a flow rate Q that varies in time, but is always positive.

As measures of the numerical error, we consider both the relative error in the flow rate Q and the relative error in bubble position z between the numerical solutions and reference solutions at the end of the simulation. Time integration is performed from $t = 0\,\text{s}$ to $t = 0.001\,44\,\text{s}$. To have control over the time step lengths, we ignore all time step criteria for now and instead set a constant Δt for each simulation.

In **Figure 5**, flow rates are plotted for each of the time integration methods. Results using a coarse time step, $\Delta t = 4 \cdot 10^{-5}\,\text{s}$, and a fine time step, $\Delta t = 1 \cdot 10^{-5}\,\text{s}$, are shown along with the reference solution.

For the forward Euler and the semi-implicit method, there is considerable discrepancy between the numerical and the reference solution with the coarse time step. The flow rate obtained from forward Euler lags behind the reference solution, while that from the semi-implicit method lies ahead of it. This may be expected, however, since forward Euler at each time step uses current information in the right hand side evaluation, whereas the semi-implicit method uses a combination of current and future information. With the fine time step, there is less difference between the reference and the numerical solutions.

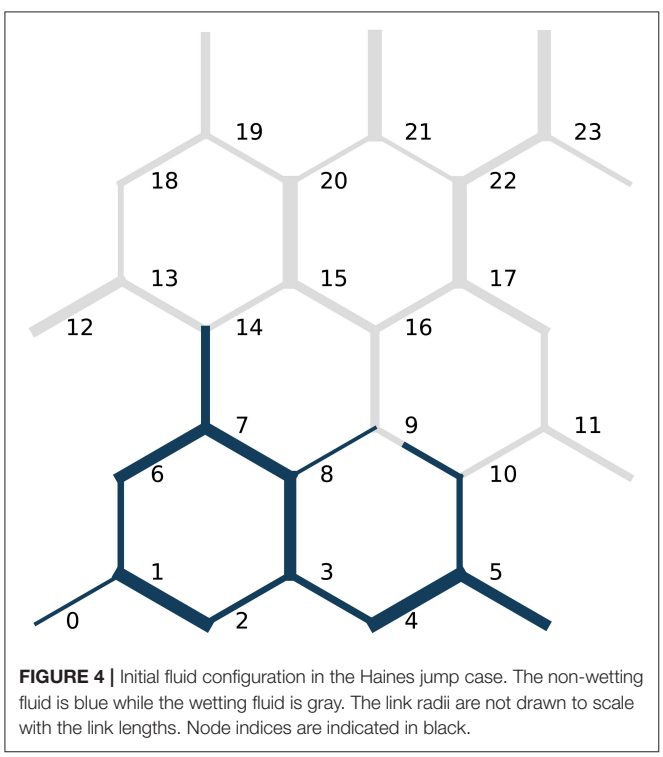

FIGURE 4 | Initial fluid configuration in the Haines jump case. The non-wetting fluid is blue while the wetting fluid is gray. The link radii are not drawn to scale with the link lengths. Node indices are indicated in black.

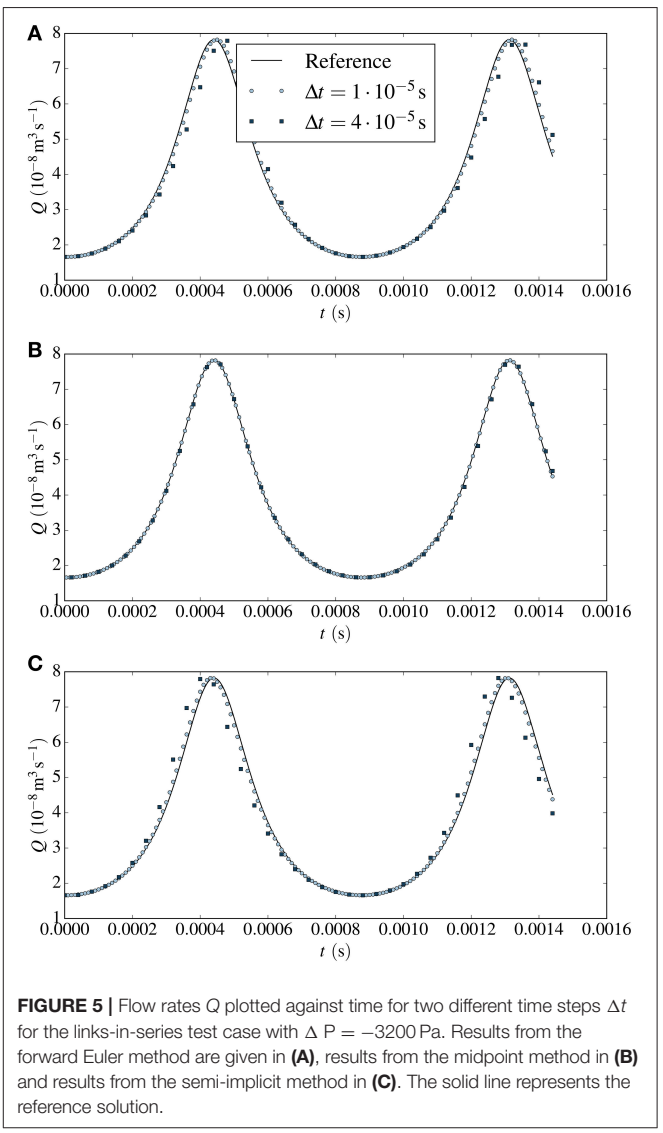

FIGURE 5 | Flow rates Q plotted against time for two different time steps Δt for the links-in-series test case with $\Delta P = -3200\,\text{Pa}$. Results from the forward Euler method are given in **(A)**, results from the midpoint method in **(B)** and results from the semi-implicit method in **(C)**. The solid line represents the reference solution.

With the more accurate midpoint method, the coarse-stepped numerical solution lies only marginally ahead of the reference solution while there is no difference between the fine-stepped numerical solution and the reference solution at the scale of representation.

The convergence of the numerical solutions to the reference solution upon time step refinement is quantified in **Tables 2–4**. Herein, the numerical errors and estimated convergence orders are given for the forward Euler, midpoint and semi-implicit method, respectively. For all methods considered, the numerical errors decrease when the time step is refined and do so at the rate that is expected. The forward Euler and the semi-implicit method exhibit first-order convergence, while the midpoint method shows second-order convergence. We note that the errors in both z and Q are similar in magnitude for the forward Euler and the semi-implicit method. The errors obtained with the midpoint method are smaller. The difference is one order of magnitude for $\Delta t = 1 \cdot 10^{-5}$ s.

In summary, we have verified that the presented time integration methods correctly solve the pore network model equations for the links-in-series test case and that the numerical errors decrease upon time step refinement at the rate that is consistent with the expected order of the methods.

TABLE 2 | Relative errors in bubble position z and flow rate Q at $t = 0.001\,44$ s and estimated convergence orders for the links-in-series test case computed with the forward Euler method.

Δt (s)	z-error	z-order	Q-error	Q-order
$4 \cdot 10^{-5}$	$1.55 \cdot 10^{-2}$		$1.33 \cdot 10^{-1}$	
$2 \cdot 10^{-5}$	$7.44 \cdot 10^{-3}$	1.06	$6.41 \cdot 10^{-2}$	1.06
$1 \cdot 10^{-5}$	$3.66 \cdot 10^{-3}$	1.02	$3.15 \cdot 10^{-2}$	1.02
$5 \cdot 10^{-5}$	$1.82 \cdot 10^{-3}$	1.01	$1.57 \cdot 10^{-2}$	1.01

TABLE 3 | Relative errors in bubble position z and flow rate Q at $t = 0.001\,44$ s and estimated convergence orders for the links-in-series test case computed with the midpoint method.

Δt (s)	z-error	z-order	Q-error	Q-order
$8 \cdot 10^{-5}$	$1.67 \cdot 10^{-2}$		$1.44 \cdot 10^{-1}$	
$4 \cdot 10^{-5}$	$4.24 \cdot 10^{-3}$	1.98	$3.65 \cdot 10^{-3}$	1.98
$2 \cdot 10^{-5}$	$1.08 \cdot 10^{-3}$	1.97	$9.33 \cdot 10^{-3}$	1.97
$1 \cdot 10^{-5}$	$2.86 \cdot 10^{-4}$	1.92	$2.46 \cdot 10^{-3}$	1.92

TABLE 4 | Relative errors in bubble position z and flow rate Q at $t = 0.001\,44$ s and estimated convergence orders for the links-in-series test case computed with the semi-implicit method.

Δt (s)	z-error	z-order	Q-error	Q-order
$4 \cdot 10^{-5}$	$1.39 \cdot 10^{-2}$		$1.18 \cdot 10^{-1}$	
$2 \cdot 10^{-5}$	$6.98 \cdot 10^{-3}$	0.99	$5.97 \cdot 10^{-2}$	0.98
$1 \cdot 10^{-5}$	$3.51 \cdot 10^{-3}$	0.99	$3.01 \cdot 10^{-2}$	0.99
$5 \cdot 10^{-5}$	$1.76 \cdot 10^{-3}$	1.00	$1.5 \cdot 10^{-2}$	1.00

9.2. Stability Tests

In this section, we demonstrate that the proposed capillary time step criterion (23) stabilizes the forward Euler method and the midpoint method at low flow rates. We simulated two different cases and varied C_c. Simulations run with low C_c turned out to be free of spurious oscillations, indicating that the proposed criterion stabilizes the methods, while simulations run with C_c significantly larger than unity produced oscillations, indicating that the proposed criterion is not unnecessarily strict.

First, consider the links-in-series test case with $\Delta P = 0$ Pa. With no applied pressure difference, the flow is driven purely by the imbalance of capillary forces on the non-wetting bubble. Therefore, there should only be flow initially and the bubble should eventually reach an equilibrium position where both interfaces experience the same capillary force and the flow rate is zero. Simulations were run with $C_a = 0.1$ and C_c equal to 2.0, 1.0, and 0.5. Results from forward Euler are shown in **Figure 6A** and results from the midpoint method are shown in **Figure 6B**. In both figures, the reference solution is also shown.

The forward Euler results are stable and qualitatively similar to the reference solution with $C_c = 0.5$. With $C_c = 1.0$, there are some oscillations initially that are dampened and eventually vanish. From comparison with the reference solution, it is clear that such oscillations have no origin in the model equations and are artifacts of the numerical method. With $C_c = 2.0$, the oscillations are severe and do not appear to be dampened by the method. Instead the non-wetting bubble keeps oscillating around its equilibrium position in a manner that is clearly unphysical.

The results from the midpoint method in **Figure 6B** follow a qualitatively similar trend as those from forward Euler with regard to stability. Results computed with $C_c = 0.5$ are stable and results with $C_c = 2.0$ exhibit severe oscillations. Still, the results from the midpoint method lie much closer to the reference solution than the results from the forward Euler method, as we would expect since the midpoint method is second-order. Both methods are, however, unstable with $C_c = 2.0$, indicating that the while the midpoint method has improved accuracy over forward Euler, it is unable to take significantly longer time steps without introducing oscillations. This is consistent with the analysis in Appendix A, since the two methods have identical stability regions in real space.

Next, consider the Haines jump case with $Q = 10^{-9}\,\mathrm{m^3\,s^{-1}}$, corresponding to $\mathrm{Ca} = 1.2 \cdot 10^{-5}$. This case was run using the forward Euler method, $C_a = 0.1$ and three different values of C_c, equal to 4.0, 2.0, and 1.0. The required pressure difference to drive the flow at the specified rate is shown in **Figure 7A**. **Figure 7B** shows the pressure from **Figure 7A** in greater detail.

For all three values of C_c, the main qualitative features of the flow are captured. We observe short transient pressure drops at $t \approx 0.08$ s and $t \approx 0.20$ s. These correspond to fluid redistribution events on the upstream side of the non-wetting ganglion, where the fluid rearranges itself to a more stable configuration with little change to the interface positions on the downstream side. The event at $t \approx 0.20$ s is illustrated in **Figure 8**. The fluid redistribution is driven by capillary forces and less external

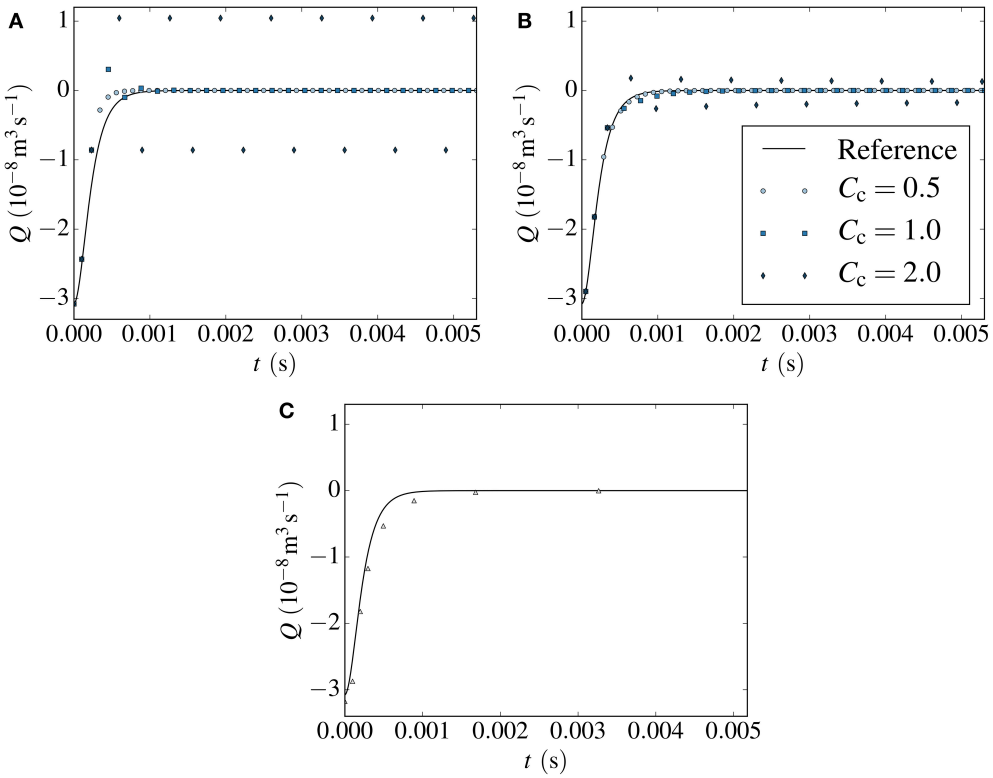

FIGURE 6 | Flow rate plotted against time in the link-in-series test case with $\Delta P = 0$ Pa. Results from the forward Euler method **(A)** and the midpoint method **(B)** are shown for different values of C_c. Severe numerical instabilities arise when $C_c = 2.0$. Results from the semi-implicit method are shown are shown in **(C)**. These are stable, even if the capillary time step criterion is not used. The solid black line represents a reference solution.

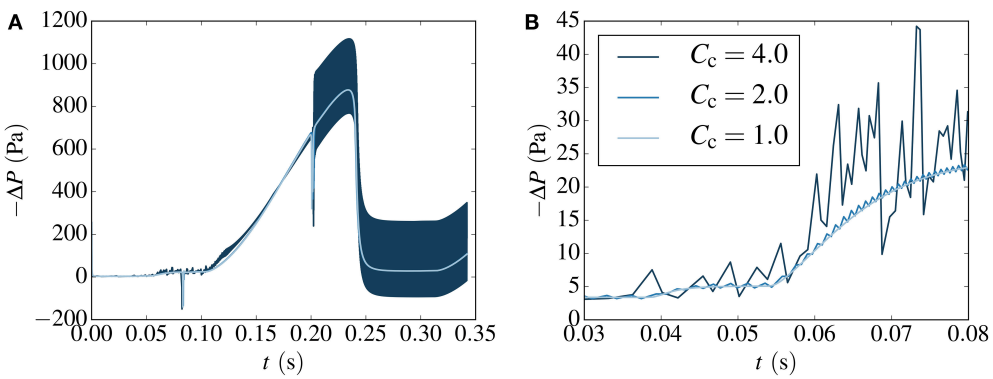

FIGURE 7 | Pressure difference required to drive the flow in the Haines jump case at a rate of $Q = 10^{-9}$ m^3 s^{-1}, corresponding to Ca $= 1.2 \cdot 10^{-5}$. In **(B)**, the results from **(A)** are shown in greater detail. Results are computed with the forward Euler method for different values of the capillary time step restriction parameter C_c. Numerical instabilities are seen to occur for $C_c > 1$.

pressure is therefore required to drive the flow during these events.

We also observe the slow pressure build-up from $t \approx 0.10$ s to $t \approx 0.23$ s, when the driving pressure becomes large enough to overcome the capillary forces and cause break-through of non-wetting fluid in the link connecting nodes 9 and 16, and we observe the subsequent Haines jump. The fluid configurations before and after the Haines jump are shown in **Figure 9**. Notice also that non-wetting fluid at the downstream end of the moving ganglion retracts during the Haines jump in links near to where the break-through occurs. This is seen e.g. in the links downstream of nodes 10 and 14. That such local imbibition occurs near the drained pore is in agreement with the observations of

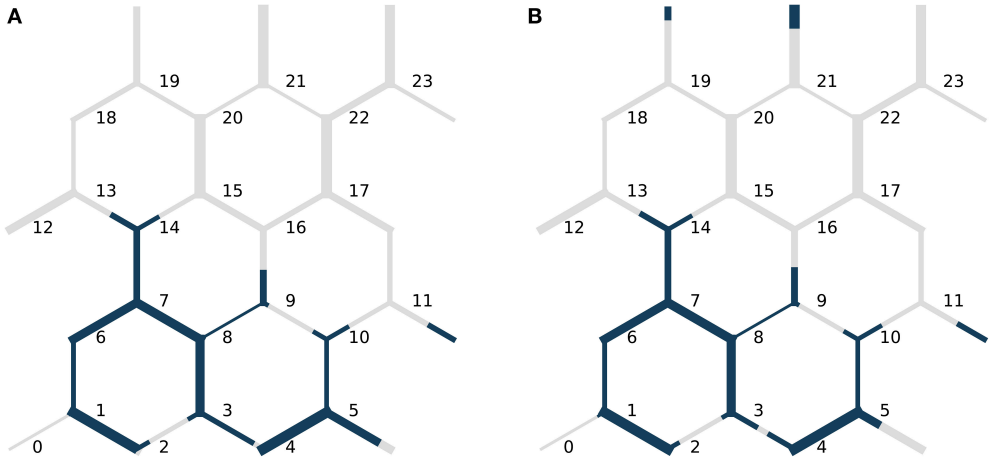

FIGURE 8 | Fluid distribution in the Haines jump case, **(A)** at $t = 0.19\,\mathrm{s}$ and **(B)** at $t = 0.21\,\mathrm{s}$, before and after the fluid redistribution event at $t \approx 0.20\,\mathrm{s}$. The link radii are not drawn to scale with the link lengths. Node indices are indicated in black.

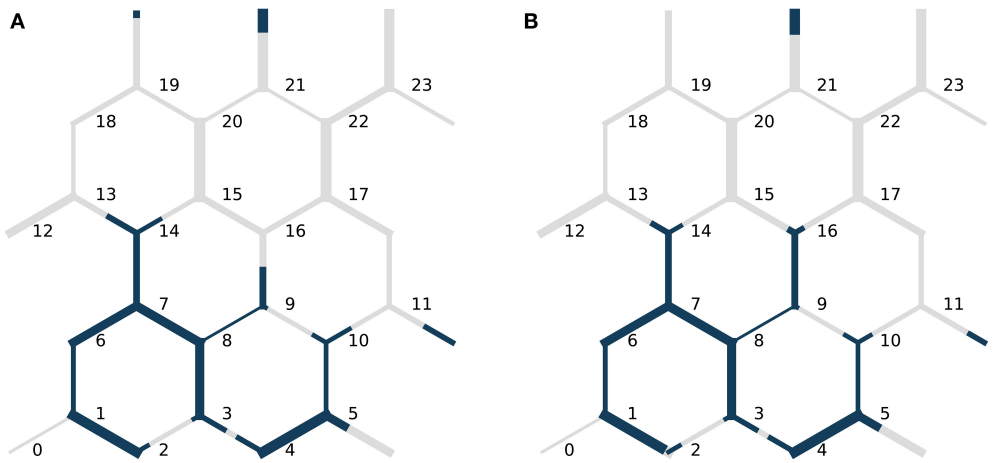

FIGURE 9 | Fluid distribution in the Haines jump case **(A)** at $t = 0.23\,\mathrm{s}$ and **(B)** at $t = 0.27\,\mathrm{s}$, before and after the Haines jump. During the jump, non-wetting fluid breaks-through the link connecting nodes 9 and 16 and invades node 16. Also, non-wetting fluid in other links at the downstream end of the moving ganglion retracts. This is seen e.g. in the links downstream of nodes 10 and 14. The link radii are not drawn to scale with the link lengths. Node indices are indicated in black.

Armstrong and Berg [15], and shows that the model is able to capture the non-local nature of pore drainage events in a numerically stable manner when the new numerical methods are used.

As in the links-in-series case, the solution exhibits oscillations for the values of C_c that are larger than unity. With $C_c = 1.0$, the results are free from oscillations and appear stable. This indicates that the stability criterion (23) is valid and not unnecessarily strict also for a network configuration that is much more complex than links in series.

Both the links-in-series case and the Haines jump case were simulated with the semi-implicit method and produced stable results with the advective time step criterion (22) only. The results from the links-in-series test case are shown in **Figure 6C**. For brevity, the results from the Haines jump case are omitted here. The reader is referred to **Figure 10A** in section 10, where stable results are shown for a lower flow rate.

To summarize, both the forward Euler and midpoint methods produce stable results for the cases considered when the capillary time step criterion (23) is used in addition to Equation (22) to select the time step lengths. By running simulations with different C_c, we have observed a transition from stable to unstable results for values of C_c near 1, in order of magnitude. In the Haines jump case, all methods presented are able to capture both the fast capillary-driven fluid redistribution events, and the slow pressure build-up before a Haines jump.

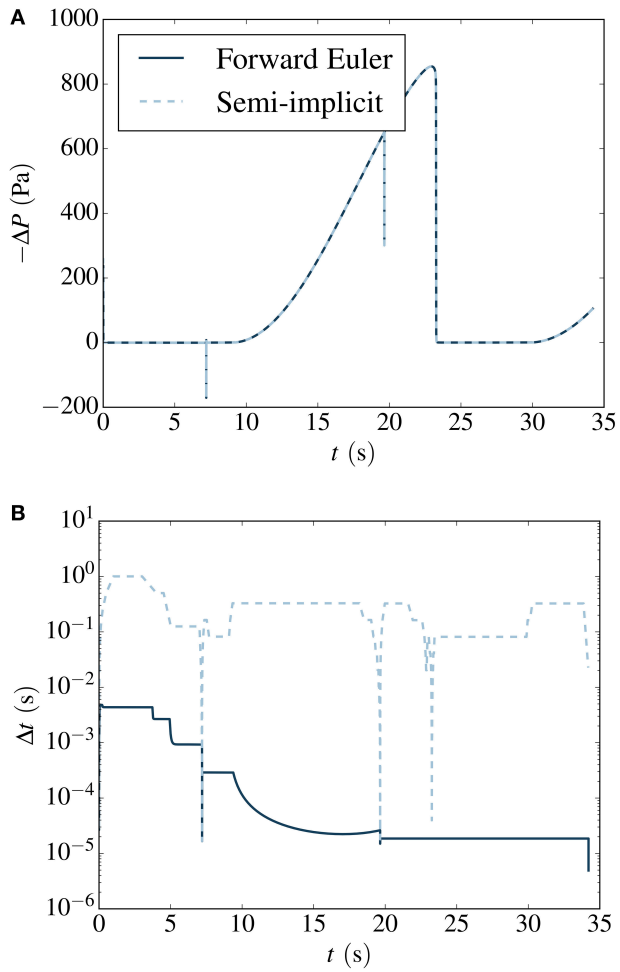

FIGURE 10 | (A) Pressure difference required to drive the flow at $Q = 10^{-11}$ m^3 s^{-1}, corresponding to Ca $= 1.2 \cdot 10^{-7}$, in the Haines jump case. Results are plotted for the forward Euler method (solid dark blue) and the semi-implicit method (dashed light blue). These lines coincide at the scale of representation. The time steps lengths used by each method are plotted in **(B)**.

10. PERFORMANCE ANALYSIS

In this section, we analyze and compare the performance of the time integration methods. In doing so, we consider the number of time steps and the wall clock time required to perform stable simulations of the Haines jump case with each of the methods at different specified flow rates Q. The flow rates simulated were 10^{-7} m^3 s^{-1}, 10^{-8} m^3 s^{-1}, 10^{-9} m^3 s^{-1}, 10^{-10} m^3 s^{-1}, 10^{-11} m^3 s^{-1}, and 10^{-12} m^3 s^{-1}. The accuracy of the methods was studied Section 9.1, and will not be part of the performance analysis. Instead, stable simulations are considered sufficiently accurate.

First, we look more closely at the results for $Q = 10^{-11}$ m^3 s^{-1}, corresponding to Ca $= 1.2 \cdot 10^{-7}$. The pressure difference required to drive the flow is shown in **Figure 10A**, and the time step lengths used are shown in **Figure 10B**. From the latter Figure, we see that the semi-implicit method is able to take longer time steps than forward Euler for most of the simulation. During the pressure build-up phase, the difference is four orders of magnitude. During the fast capillary-driven fluid redistribution events, however, the length of the semi-implicit time steps drop to the level of those used by forward Euler. This is because we here have relatively large flow rates in some links, even though Q is low, and the advective time step criterion (22) becomes limiting for both the semi-implicit method and forward Euler.

It was mentioned by Armstrong and Berg [15] that any accurate numerical simulation on the pore scale must have a time resolution fine enough to capture the fast events. The semi-implicit method accomplishes this by providing a highly dynamic time resolution, which is refined during the fast events. The method is therefore able to resolve these events, while time resolution can be coarsened when flow is governed by the slow externally applied flow rate, saving computational effort.

The time duration of the Haines jump pressure drops for all except the two largest externally applied flow rates were around 10 ms. This is in qualitative agreement with the results presented by Armstrong and Berg [15]. They found that, for their investigated range of parameters, pores were drained on the millisecond time scale regardless of externally applied flow rate. However, we stress that although we consider the same fluids, the pore network used here was approximately one order of magnitude larger in the linear dimensions than that of Armstrong and Berg [15].

The number of time steps and wall clock time required to simulate the Haines jump case at different specified flow rates Q are shown in **Figures 11A,B**, respectively.

For the explicit methods, both the number of time steps and the wall time are proportional to Ca^{-1} at low capillary numbers. This is because the capillary time step criterion (23) dictates the time step at low capillary numbers (except during fast fluid redistribution events). The criterion depends on the fluid configuration, while it is independent of the flow rate. At low enough flow rates, the system will pass through roughly the same fluid configurations during the simulation, regardless of the applied Q. The speed at which the system passes through these configurations, however, will be inversely proportional to Q and therefore, so will the required wall time and number of time steps. As the forward Euler and the midpoint method are subject to the same time step criteria, these require roughly the same number of time steps at all considered flow rates. However, since the midpoint method is a two-step method, the wall time it requires is longer and approaches twice that required by the forward Euler for long wall times.

For the semi-implicit method, on the other hand, the number of time steps required to do the simulation becomes effectively independent of the specified flow rate at capillary numbers smaller than approximately 10^{-4}. The result is that low-capillary number simulations can be done much more efficiently than with the explicit methods, in terms of wall time required to perform stable simulations. This is seen in **Figure 11B**. At Ca $\sim 10^{-5}$, the computational time needed by all three methods are similar in magnitude. The relative benefit of using the semi-implicit method increases at lower capillary numbers. For the lowest capillary number considered, the difference in wall time between

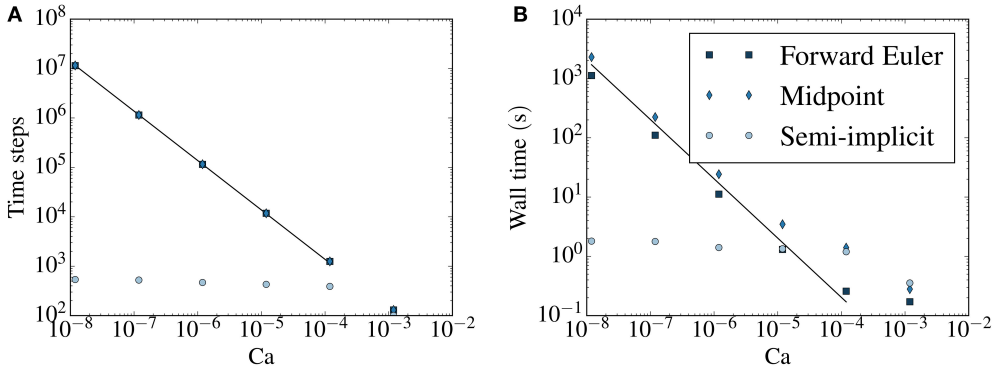

FIGURE 11 | (A) Number of time steps and **(B)** wall clock time required to simulate the Haines jump case at at different specified flow rates. In each simulation, the same volume of fluid (5% of the pore volume) flows through a network. Results from the forward Euler method (squares), the midpoint method (diamonds) and the semi-implicit method (circles) are shown. In **(A,B)**, the black lines are inversely proportional to Ca.

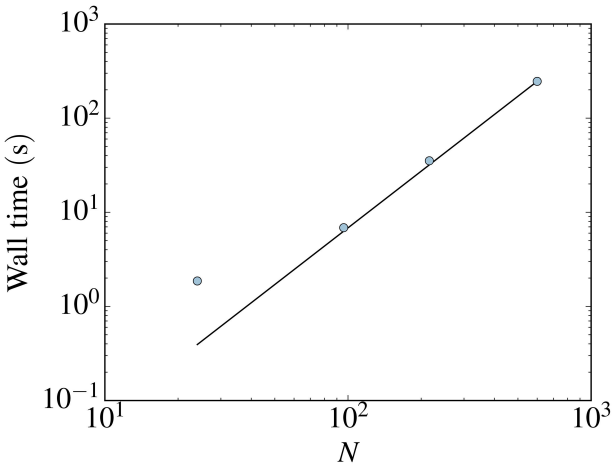

FIGURE 12 | Wall clock time time required to simulate the Haines jump case with the semi-implicit method for different network sizes. All simulations were run at Ca $\sim = 10^{-7}$ and N denotes the number of nodes in the network. The wall time is seen to increase proportionally to N^2 for the three largest networks.

the explicit methods and the semi-implicit is three orders of magnitude.

The increased efficiency of the semi-implicit method over explicit methods at low capillary numbers means that one can use the semi-implicit method to perform simulations in the low capillary number regime that are unfeasible with explicit methods. Thus, the range of capillary numbers for which the pore network model is a tractable modeling alternative is extended to much lower capillary numbers. This includes e.g. simulations of water flow in fuel cell gas diffusion layers, where capillary numbers are can be 10^{-8} [33].

Finally, to study the effect of an increase in network size on the wall time required by the semi-implicit method, the Haines jump case was run on three scaled-up versions of the network with $N = 24$ nodes considered so far, illustrated in **Figure 4**. All simulations were run at Ca $\sim 10^{-7}$. In **Figure 12** the wall clock time time required is plotted against the number of nodes N for the different networks. The wall time is seen to increase proportionally to N^2.

11. CONCLUSION

We have studied three different time integration methods for a pore network model for immiscible two-phase flow in porous media. Two explicit methods, the forward Euler and midpoint methods, and a new semi-implicit method were considered. The explicit methods have been presented and used in other works [10, 21, 24], and were reviewed here for completeness. The semi-implicit method was presented here for the first time, and therefore in detail.

The explicit methods have previously suffered from numerical instabilities at low capillary numbers. Here, a new time-step criterion was suggested in order to stabilize them and numerical experiments were performed demonstrating that stabilization was achieved.

It was verified that all three methods converged to a reference solution to a selected test case upon time step refinement. The forward Euler and semi-implicit methods exhibited first-order convergence and the midpoint method showed second-order convergence.

Simulations of a single Haines jump were performed. These showed that the all three methods were able to resolve both pressure build-up events and fluid redistribution events, including interfacial retraction after a Haines jump, which may occur at vastly different time scales when capillary numbers are low. The results from the Haines jump case were consistent with experimental observations made by Armstrong and Berg [15]. Fluid redistribution events cannot be properly captured when using solution methods that have previously been used at low capillary numbers that e.g. do not allow backflow [18].

A performance analysis revealed that the semi-implicit method was able to perform stable simulations with much less

computational effort than the explicit methods at low capillary numbers. For the case considered, the computational time needed was approximately the same for all three methods at Ca $\sim 10^{-5}$. At lower capillary numbers, the computational time needed by the explicit methods increased inversely proportional to the capillary number, while the time needed by the semi-implicit method was effectively constant. At Ca $\sim 10^{-8}$, the computational time needed by the semi-implicit methods was therefore three orders of magnitude smaller than those needed by the explicit methods.

The superior efficiency of the new semi-implicit method over the explicit methods at low capillary numbers enables simulations in this regime that are unfeasible with explicit methods. Thus, the range of capillary numbers for which the pore network model is a tractable modeling alternative is extended to much lower capillary numbers. This includes e.g. simulations of water flow in fuel cell gas diffusion layers, where capillary numbers are can be 10^{-8} [33].

In summary, use of Aker-type pore network models were previously restricted to relatively high capillary numbers due to numerical instabilities in the explicit methods used to solve them. With the new time step criterion presented here, these stability problems are removed. However, simulations at low capillary numbers still take a long time and the computational time needed increases inversely proportional to the capillary number. This problem is solved by the new semi-implicit method. With this method, the computational time needed becomes effectively independent of the capillary number, when capillary numbers are low.

AUTHOR CONTRIBUTIONS

To pursue low capillary number simulations with Aker-type pore network models was proposed by SK, MG, and AH in collaboration. MV developed the particular variation of the pore network model used. MG developed the new numerical methods and performed the simulations. MG wrote the manuscript, aided by comments and suggestions from MV, SK, and AH.

ACKNOWLEDGMENTS

The authors would like to thank Dick Bedeaux, Santanu Sinha, and Knut Jørgen Måløy for fruitful discussions. Special thanks are also given to Jon Pharoah for inspiring discussions and comments. This work was partly supported by the Research Council of Norway through its Centres of Excellence funding scheme, project number 262644.

SUPPLEMENTARY MATERIAL

The Supplementary Material for this article can be found online at: https://www.frontiersin.org/articles/10.3389/fphy.2018.00056/full#supplementary-material

REFERENCES

1. Raeini AQ, Blunt MJ, Bijeljic B. Modelling two-phase flow in porous media at the pore scale using the volume-of-fluid method. *J Comput Phys.* (2012) **231**:5653–68. doi: 10.1016/j.jcp.2012.04.011
2. Jettestuen E, Helland JO, Prodanović M. A level set method for simulating capillary-controlled displacements at the pore scale with nonzero contact angles. *Water Resour Res.* (2013) **49**:4645–61. doi: 10.1002/wrcr.20334
3. Gjennestad MA, Munkejord ST. Modelling of heat transport in two-phase flow and of mass transfer between phases using the level-set method. *Energy Proc.* (2015) **64**:53–62. doi: 10.1016/j.egypro.2015.01.008
4. Ramstad T, Øren PE, Bakke S. Simulation of two-phase flow in reservoir rocks using a lattice Boltzmann method. *SPE J.* (2010) **15**:917–27. doi: 10.2118/124617-PA
5. Hammond PS, Unsal E. A dynamic pore network model for oil displacement by wettability-altering surfactant solution. *Transport Porous Media* (2012) **92**:789–817. doi: 10.1007/s11242-011-9933-4
6. Lenormand R, Touboul E, Zarcone C. Numerical models and experiments on immiscible displacements in porous media. *J Fluid Mech.* (1988) **189**:165–87. doi: 10.1017/S0022112088000953
7. Wilkinson D, Willemsen JF. Invasion percolation: a new form of percolation theory. *J Phys A Math Gen.* (1983) **16**:3365. doi: 10.1088/0305-4470/16/14/028
8. Blunt MJ. Physically-based network modeling of multiphase flow in intermediate-wet porous media. *J Petroleum Sci Eng.* (1998) **20**:117–25. doi: 10.1016/S0920-4105(98)00010-2
9. Joekar-Niasar V, Hassanizadeh SM, Dahle H. Non-equilibrium effects in capillarity and interfacial area in two-phase flow: dynamic pore-network modelling. *J Fluid Mech.* (2010) **655**:38–71. doi: 10.1017/S0022112010000704
10. Aker E, Måløy KJ, Hansen A, Batrouni GG. A two-dimensional network simulator for two-phase flow in porous media. *Transport Porous Media* (1998) **32**:163–86. doi: 10.1023/A:1006510106194
11. Joekar-Niasar V, Hassanizadeh S. Analysis of fundamentals of two-phase flow in porous media using dynamic pore-network models: a review. *Crit Rev Environ Sci Technol.* (2012) **42**:1895–976. doi: 10.1080/10643389.2011.574101
12. Tørå G, Øren PE, Hansen A. A dynamic network model for two-phase flow in porous media. *Transport Porous Media* (2012) **92**:145–64. doi: 10.1007/s11242-011-9895-6
13. Haines WB. Studies in the physical properties of soil. v. the hysteresis effect in capillary properties, and the modes of moisture distribution associated therewith. *J Agric Sci.* (1930) **20**:97–116. doi: 10.1017/S002185960008864X
14. Berg S, Ott H, Klapp SA, Schwing A, Neiteler R, Brussee N, et al. Real-time 3D imaging of Haines jumps in porous media flow. *Proc Natl Acad Sci USA* (2013) **110**:3755–9. doi: 10.1073/pnas.1221373110
15. Armstrong RT, Berg S. Interfacial velocities and capillary pressure gradients during haines jumps. *Phys Rev E* (2013) **88**:043010. doi: 10.1103/PhysRevE.88.043010
16. Måløy KJ, Furuberg L, Feder J, Jøssang T. Dynamics of slow drainage in porous media. *Phys Rev Lett.* (1992) **68**:2161. doi: 10.1103/PhysRevLett.68.2161
17. Koplik J, Lasseter T. Two-phase flow in random network models of porous media. *Soc Petrol Eng J.* (1985) **25**:89–100. doi: 10.2118/11014-PA
18. Medici E, Allen J. The effects of morphological and wetting properties of porous transport layers on water movement in PEM fuel cells. *J Electrochem Soc.* (2010) **157**:B1505–14. doi: 10.1149/1.3474958
19. Savani I, Sinha S, Hansen A, Bedeaux D, Kjelstrup S, Vassvik M. A Monte Carlo algorithm for immiscible two-phase flow in porous media. *Transport Porous Media* (2017) **116**:869–88. doi: 10.1007/s11242-016-0804-x
20. Washburn EW. The dynamics of capillary flow. *Phys Rev.* (1921) **17**:273. doi: 10.1103/PhysRev.17.273
21. Knudsen HA, Aker E, Hansen A. Bulk flow regimes and fractional flow in 2D porous media by numerical simulations. *Transport Porous Media* (2002) **47**:99–121. doi: 10.1023/A:1015039503551

22. Sinha S, Bender AT, Danczyk M, Keepseagle K, Prather CA, Bray JM, et al. Effective rheology of two-phase flow in three-dimensional porous media: experiment and simulation. *Transport Porous Media* (2017) **119**:77–94. doi: 10.1007/s11242-017-0874-4
23. Erpelding M, Sinha S, Tallakstad KT, Hansen A, Flekkøy EG, Måløy KJ. History independence of steady state in simultaneous two-phase flow through two-dimensional porous media. *Phys Rev E* (2013) **88**:053004. doi: 10.1103/PhysRevE.88.053004
24. Sinha S, Hansen A. Effective rheology of immiscible two-phase flow in porous media. *Europhys Lett.* (2012) **99**:44004. doi: 10.1209/0295-5075/99/44004
25. Press WH, Flannery BP, Teukolsky SA, Vetterling WT. *Numerical Recipes: The Art of Scientific Computing, 3rd Edn*. New York, NY: Cambridge University Press (2007).
26. Süli E, Mayers D. *An Introduction to Numerical Analysis*. Cambridge: Cambridge University Press (2006).
27. Balay S, Abhyankar S, Adams MF, Brown J, Brune P, Buschelman K, et al. *PETSc Web Page* (2016). Available online at: http://www.mcs.anl.gov/petsc
28. Batrouni GG, Hansen A. Fourier acceleration of iterative processes in disordered systems. *J Stat Phys.* (1988) **52**:747–73. doi: 10.1007/BF01019728
29. Linstrom P, Mallard W, (eds.). *NIST Chemistry WebBook, NIST Standard Reference Database Number 69*. Gaithersburg, MD: National Institute of Standards and Technology (2017).
30. Zeppieri S, Rodríguez J, López de Ramos A. Interfacial tension of alkane + water systems. *J Chem Eng Data* (2001) **46**:1086–8. doi: 10.1021/je000245r
31. Måløy KJ, Feder J, Jøssang T. Viscous fingering fractals in porous media. *Phys Rev Lett.* (1985) **55**:2688. doi: 10.1103/PhysRevLett.55.2688
32. Tallakstad KT, Knudsen HA, Ramstad T, Løvoll G, Måløy KJ, Toussaint R, et al. Steady-state two-phase flow in porous media: statistics and transport properties. *Phys Rev Lett.* (2009) **102**:074502. doi: 10.1103/PhysRevLett.102.074502
33. Sinha PK, Wang CY. Pore-network modeling of liquid water transport in gas diffusion layer of a polymer electrolyte fuel cell. *Electrochim Acta* (2007) **52**:7936–45. doi: 10.1016/j.electacta.2007.06.061

Conflict of Interest Statement: The authors declare that the research was conducted in the absence of any commercial or financial relationships that could be construed as a potential conflict of interest.

frontiers in Physics

ORIGINAL RESEARCH
published: 08 November 2018
doi: 10.3389/fphy.2018.00126

Non-isothermal Transport of Multi-phase Fluids in Porous Media. The Entropy Production

Signe Kjelstrup[1]*, *Dick Bedeaux*[1], *Alex Hansen*[2], *Bjørn Hafskjold*[1] and *Olav Galteland*[1]

[1] PoreLab, Department of Chemistry, Norwegian University of Science and Technology, Trondheim, Norway, [2] PoreLab, Department of Physics, Norwegian University of Science and Technology, Trondheim, Norway

We derive the entropy production for transport of multi-phase fluids in a non-deformable, porous medium exposed to differences in pressure, temperature, and chemical potentials. Thermodynamic extensive variables on the macro-scale are obtained by integrating over a representative elementary volume (REV). Contributions come from porous media specific properties, phase volumes, surface areas, and contact lines. Curvature effects are neglected. Using Euler homogeneity of the first order, we obtain the Gibbs equation for the REV. From this we define the intensive variables, the temperature, pressure, and chemical potentials, and, using the balance equations, we derive the entropy production for the REV. The entropy production defines sets of independent conjugate thermodynamic fluxes and forces in the standard way. The transport of two-phase flow of immiscible components is used to give a first illustration of the equations.

Keywords: porous media, energy dissipation, two-phase flow, excess surface- and line-energies, pore-scale, representative elementary volume, macro-scale, non-equilibrium thermodynamics

OPEN ACCESS

Edited by:
Antonio F. Miguel, Universidade de Évora, Portugal

Reviewed by:
Francisco J. Valdes-Parada, Universidad Autónoma Metropolitana, Mexico
A. Murat, University of Ontario Institute of Technology, Canada

***Correspondence:**
Signe Kjelstrup
signe.kjelstrup@ntnu.no

Specialty section:
This article was submitted to Interdisciplinary Physics, a section of the journal Frontiers in Physics

Received: *05 September 2018*
Accepted: *16 October 2018*
Published: *08 November 2018*

Citation:
Kjelstrup S, Bedeaux D, Hansen A, Hafskjold B and Galteland O (2018) Non-isothermal Transport of Multi-phase Fluids in Porous Media. The Entropy Production. Front. Phys. 6:126. doi: 10.3389/fphy.2018.00126

1. INTRODUCTION

The aim of this article is to develop the basis for a macro-scale description of multi-phase flow in porous media in terms of non-equilibrium thermodynamics. The system consists of several fluid phases in a medium of constant porosity. The aim is to describe the transport of these on the scale of measurements; i.e., on the macro-scale, using properties defined on this scale, which represent the underlying structure on the micro-scale. The effort is not new; it was pioneered more than 30 years ago [1–4], and we shall build heavily on these results, in particular those of Hassanizadeh and Gray [2, 3] and Gray and Miller [5].

The aim is also still the original one; to obtain a systematic description, which can avoid arbitrariness and capture the essential properties of multi-component multi-phase flow-systems. Not only bulk energies need be taken into account to achieve this for porous media. Also excess surface- and line-energies must be considered, see e.g., [6]. But, unlike what has been done before, we shall seek to reduce drastically the number of variables needed for the description, allowing us still to make use of the systematic theory of non-equilibrium thermodynamics. While the entropy production in the porous medium so far has been written as a combination of contributions from each phase, interface and contact line, we shall write the property for a more limited set of macro-scale variables. In this sense, we deviate widely from the Thermodynamically Constrained Averaging Theory [5]. Nevertheless, we will be able to describe experiments and connect variables within the classical scheme of non-equilibrium thermodynamics. The reduction of variables is possible as long as the system is Euler homogeneous of the first kind.

The theory of non-equilibrium thermodynamics was set up by Onsager [7, 8] and further developed for *homogeneous* systems during the middle of the last century [9]. It was the favored thermodynamic basis of Hassanizadeh and Gray for their description of porous media. These authors [2, 3] discussed also other approaches, e.g., the theory of mixtures in macroscopic continuum mechanics, cf. [1, 4]. Gray and Miller [5] argued that it is the simplest of the many approaches in non-equilibrium thermodynamics.

The theory of classical non-equilibrium thermodynamics has been extended to deal with a particular case of flow in heterogeneous systems, namely transport along [10] and perpendicular [11] to layered interfaces. A derivation of the entropy production for heterogeneous systems *on the macro-scale* has not been given, however, even if one can find several uses of this property [6]. Transport in porous media takes place, not only under pressure gradients. Temperature gradients will frequently follow from transport of mass, for instance in heterogeneous catalysis [12], in polymer electrolyte fuel cells, in batteries [11, 13], or in capillaries in frozen soils during frost heave [14]. The number of this type of phenomena is enormous. We have chosen to consider first the vectorial driving forces related to changes in pressure, chemical composition, and temperature, staying away for the time being from deformations, chemical reactions, or forces leading to stress [15]. The multi-phase flow problem is thus in focus.

The development of a general thermodynamic basis for multi-phase flow started by introduction of thermodynamic properties for each component in each phase, interface, and three-phase contact line [2, 3]. A representative volume element (REV) was introduced, consisting of bulk phases, interfaces, and three-phase contact lines. Balance equations were formulated for each phase in the REV, and the total REV entropy production was the sum of the separate contributions from each phase.

Hansen et al. [16] recognized recently that the motion of fluids at the coarse-grained level could be described by extensive variables. The properties of Euler homogeneous functions could then be used to create relations between the flow rates at this level of description. This work, however, did not address the coarse-graining problem itself. We shall take advantage of Euler homogeneity also here and use it in the coarse-graining process described above.

Like Gray et al. [2, 3, 5], we use the entropy production as the governing property. But rather than dealing with the total entropy production as a sum of several parts, we shall seek to define the total entropy production directly from a basis set of a few coarse-grained variables. This will be done here for the REV, see [17] for a preliminary version. Once the entropy production has been formulated, we shall set up the independent constitutive equations. This will be done in subsequent work, see the preliminary version [18]. There we highlight the consequences of the model, and show that new experimental relations can be found. We shall find that the description is able to add insight in already published experimental results and design new experiments.

The overall aim is thus to contribute toward solving the scaling problem; i.e., how a macro-level description can be obtained consistent with the micro-level one, by defining transport equations on the macro-level. The aim of the present work, seen in this context, is to present the basis for a description of central transport phenomena, namely those due to thermal, chemical, mechanical, and gravitational forces. We shall propose a systematic, course-grained procedure that will be simple in practical use.

2. SYSTEM

Consider a heterogeneous system as illustrated by the (white) box in **Figure 1**. The system is a porous medium of fixed porosity filled with several immiscible fluids. There is net transport in one direction only, the x-direction. On the scale of measurement, the system is without structure. By zooming in, we see the pore scale. A collection of pores with two fluids is schematically shown in **Figure 2**.

A temperature, pressure, and/or chemical potential difference is applied between the inlet and the outlet, and these differences can be measured. The pressure difference Δp between the outlet and the inlet was defined for steady state conditions by Tallakstad et al. [19], as the time average of the fluctuating difference $\Delta p(t)$:

$$\Delta p = \frac{1}{t_\mathrm{e} - t_\mathrm{b}} \int_{t_\mathrm{b}}^{t_\mathrm{e}} \Delta p(t) dt. \tag{1}$$

Here t is the time. Subscript "b" denotes beginning and "e" denotes the end of the measurement. We adopt similar definitions for ΔT and $\Delta \mu_i$. It is possible, through application of separate inlet channels, to control the flow into and out of the system and find the flow of each component, to define the flow situation in **Figure 1**. In the presence of two immiscible phases, it is only possible to define the pressure difference between the inlet and the outlet for the phases, Δp^w and Δp^n, if there is continuity in the respective phases.

We will repeatedly use two-phase flow of single components as an example, where w indicates the most wetting and n the least wetting phase. We refer to them simply as the wetting and the non-wetting phase. In most of the paper we consider a multi-phase fluid. In the system pictured in **Figure 2**, there is flow within the REV in the direction of the pore. This is not necessarily the direction given by the overall pressure gradient. The flow on the macro-scale, however, is always in the direction of the pressure gradient. Net flow in other directions are zero due to isolation of the system in these directions. By flow on the macro-scale, we mean flow in the direction of the overall pressure gradient along the x-coordinate in **Figure 1**. The value of this average flow is of interest.

The representative volume element, REV, is constructed from a collection of pores like those contained in the red square in **Figure 2**. In **Figure 1**, three REVs are indicated (magenta structured squares). In a homogeneous system, statistical mechanical distributions of molecular properties lead to the macroscopic properties of a volume element. In a heterogeneous system like here, the statistical distributions are over the states within the REV. The collection of pores in the REV, cf. **Figure 2**, should be of a size that is large enough to provide meaningful

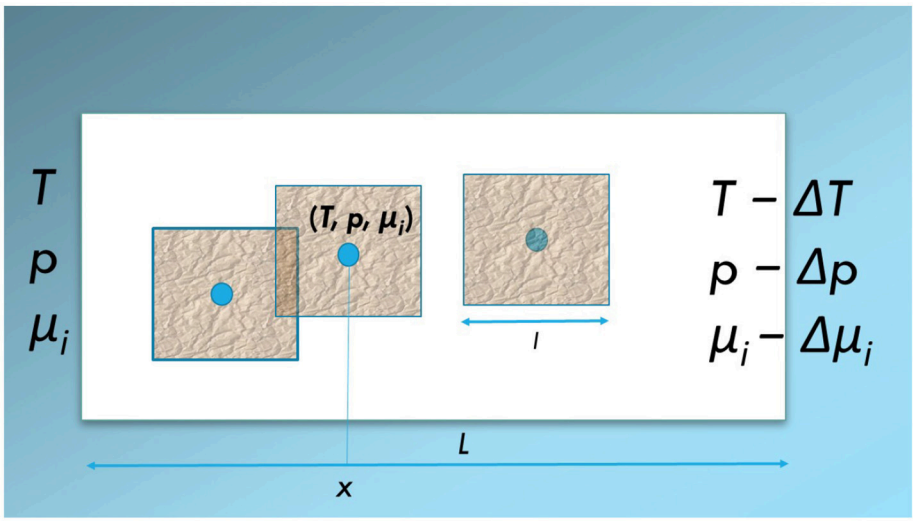

FIGURE 1 | Schematic illustration of a heterogeneous system (white box, length L) exposed to a difference in temperature, ΔT, pressure, Δp, or chemical potential $\Delta\mu_i$. The system is isolated in the $y,z-$directions. Net flows take place in the $x-$direction. Three representative elementary volumes, REVs (magenta squares, length l) are indicated. The REVs may overlap. Each is represented by a set of variables (p, T, μ_i) which defines a state (blue dot). Such states can be defined anywhere on the x-axis.

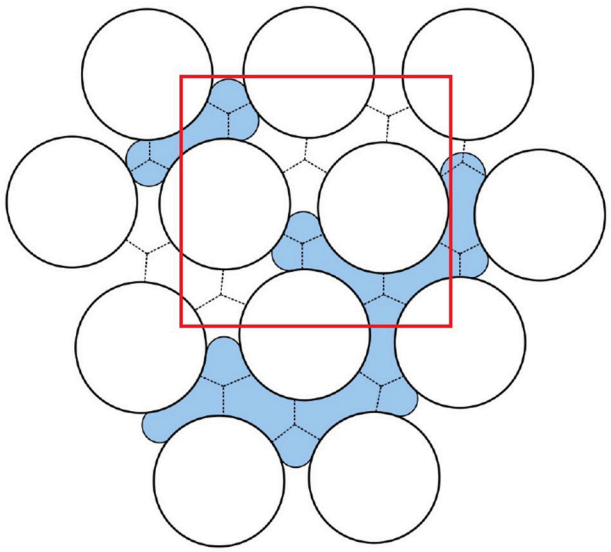

FIGURE 2 | A schematic collection of pores filled with two immiscible liquids. In order to compute the system properties, we define a REV. A REV is indicated in the figure by the red square. Courtesy of M. Vassvik.

values for the extensive variables, and therefore well defined intensive variables (see below, Equations 19 and 20), cf. section 3.2 below. Thermodynamic relations can be written for each REV.

State variables characterize the REV. They are represented by the (blue) dots in **Figure 1**. The size of the REV depends on its composition and other conditions. Typically, the extension of a REV, l, is large compared to the pore size of the medium, and small compared to the full system length L. This construction of a REV is similar to the procedure followed in smoothed particle hydrodynamics [20], cf. the discussion at the end of the work.

The REVs so constructed, can be used to make a path of states, over which we can integrate across the system. Each REV in the series of states, is characterized by variables T, p, μ_i, as indicated by the blue dots in **Figure 1**. Vice versa, each point in a porous medium can be seen as a center in a REV. The states are difficult to access directly, but can be accessed via systems in equilibrium with the states, as is normal in thermodynamics. This is discussed at the end of the work. We proceed to define the REV-variables.

3. PROPERTIES OF THE REV

3.1. Porosity and Saturation

Consider a solid matrix of constant porosity ϕ. We are dealing with a class of systems that are homogeneous in the sense that the typical pore diameter and pore surface area, on the average, are the same everywhere. There are m phases in the system. The pores are filled with a mixture of $m-1$ fluid phases; the solid matrix is phase number m. Properties will depend on the time, but this will not be indicated explicitly in the equations.

In a simple case, the phases are immiscible single components. The chemical constituents are then synonymous with a phase, and the number of phases is the number of components. The state of the REV can be characterized by the volumes of the fluid phases $V^{\alpha,\mathrm{REV}}, \alpha = 1,..,m-1$ and of the solid medium $V^{m,\mathrm{REV}}$. The total volume of the pores is

$$V^{p,\mathrm{REV}} \equiv \sum_{\alpha=1}^{m-1} V^{\alpha,\mathrm{REV}}. \tag{2}$$

while the volume of the REV is

$$V^{\mathrm{REV}} \equiv V^{m,\mathrm{REV}} + V^{p,\mathrm{REV}} + \sum_{\alpha>\beta>\delta=1}^{m} V^{\alpha\beta\delta,\mathrm{REV}}. \quad (3)$$

Superscript REV is used to indicate a property of the REV. The last term is the sum of the excess volumes of the three-phase contact lines. While the excess volume of the surfaces is zero by definition, this is not the case for the three-phase contact lines. The reason is that the dividing surfaces may cross each other at three lines which have a slightly different location. The corresponding excess volume is in general very small, and will from now on be neglected. This gives the simpler expression

$$V^{\mathrm{REV}} \equiv V^{m,\mathrm{REV}} + V^{p,\mathrm{REV}}. \quad (4)$$

All these volumes can be measured.

The porosity, ϕ, and the saturation, $\hat{S}$, are given by

$$\phi \equiv \frac{V^{p,\mathrm{REV}}}{V^{\mathrm{REV}}} \quad \text{and} \quad \hat{S}^{\alpha} \equiv \frac{V^{\alpha,\mathrm{REV}}}{V^{p,\mathrm{REV}}} = \frac{V^{\alpha,\mathrm{REV}}}{\phi V^{\mathrm{REV}}}. \quad (5)$$

The porosity and the saturation are intensive variables. They do not depend on the size of the REV. They have therefore no superscript. It follows from these definitions that

$$\sum_{\alpha=1}^{m-1} \hat{S}^{\alpha} = 1 \quad \text{and} \quad V^{m,\mathrm{REV}} = (1-\phi)\, V^{\mathrm{REV}} \quad (6)$$

In addition to the volumes of the different bulk phases (they are fluids or solids) $m \geq \alpha \geq 1$, there are interfacial areas, Ω, between each two phases in the REV: $\Omega^{\alpha\beta,\mathrm{REV}}$, $m \geq \alpha > \beta \geq 1$. The total surface area of the pores is measurable. It can be split between various contributions

$$\Omega^{p,\mathrm{REV}} = \sum_{\alpha=1}^{m-1} \Omega^{m\alpha,\mathrm{REV}} \quad (7)$$

When the surface is not completely wetted, we can estimate the surface area between the solid m and the fluid phase α, from the total pore area available and the saturation of the component.

$$\Omega^{m\alpha,\mathrm{REV}} = \hat{S}^{\alpha}\Omega^{p,\mathrm{REV}} \quad (8)$$

This estimate is not correct for strongly wetting components or dispersions. In those cases, films can form at the walls, and $\Omega^{m\alpha,\mathrm{REV}}$ is not proportional to $\hat{S}^{\alpha}$. In the class of systems we consider, all fluids touch the wall, and there are no films of one fluid between the wall and another fluid.

3.2. Thermodynamic Properties of the REV

We proceed to define the thermodynamic properties of the REV within the volume V^{REV} described above. In addition to the volume, there are other additive variables. They are the masses, the energy, and the entropy. We label the components (the chemical constituents) using italic subscripts. There are in total n components distributed over the phases, surfaces, and contact lines. The mass of component i, M_i^{REV}, in the REV is the sum of bulk masses, $M_i^{\alpha,\mathrm{REV}}$, $m \geq \alpha \geq 1$, the excess interfacial masses, $M_i^{\alpha\beta,\mathrm{REV}}$, $m \geq \alpha > \beta \geq 1$, and the excess line masses, $M_i^{\alpha\beta\delta,\mathrm{REV}}$, $m \geq \alpha > \beta > \delta \geq 1$.

$$M_i^{\mathrm{REV}} = \sum_{\alpha=1}^{m} M_i^{\alpha,\mathrm{REV}} + \sum_{\alpha>\beta=1}^{m} M_i^{\alpha\beta,\mathrm{REV}} + \sum_{\alpha>\beta>\delta=1}^{m} M_i^{\alpha\beta\delta,\mathrm{REV}} \quad (9)$$

There is some freedom in how we allocate the mass to the various phases and interfaces [11, 21]. We are e.g., free to choose a dividing surface such that one $M_i^{\alpha\beta,\mathrm{REV}}$ equals zero. A zero excess mass will simplify the description, but will introduce a reference. The dividing surface with zero $M_i^{\alpha\beta,\mathrm{REV}}$ is the equimolar surface of component i. The total mass of a component in the REV is, however, *independent* of the location of the dividing surfaces. From the masses, we compute the various mass densities

$$\rho_i \equiv \frac{M_i^{\mathrm{REV}}}{V^{\mathrm{REV}}}, \quad \rho_i^{\alpha} \equiv \frac{M_i^{\alpha,\mathrm{REV}}}{V^{\alpha,\mathrm{REV}}},$$
$$\rho_i^{\alpha\beta} \equiv \frac{M_i^{\alpha\beta,\mathrm{REV}}}{\Omega^{\alpha\beta,\mathrm{REV}}}, \quad \rho_i^{\alpha\beta\delta} \equiv \frac{M_i^{\alpha\beta\delta,\mathrm{REV}}}{\Lambda^{\alpha\beta\delta,\mathrm{REV}}} \quad (10)$$

where ρ_i and ρ_i^{α} have dimension kg.m^{-3}, $\rho_i^{\alpha\beta}$ has dimension kg.m^{-2} and $\rho_i^{\alpha\beta\delta}$ has dimension kg.m^{-1}.

All densities are for the REV. If we increase the size of the REV, by for instance doubling its size, V^{REV}, M_i^{REV} and other extensive variables will all double. They will double, by doubling all contributions to these quantities. But this is not the case for the density ρ_i or the other densities. They remain the same, independent of the size of the REV. This is true also for the densities of the bulk phases, surfaces, and contact lines. Superscript REV is therefore not used for the densities.

Within one REV there are natural fluctuations in the densities. But the densities make it possible to give a description on the macro-scale independent of the precise size of the REV. The densities will thus be used in the balance equations on the macro-scale. The density ρ_i^{α} may vary somewhat in V^{α}. We can then find M_i^{α} as the integral of ρ_i^{α} over V^{α}. Equation (10) then gives the volume-averaged densities.

The internal energy of the REV, U^{REV}, is the sum of bulk internal energies, $U^{\alpha,\mathrm{REV}}$, $m \geq \alpha \geq 1$, the excess interfacial internal energies, $U^{\alpha\beta,\mathrm{REV}}$, $m \geq \alpha > \beta \geq 1$, and the excess line internal energies, $U^{\alpha\beta\delta,\mathrm{REV}}$, $m \geq \alpha > \beta > \delta \geq 1$:

$$U^{\mathrm{REV}} = \sum_{\alpha=1}^{m} U^{\alpha,\mathrm{REV}} + \sum_{\alpha>\beta=1}^{m} U^{\alpha\beta,\mathrm{REV}} + \sum_{\alpha>\beta>\delta=1}^{m} U^{\alpha\beta\delta,\mathrm{REV}} \quad (11)$$

The summation is taken over all phases, interfaces, and contact lines (if non-negligible). We shall see in a subsequent paper how these contributions may give specific contributions to the driving force. The internal energy densities are defined by

$$u \equiv \frac{U^{\mathrm{REV}}}{V^{\mathrm{REV}}}, \quad u^{\alpha} \equiv \frac{U^{\alpha,\mathrm{REV}}}{V^{\alpha,\mathrm{REV}}},$$

$$u^{\alpha\beta} \equiv \frac{U^{\alpha\beta,\mathrm{REV}}}{\Omega^{\alpha\beta,\mathrm{REV}}}, \quad u^{\alpha\beta\delta} \equiv \frac{U^{\alpha\beta\delta,\mathrm{REV}}}{\Lambda^{\alpha\beta\delta,\mathrm{REV}}} \tag{12}$$

Their dimensions are J.m^{-3} (u, u^{α}), J.m^{-2} ($u^{\alpha\beta}$), and J.m^{-1} ($u^{\alpha\beta\delta}$), respectively.

The entropy in the REV, S^{REV}, is the sum of the bulk entropies, $S^{\alpha,\mathrm{REV}}$, $m \geq \alpha \geq 1$, the excess entropies, $S^{\alpha\beta,\mathrm{REV}}$, $m \geq \alpha > \beta \geq 1$, the excess line entropies, $S^{\alpha\beta\delta,\mathrm{REV}}$, $m \geq \alpha > \beta > \delta \geq 1$, and a configurational contribution, $S^{\mathrm{REV}}_{\mathrm{conf}}$, from the geometrical distribution of the fluid phases within the pores:

$$S^{\mathrm{REV}} = \sum_{\alpha=1}^{m} S^{\alpha,\mathrm{REV}} + \sum_{\alpha>\beta=1}^{m} S^{\alpha\beta,\mathrm{REV}} + \sum_{\alpha>\beta>\delta=1}^{m} S^{\alpha\beta\delta,\mathrm{REV}} + S^{\mathrm{REV}}_{\mathrm{conf}} \tag{13}$$

The entropy densities are defined by

$$s \equiv \frac{S^{\mathrm{REV}}}{V^{\mathrm{REV}}}, \quad s^{\alpha} \equiv \frac{S^{\alpha,\mathrm{REV}}}{V^{\alpha,\mathrm{REV}}}, \quad s^{\alpha\beta} \equiv \frac{S^{\alpha\beta,\mathrm{REV}}}{\Omega^{\alpha\beta,\mathrm{REV}}},$$
$$s^{\alpha\beta\delta} \equiv \frac{S^{\alpha\beta\delta,\mathrm{REV}}}{\Lambda^{\alpha\beta\delta,\mathrm{REV}}}, \quad s_{\mathrm{conf}} \equiv \frac{S^{\mathrm{REV}}_{\mathrm{conf}}}{V^{\mathrm{REV}}} \tag{14}$$

and have the dimensions J.K^{-1}.m^{-3} ($s, s^{\alpha}, s_{\mathrm{conf}}$), J.K^{-1}.m^{-2} ($s^{\alpha\beta}$), and J.K^{-1}.m^{-1} ($s^{\alpha\beta\delta}$), respectively. To explain the configurational contribution in more detail; consider the example of stationary two-phase flow in a single tube of varying diameter described by Sinha et al. [22]. The tube contains one bubble of one fluid in the other. The bubble touches the wall; it can not form a film between the tube wall and the other fluid. The probability per unit of length of the tube to find the center of mass of the bubble at position x_b, was $\Pi(x_b)$ [22]. Knowing this probability distribution, we can compute the entropy of an ensemble of single tubes (in this case a very long tube composed of the single ones). It is equal to

$$S^{\mathrm{REV}}_{\mathrm{conf}} = k_{\mathrm{B}} \int_0^{\ell} \Pi(x_b) \ln \ell \Pi(x_b) dx_b \tag{15}$$

For a network of pores it is more appropriate to give the probability distribution for the fluid-fluid interfaces. This has not yet been done explicitly.

For the volume, Equations (2) and (4) apply when the contact lines give a negligible contribution. The dividing surfaces have by definition no excess volume. For all the other extensive thermodynamic variables, like the enthalpy, Helmholtz energy, Gibbs energy, and the grand potential, relations similar to Equations (11) and (13) apply. We shall later show how this affects the driving forces [18].

To summarize this section; we have defined a basis set of variables for a class of systems, where these variables are additive in the manner shown. From the set of REV-variables we obtain the densities, u, s, or ρ_i to describe the heterogeneous system on the macro-scale. A series of REVs of this type, is needed for integration across the system, see section 5.

3.3. REV Size Considerations

As an illustration of the REV construction, consider the internal energy of two isothermal, immiscible and incompressible fluids (water and decane) flowing in a Hele-Shaw type cell composed of silicone glass beads. The relevant properties of the fluids can be found in **Table 1** The porous medium is a hexagonal network of 3,600 links, as illustrated in **Figure 3**. The network is periodic in the longitudinal and the transverse directions and a pressure difference of 1.8×10^4 Pa drives the flow in the longitudinal direction. The overall saturation of water is 0.4. The network flows were simulated using the method of Aker et al. [23], see [24] for details.

TABLE 1 | Fluid properties used to compute the candidate REV internal energy, for a network containing water (n) and decane (w) within silica glass beads (p) at atmospheric pressure and 293 K.

Parameter	Value	Unit	References
η^w	9.2×10^{-4}	Pa.s	[25]
η^n	1.0×10^{-3}	Pa.s	[25]
γ^{wp}	2.4×10^{-2}	N.m^{-1}	[26]
γ^{np}	7.3×10^{-2}	N.m^{-1}	[26]
γ^{wn}	5.2×10^{-2}	N.m^{-1}	[27]
$-u^w$	2.8×10^8	J.m^{-3}	[25]
$-u^n$	3.4×10^8	J.m^{-3}	[25]

The internal energy of the REV is, according to section 3.2, a sum over the two fluid bulk contributions and three interface contributions,

$$\begin{aligned} U^{\mathrm{REV}} &= U^{m,\mathrm{REV}} + \sum_{i\in\{w,n\}} \left\{U^{i,\mathrm{REV}}\right\} + U^{wn,\mathrm{REV}} + U^{np,\mathrm{REV}} \\ &\quad + U^{wp,\mathrm{REV}} \qquad (16) \\ &= U^{m,\mathrm{REV}} + V^{p,\mathrm{REV}} \sum_{i\in\{w,n\}} \left\{\hat{S}^i u^i\right\} \\ &\quad + u^{wn}\Omega^{wn,\mathrm{REV}} + u^{np}\Omega^{np,\mathrm{REV}} + u^{wp}\Omega^{wp,\mathrm{REV}}. \qquad (17) \end{aligned}$$

where, u^i is the internal energy density of phase i and u^{ij} is the excess internal energy per interfacial area between phase i and phase j. We assume u^i and u^{ij} to be constant. For simplicity, u^{ij} is approximated by interfacial tension, denoted γ^{ij}. The internal energy of the porous matrix is constant in this example and is therefore set to zero.

Candidate REVs are of different sizes, see **Table 2**. The 5.4 × 6 mm (green), and 10.4 × 12 mm (blue) candidate REVs are shown in **Figure 3**. For all candidate REVs, U^{REV} is calculated according to Equation (17) at each time step. Since the measured saturations and interfacial areas are fluctuating in time, so is the internal energy. A time-step weighted histogram of the internal energy presents the probability distribution.

The probability distributions of U^{REV} are shown in **Figure 4** for the 5.2 × 6 mm (green) and 10.4 × 12 mm (blue) candidate REVs. In both plots, the vertical lines represent the internal energy the REV would have if it were occupied by one of the fluids alone. We denote the difference in internal energy between these two single-phase states by ΔU^{REV}.

The mean value of the U^{REV} for all candidate REVs are given in **Table 2**, along with mean density $u = U^{\mathrm{REV}}/V^{\mathrm{REV}}$ and the standard deviation of U^{REV} divided by ΔU^{REV}. The latter

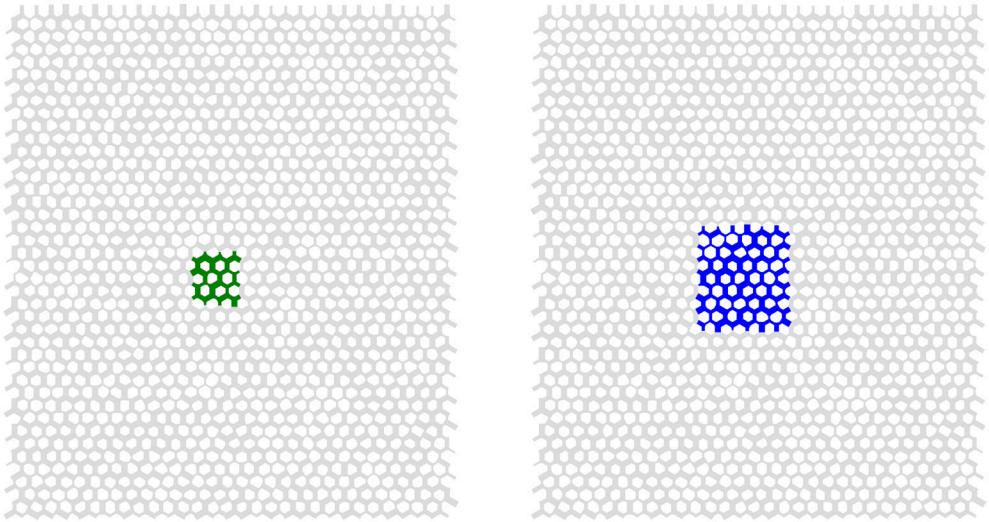

FIGURE 3 | Illustration of the link network and two of the candidate REVs under consideration. The left candidate REV (green) is 5.2 × 6 mm and the right candidate REV (blue) is 10.4 × 12 mm.

TABLE 2 | Mean values of U^{REV} and u for candidate REVs of different sizes, along with the standard deviation of U^{REV} divided by ΔU^{REV}. The latter quantity represents a measure of the relative size of the fluctuations in U^{REV}.

Candidate REV Size	Mean $\left(U^{\mathrm{REV}}\right)$ /J	$\pm\left(U^{\mathrm{REV}}\right)$ $/\Delta U^{\mathrm{REV}}$	Mean (u) / 10^7 J m^{-3}
5.2 × 6.0 mm	−2.82	0.069	−6.04
7.8 × 9.0 mm	−5.46	0.047	−5.19
10.4 × 12.0 mm	−9.60	0.037	−5.13
13.0 × 15.0 mm	−15.4	0.028	−5.25
15.6 × 18.0 mm	−22.2	0.024	−5.27
18.3 × 21.0 mm	−29.9	0.021	−5.22
20.8 × 24.0mm	−39.1	0.017	−5.23

quantity is a measure of the relative size of the fluctuations in U^{REV}. Due to the additivity of U^{REV}, the mean values of U^{REV} increases roughly proportional to the candidate REV size. But this happens only after the REV has reached a minimum size, here 7.8 × 9.0 mm. For the larger candidate REVs, the mean value of u changes little as the size increases. The relative size of the fluctuations in U^{REV} decreases in proportion to the linear size of the candidate REVs.

This example indicates that it makes sense to characterize the internal energy of a porous medium in terms of an internal energy density as defined by Equation (11), given that the size of the REV is appropriately large. About 100 links seem to be enough in this case. This will vary with the type of porous medium, cf. the 2D square network model of Savani et al. [28].

4. HOMOGENEITY ON THE MACRO-SCALE

Before we address any transport problems, consider again the system pictured in **Figure 1** (the white box). All REVs have variables and densities as explained above. By integrating to a somewhat larger volume V, using the densities defined, we obtain the set of basis variables, (U, S, M_i), in V. The internal energy U of the system is an Euler homogeneous function of first order in S, V, M_i:

$$U(\lambda S, \lambda V, \lambda M_i) = \lambda U(S, V, M_i) \tag{18}$$

where λ is a multiplication factor. The internal energy U, volume V, entropy S, and component mass M_i, obey therefore the Gibbs equation;

$$dU = \left(\frac{\partial U}{\partial S}\right)_{V,M_i} dS + \left(\frac{\partial U}{\partial V}\right)_{S,M_i} dV + \sum_{i=1}^{n} \left(\frac{\partial U}{\partial M_i}\right)_{S,V,M_j} dM_i \tag{19}$$

No special notation is used here to indicate that U, S, V, M_i are properties on the macro-scale. Given the heterogeneous nature on the micro-scale, the internal energy has contributions from all parts of the volume V, including from the excess surface and line energies. By writing Equation (18) we find that the normal thermodynamic relations apply for the heterogeneous system at equilibrium, for the additive properties U, S, V, M_i, obtained from sums of the bulk-, excess surface-, and excess line-contributions.

We can then move one more step and use Gibbs equation to *define* the temperature, the pressure, and chemical potentials on the macro-scale as partial derivatives of U:

$$T \equiv \left(\frac{\partial U}{\partial S}\right)_{V,M_i}, \quad p \equiv -\left(\frac{\partial U}{\partial V}\right)_{S,M_i}, \quad \mu_i \equiv \left(\frac{\partial U}{\partial M_i}\right)_{S,V,M_j} \tag{20}$$

The temperature, pressure, and chemical potentials on the macro-scale are, with these formulas, defined as partial derivatives of the internal energy. This is normal in

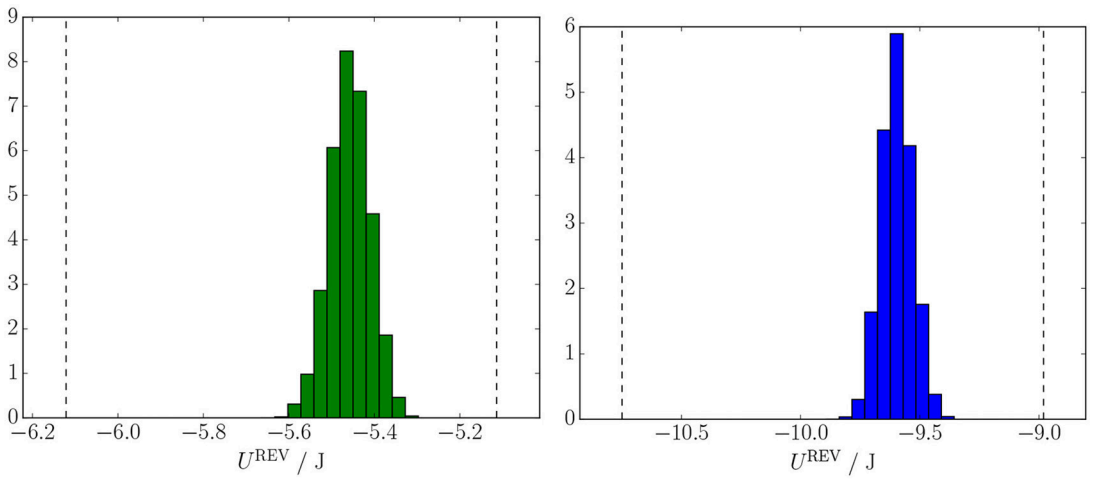

FIGURE 4 | Probability distributions of internal energy in two the candidate REVs. The left candidate REV (green) is 5.2 ×6 mm and the right candidate REV (blue) is 10.4 ×12 mm. In each plot, the left dashed line represents the internal energy the candidate REV would have if it contained non-wetting fluid only and the right dashed line represents the internal energy the candidate REV would have if it contained wetting fluid only.

thermodynamics, but the meaning is now extended. In a normal homogeneous, isotropic system at equilibrium, the temperature, pressure, and chemical equilibrium refer to a homogeneous volume element. The temperature of the REV is a temperature representing all phases, interfaces and lines combined, and the chemical potential of i is similarly obtained from the internal energy of all phases. Therefore, there are only one T, p, and μ_i for the REV. The state can be represented by the (blue) dots in **Figure 1**.

On the single pore level, the pressure and temperature in the REV will have a distribution. In the two immiscible-fluid-example the pressure, for instance, will vary between a wetting and a non-wetting phase because of the capillary pressure. One may also envision that small phase changes in one component (e.g., water) leads to temperature variations due to condensation or evaporation. Variations in temperature will follow changes in composition.

The intensive properties are *not* averages of the corresponding entities on the pore-scale over the REV. This was pointed out already by Gray and Hassanizadeh [3]. The definitions are derived from the total internal energy only, and this makes them uniquely defined. It is interesting that the intensive variables do not depend on how we split the energy into into bulk and surface terms inside the REV.

By substituting Equation (20) into Equation (19) we obtain the Gibbs equation for a change in total internal energy on the macro-scale

$$dU = TdS - pdV + \sum_{i=1}^{n} \mu_i dM_i \tag{21}$$

As a consequence of the condition of homogeneity of the first order, we also have

$$U = TS - pV + \sum_{i=1}^{n} \mu_i M_i \tag{22}$$

The partial derivatives T, p and μ_i are homogeneous functions of the zeroth order. This implies that

$$T(\lambda S, \lambda V, \lambda M_i) = T(S, V, M_i) \tag{23}$$

Choosing $\lambda = 1/V$ it follows that

$$T(S, V, M_i) = T(s, 1, \rho_i) = T(s, \rho_i) \tag{24}$$

The temperature therefore depends only on the subset of variables $s \equiv S/V, \rho_i \equiv M_i/V$ and not on the complete set of variables S, V, M_i. The same is true for the pressure, p, and the chemical potentials, μ_i. This implies that T, p and μ_i are not independent. We proceed to repeat the standard derivation of the Gibbs-Duhem equation which makes their interdependency explicit.

The Gibbs equation on the macro-scale in terms of the densities follows using Equations (21) and (22)

$$du = Tds + \sum_{i=1}^{n} \mu_i d\rho_i \tag{25}$$

which can alternatively be written as

$$ds = \frac{1}{T} du - \frac{1}{T} \sum_{i=1}^{n} \mu_i d\rho_i \tag{26}$$

The Euler equation implies

$$u = Ts - p + \sum_{i=1}^{n} \mu_i \rho_i \tag{27}$$

By differentiating Equation (27) and subtracting the Gibbs equation (25), we obtain in the usual way the Gibbs-Duhem equation:

$$dp = sdT + \sum_{i=1}^{n} \rho_i d\mu_i$$

This equation makes it possible to calculate p as a function of T and μ_i and shows how these quantities depend on one another.

We have now described the heterogeneous porous medium by a limited set of coarse-grained thermodynamic variables. These average variables and their corresponding temperature, pressure, and chemical potentials, describe a coarse-grained homogeneous mixture with variables which reflect the properties of the class of porous media. In standard equilibrium thermodynamics, Gibbs' equation applies to a homogeneous phase. We have extended this use to be applicable for heterogeneous systems at the macro-scale. On this scale, the heterogeneous system (the REV) is then regarded as being in local equilibrium. Whether or not the chosen procedure is viable, remains to be tested. We refer to the section 7 of this paper for more discussion and to a paper to follow [18] for an experimental program.

5. ENTROPY PRODUCTION IN POROUS MEDIA

Gradients in mass- and energy densities produce changes in the variables on the macro-scale. These lead to transport of heat and mass. Our aim is to find the equations that govern this transport across the REV. We therefore expose the system to driving forces and return to **Figure 1**.

The balance equations for masses and internal energy of a REV are

$$\frac{\partial \rho_i}{\partial t} = -\frac{\partial}{\partial x} J_i \tag{28}$$

$$\frac{\partial u}{\partial t} = -\frac{\partial}{\partial x} J_u = -\frac{\partial}{\partial x}\left[J_q^{'} + \sum_{i=1}^{n} J_i H_i \right] \tag{29}$$

The transport on this scale is in the $x-$direction only. The mass fluxes, J_i, and the flux of internal energy, J_u, are all macro-scale fluxes. The internal energy flux is the sum of the measurable (or sensible) heat flux, $J_q^{'}$ and the partial specific enthalpy (latent heat), H_i (in J.kg^{-1}) times the component fluxes, J_i, see [3, 9, 11] for further explanations. Component m (the porous medium) is not moving and is the convenient frame of reference for the fluxes.

The entropy balance on the macro-scale is

$$\frac{\partial s}{\partial t} = -\frac{\partial}{\partial x} J_s + \sigma \tag{30}$$

Here J_s is the entropy flux, and σ is the entropy production which is positive definite, $\sigma \geq 0$ (the second law of thermodynamics). We can now derive the expression for σ in the standard way [9, 11], by combining the balance equations with Gibbs' equation. The entropy production is the sum of all contributions within the REV.

In the derivations, we assume that the Gibbs equation is valid for the REV also when transport takes place. Droplets can form at high flow rates, while ganglia may occur at low rates. We have seen above that there is a minimum size of the REV, for which the Gibbs equation can be written. When we assume that the Gibbs equation applies, we implicitly assume that there exists a uniquely defined state. The existence of such an ergodic state was postulated by Hansen and Ramstad [29]. Valavanides and Daras used it in their DeProF model for two-phase flow in pore networks [30]. Experimental evidence for the assumption was documented by Erpelding [31].

Under the conditions that we demand valid for the REV, the Gibbs Equation (26) keeps its form during a time interval dt, giving

$$\frac{\partial s}{\partial t} = \frac{1}{T}\frac{\partial u}{\partial t} - \frac{1}{T}\sum_{i=1}^{n} \mu_i \frac{\partial \rho_i}{\partial t} \tag{31}$$

We can now introduce the balance equations for mass and energy into this equation, see [11] for details. By comparing the result with the entropy balance, Equation (30), we identify first the entropy flux, J_s,

$$J_s = \frac{1}{T} J_q^{'} + \sum_{i=1}^{n} J_i S_i \tag{32}$$

The entropy flux is composed of the sensible heat flux over the temperature plus the sum of the specific entropies carried by the components. The form of the entropy production, σ, depends on our choice of the energy flux, J_u or $J_q^{'}$. The choice of form is normally motivated by practical wishes; what is measurable or computable. We have

$$\begin{aligned} \sigma &= J_u \frac{\partial}{\partial x}(\frac{1}{T}) - \sum_{i=1}^{n} J_i \frac{\partial}{\partial x}(\frac{\mu_i}{T}) \\ &= J_q^{'} \frac{\partial}{\partial x}(\frac{1}{T}) - \frac{1}{T}\sum_{i=1}^{n} J_i \frac{\partial}{\partial x}\mu_{i,T} \end{aligned} \tag{33}$$

These expressions are equivalent formulations of the same physical phenomena. When we choose J_u as variable with the conjugate force $\partial(1/T)/\partial x$, the mass fluxes are driven by minus the gradient in the Planck potential μ_i/T. When, on the other hand we choose $J_q^{'}$ as a variable with the conjugate force $\partial(1/T)/\partial x$, the mass fluxes are driven by minus the gradient in the chemical potential at constant temperature over this temperature. The entropy production defines the independent thermodynamic driving forces and their conjugate fluxes. We have given two possible choices above to demonstrate the flexibility. The last expression is preferred for analysis of experiments.

In order to find the last line in Equation (33) from the first, we used the thermodynamic identities $\mu_i = H_i - TS_i$ and $\partial(\mu_i/T)/\partial(1/T) = H_i$ as well as the expression for the energy flux given in Equation (29). Here S_i is the partial specific entropy (in J.kg^{-1}.K^{-1}).

5.1. The Chemical Potential at Constant Temperature

The derivative of the chemical potential at constant temperature is needed in the driving forces in the second line for σ in Equation

(33). For convenience we repeat its relation to the full chemical potential [9]. The differential of the full chemical potential is:

$$d\mu_i = -S_i dT + V_i dp + \sum_{j=1}^{n} \left(\frac{\partial \mu_i}{\partial M_j}\right)_{p,T,M_i} dM_j \tag{34}$$

where S_i, V_i, and $(\partial \mu_i/\partial M_j)_{p,T,M_i}$ are partial specific quantities. The partial specific entropy and volume are equal to:

$$S_i = -\left(\frac{\partial \mu_i}{\partial T}\right)_{p,M_j}, \; V_i = \left(\frac{\partial \mu_i}{\partial p}\right)_{T,M_j} \tag{35}$$

and the last term of Equation (33) is denoted by

$$d\mu_i^c = \sum_{j=1}^{n} \left(\frac{\partial \mu_i}{\partial M_j}\right)_{p,T,M_i} dM_j \tag{36}$$

By reshuffling, we have the quantity of interest as the differential of the full chemical potential plus an entropic term;

$$d\mu_{i,T} \equiv d\mu_i + S_i dT = V_i dp + d\mu_i^c \tag{37}$$

The differential of the chemical potential at constant temperature is

$$\frac{d\mu_{i,T}}{dx} = \frac{d\mu_i^c}{dx} + V_i \frac{dp}{dx} \tag{38}$$

With equilibrium in the gravitational field, the pressure gradient is $dp/dx = -\rho g$, where ρ is the total mass density and g is the acceleration of free fall [32]. The well known separation of components in the gravitational field is obtained, with $d\mu_{i,T} = 0$ and

$$\frac{d\mu_i^c}{dx} = \frac{RT}{W_i} \frac{d \ln(\hat{S}_i y_i)}{dx} = V_i \rho g \tag{39}$$

where W_i is the molar mass (in kg.mol^{-1}), $\hat{S}_i$ the saturation, and y_i the activity coefficient of component i. The gas constant, R, has dimension J.K^{-1}.mol^{-1}. The gradient of the mole fraction of methane and decane in the geothermal gradient of the fractured carbonaceous Ekofisk oil field, was estimated to 5×10^{-4}m^{-1} [33], in qualitative agreement with observations. We replace $d\mu_{i,T}$ below using these expressions.

It follows from Euler homogeneity that the chemical potentials in a (quasi-homogeneous) mixture are related by $0 = SdT - Vdp + \sum_{j=1}^{n} \rho_j d\mu_j$, which is Gibbs-Duhem's equation. By introducing Equation 37 into this equation we obtain an equivalent expression, to be used below:

$$0 = \sum_{j=1}^{n} \rho_j d\mu_j^c \tag{40}$$

6. TRANSPORT OF HEAT AND TWO-PHASE FLUIDS

Consider again the case of two immiscible fluids of single components, one more wetting (w) and one more non-wetting (n). The entropy production in Equation (33) gives,

$$\sigma = J'_q \frac{\partial}{\partial x}\left(\frac{1}{T}\right) - \frac{1}{T}\left(J_w \frac{\partial \mu_{w,T}}{\partial x} + J_n \frac{\partial \mu_{n,T}}{\partial x}\right) \tag{41}$$

The solid matrix is the frame of reference for transport, $J_r = 0$ and does not contribute to the entropy production. The volume flux is frequently measured, and we wish to introduce this as new variable

$$J_V = J_n V_n + J_w V_w \tag{42}$$

Here J_V has dimension (m^3.m^{-2}.s^{-1} = m.s^{-1}), and the partial specific volumes have dimension m^3.kg^{-1}. The volume flows used by Hansen et al. [16] are related to ours by $J_n \upsilon_n = \hat{S}_n \upsilon_n$, $J_w \upsilon_w = \hat{S}_w \upsilon_w$ and $J_V = \upsilon = \hat{S}_n \upsilon_n + \hat{S}_w \upsilon_w$.

The chemical potential of the solid matrix may not vary much if the composition of the solid is constant across the system. We assume that this is the case ($d\mu_m^c \approx 0$), and use Equation (40) to obtain

$$0 = \rho_n d\mu_n^c + \rho_w d\mu_w^c \tag{43}$$

The entropy production is invariant to the choice of variables. We can introduce the relations above and the explicit expression for $d\mu_{i,T}$ into Equation (41), and find the practical expression:

$$\sigma = J'_q \frac{\partial}{\partial x}\left(\frac{1}{T}\right) - J_V \frac{1}{T}\frac{\partial p}{\partial x} - \nu_D \frac{\rho_w}{T}\frac{\partial \mu_w^c}{\partial x} \tag{44}$$

In the last line, the difference velocity ν_D is

$$\nu_D = \frac{J_w}{\rho_w} - \frac{J_n}{\rho_n} \tag{45}$$

This velocity (in m/s) describes the relative movement of the two components within the porous matrix on the macro-scale. In other words, it describes the ability of the medium to separate components. The main driving force for separation is the chemical driving force, related to the gradient of the saturation. The equation implies that also temperature and pressure gradients may play a role for the separation.

The entropy production has again three terms, one for each independent driving force. With a single fluid, the number of terms is two. The force conjugate to the heat flux is again the gradient of the inverse temperature. The entropy production, in the form we can obtain, Equations (41) or (44), dictates the constitutive equations of the system.

6.1. A Path of Sister Systems

As pointed out above, through the construction of the REV we were able to create a continuous path through the system, defined by the thermodynamic variables of the REVs. The path was illustrated by a sequence of dots in **Figure 1**. Such a path

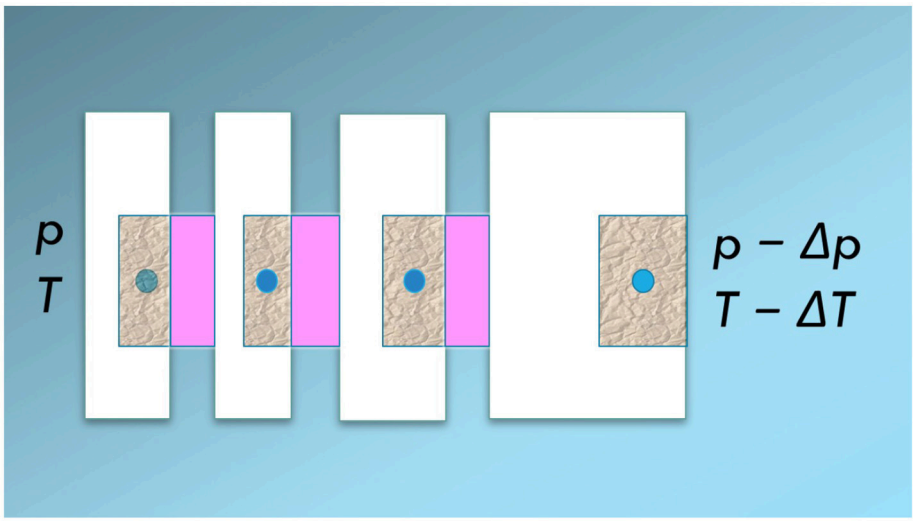

FIGURE 5 | A one-dimensional heterogeneous system cut into slices. Each cut is brought in equilibrium with a homogeneous (pink) mixture at the same temperature and pressure as the REV.

must exist, to make integration possible. Also continuum mixture theory hypothesizes such a path [4]: Hilfer introduced a series of *mixture* states, to define an integration path across the porous system, see e.g., [4].

The path created in section 2 is sufficient as a path of integration across the medium. The access to and measurement of properties in the REVs is another issue. It is difficult, if not impossible, to measure *in situ* as stated upfront. The measurement probe has a minimum extension (of some mm), and the measurement will represent an average over the surface of the probe. For a phase with constant density, the average is well-defined and measurable. A link between the state of the REV and a state where measurements are possible, is therefore needed. We call the state that provides this link a sister state.

Consider again the path of REVs in the direction of transport. To create the link between the REV and its sister state, consider the system divided into slices, see **Figure 5**. The slice (the sister system) contains homogeneous (pink) phases in equilibrium with the REV at the chosen location.

We hypothesize that we can find such sister states; in the form of a multi-component mixture with temperature, pressure, and composition such that equilibrium can be obtained with the REV-variables at any slice position. The variables of the sister state can then be measured the normal way. The chemical potential of a component in the sister state can, for instance, be found by introducing a vapor phase above this state and measure the partial vapor pressure. We postulate thus that a sister state can be found, that obey the conditions

$$T = T^s \tag{46}$$

$$p = p^s \tag{47}$$

$$\mu_i = \mu_i^s \tag{48}$$

Here $i = 1, ..., n$ are the components in the REV, and superscript s denotes the sister state. With the sister states available, we obtain an experimental handle on the variables of the porous medium. The hypothesis must be checked, of course.

The series of sister states have the same boundary conditions as the REV-states, by construction, and the overall driving forces will be the same. Between the end states, we envision the non-equilibrium system as a staircase. Each step in the stair made up of a REV is in equilibrium with a step of the sister-state-stair. Unlike the states inside the porous medium, the sister states are accessible for measurements, or determination of T, p, and μ_i. The driving forces of transport can then be described by the sequence of the sister states.

7. DISCUSSION

We have shown in this work how it is possible to extend the method of classical non-equilibrium thermodynamics [9] to describe transport in porous media. This was possible by

- constructing a REV in terms of a basis set of additive variables
- assuming that the REV is Euler homogeneous of degree one in the basis set.

The method is developed in the same manner as the classical theory is, but it extends the classical theory through the variable choice. The assumption about Euler homogeneity is the same for homogeneous (classical) as well as the heterogeneous porous media. The new variable set is necessary in order to account for the presence of the porous medium, i.e., the contributions from interfaces and contact line energies. Film formation in the pore is excluded. The properties of the porous medium will therefore enter in the definition of the variable set. The consequences of the choice will be elaborated in an article to come [18].

The classical equations have been written for single-phase systems, as these can be regarded as homogeneous on the molecular scale [34]. Equations (41) and (44), for instance, are well-established in theory of transport for polymer membranes,

see e.g., [34]. The idea of the sister states to define the state of a porous media with larger pores and immiscible phases was inspired by this. The way of dealing with lack of knowledge of variables inside the system was for instance used in polymer membrane transport long ago, see [35, 36]. The procedure, to introduce a series of equilibrium states, each state in equilibrium with the membrane at some location between the external boundaries, was first used by Scatchard [35], and experimentally verified much later [36, 37].

With the condition of Euler homogeneity we can set up the Gibbs equation, which is essential in the derivation of the entropy production. The total entropy production follows directly from the new set of variables and Euler homogeneity. This procedure is new, when compared to the literature where focus was set on the single phases, interfaces and contact lines [2, 3, 5].

The REV obeys local equilibrium in the sense that it obeys Gibbs equation. Some support for this can be found in the literature. Prigogine and Mazur [38] investigated a mixture of two fluids using non-equilibrium thermodynamics. Their system consisted of superfluid - and normal helium. Two pressures were defined, one for each of the two fluids. The interaction between the two fluids was small, meaning that one phase flowed as if the other one (aside from a small frictional force) was not there. The situation here is similar, as we may have different liquid pressures inside the REV. But the interaction between the two immiscible components in our porous medium is large, not negligible as in the helium case.

We are adding the contributions from each phase, interface, and line to overall variables for the REV. But unlike Gray and Miller [5] and others [39], we do not need to require that thermodynamic equilibrium relations are obeyed within the REV. This may seem to be drastic, but the Gibbs-Duhem equation follows from Euler homogeneity alone, cf. section 5. The assumption of Euler homogeneity is sufficient to obtain the Gibbs-Duhem equation. In this aspect, we agree with those who use that equation for porous media, see e.g., [6].

The surface areas and the contact line lengths are not *independent* variables in our representation of the REV. These variables have been included through the assumption that the basic variables of the REV are additive. This means that a REV of a double size has double the energy, entropy, and mass, but also double the surface areas of various types and double the line lengths. The contraction to the small set of variables depend on this assumption. Otherwise, we need to expand the variable set. This can be done, however. A promising route seems to include Minkovski integrals [40]. Our approach can be compared to the up-scaling method used in Smoothed Particle Hydrodynamics [20]. Inspired by the idea behind smoothed particle hydrodynamics, we can also define a normalized weight function $W(\mathbf{r})$, such that a microscopic variable $a(\mathbf{r})$ may be represented by its average, defined as

$$\overline{a}(\mathbf{r}) \equiv \int d\mathbf{r}' W(\mathbf{r}-\mathbf{r}')a(\mathbf{r}'). \tag{49}$$

For example, if $a(\mathbf{r}')$ is the local void fraction in a porous material as determined from samples of the material, $\overline{a}(\mathbf{r})$ is the average porosity of the medium. The average is assigned to the point $\mathbf{r}$ and varies smoothly in space. The average porosity $\overline{a}(\mathbf{r})$ would then be suitable for e.g., a reservoir simulation at the macro-scale.

In general, the system is subject to external forces and its properties are non-uniform. The choice of $W(\mathbf{r})$ is therefore crucial in that it defines the extent of the coarse-graining and the profile of the weighting. The illustration in **Figure 1** alludes to a weight function that is constant inside a cubic box and zero outside, but other choices are possible. Popular choices used in mesoscale simulations are the Gaussian and spline functions (see [20] for details). A convenient feature of the coarse-graining is that the average of a gradient of a property a is equal to the gradient of the average.

$$\nabla\overline{a}(\mathbf{r}) = \overline{\nabla a(\mathbf{r})} \tag{50}$$

Similarly the average of a divergence of a flux is equal to the divergence of the average. This implies that balance equations, which usually contain the divergence of a flux, remain valid after averaging. Time averages can also be introduced along the same lines.

Time scales relevant to porous media transport are usually large (minutes, hours); and much larger than times relevant for the molecular scale. Properties can change not only along the coordinate axis, but also on the time scale. In the present formulation, any change brought about in the REV must retain the validity of the Gibbs equation. As long as that is true, we can use the equations, also for transient phenomena.

The outcome of the derivations will enable us to deal with a wide range of non-isothermal phenomena in a systematic manner, from frost heave to heterogeneous catalysis, or multi-phase flow in porous media. We will elaborate on what this means in the next part of this work. In particular, we shall give more details on the meaning of the additive variables and the consequences for the REV pressure in a paper to come [18]. We will there return to the meaning of the REV variables and how they will contribute and help define new driving forces of transport.

8. CONCLUDING REMARKS

We have derived the entropy production for transport of heat and immiscible, single components (phases) in a porous medium. The derivations have followed standard non-equilibrium thermodynamics for heterogeneous systems [11]. The only, but essential, difference to current theories, has been the fact that we write all these equations for a porous medium on the macro-scale for the REV of a minimum size using its total entropy, energy and mass. These equations are mostly written for the separate contributions. Broadly speaking, we have been zooming out our view on the porous medium to first define some states that we take as thermodynamic states because they obey Euler homogeneity. The states are those illustrated by the dots in **Figure 1**. In order to define these states by experiments, we constructed the sister states of **Figure 5**.

The advantage of the present formulations is this; it is now possible to formulate the transport problem on the scale of a flow experiment in accordance with the second law of thermodynamics, with far less variables, see [18]. This opens up

the possibility to test the thermodynamic models for consistency and compatibility with the second law. Such tests will be explicitly formulated together with the constitutive equations, in the next part of this work [18].

AUTHOR CONTRIBUTIONS

SK and DB defined the variables of the REV and the sister states and wrote the first draft. AH, BH, and OG critically examined all proposals and contributed to revisions on the MS.

FUNDING

The authors are grateful to the Research Council of Norway through its Centers of Excellence funding scheme, project number 262644, PoreLab.

ACKNOWLEDGMENTS

Per Arne Slotte is thanked for stimulating discussions.

REFERENCES

1. Bedford A. Theories of immiscible and structured mixtures. *Int J Eng Sci.* (1983) **21**:863–960.
2. Hassanizadeh SM, Gray WG. Mechanics and thermodynamics of multiphase flow in porous media including interphase boundaries. *Adv Water Resour.* (1990) **13**:169–86.
3. Gray WG, Hassanizadeh SM. Macroscale continuum mechanics for multiphase porous-media flow including phases, interfaces, common lines and commpon points. *Adv Water Resour*. (1998) **21**:261–81.
4. Hilfer R. Macroscopic equations of motion for two phase flow in porous media. *Phys Rev E* (1998) **58**:2090.
5. Gray WG, Miller CT. *Introduction to the Thermodynamically Constrained Averaging Theory for Porous Medium Systems.* Cham: Springer (2014).
6. Revil A. Transport of water and ions in partially water-saturated porous media. *Adv Water Resour.* (2017) **103**:119–38. doi: 10.1016/j.advwatres.2016.07.016
7. Onsager L. Reciprocal relations in irreversible processes. I. *Phys Rev.* (1931) **37**:405–26.
8. Onsager L. Reciprocal relations in irreversible processes. II. *Phys Rev.* (1931) **38**:2265–79.
9. de Groot SR, Mazur P. *Non-Equilibrium Thermodynamics.* London: Dover (1984).
10. Bedeaux D, Albano AM, Mazur P. Boundary conditions and non-equilibrium thermodynamics. *Phys A* (1976) **82**:438–62.
11. Kjelstrup S, Bedeaux D. *Non-Equilibrium Thermodynamics of Heterogeneous Systems.* Singapore: Wiley (2008).
12. Zhu L, Koper GJM, Bedeaux D. Heats of transfer in the diffusion layer before the surface and the surface temperature for a catalytic hydrogen oxidation reaction (H_2+(1/2)O_2 = H_2O). *J Phys Chem A* (2006) **110**:4080–8. doi: 10.1021/jp056301i
13. Richter F, Gunnarshaug AF, Burheim OS, Vie PJS, Kjelstrup S. Single electrode entropy change for $LiCoO_2$ electrodes. *ECS Trans.* (2017) **80**:219–38. doi:10.1149/08010.0219ecst
14. Førland T, Ratkje SK. Irreversible thermodynamic treatment of frost heave. *Eng Geol.* (1981) **18**:225–9.
15. Huyghe JM, Nikooee E, Hassanizadeh SM. Bridging effective stress and soil water retention equations in deforming unsaturated porous media: a thermodynamic approach. *Transp Porous Med.* (2017) 117:349–65. doi: 10.1007/s11242-017-0837-9
16. Hansen A, Sinha S, Bedeaux D, Kjelstrup S, Gjennestad MA, Vassvik M. Relations between seepage velocities in immiscible, incompressible two-phase flow in porous media. arXiv:1712.06823. Availbale online at: https://arxiv.org/abs/1712.06823
17. Kjelstrup S, Bedeaux D, Hansen A, Hafskjold B, Galteland O. Non-isothermal two-phase flow in porous media. The entropy production. (2018) *arXiv.1805.03943*.
18. Kjelstrup S, Bedeaux D, Hansen A, Hafskjold B, Galteland O. Non-isothermal two-phase flow in porous media. Constitutive equations. (2018) *arXiv.1809.10378*.
19. Tallakstad KT, Løvoll G, Knudsen HA, Ramstad T, Flekkøy EG, Måløy KJ. Steady-state, simultaneous two-phase flow in porous media: an experimental study. *Phys Rev E* (2009) **80**:036308. doi: 10.1103/PhysRevE.80.036308
20. Monaghan JJ. Smoothed particle hydrodynamics. *Annu Rev Astron Astrophys.* (1992) **30**:543–74.
21. Gibbs JW. *The Scientific Papers of J.W. Gibbs.* New York, NY: Dover (1961).
22. Sinha S, Hansen A, Bedeaux D, Kjelstrup S, Savani I, Vassvik M. Effective rheology of bubbles moving in a capillary tube. *Phys Rev E* (2013) **87**:025001. doi: 10.1103/PhysRevE.87.025001
23. Aker E, Måløy KJ, Hansen A, Batrouni G. A two-dimensional network simulator for two-phase flow in porous media. *Trans Porous Media* (1998) **32**:163–86.
24. Gjennestad MA, Vassvik M, Kjelstrup S, Hansen A. Stable and efficient time integration at low capillary numbers of a dynamic pore network model for immiscible two-phase flow in porous media. *Front Phys.* (2018) 6:56. doi: 10.3389/fphy.2018.00056
25. Linstrom PJ, Mallard WG, editors. *NIST Chemistry WebBook, NIST Standard Reference Database Number 69.* Gaithersburg MD: National Institute of Standards and Technology (2018).
26. Neumann A. Contact angles and their temperature dependence: thermodynamic status, measurement, interpretation and application. *Adv Colloid Interfaces* (1974) **4**:105–91.
27. Zeppieri S, Rodríguez J, López de Ramos A. Interfacial tension of alkane + water systems. *J Chem Eng Data* (2001) **46**:1086–8. doi: 10.1021/je000245r
28. Savani I, Sinha S, Hansen A, Kjelstrup S, Bedeaux D, Vassvik M. A Monte Carlo procedure for two-phase flow in porous media. *Transp Porous Med.* (2017) **116**:869–88. doi: 10.1007/s11242-016-0804-x
29. Hansen A, Ramstad T. Towards a thermodynamics of immiscible two-phase steady-state flow in porous media. *Comp Geosci.* (2009) **13**:227. doi: 10.1007/s10596-008-9109-7
30. Valavanides MS, Daras T. Definition and counting of configurational microstates in steady-state two-phase flows in pore networks. *Entropy* (2016) **18**:1–28. doi: 10.3390/e18020054
31. Erpelding M, Sinha S, Tallakstad KT, Hansen A, Flekkøy EG, Måløy KJ. History independence of steady state in simultaneous two-phase flow through two-dimensional porous media. *Phys Rev E* (2013) **88**:053004. doi: 10.1103/PhysRevE.88.053004
32. Førland KS, Førland T, Ratkje SK. *Irreversible Thermodynamics. Theory and Applications.* Chichester: Wiley (1988).
33. Holt T, Lindeberg E, Ratkje SK. *The Effect of Gravity and Temperature Gradients on the Methane Distribution in Oil Reservoirs*. Society of Petroleum Engineers, SPE-11761-MS (1983).
34. Katchalsky A, Curran PF. *Nonequilibrium Thermodynamics in Biophysics.* Harvard University Press (1965).
35. Scatchard G. Ion exchanger electrodes. *Am Chem Soc.* (1953) **75**:2883–7.
36. Lakshminarayanaiah N, Subrahmanyan V. Measurement of membrane potentials and test of theories. *J Polym Sci Part A* (1964) **2**:4 491–502.

37. Ratkje SK, Holt T, Skrede M. Cation membrane transport:evidence for local validity of nernst–planck equations. *Berich Bunsen Gesell.* (1988) **92**: 825–32.
38. Prigogine I, Mazur P. About two formulations of hydrodynamics and the problem of liquid helium II. *Physica* (1951) **17**: 661–79.
39. Helmig R. *Multiphase Flow and Transport Processes in the Subsurface.* Berlin: Springer (1997).
40. McClure JE, Armstrong RT, Berrill MA, Schluter S, Berg S, Gray WG, et al. A geometric state function for two-fluid flow in porous media. *Phys Rev Fluids* (2018) **3**:084306. doi: 10.1103/PhysRevFluids.3.084306

Conflict of Interest Statement: The authors declare that the research was conducted in the absence of any commercial or financial relationships that could be construed as a potential conflict of interest.

APPENDIX

Mathematical symbols, superscripts, subscripts.

Symbol	Explanation
d	differential
∂	partial derivative
Δ	change in a quantity or variable
Σ	sum
i	subscript meaning component i
m	number of phases
n	subscript meaning non-wetting fluid
w	subscript meaning wetting fluid
p	superscript meaning pore
REV	abbreviation meaning representative elementary volume
r	superscript meaning solid matrix of porous medium
s	superscript meaning interface
u	superscripts meaning internal energy
$\alpha\beta$	superscripts meaning contact area between phases $\alpha\beta$
$\alpha\beta\delta$	superscripts meaning contact line between phases α, β, δ
$\bar{x}$	average of x

Greek symbols

Symbol	Dimension	Explanation
α		superscripts meaning a phase
β		superscript meaning an interface
δ		superscript meaning a contact line
ϕ		porosity of porous medium
γ	$N.m^{-1}$ (N)	surface tension (line tension)
Λ	m	length of contact line
λ		Euler scaling parameter
μ_i	$J.kg^{-1}$	chemical potential of i
ρ_i	$kg.m^{-3}$	density, $\equiv M_i/V$
σ	$J.s^{-1}.K^{-1}.m^{-3}$	entropy production in a homogeneous phase
σ^s	$J.s^{-1}.K^{-1}.m^{-2}$	surface excess entropy production
σ^c	$J.s^{-1}.K^{-1}.m^{-1}$	line excess entropy production
Ω	m^2	surface or interface area

Latin symbols.

Symbol	Dimension	Explanation
G	J	Gibbs energy
M	kg	mass
m	$kg.mol^{-1}$	
d	m	pore length
H_i	$J.kg^{-1}$	partial specific enthalpy of i
J_i	$kg.s^{-1}.m^{-2}$	mass flux of i
J_u	$J.s^{-1}.m^{-2}$	energy flux
J'_q	$J.s^{-1}.m^{-2}$	sensible heat flux
J_V	$m^3.s^{-1}.m^{-2}$	volume flux
l	m	characteristic length of representative elementary volume
L	m	characteristic length of experimental system
L_{ij}, ℓ_{ij}		Onsager conductivity
p	Pa	pressure of REV
Q	$m^3.s^{-1}$	volume flow
$\bar{r}$	m	avarage pore radius
S	$J.K^{-1}$	entropy
s	$J.K^{-1}.m^{-3}$	entropy density
S_i	$J.kg^{-1}K^{-1}$	partial specific entropy of i
$\hat{S}$		degree of saturation, $\equiv V_i/V$
T	K	temperature
t	s	time
U	J	internal energy
u	$J.m^{-3}$	internal energy density
V	m^3	volume
V_i	$m^3.kg^{-1}$	partial specific volume
v_D	$m.s^{-1}$	difference velocity
x	m	coordinate axis
x_i	-	mass fraction of i
W_i	-	$kg.mol^{-1}$ molar mass of i

frontiers in Physics

ORIGINAL RESEARCH
published: 04 January 2019
doi: 10.3389/fphy.2018.00150

Non-isothermal Transport of Multi-phase Fluids in Porous Media. Constitutive Equations

Signe Kjelstrup[1]*, *Dick Bedeaux*[1], *Alex Hansen*[2], *Bjørn Hafskjold*[1] and *Olav Galteland*[1]

[1] PoreLab, Department of Chemistry, Norwegian University of Science and Technology, Trondheim, Norway, [2] PoreLab, Department of Physics, Norwegian University of Science and Technology, Trondheim, Norway

We define a representative elementary volume of a porous medium in terms of lumped extensive variables, including properties of homogeneous phases, interfaces, and contact lines. Using the grand potential, we define the pressure of the REV in a porous medium in a new manner. From the entropy production expressed in these variables, we develop new constitutive equations for multi-component, multi-phase, macro-scale flow. The system is exposed to temperature, composition, and pressure gradients. New contributions due to varying porosity or surface tension offer explanations for non-Darcy behavior, and predict thermal osmosis special for porous media. An experimental program is suggested to verify Onsager symmetry in the transport coefficients. The analysis is limited to non-deformable systems, which obey Euler homogeneity on the REV level.

Keywords: porous media, energy dissipation, two-phase flow, representative elementary volume, macro-scale, excess surface energy, pressure, non-equilibrium thermodynamics

OPEN ACCESS

Edited by:
Jürgen Vollmer,
Institut für Theoretische Physik,
Universität Leipzig, Germany

Reviewed by:
Constantinos Siettos,
University of Naples Federico II, Italy
Soren Taverniers,
Stanford University, United States

***Correspondence:**
Signe Kjelstrup
signe.kjelstrup@ntnu.no

Specialty section:
This article was submitted to Interdisciplinary Physics, a section of the journal Frontiers in Physics

Received: *08 October 2018*
Accepted: *11 December 2018*
Published: *04 January 2019*

Citation:
Kjelstrup S, Bedeaux D, Hansen A, Hafskjold B and Galteland O (2019) Non-isothermal Transport of Multi-phase Fluids in Porous Media. Constitutive Equations. Front. Phys. 6:150. doi: 10.3389/fphy.2018.00150

1. INTRODUCTION

We have recently [1] derived a coarse-grained form of the entropy production, σ, of a representative elementary volume (REV) in a non-deformable porous medium with multi-phase, multi-component, non-isothermal fluids. The coarse-grained description of the REV was formulated for systems that obey Euler homogeneity. A Gibbs equation could therefore be formulated for the REV itself, and used as a starting point, as is normal in non-equilibrium thermodynamics [2].

Once the entropy production has been found, the driving forces and the constitutive equations can be given. These will be specified here. We shall see that we can obtain the same form of the constitutive equations as for homogeneous systems, but that the driving forces are particular for the porous medium. To write out this particularity, is one aim of the present paper. We shall see that we can obtain a new definition for the pressure in a porous medium and use this and the chemical potential to find the constitutive equations. We are also giving internal relations between experiments particular for the flows, as derived for instance from the Onsager relations.

We consider, as a premise, the REV as a complete thermodynamic system. Hansen and Ramstad [3] suggested this possibility already some time ago. Since then, the hypothesis has been supported through measurements on Hele-Shaw cells [4] and through network simulations [5]. The coarse-grained variables of the REV will fluctuate similar to the variables in a normal thermodynamic state around a mean value.

The procedure that we used to obtain the Gibbs equation for coarse-grained variables [1], assumes that the additive thermodynamic variables of the REV are Euler homogeneous functions of

order one. We give first a brief review of the procedure that defines the basis set of thermodynamic variables (section 2.1). The consequences for the chemical potential and the pressure in the context of porous media is next described (sections 2.2, 2.3). A new definition of the pressure is proposed in section 2.3.

The constitutive equations that follow from the new set of variables, allow us to revisit previously published experimental results. We shall see, for instance, that they can explain deviations from Darcy's law. Such deviations have been observed for small volume flows, also for single fluids like water and water solutions [6–10]. Thresholds and/or deviations from straight lines in plots of flow vs. the overall pressure difference, have been reported. Boersma et al. [8] found a dependency of such a threshold on the average pore radius, $\bar{r}$, for flow in a porous medium made of glass-beads. The observations have, as of yet, no final explanation. When dealing with immiscible fluids, Tallakstad et al. [11] observed a dependence of the flow rate on the square of the pressure difference under steady-state flow conditions. Sinha and Hansen [12] attributed this square dependence to a change in the conductivity, arising from the successive opening of pores due to the mobilization of interfaces when the pressure difference across the sample is increased. The explanation was supported by a mean-field calculation and numerical experiments with a network model. Sinha et al. [10] followed up the original Tallakstad study, done in a two-dimensional model porous medium, both experimentally and computationally in three-dimensional porous media, with the same result.

There is not only a need to better understand deviations from Darcy's law for volume transport. Other driving forces than those related to the pressure difference, are also relevant to porous media transport. Counter-current transport of components can lead to gradients in composition (chemical potential) or chemical driving forces. Injection of cold seawater into a warm hydrocarbon reservoir can create thermal driving forces. This leads to thermal diffusion. The separation of components in a temperature gradient is an example of the Soret effect [13]. A temperature gradient may also lead to a pressure gradient, a phenomenon called thermal osmosis. These effects are not much studied in porous media, see [14] for a review on membranes. There are, for instance, contradictory findings in the literature with respect to the impact of the porous medium on thermal diffusion. Costeseque et al. [15] found that the porous medium had no significant effect on the Soret coefficient, as determined with a horizontal thermodiffusion cell (although the component diffusion was slower in the porous medium). On the other hand, Colombani et al. [16] found by molecular dynamics simulations that both the porosity and the wettability of the porous medium had an effect on the Soret coefficient. The presence of a porous matrix had an impact on the flow pattern and therefore the Soret coefficient according to Davarzani et al. [17]. The role of a thermal driving force is therefore at best unclear. A better understanding of its role could be important. An emerging concept for water cleaning is, for instance, based on thermal osmosis [18]. This process could help produce clean water using industrial and natural heat sources, a very important topic in the world today.

It is thus an open question in porous media theory, how driving forces like the ones mentioned interact, and how the porous medium makes these interactions special [17]. It is therefore also the aim of this work to clarify the coupling that can take place due to some central forces, by constructing a non-equilibrium thermodynamic theory, particular for porous media.

The paper is structured as follows. Section 2 gives first a brief repetition of the variables used to obtain the coarse-grained Gibbs equation and the corresponding entropy production [1]. As before, the analysis applies to systems that obeys Euler homogeneity of the first order. We restrict ourselves to non-deformable media, and systems with a constant ratio of fluid surface area to volume (no film formation). For such systems we proceed to find expressions for the chemical potential and the pressure in the context of non-deformable porous media, cf. sections 2.2, 2.3. We intend to extend the theory to deformable media later.

The expression for the entropy production with these variables is detailed in section 3. The driving forces, due to temperature -, pressure -, and chemical potential gradients, are specified in section 4. They obtain new contributions compared to their normal form in homogeneous systems. In the last section 5, we detail specific cases of component and volume flow in combination with heat transport. An experimental program is suggested in the end to verify Onsager symmetry in the transport coefficients.

2. THERMODYNAMIC VARIABLES FOR THE REV

2.1. The Basis Set of Variables

The central concept in this analysis is the representative elementary volume; the REV [19, 20]. Its characteristic size, l, is small compared to the size (length) of the full system, L, but large compared to the characteristic pore length and diameter. An illustration of the REV is given by the squares in **Figure 1**. The REV (square) consists of several phases and components. The problem is to find the representation on the larger scale. For each point in the porous system, represented by a (blue) dot in **Figure 1**, Kjelstrup et al. [1] used the REV around the dot to obtain the variables of the REV ($U^{\mathrm{REV}}, S^{\mathrm{REV}}, V^{\mathrm{REV}}, M_i^{\mathrm{REV}}$). The variables were given superscript REV to indicate that they constituted the only *independent* variables of the REV. From the Euler homogeneity of these variables, the possibility followed to define the temperature, pressure, and chemical potentials of the REV, (T, p, μ_i). We refer to Kjelstrup et al. [1] and to **Tables A1–A3** in the Appendix for further details, terminology and symbols.

The value of each of these REV-variables was obtained as a sum of contributions from each phase, interface and three-phase contact line present [19, 20]. The contributions are pore-scale variables; they are not *independent* variables on the macro-scale. To assume Euler homogeneity, means to assume that a REV of the double size, for example, has double the energy, entropy, and mass, as well as double the surface areas and double the line

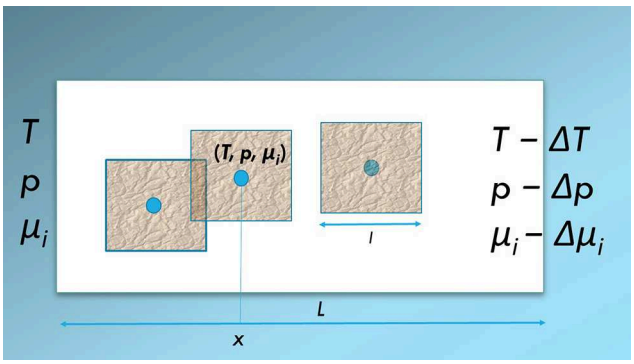

FIGURE 1 | A representative elementary volume (REV) (magenta squares, length *l*) in a system (white box of length *L*) that is exposed to for instance a pressure difference, Δp, a temperature difference, ΔT, and differences in chemical potentials $\Delta\mu_i$. A (blue) dot is used to represent the state that characterizes the REV. The set of state variables are positioned on the *x*-axis: The temperature, pressure and the chemical potentials, $(T, p, \mu_i)(x)$. The figure is adapted from Kjelstrup et al. [1].

lengths of various types. The average surface area, pore length and pore radius, as well as the curvature of the surfaces per unit of volume of the REV, are then everywhere the same. We limit ourselves to non-deformable systems with a constant ratio of fluid surface area to volume, for which this is the case. The extension to deformable systems is more complicated and will be considered later.

A system of k components in m homogeneous phases, has a volume, V^{REV}, with contributions from the homogeneous bulk phases $V^{\alpha,\mathrm{REV}}$, $m \geq \alpha \geq 1$, and the excess line volumes, $V^{\alpha\beta\delta,\mathrm{REV}}$, $m \geq \alpha > \beta > \delta \geq 1$.

$$V^{\mathrm{REV}} = \sum_{\alpha=1}^{m} V^{\alpha,\mathrm{REV}} + \sum_{\alpha>\beta>\delta=1}^{m} V^{\alpha\beta\delta,\mathrm{REV}} \approx \sum_{\alpha=1}^{m} V^{\alpha,\mathrm{REV}} \quad (1)$$

The superscripts denote the relevant phases, surfaces or contact lines. The surface area between phases α, β is denoted $\Omega^{\alpha\beta,\mathrm{REV}}$ while the contact line length between phases $\alpha\beta\delta$ is denoted $\Lambda^{\alpha\beta\delta,\mathrm{REV}}$. The surface area (line length) of the REV is the sum over all areas (lines) in the REV. The excess surface volumes are by construction zero. The excess line volumes are not, because the dividing surfaces in general cross each other along three different lines.

In this first exposition, we neglect contributions to the volume from the contact lines, which are normally small also in porous media. The volume of the pores is

$$V^{p,\mathrm{REV}} = \sum_{\alpha=1}^{m-1} V^{\alpha,\mathrm{REV}} \quad (2)$$

Superscript p is used for pore. The porosity, ϕ, and the degree of saturation, $\hat{S}^{\alpha}$ (saturation for short), are

$$\phi \equiv \frac{V^{p,\mathrm{REV}}}{V^{\mathrm{REV}}} \quad \text{and} \quad \hat{S}^{\alpha} \equiv \frac{V^{\alpha,\mathrm{REV}}}{V^{p,\mathrm{REV}}} = \frac{V^{\alpha,\mathrm{REV}}}{\phi V^{\mathrm{REV}}} \quad (3)$$

Superscript α is used for a component, which is equal to the phase in the present case. The porosity and the saturation do not depend on the size of the REV, and have therefore no REV-superscript.

The mass of component i in the REV, M_i^{REV}, is the sum of the masses in the homogeneous phases of the REV, α, $M_i^{\alpha,\mathrm{REV}}$, $m \geq \alpha \geq 1$, the excess interfacial masses, $M_i^{\alpha\beta,\mathrm{REV}}$, $m \geq \alpha > \beta \geq 1$, and the excess line masses, $M_i^{\alpha\beta\delta,\mathrm{REV}}$, $m \geq \alpha > \beta > \delta \geq 1$. We obtain:

$$M_i^{\mathrm{REV}} = \sum_{\alpha=1}^{m} M_i^{\alpha,\mathrm{REV}} + \sum_{\alpha>\beta=1}^{m} M_i^{\alpha\beta,\mathrm{REV}} + \sum_{\alpha>\beta>\delta=1}^{m} M_i^{\alpha\beta\delta,\mathrm{REV}} \quad (4)$$

where the first term on the right-hand side also can be written in terms of the (constant) densities ρ_i^{α}

$$\sum_{\alpha=1}^{m} M_i^{\alpha,\mathrm{REV}} = \sum_{\alpha=1}^{m} \rho_i^{\alpha} V_i^{\alpha,\mathrm{REV}} \quad (5)$$

Similar contributions follow for the other terms.

We shall often use the example of two immiscible one-component phases w and n in a solid porous material r of porosity ϕ, where contact line contributions are negligible. We can think of phase w as wetting, and n as non-wetting. The mass variables from Equation (4) are for n:

$$M_n^{\mathrm{REV}} = \rho_n V_n^{\mathrm{REV}} \quad (6)$$

while for the other components we obtain also surface excess contributions:

$$\begin{aligned} M_w^{\mathrm{REV}} &= M_w^{\mathrm{REV}} + M_w^{wn,\mathrm{REV}} \\ M_r^{\mathrm{REV}} &= M_r^{\mathrm{REV}} + M_r^{rn,\mathrm{REV}} + M_r^{rw,\mathrm{REV}} \end{aligned} \quad (7)$$

When an interface is formed between two phases, we are free to choose the position of the interface such that one of the components has a zero excess mass. This is the position of the equimolar surface of this component. This position is convenient because the number of variables are reduced. When we use the equimolar surface of n, $M_n^{rn} = M_n^{wn} = 0$, and when we use the equimolar surface of w at the surface of the solid, $M_w^{rw} = 0$. These choices simplify the description of the REV. Therefore, we shall later use the chemical potential of component n, which has a bulk contribution only, see section 2.2.

The expressions for U^{REV} and S^{REV} are similar to Equation (4). This way to construct a REV is reminiscent of the geometric construction of a state function, proposed for flow in porous media by McClure et al. [21].

The basis set of macro-scale variables of the REV $(U^{\mathrm{REV}}, S^{\mathrm{REV}}, V^{\mathrm{REV}}, M_i^{\mathrm{REV}})$ apply to the whole REV. The temperature, pressure and chemical potentials of the REV, (T, p, μ_i), on the macro-scale were next defined, as is normal in thermodynamics, as partial derivatives of the internal energy. These definitions are normal in the sense that they have the same form as they have in homogeneous systems. They are new because the variables (say U^{REV}) have contributions from all

parts of the heterogeneous REV. The intensive variables T, p, and μ_i are then *not* averages of the corresponding variables on the pore-scale. The importance of this was also pointed out by Hassanizadeh and Gray [11,12].

The macro-scale densities of internal energy, entropy and mass; in the example, u, s, ρ_i, do not depend on the *size* of the REV. The densities are therefore convenient when we need to integrate across the system [1]. They are, however, functions of the position of the REV, cf. **Figure 1**.

2.2. The Gibbs Energy of the REV

We proceed to define the Gibbs energy, G, as this variable is needed in the definition of driving forces of transport, see section 3. The general expression for Gibbs energy is

$$G \equiv U + pV - ST = \sum_{i=1}^{k} \mu_i M_i = \sum_{i=1}^{k} G_i \tag{8}$$

where G applies to the REV and G_i is defined for component i in the last identity. All REV variables need be taken into account. In principle, each component can exist in all phases in the REV. But component contributions to the REV are additive, cf. Equation (4). For component i we therefore have

$$\begin{aligned} G_i^{\mathrm{REV}} &\equiv \mu_i^{\mathrm{REV}} M_i^{\mathrm{REV}} \\ &= \sum_{\alpha=1}^{m} G_i^{\alpha,\mathrm{REV}} + \sum_{\alpha>\beta=1}^{m} G_i^{\alpha\beta,\mathrm{REV}} \\ &= \sum_{\alpha=1}^{m} g_i^{\alpha} V^{\alpha,\mathrm{REV}} + \sum_{\alpha>\beta=1}^{m} g_i^{\alpha\beta} \Omega^{\alpha\beta,\mathrm{REV}} \end{aligned} \tag{9}$$

The expression gives the Gibbs energy contributions of component i to the REV. We neglected again possible contributions from contact lines.

In the case of two immiscible, one-component fluids in a non-deformable porous rock, we can take advantage of the simpler description of the non-wetting fluid (see previous subsection) giving

$$G_n^{\mathrm{REV}} \equiv \mu_n M_n^{\mathrm{REV}} = G_n^{n,\mathrm{REV}} = g_n^n V^{n,\mathrm{REV}} \tag{10}$$

For immiscible, one-component fluids, the label indicating the components also gives the phase. The density g_n^n is an average over $V^{n,\mathrm{REV}}$. The local density in the pores may vary around the average.

The total differential of U is used with the definition (8), and we obtain

$$dG = -SdT + Vdp + \sum_i \mu_i dM_i \tag{11}$$

where the superscript REV is skipped for convenience.

2.3. The Pressure of the REV

We find the pressure of the REV by starting, as above, with the extensive property that holds the pressure as the variable. This is the grand potential. The compressional energy of the REV is equal to minus the grand potential:

$$\Upsilon^{\mathrm{REV}}\left(T, V^{\mathrm{REV}}, \mu_i\right) \equiv -pV^{\mathrm{REV}} = U^{\mathrm{REV}} - S^{\mathrm{REV}} T - \sum_{i=1}^{k} \mu_i M_i^{\mathrm{REV}} \tag{12}$$

The grand potential of the REV is additive, which gives

$$\Upsilon^{\mathrm{REV}} = \sum_{\alpha=1}^{m} \Upsilon^{\alpha,\mathrm{REV}} + \sum_{\alpha>\beta=1}^{m} \Upsilon^{\alpha\beta,\mathrm{REV}} + \sum_{\alpha>\beta>\delta=1}^{m} \Upsilon^{\alpha\beta\delta,\mathrm{REV}} \tag{13}$$

We introduce contributions from all phases, surfaces and contact lines. This allows us the possibility to define, in a new way, the pressure of the REV:

$$p = \frac{1}{V^{\mathrm{REV}}} \left(\sum_{\alpha=1}^{m} p^{\alpha} V^{\alpha,\mathrm{REV}} - \sum_{\alpha>\beta=1}^{m} \gamma^{\alpha\beta} \Omega^{\alpha\beta,\mathrm{REV}} - \sum_{\alpha>\beta>\delta=1}^{m} \gamma^{\alpha\beta\delta} \Lambda^{\alpha\beta\delta,\mathrm{REV}} \right) \tag{14}$$

The last equation makes it possible to compute the pressure of the REV, p, from the pressures in the bulk phases, the surface tensions and the line tensions. With knowledge of the pressure in the REV, we can find the driving force, $-dp/dx$, in the entropy production, see below, Equation (29).

We explain now how we can define and compute the pressure from Equation (14), using the example of two immiscible single fluids in a non-deformable medium. We shall neglect contact line contributions for simplicity. Such contributions can be added by the same procedure. We follow Equation (14) and sum over the n, w and r bulk phases, and the nr, wr, and nw—interfaces. The situation can be illustrated for a single cylindrical pore, see **Figure 2**.

The figure shows two phases n and w in a tube with the average radius. The wall material is r. Contact areas are therefore $\Omega^{nr,\mathrm{REV}}$, $\Omega^{wr,\mathrm{REV}}$, and $\Omega^{nw,\mathrm{REV}}$. The total surface area of the pore

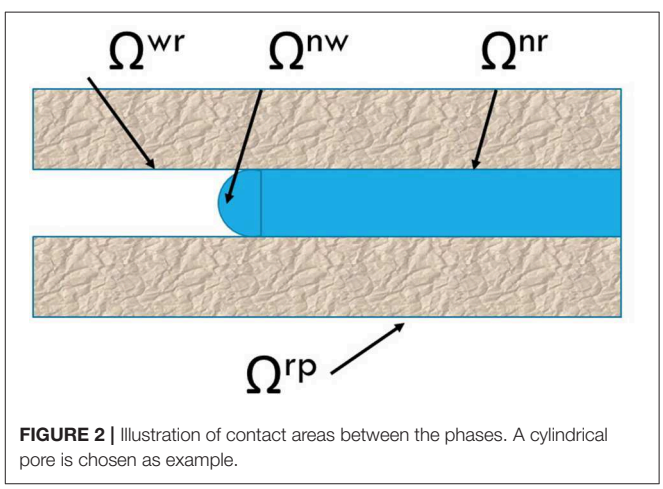

FIGURE 2 | Illustration of contact areas between the phases. A cylindrical pore is chosen as example.

is $\Omega^{rp,\mathrm{REV}} \equiv \Omega^{nr,\mathrm{REV}} + \Omega^{wr,\mathrm{REV}}$. The area $\Omega^{nw,\mathrm{REV}}$ is the smallest contact area shown in the figure. The volumes in Equation (14) depend on the saturation of the non-wetting component, $\hat{S}^n$ and the porosity, ϕ. Neither of the fluids form a film between the surface and the other fluid, so the surfaces satisfy in good approximation

$$\begin{aligned}\Omega^{nr,\mathrm{REV}} &= \hat{S}^n \Omega^{rp,\mathrm{REV}} \text{ and } \Omega^{wr,\mathrm{REV}} = \hat{S}^w \Omega^{rp,\mathrm{REV}} \\ &= (1-\hat{S}^n)\Omega^{rp,\mathrm{REV}}\end{aligned} \tag{15}$$

The pressure of the REV from Equation (14) can then be written as:

$$\begin{aligned}p = &[p^n \hat{S}^n \phi + p^w (1-\hat{S}^n)\phi + p^r(1-\phi)] \\ &-[\hat{S}^n \gamma^{nr} + (1-\hat{S}^n)\gamma^{wr}]\frac{\Omega^{rp,\mathrm{REV}}}{V^{\mathrm{REV}}} - \gamma^{nw}\frac{\Omega^{nw,\mathrm{REV}}}{V^{\mathrm{REV}}}\end{aligned} \tag{16}$$

Contact-line contributions were again not taken along, for simplicity. A consequence of the porous medium being homogeneous is that $\Omega^{rp,\mathrm{REV}}/V^{\mathrm{REV}}$ is the same everywhere. The ratio can be used as a measure of the average curvature of the pore surface, as will be explained below.

The volume-averaged contributions to the pressure from the homogeneous phases is given the symbol $\bar{p}$:

$$\begin{aligned}\bar{p} &= p^n \hat{S}^n \phi + p^w (1-\hat{S}^n)\phi + p^r(1-\phi) \\ &= \left(p^n - p^w\right)\hat{S}^n \phi + p^w \phi + p^r(1-\phi)\end{aligned} \tag{17}$$

The first term in the last equality shows that the saturation gives an important contribution to the volume-averaged pressure. The contributions of the 2nd and 3rd terms are due to p^w and p^r. These contributions are usually constant.

The surface-averaged contributions to the pressure are likewise given a separate symbol:

$$\bar{p}^c = [\hat{S}^n \gamma^{nr} + (1-\hat{S}^n)\gamma^{wr}]\frac{\Omega^{rp,\mathrm{REV}}}{V^{\mathrm{REV}}} + \gamma^{nw}\frac{\Omega^{nw,\mathrm{REV}}}{V^{\mathrm{REV}}} \tag{18}$$

The contribution of $\bar{p}^c$ to the total pressure, p, may be called the capillary pressure. The total pressure of the REV is thus, for short:

$$p = \bar{p} - \bar{p}^c \tag{19}$$

2.3.1. The Case of Approximately Cylindrical Pores

With an (approximately) cylindrical pore geometry, we can define the average radius of the pores by

$$\bar{r} \equiv \frac{2V^{p,\mathrm{REV}}}{\Omega^{rp,\mathrm{REV}}} \tag{20}$$

By introducing $\bar{r}$ into Equation (18) we obtain the capillary pressure

$$\bar{p}^c = \left(\gamma^{nr} - \gamma^{wr}\right)\hat{S}^n \frac{2\phi}{\bar{r}} + \gamma^{wr}\frac{2\phi}{\bar{r}} + \gamma^{nw}\frac{\Omega^{nw,\mathrm{REV}}}{V^{\mathrm{REV}}} \tag{21}$$

Again the first term shows that saturation gives an important contribution. The 2nd term only depends on the temperature and is usually constant. The 3rd term is proportional to the surface area of the fluid-fluid interface. In many experiments this surface area is much smaller than $\Omega^{rp,\mathrm{REV}}$. When that is the case, this term is negligible.

The three equations above give an expression for the REV pressure p for the example system.

To estimate the size of the various contributions, it is convenient to use mechanical equilibrium for the contact line and for the surface, although this condition may not apply to the REV, not even under steady flow conditions. With a balance of forces at the three-phase contact lines, Young's law applies for the surface tensions: $\gamma^{nr} - \gamma^{wr} = \gamma^{nw}\cos\theta$, where θ is the (average) contact angle. When there is furthermore mechanical equilibrium at the fluid-fluid interfaces, the pressure difference between the fluids is given by Young-Laplace's law, $p^n - p^w = 2\gamma^{nw}\cos\theta/\bar{r}$.

In the single-fluid (w) case, Equation (16) simplifies. There are volume-averaged and surface averaged contributions,

$$p = p^w\phi + p^r(1-\phi) - \gamma^{wr}\frac{2}{\bar{r}}\phi \tag{22}$$

We have defined above in detail what we mean by the pressure of a REV. We have found, using the grand potential, that it can be regarded as result of volume- and surface average properties, and we have given some examples. These contributions enter the driving force in Equations (23, 29), to be further discussed below.

3. THE ENTROPY PRODUCTION OF NON-ISOTHERMAL TWO-PHASE FLOW

Pressure-driven mass flows through porous media can lead to gradients in composition and temperature, and vice versa; temperature gradients can lead to mass flow, separation of components and pressure gradients. The interaction of such flows is of interest, and motivated the search for convenient forms of the entropy production [1].

3.1. Expression in Terms of Component Flows

From the Gibbs equation for the REV, we derived the entropy production for transport of heat and two immiscible fluid phases through the REV [1]. With transport in the x-direction only, the entropy production σ of the example system was

$$\sigma = J'_q \frac{\partial}{\partial x}\left(\frac{1}{T}\right) - \frac{1}{T}\left(J_w \frac{\partial \mu_{w,T}}{\partial x} + J_n \frac{\partial \mu_{n,T}}{\partial x}\right) \tag{23}$$

The frame of reference for the mass transport is the non-deformable solid matrix, $J_r \equiv 0$. Here J'_q is the sensible heat flux (in $\mathrm{J.m^{-2}.s^{-1}}$), T is the temperature (in K), J_i is a component flux (in $\mathrm{kg.m^{-2}.s^{-1}}$) and $\partial\mu_{i,T}/\partial x$ is the gradient of the chemical potential (in $\mathrm{J.kg^{-1}.m^{-1}}$) evaluated at constant temperature. All properties are for the REV, so superscript REV is omitted.

The thermal force conjugate to the heat flux is the gradient of the inverse temperature, where the temperature was defined for the REV as a whole, see Kjelstrup et al. [1]. The chemical force

conjugate to the mass flux is the negative gradient of $\mu_{i,T}$ over the temperature. The chemical driving forces are obtained from the full chemical potential, which is the derivative of G with respect to M_i:

$$\mu_i \equiv \left(\frac{\partial G}{\partial M_i}\right)_{T,p} \tag{24}$$

The total differential of the chemical potential is thus from Equation (11);

$$d\mu_i = -S_i dT + V_i dp + \sum_{j=1}^{k} \mu_{i,j}^c dM_j \equiv -S_i dT + V_i dp + d\mu_i^c \tag{25}$$

where $S_i = -(\partial\mu_i/\partial T)_{p,M_j}$ and $V_i = \left(\partial\mu_i/\partial p\right)_{T,M_j}$ and $\mu_{i,j}^c = (\partial\mu_i/\partial M_j)_{p,T,M_k}$ are partial specific quantities. The last term describes the change in the chemical potential by changing composition of the medium. The $d\mu_{i,T}$ is now defined as a part of the whole differential:

$$d\mu_{i,T} \equiv d\mu_i + S_i dT = V_i dp + d\mu_i^c \tag{26}$$

The last term is zero when the composition is uniform. In the expression of the entropy production in terms of component flows, Equation (23), the driving force has contributions from the composition variation and from the pressure gradient.

3.2. Expression in Terms of Volume Flow

The volume flow, rather than the component flows, is often the measured variable. A description with the volume flow is thus of interest. The volume flow of several components is $J_V = \Sigma_i J_i V_i$. We take the example of two fluids to demonstrate the principles.

$$J_V \equiv J_n V_n + J_w V_w \tag{27}$$

With two fluids in a uniform, non-deformable rock, there are three components. On the coarse-grained level, these are mixed. We assume that $d\mu_r^c = 0$, and obtain Gibbs-Duhem's equation on the form

$$\rho_n d\mu_n^c + \rho_w d\mu_w^c = 0 \tag{28}$$

where ρ_i is the density of i in the REV (in kg.m^3). This can be used with Equation (26) and J_V to change Equation (23) into

$$\sigma = J_q' \frac{\partial}{\partial x}\left(\frac{1}{T}\right) - J_V \frac{1}{T}\frac{\partial}{\partial x}p + \upsilon_D \frac{\rho_n}{T}\frac{\partial \mu_n^c}{\partial x} \tag{29}$$

We have chosen to keep the chemical potential of n, which has a simpler form than the other chemical potential ($\mu_n = \mu_n^n$), cf. section 2.2. The entropy production in Equation (23) is invariant, and this invariance defines υ_D as the relative velocity of component w and n (in m.s^{-1}):

$$\upsilon_D \equiv \frac{J_w}{\rho_w} - \frac{J_n}{\rho_n} \tag{30}$$

The entropy production 29 has also three terms. While the first term on the right-hand side is the same as before, the second term is the volume flow with minus the pressure gradient over the temperature as driving force, and the third term is the velocity difference with the chemical potential gradient times the density over the temperature as driving force.

Equations (23, 29) are equivalent. They describe the same entropy production or flow dissipation. They provide alternative choices of conjugate thermodynamic force-flux pairs. The choice to use in the particular case, is determined by practical reasons; what can be measured or not, or which terms are zero. For instance, under isothermal conditions we need not take the term containing the heat flux along, even if heat may be transported reversibly. One set may give a negative contribution to the entropy production (work is done), but the overall entropy production is positive, of course. Each set can be used to obtain constitutive equations for transport on the macro-scale. We shall proceed to find these for porous media flow, finding first more detailed expressions for the driving forces.

In the simple case of a single fluid, say w, we obtain directly from Equations (23, 26) that

$$\sigma = J_q' \frac{\partial}{\partial x}(\frac{1}{T}) - J_V \frac{1}{T}\frac{\partial p}{\partial x} \tag{31}$$

In the absence of a gradient in composition, $d\mu_i^c = 0$, the same expression applies also for more components. We may follow Hansen et al. [22] and write the component contributions as $J_n V_n = \hat{S}^n v_n$, $J_w V_w = \hat{S}^w v_w$ and $J_V = v = \hat{S}^n v_n + \hat{S}^w v_w$. where the saturation has been introduced, and v_i is the volume flow of i.

4. DEFINITION OF THE DRIVING FORCES IN THE CONTEXT OF A POROUS MEDIUM

We expand on the basis presented earlier [1], and give definitions of the driving forces in the context of porous media flow.

4.1. The Saturation-Dependent Contributions to the Chemical Potential Gradient

The specific contribution to the chemical potential gradients in the entropy production in Equation (23) is of interest. The concentration dependent part of the chemical potential of i, μ_i, for an ideal system is (in J.kg^{-1})

$$\mu_i = \mu_i^0 + \frac{RT}{W_i} \ln \frac{\rho_i}{\rho_i^{0,\mathrm{REV}}} \tag{32}$$

Here R is the gas constant (in J.K^{-1}.mol^{-1}) and W_i is the molar mass (in kg.mol^{-1}). The chemical potential is measured referred to a standard state, μ_i^0, having the local concentration ρ_i^0 in all the pores. In the description of porous media, a convenient reference state may be the state when one component is filling all pores, or when the saturation is unity, $\hat{S}^i = 1$. The mass density of i in the REV for the standard state is $\rho_i^{0,\mathrm{REV}} = \rho_i^0 V_p^{\mathrm{REV}}/V^{\mathrm{REV}} = \rho_i^0\phi$. Away from this state $\rho_i = \rho_i^0 \hat{S}^i \phi$ for $i = n, w$. When ϕ is constant, this gives

$$\frac{\rho_i}{\hat{S}^i} = \rho_i^0 \phi \tag{33}$$

By introducing these definitions into Equation (32), we obtain for the concentration dependent part of the chemical driving force of n

$$\frac{\partial \mu_n^c}{\partial x} = \frac{RT}{W_n}\frac{1}{\hat{S}^n}\frac{\partial \hat{S}^n}{\partial x} \tag{34}$$

We see that any variation in saturation between REVs along the x-axis (cf. **Figure 1**), will lead to a driving force. We integrate between two REVs and obtain the chemical driving force for porous media flow

$$\rho_n \Delta \mu_n^c = \phi \frac{\rho_n^0 RT}{W_n}\Delta \hat{S}^n \tag{35}$$

We have seen that the return to the Gibbs energy of the porous medium helped define the chemical potential in terms of properties relevant to porous media. All variables are measurable.

4.2. The Pressure Dependent Contribution

The driving force for volume flow is the negative gradient of the REV pressure over the temperature. To measure the pressure p inside the REV is difficult. The pressure in the fluid phases adjacent to the porous medium can be determined. Tallakstad et al. [11] defined the measured pressure difference, $\Delta p'$, at steady state, as an average over the value $\Delta p(t)$ over the time of measurement:

$$\Delta p' = \frac{1}{t_e - t_s}\int_{t_s}^{t_e} \Delta p(t) dt \tag{36}$$

Here t is the time and Δ refers to the extension of the system. Subscript 's' denotes the start and 'e' denotes the end of the measurement. We will take this pressure difference as our Δp. The pressure differences Δp^w and Δp^n can also be measured when there is continuity in the fluids, w and n, respectively.

The pressure variation across the REV is given by Equation (19), we have an interpretation of the pressure difference external to the porous medium;

$$\frac{d}{dx}p = \frac{d}{dx}(\bar{p} - \bar{p}^c) \tag{37}$$

We integrate over the system and obtain an interpretation of the total pressure difference:

$$\Delta p = \Delta \bar{p} - \Delta \bar{p}^c \tag{38}$$

We can assess the right-hand side of this equation using Equations (17, 18).

4.2.1. The Case of Large Pressure Differences

When the pressure drop across the porous plug is large compared to the capillary pressure contribution, the surface contributions and therefore $\bar{p}^c$ can be neglected. This is the case of large capillary numbers. Furthermore $p^n = p^w$. In the pressure difference, the terms with constant ϕ and p^r disappears, and the pressure difference is:

$$\Delta p = \Delta \bar{p} = \phi \Delta p^w \tag{39}$$

The pressure is applied to the whole cross-sectional area. This explains that the net driving force becomes a fraction, ϕ, of Δp^w. In other words, the force applies to the fraction ϕ of the pore area.

The conditions leading to Equation (39) are common in the laboratory. Some numerical values for the air-glycerol system, [4], can illustrate when the conditions apply. The value of $2\phi\gamma^{wr}/\bar{r}$ is of the same order of magnitude as $p^c\hat{S}^n\phi$ (400 Pa) when the surface tension $\gamma = 6.4 \cdot 10^{-2}$N m^{-2}, the average pore radius $\bar{r}$ = 0.2 mm and the porosity ϕ = 0.63. A typical value of $\Delta\bar{p}$ in the experiments is close to 30 kPa, which is far from the limit where capillary effects are significant.

4.2.2. The Case of Small Pressure Differences

For small capillary numbers the effective pressure drop across a porous plug is comparable to or smaller than the capillary pressure. Surface contributions need be taken into account. Equation (38) gives the effective pressure difference. When we can assume a constant average radius $\bar{r}$, and constant porosity, we obtain

$$\Delta p = \Delta \bar{p} - \frac{2\phi}{\bar{r}}\Delta\left[\left(\gamma^{nr} - \gamma^{wr}\right)\hat{S}^n + \gamma^{wr}\right] - \Delta\left(\gamma^{nw}\frac{\Omega^{nw,\mathrm{REV}}}{V^{\mathrm{REV}}}\right) \tag{40}$$

A fluid will be transported when the surface tensions of the fluids with the wall are different and there is a difference in the saturation. When there is only one fluid in the porous medium, cf. Equation (22), and we have constant $\bar{r}$ and porosity, the pressure difference becomes

$$\Delta p = \Delta \bar{p} - \frac{2\phi}{\bar{r}}\Delta\gamma^{wr} \tag{41}$$

The last term can lead to mass transport, when the surface tension changes.

5. CONSTITUTIVE EQUATIONS. EXAMPLES

5.1. Constitutive Equations for Non-isothermal, Two-Phase, Immiscible Fluids

The constitutive equations follow from the entropy production. We present these on differential form for two incompressible flows. From Equation (23) we have:

$$\begin{aligned} J_q' &= l_{qq}\frac{\partial}{\partial x}(\frac{1}{T}) - l_{qw}\frac{1}{T}\frac{\partial \mu_{w,T}}{\partial x} - l_{qn}\frac{1}{T}\frac{\partial \mu_{n,T}}{\partial x} \\ J_w &= l_{wq}\frac{\partial}{\partial x}(\frac{1}{T}) - l_{ww}\frac{1}{T}\frac{\partial \mu_{w,T}}{\partial x} - l_{wn}\frac{1}{T}\frac{\partial \mu_{n,T}}{\partial x} \\ J_n &= l_{nq}\frac{\partial}{\partial x}(\frac{1}{T}) - l_{nw}\frac{1}{T}\frac{\partial \mu_{w,T}}{\partial x} - l_{nn}\frac{1}{T}\frac{\partial \mu_{n,T}}{\partial x} \end{aligned} \tag{42}$$

We can also use Equation (29) and obtain

$$\begin{aligned} J_q' &= l_{qq}\frac{\partial}{\partial x}\left(\frac{1}{T}\right) - l_{qp}\frac{1}{T}\frac{\partial}{\partial x}p + l_{qd}\frac{\rho_n}{T}\frac{\partial \mu_n^c}{\partial x} \\ J_V &= l_{pq}\frac{\partial}{\partial x}\left(\frac{1}{T}\right) - l_{pp}\frac{1}{T}\frac{\partial}{\partial x}p + l_{pd}\frac{\rho_n}{T}\frac{\partial \mu_n^c}{\partial x} \\ \upsilon_D &= l_{dq}\frac{\partial}{\partial x}\left(\frac{1}{T}\right) - l_{dp}\frac{1}{T}\frac{\partial}{\partial x}p + l_{dd}\frac{\rho_n}{T}\frac{\partial \mu_n^c}{\partial x} \end{aligned} \tag{43}$$

The flux-force relations are linear on the REV-level. Our construction of the coarse-grained entropy production has followed the standard line in non-equilibrium thermodynamic theory, meaning that the Onsager relations holds for each matrix of coefficients. They may not hold, when the REV no longer can be constructed using Euler homogeneity (i.e., can be regarded as a thermodynamic state) or when the balance equations fail. Some evidence exists that the REV is a thermodynamic state [4, 5]. Also, there is theoretical and computational proof that the Onsager relations apply, $l_{ij} = l_{ji}$ [23–25]. Experimental proof for the Onsager relations exists for one-phase flow in porous media[26], but as far as we know, not for two-phase flow. We continue to specify how this possibly can be achieved.

One set of conductivities can be expressed by the other, using entropy production invariance. The element l_{qq} is the same in both formulations.

We have discussed above how the local and overall driving forces can be determined. We integrate across the system in order to relate experimental results to theory. We integrate the linear laws 43 across the REV, and obtain

$$\begin{aligned} J'_q &= L_{qq}\Delta(\frac{1}{T}) - L_{qw}\frac{1}{T}\Delta\mu_{w,T} - L_{qn}\frac{1}{T}\Delta\mu_{n,T} \\ J_w &= L_{wq}\Delta(\frac{1}{T}) - L_{ww}\frac{1}{T}\Delta\mu_{w,T} - L_{wn}\frac{1}{T}\Delta\mu_{n,T} \\ J_n &= L_{nq}\Delta(\frac{1}{T}) - L_{nw}\frac{1}{T}\Delta\mu_{w,T} - L_{nn}\frac{1}{T}\Delta\mu_{n,T} \end{aligned} \tag{44}$$

and

$$\begin{aligned} J'_q &= L_{qq}\Delta\left(\frac{1}{T}\right) - L_{qp}\frac{1}{T}\Delta p + L_{qd}\frac{\rho_n}{T}\Delta\mu_n^c \\ J_V &= L_{pq}\Delta\left(\frac{1}{T}\right) - L_{pp}\frac{1}{T}\Delta p + L_{pd}\frac{\rho_n}{T}\Delta\mu_n^c \\ \upsilon_D &= L_{dq}\Delta\left(\frac{1}{T}\right) - L_{dp}\frac{1}{T}\Delta p + L_{dd}\frac{\rho_n}{T}\Delta\mu_d^c \end{aligned} \tag{45}$$

Here $L_{ij} \equiv l_{ij}/l$ and l is the length of the REV, and the driving forces are defined by Equations (35, 38).

The coefficients may become dependent on the force through the integration as shown by Sinha et al. [27]. The averaging procedure gave the conductivity as a function of ($\Delta\bar{p}$ - Δp^c) in the terminology of this paper. In the remainder of this work we will discuss experimental conditions that allow us to determine these coefficients. The presentation follows closely the derivation of Stavermann [28] and Katchalsky et al. [29]. For transport in discrete systems with polymer membranes, see also [30]. We refer to these works for further definitions of transport coefficients.

5.2. Constitutive Equation for Isothermal, Single Fluid

For an isothermal single fluid *w*, flowing inside a porous medium, the entropy production 45 has one term; the volume flow times the negative pressure difference over the temperature. By including the constant temperature in the transport coefficient, we obtain the common linear law. With the permeability L_p, we write

$$J_V = -L_p\Delta p \tag{46}$$

where $L_p \equiv L_{pp}/T$. The permeability is normally a function of state variables (pressure, temperature). In the hydrodynamic regime it is a function of viscosity, $L_p = L_p(p, T, \eta)$. By introducing the new expression for the pressure, Equation (22), we obtain

$$J_V = -L_{VV}\left(\Delta p^w - \frac{2}{\bar{r}}\Delta\gamma^{wr}\right) \tag{47}$$

When the permeability and porosity are constant, $L_{VV} \equiv L_p\phi$. The equation predicts a threshold value for flow if there is a (significant) change in the surface tension across the REV. Transport will take place, when $\Delta p^w > 2\Delta\gamma^{wr}/\bar{r}$. The permeability L_{VV} is inversely proportional to the viscosity η of the fluid in the hydrodynamic regime. Interestingly, Boersma et al. [8] and Miller et al. [7] plotted the volume flow vs. the hydrostatic pressure difference Δp^w and found a deviation from Darcy's law in the form of a pressure threshold, for water or water solutions in clay. They offered no explanation for this. Also Bernadiner et al. [9] and Swartzendruber [6] plotted the volume flow of water solution J_V vs. the pressure gradient in sandstone with low clay content [9], and in NaCl-saturated Utah bentonite [6]. The thresholds that they observed depended on the content of salt in the permeating solution. They explained the thresholds by water adsorption and pore clogging by colloids [9]. According to Equation (47), a varying surface tension (due to a varying adsorption and clogging) might explain the existence of a threshold or a non-linear flux-force relation. There is no reason to believe that the non-linear flux-force relation is not caused by creation of system disorder, as was shown analytically for a tube [27] and in Sinha and Hansen [12] for a porous medium.

5.3. Constitutive Equations for Isothermal, Two-Phase Fluids

The entropy production in Equation (29) has two terms when two immiscible components flow at isothermal conditions. We choose the formulation that has variables J_V and υ_D; volume flux and interdiffusion flux, respectively. Equation (45) gives then:

$$\begin{aligned} J_V &= -L_{pp}\Delta p + L_{pd}\left(\rho_n\Delta\mu_n^c\right) \\ \upsilon_D &= -L_{dp}\Delta p + L_{dd}\left(\rho_n\Delta\mu_n^c\right) \end{aligned} \tag{48}$$

where $L'_{ij} \equiv L_{ij}/T$. The coefficients reflect, as above, the mechanism of flow (pressure, diffusion). Four experiments can be done to determine the four coefficients. There are only three independent coefficients. When four experiments are done, we can check the Onsager relations.

5.3.1. Main Coefficient: The Hydraulic Permeability

The (hydraulic) permeability K is related to the mobility coefficient L_{pp}, by $L_{pp} = K/\eta$ where η is the fluid viscosity. Both coefficients are measured at uniform composition. By

introducing the driving force for the volume flow from Equation (38), we obtain [the last term on Equation (48)] is zero:

$$J_V = -L_{pp}\Delta p = -L_{pp}\Delta(\bar{p} - \bar{p}^c) \tag{49}$$

With the present definition of variables the equation applies to the overall behavior of the system. A plot of J_V vs. $\Delta\bar{p}$ may show a threshold. This threshold has more contributions than in the single component system, as there are contributions to the pressure from surface and line energies. A threshold may be detectable at low capillary numbers.

The hydraulic permeability, is found by measuring the volume flow caused by the overall pressure difference at uniform composition;

$$K = -\eta\left(\frac{J_V}{\Delta p}\right)_{d\mu_n^c=0} \tag{50}$$

The mobility is a function of the saturation, $L_{pp} = L_{pp}(p, T, \eta, \hat{S}^w)$. In the hydrodynamic regime, the coefficient can be modeled, assuming Poiseuille flow and the effective viscosity $\eta^{\text{eff}} = \eta_w\hat{S}^w + \eta_n\hat{S}^n$ [27]. Using a pore model, Sinha et al. [27] found a dependence of the coefficient L_{pp} on the threshold pressure. This non-linearity does not prevent the use of non-equilibrium thermodynamics.

5.3.2. Main Coefficient: The Interdiffusion Coefficient

The main coefficient L_{dd} is an interdiffusion coefficient. It is defined at uniform pressure from the difference flux created by a difference in saturation;

$$L_{dd} = \left(\frac{\upsilon_D}{\rho_n\Delta\mu_n^c}\right)_{\Delta p=0} = \frac{W_n}{\phi RT\rho_n^0}\left(\frac{\upsilon_D}{\Delta\hat{S}^n}\right)_{\Delta p=0} \tag{51}$$

where we used Equation (35) for the driving force.

5.3.3. The Two Coupling Coefficients

The coupling coefficients in Equations (48) express that a separation of components can be caused by a pressure gradient (L_{dp}) and that a volume flow can be promoted by a gradient in saturation (L_{pd}).

Consider first the determination of L_{dp}. A pressure gradient may build as a consequence of a difference in composition [30]. The volume flux continues until a balance of forces is reached:

$$\Delta p = \frac{L_{pd}}{L_{pp}}\rho_n\Delta\mu_n^c \tag{52}$$

From the force-balance across the system, we obtain:

$$\left(\frac{\Delta p}{\Delta\hat{S}_n}\right)_{J_V=0} = \frac{L_{pd}}{L_{pp}}\phi\frac{\rho_n^0 RT}{W_n} \tag{53}$$

This condition can be used to find the unknown coupling coefficient, once the hydraulic permeability is known.

The remaining coupling coefficient can be found from the flux ratio, r, that has been called the reflection coefficient r, see also [30]. At constant saturation, we have

$$r = -\left(\frac{\upsilon_D}{J_V}\right)_{\Delta\mu_n^c=0} = -\frac{L_{dp}}{L_{pp}} \tag{54}$$

We are now in a position to compare L_{pd} and L_{dp} and verify the Onsager relations. The state of the system must be (approximately) the same, when the comparison is made.

5.4. Constitutive Equations for Non-isothermal, Two-Phase Fluids

The full set of equations given in Equation (45) must be used to describe non-isothermal flow in porous media. The coefficients, L_{pp}, $L_{pd} = L_{dp}$, L_{dd} in the lower right-hand side corner of the conductivity matrix, were discussed above. The new coefficients are those related to heat transport. The coefficient L_{qq} represents the Fourier type heat conductivity at uniform composition and pressure. The coefficients L_{pq} and L_{dq} are coupling coefficients.

Non-zero coefficients L_{pq} and L_{dq} mean that we can obtain separation in a temperature gradient. Injection of cold water into warm reservoirs may thus lead to separation. Likewise, a pressure difference can arise from a temperature difference. This is thermal osmosis [14].

Separation caused by a thermal driving force was observed in clay-containing soils where water was transported in clay capillaries against a pressure gradient. The coefficient, measured at constant pressure, was called the segregation potential [31]. The coefficient L_{pq} can be obtained from Equation (45), setting $\Delta p = 0$ and $\Delta\mu_n^c = 0$ ($\Delta\hat{S}^n$=0) in the second line. We obtain

$$\left(\frac{J_V}{\Delta T}\right)_{\Delta p=0,\Delta\mu_n^c=0} = -\frac{1}{T^2}L_{pq} \tag{55}$$

This coefficient can also be found from steady state conditions, when the thermal gradient is balanced by a gradient in saturation (chemical potential)

$$\begin{aligned} L_{pq}\frac{1}{T^2}\Delta T &= L_{pd}\rho_n\Delta\mu_n^c = L_{pd}\phi\frac{RT\rho_n^0}{W_n}\Delta\hat{S}^n \\ \left(\frac{\Delta\hat{S}^n}{\Delta T}\right)_{\upsilon_D=0} &= \frac{W_n}{RT^3\rho_n^0}\frac{L_{pq}}{L_{pd}} \end{aligned} \tag{56}$$

This determination of L_{pq} requires knowledge of L_{pd}. Alternatively, we may obtain the coefficient from the thermal osmosis experiment

$$\left(\frac{\Delta p}{\Delta T}\right)_{J_V=0,\Delta\mu_n^c=0} = -\frac{1}{T}\frac{L_{pq}}{L_{pp}} \tag{57}$$

The coupling coefficient L_{qp} can also be found by measuring the heat flux that accompanies the volume flux for constant composition and at isothermal conditions.

$$\left(\frac{J_q'}{J_V}\right)_{\Delta T=0,\Delta\mu_n^c=0} = \frac{L_{qp}}{L_{pp}} \tag{58}$$

These interrelated effects are well-known in homogeneous media [14], but have to the best of our knowledge, not been measured for porous media with two-phase flow.

6. DISCUSSION AND CONCLUSION

We have further developed a new coarse-grained formulation of the entropy production [1] for porous media, and specified the constitutive equations for flow of two immiscible fluids under uniform or varying temperature, pressure and composition. Several of the equations are new in the context of porous media, but they follow well-documented tracks in classical non-equilibrium thermodynamics [1, 28–30]. Experimental observations exist on single fluid flow, that give support to the theoretical description.

We have given a new definition of the pressure of the representative elementary volume (REV), and used it to obtain the pressure part of the driving force. The force obtains contributions from homogeneous phases, surfaces—and, in principle also line—tensions of the system. This distinguishes the present formulation from their counterpart for homogeneous systems [1, 28–30].

We have seen that surface contributions can be spelled out for varying conditions, under the assumption that the additive properties of the REV are Euler homogeneous of the first order. Doing this, we have been able to explain for instance deviations from Darcy's law, or the occurrence of threshold pressures in plots of flow vs pressure difference. We have pointed at possibilities to describe non-isothermal phenomena.

As for instance sections 5.1–5.3 show, there is a multitude of scenarios that can be further investigated, and used to check the theory. The expressions open up the possibility to test the thermodynamic models in use, for their compatibility with the second law.

The basic assumption used is that the REV set of basis variables are Euler homogeneous functions of degree one. This means in essence that *one* temperature, *one* pressure and *one* chemical potential per component can be defined for the REV. Some evidence already supports the idea that the REV is a thermodynamic state [4], [5], originally proposed by Hansen and Ramstad [3] and Tallakstad et al. [11]. We did neither consider surface areas, nor their curvature or the contact line length as independent variables, but these may be included, cf.[21].

We have illustrated relations for some specific cases; the non-isothermal flow of one or two immiscible single fluids in a non-deformable medium. It is straight forward to include more terms in the chemical potential (*e.g.* gravity). To include stress fields or other fields that deform the porous medium is more problematic, and has been postponed.

Flow of two isothermal, immiscible fluids in a porous medium has often been described by Darcy's law, using the relative permeability concept. The seepage velocities v_n and v_w are related to fluxes used here by $v_n = J_n V_n$ and $v_w = J_w V_w$. The expressions for the seepage velocities must be contained or be equivalent to the expressions given here, using the condition of invariance for the entropy production. A comparison can elucidate assumptions that are made. Hilfer and Standnes et al. [32, 33] gave a set of linear relations for the seepage velocities. Their driving forces were the gradients in the single component pressures, obtained by pressure measurements in the single phases. Their description implies e.g., that the composition is uniform.

We have seen through these examples how non-equilibrium thermodynamic theory can provide a fundamental basis for constitutive equations, also in porous media. For systems that obey entropy production invariance and Onsager symmetry, we have obtained relations between variables, which have been used to a limited degree for two-phase systems.

AUTHOR CONTRIBUTIONS

SK and DB defined the variables of the REV and wrote the first draft. AH, BH, and OG critically examined all proposals and contributed to revisions of the Manuscript.

ACKNOWLEDGMENTS

Per Arne Slotte is thanked for stimulating discussions. The authors are grateful to the Research Council of Norway through its Centers of Excellence funding scheme, project number 262644, PoreLab.

REFERENCES

1. Kjelstrup S, Bedeaux D, Hansen A, Hafskjold B, Galteland O. Non-isothermal two-phase flow in porous media. The entropy production. *Front Phys.* (2018) **6**:126. doi: 10.3389/fphy.2018.00126
2. de Groot SR, Mazur P. *Non-Equilibrium Thermodynamics*. London: Dover (1984).
3. Hansen A, Ramstad T. Towards a thermodynamics of immiscible two-phase steady-state flow in porous media. *Comp Geosci.* (2009) **13**:227–34. doi: 10.1007/s10596-008-9109-7
4. Erpelding M, Sinha S, Tallakstad KT, Hansen A, Flekkøy EG, Måløy KJ. History independence of steady state in simultaneous two-phase flow through two-dimensional porous media. *Phys Rev E* (2013) **88**:053004. doi: 10.1103/PhysRevE.88.053004
5. Savani I, Sinha S, Hansen A, Kjelstrup S, Bedeaux D, Vassvik M. A Monte Carlo procedure for two-phase flow in porous media. *Transp Porous Med.* (2017) **116**:869–88. doi: 10.1007/s11242-016-0804-x
6. Swartzendruber D. Non-Darcy flow behaviour in liquid-saturated porous media. *J Geophys Res.* (1962) **67**:5205. doi: 10.1029/JZ067i013p05205
7. Miller RJ, Low PF. Threshold Gradient for Water Flow in Clay Systems. *Soil Sci Soc Am Proc.* (1963) **27**:605–9.
8. Boersma L, Lindstrom FT, Saxena SK. Limitations of Darcy's law in glass bead porous media. *Soil Sci Soc Am Proc.* (1973) **37**:333–5.
9. Bernadiner MG, Protopapas AL. Progress on the theory of flow in geologic media with treshold gradient. *J Environ Sci Health* (1994) **A29**:249–75.
10. Sinha S, Bender AT, Danczyk M, Keepseagle K, Prather CA, Bray JM, et al. Effective rheology of two-phase flow in three-dimensional porous media: experiment and simulation. *Transp Porous Med.* (2017) **119**:77–94. doi: 10.1007/s11242-017-0874-4
11. Tallakstad KT, Knudsen HA, Ramstad T, Løvoll G, Måløy KJ, Toussaint R, et al. Steady-state, two-phase flow in porous media: Statistics and transport properties. *Phys Rev Lett.* (2009) **102**:074502. doi: 10.1103/PhysRevLett.102.074502

12. Sinha and Hansen Sinha S, Hansen A. Effective rheology of immiscible two-phase flow in porous media. *Europhys Lett.* (2012) **99**:44004. doi: 10.1209/0295-5075/99/44004
13. Kjelstrup S, Bedeaux D. *Non-Equilibrium Thermodynamics of Heterogeneous Systems.* Singapore: Wiley (2008).
14. Barragan VM, Kjelstrup S. Thermo-osmosis in membrane systems. *J NonEq Thermodyn.* (2017) **42**:217–36. doi: 10.1515/jnet-2016-0088
15. Costeseque P, Pollak T, Platten JK, Marcoux M. Transient-state method for coupled evaluation of Soret and Fick coefficients, and related tortuosity factors, using free and porous packed thermodiffusion cells: applications to $CuSO_4$ aqueous solution (0.25 M). *Eur Phys J E* (2004) **15**:249–53. doi: 10.1140/epje/i2004-10064-6
16. Colombani J, Galliero G, Duguay B, Caltagirone JP, Montel F, Bopp PA. A molecular dynamics study of the thermal diffusion in a porous medium. *Phys Chem Chem Phys.* (2002) **4**:313–21. doi: 10.1039/B106800H
17. H Davarzani MQ M Marcoux. Theoretical predictions of the effective thermodiffusion coefficients in porous media. *Int J Heat and Mass Transfer* (2010) **53**:1514–28. doi: 10.1016/j.ijheatmasstransfer.2009.11.044
18. Keulen L, van der Ham LV, Kuipers NJM, Hanemaaijer JH, Vlugt TJH, Kjelstrup S. Membrane distillation against a pressure difference. *J Membr Sci.* (2017) **524**:151–62. doi: 10.1016/j.memsci.2016.10.054
19. Hassanizadeh SM, Gray WG. Mechanics and thermodynamics of multiphase flow in porous media including interphase boundaries. *Adv Water Resour.* (1990) **13**:169–86.
20. Gray WG, Hassanizadeh SM. Macroscale continuum mechanics for multiphase porous-media flow including phases, interfaces, common lines and commpon points. *Adv Water Resour.* (1998) **21**:261–81.
21. McClure JE, Armstrong RT, Berrill MA, Schluter S, Berg S, Gray WG, et al. A geometric state function for two-fluid flow in porous media. *arXiv:1805.11032* (2018). doi: 10.1103/PhysRevFluids.3.084306
22. Hansen A, Sinha S, Bedeaux D, Kjelstrup S, Gjennestad MA, Vassvik M. Relations between seepage velocities in immiscible, incompressible two-phase flow in porous media. *Transp Porous Med.* (2018) **125**:565–87. doi: 10.1007/s11242-018-1139-6
23. Flekkøy EG, Pride SR, Toussaint R. Onsager symetry from mesoscopic time reversibility and the hydrodynamic dispersion tensor for coarse-grained systems. *Phys Rev E.* (2017) **95**:022136. doi: 10.1103/PhysRevE.95.022136
24. Pride S, Vasco D, Flekkøy E, Holtzmann R. Dispersive transport and symmetry of the dispersion tensor in porous media. *Phys Rev E* (2017) **95**:043103. doi: 10.1103/PhysRevE.95.043103
25. Burelbach J, Bruckner DB, Frenkel D, Eiser E. Thermophoretic forces on a mesoscopic scale. *Soft Matter.* (2018) **14**:7446–54. doi: 10.1039/C8SM01132J
26. Li SX, Pengra DB, Wong P. Onsager's reciprocal relation and the hydraulic permeability of porous media. *Phys Rev E.* (1995) **51**: 5748–51.
27. Sinha S, Hansen A, Bedeaux D, Kjelstrup S, Savani I, Vassvik M. Effective rheology of bubbles moving in a capillary tube. *Phys Rev E* (2013) **87**:025001. doi: 10.1103/PhysRevE.87.025001
28. Stavermann AJ. Non-equilibrium thermodynamics of membrane processes. *Trans Farad Soc.* (1952) **48**:176–85.
29. Katchalsky A, Curran PF. *Nonequilibrium Thermodynamics in Biophysics.* Cambridge, MA: Harvard University Press (1965).
30. Førland KS, Førland T, Ratkje SK. *Irreversible Thermodynamics. Theory and Applications.* Chichester: Wiley (1988).
31. Konrad JM. Frost susceptibility related to soil index properties. *Can Geotech J.* (1999) **36**:403–17.
32. Hilfer R. Macroscopic equations of motion for two phase flow in porous media. *Phys Rev E* (1998) **58**:2090.
33. Standnes DC, Evje S, Andresen PØ. A novel relative permeability model based on mixture theory approach accounting for solid-fluid and fluid-fluid interaction. *Transp Porous Med.* (2017) **119**:707–38. doi: 10.1007/s11242-017-0907-z

Conflict of Interest Statement: The authors declare that the research was conducted in the absence of any commercial or financial relationships that could be construed as a potential conflict of interest.

APPENDIX
Symbol Lists

TABLE A1 | Mathematical symbols, superscripts, subscripts.

Symbol	Explanation
c	Superscript meaning capillary pressure
d	Differential
∂	Partial derivative
Δ	Change in a quantity or variable
$\Delta_{f,t}$	The change is taken from f on the right to t On the left hand side
Σ	Sum
i	Subscript meaning component i
m	Number of fluids
n	Subscript meaning non-wetting fluid
w	Subscript meaning wetting fluid
p	Superscript meaning pore
REV	Abbreviation meaning representative elementary volume
r	Superscript meaning rock, solid matrix of medium
s	Superscript meaning interface
u	Subscript meaning internal energy
α, β	Superscripts meaning surface between phases α and β
α, β, δ	Superscripts meaning contact line between phases α, β, δ
θ	Contact angle, average

TABLE A2 | latin symbols

Symbol	Dimension	Explanation
G	J	Gibbs energy
M	kg	Mass
d	m	Pore length
H_i	$\mathrm{J.kg^{-1}}$	Partial specific enthalpy of i
J	$\mathrm{kg.s^{-1}.m^{-2}}$	Mass flux
J'_q	$\mathrm{J.s^{-1}.m^{-2}}$	Sensible heat flux
l	m	Characteristic length of representative elementary volume
L	m	Characteristic length of experimental system
L_{ij}		Onsager conductivity
p	Pa	Pressure of REV
$\bar{r}$	m	Average pore radius
S	$\mathrm{J.K^{-1}}$	Entropy
s	$\mathrm{J.K^{-1}.m^{-3}}$	Entropy density
S_i	$\mathrm{J\ kg^{-1}.K^{-1}}$	Partial specific entropy of i
$\hat{S}_i$		Degree of saturation of i, $\equiv V_i/V$
T	K	Temperature
t	s	Time
U	J	Internal energy
u	$\mathrm{J.m^{-3}}$	Internal energy density
V	$\mathrm{m^3}$	Volume
V_i	$\mathrm{m^3.kg^{-1}}$	Partial specific volume
x	m	Axis of transport
W_i	$\mathrm{kg.mol^{-1}}$	Molar mass of i

TABLE A3 | greek symbols, continued

Symbol	Dimension	Explanation
α		Superscripts meaning a phase
β		Superscript meaning an interface
δ		Superscript meaning a contact line
ϕ		Porosity of porous medium
γ	$\mathrm{N.m^{-1}}$	Surface tension
μ_i	$\mathrm{J.kg^{-1}}$	Chemical potential of i
ρ_i	$\mathrm{kg.m^{-3}}$	Density, $\equiv M_i/V_i$
σ	$\mathrm{J.s^{-1}.K^{-1}.m^{-3}}$	Entropy production in a homogeneous phase
Ω	$\mathrm{m^2}$	Surface or interface area

frontiers in Physics

ORIGINAL RESEARCH
published: 08 January 2019
doi: 10.3389/fphy.2018.00148

Predicting the Dielectric Response of Saturated Sandstones Using a 2-electrode Measuring System

Alex Kirichek[1,2]*, *Claire Chassagne*[2] *and Ranajit Ghose*[3]

[1] Deltares, Delft, Netherlands, [2] Department of Hydraulic Engineering, Faculty of Civil Engineering and Geosciences, TU Delft, Delft, Netherlands, [3] Department of Geoscience and Engineering, Faculty of Civil Engineering and Geosciences, TU Delft, Delft, Netherlands

4-electrode setups are usually used to measure the dielectric response (complex conductivity) of sandstones, as it is known that 2-electrode systems are sensitive to unwanted electrode polarization at low frequency. Moreover, electrode polarization (EP) occurs in the frequency range where the characteristic relaxation associated to the grain size also occurs, which can therefore theoretically be assessed using 4-electrode setups. Nonetheless, we find that other parameters of interest (porosity, salinity) can easily be extracted from the frequency range ∼ 1–10 kHz, beyond the one affected by EP using a 2-electrode setup. An additional unwanted effect ("pseudo-inductance") is observed in the frequency range 10 kHz–1 MHz during our experiments. Even though the origin of this effect remains unknown, it is shown to be correlated with the ionic strength of the system and the electrode separation. The bulk polarization region, i.e., the region of intermediate frequencies devoid of EP and pseudo-inductance polarizations, is the one of interest, as the complex conductivity of the system is there only dependent on material parameters such as the porosity of the sandstone and the conductivity of the electrolyte. We demonstrate that in the bulk region the model predicts the complex conductivity response, when these porosity and ionic strength are known. The model has been validated using laboratory measurements on a Bentheim sandstone saturated with five different NaCl concentrations: 5, 10, 100, 170, and 540 mM.

Keywords: dielectric spectroscopy, sandstone, electrode polarization, 2-electrode setup, impedance

OPEN ACCESS

Edited by:
Dick Bedeaux,
Norwegian University of Science and Technology, Norway

Reviewed by:
Siddharth Surajbhan Gautam,
The Ohio State University, United States
Miguel Rubi,
University of Barcelona, Spain

***Correspondence:**
Alex Kirichek
alex.kirichek@deltares.nl

Specialty section:
This article was submitted to Physical Chemistry and Chemical Physics, a section of the journal Frontiers in Physics

Received: *24 October 2018*
Accepted: *05 December 2018*
Published: *08 January 2019*

Citation:
Kirichek A, Chassagne C and Ghose R (2019) Predicting the Dielectric Response of Saturated Sandstones Using a 2-electrode Measuring System. Front. Phys. 6:148. doi: 10.3389/fphy.2018.00148

1. INTRODUCTION

Frequency dependent electrical measurements have been widely used during the last decades for environmental and engineering studies [e.g., 1–4]. All these measurements have been typically done using a 4-electrode cell, a measurement technique that is in principle devoid of (unwanted) electrode polarization effect. Numerous laboratory experiments have been conducted to investigate the frequency-dependence of the electrical conductivity of porous rocks, unconsolidated sands and sandstones using 4-electrode setups in the frequency range between 0.01 Hz and 10 MHz [e.g., 1, 5–8]. The electrokinetic polarization response is however difficult to interpret quantitatively due to crosstalks between the 4 electrodes in the frequency range > 1 kHz, dependent on the electrode separation and unwanted interactions between the measuring equipment, electrodes and the sample. For the high frequency range 2-electrode setups are generally used, as they are less sensitive to cross talks in that range [9]. The bulk impedance, i.e., the impedance of the saturated sandstone (devoid of parasitic impedances), can be masked

by electromagnetic pseudo-inductance effects which produce inductive loops yielding positive values in the phase spectra at high frequencies. These loops can be triggered by the wiring of the measurement system [10]. Normally, this effect is taken into account during the design of the measurement cell so that its contribution is reduced. Even though crosstalks between electrodes are avoided when 2-electrode systems are used, wiring induced and other unwanted polarizations can still arise as we will demonstrate with our measurements.

Electrode polarization (EP) is the most common electrode/bulk effect reported in the literature for dielectric spectroscopy measurements, which are conducted with 2-electrode systems [11–14]. This phenomenon occurs due to the build-up of ions close to the surface of the electrodes (which are assumed to be perfectly blocking) at low frequencies. As the impedance measurements presented in this article are done with 2-electrode system, EP is dominant in the impedance spectra at low frequencies. Several relaxation frequencies can be observed in the spectra, an important one being associated to the relaxation of the double layer of the grains which occurs at high frequencies [6, 9].

Mechanistic models describing the overlapping of the polarization effects at low and high frequencies are given in Leroy and Revil [15], Jougnot et al., [2], and Okay et al. [16] among others. These models have been successfully used to connect the complex conductivity to the changes in the pore fluid chemistry [e.g., 9, 32, 38]. Recently, we have proposed a new model for the dielectric response of sands and sandstones that in most cases require no adjustable parameters [17]. The model we presented was for dielectric spectra that are not affected by unwanted (parasitic) polarization effects. They were tested using data from literature that were obtained with 4-electrode setups, and the mismatches found between models and experimental data were attributed to the unwanted polarization effects generated from the measuring equipment.

In the present article, we will show that the model can be adapted to account for unwanted polarization effects in the case of 2-electrode systems. Unlike 4-electrode setups, 2-electrode setups have the advantage to be less sensitive to crosstalks in the frequency range > kHz. We will show that in a given frequency range, (1–10 kHz), the impedance of the saturated sandstone (devoid of parasitic impedances) can be obtained and that 2-electrode measurements are reliable. For higher frequencies, we found that an unwanted pseudo-inductance affected our measurements. This pseudo-inductance was also accounted for in the model.

The dielectric spectroscopy measurements presented in this article were performed using a 2-electrode system on fully saturated sandstones in the frequency range 20 Hz–3 MHz, where EP, bulk polarization (the polarization of the saturated sandstone) and pseudo-inductance effects are present. We compare the data with the response of an equivalent circuit model that is built as a sum of three complex impedances. Two of these impedances are directly linked to the theoretical complex conductivities of EP and bulk, and are, therefore only dependent on the system parameters (fluid, grain and electrode properties). The last impedance is introduced to model the pseudo-inductance effect measured at high frequencies. This impedance is a function of one adjustable parameter. Frequency ranges where one of the polarization effects (EP, bulk or pseudo-inductance) is dominant will be mathematically defined from the analysis of the full equivalent circuit expression. The theoretical range corresponding to the dominance of the bulk polarization will be compared to the experimental one.

This paper consists of four sections. In the first section we formulate theoretical descriptions of electrode polarization, bulk polarization, and pseudo-inductance complex conductivities as functions of the system parameters, i.e., porosity, conductivity and dielectric permittivity of water and grains. The model is compared with other models available in literature. In the second section we give an equivalent circuit model, for which the circuit elements can be identified with the complex conductivities found in the first section. In the third section a short overview of the laboratory experimental setup, which is used to measure the dielectric spectroscopy of reservoir rock that is saturated with NaCl solution, is given. Finally, in the fourth section we test the new model by predicting the desired bulk properties from the measured electrokinetic response of a fully saturated reservoir rock for 5 different NaCl solution concentrations.

2. THEORY

2.1. Bulk Polarization

In Kirichek et al. [17], we show (see Equation 8 in that article) that the complex conductivity of the bulk, $\sigma_b^*(\omega)$, can be expressed using the Maxwell-Wagner model as

$$\sigma_b^*(\omega) = \sigma_b(\omega) + i\omega\varepsilon_0\varepsilon_b(\omega) = \sigma_e^*(\omega)\frac{1+2(1-\phi)\beta^*(\omega)}{1-(1-\phi)\beta^*(\omega)}, \quad (1)$$

where $\sigma_b(\omega)$ and $\varepsilon_b(\omega)$ are, respectively, the conductivity and relative dielectric permittivity of the bulk, ω is the angular frequency, ε_0 is the permittivity of vacuum, $\sigma_e^*(\omega) = \sigma_e + i\omega\varepsilon_0\varepsilon_e$, σ_e is the conductivity of electrolyte, ε_e is the relative dielectric permittivity of electrolyte. Note that $\sigma_b(\omega)$ and $\varepsilon_b(\omega)$ are frequency dependent whereas σ_e and ε_e are not in the frequency range of interest, i.e., < GHz. Furthermore, ϕ is the porosity, $\beta^*(\omega)$ is the dipolar coefficient that is linked to the polarization $P(\omega)$ of a grain and its double layer by $P(\omega) = \alpha^*(\omega)E_0(\omega)$. $E_0(\omega)$ is the electrical field that is applied on the porous media and the polarizability, $\alpha^*(\omega)$, is given by: $\alpha^*(\omega) = 4\pi\varepsilon_e\varepsilon_0 a^3\beta^*(\omega)$, where a is the radius of a grain.

For an electrolyte (with no grains) $\phi = 1$, and one gets $\sigma_b^*(\omega) = \sigma_e^*(\omega)$, as expected. One can show that the dipolar coefficient $\beta^*(\omega)$ of a spherical grain with complex conductivity $\sigma_g^*(\omega)$ immersed in an electrolyte of conductivity $\sigma_e^*(\omega)$ can be written as [17, 18]:

$$\beta^*(\omega) = \frac{\sigma_g^*(\omega) - \sigma_e^*(\omega)}{\sigma_g^*(\omega) + 2\sigma_e^*(\omega)}, \quad (2)$$

where $\sigma_g^*(\omega) = i\omega\varepsilon_0\varepsilon_g$, ε_g being the relative dielectric permittivity of the grains. For silica grains, we take $\varepsilon_g \approx 4.5$ [19]. This expression for $\beta^*(\omega)$ is based on the hypothesis that

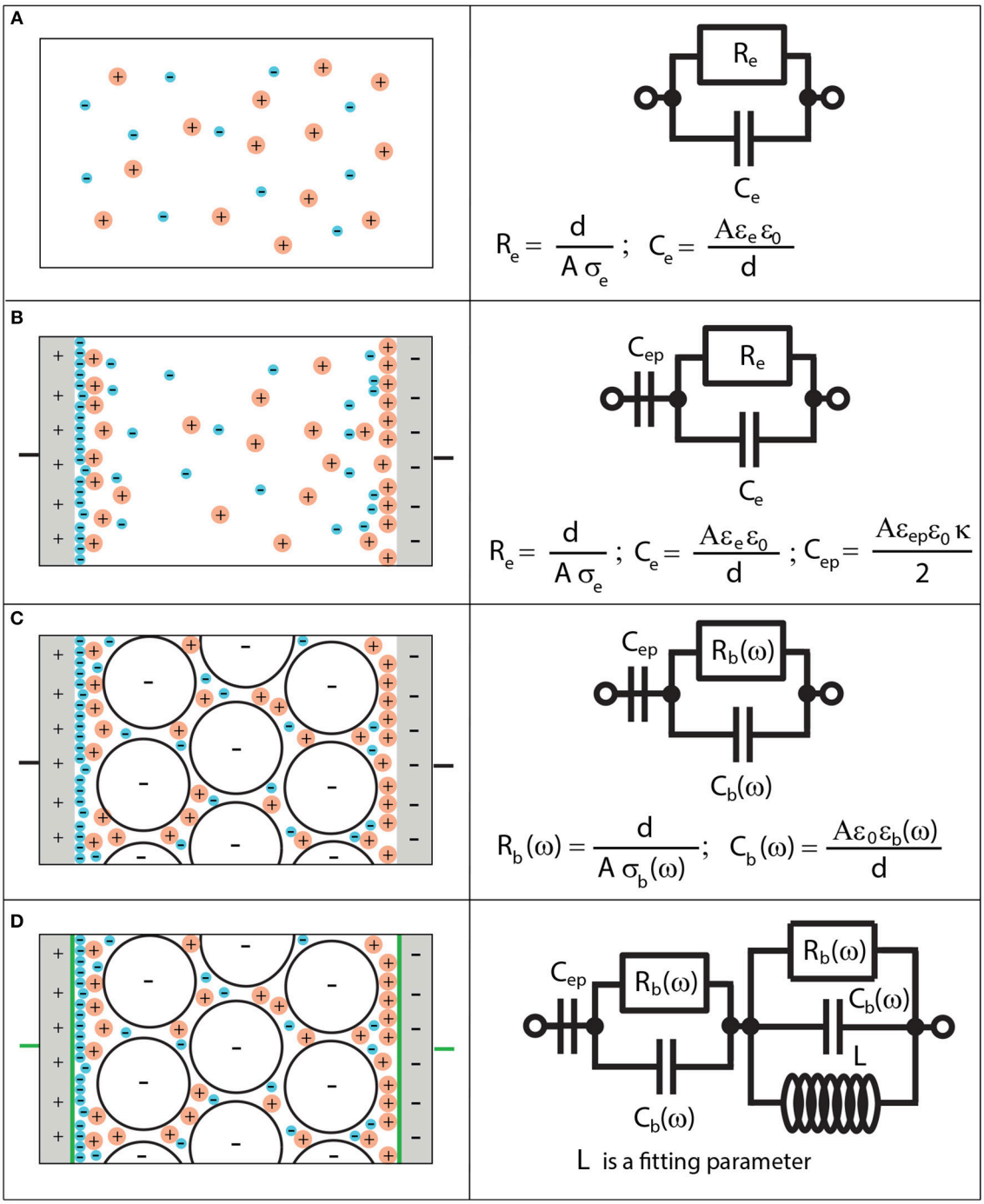

FIGURE 1 | Equivalent circuit representation of the measured electrical impedance. **(A)** Equivalent circuit representation for an electrolyte solution. R_e and C_e are resistance and capacitance of the electrolyte, A is the area of the electrode, d is the distance between the electrodes, ε_0 is the permittivity of vacuum, σ_e and ε_e are electrical conductivity and permittivity of an electrolyte, respectively. **(B)** Equivalent circuit representation for an electrolyte solution with electrode polarization. C_{ep} is the capacitance of electrode polarization, ε_{ep} is the permittivity of electrode polarization and κ^{-1} is the electric double layer thickness. **(C)** Equivalent circuit representation for an electrolyte saturated sandstone with electrode polarization. $R_b(\omega)$ and $C_b(\omega)$ are resistance and capacitance of the bulk, $\sigma_b(\omega)$ and $\varepsilon_b(\omega)$ are electrical conductivity and permittivity of the bulk, respectively. **(D)** Equivalent circuit representation for a bulk in presence of electrode polarization and pseudo-inductance. L is used as a fitting parameter.

the polarization of the double layer is negligible compared to the polarization of the core of the grain. This hypothesis is valid for $\kappa a >> 1$, where κ^{-1} is the Debye length given in Equation 6, and moderate zeta potentials [18]. We showed in Kirichek et al. [17] how the corresponding parameter, the Dukhin number influences the expression for $\beta^*(\omega)$ and hence the complex conductivity of sands and sandstones. The Dukhin number reads

$$Du = \frac{2}{\kappa a}\left[\exp\left(\frac{e\zeta}{2kT}\right) - 1\right], \tag{3}$$

where e is the elementary charge, ζ is the zeta potential, k the Boltzmann constant and T the temperature. In our case, we can estimate that on an average $\kappa a \sim 10^4 \gg 1$, where the inverse of the Debye length, κ is defined in Equation 6. The Dukhin number is therefore small, which implies that the grain bulk polarization will dominate the total (grain and double layer) polarization. In the case of small charged grains, there are models which take into account the electric double layer polarization, and even account for additional layers, like Stern layers [17, 18], in the evaluation of $\beta^*(\omega)$, see also the **Appendix** of the present article.

The conductivity of the electrolyte σ_e can be evaluated by:

$$\sigma_e \equiv \sum_i D_i \frac{e^2 z_i^2 \nu_i n_\infty}{k_B T}, \tag{4}$$

where D_i is the diffusion constant of ion i, z_i is the valency of ion i, ν_i are stoichiometric coefficients, k_B is the Boltzman constant, T is temperature, and n_∞ is the ionic density. The latter is given by

$$n_\infty[m^{-3}] = C_s[mM] \cdot N_a[mol^{-1}], \tag{5}$$

with C_s and N_a being the salt concentration and the Avogadro constant, respectively. The Debye length κ^{-1} is a measure for the electric double layer thickness. It can be calculated using

$$\kappa^2 \equiv \frac{e^2 n_\infty}{\varepsilon_e \varepsilon_0 k_B T} \sum_i \nu_i z_i^2. \tag{6}$$

Substituting Equation 6 in Equation 4 and using the electroneutrality relation $\sum \nu_i z_i = 0$ leads to

$$\sigma_e \equiv \varepsilon_e \varepsilon_0 \kappa^2 D_0 \qquad \text{with} \qquad D_0 = \frac{z_+ D_+ - z_- D_-}{z_+ - z_-}. \tag{7}$$

In this work we consider NaCl solution as the pore-filling electrolyte. Hence, we assume the following: $D_+ \approx D_- \approx 2{\cdot}10^{-9}$ m^2/s, $z_+ = -z_- = \nu_+ = \nu- = 1$.

2.2. Electrode Polarization

Electrode polarization (EP) is observed at low frequencies in a 2-electrode measurement system and arises due to ion build-up close to the surface of the electrodes, as both electrodes are considered to be blocking. This effect is associated with a characteristic frequency ω_{ep}, which is defined as [11, 14]

$$\omega_{ep} = \frac{2D_0\kappa}{d}, \tag{8}$$

where d is the distance between the electrodes. We found that EP is indeed shifted to higher frequencies in our experiments, in accordance with Equation 8, as the ionic strength is increased and/or d is diminished.

In this article, C_s is in the range 5–540 mM, and two electrodes separations are used: d = 0.03 m and d = 0.074 m. The characteristic frequency for the EP effect is, thus, in the frequency range below 1 kHz (from Equation 8). EP complex conductivity can also be derived from the set of electrokinetic equations presented in Buck [11] and Chassagne et al. [14]. The expression for EP reads

$$\sigma^*_{ep}(\omega) = \frac{i\omega\varepsilon_{ep}\varepsilon_0\kappa d}{2}. \tag{9}$$

For electrolyte solutions (no porous media), $\varepsilon_{ep} = \varepsilon_e$. In the case of two-phase systems, such as suspensions or porous media made of electrolyte and grains, it remains to be investigated if $\varepsilon_{ep} = \varepsilon_e$ or $\varepsilon_{ep}(\omega) = \varepsilon_b(\omega)$ [14], where $\varepsilon_b(\omega)$ is the dielectric permittivity of the two-phase system that is connected to the bulk conductivity (Equation 1).

2.3. Pseudo-Inductance Effect

Our dielectric spectroscopy experiments (see **Figure 4**) show that the electrical impedance has a positive phase in the frequency range [10 kHz–1 MHz]. A positive phase is usually the signature of the presence of parasitic inductors due to the proximity of wires in electric circuits. Therefore, we call this effect "pseudo-inductance." We have observed that the characteristic frequency of this polarization depends on the electrode separation d, and its magnitude depends on the ionic strength. The pseudo-inductance complex conductivity is not modeled using first principles as is done for EP and bulk polarizations. We show in the next section how we account for it by using the concept of equivalent circuits.

3. FULL MODEL

Traditionally, dielectric spectroscopy measurements have been analyzed by means of equivalent electrical circuits. The classical equivalent circuit approach is based on the use of simple R, C, L elements. It has been shown explicitly that two-phase systems can also be modeled by equivalent circuits, where each circuit element can be linked to a theoretical complex conductivity, as defined in the previous section [14].

We looked for the same type of equivalence when setting up our full model. We wanted each polarization to be identifiable as a separate impedance in series with the others. This constraint led us to the equivalent circuits which are illustrated in **Figure 1**. The total impedance of the system is represented by:

$$Z_{theo} = Z_{ep} + Z_b + Z_{hf}, \tag{10}$$

where Z_{ep} and Z_b are the electrical impedances that arise from electrode and bulk polarizations, respectively. Z_{hf} accounts for the pseudo-inductance effect observed at high frequencies.

The complex electrical conductivity and complex electrical impedance are linked by

$$Z_k = \frac{d}{A\sigma_k^*(\omega)}, \tag{11}$$

where A is the area of an electrode, d is the distance between the electrodes, and $k = theo$, b, hf or ep. The ratio d/A is called the cell constant.

3.1. The Dielectric Response of Electrolyte Suspensions

For a simple electrolyte solution illustrated in **Figure 1A**, one can show that

$$\frac{1}{Z_{theo}} = \frac{1}{Z_e} = \frac{1}{R_e} + i\omega C_e \tag{12}$$

where R_e and C_e are linked to σ_e and ε_e by

$$R_e = \frac{d}{A\sigma_e} \quad \text{and} \quad C_e = \frac{A\varepsilon_0\varepsilon_e}{d}, \tag{13}$$

respectively. Note that, in this case, EP is not accounted for. Therefore, this equivalent circuit is valid for $\omega > \omega_{ep}$. In order to account for EP, one should consider **Figure 1B** [11], where the complex electrical conductivity of EP is connected to the EP impedance by:

$$Z_{ep} = \frac{d}{A\sigma_{ep}^*(\omega)} = \frac{1}{i\omega C_{ep}}. \tag{14}$$

The capacitance is given by $C_{ep} = A\kappa\varepsilon_{ep}\varepsilon_0/2$ and the impedance corresponding to EP and bulk polarization of the electrolyte is given by $Z_{theo} = Z_{ep} + Z_e$. The frequency range of validity is now in principle [mHz–MHz].

3.2. The Dielectric Response of Colloidal Suspensions and Sandstones

When the electrolyte solution is replaced by a suspension or a porous medium, the equivalence can still be considered valid [14, 17], but the circuit elements are then frequency-dependent so that $R_b(\omega)$ and $C_b(\omega)$ have the dimension of resistance and capacitance, but cannot actually be substituted by real resistance and capacitance as in traditional equivalent circuits. They are given by

$$R_b(\omega) = \frac{d}{A\sigma_b(\omega)} \quad \text{and} \quad C_b(\omega) = \frac{A\varepsilon_0\varepsilon_b(\omega)}{d}. \tag{15}$$

This case is shown in **Figure 1C**, where $Z_{theo} = Z_{ep} + Z_b$. The frequency range of validity in this case is in principle [mHz–MHz]. When $\phi = 1$ (only electrolyte), we get $\sigma_b^*(\omega) = \sigma_e^*(\omega)$ and $Z_b = Z_e$. In this case, the equivalent circuit reduces to the one given in **Figure 1B**.

3.3. Accounting for the Measured Pseudo-Inductance

The equivalent circuit presented in **Figure 1C** is valid in order to fit the data in the frequency range [mHz–≈ 10 kHz], as will be shown in the experiment section (Section 4). We found a pseudo-inductance signature in the impedance spectra for frequencies higher than 10 kHz. In order to account for the pseudo-inductance occurring at higher frequencies, the equivalent circuit presented in **Figure 1D** is used. Using the equivalent circuit, where $Z_{theo} = Z_{ep} + Z_b + Z_{hf}$, the data can be modeled for the whole frequency range [mHz– MHz]. At higher frequencies, the dielectric relaxation of water occurs [20], which is not accounted for in the present model. From the circuit element analysis, one finds the following characteristic frequencies:

$$\omega_{ep} = \frac{1}{R_e C_{ep}} = \frac{2\kappa}{d} D_0; \quad \omega_{hf1} = \frac{R_b}{L}; \quad \omega_0 = \frac{1}{R_b C_b} \simeq \kappa^2 D_0;$$
$$\text{and} \quad \omega_{hf2} = \sqrt{\omega_0 \omega_{hf1}} = \frac{1}{\sqrt{LC_b}}. \tag{16}$$

The frequency ω_{ep} corresponds to the characteristic frequency associated to EP, below which charges can fully build-up a double layer close to the blocking electrodes. Above ω_{ep}, EP effects can be considered to be negligible. The frequency ω_{hf1} corresponds to the frequency above which pseudo-inductance effects can affect the electrokinetic response. For extremely large L there is no pseudo-inductance effect, the frequencies ω_{hf1} and ω_{hf2} tend to infinity, and Z_{hf} can be represented by a wire. The equivalent circuit shown in **Figure 1D** then reduces to the one shown in **Figure 1C** for the frequency range $[\omega_{ep} - \omega_0]$. The frequency ω_{hf2} corresponds to the frequency where the charges cannot totally be dissipated in the system start to play a role. Above ω_0 (the Maxwell-Wagner frequency) no double layer can be established at the electrodes and the double layers around the grains cannot polarize anymore. Below ω_0 one can verify using Equations 1, 2, and 15, that R_b and C_b are in good approximation constant as function of frequency as we are in the special case where the Dukhin number, Equation 3, is small (large κa and moderate zeta potentials). This is why we could define proper characteristic frequencies in Equations 16 using R_b and C_b. In these definitions, we imply that we take the values of R_b and C_b below ω_0. The same holds for **Table 1** and **Table A1** (see Appendix) where the value for R_b is the value of R_b below ω_0. For larger Dukhin numbers, R_b and C_b become frequency-dependent below ω_0, but it is then also possible to define characteristic frequencies [14]. One can then find the approximations for the amplitude and phase in each frequency domain given in **Table 1**. An example is given in **Figure 2**. The individual contributions of Z_{ep}, Z_b, and Z_{hf} to Z_{theo} are indicated in color. An alternative equivalent circuit is given and discussed in the **Appendix**.

3.4. Comparison Between Models

Most models used in geophysics concentrate on the bulk polarization [e.g., 23, 27, 33, 37] as these authors use 4-electrode cells, for which EP effects are in theory avoided. 4-electrode cells are in fact not devoid of parasitic impedances due to cross-talks between the electrodes and some EP effects have been measured

TABLE 1 | Evolution of the amplitude $|Z_{theo}|$ and phase φ as function of the applied electric field frequency ω for the equivalent circuit presented in **Figure 1D**.

	$\omega_{ep} < \omega < \omega_{hf1}$	$\omega_{hf1} < \omega < \omega_{hf2}$	$\omega_{hf2} < \omega < \omega_0$
$\lvert Z_{theo}\rvert \simeq$	R_b	$R_b\left[1+(\omega/\omega_{hf1})/\left(\sqrt{1+(\omega/\omega_{hf1})^2}\right)\right]$	$2R_b/\sqrt{1+(\omega/\omega_0)^2}$
$\tan\varphi \simeq$	0	$(\omega/\omega_{hf1})/\left[1+2(\omega/\omega_{hf1})^2\right]$	$-\omega/\omega_0$

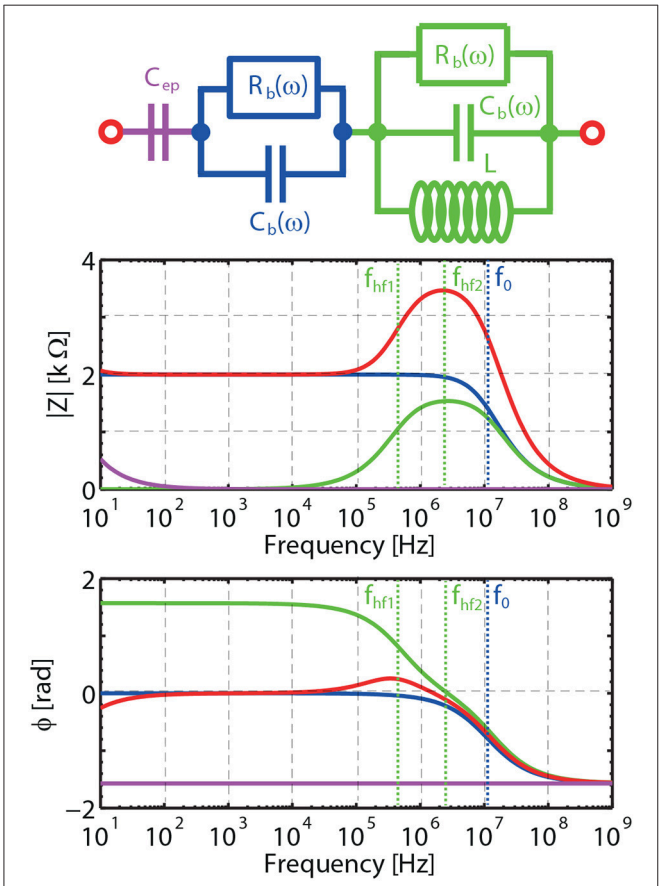

FIGURE 2 | Predicted magnitude $|Z|$ and phase φ of the electrical impedance of a sandstone saturated with a 50 mM NaCl electrolyte, including the effects of EP, bulk polarization and pseudo-inductance with $L = 5{\cdot}10^{-4}$ H, that is representative for our measurements. The individual contributions of Z_{ep} (magenta line), Z_b (blue line) and Z_{hf} (green line) to Z_{theo} (red line). f_{hf1}, f_{hf2} and f_0 are characteristic frequencies.

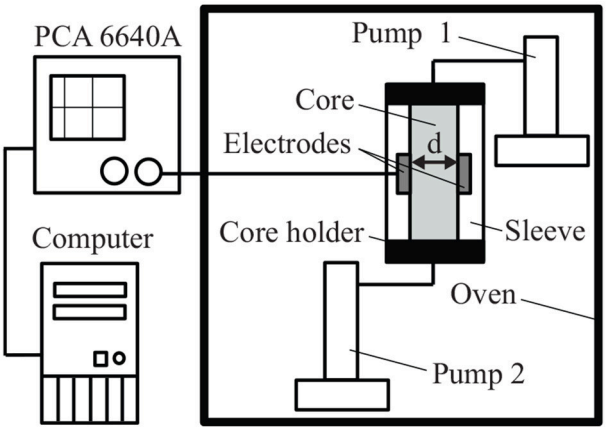

FIGURE 3 | Sketch of the experimental setup. Wayne Kerr Precision Component Analyser 6640A (PCA 6640A) is used to measure $|Z|$ and φ at the frequency range 20 Hz–3 MHz.

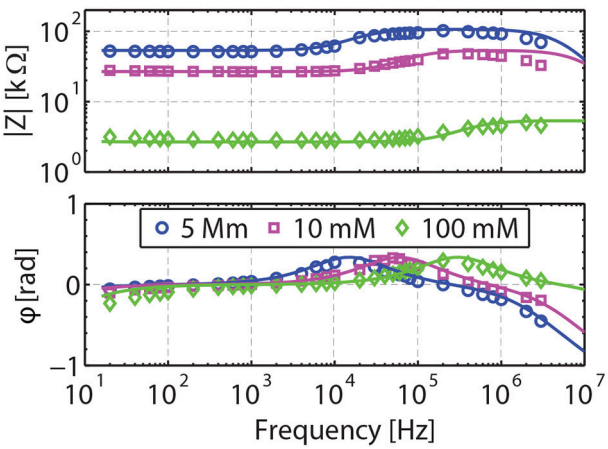

FIGURE 4 | Validation of the model for $d = 0.074$ m. Measured impedances are shown in symbols for NaCl concentration of 5, 10, and 100 mM. The full model is shown by the solid lines. Only the inductance L is fitted to match the pseudo-inductance response measured at $\omega > 10$ kHz. The response of the bulk (1–10 kHz) is obtained with no adjustable parameter, as in particular both porosity and salinity are known.

[e.g., 28, 34]. Moreover, 4-electrode systems and its additional electronics (as compared to 4-electrode systems) is in general less suitable for high frequencies. In their measurements, done using both 4 and 2 electrodes on a Berea sandstone saturated with NaCl, [9] found a good overlap between the two devices in the frequency range $[10^2$–$10^3]$ Hz. The 4-electrode setup was used in the frequency range $[10^{-3}$–$10^3]$ Hz, whereas the 2-electrode cell was used in the frequency range $[10^2$–$10^6]$ Hz. The relaxation frequencies associated to the electrolyte saturated sandstone are linked to its characteristic length scales. One of this length scale is the double layer thickness κ^{-1} and depending on ionic strength the associated characteristic frequency ω_0 is of the order of $[10^5$–$10^9]$ Hz a frequency range best probed using a 2-electrode device. The other length scale is the characteristic of a sandstone grain size, a, and the associated frequency is given by $\omega_a = D_0/a^2$ [14], which gives values of the order of 1–500 Hz for micrometric particles. This frequency range is therefore best probed by 4-electrode cells in principle. However, as stated above,

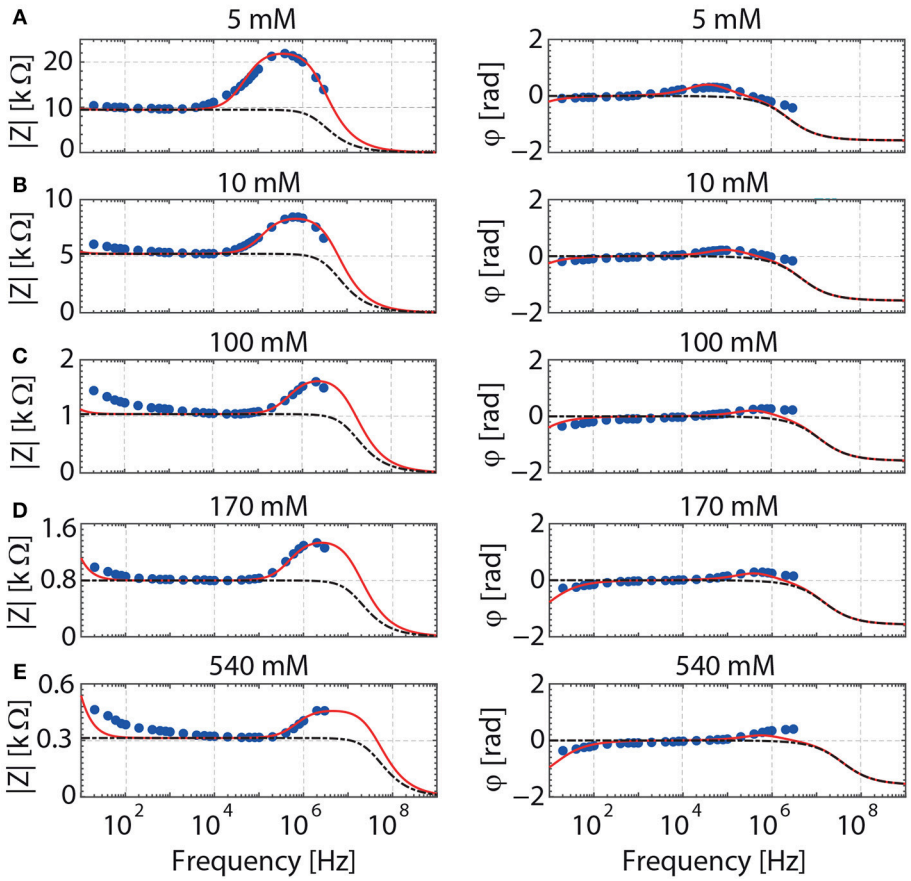

FIGURE 5 | Contribution of the bulk polarization (black line) to the total impedance (red line) of a fully saturated reservoir rock. The model for the impedance is given in **Figure 1**. No adjustable parameter is used to generate the bulk impedance. Measured impedances are shown in symbols for NaCl concentrations of 5, 10, 100, 170, and 540 mM. The electrode separation is 0.03 m.

EP can also contaminate the signal of 4-electrode devices, as such low frequencies and interpretation of data at these frequencies can be complicated [17, 21].

Some authors using 2-electrode cells try to mathematically "clean" the measured signal for EP [22]. A discussion about how to compensate for EP can be found in Chassagne et al. [14]. Experimental evidence however shows that even though it is theoretically possible to compensate for EP, in practice it is very difficult due to the non-ideality of the electrodes. In the present article we explicitly define the frequency range where the bulk properties of the system can be obtained without any correction.

Regarding the modeling of this bulk polarization part, different formulations for the related complex conductivity have been presented in the literature. A review has been provided by Chelidze et al. [23]. There has been some debate in literature regarding the origin of the low-frequency polarization (see Scott [24] for a review), which corresponds, in our terminology, to the frequency range below ω_0, where the double layers around charged grains can still polarize under the action of the electric field. It has been argued by some authors [e.g., [25]] that so-called membrane polarization could be causing this effect. Membrane polarization is caused in a pore constriction (pore throat), where ions in the pore fluid can encounter resistance to their movement, causing charge buildup. The first reference to membrane polarization is to be found in Marshall and Madden [26], where Marshall and Madden explicitly state that the conductive grains i.e., metallic particles within the rock are responsible for this phenomenon. Due to the voltage gradient in the vicinity of the conductive grains, a charge build-up can be created close to the conductive grains (much like what happens close to the electrodes) and electric double layers can be established. This is quite similar to what happens close to the surface of charged grains (with a dielectric core) which have electric double layers when they are in contact with an electrolyte. When grains are very close it is possible that their double layers overlap and it is argued that this might be the reason for the restriction in the pore throat (the pore throat being the space between the two grains). As discussed in Scott [24], and as the

reader can verify from Equation 6, the size of the double layer for most systems is generally in the nm range, much smaller than the average pore throat. Most rocks formed by grains (like sandstones) are well interconnected pores, see Sen et al. [27] for a discussion. In fact, from simple mathematical consideration, a pile of grains can be seen as having (average) pore throats of the order of a grain diameter. It is, therefore, not surprising that the effective-medium approach based on a collection of grains is giving good results, as for large grains and any ionic strength $\kappa a \gg 1$ any grain's double layer can polarize without being affected by a neighboring one. In Kirichek et al. [17], we moreover showed that the effective medium approach, as originally proposed by Maxwell-Wagner and Bruggeman, can be modified so as to include surface conductivities without the use of approximations (large κa, large ζ), which lead to formulations comparable to Equation 48 in Chelidze et al. [23]. In the present article, as discussed above, surface conduction due to the polarization of the grain double layer is negligible and our expression reduces to the self-similar model presented in Sen et al. [27], see their Equation 5.

We will show in the next section how our equivalent circuit model adequately reproduce our measured data for the whole range of frequencies investigated and how indeed the bulk polarization part can be estimated without any adjustable parameter in a well-defined frequency range.

4. LABORATORY EXPERIMENTS

A simplified sketch of the experimental setup is shown in **Figure 3**. The relatively high porosity (21.8%) and grain diameter (0.1–0.3 mm) of Bentheim sandstone makes it a good testing material for the core-flooding experiments. The sample is encased in a silicone sleeve and placed in a stainless steel core holder. An insulating silicon rubber is used as a material for the sleeve. Thus, current leakages from the system to the core holder can be disregarded. A temperature-controlled oven is used to reproduce realistic reservoir conditions of temperature and to eliminate complication of data analysis due to fluctuations in the external temperature.

Each end of the core holder contains a port for fluid injection. The sandstone is fully saturated with NaCl solution before each experiment.

A Wayne Kerr Precision Component Analyser 6640A is used as the impedance measuring system. Coaxial cables connect the measuring device to the electrodes, which are directly attached to the lateral surface of the core on diametrically opposite sides. We use a 2-terminal electrode system in this study. Both electrodes act as current and potential terminals. Residual stray impedances were filtered out using a standard open/short/load calibration [28]. The measurements of magnitude $|Z|$ and phase φ of the electrical impedance are conducted over the frequency range 20 Hz–3 MHz. The electrical conductivity $\sigma^*(\omega)$ is converted from the measured $|Z|$ and φ from

$$\sigma^*(\omega) = \frac{d}{A|Z|e^{i\varphi}}. \tag{17}$$

TABLE 2 | The fitting parameter L is used to generate the red curves in **Figures 4**, **5**.

	d = 0.03 m			d = 0.074 m		
Cs [mM]	f_{ep}[Hz]	f_{hf1}[Hz]	L[H]	f_{ep}(Hz)	f_{hf1}(Hz)	L(H)
5	20	$7 \cdot 10^3$	$2.2 \cdot 10^{-2}$	8	945	0.4
10	28	$1.5 \cdot 10^4$	$5 \cdot 10^{-3}$	11	$3.8 \cdot 10^3$	0.05
100	90	$5 \cdot 10^4$	$1.5 \cdot 10^{-4}$	36	$6.3 \cdot 10^3$	0.003
170	117	$5.6 \cdot 10^4$	$8 \cdot 10^{-5}$			
540	209	$1.4 \cdot 10^5$	$1 \cdot 10^{-5}$			

The characteristic frequencies are evaluated using Equations 16. The characteristic frequencies f_{ep} and f_{hf1} are related to the angular frequencies ω_{ep} and ω_{hf1} by $f_{ep} = \omega_{ep}/2\pi$ and $f_{hf1} = \omega_{hf1}/2\pi$, respectively.

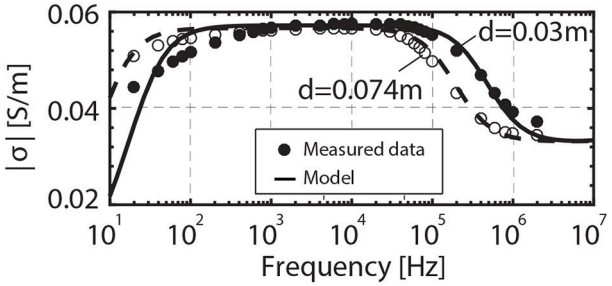

FIGURE 6 | Electrical conductivity spectrum of the porous rock saturated with 100 mM NaCl solution for electrode separation of 0.074 and 0.03 m.

We have conducted two sets of experiments. For the first set, we use a NaCl solution with C_s = 5, 10, 100, 170, and 540 mM. The distance between the electrodes d =0.03 m and the area is A =0.01×0.05 m^2. For the second set of experiments, NaCl solutions with C_s = 5, 10, and 100 mM are used. For this case, the parameters are d =0.074 m and A =0.01×0.025 m^2. Other parameters are the relative permittivity of water ε_e = 80, the relative permittivity of the sandstone ε_b = 4.5, the temperature is T = 25 degrees C.

5. RESULTS AND DISCUSSION

The dielectric response of the reservoir rock filled with NaCl solutions of various salinities is shown in **Figures 4**, **5**. A frequency region can be identified, where the contribution of the (desired) bulk polarization is dominant. For our measured data, this is [$\approx 10\ \omega_{ep}$–ω_{hf1}], as can be seen from comparing the regions where the bulk impedance is overlapping the total impedance in **Figures 4**, **5** and the values given in **Table 2**. This implies that within this frequency range the relevant parameters (porosity, salinity) can be extracted. In our case, both the porosity of the sandstone and the salinity of pore-filling electrolyte are known. Hence, the bulk polarization could be predicted with no adjustable parameters.

The characteristic frequency of EP, ω_{ep} is increasing with salinity in accordance with Equation 8. In Chassagne et al. [14]

the question was raised whether, in estimating C_{ep}, one should take $\varepsilon_{ep} = C_{ep}/(A\kappa\varepsilon_0) = \varepsilon_e$ or ε_b. We find that $\varepsilon_{ep}(\omega) \simeq \varepsilon_b(\omega)$ in the whole range of the considered salinity. This implies that the grains close to the electrodes certainly contribute to EP.

From **Figure 5** and the values given in **Table 2**, one realizes that the frequency range where EP is dominant [mHz–ω_{ep}] is underestimated. The frequency region where the bulk polarization is dominant is on average starting above $\approx 10\ \omega_{ep}$. The estimated value of ω_{ep} is based on the assumption that the electrodes are perfectly blocking and that the contact between these electrodes and the porous sandstone is ideal (the electrodes are not porous and extremely clean). In practice a discrepancy between theory and experiment is always observed when studying electrode polarization as these conditions are never met. Taking $\approx 10\omega_{ep}$ as an estimation from the characteristic frequency above which EP is negligible is found to be appropriate for the large range of salinity studied for the shortest electrode separation used (d = 0.03 m). For the larger electrode separation, d = 0.074 m, (see **Figure 4**), EP is barely affecting the measurements as ω_{ep} is found to be very low (see **Table 2**).

The effect of electrode separation is better illustrated in **Figure 6**, where the data is plotted in terms of conductivity in order to avoid the cell constant (d/A) dependence of the impedance. For $\omega_{ep} \ll \omega < \omega_{hf1}$, we have $Z_{theo} = Z_b$, and no adjustable parameters are required to predict the measured impedance.

The fact that the phase becomes positive in the frequency range [ω_{hf1}– ω_{hf2}] indicates the development of an inductive effect in the system. There are several possible explanations for the origin of this phenomenon. Inductive loops can be generated by a chemical reaction between electrode and electrolyte, e.g., oxidation of the electrodes [10]. Another trigger for inductive loops can be due to inductive connecting cables [10]. In this case the inductance signatures occur at high frequencies in the impedance spectrum. The coaxial cables used in the present study were perfectly shielded, so we do not expect they create a parasitic inductance. Fleig et al. [29] suggests that inductive loops can be induced in the impedance spectra at high frequencies due to the capacitive leakage to the ground. Since the measurement system used in this study is grounded, the occurrence of this artifact is highly unlikely.

Other authors [e.g., 30, 36] found a pseudo-inductance by measuring electrolyte solutions using 4-electrode setups. Zimmermann et al. [30] refers to this phenomenon as "contact impedance," and attributed it to a phase error due to the inhomogeneous contact impedance of the current electrodes. They found that the pseudo-inductance depends on the nature of the electrodes used. The surface properties of the electrodes (roughness, contamination) could, therefore, play a major role in the pseudo-inductance effect. An alternative possibility is proposed in the **Appendix**. We there demonstrate that the contribution of a Stern layer around the grains can generate pseudo-inductance effects. The demonstration is only theoretical as there is no proof that such contribution is present in the system we have investigated.

6. CONCLUSION

We have demonstrated that the dielectric response of a porous sandstone saturated with NaCl solutions of different concentrations measured with a 2-electrode setup can correctly be modeled using the theory presented in this article. The model accounts for 3 distinct polarization phenomena: electrode polarization, bulk polarization, and pseudo-inductance effect, that all three were found in our experiments. Different characteristic frequencies (ω_{ep}, ω_{hf1}, ω_0, and ω_{hf2}) were defined, see Equations 16. Each frequency range was studied theoretically to find its dominant polarization mechanism. A suitable frequency range was identified [$\approx 10\ \omega_{ep}$–ω_{hf1}] in our experiments, where the bulk polarization is the dominant part of the measured impedance. As both the porosity of the sandstone and the salinity of the pore fluid were known in our system, no adjustable parameter was required to predict the complex impedance response in the bulk polarization region. A good match was found between the predictions and measurements for a large range of ionic strengths and two different setups.

AUTHOR CONTRIBUTIONS

AK wrote the article, performed the experiments and analyzed the data. CC developed the theory and helped with the writing. RG was the formal supervisor of AK during his Ph.D.

ACKNOWLEDGMENTS

This research has been carried out in the context of the CATO2 program with grant number FES10036GXDU. CATO2 was the Dutch National Research Program on Carbon Capture and Storage (CCS) Technology. The program was financially supported by the Dutch Government (Ministry of Economic Affairs) and the CATO2 consortium parties. Part of the work presented here was published in the Ph.D. thesis of AK [31]. We thank Karel Heller for his help in the laboratory.

SUPPLEMENTARY MATERIAL

The Supplementary Material for this article can be found online at: https://www.frontiersin.org/articles/10.3389/fphy.2018.00148/full#supplementary-material

REFERENCES

1. Slater LD, Glaser DR. Controls on induced polarization in sandy unconsolidated sediments and application to aquifer characterization. *Geophysics* (2003) **68**:1547–88. doi: 10.1190/1.1620628
2. Jougnot D, Ghorbani A, Revil A, Leroy P, Cosenza P. Spectral induced polarization of partially saturated clay-rocks: a mechanistic approach. *Geophys J Int.* (2010) **180**:210–24. doi: 10.1111/j.1365-246X.2009.04426.x
3. Revil A, Karaoulis M, Johnson T, Kemna A. Review: some low-frequency electrical methods for subsurface characterization and

monitoring in hydrogeology. *Hydrogeol J.* (2012) **20**:617–58. doi: 10.1007/s10040-011-0819-x
4. Kemna A, Binley A, Cassiani G, Niederleithinger E, Revil A, Slater L, et al. An overview of the spectral induced polarization method for near-surface applications. *N Surf Geoph.* (2012) **10**:453–68. doi: 10.3997/1873-0604.2012027
5. Knight RJ. Hysteresis in the electrical resistivity of partially saturated sandstones. *Geophysics* (1991) **56**:2139–47. doi: 10.1190/1.1443028
6. Garrouch AA, Sharma MM. The influence of clay content, salinity, stress, and wettability on the dielectric properties of brine-saturated rocks: 10 Hz to 10 MHz. *Geophysics* (1994) **59**:909–17. doi: 10.1190/1.1443650
7. Ulrich C, Slater LD. Induced polarization measurements on unsaturated, unconsolidated sands. *Geophysics* (2004) **69**:762–71. doi: 10.1190/1.1759462
8. Binley A, Slater LD, Fukes M, Cassiani G. Relationship between spectral induced polarization and hydraulic properties of saturated and unsaturated sandstone, *Water Resour Res.* (2005) **41**:W12417. doi: 10.1029/2005WR004202
9. Lesmes DP, Frye KM. Influence of pore fluid chemistry on the complex conductivity and induced polarization responses of Berea sandstone. *J Geophys Res.* (2001) **106**:4079–90. doi: 10.1029/2000JB900392
10. Macdonald JR, Kenan WR. *Impedance Spectroscopy*. New York, NY: John Wiley and Sons (1987).
11. Buck RP. Diffuse layer charge relaxation at the ideally polarized electrode. *J Electroanal Chem.* (1969) **23**:219–40. doi: 10.1016/S0022-0728(69)80212-3
12. Scheider W. Theory of the frequency dispersion of electrode polarization. topology of networks with ractional power frequency dependence. *J Phys Chem.* (1975) **79**:127–36. doi: 10.1021/j100569a008
13. Volkmann J, Klitzsch N. Wideband impedance spectroscopy from 1 mHz to 10 MHz by combination of four- and two-electrode methods. *J Appl Geophs.* (2015) **114**:191–201. doi: 10.1016/j.jappgeo.2015.01.012
14. Chassagne C, Dubois E, Jimenez ML, van der Ploeg JPM, van Turnhout J. Compensating for electrode polarization in dielectric spectroscopy studies of colloidal suspensions: theoretical assessment of existing methods. *Front Chem.* (2016) **4**:30. doi: 10.3389/fchem.2016.00030
15. Leroy P, Revil A. A mechanistic model for the spectral induced polarization of clay materials. *J Geophys Res.* (2009) **114**:1–21. doi: 10.1029/2008JB006114
16. Okay G, Leroy P, Ghorbani A, Cosenza P, Camerlynck C, Cabrera J, et al. Spectral induced polarization of clay-sand mixtures: experiments and modeling. *Geophysics* (2014) **79**:E353–75. doi: 10.1190/geo2013-0347.1
17. Kirichek A, Chassagne C, Ghose R. Dielectric spectroscopy of granular material in an electrolyte solution of any ionic strength. *Coll Surf A* (2017) **533**:356–70. doi: 10.1016/j.colsurfa.2017.07.040
18. Chassagne C, Bedeaux D. The dielectric response of a colloidal spheroid. *J Coll Interf Sci.* (2008) **326**:240–53. doi: 10.1016/j.jcis.2008.06.055
19. Kirichek A, Ghose R, Heller HKJ. Laboratory monitoring of CO_2 migration and phase transition using complex electrical conductivity. In: *75th EAGE Conference and Exhibition Incorporating SPE EUROPEC 2013* London (2013).
20. Ngai KL. Interpretation of the ghz to thz dielectric relaxation dynamics of water in the framework of the coupling model. *J Mol Liq.* (2018) **253**:113–18. doi: 10.1016/j.molliq.2018.01.039
21. Niu Q, Revil A, Saidian M. Salinity dependence of the complex surface conductivity of the portland sandstone. *Geophysics* (2016) **81**:D125–14. doi: 10.1190/geo2015-0426.1
22. Prodan C, Bot C. Correcting the polarization effect in very low frequency dielectric spectroscopy. *J Phys D Appl Phys.* (2009) **42**:175505. doi: 10.1088/0022-3727/42/17/175505
23. Chelidze T, Gueguen Y. Electrical spectroscopy of porous rocks: a review - I. Theoretical models. *Geoph J Int.* (1999) **137**:1–15. doi: 10.1046/j.1365-246x.1999.00799.x
24. Scott JBT. The origin of the observed low-frequency electrical polarization in sandstones. *Geo phys.* (2006) **72**:G235–8. doi: 10.1190/1.2258092
25. Titov K, Komarov V, Tarasov V, Levitski A. Theoretical and experimental study of time domain-induced polarization in water-saturated sands. *J Appl Geophs.* (2002) **50**:417–33. doi: 10.1016/S0926-9851(02)00168-4
26. Marshall DJ, Madden TR. Induced polarization, a study of its causes. *Geophysics* (1959) **24**:790–816. doi: 10.1190/1.1438659
27. Sen PN, Scala C, Cohen MH. A self-similar model for sedimentary rocks with application to the dielectric constant of fused glass beads. *Geophysics* (1981) **46**:781–95. doi: 10.1190/1.1441215
28. Lvovich VF. *Impedance Spectroscopy: Applications to Electrochemical and Dielectric Phenomena*. New York, NY: John Wiley and Sons (2012).
29. Fleig J, Jamnik J, Maier J. Inductive loops in impedance spectroscopy caused by electrical shielding. *J Electrochem Soc.* (1996) **143**:3636–41. doi: 10.1149/1.1837263
30. Zimmermann E, Kemna A, Berwix J, Glaas W, Münch HM, Huisman JA. A high-accuracy impedance spectrometer for measuring sediments with low polarizability. *Meas Sci Technol.* (2008) **19**:105603. doi: 10.1088/0957-0233/19/10/105603
31. Kirichek A. *Electrokinetic and poroelastic Characterization of Porous Media: Application to CO_2 Storage Monitoring*. ISBN: 978-94-6186-902-9 (2018).
32. Schmutz M, Revil A, Vaudelet P, Batzle M, Femenía Viñao P, Werkema DD. Influence of oil saturation upon spectral induced polarization of oil bearing sands. *Geophys J Int.* (2010) **183**:211–24. doi: 10.1111/j.1365-246X.2010.04751.x
33. Vinegar HJ, Waxman MH. Induced polarization of shaly sands. *Geophysics* (1984) 49:1267–87. doi: 10.1190/1.1441755
34. Mazzeo BA. Parasitic capacitance influence of potential-sensing electrodes on four-electrode liquid impedance measurements. *J Appl Phys.* (2009) **105**:094106. doi: 10.1063/1.3124365
35. Hollingsworth AD, Saville DA. A broad frequency range dielectric spectrometer for colloidal suspensions: cell design, calibration, and validation. *J Colloid Interface Sci.* (2003) **257**:65–76. doi: 10.1016/S0021-9797(02)00029-2
36. Abdulsamad F, Florsch N, Schmutz M, Camerlynck C. Assessing the high frequency behavior of non-polarizable electrodes for spectral induced polarization measurements. *J Appl Geophs.* (2016) **135**:449–55. doi: 10.1016/j.jappgeo.2016.01.001
37. Leroy P, Revil A, Kemna A, Cosenza P, Ghorbani A. Complex conductivity of water-saturated packs of glass beads. *J Coll Int Sci.* (2008) **321**:103–17. doi: 10.1016/j.jcis.2007.12.031
38. Vaudelet P, Revil A, Schmutz M, Franceschi M, Bégassat P. Changes in induced polarization associated with the sorption of sodium, lead, and zinc on silica sands. *J Coll Int Sci.* (2011) **360**:739–52. doi: 10.1016/j.jcis.2011.04.077

Conflict of Interest Statement: The authors declare that the research was conducted in the absence of any commercial or financial relationships that could be construed as a potential conflict of interest.

frontiers in Physics

METHODS
published: 04 March 2019
doi: 10.3389/fphy.2019.00021

Bernaise: A Flexible Framework for Simulating Two-Phase Electrohydrodynamic Flows in Complex Domains

Gaute Linga, Asger Bolet and Joachim Mathiesen*

Niels Bohr Institute, University of Copenhagen, Copenhagen, Denmark

Bernaise (Binary Electrohydrodynamic Solver) is a flexible high-level finite element solver of two-phase electrohydrodynamic flow in complex geometries. Two-phase flow with electrolytes is relevant across a broad range of systems and scales, from "lab-on-a-chip" devices for medical diagnostics to enhanced oil recovery at the reservoir scale. For the strongly coupled multi-physics problem, we employ a recently developed thermodynamically consistent model which combines a generalized Nernst–Planck equation for ion transport, the Poisson equation for electrostatics, the Cahn–Hilliard equation for the phase field (describing the interface separating the phases), and the Navier–Stokes equations for fluid flow. We present an efficient linear, decoupled numerical scheme which sequentially solves the three sets of equations. The scheme is validated by comparison to cases where analytical solutions are available, benchmark cases, and by the method of manufactured solution. The solver operates on unstructured meshes and is therefore well suited to handle arbitrarily shaped domains and problem set-ups where, e.g., very different resolutions are required in different parts of the domain. *Bernaise* is implemented in Python via the FEniCS framework, which effectively utilizes MPI and domain decomposition. Further, new solvers and problem set-ups can be specified and added with ease to the *Bernaise* framework by experienced Python users.

Keywords: electrokinectic, electrohydrodynamics (EHD), porous flow, phase field method, capillarity, numerical simulation, finite element method (FEM)

OPEN ACCESS

Edited by:
Alex Hansen,
Norwegian University of Science and Technology, Norway

Reviewed by:
Iver Hakon Brevik,
Norwegian University of Science and Technology, Norway
Christian F. Klingenberg,
Universität Würzburg, Germany

****Correspondence:***
Gaute Linga
linga@nbi.dk

Specialty section:
This article was submitted to Interdisciplinary Physics, a section of the journal Frontiers in Physics

Received: *26 October 2018*
Accepted: *04 February 2019*
Published: *04 March 2019*

Citation:
Linga G, Bolet A and Mathiesen J (2019) Bernaise: A Flexible Framework for Simulating Two-Phase Electrohydrodynamic Flows in Complex Domains. Front. Phys. 7:21. doi: 10.3389/fphy.2019.00021

1. INTRODUCTION

Two-phase flow with electrolytes is encountered in many natural and industrial settings. Although Lippmann already in the nineteenth century [1, 2] made the observation that an applied electric field changes the wetting behavior of electrolyte solutions, the phenomenon of electrowetting has remained elusive. Recent decades have seen an increased theoretical and experimental interest in understanding the basic mechanisms of electrokinetic or electrohydrodynamic flow [3, 4]. Progress in micro- and nanofluidics [5, 6] has enabled the use of electrowetting to control small amounts of fluid with very high precision (see e.g., the comprehensive reviews by [2, 7, 8] and references therein). This yields potential applications in, e.g., "lab-on-chip" biomedical devices or microelectromechanical systems [9–11], membranes for harnessing blue energy [12], energy storage in fluid capacitors, and electronic displays [13–16].

It is known that electrohydrodynamic phenomena affects transport properties and energy dissipation in geological systems, as a fluid moving in a fluid-saturated porous medium sets up an electric field that counteracts the fluid motion [17–19]. Electrowetting may also be an important factor in enhanced oil recovery [20, 21]. Here, the injection of water of a particular salinity, or "smart water" [22], is known to increase the recovery of oil from reservoirs as compared to brine [23]. Further, transport in sub-micrometer scale pores in low-permeability rocks in the Earth's crust may be driven by gradients in the electrochemical potential [24], which may have consequences for, e.g., transport of methane-water mixtures in dense rocks.

Hence, a deepened understanding of electrowetting and two-phase electrohydrodynamics would be of both geological and technological importance. While wetting phenomena (or more generally, two-phase flow) on one hand, and electrohydrodynamics on the other, remain in themselves two mature and active areas of research which both encompass a remarkably rich set of phenomena, this article is concerned with the interface between these fields. For interested readers, there are several reviews available regarding wetting phenomena [25–27] and electrohydrodynamics [28–30]. Notably, the "leaky dielectric" model originally proposed by Taylor [31] (and revisited by [28]) to describe drop deformation, is arguably the most popular description of electrohydrodynamics, but it does not describe ionic transport and considers all dielectrics to be weak conductors. In this work, we shall employ a model that does not make such simplifications. Recently, Schnitzer and Yariv [32] showed rigorously that models of the latter type reduce to the Taylor–Melcher model in the double limit of small Debye length and strong electric fields. The simplified model may therefore have advantages in settings where those assumptions are justified, e.g., in simulations on larger scales; while the class of models considered here are more general and expected to be valid down to the smallest scale where the continuum hypothesis still holds.

Experimental and theoretical approaches [33–35] in two-phase electrohydrodynamic flows need to be supplemented with good numerical simulation tools. This is a challenging task, however: the two phases have different densities, viscosities and permittivities, the ions have different diffusivities and solubilites in the two phases, and moreover, the interface between the phases must be described in a consistent manner. Hence, much due to the complex physics involved, simulation of two-phase electrohydrodynamic phenomena with ionic transport is still in its infancy. It has been carried out with success e.g., in order to understand deformation of droplets due to electric fields [36–38], or for the purpose of controlling microfluidic devices (see e.g., [39]). Lu et al. [40] simulated and performed experiments on droplet dynamics in a Hele-Shaw cell. Notably, Walker et al. [41] simulated electrowetting with contact line pinning, and compared to experiments. In practical applications, such as in environmental remediation or oil recovery, the complex pore geometry is essential and it is therefore of interest to simulate and study electrowetting in such configurations. However, to our knowledge, there have been few numerical studies of these phenomena in the context of more complex geometries.

In this article, we introduce and describe *Bernaise* (Binary ElectRohydrodyNAmIc SolvEr), which is an open-source software/framework for simulating two-phase electrohydrodynamics. It is suitable for use in complex domains, operating on arbitrary unstructured meshes. The finite-element solver is written entirely in Python and built on top of the FEniCS framework [42], which (among other things) effectively uses the PETSc backend for scalability. FEniCS has in recent years found success in related applications, such as in high-performance simulation of turbulent flow [43], and for single-phase, steady-state electrohydrodynamic flow simulation in nanopores [44] and model fractures [45]. Since *Bernaise* was inspired by the *Oasis* solver for fluid flow [43], it is similar to the latter in both implementation and use.

In this work, we employ a phase-field model to propagate the interface between the two phases. Such *diffuse interface* models, as opposed to e.g., sharp interface models (see for instance [46]), assume that the fluid-fluid interface has a finite size, and have the advantage that no explicit tracking of the interface is necessary. Hence, using a phase-field model has several advantages in our setting: it takes on a natural formulation using the finite element method; in sub-micrometer scale applications, the diffuse interface and finite interface thickness present in these models might correspond to the physical interface thickness (typically nanometer scale [47]); and the diffuse interface may resolve the moving contact line conundrum [27, 48]. Note that although *ab initio* and molecular dynamics simulation methods are in rapid growth due to the increase in computational power, and do not require explicit tracking of the interface or phenomenological boundary conditions, such methods are restricted to significantly smaller scales than continuum models are. Nevertheless, they serve as valuable tools for calibration of the continuum methods [48–51]. We note also that sharp-interface methods such as level-set [52, 53] and volume-of-fluid methods [38, 54, 55] are viable options for simulating electrohydrodynamics, but such methods shall not be considered here.

The use of phase field models to describe multiphase flow has a long history in fluid mechanics [56]. Notably, the "Model H" of Hohenberg and Halperin [57], for two incompressible fluids with matched densities and viscosities, is based on the coupled Navier–Stokes–Cahn–Hilliard system, and was introduced to describe phase transitions of binary fluids or single-phase fluid near the critical point. Lowengrub and Truskinovsky [58] later derived a thermodynamically consistent generalization of Model H where densities and viscosities were different in the two phases, however with the numerical difficulty that the velocity field was not divergence free. To circumvent this issue, Abels et al. [59] developed a thermodynamically consistent and frame invariant phase-field model for two-phase flow, where the velocity field was divergence free, allowing for the use of more efficient numerical methods. Lu et al. [40] proposed a phase-field model to describe electrohydrodynamics, but was restricted to flow in Hele-Shaw cells, using a Darcy equation to describe the flow between the

parallel plates[1]. A phase-field approach to the leaky-dielectric model was presented by Lin et al. [60]. Using the Onsager variational principle, Campillo-Funollet et al. [61] augmented the model of Abels et al. [59] with electrodynamics, i.e., inclusion of ions, electric fields and forces. This can be seen as a more physically sound version of the model proposed by Eck et al. [62], which only contained a single "net charge" electrolyte species. A model for two-phase electrohydrodynamics was derived, with emphasis on contact line pinning, by Nochetto et al. [63], but this does not appear to be frame-invariant, as the chemical potential depends quadratically on velocity [61]. In this work, we will therefore focus on the model by Campillo-Funollet et al. [61].

There is a vast literature on the discretization and simulations of immiscible two-phase flows including phase-field models (see e.g., [46, 56]), but here we focus on research which is immediately relevant concerning the discretization and implementation of the model by Campillo-Funollet et al. [61]. Grün and Klingbeil [64] discretized the model in Abels et al. [59] (without electrohydrodynamics) with a dual mesh formulation, using a finite volume method on the dual mesh for advection terms, and a finite element method for the rest. Based on the sharp-interface model benchmarks of Hysing et al. [65], Aland and Voigt [66] provided benchmarks of bubble dynamics comparing several formulations of phase-field models (without electrodynamics). Energy-stable numerical schemes for the same case were presented and analyzed in Guillén-González and Tierra [67] and Grün et al. [68]. Campillo-Funollet et al. [61] provided preliminary simulations of the two-phase electrohydrodynamics model in their paper, however with a simplified formulation of the chemical potential of the solutes. A scheme for the model in Campillo-Funollet et al. [61] which decouples the Navier–Stokes equations from the Cahn–Hilliard–Poisson–Nernst–Planck problem, was presented and demonstrated by Metzger [69, 70]. In the particular case of equal phasic permittivities, the Cahn–Hilliard problem could be decoupled from the Poisson–Nernst–Planck problem. Recently, a stable finite element approximation of two-phase EHD, with the simplifying assumptions of Stokes flow and no electrolytes, was proposed by Nurnberg and Tucker [71].

The main contributions of this article is to give a straightforward description of *Bernaise*, including the necessary background theory, an overview of the implementation, and a demonstration of its ease of use. Solving the coupled set of equations in a monolithic manner (as is done in [61] using their in-house EconDrop software) is a computationally expensive task, and we therefore propose a new linear splitting scheme which sequentially solves the phase-field, chemical transport and the fluid flow *subproblems* at each time step. A major point of this article is to demonstrate the validity of the approach and numerical convergence of the proposed scheme. We do this through comparing our numerical solutions to limiting cases where analytical solutions are available, benchmark solutions, and using the method of manufactured solution. We also demonstrate how the framework can be extended by supplying user-specified problems and solvers. We believe that due to its flexibility, scalability and open-source licensing, this framework has advantages over software which to our knowledge may have *some* of the same functionality, such as EconDrop (in-house code of Grün and co-workers) and Comsol (proprietary). Compared to sharp-interface methods, the method employed in the current framework is automatically capable of handling topological changes and contact line motion, and the full three-dimensional (3D) capabilities allows to study more general phenomena than what can be achieved by axisymmetric formulations [38]. We expect *Bernaise* to be a valuable tool that may facilitate the development of microfluidic devices, as well as a deepened understanding of electrohydrodynamic phenomena in many natural or industrial settings.

The outline of this paper is as follows. In section 2, we introduce the sharp-interface equations describing two-phase electrohydrodynamics; then we present the thermodynamically consistent model of electrohydrodynamics by Campillo-Funollet et al. [61]. In section 3, we write down the variational form of the model, present the monolithic scheme, and present a linear splitting scheme for solving the full-fledged two-phase electrohydrodynamics. section 4 gives a brief presentation of *Bernaise*, and demonstrates its ease use through a minimal example. Further, we describe how *Bernaise* can be extended with user-specified problems and solvers. In section 5, we validate the approach as described in the preceding paragraph. In section 6, we apply the framework to a geologically relevant setting where dynamic electrowetting effects enter, and present full 3D simulations of droplet coalescence and breakup. Finally, in section 7 we draw conclusions and point to future work.

We expect the reader to have a basic familiarity with the finite element method, the Python language, and the FEniCS package. Otherwise, we refer to the tutorial by Langtangen and Logg [72].

2. MODEL

The governing equations of two-phase electrohydrodynamics can be summarized as the coupled system of two-phase flow, chemical transport (diffusion and migration), and electrostatics [61]. We will now describe the sharp-interface equations that the phase-field model should reproduce, and subsequently the phase-field model for electrohydrodynamics. For the purpose of keeping the notation short, we consider a general electrokinetic scaling of the equations. The relations between the dimensionless quantities and their physical quantities are elaborated in **Appendix A** in Supplementary Material.

2.1. Sharp-Interface Equations

In the following, we present each equation of the physical (sharp-interface) model. With validity down to the nanometer scale, the fluid flow is described by the incompressible Navier–Stokes equations, augmented by some additional force terms due to electrochemistry:

[1]Instead of the full Navier–Stokes equations, which would be necessary in the presence of boundaries in the two in-plane dimensions.

$$\rho_i \left(\partial_t \mathbf{v} + (\mathbf{v}\cdot\nabla)\mathbf{v}\right) - \mu_i \nabla^2 \mathbf{v} + \nabla p = -\sum_j c_j \nabla g_{c_j}, \quad (1)$$

$$\nabla \cdot \mathbf{v} = 0. \quad (2)$$

Here, ρ_i is the density of phase i, $\mathbf{v}$ is the velocity field, μ_i is the dynamic viscosity of phase i, $p(\mathbf{x}, t)$ is the pressure field[2], $c_j(\mathbf{x}, t)$ is the concentration of solute species j, and g_{c_j} is the associated electrochemical potential. The form of the right hand side of Equation (1) is somewhat unconventional (and relies on a specific interpretation of the pressure), but has numerical advantages over other formulations as it avoids, e.g., pressure build-up in the electrical double layers [73].

The transport of the concentration field of species i is governed by the conservative (advection–diffusion–migration) equation:

$$\partial_t c_j + \mathbf{v}\cdot\nabla c_j - \nabla\cdot(K_{ij} c_j \nabla g_{c_j}) = 0, \quad (3)$$

where K_{ij} is the diffusivity of species j in phase i. The electrochemical potential is in general given by

$$g_{c_j}(c_j, V) = \alpha'(c_j) + \beta_{ij} + z_j V, \quad (4)$$

where $\alpha'(c) = \partial\alpha/\partial c(c)$, and $\alpha(c)$ is a convex function describing the chemical free energy, β_{ij} is a parameter describing the solubility of species j in phase i, z_j is the charge if solute species j, and V is the electric potential. Equation (3) can be seen as a generalized Nernst–Planck equation. With an appropriate choice of $\alpha(c)$, Equation (3) reduces to the phenomenological Nernst–Planck equation, which has been established for the transport of charged species in dilute solutions under influence of an electric field. The latter amounts to a dilute solution, using the ideal gas approximation,

$$\alpha(c_j) \propto c_j(\ln c_j - 1). \quad (5)$$

With this choice of α, the solubility parameter β_{ij} can be interpreted as related to a reference concentration $c_j^{\mathrm{ref},i}$, through the relation

$$\beta_{ij} = -\ln c_j^{\mathrm{ref},i}. \quad (6)$$

This gives a chemical energy $\mathcal{G}_j = \alpha(c_j) + \beta_{ij} c_j = c_j(\ln(c_j/c_j^{\mathrm{ref},i}) - 1)$ which has a minimum at $c_j = c_j^{\mathrm{ref},i}$ (see also Linga et al. (Submitted)).

Since the dynamics of the electric field is much faster than that of charge transport, we can safely assume electrostatic conditions (i.e., neglect magnetic fields). This amounts to solving the Poisson problem (Gauss' law):

$$\nabla\cdot(\varepsilon_i \nabla V) = -\rho_e, \quad (7)$$

Here, ε_i is the electrical permittivity of phase i, and $\rho_e = \sum_j z_j c_j$ is the total charge density.

In the absence of advection, for the case of two symmetric charges, and under certain boundary conditions, Equations (3–7) lead to the simpler Poisson–Boltzmann equation (see **Appendix B** in Supplementary Material).

[2]The interpretation of this pressure depends on the formulation of the force on the right hand side of Equation (2).

2.1.1. Fluid-Fluid Interface Conditions

It is necessary to define jump conditions over the interface between the two fluids. We denote the jump in a physical quantity χ across the interface by $[\chi]_-^+$, and the unit vector $\hat{\mathbf{n}}_{\mathrm{int}}$ normal to the interface.

Firstly, due to incompressibility, the velocity field must be continuous:

$$[\mathbf{v}]_-^+ = 0. \quad (8)$$

The electrochemical potential must be continuous across the interface,

$$\left[g_{c_j}\right]_-^+ = 0. \quad (9)$$

Due to conservation of the electrolytes, the flux of ion species j *into* the interface must equal the flux *out of* the interface,

$$\left[K_{ij} c_j \nabla g_{c_j}\right]_-^+ \cdot \hat{\mathbf{n}}_{\mathrm{int}} = 0, \quad (10)$$

and the normal flux of the electric displacement field $\mathbf{D} = -\varepsilon_i \nabla V$, and the electric potential, should be continuous (since by assumption, no free charge is located *between* the fluids):

$$[\varepsilon_i \nabla V]_-^+ \cdot \hat{\mathbf{n}}_{\mathrm{int}} = 0, \quad [V]_-^+ = 0. \quad (11)$$

Finally, interfacial stress balance yields the condition

$$\left[p\right]_-^+ \hat{\mathbf{n}}_{\mathrm{int}} - [2\mu_i \mathcal{D}\mathbf{v}]_-^+ \cdot \hat{\mathbf{n}}_{\mathrm{int}} - \left[\varepsilon_i \mathbf{E}\otimes\mathbf{E} - \frac{1}{2}\varepsilon_i |\mathbf{E}|^2 \mathbf{I}\right]_-^+ \cdot \hat{\mathbf{n}}_{\mathrm{int}} = \sigma\kappa\hat{\mathbf{n}}_{\mathrm{int}}, \quad (12)$$

where σ is the surface tension, κ is the curvature, and $\mathbf{E} = -\nabla V$ is the electric field. Moreover, we have defined the shorthand symmetric (vector) gradient,

$$\mathcal{D}\mathbf{v} = \mathrm{sym}\,(\nabla\mathbf{v}) = \frac{1}{2}\left(\nabla\mathbf{v} + \nabla\mathbf{v}^T\right). \quad (13)$$

Further, all gradient terms have been absorbed into the pressure. Note that Equation (12) leads to a modified Young–Laplace law in equilibrium, which include Maxwell stresses.

2.1.2. Boundary Conditions

There are a range of applicable boundary conditions for two-phase electrohydrodynamics. Here, we briefly discuss a few viable options. In the following, we let $\hat{\mathbf{n}}$ be a unit normal vector pointing out of the domain, and $\hat{\mathbf{t}}$ be a tangent vector to the boundary.

For the velocity, it is customary to use the no-slip condition $\mathbf{u} = \mathbf{0}$ at the solid boundary. Alternatively, the Navier slip condition, which is useful for modeling moving contact lines [50], could be used:

$$\hat{\mathbf{n}}\cdot\mathbf{v} = 0, \quad (\gamma\mathbf{v} - 2\mu\mathcal{D}\mathbf{v}\,\hat{\mathbf{n}})\times\hat{\mathbf{n}} = \mathbf{0}, \quad (14)$$

where γ is a slip parameter. The slip length μ/γ is typically of nanometer scale and dependent on the materials in question.

However, since the implementation of such conditions may become slightly involved, we omit it in the following.

With regards to the electrolytes, it is natural to specify either a prescribed concentration at the boundary, $c_i = c_0$, or a no-flux condition out of the domain,

$$\hat{\mathbf{n}} \cdot \left(-\mathbf{v}c_j + K_{ij}c_j \nabla g_{c_j}\right) = 0. \tag{15}$$

For the electric potential, it is natural to prescribe either the Dirichlet condition $V = \bar{V}$, or a prescribed surface charge $\sigma_e(\mathbf{x})$,

$$\hat{\mathbf{n}} \cdot \nabla V = \frac{\sigma_e}{\epsilon_i}. \tag{16}$$

2.2. Phase-Field Formulation

In order to track the interface between the phases, we introduce an order parameter field ϕ which attains the values ± 1, respectively, in the two phases, and interpolates between the two across a diffuse interface of thickness ϵ. In the sharp-interface limit $\epsilon \to 0$, the equations should reproduce the correct physics, and reduce to the model above, including the interface conditions. A thermodynamically consistent phase-field model which reduces to this formulation was proposed by Campillo-Funollet et al. [61]:

$$\begin{aligned} \partial_t(\rho(\phi)\mathbf{v}) + \nabla \cdot \left(\rho(\phi)\mathbf{v} \otimes \mathbf{v}\right) - \nabla \cdot \left[2\mu(\phi)\mathcal{D}\mathbf{v}\right. \\ \left. + \mathbf{v} \otimes \rho'(\phi)M(\phi)\nabla g_\phi\right] + \nabla p = -\phi \nabla g_\phi - \sum_i c_i \nabla g_{c_i}, \end{aligned} \tag{17}$$

$$\nabla \cdot \mathbf{v} = 0, \tag{18}$$

$$\partial_t \phi + \mathbf{v} \cdot \nabla \phi - \nabla \cdot (M(\phi)\nabla g_\phi) = 0, \tag{19}$$

$$\partial_t c_j + \mathbf{v} \cdot \nabla c_j - \nabla \cdot (K_j(\phi)c_j \nabla g_{c_j}) = 0, \tag{20}$$

$$\nabla \cdot (\varepsilon(\phi)\nabla V) = -\rho_e. \tag{21}$$

Here, ϕ is the phase field, and it takes the value $\phi = -1$ in phase $i = 1$, and the value $\phi = 1$ in phase $i = 2$. Equation (19) governs the conservative evolution of the phase field, wherein the diffusion term is controlled by the phase field mobility $M(\phi)$. Here, ρ, μ, ε, K_j depend on which phase they are in, and are considered slave variables of the phase field ϕ. Across the interface these quantities interpolate between the values in the two phases:

$$\rho(\phi) = \frac{\rho_1 + \rho_2}{2} + \frac{\rho_1 - \rho_2}{2}\phi, \tag{22}$$

$$\mu(\phi) = \frac{\mu_1 + \mu_2}{2} + \frac{\mu_1 - \mu_2}{2}\phi, \tag{23}$$

$$\varepsilon(\phi) = \frac{\varepsilon_1 + \varepsilon_2}{2} + \frac{\varepsilon_1 - \varepsilon_2}{2}\phi, \tag{24}$$

$$K_j(\phi) = \frac{K_{1,j} + K_{2,j}}{2} + \frac{K_{1,j} - K_{2,j}}{2}\phi. \tag{25}$$

These averages are all weighted arithmetically, although other options are available. For example, Tomar et al. [54] found that, in the case of a level-set method with smoothly interpolated phase properties, using a weighted harmonic mean gave more accurate computation of the electric field. However, Lopez-Herrera et al. [55] found no indication that the harmonic mean was superior when free charges were present, and hence we adopt for simplicity and computational performance the arithmetic mean, although it remains unsettled which mean would yield the most accurate result.

Further, the chemical potential of species c_j is given by

$$g_{c_j}(c_j, \phi) = \alpha'(c_j) + \beta_j(\phi) + z_j V, \tag{26}$$

where we, for dilute solutions, may model $\alpha(c) = c(\log c - 1)$ to obtain consistency with the standard Nernst–Planck equation. Further, we use a weighted arithmetic mean for the solubility parameters β_j:

$$\beta_j(\phi) = \frac{\beta_{1,j} + \beta_{2,j}}{2} + \frac{\beta_{1,j} - \beta_{2,j}}{2}\phi, \tag{27}$$

which, under the assumption of dilute solutions and with the interpretation (6), corresponds to a weighted geometric mean for the reference concentrations:

$$c_j^{\mathrm{ref}}(\phi) = \left(c_j^{\mathrm{ref},1}\right)^{\frac{1+\phi}{2}} \cdot \left(c_j^{\mathrm{ref},2}\right)^{\frac{1-\phi}{2}}. \tag{28}$$

In analogy with g_{c_j} being the chemical potential of species c_j, we denote g_ϕ as the chemical potential of the phase field ϕ. It is given by:

$$g_\phi = \frac{\partial f}{\partial \phi} - \nabla \cdot \frac{\partial f}{\partial \nabla \phi} + \sum_j \beta_j'(\phi)c_j - \frac{1}{2}\varepsilon'(\phi)|\nabla V|^2. \tag{29}$$

The free energy functional f of the phase field is defined by

$$f(\phi, \nabla\phi) = \frac{3\sigma}{2\sqrt{2}}\left[\frac{\epsilon}{2}|\nabla\phi|^2 + \epsilon^{-1}W(\phi)\right] = \tilde{\sigma}\left[\frac{\epsilon}{2}|\nabla\phi|^2 + \epsilon^{-1}W(\phi)\right], \tag{30}$$

where σ is the surface tension, ϵ is the interface thickness, and $W(\phi)$ is a double well potential. Here, we use $W(\phi) = (1-\phi^2)^2/4$. We have also implicitly defined the scaled surface tension $\tilde{\sigma}$ for convenience of notation. With this free energy, we obtain

$$g_\phi = \tilde{\sigma}\epsilon^{-1}W'(\phi) - \tilde{\sigma}\epsilon\nabla^2\phi + \sum_j \beta_j'(\phi)c_j - \frac{1}{2}\varepsilon'(\phi)|\nabla V|^2. \tag{31}$$

We will assume this form throughout.

After some rewriting, exploiting Equation (18) and the fact that $\rho'(\phi)$ is constant due to Equation (22), Equation (18) can be expressed as

$$\begin{aligned} \rho(\phi)\partial_t\mathbf{v} + \left(\left(\rho(\phi)\mathbf{v} - \rho'(\phi)M(\phi)\nabla g_\phi\right) \cdot \nabla\right)\mathbf{v} - \nabla \cdot \left[2\mu(\phi)\mathcal{D}\mathbf{v}\right] + \nabla p \\ = -\phi\nabla g_\phi - \sum_j c_j \nabla g_{c_j}. \end{aligned} \tag{32}$$

2.2.1. Phase Field Mobility

Given a proper definition of the phase-field mobility $M(\phi)$, the phase-field model should reduce to the sharp-interface model given in the previous section. As discussed at length in Campillo-Funollet et al. [61], the two following ways are viable options:

$$M(\phi) = \epsilon M_0, \tag{33a}$$

$$M(\phi) = M_0(1-\phi^2)_+. \tag{33b}$$

Here M_0 is a constant, and $(\cdot)_+ = \max(\cdot, 0)$. Other formulations of M are possible; some of these will in the limit of vanishing interface width reduce to a sharp-interface model where the interface velocity does not equal the fluid velocity [59, 61].

2.2.2. Boundary Conditions

Some of the interface conditions from the sharp-interface model carry over to the phase field model, but in addition, some new conditions must be specified for the phase field. Here we give a brief summary. We assume that the boundary of the domain Ω, $\partial\Omega$, can be divided into an inlet part $\partial\Omega_{\text{in}}$, an outlet part $\partial\Omega_{\text{out}}$, and a wall part $\partial\Omega_{\text{wall}}$. We shall primarily discuss the latter here.

For the velocity field, we assume the no-slip condition

$$\mathbf{v}(\mathbf{x}, t) = \mathbf{0} \quad \text{for} \quad \mathbf{x} \in \partial\Omega_{\text{wall}}. \tag{34}$$

Alternatively, a no-flux condition and a slip law could have been used; in particular, a generalized Navier boundary condition (GNBC) has been shown to hold yield a consistent description of the contact line motion [48, 49]. However, to limit the scope, the moving contact line paradox will in this work be overcome by interface diffusion.

With regards to the flow problem, the pressure gauge needs to be fixed. To this end, the pressure could be fixed somewhere on the boundary, or the pressure nullspace could be removed.

For the concentrations c_j, we may use a prescribed concentration, or the no-flux condition

$$\hat{\mathbf{n}} \cdot \left(K_j(\phi) c_j \nabla g_{c_j}\right) = 0 \quad \text{on} \quad \partial\Omega_{\text{wall}}. \tag{35}$$

For the electric potential, we use either the Dirichlet condition $V = \bar{V}$ (which is reasonable at either inlet or outlet), or in the presence of charged (or neutral) boundaries, the condition

$$\hat{\mathbf{n}} \cdot \nabla V = \frac{\sigma_e}{\varepsilon(\phi)} \quad \text{on} \quad \partial\Omega_{\text{wall}}, \tag{36}$$

similar to the sharp-interface condition. Note that $\sigma_e(\mathbf{x})$ is prescribed and can vary over the boundary.

We assume that the no-flux conditons hold on the phase field chemical potential,

$$\hat{\mathbf{n}} \cdot \nabla g_\phi = 0 \quad \text{on} \quad \partial\Omega_{\text{wall}}. \tag{37}$$

For the phase field itself, a general dynamic wetting boundary condition can be expressed as [74]:

$$\epsilon \tau_w \partial_t \phi = -\tilde{\sigma}\epsilon \hat{\mathbf{n}} \cdot \nabla\phi + \sigma \cos(\theta_e) f_w'(\phi), \tag{38}$$

where θ_e is the equilibrium contact angle, τ_w is a relaxation parameter, and $f_w(\phi) = (2 + 3\phi - \phi^3)/4$ interpolates smoothly between 0 (at $\phi = -1$) and 1 (at $\phi = 1$). In this work, we limit ourselves to studying fixed contact angles, i.e., considering Equation (38) with $\tau_w = 0$. For a GNBC, the phase-field boundary condition (38) must be modeled consistently with the slip condition on the velocity [48].

3. DISCRETIZATION

For solving the equations of two-phase EHD, i.e., the model consisting of Equations (18)–(21), there are four operations that must be performed:

1. Propagate the phase field ϕ.
2. Propagate the chemical species concentrations c_i.
3. Update the electric potential V
4. Propagate the velocity $\mathbf{v}$ and pressure p.

The whole system of equations could in principle be solved simultaneously using implicit Euler discretization in time and e.g., Newton's method to solve the nonlinear system. However, in order to simulate larger systems faster, it is preferable to use a splitting scheme to solve for each field sequentially. One such splitting scheme was outlined in Metzger [69], based on the energy-stable scheme without electrochemistry as developed by Guillen-Gonzalez F and Tierra [67], Grün et al. [68]. However, that scheme did not take into account that the electric permittivities in the two fluids may differ, and when they do, the phase field and the electrochemistry computations become coupled through the electric field [70]. We will here discuss two strategies for solving the coupled problem of two-phase electrohydrodynamics. First, we present the fully monolithic, non-linear scheme, and secondly, we propose a new, fully practical linear operator splitting scheme. As we are not aware of any splitting schemes that are second-order accurate in time for the case of unmatched densities, we shall constrain our discussion to first-order in time schemes.

In the forthcoming, we will denote the inner product of any two scalar, vector, or tensor fields $\mathcal{A}, \mathcal{B}$ by $(\mathcal{A}, \mathcal{B})$. Further, we consider a discrete time step τ, and denote the (first-order) discrete time derivative by

$$\partial_\tau^- \mathcal{A}^k = \frac{\mathcal{A}^k - \mathcal{A}^{k-1}}{\tau}. \tag{39}$$

The equations are discretized on the domain $\Omega \subset \mathbb{R}^d$, $d = 2, 3$, with the no-slip boundary Γ. Since we do not consider explicitly in- and outlet boundary conditions in this work, we will omit this possible part of the domain for the sake of brevity.

We define the following finite element subspaces:

$$\mathbf{V}_h = (V_h)^d \quad \text{where} \quad V_h = \left\{v \in H^1(\Omega)\right\} \quad \text{for velocity,} \tag{40}$$

$$P_h = \left\{p \in L_0^2(\Omega)\right\} \quad \text{for pressure,} \tag{41}$$

$$\Phi_h = \left\{\phi \in H^1(\Omega)\right\} \quad \text{for phase field,} \tag{42}$$

$$G_h = \left\{g \in H^1(\Omega)\right\} \quad \text{for phase field chemical potential,} \tag{43}$$

$$C_h = \left\{c \in H^1(\Omega)\right\} \quad \text{for concentrations,} \tag{44}$$

$$U_h = \left\{V \in H^1(\Omega)\right\} \quad \text{for the electrostatic potential.} \tag{45}$$

3.1. Monolithic Scheme

Here we give the fully implicit scheme that follows from a naïve implicit Euler discretizion of the model (18)–(21), and supplemented by Equation (31).

Assume that $(\mathbf{v}^{k-1}, p^{k-1}, \phi^{k-1}, g_\phi^{k-1}, c_1^{k-1}, \ldots, c_M^{k-1}, V^{k-1})$ is given. The scheme can then be summarized by the following. Find $(\mathbf{v}^k, p^k, \phi^k, g_\phi^k, c_1^k, \ldots, c_N^k, V^k) \in \mathbf{V}_h \times P_h \times \Phi_h \times G_h \times (C_h)^N \times \mathcal{U}_h$ such that

$$\left(\rho^k \partial_\tau^- \mathbf{v}^k, \mathbf{u}\right) + \left(\left(\mathbf{m}^k \cdot \nabla\right)\mathbf{v}^k, \mathbf{u}\right) + \left(2\mu^k \mathcal{D}\mathbf{v}^k, \mathcal{D}\mathbf{u}\right) - \left(p^k, \nabla \cdot \mathbf{u}\right) = -\left(\phi^k \nabla g_\phi^k, \mathbf{u}\right) - \sum_j \left(c_j^k \nabla g_{c_j}^k, \mathbf{u}\right), \tag{46a}$$

$$\left(\nabla \cdot \mathbf{v}^k, q\right) = 0, \tag{46b}$$

$$\left(\partial_\tau^- \phi^k, \psi\right) - \left(\mathbf{v}^k \phi^k, \nabla\psi\right) + \left(M^k \nabla g_\phi^k, \nabla\psi\right) = 0, \tag{46c}$$

$$\left(g_\phi^k, g_\psi\right) = \left(\tilde{\sigma}\epsilon^{-1} W'(\phi^k), g_\psi\right) - \sigma\cos(\theta_e)\int_\Gamma f_w'(\phi^k) g_\psi \,\mathrm{d}\Gamma + \left(\tilde{\sigma}\epsilon \nabla\phi^k, \nabla g_\psi\right) + \sum_j \left(\beta_j' c_j^k, g_\psi\right) - \left(\frac{1}{2}\varepsilon' |\nabla V^k|^2, g_\psi\right), \tag{46d}$$

$$\left(\partial_\tau^- c_j^k, b_j\right) - \left(\mathbf{v}^k c_j^k, \nabla b_j\right) + \left(K_j^k c_j^k \nabla g_{c_j}^k, \nabla b_j\right) = 0, \tag{46e}$$

$$\left(\varepsilon^k \nabla V^k, \nabla U\right) = \left(\rho_e^k, U\right) + \int_\Gamma \sigma_e U \,\mathrm{d}\Gamma, \tag{46f}$$

for all test functions $(\mathbf{u}, q, \psi, g_\psi, b_1, \ldots, b_N, U) \in \mathbf{V}_h \times P_h \times \Phi_h \times G_h \times (C_h)^N \times \mathcal{U}_h$. Here we have used

$$\mathbf{m}^k = \rho^k \mathbf{v}^k - \rho' M^k \nabla g_\phi^k \tag{47}$$

and the shorthands

$$\rho^k = \rho(\phi^k), \quad \mu^k = \mu(\phi^k), \quad M^k = M(\phi^k), \quad \varepsilon^k = \varepsilon(\phi^k), \quad K_j^k = K_j(\phi^k), \quad \text{and} \quad \rho_e^k = \rho_e(\{c_j^k\}).$$

Note that Equations (46) constitute a fully coupled non-linear system and the equations must thus be solved simultaneously, preferably using a Newton method. This results in a large system matrix which must be assembled and solved iteratively, and for which there are in general no suitable preconditioners available. On the other hand, the scheme is fully implicit and hence expected to be fairly robust with regards to e.g., time step size. There are in general several options for constructing the linearized variational form to be used in a Newton scheme.

3.2. A Linear Splitting Scheme

Now, we introduce a linear operator splitting scheme. This scheme splits between the processes of phase-field transport, chemical transport under an electric field, and hydrodynamic flow, such that the equations governing each of these processes are solved separately.

3.2.1. Phase Field Step

Find $(\phi^k, g_\phi^k) \in \Phi_h \times G_h$ such that

$$\left(\partial_\tau^- \phi^k, \psi\right) - \left(\mathbf{v}^{k-1}\phi^k, \nabla\psi\right) + \left(M^{k-1}\nabla g_\phi^k, \nabla\psi\right) = 0 \tag{48a}$$

$$\left(g_\phi^k, g_\psi\right) = \tilde{\sigma}\epsilon^{-1}\left(\overline{W'}(\phi^k, \phi^{k-1}), g_\psi\right) + \tilde{\sigma}\epsilon\left(\nabla\phi^k, \nabla g_\psi\right) - \sigma\cos(\theta_e)\int_\Gamma \overline{f_w'}(\phi^k, \phi^{k-1})\, g_\psi \,\mathrm{d}\Gamma + \sum_j \beta_j'\left(c_j^{k-1}, g_\psi\right) - \frac{1}{2}\varepsilon'\left(|\nabla V^{k-1}|^2, g_\psi\right), \tag{48b}$$

for all test functions $(\psi, g_\psi) \in \Phi_h \times G_h$. Here, $\overline{W'}(\phi^k, \phi^{k-1})$ is a linearization of $W'(\phi^k)$ around ϕ^{k-1}:

$$\overline{W'}(\phi^k, \phi^{k-1}) = W'(\phi^{k-1}) + W''(\phi^{k-1})(\phi^k - \phi^{k-1}). \tag{49}$$

We have also used the discretization of Equation (38)

$$\tilde{\sigma}\epsilon \mathbf{n}\cdot\nabla\phi^k = \sigma\cos(\theta_e)\overline{f_w'}(\phi^k, \phi^{k-1}), \tag{50}$$

where we have used the linearization

$$\overline{f_w'}(\phi^k, \phi^{k-1}) = f_w'(\phi^{k-1}) + f_w''(\phi^{k-1})(\phi^k - \phi^{k-1}). \tag{51}$$

3.2.2. Electrochemistry Step

Find $(c_1, \ldots, c_N, V) \in (C_h)^N \times U_h$ such that

$$\left(\partial_\tau^- c_j^k, b_j\right) - \left(\mathbf{v}^{k-1} c_j^k, \nabla b_j\right) + \left(\bar{\mathbf{J}}_{c_j}^k, \nabla b_i\right) = 0 \tag{52a}$$

$$\left(\varepsilon^k \nabla V^k, \nabla U\right) + \int_\Gamma \sigma_e U \,\mathrm{d}\Gamma + \left(\rho_e^k, U\right) = 0 \tag{52b}$$

for all test functions $(b_1, \ldots, b_N, U) \in (C_h)^N \times U_h$. Here $\bar{\mathbf{J}}_{c_j}^k$ is a linear approximation of the diffusive chemical flux $\mathbf{J}_{c_j} = K_j(\phi) c_j \nabla g_{c_j}$. For conciseness, we here constrain our analysis to ideal chemical solutions, i.e., we assume a common chemical energy function on the form $\alpha(c) = c(\ln c - 1)$. To this end, we approximate the flux by:

$$\bar{\mathbf{J}}_{c_j}^k = K_j^k(\nabla c_i^k + c_i^k \beta_i' \nabla\phi^k + z_i c_i^{k-1}\nabla V^k). \tag{53}$$

3.2.3. Fluid Flow Step

Find $(\mathbf{v}^k, p^k) \in \mathbf{V}_h \times P_h$ such that

$$\left(\rho^{k-1}\partial_\tau^- \mathbf{v}^k, \mathbf{u}\right) + \left(\left(\bar{\mathbf{m}}^{k-1}\cdot\nabla\right)\mathbf{v}^k, \mathbf{u}\right) + \frac{1}{2}\left(\mathbf{v}^k\partial_\tau^-\rho^k, \mathbf{u}\right) - \frac{1}{2}\left(\bar{\mathbf{m}}^{k-1}, \nabla(\mathbf{v}^k\cdot\mathbf{u})\right) + \left(2\mu^k\mathcal{D}\mathbf{v}^k, \mathcal{D}\mathbf{u}\right) - \left(p^k, \nabla\cdot\mathbf{u}\right) = -\left(\phi^k\nabla g_\phi^k, \mathbf{u}\right) - \sum_j\left(c_j^k\nabla g_{c_j}^k, \mathbf{u}\right) \quad (54a)$$

$$\left(q, \nabla\cdot\mathbf{v}^k\right) = 0 \quad (54b)$$

for all test functions $(\mathbf{u}, q) \in \mathbf{V}_h \times P_h$. Here, we have used the following approximation of the advective momentum:

$$\bar{\mathbf{m}}^{k-1} = \rho^{k-1}\mathbf{v}^{k-1} - \rho' M^k\nabla g_\phi^k. \quad (55)$$

Note that the terms in (54a) involving $\partial_\tau^-\rho^k + \nabla\cdot\bar{\mathbf{m}}^{k-1}$, which is a discrete approximation of $\partial_t\rho + \nabla\cdot\mathbf{m} = 0$, is included to satisfy a discrete energy dissipation law [75] (i.e., to improve stability). This step requires solving for the velocity and pressure in a coupled manner. This has the advantage that it yields accurate computation of the pressure, but the drawback that it is computationally challenging to precondition and solve, related to the Babuska–Brezzi (BB) condition (see e.g., [76]). Alternatively, it might be worthwhile to further split the fluid flow step into the following three substeps, at the cost of some lost accuracy [77].

- Tentative velocity step: Find $\tilde{\mathbf{v}}^k \in \mathbf{V}_h$ such that for all $\mathbf{u} \in \mathbf{V}_h$,

$$\left(\rho^{k-1}\frac{\tilde{\mathbf{v}}^k - \mathbf{v}^{k-1}}{\tau}, \mathbf{u}\right) + \left((\bar{\mathbf{m}}^{k-1}\cdot\nabla)\tilde{\mathbf{v}}^k, \mathbf{u}\right) + \left(2\mu^k\mathcal{D}\tilde{\mathbf{v}}^k, \mathcal{D}\mathbf{u}\right) - \left(p^{k-1}, \nabla\cdot\mathbf{u}\right) + \frac{1}{2}\left(\tilde{\mathbf{v}}^k\partial_\tau^-\rho^k, \mathbf{u}\right) - \frac{1}{2}\left(\bar{\mathbf{m}}^{k-1}, \nabla(\tilde{\mathbf{v}}^k\cdot\mathbf{u})\right) = -\left(\phi^k\nabla g_\phi^k, \mathbf{u}\right) - \sum_i\left(c_i^{k-1}\nabla g_i^k, \mathbf{u}\right), \quad (56a)$$

  with the Dirichlet boundary condition $\tilde{\mathbf{v}}^k = \mathbf{0}$ on Γ.
- Pressure correction step: Find $p^k \in P_h$ such that for all $q \in P_h$, we have

$$\left(\frac{1}{\rho_0}\nabla(p^k - p^{k-1}), \nabla q\right) = -\frac{1}{\tau}\left(\nabla\cdot\tilde{\mathbf{v}}^k, q\right). \quad (56b)$$

- Velocity correction step: Then, find $\mathbf{v}^k \in \mathbf{V}_h$ such that for all $\mathbf{u} \in \mathbf{V}_h$,

$$\left(\rho^k\frac{\mathbf{v}^k - \tilde{\mathbf{v}}^k}{\tau}, \mathbf{u}\right) = \left(p^k - p^{k-1}, \nabla\cdot\mathbf{u}\right), \quad (56c)$$

  which we solve by explicitly imposing the Dirichlet boundary condition $\mathbf{u}^k = \mathbf{0}$ on Γ.

Equations (56a), (56b), and (56c) should be solved sequentially, and constitutes a variant of a projection scheme, i.e., a fractional-step approach to the fluid flow equations [75, 77–80]. We will in this paper refer to the coupled solution of the fluid flow equations, unless stated otherwise. Specifically, the fractional-step fluid flow scheme will only be demonstrated in the full 3D simulations in section 6.2.

The scheme presented above consists in sequentially solving three decoupled subproblems (or five decoupled subproblems for the fractional-step fluid flow alternative). The subproblems are all linear, and hence attainable for specialized linear solvers which could improve the efficiency. We note that the splitting introduces an error of order τ, i.e., the same as the scheme itself. Moreover, our scheme does not preserve the same energy dissipation law on the discrete level, that the original model does on the continuous level. We are currently not aware of any scheme for two-phase electrohydrodynamics with this property, apart from the fully implicit scheme presented in the previous section.

4. BERNAISE

We have now introduced the governing equations and two strategies for solving them. Now, we will introduce the Bernaise package, and describe an implementation of a generic simulation problem and a generic solver in this framework. For a complete description of the software, we refer to the online Git repository [81].

The work presented herein refers to version 1.0 of *Bernaise*. It is compatible with version 2017.2.0 of FEniCS [42] running in Python 2.7, and version 2018.1.0 of FEniCS, which is the latest stable version available for Python 3.6 at the time of writing. The simulations presented herein were carried out using the 2017.2.0 version of FEniCS (installed from the standard PPA) in combination with Python 2.7 on a Ubuntu 16.04 system. Future releases of Bernaise will (as FEniCS) primarily be compatible with Python 3.6 and follow the update cycle of FEniCS.

4.1. Python Package

Bernaise is designed as a Python package, and the main structure of the package is shown in **Figure 1**. The package contains two main submodules, `problems` and `solvers`. As suggested by the name, the `problems` submodule contains scripts where problem-specific geometries (or meshes), physical parameters, boundary conditions, initial states, etc., are specified. We will in section 4.2 dive into the constituents of a problem script. The `solvers` submodule, on the other hand, contains scripts that are implementations of the numerical schemes required to solve the governing equations. Two notable examples that are implemented in *Bernaise* are the monolithic scheme (implemented as `basicnewton`) and the linear splitting scheme (implemented as `basic`). We shall in section 4.3 describe the building blocks of such a solver. Further, a default solver compatible with a given problem is specified in the problem, but this setting can—along with most other

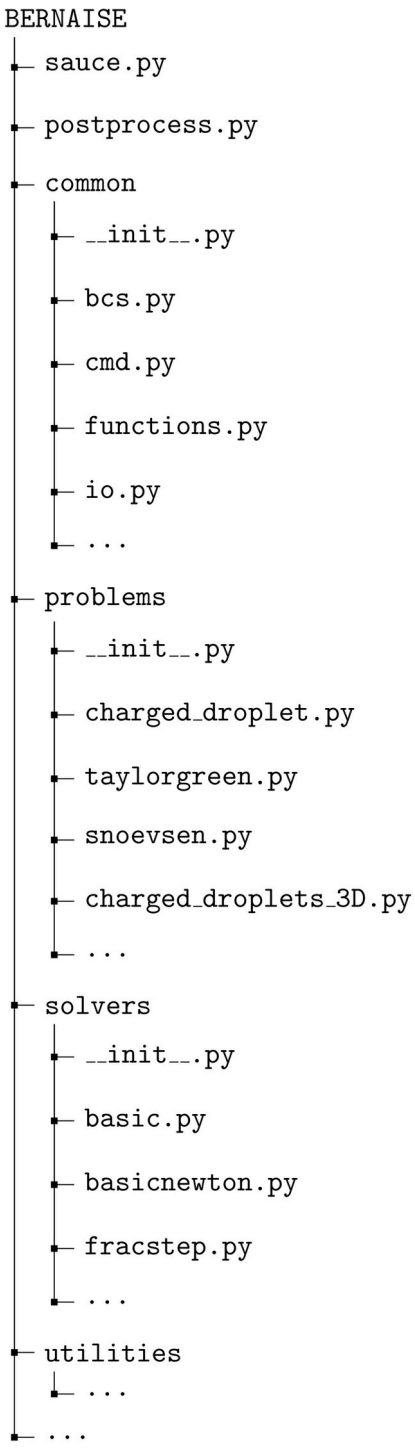

FIGURE 1 | Part of the directory structure of Bernaise.

settings specified in a problem—be overridden by providing an additional keyword to the main script call (see below). Note that *not all* solvers are compatible with *all* problems, and vice versa.

A simulation is typically run from a terminal, pointing to the *Bernaise* directory, using the command

```
>> python sauce.py problem=charged_droplet
```

where `charged_droplet` may be exchanged with another problem script of choice; albeit we will use `charged_droplet` as a pedagogical example in the forthcoming. The main script `sauce.py` fetches a `problem` and connects it with the `solver`. It sets up the finite element problem with all the given parameters, initializes the finite element fields with the specified initial state, and solves it with the specified boundary condition at each time step, until the specified (physical) simulation time `T` is exceeded. Any parameter in the problem can be overridden by specifying an additional keyword from the command line; for example, the simulation time can be set to 1,000 by running the command:

```
>> python sauce.py problem=charged_droplet T=1000
```

After every given interval of steps, specified by the parameter `checkpoint_interval`, a checkpoint is stored, including all fields, and all problem parameters at the time of writing to file. The checkpoint can be loaded, and the simulation can be continued, by running the command:

```
>> python sauce.py problem=charged_droplet
   restart_folder=results_charged_droplet/1/
   Checkpoint/
```

where the `restart_folder` points to an appropriate checkpoint folder. Here, the problem parameters stored within the checkpoint have precedence over the default parameters given in the `problem` script. Further, any parameters specified by command line keywords have precedence over the checkpoint parameters.

The role of the main module `sauce.py` is to allocate the required variables to run a simulation, to import routines from the specified problem and solver, to iterate the solver in time, and to output and store data at appropriate times. Hence, the main module works as a general interface to problems and solvers. This is enabled by overloading a series of functions, such that problem- and solver-specific functions are defined within the problem and solver, respectively. The structure of `sauce.py` is by choice similar to the `NSfracStep.py` script in the *Oasis* solver [43]; both in order to appeal to overlapping user bases, and to keep the code readable and consistent with and similar to common FEniCS examples. However, an additional layer of abstraction in e.g., setting up functions and function spaces is necessary in order to handle a flexible number of subproblems and subspaces, depending on e.g., whether phase field, electrochemistry or flow is disabled, or whether we are running with a monolithic or operator splitting scheme. To keep the *Bernaise* code as readable and easily maintainable as possible, we have consciously avoided uneccessary abstraction. Only the boundary conditions (found in `common/bcs.py`) are implemented as classes.

4.2. The Problems Submodule

The basic user typically interacts with *Bernaise* by implementing a *problem* to be solved. This is accessible to *Bernaise* when put

in the subfolder `problems`. The implementation consists in overloading a certain set of functions; all of which are listed in the `problems/__init__.py` file in the problems folder. The mandatory functions that must be overloaded for each problem are:

- `mesh`: defines the geometry. Equivalent to the `mesh` function in *Oasis* [43].
- `problem`: sets up all parameters to be overloaded, including defining solutes and types of finite elements. The default parameters are defined in the `problems/__init__.py` file.
- `initialize`: initializes all fields.
- `create_bcs`: sets all subdomains, and defines boundary conditions (including pointwise boundary condtions, such as pressure pinning). The boundary conditions are more thoroughly explained below.

Further, there are functions that *may* be overloaded.

- `constrained_domain`: set if the boundary is to be considered periodic.
- `pf_mobility`: phase field mobility function; cf. (33a) and (33b).
- `start_hook`: hook called before the temporal loop.
- `tstep_hook`: hook called at each time step in the loop.
- `end_hook`: hook called at the end of the program.
- `rhs_source`: explicit source terms to be added to the right hand side of given fields; used e.g., in the method of manufactured solution.

Note here the use of three *hooks* that are called during the course of a simulation. These are useful for outputting certain quantities during a simulation, e.g., the flux through a cross section, or total charge in the domain. The `start_hook` could also be used to call a steady-state solver to initialize the system closer to equilibrium, e.g., a solver that solves only the electrochemistry subproblem such that we do not have to resolve the very fast time scale of the initial charge equilibration.

In Listing 1, we show an implementation of the `problems` function, which sets the necessary parameters that are required for the `charged_droplet` case to run. Here, the `solutes` array (which defines the solutes), contains only one species, but it can in principle contain arbitrarily many.

In Listing 2, we show the code for the initialization stage. Here, `initial_pf` and `initial_c` are functions defined locally inside the `charged_droplet.py` problem script, that set the initial distributions of the phase field and the concentration field, respectively. Here, it should be noted how the (boolean) parameters `enable_PF`, `enable_EC` and `enable_NS` allow to switch on or off either the phase field, the electrochemistry or the hydrodynamics, respectively.

Listing 1 | The `problems` function for the `charged_droplet` case.

```
def problem():
    info_cyan("Charged droplet in an electric field.")

    # Define solutes
    # Format: name, valency, diffusivity in phase 1, diffusivity in phase 2,
    #         solubility energy in phase 1, solubility energy in phase 2
    solutes = [["c_p",  1, 1e-5, 1e-3, 4., 1.]]

    # Default parameters to be loaded unless starting from checkpoint.
    parameters = dict(
        solver="basic",                     # Solver to be used.
        folder="results_charged_droplet",   # Folder to store results in.
        dt=0.08,                            # Timestep
        t_0=0.,                             # Starting time
        T=8.,                               # Total simulation time
        grid_spacing=1./32,                 # Mesh size
        interface_thickness=0.03,           # Extent of diffuse interface
        solutes=solutes,                    # Array of solutes defined above
        Lx=2.,                              # Length of domain along x
        Ly=1.,                              # Length of domain along y
        rad_init=0.25,                      # Initial droplet radius
        V_left=10.,                         # Potential at left side
        V_right=0.,                         # Potential at right side
        surface_tension=5.,                 # Surface tension
        concentration_init=10.,             # Initial (total) concentration
        pf_mobility_coeff=0.00002,          # Phase field mobility coeff. (M_0)
        density=[200., 100.],               # Density in phase 1, phase 2
        viscosity=[10., 1.],                # Viscosity in phase 1, phase 2
        permittivity=[1., 1.]               # Permittivity in phase 1, phase 2
    )
    return parameters
```

Listing 2 | The `initialize` function for the `charged_droplet` case.

```
def initialize(Lx, Ly, rad_init, interface_thickness, solutes,
               concentration_init, restart_folder, field_to_subspace,
               enable_NS, enable_PF, enable_EC, **namespace):
    """ Create the initial state. """
    w_init_field = dict()
    if not restart_folder:
        x0, y0, rad0, c0 = Lx/4, Ly/2, rad_init, concentration_init
        # Initialize phase field
        if enable_PF:
            w_init_field["phi"] = initial_pf(
                x0, y0, rad0, interface_thickness,
                field_to_subspace["phi"].collapse())

        # Initialize electrochemistry
        if enable_EC:
            w_init_field[solutes[0][0]] = initial_c(
                x0, y0, rad0/3., c0, interface_thickness,
                field_to_subspace[solutes[0][0]].collapse())

    return w_init_field
```

Listing 3 | The `get_subproblems` subroutine of the `basic` solver.

```
def get_subproblems(solutes, enable_NS, enable_PF, enable_EC, **namespace):
    """ Returns dict of subproblems the solver splits the problem into. """
    subproblems = dict()
    if enable_NS:
        subproblems["NS"] = [dict(name="u", element="u"),
                             dict(name="p", element="p")]
    if enable_PF:
        subproblems["PF"] = [dict(name="phi", element="phi"),
                             dict(name="g", element="g")]
    if enable_EC:
        subproblems["EC"] = ([dict(name=solute[0], element="c")
                              for solute in solutes]
                             + [dict(name="V", element="V")])
    return subproblems
```

4.3. The Solvers Submodule

Advanced users may develop solvers that can be placed in the `solvers` subdirectory. In the same way as with the `problems` submodule, a solver implementation constists of overloading a range of functions which are defined in `solvers/__init__.py`.

- `get_subproblems`: Returns a dictionary (`dict`) of the subproblems which the solver splits the problem into. This dictionary has points to the name of the fields and the elements (specified in problem) which the subspace is made up of.
- `setup`: Sets up the FEniCS solvers for each subproblem.
- `solve`: Defines the routines for solving the finite element problems, which are called at every time step.
- `update`: Defines the routines for assigning updated values to fields, which are called at the end of every time step.

The module `solvers/basicnewton.py` implements the monolithic scheme, while the module `solvers/basic.py` implements the segregated solver[3]. The problem is split up into the subproblems corresponding to whether we have a monolothic or segragated solver in the function `get_subproblems`. Within the `setup` function, the variational forms are defined, and the solver routines are initialized. The latter are eventually called in the `solve` routine at every time step. Note that the element types are defined within the problem, and that the solvers in general can be applied for higher-order spatial accuracy without further ado. The task of `get_subproblems` is simply to link the subproblem to the element specification.

In Listing 3, we show how the `get_subproblems` function is implemented in the `basic` solver. As can be readily seen, the function formally splits the problem into the three subproblems `NS`, `PF`, and `EC`.

The other functions (such as `setup`) are somewhat more involved, but can be found at the Git repository [81].

Note that the implementations of the solvers presented above are sought to be short and humanly readable, and therefore quite straightforwardly implemented. There are several ways to improve the efficiency (and hence scalability) of a solver, at the cost of lost intuitiveness [43].

[3]The latter also contains an equilibrium solver for the quiescent electrochemistry problem, mainly to be used for initialization purposes.

Listing 4 | The `create_bcs` function within the `charged_droplet` case.

```
def create_bcs(field_to_subspace, Lx, Ly, solutes, V_left, V_right,
               enable_NS, enable_PF, enable_EC,
               **namespace):
    """ The boundary conditions are defined in terms of field. """

    boundaries = dict(
        wall=[Wall(Lx)],
        left=[Left()],
        right=[Right(Lx)]
    )

    noslip = Fixed((0., 0.))

    bcs = dict()
    bcs_pointwise = dict()

    bcs["wall"] = dict()
    bcs["left"] = dict()
    bcs["right"] = dict()

    if enable_NS:
        bcs["wall"]["u"] = noslip
        bcs["left"]["u"] = noslip
        bcs["right"]["u"] = noslip
        bcs_pointwise["p"] = (0., "x[0] < DOLFIN_EPS && x[1] < DOLFIN_EPS")

    if enable_EC:
        bcs["left"]["V"] = Fixed(V_left)
        bcs["right"]["V"] = Fixed(V_right)

    return boundaries, bcs, bcs_pointwise
```

4.4. Boundary Conditions

Boundary conditions are among the few components of *Bernaise* which are implemented as classes. Physical boundary conditons may consist of a combination of Dirichlet and Neumann (or Robin) conditions, and the latter must be incorporated into the variational form. The boundary conditions are specified in the specific problem script, while the variational form is set up in the solver. To promote code reuse, keeping the physical boundary conditions accessible from the problems side, and simultaneously independent of the solver, the various boundary conditions are stored as classes in a separate module. The boundaries themselves should be set by the user within the `problem`. By importing various boundary condition classes from `common/bcs.py`, the boundary conditions can be inferred at user-specified boundaries.

Within the `bcs` module, the base class `GenericBC` is defined. The boolean member functions `is_dbc` and `is_nbc` specifies, respectively, whether the concrete boundary conditions impose a Dirichlet and Neumann condition, and both return false by default. The base class is inherited by various concrete boundary conditon classes, and by overloading these two member functions, the member functions `dbc` or `nbc` are, respectively called at appropriate times in the code. There is a hierarchy of boundary conditions which inherit from each other. Some of the boundary conditions currently implemented in *Bernaise* are:

- `GenericBC`: Base class for all boundary conditions.
  - `Fixed`: Dirichlet condition, applicable for all fields.
    - `NoSlip`: The no-slip condition—a pure Dirichlet condition with the value **0**, applicable for velocity.
    - `Pressure`: Constant pressure boundary condition—adds a Neumann condition to the velocity, i.e., a boundary term in the variational form.
  - `Charged`: A charged boundary—a Neumann conditon intended for use with the electric potential V.
  - `Open`: An open boundary—a Neumann condition is applied.

We note that when a no-flux condition is to be applied, no specific boundary condition class needs to be supplied, since the boundary term in the variational form then disappears (in particular when considering conservative PDEs).

As an example, we show in Listing 4 the `create_bcs` function within the `charged_droplet` case. Here, the boundaries `Wall`, `Left`, etc., are defined in the standard FEniCS/DOLFIN way as instances of a `SubDomain` class.

4.5. Post-processing

An additional module provided in *Bernaise* is the post-processing module. It operates with methods analogously to how the

main *Bernaise* script operates with problems. The base script `postprocess.py` pulls in the required method and analyses or operates on a specified folder. The methods are located in the folder `analysis_scripts/` and new methods can be implemented by users by adding scripts to this folder.

To exemplify its usage, we consider a method to analyse the temporal development of the energy. This is done by navigating to the root folder and calling

```
>> python postprocess.py method=energy_in_time
   folder=results_charged_droplet/1/
```

where we assume that the output of the simulation, we want to analyse, is found in the folder `results_charged_droplet/1/`. The analysis method `energy_in_time` above can, of course, be exchanged with another method of choice. A list of available methods can be produced by supplying the help argument from a terminal call:

```
>> python postprocess.py -h
```

Similar to the `problems` submodule, the methods are implemented by overloading a set of routines, where default routines are found in `analysis_scripts/__init__.py`. The routines required to implement an analysis method are the following:

- `description`: routine called when a question mark is added to the end of the method name during a call from the terminal, meant to obtain a description of the method without having to inspect the code.
- `method`: the routine that performs the desired analysis.

The implementation hinges on the `TimeSeries` class (located in `utilities/TimeSeries.py`), which efficiently imports the XDMF/HDF5 data files and the parameter files produced by a *Bernaise* simulation. Several plotting routines are implemented in `utilities/plot.py`, and these are extensively used in various analysis methods.

5. VALIDATION

With the aim of using *Bernaise* for quantitative purposes, it is essential to establish that the schemes presented in the above converges to the correct solution—in two senses:

- The numerical schemes should converge to the correct solution of the phase-field model.
- The solution of the phase-field model should converge to the correct sharp-interface equations[4].

Unless otherwise stated, we mean by convergence that the error in all fields χ should behave like,

$$\|\chi - \chi_e\|_h \sim C_h h^{k_h} + C_\tau \tau^{k_\tau} \tag{57}$$

where $\|\cdot\|_h$ is an L^2 norm, χ is the simulated field, χ_e is the exact solution, h is the mesh size, τ is the time step, k_h is the order of spatial convergence, k_τ is the order of temporal convergence ($k_\tau = 1$ in this work), and C_h and C_τ are constants.

[4]Obviously, when the physical interface thickness may be resolved by the phase field, the sharp-interface assumption might be less sensible than the diffuse. Hence, in such cases this point might be too crude.

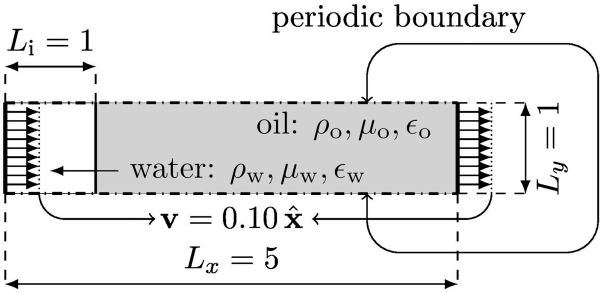

FIGURE 2 | Schematic set-up of the stable bulk flow intrusion test case. Here, the "water" (subscript w) displaces the "oil" (subscript o). At the left and right boundaries, a constant velocity is prescribed.

In the following, we present convergence test in three cases. Firstly, in the limiting case of a stable bulk intrusion without electrochemistry, an analytical solution is available to test against. Secondly, using the method of manufactured solution, convergence of the full two-phase EHD problem to an augmented Taylor–Green vortex is shown. Thirdly, we show convergence toward a highly resolved reference solution for an electrically driven charged droplet.

We note that the aim of *Bernaise* is to solve coupled multi-physics problems, and while the solvers may contain subtle errors, they may be negligible for many applications, and dominant only in limiting cases. In addition to testing the whole, coupled multi-physics problem of two-phase EHD, a proper testing should also consider simplified settings where fewer physical mechanisms are involved simultaneously. A brief discussion of testing and such reduced models is given in **Appendix C** in Supplementary Material. In this section, we show the convergence of the schemes in a few relevant cases, which we believe represent the efficacy of our approach. Tests of simplified-physics problems are found in the Git repository [81].

5.1. Stable Bulk Intrusion

A case where an analytic solution is available, is the stable intrusion of one fluid into another, in the absence of electrolytes and electric fields. A schematic view of the initial set-up is shown in **Figure 2**. A constant velocity $\mathbf{v} = v_0\hat{\mathbf{x}}$ ($\hat{\mathbf{x}}$ is the unit vector along the x axis) is applied at both the left and right sides of the reservoir, and periodic boundary conditions are imposed at the perpendicular direction. We shall here consider the convergence to the solution of the phase-field equation, i.e., retaining a finite interface thickness ϵ. This effectively one-dimensional problem is implemented in `problems/intrusion_bulk.py`.

Due to the Galilean invariance, we expect the velocity field to be uniformly equal to the inlet and outlet velocities, i.e., $\mathbf{v}(\mathbf{x}, t) = v_0\hat{\mathbf{x}}$. The exact analytical solution for the phase field is given by

$$\phi(\mathbf{x}, t) = \tanh\left(\frac{x - x_0 - v_0 t}{\sqrt{2}\epsilon}\right), \tag{58}$$

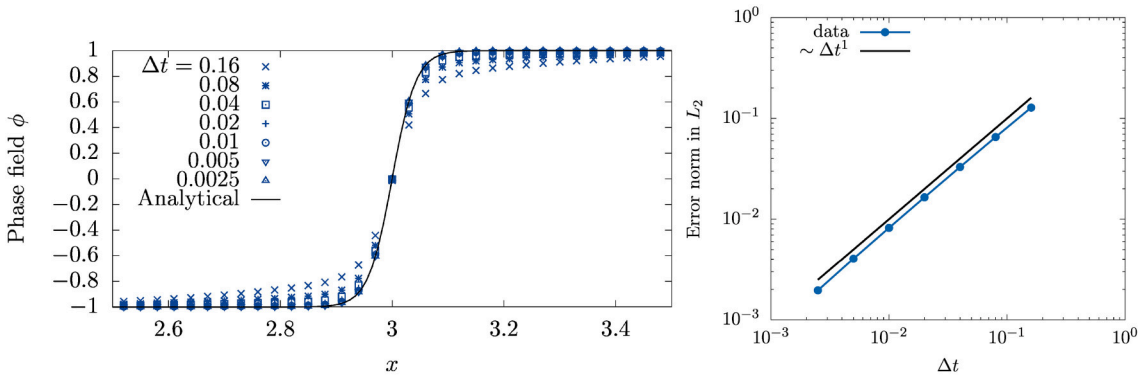

FIGURE 3 | Convergence in time for the case of stable intrusion. The mesh size is held fixed at $h = 0.0039$. **(Left)** We show the phase field interpolated at equidistant points along the centerline for increasing temporal resolution. The solid black line is the analytical solution. **(Right)** The integrated L^2 norm of the phase field plotted against time step. The solid black line shows the theoretical convergence order of the scheme ($\sim \tau$). As can be seen from the figure, it displays close to ideal scaling.

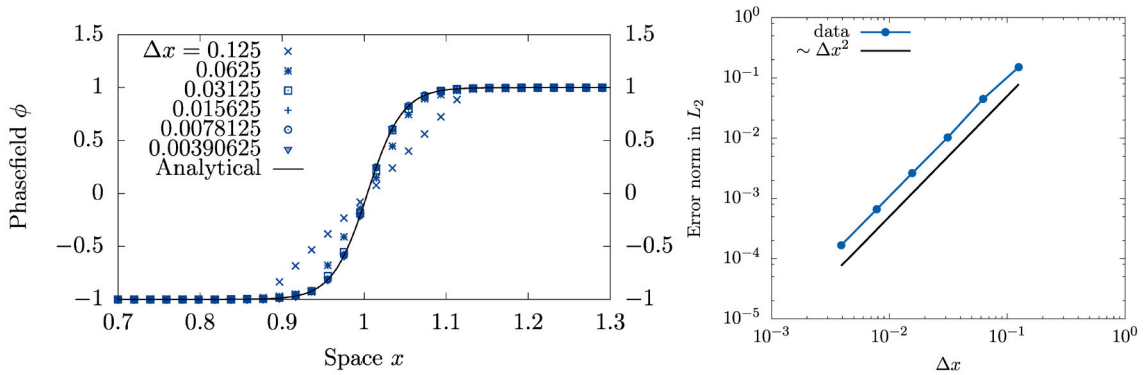

FIGURE 4 | Convergence in space for the case of stable intrusion. The time step is held fixed at $\tau = 0.0025$. **(Left)** Phase field interpolated at equidistant points along the centerline for increasing spatial resolution. **(Right)** The L^2 norm of the phase field is plotted against mesh resolution. The solid black line shows the theoretical convergence order ($\sim h^2$).

for which we shall consider the error norm. Note that the only parameters this analytical solution depends on are the initial position of the interface x_0, the injection velocity v_0, and the interface width ϵ. We consider the parameters $\rho_1 = \rho_2 = 1000$, $\mu_1 = 100$, $\mu_2 = 1$, $\sigma = 2.45$, $\epsilon = 0.03$, $M(\phi) = M_0 = 2 \cdot 10^{-5}$, $x_0 = 1$, $L_x = 5$, $L_y = 1$ and $v_0 = 0.1$.

Figure 3 shows the convergence to the analytical solution with regards to temporal resolution. The order of convergence is consistent with the order of the scheme, indicating that the scheme is appreciable at least in the lack of electrostatic interactions.

Figure 4 shows the convergence of the phase field with regards to the spatial resolution. The scheme is seen to converge at the theoretical rate, $\sim h^2$.

5.2. Method of Manufactured Solution: A Two-Phase Electrohydrodynamic Taylor–Green Vortex

Having established convergence in the practically one-dimensional case, we now consider a slightly more involved setting where we use the method of manufactured solution to obtain a quasi-analytical test case.

The Taylor–Green vortex is a standard benchmark problem in computational fluid dynamics because it stands out as one of the few cases where exact analytical solutions to the Navier–Stokes equations are available. However, in the case of two-phase electrohydrodynamics, the Navier–Stokes equations couple to both the electrochemical and the phase field subproblems. In Linga et al. (Submitted) the authors augmented the Taylor–Green vortex with electrohydrodynamics, and in this work we supplement the latter with a phase field and non-matching densities of the two phases.

We consider the full set of equations on the domain $\Omega = [0, 2\pi] \times [0, 2\pi]$, where all quantities may differ in the two phases. The two ionic species have opposite valency $\pm z$. The fields are given by

$$\mathbf{u} = U(t)(\hat{\mathbf{x}} \cos x \sin y - \hat{\mathbf{y}} \sin x \cos y), \tag{59a}$$

$$p = -\sum_{mn} \mathcal{P}_{mn}(t) \cos(2mx) \cos(2ny), \tag{59b}$$

$$\phi = \Phi(t)\cos x \cos y, \tag{59c}$$

$$c_{\pm} = c_0(1 \pm \cos x \cos y\, C(t)), \tag{59d}$$

$$V = \frac{zc_0 C(t)}{\varepsilon}\cos x \cos y. \tag{59e}$$

Here, the time-dependent coefficients are given by

$$U(t) = U_0 \exp\left(-\frac{2\bar{\mu}}{\bar{\rho}}t\right), \tag{60}$$

$$C(t) = C_0 \exp\left(-2\bar{D}\left(1 + \frac{c_0}{\bar{\varepsilon}}\right)t\right), \tag{61}$$

$$\Phi(t) = \Phi_0 \exp\left(-2M\tilde{\sigma}\left(2\epsilon - \frac{1}{\epsilon}\right)t\right), \tag{62}$$

where U_0, C_0 and Φ_0 are scalars, and

$$\mathcal{P}_{mn} = \begin{cases} \mathcal{Q}_1(t) + \mathcal{Q}_2(t) \quad \text{for} \quad (m,n) \in \{(0,1),(1,0)\}, \\ \mathcal{Q}_2(t) \quad \text{for} \quad (m,n) \in \{(1,1)\}, \\ 0 \quad \text{otherwise.} \end{cases} \tag{63}$$

where

$$\mathcal{Q}_1 = \frac{1}{4}\rho U_0^2(t), \quad \text{and} \quad \mathcal{Q}_2 = \frac{z^2 c_0^2 C^2(t)}{4\epsilon}. \tag{64}$$

Further, a bar indicates the arithmetic average over the value in the two phases, i.e., $\bar{\chi} = (\chi_1 + \chi_2)/2$ for any quantity χ, and $\bar{D} = (\bar{D}_+ + \bar{D}_-)/2 = (D_{+,1} + D_{+,2} + D_{-,1} + D_{-,2})/4$ is the arithmetic average over all diffusivities. The time-dependent boundary conditions are set by prescribing the reference solutions at the boundary of Ω for all fields given in (59a)–(59e), except the pressure p, which is set (to the reference value) only at the corner point $(x, y) = (0, 0)$. The method of manufactured solution now consists in augmenting the conservation Equations (18), (19), (20) and (21) by appropriate source terms, such that the reference solution (59a)–(59e) solves the system exactly. These source terms were computed in Python using the *Sympy* package, and are rather involved algebraic expressions. The expressions are therefore omitted here, but can be found as a utility script in the *Bernaise* package. Note that in the special case of single-phase flow without electrodynamics, i.e., $\phi \equiv 1$ and $z = 0$, we retrieve the classic Taylor–Green flow (with a passive tracer concentration field), where all artificial source terms vanish.

We consider now the convergence toward the manufactured solution. We let the grid size $h \in [2\pi/256, 2\pi/16]$ and the time step $\tau \in [0.0001, 0.01]$, and evaluate the solution at the final time $T = 0.1$. The parameters for two phases used the simulation are given in **Table 1**, while the non-phase specific parameters are given in **Table 2**. Note that in order to test all parts of the implementation, all parameters are kept roughly in the same order of magnitude. When all the physical processes are included, the manufactured solution becomes an increasingly bad approximation and thus the resulting source terms become large. Thus, in order to avoid numerical instabilities, it was necessary to evaluate the error at a relatively short final time T. However, it should be enough to locate errors in most parts of the code.

TABLE 1 | Phasic parameters used in the Taylor–Green simulations.

Parameter	Symbol	Value in phase 1	Value in phase 2
Density	ρ	3	1
Viscosity	μ	3	5
Permittivity	ε	3	4
Cation diffusivity	D_+	3	1
Anion diffusivity	D_-	4	2
Cation solubility	β_+	2	−2
Anion solubility	β_-	1	−1

TABLE 2 | Non-phase-specific parameters used in the Taylor–Green simulations.

Parameter	Symbol	Value
Surface tension	σ	0.1
Interface thickness	ϵ	$1/\sqrt{2}$
Phase field mobility	M	1
Initial velocity	U_0	1
Initial concentration	c_0	1
Initial phase field	Φ_0	1
Initial conc. deviation	C_0	0.5

We plot the L^2 errors of all the fields as a function of the grid size h in **Figure 5**. In these simulations, we used a small time step $\tau = 0.0001$ to rule out the contribution of time discretization to the error, cf. Equation (57). It is clear that the spatial convergence is close to ideal for all fields, indicating that the scheme approaches the correct solution. The pressure p displays slightly worse convergence and higher error norm than the other fields, which may be due to the pointwise way of enforcing the pressure boundary condition (all other fields have Dirichlet conditions on the entire boundary).

In **Figure 6**, we plot the L^2 errors of the same fields as in **Figure 5**, but as a function of the time step τ. In the simulations plotted here, we used a fine grid resolution with $h = 2\pi/256$ to rule out the contribution of spatial discretization to the error, cf. Equation (57). Clearly, first order convergence is achieved for sufficient refinement, for all fields including the pressure.

5.3. Droplet Motion Driven by an Electric Field

We now consider a charged droplet moving due to an imposed electric field; a problem for which there is no analytical solution available. However, by comparing to a highly resolved numerical solution, convergence for the fully coupled two-phase electrohydrodynamic problem can be verified. This problem has already been partly presented in the above, and is implemented in `problems/charged_droplet.py`. A sketch showing the initial state is shown in **Figure 7**. We consider an initially circular droplet, where a positive charge concentration is initiated as a Gaussian distribution, with variance δ_c^2, in the middle of the droplet. In this set-up, we consider only a single, positive species. The total amount of solute, i.e., integrated concentration, is

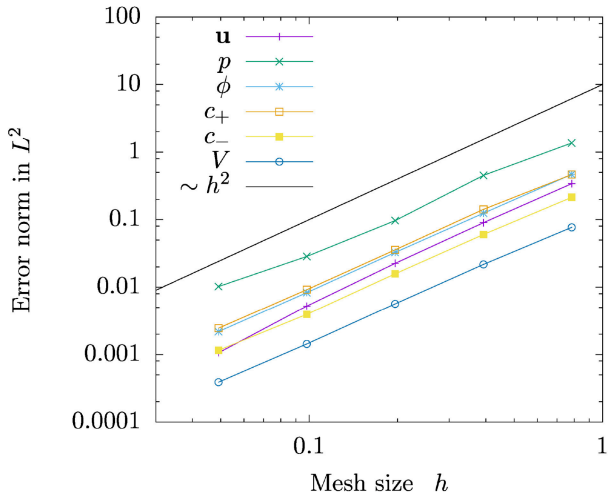

FIGURE 5 | Convergence in space for the two-phase electrohydrodynamic Taylor–Green manufactured solution. The solid black line shows the theoretical convergence rate based on the order of the finite elements chosen ($\sim h^2$). All fields display close to ideal convergence.

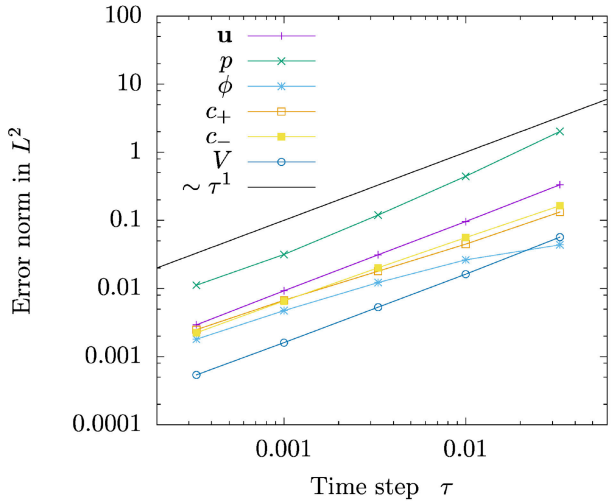

FIGURE 6 | Convergence in time for the two-phase electrohydrodynamic Taylor–Green manufactured solution. The solid black line shows the theoretical convergence rate of the scheme ($\sim \tau^1$). All fields display close to ideal convergence.

$C_0 = \int_\Omega c_0 \, \mathrm{d}A$. The left wall of the reservoir is kept at a positive potential, $V = \Delta V$, while the right wall is grounded, $V = 0$. The top and bottom walls are assumed to be perfectly insulating, i.e., a no-flux condition is applied on concentration fields and electric fields, and a no-slip condition is applied on the velocity. The fluid surrounding the droplet is neutral, and its parameters are chosen such that the solute is only very weakly soluble in the surrounding fluid, and the diffusivity here is very low here to prevent leakage. The droplet is accelerated by the electric field toward the right, before it is slowed down due to viscous effects upon approaching the wall.

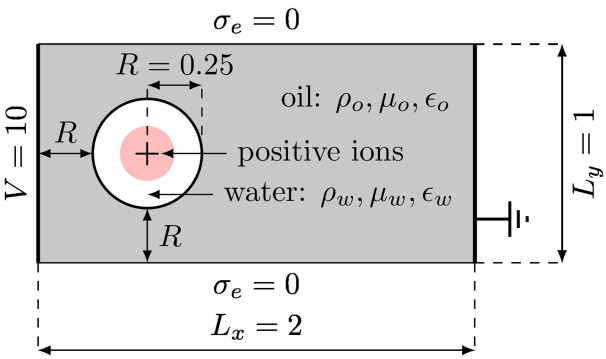

FIGURE 7 | Schematic set-up of the test case of droplet motion driven by an electric field. The "water" droplet contains positive ions and is driven by the electric field set up between the high potential on the left wall and the grounded right wall.

TABLE 3 | Numerical parameters that vary with resolution in the charged droplet simulations: Mesh size h, time step τ, and interface thickness ϵ.

h	τ	ϵ
0.04	0.04	0.06
0.02	0.02	0.03
0.01	0.01	0.015
0.005	0.005	0.0075
0.0025	0.0025	0.00375

With regard to reproducing the sharp-interface equations, we consider now the case of reducing the interface thickness $\epsilon \to 0$. To this end, we keep the ratio h/τ between mesh size and time step fixed, and further we keep the interface thickness ϵ proportional to h. The latter spans roughly 3–4 elements. Since the interface thickness ϵ changes, an important parameter in the phase-field model changes, which couples back to the equations, and thus the L_2 norm does not necessarily constitute a proper convergence measure. We therefore resort to using the *picture norm* or contour of the droplet as a measure, i.e., the zero-level set of the phase field $\phi = 0$. In particular, we will consider two observables: circumference and the center of mass (along x) of the droplet, as a function of resolution. A similar approach was taken for the case of phase-field models without electrodynamics by Aland and Voigt [66] who compared their benchmarks to sharp interface results by Hysing et al. [65].

The resolutions used in our simulations are given in **Table 3**. In order not to have to adjust the phase field mobility when refining, whilst still expecting to retrieve the sharp-interface model in the limit $\epsilon \to 0$, we choose the phase field mobility given by (33b). All parameters for the phasic quantities are given in **Table 4**, while the remaining parameters are given in **Table 5**. From these parameters, using the unit scaling adopted in this paper, we find an approximate Debye length $\lambda_D = \sqrt{\varepsilon/(2z^2 c_R)} \simeq \sqrt{1/(2 \cdot 10)} \simeq 0.2$ (see section B2 in the Appendix for

TABLE 4 | Numerical parameters for the phases that are common for all charged droplet simulations.

Parameter	Symbol	Value, phase 1	Value, phase 2
Density	ρ	200.0	100.0
Permittivity	ε	1.0	1.0
Diffusivity	D	$1 \cdot 10^{-5}$ ($\simeq 0$)	0.001
Solubility	β	4.0	1.0
Viscosity	μ	10.0	1.0

TABLE 5 | Numerical parameters not specific to phase for the charged droplet simulations.

Parameter	Symbol	Value
Potential difference	ΔV	10.0
Integrated concentration	C_0	10.0
Phase field mobility coeff.	M_0	$1.5 \cdot 10^{-5}$
Initial droplet radius	R	0.25
Initial conc. std. dev.	δ_C	0.0833
Surface tension	σ	5.0
Length in x-direction	L_x	2.0
Length in y-direction	L_y	1.0

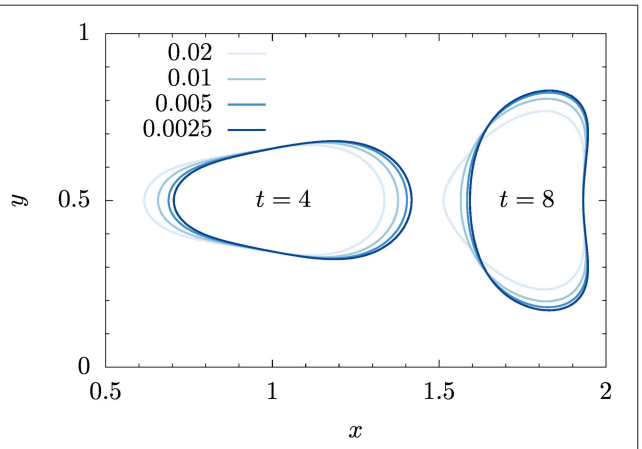

FIGURE 8 | Shape comparison of electrically driven charged droplet at two time instances. The effect of the four resolutions given in **Table 3** is shown. The legend shown in the figure refers to both spatial (h) and temporal resolution (τ).

this expression), since we can approximate the order of magnitude of $c_R < C/(\pi R^2) = 10/(\pi \cdot 0.25^2)$ for a moderate screening.

In **Figure 8**, we show the contour of the driven droplet at two time instances $t = 4$ and $t = 8$, and compare increasing resolution (simultaneously in space, time and interface thickness). Qualitatively inspecting the contours by eye, the droplet shapes seem to converge to a well defined shape with increasing resolution at both time instances.

However, qualitive comparison is clearly not enough to assess the convergence. As in Hysing et al. [66] and Aland and Voigt [65], we define three observables:

- Center of mass: We consider the center of mass of the dispersed phase (phase 2, i.e., $\phi < 0$),

$$x_{\mathrm{CM}} = \frac{\int_{\phi<0} x \,\mathrm{d}A}{\int_{\phi<0} \mathrm{d}A}, \tag{65}$$

  where we approximate the integral over the droplet (phase 2) by $\int_{\phi<0}(\cdot)\,\mathrm{d}A = \int_\Omega (1-\phi)(\cdot)/2\,\mathrm{d}A$.
- Drift velocity: Similarly as above, the velocity at which the droplet is driven is measured by

$$\mathcal{V} = \frac{\int_{\phi<0} \mathbf{u}\cdot\hat{\mathbf{x}}\,\mathrm{d}A}{\int_{\phi<0}\mathrm{d}A}. \tag{66}$$

- Circularity: Defined as the ratio of the circumference of the area-equivalent circle to the droplet circumference,

$$\mathcal{C} = \frac{2\sqrt{\pi \int_{\phi<0}\mathrm{d}A}}{\ell}. \tag{67}$$

The circumference ℓ and the integrals are computed by the post-processing method `geometry_in_time` which is built into *Bernaise*.

Figure 9 shows the three quantities as a function of time for increasing resolution. (Here we have omitted the coarsest resolution $h = 0.04$ for visual clarity.) The curves seem to converge toward well-defined trajectories with resolution.

For a more quantitative comparison, we define the time-integrated error norm,

$$\|e\|_p = \left(\frac{\int_0^T |q_{\mathrm{ref}}(t) - q(t)|^p \,\mathrm{d}t}{\int_0^T |q_{\mathrm{ref}}(t)|^p \,\mathrm{d}t} \right)^{1/p} \tag{68}$$

for a given quantity q. We can compute an empirical convergence rate of this norm,

$$k_{p,i} = \frac{\log\left(\|e\|_p(h_{i+1})/\|e\|_p(h_i)\right)}{\log\left(h_{i+1}/h_i\right)} \tag{69}$$

for two successive resolutions ($h_{i+1} > h_i$). Here we shall consider the L^2 error norm in time, i.e., $p = 2$, and in practice we compute the integrals in time by cubic spline interpolation of measurement points saved at every 5 time steps. There is no exact solution, or reference high-resolution sharp-interface solution available for this set-up. However, if we now assume that the finest resolution *is* the exact solution, and use this as the reference field in Equation (68), we can compute error norms and convergence rates. These values are reported in **Table 6**.

The computed convergence rates increase for all three observables and reach 1.6–1.7 with increasing resolution, indicating also quantitatively a convergence that is in agreement with the anticipated convergence rate. Considering Equation (57), from the temporal discretization, we expect $k_2 \simeq 1$, and from the spatial $k_2 \simeq 2$. Depending on which term contributes most to the error, we will measure either of

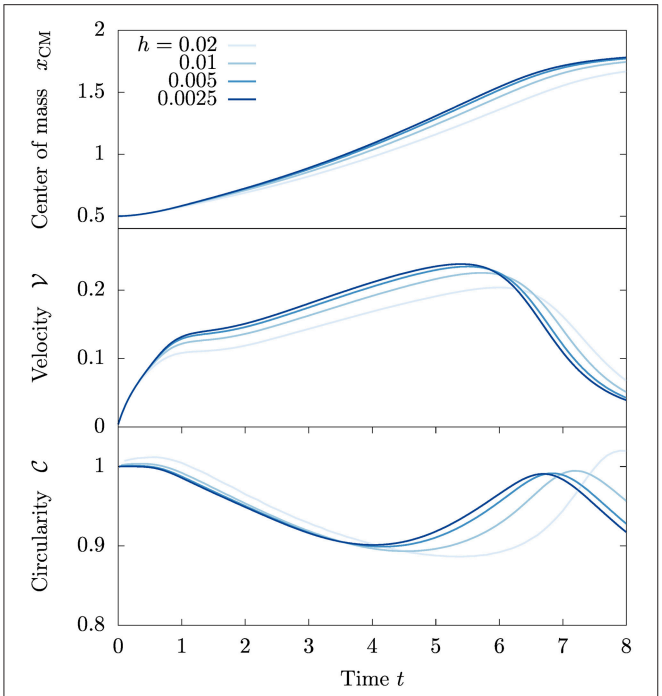

FIGURE 9 | Observable quantities as a function of time. Increasing resolutions (spatial and temporal) are compared.

TABLE 6 | Mesh size h, error norm $\|e\|_2$, and empirical convergence rate k_2 for increasing grid refinement, assuming the solution for the finest resolution to be exact.

h	$\|e\|_2$	k_2
CENTER OF MASS		
0.04	0.1798	
0.02	0.0955	0.9129
0.01	0.0410	1.2186
0.005	0.0126	1.7033
DRIFT VELOCITY		
0.04	0.3427	
0.02	0.2067	0.7293
0.01	0.1032	1.0025
0.005	0.0341	1.5932
CIRCULARITY		
0.04	0.0891	
0.02	0.0423	1.0757
0.01	0.0205	1.0467
0.005	0.0060	1.7612

these rates. The values measured here indicate that both terms may be comparable in magnitude; however if we instead of using directly the finest solution as reference, extrapolated the trajectories further, we would presumptively have achieved lower convergence rates. This might indicate that the convergence error is eventually dominated by the temporal discretization, cf. Equation (57).

6. APPLICATIONS

6.1. Oil Expulsion From a Dead-End Pore

Here, we present a demonstration of the method in a potential geophysical application. We consider a shear flow of one phase ("water") over a dead-end pore which is initially filled with a second phase ("oil"). The water phase contains initially a uniform concentration of positive and negative ions, $c_\pm|_{t=0} = c_0$, and the water–oil interface is modeled to be impermeable. The simulation of the dead-end pore is carried out to preliminarily assess the hypothesis that electrowetting could be responsible for the increased expelling of oil in low-salinity enhanced oil recovery. The problem set-up is schematically shown in **Figure 10**. The phasic parameters used in the simulations are given in **Table 7**, and the remaining parameters are given in **Table 8**. This problem is implemented in the file `problems/snoevsen.py`.

To investigate the effect of including electrostatic interactions, we show in **Figure 11** instantaneous snapshots of simulations with and without surface charge at different times. The left column, **Figures 11A,C,E**, shows the results for vanishing surface charge, and the right column, **Figures 11B,D,F**, shows the results for a surface charge of $\sigma_e = -10$.

For the uncharged case, the frames that are shown are almost indistinguishable. In fact, the main difference is the numerical noise of the total charge, which is due to roundoff errors of machine precision. The initial dynamics of the oil plug interface, which is to equilibrate with the neutral contact angle and the shear flow, mainly happens before the first frame presented; compare **Figure 10** and **Figure 11A**.

A markedly different behavior is displayed in the right column, **Figures 11B,D,F**, where a uniform surface charge density is enforced at the walls at the simulation start, $t = 0$. Here, we see first that two tongues are intruding on both sides of the droplet, which push the droplet out into the center of the dead-end pore. The process is continued, as shown in the second frame, and finalized, as shown in the third frame, with the complete release of the droplet as the two tongues meet at the bottom of the dead-end pore, cutting the final contact point.

With these simulations, we have demonstrated the effects when a surface charge couples to hydrodynamics. This has lead to the observation that oil phase, on a larger scale than the Debye length, behaves like it is completely dewetting even when we locally enforce a neutral contact angle.

6.2. 3D Simulations of Droplet Coalescence and Breakup in an Electric Field

Finally, to demonstrate the ability of *Bernaise* to simulate 3D configurations, we present simulations of two oppositely charged droplets that coalesce. In order to achieve this efficiently, a fully iterative solver was implemented. The solver consists of a fractional step version of the `basic` solver, in the sense that within the fluid flow step, it splits between the velocity and pressure computations, as shown in Equations (56a), (56b), and (56c). The splitting introduces a weak compressibility which suffices to stabilize the problem [77] (with respect to the BB condition) and thus we can use P_1 finite elements also for the velocity. The combination of fewer degrees of freedom and

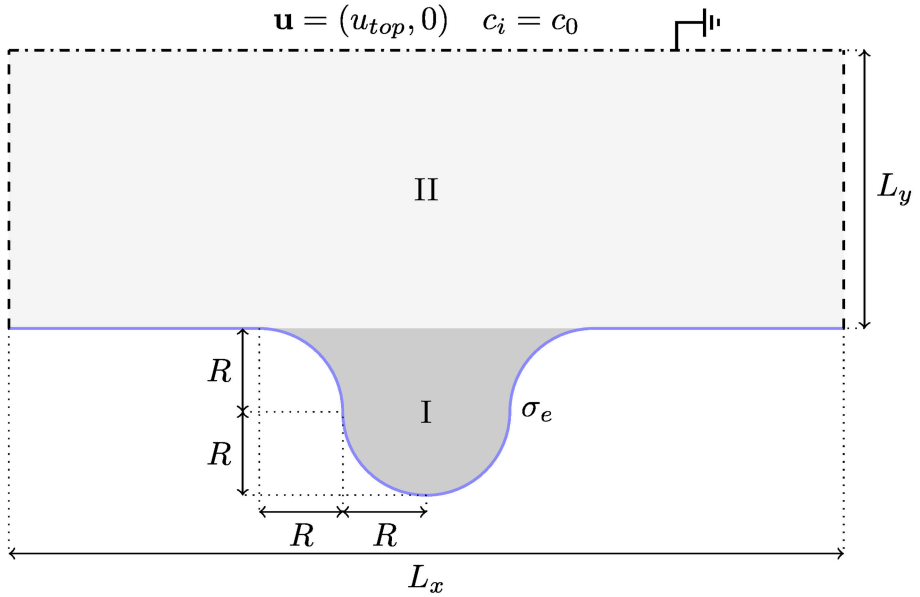

FIGURE 10 | A schematic depiction of the "dead-end pore" geometry, with the appropriate boundary conditions for the problem and specified initial conditions for the phase field. The geometry is specified by the two lengths L_x, L_y, and the radius R used to define the dead-end pore in the center of the channel by a circle and a circular smoothed inlet. The roman numerals indicate the phase, along with the tone of gray. The darker phase is the oil-like phase (I), and the lighter one is the water-like phase (II).

TABLE 7 | Phasic parameters for the simulations of shear flow over a dead-end pore.

Parameter	Symbol	Value in phase 1	Value in phase 2
Viscosity	μ	1.0	1.0
Density	ρ	10.0	10.0
Permittivity	ε	1.0	1.0
Solution energy	$\beta_\pm$	4	1
Ion mobility	$D_\pm$	0.0001	0.01

The subscript ± indicates the value for both the positive and negative ions.

TABLE 8 | Simulation parameters for the simulations of shear flow over a dead-end pore.

Parameter	Symbol	Value
Length	L_x	3.0
Height	L_y	1.0
Total simulation time	T	20
Radius	R	0.3
Time step	τ	0.01
Resolution	h	1/120
Interface thickness	ϵ	0.02
Phase field mobility	M_0	$2.5 \cdot 10^{-6}$
Surface tension	σ	2.45
Surface charge	σ_e	$\{-10, 0\}$
Reference concentration	c_0	2
Shear velocity	u_{top}	0.2

the applicability of iterative linear solvers imparts significant speed-up compared to coupled solvers, which is of paramount importance for 3D simulations. This yields advantages over solvers which rely on a mixed-element formulation of the hydrodynamic subproblem [70]. The detailed analysis of the fractional step solver will be published in a separate paper, but the implementation can be found in `solvers/fracstep.py`. For solving the linear systems iteratively, we use an algebraic multigrid (AMG) preconditioner and a generalized minimal residual (GMRES) linear solver for the electrochemical and the pressure correction step; Jacobi preconditioner (Jacobi) and a stabilized bi-conjugate gradient method (BiCGStab) for the velocity prediction, and Jacobi and GMRES for the velocity correction. For the phase field we use Jacobi and a conjugate gradient method.

To prevent leakage of ions out of the two coalescing droplets, a weighted geometric mean was used for the diffusivities:

$$K_j(\phi) = K_{j,1}^{\frac{1+\phi}{2}} \cdot K_{j,2}^{\frac{1-\phi}{2}}, \tag{70}$$

instead of the arithmetic mean (25) used in most of the article.

We consider a setup of two initially spherical droplets in a domain $\Omega = [0, L_x] \times [0, L_y] \times [0, L_z]$. The droplets are centered at $(L_x/2, L_y/2, (L_z \pm L_x)/2)$ and have a radius R. The lower droplet (along the z-axis) is initialized with a Gaussian concentration distribution of negative ions ($z_- = -1$), whereas the upper droplet is initialized with positive ions ($z_+ = 1$). The average concentration of the respective ion species within each droplet is c_0, such that the total charge in the system is zero, and the initial

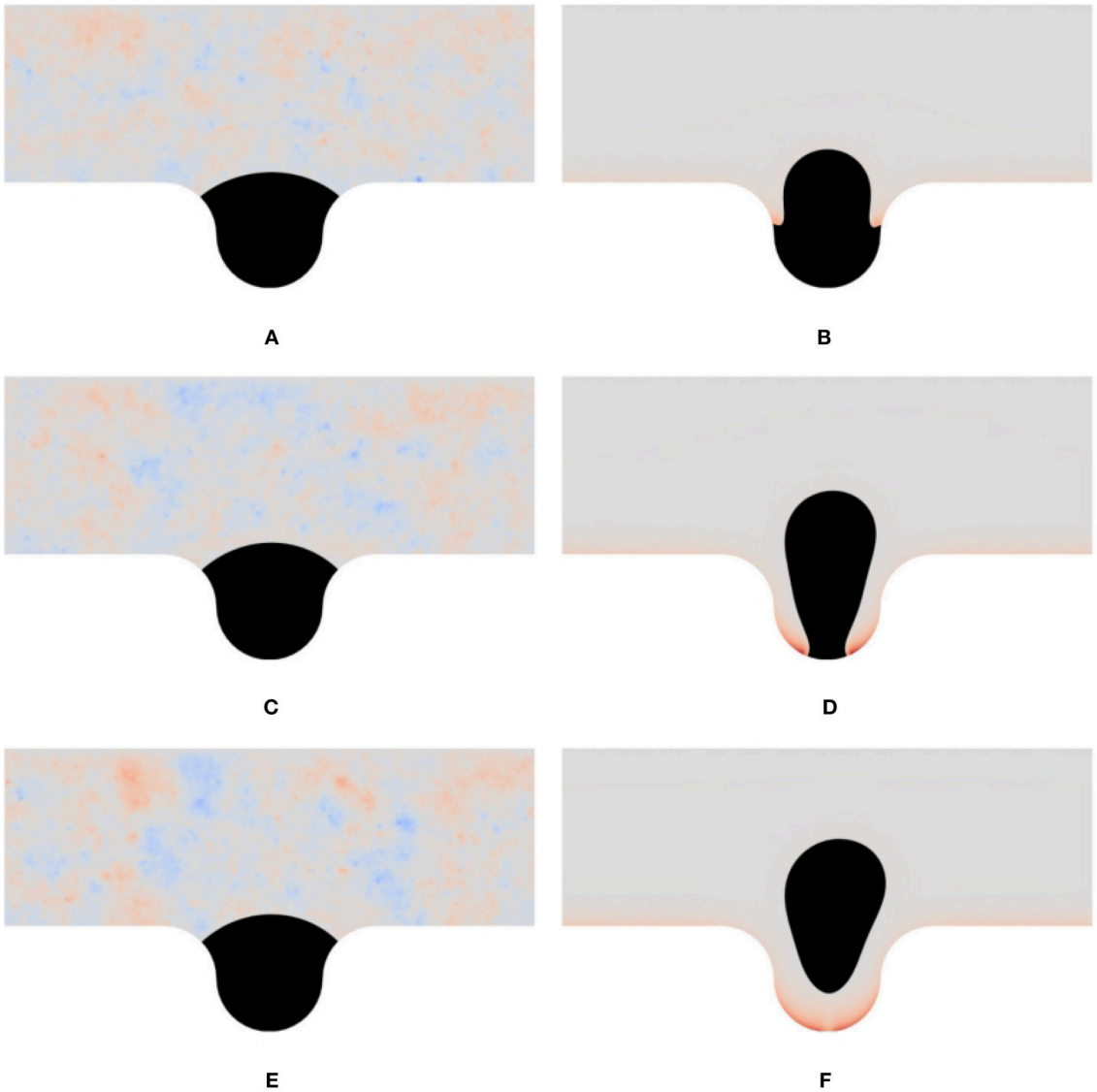

FIGURE 11 | Oil released from a dead-end pore. We show instantaneous snapshots from the simulations of the dead-end pore under a shear flow. The black phase is the oil phase, which does not contain solutes, and the other phase is the water phase, which contains monovalent positive and negative ions. The color in the lighter phase indicates the local net charge, red meaning positive charge, blue negative charge, and gray neutral charge. The color scale is relative to the maximum deviation from neutral charge for an entire simulation; therefore the neutral simulations display numerical noise (which is of the order of machine precision). In the left column the surface charge is zero, and in the right column, a uniform surface charge density $\sigma_e = -10$ is set. The rows show snapshots at different times t. **(A)** t = 3.0, σ_e = 0. **(B)** t = 3.0, σ_e = -10. **(C)** t = 6.0, σ_e = 0. **(D)** t = 3.0, σ_e = -10. **(E)** t = 9.0, σ_e = 0. **(F)** t = 9.0, σ_e = -10.

spread (standard deviation) of the Gaussian distribution is $R/3$. A potential V_0 is set on the top plane at $z = L_z$ and the bottom plane at $z = 0$ is taken to be grounded. We assume no-slip and no-flux conditions on all boundaries, except for the electrostatic potential V at the top and bottom planes, and the fluid is taken to be in a quiescent state at the initial time $t = 0$. The phasic parameters used in the simulations are given in **Table 9**, and the remaining parameters are given in **Table 10**. The problem is implemented in the file `problems/charged_droplets_3D.py`.

Figure 12 shows snapshots from the simulations at several instances of time. As seen from the figure, the droplets are set in motion toward each other by the electric field and collide with each other. Subsequently, the unified droplet is stretched, until it touches both electrodes. The middle part then breaks off, and as it is unstable, it further emits droplets that are released to two two sides. Finally, two spherical caps form at each electrode, and a neutral drop is left in the middle, due to the initial symmetry. Similar behavior has been observed in axisymmetric simulations (e.g., [82]).

We finally carry out a strong scaling test of the linear iterative solver on a single in-house server with 80 dedicated cores. The results of average computational time per time step (averaged

TABLE 9 | Phasic parameters for the simulations of droplet coalescence and breakup in an electric field.

Parameter	Symbol	Value in phase 1	Value in phase 2
Viscosity	μ	1.0	0.5
Density	ρ	500.0	50.0
Permittivity	ε	1.0	2.0
Solution energy	$\beta_{\pm}$	2	0
Ion mobility	$D_{\pm}$	0.0001	0.1

The subscript $\pm$ indicates the value for both the positive and negative ions.

TABLE 10 | Simulation parameters for the simulations of droplet coalescence and breakup in an electric field.

Parameter	Symbol	Value
Length along x	L_x	1.0
Length along y	L_y	1.0
Height	L_z	2.0
Total simulation time	T	20
Initial radius	R	0.2
Time step	τ	0.005
Resolution	h	1/64
Interface thickness	ϵ	0.01
Phase field mobility	M_0	$1 \cdot 10^{-5}$
Surface tension	σ	2.0
Initial avg. concentration	c_0	20.0

over 10 time steps) vs. number of cores are shown in **Figure 13**. We show here the amount of time spent per time step for all substeps in order to illuminate where most of the computational resources are spent. As can be seen, a significant portion of the computational time is spent on the electrochemical substep. Overall, the solver displays sublinear scaling with the number of cores, but the results are promising given that neither the solver nor the FEniCS install (a standard PPA install of FEniCS 2017.2.0 on Ubuntu 16.04 server) are fully optimized. Much could be gained by improving the two steps where solving a Poisson equation is involved; in particular it seems possible that more specifically tailored preconditioners than the straightforward AMG preconditioning could impart speedup. However, we stress that the division of labor between the steps is highly problem-dependent, and in particular, the electrochemical subproblem is susceptible to how far into the non-linear regime we are (see e.g., [45]).

7. DISCUSSION AND CONCLUSION

We have in this work presented *Bernaise*, a flexible open-source framework for simulating two-phase electrohydrodynamics in complex geometries using a phase-field model. The solver is written in its entirety in Python, and is built on top of the FEniCS/DOLFIN framework [42, 83] for solving partial differential equations using the finite element method on unstructured meshes. FEniCS in turn interfaces to, e.g., scalable state-of-the art linear solvers through its PETSc backend [84]. We have proposed a linear operator-splitting scheme to solve the coupled non-linear equations of two-phase electrohydrodynamics. In contrast to solving the equations directly in a monolithic manner, the scheme sequentially solves the Cahn–Hilliard equation for the phase field describing the interface, the Poisson–Nernst–Planck equations for the electrochemistry (solute transport and electrostatics), and the Navier–Stokes equations for the hydrodynamics, at each time step. Implementation of new solvers and problems has been demonstrated through representative examples. Validation of the implementation was carried out by three means: (1) By comparison to analytic solutions in limiting cases where such are available, (2) by the method of manufactured solution through an augmented Taylor–Green vortex, and (3) through convergence to a highly resolved solution of a new two-phase electrohydrodynamics benchmark problem of an electrically driven droplet. Finally, we have presented applications of the framework in non-trivial settings. Firstly, to test the applicability of the code in a complicated geometry, and to illuminate the effects of dynamic electrowetting, we simulated a shear flow of water containing an electrolyte over a dead-end pore initially filled with oil. This problem is relevant from a geophysical standpoint, and exemplifies the potential of the method to simulate the dynamics of the interaction between two-phase flow and electric double layers. Secondly, the ability of the framework to simulate three-dimensional configurations was demonstrated using a fully iterative version of the operator-splitting scheme, by simulating the coalescence and subsequent breakup of two oppositely charged droplets in an electric field. The parallel scalability of the latter solver was tested on in-house computing facilities. The results presented herein underpin our aim that *Bernaise* can become a valuable tool both within the micro- and nanofluidics community and within geophysical simulation.

We have in this article not considered situations with multiple interacting droplets, complicated background flows, or complex mesh topologies. While the numerical procedure is capable of handling this, the main purpose of this article (in addition to presenting the software) has been to establish the validity of the approach, and to demonstrate its use through fairly rudimentary examples. Hence, we plan to use the present work as a basis for studying more complicated systems in the future.

There are several possible avenues for further development and use of *Bernaise*. With regard to computational effort, the linear operator-splitting scheme constitutes a major computational improvement over a corresponding monolithic scheme. For the resulting smaller and simpler subproblems, more specialized linear solvers and preconditioners can be used. However, the implementation of the schemes are still not fully optimized, as in many cases it is not strictly necessary to reassemble entire system matrices (multiple times) at every time step. Using ideas e.g., from Mortensen and Valen-Sendstad [43] on how to effectively preassemble system matrices in FEniCS, one could achieve an implementation that is to a larger extent dominated by the backend linear solvers. However, as the phase field is updated at every time step, there may be less to gain in performance than what was the case in the latter reference.

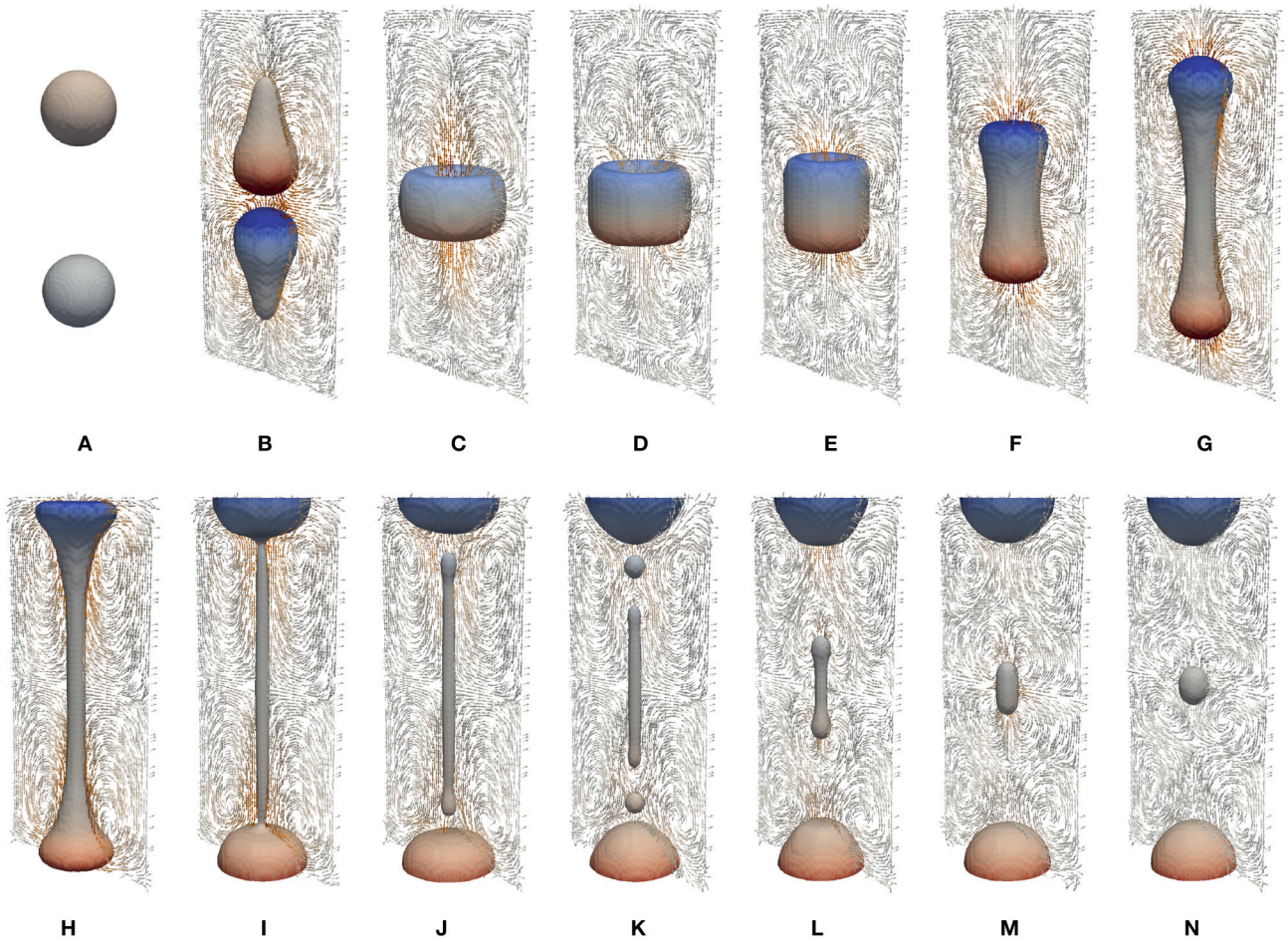

FIGURE 12 | Snapshots from the simulations of droplet coalescence and subsequent breakup in an electric field. The phase boundary shows the $\phi = 0$ isosurface of the phase field. The coloring indicates charge: red is positive and blue is negative. The color bar goes from -20 (deep blue) to 20 (deep red). The quivers show the velocity field in the $x = 0.5$ plane (color indicates intensity). **(A)** $t = 0.0$. **(B)** $t = 0.25$. **(C)** $t = 0.5$. **(D)** $t = 0.75$. **(E)** $t = 1.0$. **(F)** $t = 1.25$. **(G)** $t = 1.5$. **(H)** $t = 1.75$. **(I)** $t = 2.0$. **(J)** $t = 2.25$. **(K)** $t = 2.5$. **(L)** $t = 2.75$. **(M)** $t = 3.0$. **(N)** $t = 4.0$.

With regard to solving the Navier–Stokes equations, the solvers considered herein either rely on a coupled approach (the `basic` and `basicnewton` solvers) or a fractional step approach that splits between the computations of velocity and pressure (the `fracstep` solver that was considered in section 6.2). Using direct linear solvers, the coupled solvers yield accurate prediction of the pressure and can be expected to be more robust. However, direct solvers have numerical disadvantages when it comes to scalability, and Krylov solvers require specifically tailored preconditioners to achieve robust convergence. An avenue for further research is to refine the `fracstep` solver and develop decoupled energy-stable schemes for this problem, which seems possible by building on literature on similar systems [67–70, 75], Linga et al. (Submitted). The implementation of such enhanced schemes in *Bernaise* is straighforward, as demonstrated in this paper. On the other hand, in problems where interface forces and electric fields become sufficiently strong, and the equations become strongly nonlinearly coupled, it may be necessary to use a fully-implicit approach (along the lines of `basicnewton`), combined with direct linear solvers, to obtain a converged solution. In the future we aim to compare the ranges of applicability of various fully-implicit, semi-implicit, and splitting-based schemes for practical settings.

A clear enhancement of *Bernaise* would be adaptivity, both in time and space. Adaptivity in time should be implemented such that time step is variable and controlled by the globally largest propagation velocity (in any field), and a Courant number of choice. Adaptivity in space is presently only supported as a one-way operation. Adaptive mesh refinement is already used in the mesh initialization phase in many of the implemented problems. However, mesh coarsening has currently limited support in FEniCS and to the authors' knowledge there are no concrete plans of adding support for this. Hence, *Bernaise* lacks an adaptive mesh functionality, but this could be implemented in an *ad hoc* manner with some code restructuring.

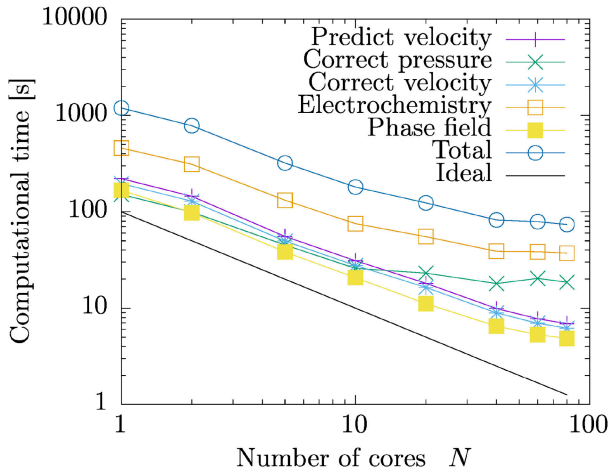

FIGURE 13 | Strong scaling test. We show computational time per timestep vs. number of processor cores for the coalescence and breakup of droplets in 3D. The results are averaged over the 10 first timesteps for simulations with $128 \times 128 \times 256 = 4{,}194{,}304$ degrees of freedom, with a time step $\tau = 0.02$.

In this article, we have not considered any *direct* dependence of the contact angle (i.e., the surface energies) on an applied electric field. However, the contact angle on scales below the Debye length is generally thought to be unaffected, albeit on scales larger than the insulator thickness, an apparent contact angle forms [85, 86]. Using the full two-phase electrohydrodynamic model presented herein, effective contact angle dependencies upon the zeta potential could be measured and used in simulations of more macroscopic models; i.e., models admissible on scales where the electrical double layers are not fully resolved [86]. This would result in a modified contact angle energy that would be enforced as a boundary condition in a phase field model [87].

Physically, several extensions of the model could be included in the simulation framework. Surfactants may influence the dynamics of droplets and interfaces, and could be included as in e.g., the model by Teigen et al. [88]. The model in its current form further assumes that we are concerned with dilute solutions (i.e., ideal gas law for the concentration), and hence more complicated electrochemistry could to some extent be incorporated into the chemical free energy $\alpha(c)$.

Finally, the requirement of the electrical double layer to be well-resolved constitutes the main constraint for upscaling of the current method. Thus, for simulation of two-phase electrohydrodynamic flow on larger scales, if ionic transport need not be accounted for, it would only require minor modifications of the code to run the somewhat simpler Taylor–Melcher leaky dielectric model, e.g., in the formulation by Lin et al. [60], within the current framework.

AUTHOR CONTRIBUTIONS

AB, GL, and JM: designed the study; GL: developed the numerical scheme and methods; GL and AB: performed simulations; GL: wrote the first draft.

FUNDING

This project has received funding from the European Union's Horizon 2020 research and innovation program through a Marie Curie initial training networks under grant agreement no. 642976 (NanoHeal), and from the Villum Fonden through the grant Earth Patterns.

SUPPLEMENTARY MATERIAL

The Supplementary Material for this article can be found online at: https://www.frontiersin.org/articles/10.3389/fphy.2019.00021/full#supplementary-material

REFERENCES

1. Lippmann G. *Relations Entre les Phénomènes Électriques et Capillaires*. Paris: Sorbonne (1875).
2. Mugele F, Baret JC. Electrowetting: from basics to applications. *J Phys Condens Matter.* (2005) **17**:R705. doi: 10.1088/0953-8984/17/28/R01
3. Ristenpart W, Bird J, Belmonte A, Dollar F, Stone H. Non-coalescence of oppositely charged drops. *Nature.* (2009) **461**:377–80. doi: 10.1038/nature08294
4. Mugele F. Fluid dynamics: to merge or not to merge. *Nature.* (2009) **461**:356. doi: 10.1038/461356a
5. Squires TM, Quake SR. Microfluidics: fluid physics at the nanoliter scale. *Rev Mod Phys.* (2005) **77**:977. doi: 10.1103/RevModPhys.77.977
6. Schoch RB, Han J, Renaud P. Transport phenomena in nanofluidics. *Rev Mod Phys.* (2008) **80**:839. doi: 10.1103/RevModPhys.80.839
7. Mugele F, Duits M, Van den Ende D. Electrowetting: a versatile tool for drop manipulation, generation, and characterization. *Adv Colloid Interface Sci.* (2010) **161**:115–23. doi: 10.1016/j.cis.2009.11.002
8. Nelson WC, Kim CJ. Droplet actuation by electrowetting-on-dielectric (EWOD): a review. *J Adhes Sci Technol.* (2012) **26**:1747–71. doi: 10.1163/156856111X599562
9. Pollack M, Shenderov A, Fair R. Electrowetting-based actuation of droplets for integrated microfluidics. *Lab Chip.* (2002) **2**:96–101. doi: 10.1039/b110474h
10. Srinivasan V, Pamula VK, Fair RB. An integrated digital microfluidic lab-on-a-chip for clinical diagnostics on human physiological fluids. *Lab Chip.* (2004) **4**:310–5. doi: 10.1039/b403341h
11. Lee J, Kim CJ. Surface-tension-driven microactuation based on continuous electrowetting.*J Microelectromech Syst.* (2000) **9**:171–80. doi: 10.1109/84.846697
12. Siria A, Bocquet ML, Bocquet L. New avenues for the large-scale harvesting of blue energy. *Nat Rev Chem.* (2017) **1**:0091. doi: 10.1038/s41570-017-0091
13. Beni G, Hackwood S. Electro-wetting displays. *Appl Phys Lett.* (1981) **38**:207–9. doi: 10.1063/1.92322
14. Beni G, Tenan M. Dynamics of electrowetting displays. *J Appl Phys.* (1981) **52**:6011–5. doi: 10.1063/1.329822
15. Beni G, Hackwood S, Jackel J. Continuous electrowetting effect. *Appl Phys Lett.* (1982) **40**:912–4. doi: 10.1063/1.92952
16. Hayes RA, Feenstra BJ. Video-speed electronic paper based on electrowetting. *Nature.* (2003) **425**:383. doi: 10.1038/nature01988
17. Pride SR, Morgan F. Electrokinetic dissipation induced by seismic waves. *Geophysics.* (1991) **56**:914–25. doi: 10.1190/1.1443125

18. Fiorentino EA, Toussaint R, Jouniaux L. Lattice Boltzmann modelling of streaming potentials: variations with salinity in monophasic conditions. *Geophys J Int.* (2016) **205**:648–64. doi: 10.1093/gji/ggw041
19. Fiorentino EA, Toussaint R, Jouniaux L. Two-phase lattice Boltzmann modelling of streaming potentials: influence of the air-water interface on the electrokinetic coupling. *Geophys J Int.* (2016) **208**:1139–56. doi: 10.1093/gji/ggw417
20. Hassenkam T, Pedersen CS, Dalby K, Austad T, Stipp SLS. Pore scale observation of low salinity effects on outcrop and oil reservoir sandstone. *Colloids Surf A.* (2011) **390**:179–88. doi: 10.1016/j.colsurfa.2011.09.025
21. Hilner E, Andersson MP, Hassenkam T, Matthiesen J, Salino P, Stipp SLS. The effect of ionic strength on oil adhesion in sandstone–the search for the low salinity mechanism. *Sci Rep.* (2015) **5**:9933. doi: 10.1038/srep09933
22. RezaeiDoust A, Puntervold T, Strand S, Austad T. Smart water as wettability modifier in carbonate and sandstone: a discussion of similarities/differences in the chemical mechanisms. *Energy Fuels.* (2009) **23**:4479–85. doi: 10.1021/ef900185q
23. Pedersen N, Hassenkam T, Ceccato M, Dalby KN, Mogensen K, Stipp SLS. Low salinity effect at pore scale: probing wettability changes in Middle East limestone. *Energy Fuels.* (2016) **30**:3768–75. doi: 10.1021/acs.energyfuels.5b02562
24. Plümper O, Botan A, Los C, Liu Y, Malthe-Sørenssen A, Jamtveit B. Fluid-driven metamorphism of the continental crust governed by nanoscale fluid flow. *Nat Geosci.* (2017) **10**:685. doi: 10.1038/ngeo3009
25. De Gennes PG. Wetting: statics and dynamics. *Rev Mod Phys.* (1985) **57**:827. doi: 10.1103/RevModPhys.57.827
26. Bonn D, Eggers J, Indekeu J, Meunier J, Rolley E. Wetting and spreading. *Rev Mod Phys.* (2009) **81**:739. doi: 10.1103/RevModPhys.81.739
27. Snoeijer JH, Andreotti B. Moving contact lines: scales, regimes, and dynamical transitions. *Ann Rev Fluid Mech.* (2013) **45**:269–92. doi: 10.1146/annurev-fluid-011212-140734
28. Melcher J, Taylor G. Electrohydrodynamics: a review of the role of interfacial shear stresses. *Ann Rev Fluid Mech.* (1969) **1**:111–46. doi: 10.1146/annurev.fl.01.010169.000551
29. Saville DA. Electrohydrodynamics: the Taylor-Melcher leaky dielectric model. *Ann Rev Fluid Mech.* (1997) **29**:27–64. doi: 10.1146/annurev.fluid.29.1.27
30. Fylladitakis ED, Theodoridis MP, Moronis AX. Review on the history, research, and applications of electrohydrodynamics. *IEEE Trans Plasma Sci.* (2014) **42**:358–75. doi: 10.1109/TPS.2013.2297173
31. Taylor G. Studies in electrohydrodynamics. I. The circulation produced in a drop by electrical field. *Proc R Soc Lond Ser A Math Phys Sci.* (1966) **291**:159–66.
32. Schnitzer O, Yariv E. The Taylor–Melcher leaky dielectric model as a macroscale electrokinetic description. *J Fluid Mech.* (2015) **773**:1–33. doi: 10.1017/jfm.2015.242
33. Zholkovskij EK, Masliyah JH, Czarnecki J. An electrokinetic model of drop deformation in an electric field. *J Fluid Mech.* (2002) **472**:1–27. doi: 10.1017/S0022112002001441
34. Monroe CW, Daikhin LI, Urbakh M, Kornyshev AA. Electrowetting with Electrolytes. *Phys Rev Lett.* (2006) **97**:136102. doi: 10.1103/PhysRevLett.97.136102
35. Monroe CW, Daikhin LI, Urbakh M, Kornyshev AA. Principles of electrowetting with two immiscible electrolytic solutions. *J Phys Condens Matter.* (2006) **18**:2837. doi: 10.1088/0953-8984/18/10/009
36. Yang Q, Li BQ, Ding Y. 3D phase field modeling of electrohydrodynamic multiphase flows. *Int J Multiph Flow.* (2013) **57**:1–9. doi: 10.1016/j.ijmultiphaseflow.2013.06.006
37. Yang Q, Li BQ, Shao J, Ding Y. A phase field numerical study of 3D bubble rising in viscous fluids under an electric field. *Int J Heat Mass Transf.* (2014) **78**:820–9. doi: 10.1016/j.ijheatmasstransfer.2014.07.039
38. Berry J, Davidson M, Harvie DJ. A multiphase electrokinetic flow model for electrolytes with liquid/liquid interfaces. *J Comput Phys.* (2013) **251**:209–22. doi: 10.1016/j.jcp.2013.05.026
39. Zeng J. Non-linear electrohydrodynamics in microfluidic devices. *Int J Mol Sci.* (2011) **12**:1633–49. doi: 10.3390/ijms12031633
40. Lu HW, Glasner K, Bertozzi A, Kim CJ. A diffuse-interface model for electrowetting drops in a Hele-Shaw cell. *J Fluid Mech.* (2007) **590**:411–35. doi: 10.1017/S0022112007008154
41. Walker SW, Shapiro B, Nochetto RH. Electrowetting with contact line pinning: computational modeling and comparisons with experiments. *Phys Fluids.* (2009) **21**:102103. doi: 10.1063/1.3254022
42. Logg A, Mardal KA, Wells G. *Automated Solution of Differential Equations by the Finite Element Method: The FEniCS Book*, Vol. 84. Springer Science & Business Media (2012).
43. Mortensen M, Valen-Sendstad K. Oasis: a high-level/high-performance open source Navier–Stokes solver. *Comput Phys Commun.* (2015) **188**:177–88. doi: 10.1016/j.cpc.2014.10.026
44. Mitscha-Baude G, Buttinger-Kreuzhuber A, Tulzer G, Heitzinger C. Adaptive and iterative methods for simulations of nanopores with the PNP–Stokes equations. *J Comput Phys.* (2017) **338**:452–76. doi: 10.1016/j.jcp.2017.02.072
45. Bolet A, Linga G, Mathiesen J. Electrohydrodynamic channeling effects in narrow fractures and pores. *Phys Rev E.* (2018) **97**:043114. doi: 10.1103/PhysRevE.97.043114
46. Prosperetti A, Tryggvason G. *Computational Methods for Multiphase Flow*. New York, NY: Cambridge University Press (2009).
47. Yang C, Li D. A method of determining the thickness of liquid-liquid interfaces. *Colloids Surf A.* (1996) **113**:51–9. doi: 10.1016/0927-7757(96)03544-3
48. Qian T, Wang XP, Sheng P. A variational approach to moving contact line hydrodynamics. *J Fluid Mech.* (2006) **564**:333–60. doi: 10.1017/S0022112006001935
49. Qian T, Wang XP, Sheng P. Molecular scale contact line hydrodynamics of immiscible flows. *Phys Rev E.* (2003) **68**:016306. doi: 10.1103/PhysRevE.68.016306
50. Sui Y, Ding H, Spelt PDM. Numerical simulations of flows with moving contact lines. *Ann Rev Fluid Mech.* (2014) **46**:97–119. doi: 10.1146/annurev-fluid-010313-141338
51. Ervik Å, Lysgaard MO, Herdes C, Jimnez-Serratos G, Müller EA, Munkejord ST, et al. A multiscale method for simulating fluid interfaces covered with large molecules such as asphaltenes. *J Comput Phys.* (2016) **327**:576–611. doi: 10.1016/j.jcp.2016.09.039
52. Walker SW, Shapiro B. Modeling the fluid dynamics of electrowetting on dielectric (EWOD). *J Microelectromech Syst.* (2006) **15**:986–1000. doi: 10.1109/JMEMS.2006.878876
53. Teigen KE, Munkejord ST. Influence of surfactant on drop deformation in an electric field. *Phys Fluids.* (2010) **22**:112104. doi: 10.1063/1.3504271
54. Tomar G, Gerlach D, Biswas G, Alleborn N, Sharma A, Durst F, et al. Two-phase electrohydrodynamic simulations using a volume-of-fluid approach. *J Comput Phys.* (2007) **227**:1267–85. doi: 10.1016/j.jcp.2007.09.003
55. López-Herrera J, Popinet S, Herrada M. A charge-conservative approach for simulating electrohydrodynamic two-phase flows using volume-of-fluid. *J Comput Phys.* (2011) **230**:1939–55. doi: 10.1016/j.jcp.2010.11.042
56. Anderson DM, McFadden GB, Wheeler AA. Diffuse-interface methods in fluid mechanics. *Ann Rev Fluid Mech.* (1998) **30**:139–65. doi: 10.1146/annurev.fluid.30.1.139
57. Hohenberg PC, Halperin BI. Theory of dynamic critical phenomena. *Rev Mod Phys.* (1977) **49**:435. doi: 10.1103/RevModPhys.49.435
58. Lowengrub J, Truskinovsky L, The Royal Society. Quasi-incompressible Cahn–Hilliard fluids and topological transitions. *Proc R Soc A.* (1998) **454**:2617–54. doi: 10.1098/rspa.1998.0273
59. Abels H, Garcke H, Grün G. Thermodynamically consistent, frame indifferent diffuse interface models for incompressible two-phase flows with different densities. *Math Models Methods Appl Sci.* (2012) **22**:1150013. doi: 10.1142/S0218202511500138
60. Lin Y, Skjetne P, Carlson A. A phase field model for multiphase electro-hydrodynamic flow. *Int J Multiphase Flow* (2012) **45**:1–11. doi: 10.1016/j.ijmultiphaseflow.2012.04.002
61. Campillo-Funollet E, Grün G, Klingbeil F. On modeling and simulation of electrokinetic phenomena in two-phase flow with general mass densities. *SIAM J Appl Math.* (2012) **72**:1899–925. doi: 10.1137/120861333
62. Eck C, Fontelos M, Grün G, Klingbeil F, Vantzos O. On a phase-field model for electrowetting. *Interf Free Boundaries.* (2009) **11**:259–90. doi: 10.4171/IFB/211

63. Nochetto RH, Salgado AJ, Walker SW. A diffuse interface model for electrowetting with moving contact lines. *Math Models Methods Appl Sci.* (2014) **24**:67–111. doi: 10.1142/S0218202513500474
64. Grün G, Klingbeil F. Two-phase flow with mass density contrast: stable schemes for a thermodynamic consistent and frame-indifferent diffuse-interface model. *J Comput Phys.* (2014) **257**:708–25. doi: 10.1016/j.jcp.2013.10.028
65. Hysing SR, Turek S, Kuzmin D, Parolini N, Burman E, Ganesan S, et al. Quantitative benchmark computations of two-dimensional bubble dynamics. *Int J Numer Methods Fluids.* (2009) **60**:1259–88. doi: 10.1002/fld.1934
66. Aland S, Voigt A. Benchmark computations of diffuse interface models for two-dimensional bubble dynamics. *Int J Numer Methods Fluids.* (2012) **69**:747–61. doi: 10.1002/fld.2611
67. Guillén-González F, Tierra G. Splitting schemes for a Navier–Stokes–Cahn–Hilliard model for two fluids with different densities. *J Comp Math.* (2014) **32**:643–64. doi: 10.4208/jcm.1405-m4410
68. Grün G, Guillén-González F, Metzger S. On fully decoupled, convergent schemes for diffuse interface models for two-phase flow with general mass densities. *Commun Comput Phys.* (2016) **19**:1473–502. doi: 10.4208/cicp.scpde14.39s
69. Metzger S. On numerical schemes for phase-field models for electrowetting with electrolyte solutions. *Proc Appl Math Mech.* (2015) **15**:715–8. doi: 10.1002/pamm.201510346
70. Metzger S. On stable, dissipation reducing splitting schemes for two-phase flow of electrolyte solutions. In: *Numerical Algorithms.* (2018). p. 1–30. doi: 10.1007/s11075-018-0530-2
71. Nürnberg R, Tucker EJW. Stable finite element approximation of a Cahn–Hilliard–Stokes system coupled to an electric field. *Eur J Appl Math.* (2017) **28**:470–98. doi: 10.1017/S0956792516000395
72. Langtangen HP, Logg A. *Solving PDEs in Python*. Berlin: Springer (2017). Available online at: https://link.springer.com/book/10.1007/978-3-319-52462-7
73. Nielsen CP, Bruus H. Concentration polarization, surface currents, and bulk advection in a microchannel. *Phys Rev E.* (2014) **90**:043020. doi: 10.1103/PhysRevE.90.043020
74. Carlson A, Bellani G, Amberg G. Universality in dynamic wetting dominated by contact-line friction. *Phys Rev E.* (2012) **85**:045302. doi: 10.1103/PhysRevE.85.045302
75. Shen J, Yang X. Decoupled, energy stable schemes for phase-field models of two-phase incompressible flows. *SIAM J Numer Anal.* (2015) **53**:279–96. doi: 10.1137/140971154
76. Brenner SC, Scott LR. *The Mathematical Theory of Finite Element Methods*, Vol. 15. New York, NY: Springer Science and Business Media (2007).
77. Langtangen HP, Mardal KA, Winther R. Numerical methods for incompressible viscous flow. *Adv Water Resour.* (2002) **25**:1125–46. doi: 10.1016/S0309-1708(02)00052-0
78. Chorin AJ. A numerical method for solving incompressible viscous flow problems. *J Comput Phys.* (1967) **2**:12–26. doi: 10.1016/0021-9991(67)90037-X
79. Chorin AJ. Numerical solution of the Navier-Stokes equations. *Math Comput.* (1968) **22**:745–62. doi: 10.1090/S0025-5718-1968-0242392-2
80. Guermond JL, Minev P, Shen J. An overview of projection methods for incompressible flows. *Comput Methods Appl Mech Eng.* (2006) **195**:6011–45. doi: 10.1016/j.cma.2005.10.010
81. Linga G, Bolet A. *Bernaise: Git repository*. (2018). Available online at: https://www.github.com/gautelinga/BERNAISE
82. Pillai R, Berry J, Harvie D, Davidson M. Electrolytic drops in an electric field: a numerical study of drop deformation and breakup. *Phys Rev E.* (2015) **92**:013007. doi: 10.1103/PhysRevE.92.013007
83. Logg A, Wells GN. DOLFIN: automated finite element computing. *ACM Trans Math Softw.* (2010) **37**:20:1–20:28.
84. Balay S, Abhyankar S, Adams MF, Brown J, Brune P, Buschelman K, et al. *PETSc Web page*. (2017). Available online at: http://www.mcs.anl.gov/petsc
85. Mugele F, Buehrle J. Equilibrium drop surface profiles in electric fields. *J Phys Condens Matter.* (2007) **19**:375112. doi: 10.1088/0953-8984/19/37/375112
86. Linga G, Bolet A, Mathiesen J. Controlling wetting with electrolytic solutions: phase-field simulations of a droplet-conductor system. *Phys Rev E.* (2018) 98:013101. doi: 10.1103/PhysRevE.98.013101
87. Huang JJ, Huang H, Wang X. Wetting boundary conditions in numerical simulation of binary fluids by using phase-field method: some comparative studies and new development. *Int J Numer Methods Fluids.* (2015) **77**:123–58. doi: 10.1002/fld.3975
88. Teigen KE, Song P, Lowengrub J, Voigt A. A diffuse-interface method for two-phase flows with soluble surfactants. *J Comput Phys.* (2011) **230**:375–93. doi: 10.1016/j.jcp.2010.09.020

Conflict of Interest Statement: The authors declare that the research was conducted in the absence of any commercial or financial relationships that could be construed as a potential conflict of interest.

frontiers in Physics

REVIEW
published: 01 April 2019
doi: 10.3389/fphy.2019.00041

Relations and Links Between Soil Mechanics, Porous Media Physics, Physiochemical Theory, and Effective Medium Theory

Gustav Grimstad, Seyed Ali Ghoreishian Amiri and Steinar Nordal*

PoreLab, Department of Civil and Environmental Engineering, Norwegian University of Science and Technology, Trondheim, Norway

Modern soil mechanics (geotechnical engineering) was developed as a branch of civil engineering from the 1920's. While modern porous media physics was developed as a branch of physics and applied mathematics from roughly the same period of time. In soil mechanics the main concern is often on the deformations, resulting from mechanical, hydraulic, or thermal actions. In application of porous media physics the main concern is historically on the flow part, putting less emphasis on the mechanical part. However, deformation and flow are highly linked processes, especially in unconsolidated porous media (soil). This paper makes some links between concepts used in porous media physics, like the effective medium theory, and concepts in soil mechanics, like choice of stress measures. As an example, it shows that the use of Terzaghi effective stress is a matter of choice and can be consistently used also for cases where other effective stress measures are used in literature, like Biot effective stress. The requirement, to be consistent, is that the state variables considered, at the constitutive level, includes all relevant variables.

Keywords: soil mechanics, porous media physics, effective medium theory, effective stress, constitutive model

OPEN ACCESS

Edited by:
Sergey G. Abaimov, Skolkovo Institute of Science and Technology, Russia

Reviewed by:
Ignazio Licata, Institute for Scientific Methodology (ISEM), Italy
Irina Bayuk, Institute of Physics of the Earth (RAS), Russia

****Correspondence:***
Gustav Grimstad
gustav.grimstad@ntnu.no

Specialty section:
This article was submitted to Interdisciplinary Physics, a section of the journal Frontiers in Physics

Received: *07 November 2018*
Accepted: *06 March 2019*
Published: *01 April 2019*

Citation:
Grimstad G, Ghoreishian Amiri SA and Nordal S (2019) Relations and Links Between Soil Mechanics, Porous Media Physics, Physiochemical Theory, and Effective Medium Theory. Front. Phys. 7:41. doi: 10.3389/fphy.2019.00041

INTRODUCTION

Geotechnical engineering is the part of civil engineering concerns about the hydro-mechanical (or thermo-hydro mechanical) behavior of soils. In classical soil mechanics (geotechnical engineering) the basics principles used are:

- Equilibrium (Conservation of linear momentum)
- Mass balance (Conservation of mass)
- Heat balance (conservation of energy)
- Effective stress principle (Terzaghi or Bishop) for the stress carried by the soil skeleton and responsible for deformation.
- Stress-strain constitutive relations
- Darcy flow for the pore fluid(s)
- Fourier's law for heat conduction

The continuum approach is the most used approach to satisfy the momentum balance, compatibility, mass balance and heat balance equations. Deformation of and/or stresses (forces) acting on structures are one of the main problems for the geotechnical engineer to solve. In

air-saturated soil systems (dry soils), when the loading rate is not too high (like the load coming from an explosion), the equilibrium equation is the only equation that should be solved. In water-saturated systems (and also in partially saturated systems), the volumetric deformation of the system is directly linked with the ability of the porous system for draining/absorbing of water, thus the mass balance equation should also be taken into account. Practical engineering problems involving non-isothermal conditions, e.g., artificial ground freezing projects, require the heat balance equation to be taken into account, too.

In classical soil mechanics, by assuming incompressible grains, the deformation of the system is considered as the result of the process of slippage, widening, and closing between granular medium particles. The slippage, widening, and closing between the granular materials will continue until reaching a locked state. Geotechnical engineers call this state as the "critical state" of the soil. At the onset of critical state, the volume of the system will be locked and the system can only be distorted. The critical state is a kind of geometrical state and can be found analytically. However, geotechnical engineers find this state experimentally, and use a mechanical constitutive framework to link the deformation gradients to an effective stress measure of the system [1].

The mechanical constitutive model is the key aspect of computational geotechnical engineering. Traditionally, in classical geotechnical engineering, these models are developed in the framework of plasticity theory. However, it is also possible to find deformation gradient- effective stress links, based on the effective medium theory. For the reader not used to the terminology, Effective Medium Theory (EMT) is a way to describe the macroscopic properties of a composite material from some sort of averaging of the multiple values of the constituents of this composite (e.g., [2–5]). The properties of the system are calculated from constituents' properties knowing the volume fraction of the constituents and geometrical details. This is typically used to find conductivities (hydraulic, thermal, or electric) in composite systems. In case of mechanical properties of material like rocks, EMT can be used to find elastic moduli of the composite from elastic moduli of the constituents (e.g., [6]). The volume fraction and the individual properties of the constituents are often the easy parts to establish, however, the geometry of the arrangement of the constituents is difficult to assess [7, 8]. Hence, effective medium theory will often result in rigorous upper and lower bounds from the extreme assumptions on geometrical arrangements and a representative model in between these two extremes, which needs experimental calibration.

This paper will give some relations between the macroscopic material behavior (i.e., constitutive laws) and the equivalent properties that can be obtained from effective medium theory. The main attempt is made on mechanical constitutive relations; however, it will also address the possibilities of using relations obtained from the use of effective medium theory for calculating hydraulic and thermal conductivities of the mixture.

EFFECTIVE MEDIUM THEORY AND DEFORMATION PROPERTIES OF DRY SOILS

As an example of effective medium theory and the application to soil, the case of compressibility/stiffness is selected as a start point. For the case of soils, or to what is often in porous media physics referred to as "unconsolidated" porous materials, effective medium theory has been applied by several researchers to e.g., establish the dry bulk compressibility and shear modulus of the composite, assuming a system of spheres and the Hertz-Mindlin contact model (e.g., [9, 10]). In the geotechnical engineering community, a similar attempt, but under a different name "discrete element method," have been made to find the deformation characteristics of the composite (e.g., [11–13]).

The dry bulk compressibility derived from effective medium theory, which will be a function of mean (effective) stress and/or porosity (or void ratio) in addition to the contact stiffness (grain compressibility) of the Hertz-Mindlin model, seems to be relatively in line with the measured values from course-graded soils (e.g., [14]). As seen from traditional geotechnical testing of sand samples under isotropic stress condition, the dry bulk compressibility, or the reciprocal property being the bulk stiffness, is shown to be a function of porosity and/or mean stress [1]. The empirical data typically gives that the bulk stiffness of sand varies with the square root of the mean stress, at least under the working stress levels normally encountered in geotechnical engineering practice. Houlsby et al. [15] derived a hyperelastic formulation, proposing a function for the elastic strain energy (Helmholtz free energy) and/or the complementary Gibbs free energy. The derivation from Houlsby et al. [15] gives not only the variation of the bulk stiffness under isotopic condition, as function of mean stress, but also the rest of the 4th order stiffness tensor and its stress dependency. As reviled from the hyperelastic description, under general stress condition, the stiffness is dependent on the general stress state not only the mean stress. However, the formulation gives, under the assumption of isotropic condition, a mean stress dependent bulk stiffness, that then agrees very well with the results obtained with effective medium theory [14]. It is worth noting, the power dependency according to hyperelasticity can vary between one (linear variation) and zero (constant stiffness), like the experimental finding of e.g., Janbu [16]. Effective medium theory under non-isotropic condition shows, as e.g., seen in Norris and Johnson [17], that the bulk compressibility will become a function of the tangential slip displacement in the contacts and the tangential contact stiffness in the Hertz-Mindlin model. This relates back to the general (shear) stress dependency found by Houlsby et al. [15] and will also generate coupling terms between bulk and shear stiffness in the medium in a similar way.

THE EFFECTIVE STRESS PRINCIPLE IN SOILS, EFFECT OF PORE FLUID

The section above shows that the effective medium theory essentially produces similar results for dry granular media as

those relations already used in soil mechanics when it comes to deformation of the medium. The natural next step would be to see the relationship between effective medium theory and an effective stress measure, in fully saturated soils. This is important since, in geotechnical engineering, the effective stress is considered as the only stress variable controlling the deformation of the soil. It is well-established, through experimental work and theory, that for saturated condition and for course-graded soils (i.e., sand and gravel) the effective stress principle of Terzaghi is valid (see for instance [18]). In the following, this concept is summarized. In saturated condition, due the small contact area between the relatively large grains, one may simply write up Equation (1) considering one component of normal stress and the buoyancy of the grains in water.

$$\sigma' = \frac{1}{A} \cdot \left(A \cdot \sigma - A_w \cdot \left(p_w - p_{am}\right) - A \cdot p_{am}\right) = \sigma - p_{am} + \frac{A_w}{A} \cdot \left(p_{am} - p_w\right) \quad (1)$$

Where A is the total area of a cross section taken through the contact points, A_w is the area covered by water (note that water can be replaced by any other non-reactive pore-fluids), σ' and σ are the effective and total normal stress respectively, p_w and p_{am} are the water and ambient pressures. This is in accordance with the expression found by Bishop [19]. Further setting $A_w/A = 1$ (i.e., ignoring the contact area between grains) and redefining total stress as $\sigma - p_{am}$, and pore pressure as $p_w - p_{am}$, yields the Terzaghi effective stress as:

$$\sigma' = \sigma - p_w \quad (2)$$

Note that, in the above, compression and pressure is considered as positive.

De Boer and Ehlers [20] used the concept of *mixture theory* and free energy to show that, when the constituents are considered as incompressible (incompressible grains and incompressible fluid) and that the fluid are considered to have negligible shear stress, the total partial solid stress tensor (acting over the whole area) is additively decomposed into the pore-liquid pressure and the effective stress tensor Equation (3). The above assumption holds, as the shear stiffness of the fluid is zero for Newtonian fluids and the viscosity times shear strain rate, in the fluid, is negligible or zero (which holds for the assumption of Darcy flow).

$$\sigma_{ij}{}^S = \sigma'_{ij}{}^S + n^S \cdot p_F \cdot \delta_{ij} \quad (3)$$

Where n^S is the volume fraction of solid and p_F is fluid pressure.

Similar for the partial pore-fluid stress tensor (acting over the whole area), the equation by de Boer and Ehlers yields:

$$\sigma_{ij}{}^F = n^F \cdot p_F \cdot \delta_{ij} \quad (4)$$

where n^F is the volume fraction of fluid, which in geotechnical engineering, in the case of saturated medium, is called porosity n (the ratio between pore volume and total volume).

When combining Equations (3, 4) in to the total stress of the effective medium, the following is obtained, since for saturated case $n^S + n^F = 1$:

$$\sigma_{ij} = \sigma_{ij}{}^S + \sigma_{ij}{}^F = \sigma'_{ij}{}^S + \left(n^S + n^F\right) \cdot p_F \cdot \delta_{ij} = \sigma'_{ij}{}^S + p_F \cdot \delta_{ij} \quad (5)$$

This further clarifies, into the classical Terzaghi effective stress [21], by replacing fluid with water and omitting the index S for solid:

$$\sigma'_{ij} = \sigma_{ij} - p_w \cdot \delta_{ij} \quad (6)$$

It will be for this effective stress that the constitutive equation, for the mechanical behavior of the saturated mixture, should be formulated.

For the case of partially saturated soil (which can be extended to the case of more than one type of pore fluid), Nikooee et al. [22] derived from a thermodynamic approach an analog stress to the Bishop effective stress [23]:

$$\sigma'^{(B)}_{ij} = \sigma_{ij} - p_a \cdot \delta_{ij} + \chi \cdot \left(p_a - p_w\right) \cdot \delta_{ij} \quad (7)$$

where p_a is pore air pressure. Equation introduces the effective stress parameter χ. The parameter χ is a function of the water saturation (including the air entry value) and the specific air-water interfacial area. Notice the similarity of Equations (7) to if one sets $\chi = A_w/A$. Other works, like that of Borja [24], show, by using mixture theory, that the parameter χ can be set to be equal to the degree of water saturation (S_w), meaning that the specific air-water interfacial area would only be dependent on the soil and degree of saturation and not if the soil is going through wetting or drying. This is probably an assumption that does not hold in reality and is easily proven incorrect by experimental testing (e.g., [25]). Others like the work of Jiang et al. [26] and Huyghe et al. [27] discuss the form of χ including the effect of wetting and drying. In addition, as discussed by e.g., Molenkamp et al. [28] and Manahiloh et al. [29], the Bishop effective stress actually should be take a form like Equation (8), as due to soil fabric, the effect of suction is not isotropic.

$$\sigma'^{(B^*)}_{ij} = \sigma_{ij} - p_a \cdot \delta_{ij} + \chi \cdot \left(p_a - p_w\right) \cdot \left(\delta_{ij} + \hat{\chi} \cdot \left(\alpha_{ij} - \delta_{ij}\right)\right) \quad (8)$$

Where A is introduced to account for the anisotropic effect of suction due to the fabric tensor α_{ij}. The consequence of soil fabric leads to an effective stress measure that is dependent on the state variable (fabric). Therefore, it might be more appropriate to work with Terzaghi's definition of effective stress, Equation (6), and suction ($p_a - p_w$) as an independent stress variable, at the constitutive level.

As the effective stress is a well-established framework, working well for coarse graded soil and has solid theoretical explanations,

the next step is to look into more of the fine graded soils like clay. Authors like Osipov [30] emphasizes on that the effective stress principle above does not consider the influence of any physicochemical forces on the effective stress. Mitchell and Soga [31] found that the effective stress principle can be modified to include the "far distance" attractive and repulsive electrostatic forces and the close distance chemical bounds. After integrating the effect of the close chemical bounding and the contact stresses, this results in the following expression for effective stress:

$$\sigma'_{ij} = \sigma_{ij} + \mathrm{A} - p_w \cdot \delta_{ij} \tag{9}$$

where A (capital α, not Latin *A*) is representing the integral of electrostatic attraction forces divided by area. However, the actual value of A is very difficult to assess. The size and the sign of which will be a function of particle orientation and distance, the double layer thickness etc. For water saturated clays, with no direct contact between particles, as in soft natural clays with fully open pore structure, A is equal to the integral over the local net disjoining/attractive pressure over the working areas, divided by the total area. The net A is then a function of the particle-to-particle distance, which in average is represented by the porosity of the clay (i.e., the volume fraction of free water). The link between this and the classical geotechnical terminology is what we experience as the effect of the *pre-consolidation* stress, p_c', of the clay. In terms of constitutive modeling, this allows for two options: A constitutive model formulated in terms of an effective stress considering 'A'; or using the previous definition of effective stress, for saturated soils, and add an additional state variable being the pre-consolidation stress. The latter being the way it is often done in soil mechanics today. As an alternative, a measure of porosity can be used as state variable. For a denser clay, there might be formation of closed pores. In such case even for saturated condition, the χ (as the ratio "A_w/A") parameter may locally be interpreted as less than one; and the local pore pressure might be higher than hydrostatic pressure, as the local encapsulated pressure cannot consolidate. Such behavior typical the case for e.g., smectite rich clays (swelling clays). However, this behavior may also be treated at a constitutive level considering Terzaghi effective stress [32], since the local effective stress is not needed for considering the macroscopic behavior of clay aggregates, and the microscopic effects (particle-particle interaction) can be included by state variables in the model (i.e., through fabric).

CONSTITUTIVE MODELING AND CHOICE OF EFFECTIVE STRESS MEASURE

The relations between two physical quantities specified to a material are called constitutive relations. Examples of constitutive relations are that between potential differences and mean fluxes (fluid, electrical, heat etc.) or between deformation gradients and stresses (mechanical behavior). For soils, in the context of soil mechanics, there are three main constitutive relationships that needs to be addressed. Namely, for the hydraulic part (the hydraulic conductivity, i.e., the fluid flux due to the gradient in hydraulic potential, Darcy law, i.e., the 2nd order tensor, **k**), for the thermal part (the thermal conductivity, i.e., the heat flux due to temperature gradient, Fourier's law, i.e., the 2nd order tensor λ) and for the mechanical part (change in effective stress in relation to change in strain, i.e., the 4th order tangential stiffness tensor, **D**).

The hydraulic conductivity, **k**, is a function of the soil permeability (as a function of *porosity* and *anisotropy*) and the fluid viscosity (as a function of *temperature*). In addition, the gradient of hydraulic potential is linked through pressure gradient and density (the fluid density is also a function of temperature).

Even though the exact description on a macro level for establishing the effective hydraulic and thermal conductivity tensors are complicated, from the effective medium theory perspective, the derivation of it is the same for both consolidated and unconsolidated porous media.

The deformation properties of a dry porous media are discussed in a previous section. Accepting that the effective stress will be the only stress variable responsible for the mechanical behavior, the same constitutive rules will apply to saturated or partially saturated soils as for dry soils. Hence, the elastic stiffness relations found from effective medium theory applies also here. However, actually the elastic deformation of an unconsolidated porous medium (i.e., the elastic portion of strain in the soil material) normally only contributes with a small amount to the total deformation. Actually, most of the deformations within a soil material will be plastic deformations (strain that does not contribute to increase in internal reversible energy).

By the assumption of incompressible solid constituents, as shown by e.g., Gajo [33], the plastic strains in the medium (soil skeleton) can be found from a formulation considering a yield and potential surface that are formulated in terms of the effective stresses defined in the previous section.

In case of compressible constituents, the tradition in soil/rock mechanics community is to use the so-called Biot effective stress definition instead of Terzaghi effective stress. In accordance with Biot and Willis [34], the Biot effective stress, σ''_{ij}, is defined in Equation .

$$\dot{\sigma}''_{ij} = \dot{\sigma}_{ij} - \alpha \cdot \dot{p}_w \cdot \delta_{ij} \tag{10}$$

Where α is the Biot parameter(assumed here as a constant). Note that when both the soil skeleton and the solid grains behave isotropically elastic, the volumetric deformation of the solid grains can be included into the Biot parameter, from the ratio of the bulk stiffness of the soil skeleton grain system to the bulk stiffness of solid grains. Which, then in saturated condition would be:

$$\alpha = 1 - \frac{K''}{K_S} \tag{11}$$

where K'' is bulk stiffness of the solid system (skeleton and grains) and K_S is supposed to be the stiffness of the solid grains.

Then, the volumetric deformation of the system can simply be calculated as:

$$\dot{\varepsilon}_v = \frac{\dot{p}''}{K''} \tag{12}$$

where p'' is the mean Biot effective stress ($p'' = \sigma''_{ii}/3$).

The other option is to use the Terzaghi effective stress principle for the soil skeleton, and the effective medium theory to find the effect of compressible constituents in the constitutive level. In this case, the total volumetric strain in the system is distributed into volumetric strain in the solid particles themselves and volumetric strain of the soil skeleton. While the volumetric strain in the soil skeleton is connected to the change in effective mean stress (p'), the volumetric strain in the solid particles is connected to the change in solid grains mean stress (p_s). According to Equation (3) the stress in solid grains depends on both effective stress, p', and pore pressure, p_w. However, the solid stress in Equation (3) is acting over the whole area, and it could be rescaled on the solid surface forming the stress σ_S:

$$(\sigma_S)_{ij} = \frac{\sigma_{ij}{}^S}{1-n} = \frac{\sigma'_{ij}{}^S}{1-n} + p_F \cdot \delta_{ij} \tag{13}$$

One can rewrite this equation in terms of mean stress rate as

$$\dot{p}_S = \frac{\dot{p}'}{1-n} + \frac{p'}{(1-n)^2} \cdot \dot{n} + \dot{p}_w \tag{14}$$

where the Terzaghi definition is used:

$$p' = p - p_w \tag{15}$$

and p is the total mean stress and p' is the effective mean stress.

The increment in volumetric strain in the particles is related to p_S through the bulk stiffness of the solid constituent, if the solid grains behave isotropically elastic.

$$(\dot{\varepsilon}_S)_v = \frac{\dot{p}_S}{K'_S} \tag{16}$$

where $(\varepsilon_s)_v$ is the volumetric strain of the particles and $K_S{}'$ is the actual effective bulk stiffness of the solid material.

The increment in volumetric strain in the skeleton is related to p' through the bulk stiffness of the skeleton, if the skeleton behaves isotropically elastic.

$$\dot{\varepsilon}'_v = \frac{\dot{p}'}{K'} \tag{17}$$

where ε'_v is the volumetric strain of the skeleton and K' is the effective bulk stiffness of the soil skeleton. The total volumetric strain of the system then can be calculated as

$$\dot{\varepsilon}_v = (1-n) \cdot (\dot{\varepsilon}_S)_v + \dot{\varepsilon}'_v \tag{18}$$

Now, one can connect the Biot stiffness parameters to the effective stiffness parameters through: (full derivation is given in the **Appendix**)

$$K_S = \frac{K'_S}{1-n} \cdot \left(1 - \frac{p'}{K'_S} \cdot \frac{n}{1-n}\right) \tag{19}$$

$$K'' = \left(1 - \frac{p'}{K'_S} \cdot \frac{n}{1-n}\right) \cdot \left(\left(1 - \frac{p'}{K'_S} \cdot \frac{1}{1-n}\right) \cdot \frac{1}{K'} + \frac{1}{K'_S}\right)^{-1|}$$

Note that normally both K'' and K' are function of n and/or p'. If $K_S{}' \gg p'$ then the relations are simplified to Equation (20), and only porosity dependency is present.

$$\begin{aligned} K_S &\simeq \tfrac{1}{1-n} \cdot K'_S \\ K'' &\simeq \left(\tfrac{1}{K'_S} + \tfrac{1}{K'}\right)^{-1} \end{aligned} \tag{20}$$

Giving the Biot coefficient, as a function of porosity, as follows:

$$\alpha \simeq \frac{K'_S + n \cdot K'}{K'_S + K'} \tag{21}$$

The difference between using the Biot effective stress measure and the Terzaghi effective stress is then simply the use of K' or K'' for bulk stiffness of the soil skeleton alone or for the solid system in total, respectively, and K_S or $K_S{}'$ for the grain contribution. It means that selection of the stress measure is a choice as long as one considers the effects at the constitutive level. Note that the above relation with Terzaghi effective stress definition can be extended to anisotropic elasticity, for the soil grains or the soil skeleton, by modifying Equations or respectively. **Table 1** gives a brief summary of three of the stress measures, found in the article, and the connection with required variables.

Since soil actually does not behave in an isotropic linear elastic manner (see the section on effective medium theory and deformation properties of dry soils), the Biot definition of effective stress will be response dependent. Therefore, for a non-linear, anisotropic and/or inelastic material response, it is more convenient to have an effective stress measure that is independent of response (Equation, 6), i.e., the Terzaghi effective stress definition and solid stress as the stress state variables for the mechanical constitutive model.

CONSTITUTIVE MODELING, CHOICE OF FUNCTIONS AND STATE VARIABLES

For e.g., soft clays, it is often found that there is a linear relationship between mean effective stress and elastic bulk stiffness, for small variation in porosity. Such an observation and others like it is essential information to be able to formulate constitutive models for the mechanical behavior of soils. However, the constitutive equations cannot be formulated in an arbitrarily manner, the following should apply (not in a specially ordered manner):

1. Behave in a deterministic manner or more strictly described: Principle of causality

TABLE 1 | Summary table of some stress measures.

	Terzaghi	Biot	Bishop
Effective Stress	σ'	σ''	$\sigma'^{(B)}$
Purpose for modification	N.A.	Deformable grains	Unsaturated soil
Isotropic parameters/variables under "normal" isothermal working condition	K'	K'' and α	K' and χ
Additional variables needed in the constitutive model when deformable grains should be modeled under isotropic isothermal condition	p_w, K'_S	No new variables Note that α is function of porosity (and σ', K'_S and K')	Not part of this work
Additional variables needed in the constitutive model when unsaturated soil should be modeled under isotropic isothermal condition	p_w, χ (and p_a)	Not part of this work	No new variables Note that χ is a function of $p_w - p_a$

2. Obey the 2nd law of thermodynamics (Entropy principle)
3. Behave objectively (Principle of material frame-indifference)
4. Preserve material symmetry, meaning that there is a consistency between material symmetry and constitutive equation.
5. Principle of equipresence, meaning that all constitutive equations should include the all the same state variables. Unless these are shown to have no effect. Or, that such a presence is in violation with physical laws (i.e., reduced by the other principles).
6. Finally, the constitutive behavior is to be described locally (Principle of local action). Which means that it is only the action on an infinitesimal space, which gives an effect in this infinitesimal space. However, deviation from this point is allowed in some cases, e.g., in order to use a continuum description for a local phenomenon.

Constitutive Model for the Mechanical Behavior

Houlsby and Puzrin [35] uses the fact that, in order to have a hyper-elastoplastic description of the mechanical behavior of a material, the constitutive equations should be formulated based on the 1st and 2nd law of thermodynamics. As a consequence of their derivation, it is possible to come up with a formulation of so called yield and potential surfaces, formulated in the conventional stress space (i.e., in terms of $\sigma'_{ij}, p_w, p_a, \theta, \nabla\theta, d\theta/dt$, $\nabla(d\theta/dt)$, $\boldsymbol{\kappa}$). Where θ is temperature and $\boldsymbol{\kappa}$ is a set of internal state variables. In the simplest form, $\boldsymbol{\kappa}$ is expressed simply by the plastic strain tensor, ε^p_{ij}. Note that Houlsby and Puzrin uses the dissipative generalized stress "X_{ij}" to formulate the framework in their paper and also assuming that the mechanical work itself must be dissipative (to obey the 2nd law of thermodynamics). However, a transformation between a formulation in terms of the dissipative generalized stress and conventional stress tensor is possible. Normally, the elastoplastic description of soil materials is not derived from energy potentials and dissipation functions, but rather suggested expressions for yield surfaces, potential surfaces and hardening rules, for the plastic or viscoplastic part. For the elastic part, some uses a hypo-elastic description, in other case a hyper-elastic description is used (where the latter is definitely preferable).

Constitutive Relations for the Fluid Flow

Darcy's law, for quasi-static condition (steady state) of a single-phase flow in saturated porous media, gives that the fluid velocity tensor, $\mathbf{w}$, over the total area, with respect to the soil skeleton grain system, is proportional to the difference in hydraulic potential:

$$\mathbf{w} = -\frac{\mathbf{k}}{\rho_w \cdot g} \cdot \left(\nabla p_w - \rho_w \cdot \mathbf{g}\right) \tag{22}$$

Where:

$$\mathbf{w} = n \cdot (\mathbf{v}_w - \mathbf{v}) \tag{23}$$

and $\mathbf{k}$ is the hydraulic conductivity tensor (in geotechnical engineering, referred to as permeability tensor, which for isotropic condition is replaced by a single value k), $\mathbf{v}_w$ is the actual velocity tensor of the water, $\mathbf{v}$ is the velocity tensor of the skeleton grain system, ρ_w is mass density of water, $\mathbf{g}$ is the gravitational tensor $[0\ 0\ -g]^{\mathrm{T}}$. The hydraulic conductivity is found from:

$$\mathbf{k} = \kappa \cdot \frac{\rho_w \cdot g}{\mu_w} \tag{24}$$

where $\boldsymbol{\kappa}$ is the absolute permeability tensor and μ_w is dynamic viscosity of water. The absolute permeability tensor is expected to be a function of the porosity, n, and anisotropy/fabric $\boldsymbol{\alpha}$. μ_w and ρ_w are functions of temperature (θ) [and fluid pressure (p_w)]. The geotechnical engineering practice is to establish this experimentally. However, effective medium theory can be used to establish such a relationship. For the case of partially saturated soil the concept of relative permeability as described in Brooks and Corey [36] is normally followed. A concept easily extended to anisotropic medium, e.g., [37].

Constitutive Relation for Heat Flow

Unlike the hydraulic conductivity, that depends on the absolute permeability tensor, a property of the pore space, and the properties of the fluid, the thermal conductivity depends on structure of the skeleton, properties the solid part, structure of the pores and properties of the pore fluid. Wang et al. [38] and

Gong et al. [39] considered an isotropic representative volume and showed that an unified equation, for a modified effective medium theory model for the thermal conductivity of a two phase system (particular case of a multiphase system), is in accordance with Equation (25).

$$\lambda' = \frac{\lambda_S \cdot \lambda_w + 2\lambda_m \cdot ((1-n)\cdot\lambda_S + n\cdot\lambda_w)}{(1-n)\cdot\lambda_w + n\cdot\lambda_S + 2\lambda_m} \tag{25}$$

Where λ' is the effective thermal conductivity, λ_S and λ_w are thermal conductivities of the solid and fluid (water), respectively, λ_m is the unknown effective medium conductivity parameter that gives the coupling, extremes being series, or parallel coupling ($\lambda_m = 0$ or $\lambda_m = \infty$). By setting $\lambda_m = \lambda'$, one retrieves a more original form of the EMT model (for electrical conductivity with spherical inclusions) by Landauer [40]. Note that λ_m likely itself will be porosity dependent, but this dependency is not significant, as discussed in e.g., Gong et al. [39] for the case of a sand, where empirical findings agreed well with the use of Equation (25). However, in general in a soil, it is expected that the thermal conductivity may not be isotropic, but expressed by a tensor ($\boldsymbol{\lambda}'$). Which, also like the hydraulic conductivity, depends on the fabric tensor, $\boldsymbol{\alpha}$. Establishing the full $\boldsymbol{\lambda}'$ tensor can be done following the procedure of a modified EMT with different structure in different directions, but little references to such work can be found in literature. Even from an experimental point of view, measurement of anisotropic thermal conductivity is challenging [41]. Finally, the Fourier law gives that the heat flux $\mathbf{q}$ is expressed as:

$$\mathbf{q} = -\boldsymbol{\lambda}' \cdot \nabla\theta \tag{26}$$

Note that in the above, properties as K'_S and λ_S are assumed to be reflected by a single mineralogical composition. However, natural soil is composed of a variety of different minerals with varying K_S and λ_S. The calculation of these two average quantities for the bulk of grains are ideal exercise in using EMT. For the case of effective bulk stiffness of the solid such a relation will be of the form of Equation (27) after modifying and extending the Landauer [40] relation.

$$\sum\left(n_i^S \cdot \frac{K'_S - K_S^i}{f\cdot K'_S + K_S^i}\right) = 0 \tag{27}$$

Where n_i^S is the volume fraction of the solid constituent, i, and f is a geometrical factor between zero and infinity. For the effective (combined) solid thermal conductivity of the solid, λ'_S, the following relation may be used:

$$\sum\left(n_i^S \cdot \frac{\lambda'_S - \lambda_S^i}{f\cdot \lambda'_S + \lambda_S^i}\right) = 0 \tag{28}$$

Equations (27, 28) are not the exact form of the effective quantities for the solid, because it does not reflect on the anisotropy, but it is a simple suggestion as a start point.

Thermal Expansion

Based on the individual constituent the volumetric thermal expansion follows the Equation (29)

$$\dot{\varepsilon}_{\theta,v} = -\sum_i \left(n^i \cdot \alpha_i\right)\cdot\dot{\theta} \tag{29}$$

where α_i is the volumetric thermal expansion of the constituent. However, for the solid grains when combined in a soil skeleton grain system, consisting of several different minerals, the thermal expansion coefficient is not necessary isotropic.

FINAL GOVERNING EQUATIONS

Governing equations for a saturated porous media, in tensorial form, are presented below. The mass balance equation is written with an Eulerian description for the fluid phase with respect to the Lagrangian solid:

$$n\dot{\rho}_w - \rho_w\left(\dot{\varepsilon}'_v - \dot{\varepsilon}_{\theta,v}\right) + \nabla.\left(\rho_w \mathbf{w}_w\right) = 0 \tag{30}$$

The first term in Equation (30) can be found by the bulk modulus of water (K_w):

$$\dot{\rho}_w = \frac{\dot{p}_w}{K'_w} \tag{31}$$

Substituting Equations (18, 31, 29) in Equation (30), result in:

$$\frac{n}{K'_w}\dot{p}_w - \rho_w\left[\dot{\varepsilon}_v - (1-n)\cdot(\dot{\varepsilon}_S)_v + \left((1-n)\cdot\alpha'_{S,v} + n\cdot\alpha_w\right)\cdot\dot{\theta}\right] + \nabla.\left(\rho_w\mathbf{w}_w\right) = 0 \tag{32}$$

Considering Equations (16, 32) can be rewritten as:

$$\frac{n}{K'_w}\dot{p}_w - \rho_w\left[\dot{\varepsilon}_v - (1-n)\cdot\frac{\dot{p}_s}{K'_s} + \left((1-n)\cdot\alpha'_{S,v} + n\cdot\alpha_w\right)\cdot\dot{\theta}\right] + \nabla.\left(\rho_w\mathbf{w}_w\right) = 0 \tag{33}$$

Where the total volumetric strain is found from:

$$\dot{\varepsilon}_v = -\nabla\cdot\mathbf{v} \tag{34}$$

Introducing Equations (14, 34) into Equation (33) and rearranging, one find the final form of the mass balance equation as:

$$\left(\nabla\cdot\mathbf{v} + \frac{\dot{p}' + \frac{p'}{1-n}\cdot\dot{n}}{K'_S} + \left(\frac{1-n}{K'_S} + \frac{n}{K_w}\right)\cdot\dot{p}_w - \left((1-n)\cdot\alpha'_{S,v} + n\cdot\alpha_w\right)\cdot\dot{\theta}\right)\cdot\rho_w + \nabla\cdot(\rho_w\cdot\mathbf{w}) = 0 \tag{35}$$

Where $\alpha'_{S,v}$ and α_w is the effective volumetric thermal expansion coefficient of solid and thermal expansion coefficient of water,

respectively. The particular form of Equation (35) is chosen such that it includes the relative change in fluid pressure to solid stress through Equation (14), by the change in effective mean stress and/or due to change in porosity.

Equilibrium equation is written using the Terzaghi effective stress definition plus solid stress, stand for describing the hydro-mechanical behavior of a fully saturated system.

$$\nabla \cdot \boldsymbol{\sigma}' + \nabla p_w - \rho \cdot \mathbf{g} = 0 \tag{36}$$

And finally for heat balance:

$$\left((1-n)\cdot \rho_S \cdot C_S + n \cdot \rho_w \cdot C_w\right)\cdot \dot{\theta} + \rho_w \cdot C_w \cdot \mathbf{w} \cdot \nabla\theta + \nabla \cdot \mathbf{q} - Q = 0 \tag{37}$$

where Q is the total heat supply (or loss). C_S and C_w are heat capacity of solid and fluid, respectively.

CONCLUSION

This article tries to connect the use of different concepts with porous media physics, like effective medium theory, to the classical concepts in soil mechanics/geotechnical engineering. The article demonstrates that the use of the Terzaghi effective stress principle is valid, for all types of geomaterials, as long as the constitutive model for the material behavior considers all relevant state variables. This means that there is no actual need for a Biot or Bishop effective stress, or any modification of such effective stress, to take into account of e.g., physiochemical forces, grain compressibility or the capillary suction in partially saturated soil. Especially since, the Biot parameter is anyway not a constant, but is deformation dependent, the physiochemical forces cannot be assessed properly and the capillary suction anyway must be treated as a state variable at constitutive level to account for soil fabric. For the case of compressible grains this article proposes a modified mass balance equation where the solid stress is included (rather that the Biot parameter). The understanding, of the geomaterials, obtained from effective medium theory and thermodynamics, shows that the conventional methodology, as used in modern numerical modeling in geotechnical engineering practice, is theoretically sound. This includes things like effective stress dependent stiffness, for the mechanical part, and the description of hydraulic and thermal conductivities where empirically based values fits with well with theoretical EMT studies, as recorded in various literature.

DATA AVAILABILITY

No datasets were generated or analyzed for this study.

AUTHOR CONTRIBUTIONS

All authors made substantial contributions to the conception or design of the work, and were part of drafting the work or revising it critically for important intellectual content, thus approving the publication of the content. All authors agree to be accountable for all aspects of the work in ensuring that questions related to the accuracy or integrity of any part of the work are appropriately investigated and resolved.

ACKNOWLEDGMENTS

This work is supported by the Research council of Norway through its Centers of Excellence funding Scheme, project number 262644.

REFERENCES

1. Schofield A, Wroth P. *Critical State Soil Mechanics*. New York, NY: McGraw-Hill (1968).
2. Johnson DL, Koplik J, Dashen R. Theory of dynamic permeability and tortuosity in fluid-saturated porous media. *J Fluid Mechan.* (1987) **176**:379–402. doi: 10.1017/S0022112087000727
3. Burganos VN, Sotirchos SV. Diffusion in pore networks: effective medium theory and smooth field approximation. *AICHE J.* (1987) **33**:1678–89. doi: 10.1002/aic.690331011
4. Brinkman HC. A calculation of the viscous force exerted by a flowing fluid on a dense swarm of particles. *Appl Sci Res.* (1947) **A1**:27.
5. Harris CK. Application of generalised effective-medium theory to transport in porous media. *Transport Porous Media*. (1990) **5**:517–42. doi: 10.1007/BF01403480
6. Kuster GT, Toksöz MN. Velocity and attenuation of seismic waves in two-phase media: part i. Theoretical formulations. *Geophysics*. (1974) **39**:587–606. doi: 10.1190/1.1440450
7. Makse HA, Gland N, Johnson DL, Schwartz LM. Why effective medium theory fails in granular materials. *Phys Rev Lett.* (1999) **83**:5070–3. doi: 10.1103/PhysRevLett.83.5070
8. Garboczi EJ, Berryman JG. Elastic moduli of a material containing composite inclusions: effective medium theory and finite element computations. *Mech Mater.* (2001) **33**:455–70. doi: 10.1016/S0167-6636(01)00067-9
9. Goddard JD. Nonlinear elasticity and pressure-dependent wave speeds in granular media. *Proc R Soc London Series A Math Phys Sci.* (1990) **430**:105. doi: 10.1098/rspa.1990.0083
10. Makse HA, Gland N, Johnson DL, Schwartz L. The apparent failure of effective medium theory in granular materials. *Phys Chem Earth Part A Solid Earth Geodesy*. (2001) **26**:107–11. doi: 10.1016/S1464-1895(01)00033-3
11. Dobry R, Tang-Tat NG A. Discrete modelling of stress-strain behaviour of granular media at small and large strains. *Eng Comp.* (1992) **9**:129–43. doi: 10.1108/eb023853
12. Ting JM, Khwaja M, Meachum LR, Rowell JD. An ellipse-based discrete element model for granular materials. *Int J Numer Anal Methods Geomechan.* (1993) **17**:603–23. doi: 10.1002/nag.1610170902
13. O'Sullivan C. Particle-based discrete element modeling: geomechanics perspective. *Int J Geomech.* (2011) **11**:449–64. doi: 10.1061/(ASCE)GM.1943-5622.0000024
14. Johnson DL, Makse HA, Gland N, Schwartz L. Nonlinear elasticity of granular media. *Phys B Conden Matter*. (2000) **279**:134–8. doi: 10.1016/S0921-4526(99)00700-0
15. Houlsby GT, Amorosi A, Rojas E. Elastic moduli of soils dependent on pressure: a hyperelastic formulation. *Géotechnique*. (2005) **55**:383–392. doi: 10.1680/geot.55.5.383.66021
16. Janbu N. Soil compressibility as determined by oedometer and triaxial tests. *Proc. ECSMFE Wiesbaden*. (1963) **1**:19–25.
17. Norris AN, Johnson DL. Nonlinear elasticity of granular media. *J Appl Mech.* (1997) **64**:39–49. doi: 10.1115/1.2787292

18. Laloui L, Hutter K, Vulliet L. Thermodynamics of saturated and unsaturated soils. In: *Biot Conference on Poromechanics*. Louvain-La-Neuve (1998). p. 93–97.
19. Bishop AW. The principle of effective stress. *Teknisk Ukeblad*. (1959) **39**:859–63.
20. de Boer R, Ehlers W. The development of the concept of effective stresses. *Acta Mech.* (1990) **83**:77–92. doi: 10.1007/BF01174734
21. Terzaghi K. *Erdbaumechanik Auf Bodenphysikalischer Grundlage*. Leipzig: F. Deuticke (1925).
22. Nikooee E, Habibagahi G, Hassanizadeh SM, Ghahramani A. Effective stress in unsaturated soils: a thermodynamic approach based on the interfacial energy and hydromechanical coupling. *Transport Porous Media*. (2013) **96**:369–96. doi: 10.1007/s11242-012-0093-y
23. Bishop AW, Blight GE. Some aspects of effective stress in saturated and partly saturated soils. *Géotechnique*. (1963) **13**:177–97. doi: 10.1680/geot.1963.13.3.177
24. Borja RI. On the mechanical energy and effective stress in saturated and unsaturated porous continua. *Int J Solids Struc.* (2006) **43**:1764–86. doi: 10.1016/j.ijsolstr.2005.04.045
25. Fredlund Delwyn G. Unsaturated soil mechanics in engineering practice. *J Geotech Geoenviron Eng.* (2006) **132**:286–321. doi: 10.1061/(ASCE)1090-0241(2006)132:3(286)
26. Jiang Y, Einav I, Liu M. A thermodynamic treatment of partially saturated soils revealing the structure of effective stress. *J Mech Phys Solids*. (2017) **100**:131–146. doi: 10.1016/j.jmps.2016.11.018
27. Huyghe JM, Nikooee E, Hassanizadeh SM. Bridging effective stress and soil water retention equations in deforming unsaturated porous media: a thermodynamic approach. *Transport Porous Media*. (2017) **117**: 349–365. doi: 10.1007/s11242-017-0837-9
28. Molenkamp F, de Jager RR, F.A.Mathijssen JM. Stress measures affecting deformation of granular materials. *Vadose Zone J.* (2014) **13**. doi: 10.2136/vzj2013.07.0130
29. Manahiloh KN, Muhunthan B, Likos WJ. Microstructure-based effective stress formulation for unsaturated granular soils. *Int J Geomech.* (2016) **16**:D4016006. doi: 10.1061/(ASCE)GM.1943-5622.0000617
30. Osipov VI. *Physicochemical Theory of Effective Stresses, Physicochemical Theory of Effective Stress in Soils*. Cham: Springer International Publishing (2015). p. 39–54.
31. Mitchell JK, Soga K. *Fundamentals of Soil Behavior*, 3rd Edn. New York, NY: John Wiley and Sons Inc. (2005).
32. Mašín D, Khalili N. Swelling phenomena and effective stress in compacted expansive clays. *Can Geotech J.* (2015) **53**:134–47. doi: 10.1139/cgj-2014-0479
33. Gajo A. Finite strain hyperelastoplastic modelling of saturated porous media with compressible constituents. *Int J Solids Struc.* (2011) **48**:1738–53. doi: 10.1016/j.ijsolstr.2011.02.021
34. Biot M, Willis D. The elastic coeff cients of the theory of consolidation. *J Appl Mech*. (1957) **15**:594–601.
35. Houlsby GT, Puzrin AM. A thermomechanical framework for constitutive models for rate-independent dissipative materials. *Int J Plastic.* (2000) **16**:1017–47. doi: 10.1016/S0749-6419(99)00073-X
36. Brooks R, Corey T. *HYDRAU uc Properties of Porous Media*. Hydrology Papers, Colorado State University (1964). 24:37.
37. Bear J, Braester C, Menier PC. Effective and relative permeabilities of anisotropie porous media. *Transport Porous Media*. (1987) **2**:301–16. doi: 10.1007/BF00165786
38. Wang J, Carson JK, North MF, Cleland DJ. A new approach to modelling the effective thermal conductivity of heterogeneous materials. *Int J Heat Mass Transfer*. (2006) **49**:3075–83. doi: 10.1016/j.ijheatmasstransfer.2006.02.007
39. Gong L, Wang Y, Cheng X, Zhang R, Zhang H. A novel effective medium theory for modelling the thermal conductivity of porous materials. *Int J Heat Mass Transfer*. (2014) **68**:295–8. doi: 10.1016/j.ijheatmasstransfer.2013.09.043
40. Landauer R. The electrical resistance of binary metallic mixtures. *J Appl Phys.* (1952) **23**:779–84. doi: 10.1063/1.1702301
41. Li M, Kang JS, Hu Y. Anisotropic thermal conductivity measurement using a new Asymmetric-Beam Time-Domain Thermoreflectance (AB-TDTR) method. *Rev Sci Instr.* (2018) **89**:084901. doi: 10.1063/1.5026028

Conflict of Interest Statement: The authors declare that the research was conducted in the absence of any commercial or financial relationships that could be construed as a potential conflict of interest.

APPENDIX

Derivation of the stiffness relation Equation (19).

Setting the rate of total stress in Equation (10) equal to the rate of total stress derived from Equation (6) combined with Equation (11) gives:

$$\dot{\sigma}'_{ij} = \dot{\sigma}''_{ij} - \frac{K''}{K_S} \cdot \dot{p}_w \cdot \delta_{ij} \tag{A1}$$

Taking the trace and inserting Equations (12, 17)

$$K' \cdot \dot{\varepsilon}'_v = K'' \cdot \dot{\varepsilon}_v - \frac{K''}{K_S} \cdot \dot{p}_w \tag{A2}$$

Combined with Equation (18)

$$K' \cdot \dot{\varepsilon}_v - K' \cdot (1-n) \cdot (\dot{\varepsilon}_S)_v = K'' \cdot \dot{\varepsilon}_v - \frac{K''}{K_S} \cdot \dot{p}_w \tag{A3}$$

Writing porosity change as:

$$\dot{n} = -\dot{\varepsilon}'_v + n \cdot \dot{\varepsilon}_v \tag{A4}$$

Inserting Equation (A4) into Equation (14) and combining with Equation (16, 17)

$$K'_S \cdot (\dot{\varepsilon}_S)_v = \frac{K' \cdot \dot{\varepsilon}'_v}{1-n} + \frac{p'}{(1-n)^2} \cdot \left(-\dot{\varepsilon}'_v + n \cdot \dot{\varepsilon}_v\right) + \dot{p}_w \tag{A5}$$

Then, replacing the $\varepsilon_v{}'$ by using Equation (18) gives:

$$K'_S \cdot (\dot{\varepsilon}_S)_v = \frac{K' \cdot \left(\dot{\varepsilon}_v - (1-n) \cdot (\dot{\varepsilon}_S)_v\right)}{1-n} - \frac{p'}{1-n} \cdot \left(\dot{\varepsilon}_v - (\dot{\varepsilon}_S)_v\right) + \dot{p}_w \tag{A6}$$

Which solved for (ε_v) gives:

$$(\dot{\varepsilon}_S)_v = \frac{\left(K' - p'\right) \cdot \dot{\varepsilon}_v + (1-n) \cdot \dot{p}_w}{(1-n) \cdot K'_S + (1-n) \cdot K' - p'} \tag{A7}$$

Inserting the resulting Equation (A7) into Equation (A3) and rearranging gives:

$$\left(\frac{K'_S - \frac{n}{1-n} \cdot p'}{K'_S + K' - \frac{p'}{1-n}}\right) \cdot K' \cdot \dot{\varepsilon}_v - \frac{K' \cdot (1-n)}{K'_S + K' - \frac{p'}{1-n}} \cdot \dot{p}_w = K'' \cdot \dot{\varepsilon}_v - \frac{K''}{K_S} \cdot \dot{p}_w \tag{A8}$$

Where, by grouping:

$$\left(\frac{K'_S - \frac{n}{1-n} \cdot p'}{K'_S + K' - \frac{p'}{1-n}}\right) \cdot K' = K'' \text{and} \frac{K' \cdot (1-n)}{K'_S + K' - \frac{p'}{1-n}} = \frac{K''}{K_S} \tag{A9}$$

Which, finally gives Equation (19).

frontiers in Physics

ORIGINAL RESEARCH
published: 24 April 2019
doi: 10.3389/fphy.2019.00060

Pressures Inside a Nano-Porous Medium. The Case of a Single Phase Fluid

Olav Galteland, Dick Bedeaux, Bjørn Hafskjold and Signe Kjelstrup*

PoreLab, Department of Chemistry, Norwegian University of Science and Technology, Trondheim, Norway

We define the pressure of a porous medium in terms of the grand potential and compute its value in a nano-confined or nano-porous medium, meaning a medium where thermodynamic equations need be adjusted for smallness. On the nano-scale, the pressure depends in a crucial way on the size and shape of the pores. According to Hill [1], two pressures are needed to characterize this situation; the integral pressure and the differential pressure. Using Hill's formalism for a nano-porous medium, we derive an expression for the difference between the integral and the differential pressures in a spherical phase α of radius R, $\hat{p}^\alpha - p^\alpha = \gamma/R$. We recover the law of Young-Laplace for the differential pressure difference across the same curved surface. We discuss the definition of a representative volume element for the nano-porous medium and show that the smallest REV is a unit cell in the direction of the pore in the fcc lattice. We also show, for the first time, how the pressure profile through a nano-porous medium can be defined and computed away from equilibrium.

Keywords: nano-porous media, thermodynamics of small systems, representative elementary volume, single phase fluid, molecular dynamics simulations

OPEN ACCESS

Edited by:
Daniel Bonamy, Commissariat á l'Energie Atomique et aux Energies Alternatives (CEA), France

Reviewed by:
Alberto Rosso, Centre National de la Recherche Scientifique (CNRS), France
Reinaldo Roberto Rosa, Instituto Nacional de Pesquisas Espaciais (INPE), Brazil

****Correspondence:***
Olav Galteland
olav.galteland@ntnu.no

Specialty section:
This article was submitted to Interdisciplinary Physics, a section of the journal Frontiers in Physics

Received: *30 January 2019*
Accepted: *29 March 2019*
Published: *24 April 2019*

Citation:
Galteland O, Bedeaux D, Hafskjold B and Kjelstrup S (2019) Pressures Inside a Nano-Porous Medium. The Case of a Single Phase Fluid. Front. Phys. 7:60. doi: 10.3389/fphy.2019.00060

1. INTRODUCTION

The description of transport processes in porous media poses many challenges that are well described in the literature (see e.g., [2–6]). There is, for instance, no consensus, neither on the definition nor on the measurement or the calculation, of the pressure in a porous medium with flow of immiscible fluids. The problem with the ill-defined microscopic pressure tensor [5, 7] is accentuated in a heterogeneous system with interfaces between solids and fluids. In a homogeneous fluid phase one may define and calculate a pressure and a pressure gradient from the equation of state. In a porous medium the presence of curved surfaces and fluid confinements makes it difficult to apply accepted methods for calculation of the microscopic pressure tensor and, consequently, the pressure gradient as driving force for fluid flow. The scale at which we choose to work will be decisive for the answer. Moreover, the scale that the hydrodynamic equations of transport refer to, remains to be given for nano-porous as well as micro-porous media.

A central element in the derivation of the equations of transport on the macro-scale is the definition of a representative elementary volume (REV) (see e.g., [8, 9]). The size of the REV should be large compared to the pore size and small compared to size of the porous medium. It should contain a statistically representative collection of pores. We have recently discussed [10] a new scheme to define a basis set of additive variables: the internal energy, entropy, and masses of all the components of the REV. These variables are additive in the sense that they are sums of contributions of all phases, interfaces and contact lines within the REV. Using Euler homogeneity of the first kind, we were able to derive the Gibbs equation for the REV. This equation defines

the temperature, pressure and chemical potentials of the REV as partial derivatives of the internal energy of the REV [10].

As discussed in Kjelstrup et al. [11] the grand potential, Υ, of the REV is given by minus $k_B T$ times the logarithm of the grand partition function, Z_g, where k_B is Boltzmann's constant and T is the temperature. The grand potential is equal to minus the contribution to the internal energy from the pressure-volume term, $k_B T \ln Z_g = \Upsilon = -pV$, which we will from now on refer to as the compressional energy. For a single fluid f in a porous medium r, the result was [10, 11]

$$pV = p^f V^f + p^r V^r - \gamma^{fr}\Omega^{fr}, \tag{1}$$

where p and V are the pressure and the volume of the REV. Furthermore p^f and V^f are the pressure and the volume of the fluid in the REV, p^r and V^r are the pressure and the volume in the grains in the REV, and γ^{fr} and Ω^{fr} are the surface tension and the surface area between the fluid and the grain. The assumption behind the expression was the additive nature of the grand potential. This definition of the REV, and the expression for the grand potential, opens up a possibility to define the pressure on the hydrodynamic scale. The aim of this work is to explore this possibility. We shall find that it will work very well for flow of a single fluid in a porous medium. As a non-limiting illustrative example, we use grains positioned in a fcc lattice. The work can be seen as a continuation of our earlier works [10, 11].

The work so far considered transport processes in micro-porous, not nano-porous media. In micro-porous media, the pressure of any phase (the surface tension of any interface) is independent of the volume of the phase (the area between the phases). This was crucial for the validity of equation 1. For nano-porous systems, we need to step away from Equation (1). Following Hill's procedure for small systems' thermodynamics [1], we generalize Equation (1) to provide an expression for the thermodynamic pressure in a nano-porous medium. We shall see that not only one, but two pressures are needed to handle the additional complications that arise at the nano-scale; the impact of confinement and of radii of curvature of the interfaces. In the thermodynamic limit, the approach presented for the nano-scale must simplify to the one for the macro-scale. We shall see that this is so. In order to work with controlled conditions, we will first investigate the pressure of a fluid around a single solid nano-scale grain and next around a lattice of solid nano-scale grains. The new expression, which we propose as a definition of the pressure in a nano-porous medium, will be investigated for viability and validity for this case. The present work can be seen as a first step in the direction toward a definition and use of pressure and pressure gradients in real porous media.

The pressure is not uniquely defined at molecular scale. This lack of uniqueness becomes apparent in molecular dynamics (MD) simulations, for which the computational algorithm has to be carefully designed [7]. The predominant method for pressure calculations in particular systems is using the Irving-Kirkwood contour for the force between two particles [12]. This algorithm works for homogeneous systems, but special care must be taken for heterogeneous systems [5, 6]. However, if the control volume (REV) used for pressure calculation is large compared with the heterogeneity length scale, one may argue that the algorithm for homogeneous systems gives a good approximation to the true result. We are interested in the isotropic pressure averaged over the REV, on a scale where the porous medium can be considered to be homogeneous.

The paper is organized as follows. In section 2 we derive the pressure of a REV for one solid grain surrounded by fluid particles (Case I) and for a three-dimensional face-centered cubic (fcc) lattice of solid grains (Case II). Section 3 describes the molecular dynamics simulation technique when the system is in equilibrium and in a pressure gradient. In section 4 we use the theory to interpret results of equilibrium molecular dynamics simulations for one solid grain and for an array of solid grains in a fluid. Finally we apply the results to describe the system under a pressure gradient. We conclude in the last section that the expressions and the procedure developed provide a viable definition of the pressures and pressure gradients in nano-porous media.

2. THE PRESSURE OF A NANO-POROUS MEDIUM

Equation (1) applies to a micro-porous medium, a medium where the pore-size is in the micrometer range or larger [10, 11]. For a nano-porous medium we need to apply the thermodynamics of small systems [1]. In nano-porous media, this technique is therefore well suited for the investigation. The thermodynamic properties like internal energy, entropy and masses of components of a small system are not proportional to the system's volume. As Hill explained, this leads to the definition of two different pressures, for which he introduced the names integral and differential pressure, $\hat{p}$ and p, respectively. For a system with a volume V, these pressures are related by

$$p(V) = \frac{\partial\left(\hat{p}\,(V)\,V\right)}{\partial V} = \hat{p}\,(V) + V\frac{\partial\left(\hat{p}\,(V)\right)}{\partial V}. \tag{2}$$

The symbol p (the differential pressure) is given to the variable that we normally understand as the pressure on the macroscopic level. It is only when $\hat{p}$ depends on V, that the two pressures are different. For large systems, $\hat{p}$ does not depend on V and the two pressures are the same.

The integral and differential pressures connect to different types of mechanical work on an ensemble of small systems. The differential pressure times the change of the small system volume is the work done on the surroundings by this volume change. The name differential derives from the use of a differential volume. This work is the same, whether the system is large or small. The integral pressure times the volume per replica, however, is the work done by adding one small system of constant volume to the remaining ones, keeping the temperature constant. This work is special for small systems. It derives from an ensemble view, but is equally well measurable. The word integral derives from the addition of a small system.

From statistical mechanics of macro-scale systems, we know that pV equals $k_B T$ times the natural logarithm of the grand-canonical partition function. For a small (nano-sized) system,

Hill ([1], Equations 1–17), showed that this logarithm gives $\hat{p}V$. In nano-porous media this product is different from pV, cf. Equation (1). Energies are still additive and the total compressional energy within the small system is similar to Equation (1). We replace Equation (1) by:

$$\hat{p}V = \hat{p}^f V^f + \hat{p}^r V^r - \hat{\gamma}^{fr}\Omega^{fr}, \tag{3}$$

where $\hat{p}^f$, $\hat{p}^r$ are integral pressures of the sub-volumes V^f and V^r, and $\hat{\gamma}^{fr}$ is the integral surface tension.

We consider here a nano-porous medium, so integral pressures and integral surface tensions apply. The integral pressure and integral surface tension normally depend on the system size. In the porous medium there are two characteristic sizes: the size of a grain and the distance between the surfaces of two grains[1]. The quantities $\hat{p}$, $\hat{p}^f$, $\hat{p}^r$ and $\hat{\gamma}^{fr}$ may depend on both. We shall here examine a system (cf. section 3) of spherical, monodisperse grains, for which the radius R is a good measure of the size. The volume of the grains may be a good alternative measure, which we will also use. The dependence on the grain size and on the distance between the surfaces of the grains will be studied in an effort to establish Equation (3).

In the following, we consider a single spherical grain confined by a single phase fluid (Case I) and a face-centered cubic (fcc) lattice of spherical grains confined by a single phase fluid (Case II). The size of the REV does not need to be large, and we will show in section 4.2 that the smallest REV is a unit cell in the direction of the pore in the fcc lattice.

2.1. Case I. Single Spherical Grain

Consider the inclusion of a spherical grain r in a box with fluid phase f. This is system A in **Figure 1**. Phase f has volume V^f and phase r has volume V^r. The total volume is $V = V^f + V^r$. The surface area between phase f and r is Ω^{fr}. The compressional energy of system A has contributions, in principle, from all its small parts

$$\hat{p}^A V = \hat{p}^f V^f + \hat{p}^r V^r - \hat{\gamma}^{fr}\Omega^{fr} \tag{4}$$

where $\hat{p}^A$ is the unknown pressure in Equation (3). There is a hat on the pressures and the surface tension, in the outset, because the system is small. The pressure of the fluid in A is, however, p^f, meaning that $\hat{p}^f = p^f$. When the surface tension depends on the curvature, there is a dependence of $\hat{\gamma}^{fr}$ on Ω^{fr} [13, 14]. This interesting effect, which we will not consider here, becomes relevant as the grain size decreases. Only $\hat{p}^r$ depends on the volume of the phase, V^r. This gives

$$\hat{p}^A V = p^f V^f + \hat{p}^r V^r - \gamma^{fr}\Omega^{fr} \tag{5}$$

We now introduce a system B in contact with A. System B has volume V, contains pure fluid, and is tuned so that it is in thermodynamic equilibrium with A. The equilibrium condition requires that their grand canonical partition functions are equal,

[1]Another valid characteristic size is the size of the pores between the grains, but this follows from the two we have chosen.

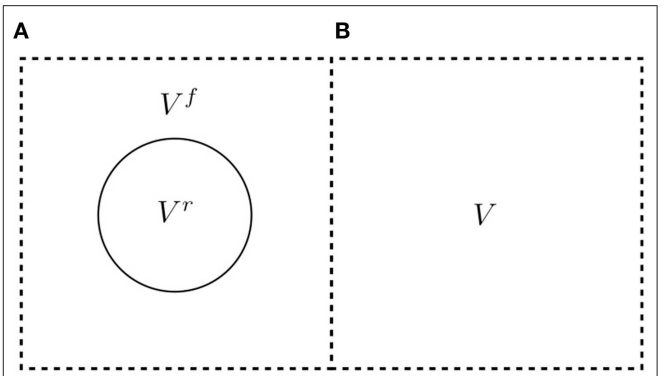

FIGURE 1 | A particle in a confined system **(A)** in equilibrium with a bulk fluid phase **(B)**.

which implies $\hat{p}^A V = \hat{p}^B V$, and with equal volumes this means $\hat{p}^A = \hat{p}^B$. Furthermore, system B is not a small system in Hill's sense, which leads to:

$$\hat{p}^A = \hat{p}^B = p^B = p^f \tag{6}$$

The fluid pressure p^f is the same in phases A and B. We obtain

$$p^f V = p^f V^f + \hat{p}^r V^r - \gamma^{fr}\Omega^{fr}, \tag{7}$$

and by rearranging the terms,

$$\hat{p}^r = p^f + \frac{\gamma^{fr}\Omega^{fr}}{V^r} = p^f + \frac{3\gamma^{fr}}{R}. \tag{8}$$

where we have used that $V^r + V^f = V$ and $\frac{\Omega^{fr}}{V^r} = \frac{3}{R}$ for a spherical phase r.

The pressure of the rock particle depends on the volume of the particle. The relation of the two pressures is according to Hill

$$p^r = \frac{\partial(\hat{p}^r V^r)}{\partial V^r} \tag{9}$$

When this is combined with the equation right above, we find the relation we are after

$$p^r - p^f = \frac{2\gamma}{R}, \tag{10}$$

which is the familiar Young-Laplace's law. By subtracting Equation (10) from Equation (8), we obtain an interesting new relation

$$\hat{p}^r - p^r = \frac{\gamma^{fr}}{R} \tag{11}$$

The expression relates the integral and differential pressure for a spherical phase r of radius R. It is clear that this pressure difference is almost equally sensitive to the radius of curvature as is the pressure difference in Young-Laplace's law.

We see from this example how the integral pressure enters the description of small systems. The integral pressure is not equal

to our normal bulk pressure, called the differential pressure by Hill, $\hat{p}^r \neq p^r$. While two differential pressures satisfy Young-Laplace's law in Equation (10), the integral pressures do not. The integral pressure has the property that when averaged over system A using Equation (4), it is the same as in system B, cf. Equation (6). This analysis shows that system A is a possible, or as we shall see proper, choice of a REV that contains the solid grain, while system B is a possible choice of a REV that contains only fluid.

2.2. Case II. Lattice of Spherical Grains

The above explanation concerned a single spherical grain and was a first step in the development of a procedure to determine the pressure of a nano-porous medium. To create a more realistic model, we introduce now a lattice of spherical grains. The integral pressure of a REV containing n grains is given by an extension of Equation (3)

$$\hat{p}^A V = p^f V^f + \sum_{i=1}^{n} \hat{p}_i^r V_i^r - \sum_{i=1}^{n} \hat{\gamma}_i^{fr} \Omega_i^{fr}, \tag{12}$$

For each grain one may follow the same derivation for the integral and differential pressure as for the single grain. By using Equation (8), we obtain

$$\hat{p}_i^r = p^f + \gamma_i^{fr} \frac{\Omega_i^{fr}}{V_i^r} = p^f + \frac{3\gamma_i^{fr}}{R_i}, \tag{13}$$

where the last identity applies to spherical grains only. The differential pressure of the grains is given by a generalization of Equation (10)

$$\begin{aligned} p_i^r &= \frac{\partial(\hat{p}_i^r V_i^r)}{\partial V_i^r} = \frac{\partial(p^f V_i^r)}{\partial V_i^r} + \gamma_i^{fr} \frac{\partial \Omega_i^{fr}}{\partial V_i^r} \\ &= p^f + \gamma_i^{fr} \frac{\partial \Omega_i^{fr}}{\partial V_i^r} = p^f + \frac{2\gamma_i^{fr}}{R_i}, \end{aligned} \tag{14}$$

where the last identity is only for spherical grains. The differential pressures again satisfy Young-Laplace's law at equilibrium.

When all grains are identical spheres and positioned on a fcc lattice, a properly chosen layer covering half the unit cell can be a proper choice of the REV. We shall see how this can be understood in more detail from the molecular dynamics simulations below. The REV is larger if the material is amorphous.

3. MOLECULAR DYNAMICS SIMULATIONS

Cases I and II were simulated at equilibrium, while case II was simulated also away from equilibrium. **Figures 3–8** illustrate the equilibrium simulations of the two cases.

3.1. Systems

The simulation box was three-dimensional with side lengths L_x, L_y, L_z.The box was elongated in the x-direction, $L_x > L_y = L_z$. Periodic boundary conditions were used in all directions in the equilibrium simulations. In the non-equilibrium simulation, reflecting particle boundaries [15] were applied to the x-direction, cf. section 3.5. Along the x-axis, the simulation box was divided into n rectangular cuboids (called layers) of size $\Delta x, L_y, L_z$, where $\Delta x = L_x/n$. The volume of each layer is $V_l = \Delta x L_y L_z$. There are two regions A and B in the simulation box. Region A contains fluid (red particles) and grains (blue particles) and region B contains only fluid, see **Figure 2**. The regions, $\mathrm{B} = \mathrm{B}_1 + \mathrm{B}_2$ and A do not have the same size, but the layers have the same thickness, Δx. The compressional energy of the fluid in one layer is, $\hat{p}_l^f V_l^f = p_l V_l^f$.

The simulation was carried out with LAMMPS [16] in the canonical ensemble using the Nosé-Hoover thermostat [17], at constant temperature $T^* = 2.0$ (in Lennard-Jones units). The critical temperature for the Lennard-Jones/spline potential (LJ/s) is approximately $T_c^* \approx 0.9$. Fluid densities range from $\rho^* = 0.01$ to $\rho^* = 0.7$.

3.2. Case Studies

In case I the single spherical grain was placed in the center of the box. A periodic image of the spherical grain is a distance L_x, L_y and L_z away in the x, y and z-directions, see **Figure 4A**. The surface to surface distance of the spherical grains is $d = L_\alpha - 2R$, where R is the radius of the grain, and $\alpha = y, z$. In case I, each spherical grain has four nearest neighbors in the periodic lattice that is built when we use periodic boundary conditions. We considered two nearest neighbor distances; $d = 4\sigma_0$ and $d = 11\sigma_0$, where σ_0 is the diameter of the fluid particles.

In case II, the spherical grains were placed in a fcc lattice with lattice constant a. The two shortest distances between the surfaces were characterized by $d_1 = \frac{1}{2}(\sqrt{2}a - 4R)$ and $d_2 = a - 2R$, see **Figure 2**, where $d_1 < d_2$. We used $d_1 = 4.14\sigma_0$ and $d_1 = 11.21\sigma_0$, which is almost the same as the distances considered in case I. The corresponding other distances were $d_2 = 10\sigma_0$ and $d_2 = 20\sigma_0$. Each grain has 12 nearest neighbors at a distance d_1.

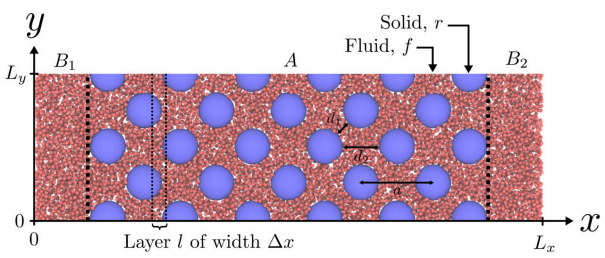

FIGURE 2 | A slice of the simulation box in case II. The box has side lengths L_x, L_y, L_z, and properties are calculated along the x-axis in layers l of width Δx. Blue particles are grain r and red particles are fluid f. The A is the lattice constant of the fcc lattice, d_1 and d_2 are the two shortest surface-to-surface distances.

In all cases we computed the volume of the grains V_l^r, the surface area Ω_l^{fr} and the compressional energy of each layer, l, in the x-direction.

3.3. Particle Interaction Potential

The particles interact with the Lennard-Jones/spline potential,

$$u_{ij}(r) = \begin{cases} \infty & \text{if } r < R_{ij} \\ 4\epsilon_{ij}\left[\left(\frac{\sigma_{ij}-R_{ij}}{r-R_{ij}}\right)^{12} - \left(\frac{\sigma_{ij}-R_{ij}}{r-R_{ij}}\right)^{6}\right] & \text{if } R_{ij} < r < r_{s,ij} \\ a_{ij}(r-r_{c,ij})^2 + b_{ij}(r-r_{c,ij})^3 & \text{if } r_s < r < r_{c,ij} \\ 0 & \text{if } r > r_{c,ij} \end{cases}. \tag{15}$$

Each particle type has a hard-core diameter R_{ii} and a soft-core diameter σ_{ii}. There were two types of particles, small particles with $\sigma_{ff} = \sigma_0$, $R_{ff} = 0$ and large particles with $\sigma_{rr} = 10\sigma_0$, $R_{rr} = 9\sigma_0$. The small particles are the fluid (f), and the large particles are the grain (r). The hard-core and soft-core diameters for fluid-grain pairs are given by the Lorentz mixing rule

$$R_{fr} = \frac{1}{2}\left(R_{ff} + R_{rr}\right) \quad \text{and} \quad \sigma_{fr} = \frac{1}{2}\left(\sigma_{ff} + \sigma_{rr}\right). \tag{16}$$

We define the radius of the grain particles as $R \equiv (\sigma_{ff} + \sigma_{rr})/2 = 5.5\sigma_0$, which is the distance from the grain center where the potential energy is zero. Fluid particles can occupy a position closer to the grain than this, this is illustrated in **Figure 3**. The figure shows the radial distribution function, $g(r)$, of fluid particles around a single spherical grain. The density of fluid varied between $\rho^* = 0.1$ and $\rho^* = 0.7$. This shows that the average distance from the grain particle and the closest fluid particle is approximately $5.5\sigma_0$, but the fluid particles are able to occupy positions closer to the grain particle.

The interaction strength ϵ_{ij} was set to ϵ_0 for all particle-particle pairs. The potential and its derivative are continuous in $r = r_{c,ij}$. The parameters a_{ij}, b_{ij} and $r_{s,ij}$ were determined so that the potential and the derivative of the potential (the force) are continuous at $r = r_{s,ij}$.

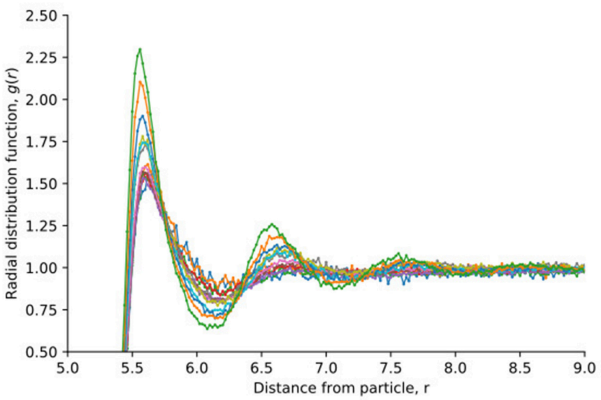

FIGURE 3 | The radial distribution function of fluid particles around a grain, as shown in **Figure 4**. Results are shown for densities that vary between $\rho^* = 0.1$ and $\rho^* = 0.7$.

3.4. Pressure Computations

The contribution of the fluid to the grand potential of layer l is [12]

$$p_l^f V_l^f = \frac{1}{3}\left\langle \sum_{i\in l} m_i(\mathbf{v}_i \cdot \mathbf{v}_i) \right\rangle - \frac{1}{6}\left\langle \sum_{i\in l}\sum_{j=1}^{N} (\mathbf{r}_{ij} \cdot \mathbf{f}_{ij}) \right\rangle, \tag{17}$$

where p_l^f is the fluid differential pressure, V_l^f the fluid volume, m_i and $\mathbf{v}_i$ are the mass and velocity of fluid particle i. The first two sums are over all fluid particles i in layer l, while the second sum is over all other particles j. Half of the virial contribution, the second term in Equation (17), is assigned to particle i and the other half to particle j. The virial contribution assigned to the solid particles are not included. $\mathbf{r}_{ij} \equiv \mathbf{r}_i - \mathbf{r}_j$ is the vector connecting particle i and j, and $\mathbf{f}_{ij} = -\partial u_{ij}/\partial \mathbf{r}_{ij}$ is the force between them. The $\cdot$ means an inner product of the vectors. The computation gives $\hat{p}_l^f$, which is the contribution to the integral pressure in layer l from the fluid particles, accounting for their interaction with the grain particles.

3.5. The Porous Medium in a Pressure Gradient

We used the reflecting particle boundary method developed by Li et al. [15] to generate a pressure difference across the system along the x-axis. Particles moving from right to left pass the periodic boundary at $x = 0$ and $x = L_x$ with probability $(1 - \alpha_p)$ and reflected with probability α_p, whereas particles moving from left to right pass freely through the boundary. A large α_p gives a high pressure difference and a low α_p gives a low pressure difference.

4. RESULTS AND DISCUSSION

The results of the molecular dynamics simulations are shown in **Figures 4–8** (equilibrium) and **Figures 9**, **10** (away from equilibrium). The porous medium structure was characterized by its pair correlation function, cf. **Figure 3**. The compressional energy was computed according to equation 4 in case I with a single spherical grain and case II with a lattice of spherical grains.

We computed the compressional energy, $p_l V_l$, in the bulk liquid (region B) and in the nano-porous medium (region A). In the bulk liquid we computed the pressure directly from the compressional energy, because $p_l V_l = p_l^f V_l^f$ (not shown).

Figures 4, **6** show the various contributions to the compressional energy, cf. equation 4. The grain particles were identical and the system was in equilibrium, so the integral pressure in the grains was everywhere the same, $\hat{p}_l^r = \hat{p}^r$. Similarly, the surface tension was everywhere the same, $\gamma_l^{fr} = \gamma^{fr}$.

The grain pressure $\hat{p}^r$ and surface tension γ^{fr} were fitted such that the pressure is everywhere the same and are plotted as a function of the fluid pressure p^f. The results for case II were next used in **Figures 9**, **10** to determine the pressure gradient across the sequence of REVs in the porous medium.

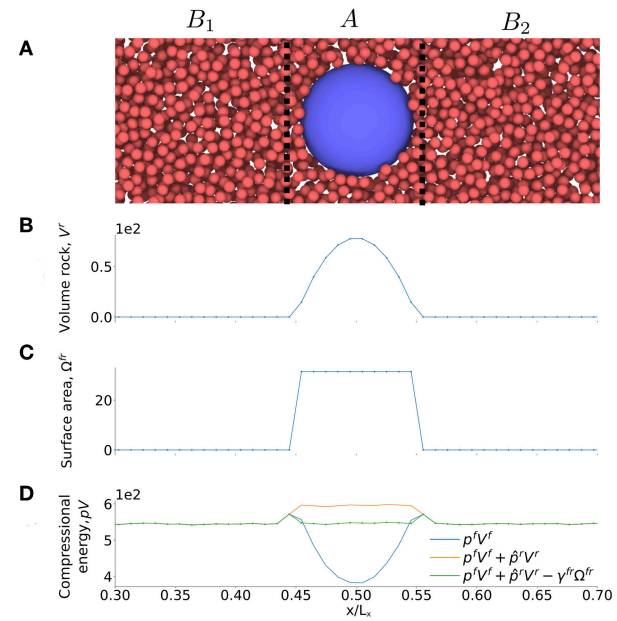

FIGURE 4 | (A) Illustration of case I, a single spherical grain surrounded by a fluid phase with $d = 4\sigma_0$. **(B)** Volume of grain, V^r, **(C)** surface area Ω^{fr} and **(D)** compressional energy pV as a function of the x-axis of the simulation box.

4.1. Case I. Single Spherical Grain. Equilibrium

The single sphere case is illustrated in **Figure 4A**. **Figures 4B,C** show the variation in the volume of the porous medium (rock), V_l^r, and the surface area between the rock and the fluid, Ω^{fr}, along the x-axis of the simulation box. The two quantities were determined for all layers, l, and these results were used in the plots of **Figures 4B,C**. To be representative, the REV must include the solid sphere with boundaries left and right of the sphere. In order to obtain $p^{\text{REV}}V^{\text{REV}}$ we summed p_lV_l over all the layers in the REV. At equilibrium, $p^{\text{REV}} = p$, where p is the pressure in the fluid in region B. For the REV we then have

$$pV^{\text{REV}} = \sum_{l\in\text{REV}} p_l^f V_l^f + \hat{p}^r \sum_{l\in\text{REV}} V_l^r - \gamma^{fr} \sum_{l\in\text{REV}} \Omega_l^{fr}, \qquad (18)$$

where we used that $\hat{p}_l^r = \hat{p}^r$ and $\gamma_l^{fr} = \gamma^{fr}$. We know the values of all the elements in this equation, except $\hat{p}^r$ and γ^{fr}. The values of $\hat{p}^r$ and γ^{fr} are fitted such that the pressure, p in Equation (18) is everywhere the same. With these fitted values available, we calculated p_lV_l of each layer from

$$p_lV_l = p_l^f V_l^f + \hat{p}^r V_l^r - \gamma^{fr}\Omega_l^{fr}. \qquad (19)$$

The contributions to the compressional energy in this equation for case I are shown in the bottom **Figure 4D**. We see the contribution from (1) the bulk fluid $p_l^f V_l^f$, (2) the bulk fluid and grain $p_l^f V_l^f + \hat{p}^r V_l^r$ and (3) the total compressional energy, $p_lV_l = p_l^f V_l^f + \hat{p}^r V_l^r - \gamma^{fr}\Omega^{fr}$, which gives the pressure of the REV when summed and divided with the volume of the REV.

Figure 4D shows clearly that the bulk pressure energy gives the largest contribution, as one would expect. It is also clear that the surface energy is significant. As the surface to volume ratio increases, the bulk contributions may become smaller than the surface contribution (not shown). In the present case, this will happen when the radius of the sphere is $2.25\sigma_0$. For our grains with $R = 5.5\sigma_0$, this does not happen.

The plots of $\hat{p}^r$ and γ^{fr} as functions of p in region B are shown in **Figure 5**. The values for $d = 4\sigma_0$ and $d = 11\sigma_0$ are given in the same plots. We see that the plots fall on top of each other. This shows that the integral pressure and the surface tension are independent of the distance d in the interval considered. If confinement effects were essential, we would expect that $\hat{p}^r$ and γ^{fr} were functions of the distance d between the surfaces of the spheres. When the value of d decreases below $4\sigma_0$, deviations may arise, for instance due to contributions from the disjoining pressure. Such a contribution is expected to vary with the surface area, and increase as the distance between interfaces become shorter. In plots like **Figure 5**, we may see this as a decrease in the surface tension.

4.2. Case II. Lattice of Spherical Grains. Equilibrium

Consider next the lattice of spherical grains, illustrated in **Figure 6A**. **Figures 6B,C** give the variation in the volume of the porous medium V_l^r and surface area, Ω^{fr}, along the x-axis.

When the REV in region A is properly chosen, we know that $p^{\text{REV}} = p$. In equilibrium, the pressure of the REV is constant in the bulk liquid phases, in regions B_1 or B_2, where p is the pressure of the fluid in region B. In order to obtain pV^{REV} in region A, we sum p_lV_l over all the layers that make up the REV, and obtain

$$pV^{\text{REV}} = \sum_{l\in\text{REV}} p_l^f V_l^f + \hat{p}^r \sum_{l\in\text{REV}} V_l^r - \gamma^{fr} \sum_{l\in\text{REV}} \Omega_l^{fr}, \qquad (20)$$

To proceed, we find first the values of all the elements in this equation, except $\hat{p}^r$ and γ^{fr}. The values of $\hat{p}^r$ and γ^{fr} are fitted such that the pressure is everywhere the same. Using these fitted values, we next calculated $\hat{p}_lV_l$ of each layer using

$$p_lV_l = p_l^f V_l^f + \hat{p}^r V_l^r - \gamma^{fr}\Omega_l^{fr} \qquad (21)$$

The contributions to the compressional energy in this equation are shown in three stages in **Figure 6D**: (1) bulk fluid contribution $p_l^f V_l^f$, (2) bulk fluid and grain contribution $p_l^f V_l^f + \hat{p}^r V_l^r$ and (3) the total compressional energy, $p_lV_l = p_l^f V_l^f + \hat{p}^r V_l^r - \gamma^{fr}\Omega^{fr}$. **Figure 6D** shows clearly that the bulk contribution is largest, as is expected. However, the surface energy is significant.

From **Figure 6B** it follows that a proper choice of the REV is a unit cell, because all REVs are then identical, (except the REVs at the boundaries). The integral over p_lV_l in these REVs is the same and equal to pV^{REV}. The layers l are smaller than the REV and as a consequence $\hat{p}_lV_l$ will vary, a variation that is seen in **Figure 6D**.

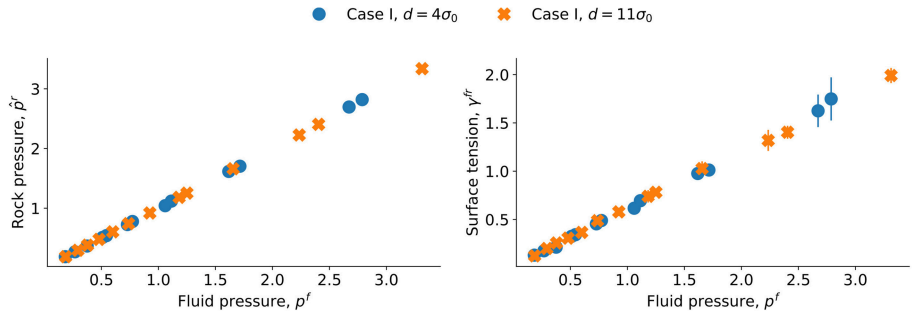

FIGURE 5 | Fitted grain pressure $\hat{p}^r$ and surface tension γ^{fr} as a function of pressure p for a sphere (characteristic length $d = 4\sigma_0$ and $d = 11\sigma_0$).

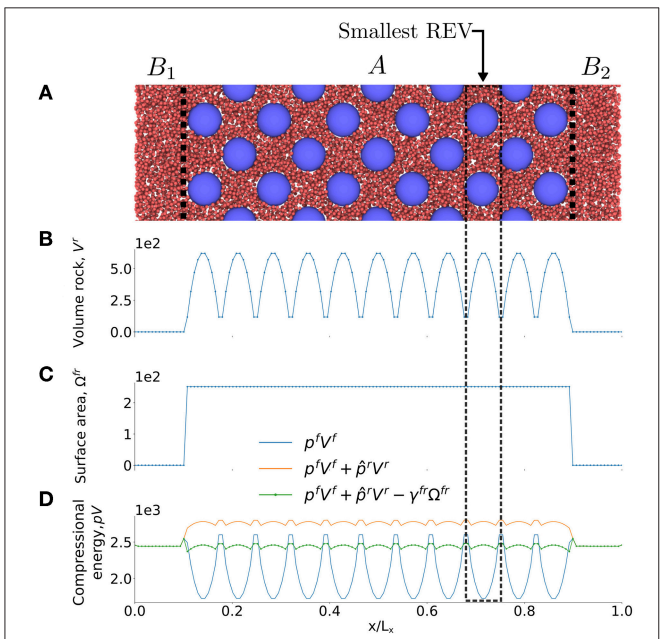

FIGURE 6 | (A) Illustration of case II, a lattice spherical grain surrounded by a fluid phase with $a = 20\sigma_0$. **(B)** Volume of grain, V^r, **(C)** surface area Ω^{fr} and **(D)** compressional energy pV as a function of the x-axis of the simulation box. The smallest REV is a unit cell.

The values for $\hat{p}^r$ and γ^{fr} are shown as a function of p^f for case II in **Figure 7** for $d_1 = 4.14\sigma_0$ and $d_1 = 11.21\sigma_0$. We see now a systematic difference between the values of $\hat{p}^r$ and γ^{fr} in the two cases. The integral pressure and the surface tension increases as the distance between the grains decreases. The difference in one set can be estimated from the other. Say, for a difference in surface tension $\Delta\gamma^{fr}$ we obtain for the same fluid pressure from equation 11, a difference in integral pressure of $\Delta\hat{p}^r = 3\Delta\gamma^{fr}/R$. This is nearly what we find by comparing the lines in **Figure 6**, the lines can be predicted from one another using $R = 6.5\sigma_0$ while the value in **Figure 3** is $R = 5.5\sigma_0$. The difference may be due to the disjoining pressure. Its distribution is not spherically symmetric, which may explain the difference between $6.5\sigma_0$ and $5.5\sigma_0$.

The results should be the same as for case I for the larger distance, and indeed that is found, cf. **Figure 8**. As the distance between the grain surfaces increases, we expect the dependence on confinement to disappear, and this is documented by **Figure 8** where the two cases are shown with distances $d = 11\sigma_0$ and $d_1 = 11.21\sigma_0$, respectively. The curves for the single grain and lattice of grains overlap.

The knowledge gained above on the various pressures at equilibrium is needed to construct the REV. The size of the REV includes the complete range of potential interactions available in the system, but not more. To find a REV-property, we need to sample the whole space of possible interactions. The thickness of the REV is larger than the layer thickness used in the simulations.

Our analysis therefore shows that the pressure inside grains in a fcc lattice and the surface tension, depends in particular on the distances between the surfaces of the spheres, including on their periodic replicas. A procedure has been developed to find the pressure of a REV, from information of the (equilibrium) values of $\hat{p}^r$ and γ^{fr} as a function of p^f. It has been documented in particular for nano-porous medium, but is likely to hold for other lattices, even amorphous materials when the REV can be defined properly.

4.3. Case II. Lattice of Spherical Grains. Non-equilibrium

Figure 9 illustrates the system in the pressure gradient, where **Figure 9B** shows the compressional energy, pV, along the x-axis. The dip in the pressure close to $x = 0$ is caused by the reflecting particle boundary, cf. section 3.5. The reflecting particle boundary introduces a surface between the high pressure on the left side and the low pressure on the right side.

To show first how a REV-property is determined from the layer-property, consider again the compressional energies of each layer. In the analysis we used the fcc lattice with lattice parameter $a = 20\sigma_0$. The volume of the grain, V^r, and the surface area, Ω^{fr}, varied of course in the exact same way as in **Figures 6B,C**. The pressure gradient was generated as explained in section 3.5. The pressure difference between the external reservoirs B_1 and B_2 was large, giving a gradient with order of magnitude 10^{12} bar/m. The fluid on the left side is liquid-like, while the fluid on the right side is gas-like. The smallest REV as obtained in the analysis at equilibrium is indicated in the figure.

In order to compute a REV variable away from equilibrium, we therefore follow the procedure described by Kjelstrup et al.

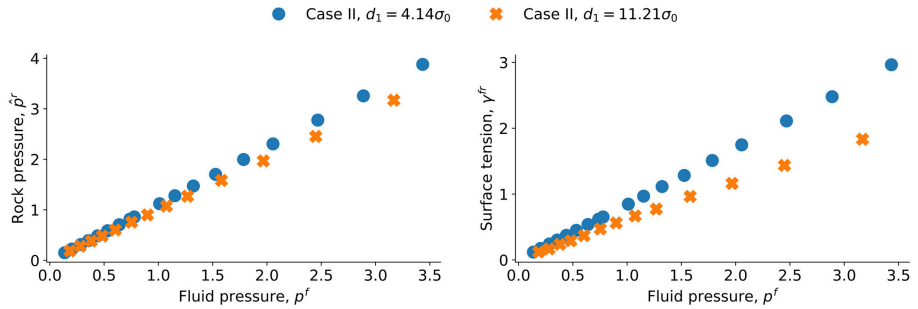

FIGURE 7 | Fitted grain pressure $\hat{p}^r$ and surface tension γ^{fr} as a function of pressure p for the lattice of spheres (characteristic length $d_1 = 4.14\sigma_0$ and $d_1 = 11.21\sigma_0$).

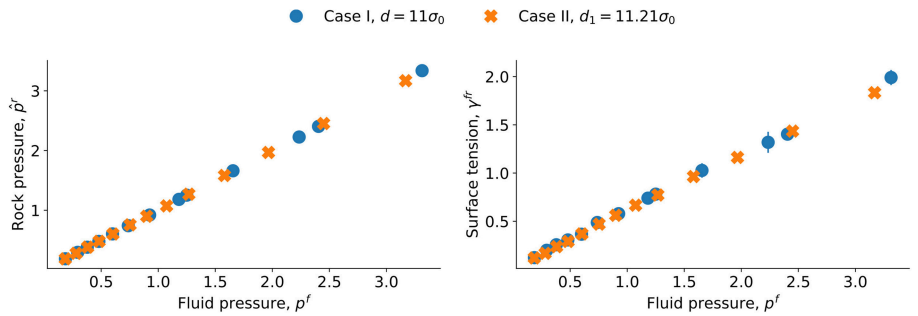

FIGURE 8 | Fitted grain pressure $\hat{p}^r$ and surface tension γ^{fr} as a function of pressure p for the sphere (characteristic length $d = 11\sigma_0$) and a lattice of spheres (characteristic length $d_1 = 11.21\sigma_0$).

[10] and choose a layer as a reference point. We then compute the average using five layers, two to the left, two to the right and the central layer. Moving one layer down the gradient, we repeat the procedure, and in this manner we obtain the property variation on the REV scale. The results of the simulation gave, for each individual layer, $p_l^l V_l^l$, as plotted in **Figure 9B**. The profile created by the REV-centers is shown in **Figure 10**. We see a smooth linear profile (central curve) as one would expect from the boundary conditions that are imposed on the system. Some traces of oscillation are still left in the separate contributions to the total compressional energy.

We have seen that a nano-porous medium is characterized by pressures in the fluid and the solid phases, as well as the surface tension between the fluid and the solid. When one reduces the size of a thermodynamic system to the nano-meter size, the pressures and the surface tensions become dependent on the size of the system. An important observation is then that there are two relevant pressures rather than one. Hill [1] called them the integral and the differential pressure, respectively. It is maybe surprising that the simple virial expression works so well for all pressure calculations in a fluid, but we have found that it can be used. We will next be able to study transport processes, where the external pressure difference is a driving force. The method, to compute the mechanical force intrinsic to the porous medium, may open interesting new possibilities to study the effects that are characteristic for porous media.

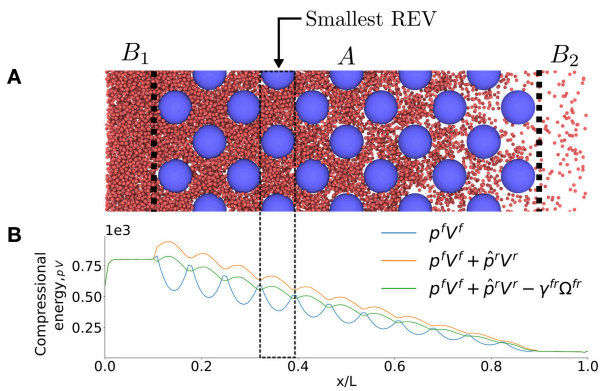

FIGURE 9 | (A) Illustration of case II in a pressure gradient. **(B)** Compressional energy pV variation across the system.

In a macro-scale description, the so-called representative elementary volume (REV) is essential. The REV makes it possible to obtain thermodynamic variables on this scale. We have here discussed how the fact that the macro-scale pressure is constant in equilibrium makes it possible to obtain the integral pressure in the solid, as well as the surface tension, of the liquid-solid contacts in the REV. An observation which confirms the soundness of the procedure is that we recover Young-Laplace's law for the differential pressures. The existence of a REV for

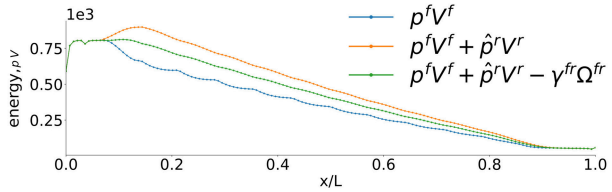

FIGURE 10 | Compressional energy pV variation across the system smoothed over the representary elementary volume.

systems on the nano-scale supports the idea of a REV that can be defined for pores also of micrometer dimension [10]. There is no conflict between the levels of description as they merge in the thermodynamic limit. The REV, as defined in the present work, may allow us to develop a non-equilibrium thermodynamic theory for the nano-scale.

5. CONCLUSIONS

The following conclusions can be drawn from the above studies

- We have obtained the first support for a new way to compute the pressure in a nano-porous medium. The integral pressure of the medium is defined by the grand potential. The definition applies to the thermodynamic limit, as well as to systems which are small, according to the definition of Hill [1].
- It follows that nano-porous media need two pressures in their description, the integral and the differential pressure. This is new knowledge in the context of nano-porous media.
- For a spherical rock particle of radius R, we derive a relation between the integral and the differential pressure in terms of the surface tension, $\hat{p}^r - p^r = \gamma/R$. Their difference is non-negligible in the cases where Young-Laplace's law applies.
- We have constructed two models of a porous medium, case I with a single spherical grain and case II with a fcc lattice of spherical grains. The new method to compute the pressure in these nano-porous mediums is not specific to these two cases, it is general. The method can be used on, e.g., a random distribution of spherical grains, but the REV will need to be larger in order to include all possible microstates. The REV needs in general to be larger as the heterogeneity of the porous medium increases.
- To illustrate the concepts, we have constructed a system with a single fluid. The rock pressure and the surface tension are constant throughout the porous medium at equilibrium. The assumptions were confirmed for a porosity change from $\phi = 0.74$ to 0.92, for a REV with minimum size of a unit cell.
- From the assumption of local equilibrium, we can find the pressure internal to a REV of the porous medium, under non-equilibrium conditions, and a continuous variation in the pressure on a macro-scale.

To obtain these conclusions, we have used molecular dynamics simulations of a single spherical grain in a pore and then for face-centered lattice of spherical grains in a pore. This tool is irreplaceable in its ability to test assumptions made in the theory. The simulations were used here to compute the integral rock pressure and the surface tension, as well as the pressure of the representative volume, and through this to develop a procedure for porous media pressure calculations.

Only one fluid has been studied here. The situation is expected to be more complicated with two-phase flow and an amorphous medium. Nevertheless, we believe that this first step has given useful information for the work to follow. We shall continue to use the grand potential for the more complicated cases, in work toward a non-equilibrium thermodynamic theory for the nano-scale.

AUTHOR CONTRIBUTIONS

All authors contributed equally to the work done. OG carried out the simulations.

ACKNOWLEDGMENTS

The calculation power was granted by The Norwegian Metacenter of Computational Science (NOTUR). We thank the Research Council of Norway through its Centres of Excellence funding scheme, project number 262644, PoreLab.

REFERENCES

1. Hill TL. *Thermodynamics of Small Systems*. New York, NY: Dover (1964).
2. Gray WG, Miller CT. Thermodynamically constrained averaging theory approach for modeling flow and transport phenomena in porous medium systems: 8. Interface and common curve dynamics. *Adv Water Resour.* (2010) **33**:1427–43. doi: 10.1016/j.advwatres.2010.07.002
3. Bennethum LS, Weinstein T. Three pressures in porous media. *Transp Porous Media.* (2004) **54**:1–34. doi: 10.1023/A:1025701922798
4. Magda J, Tirrell M, Davis H. Molecular dynamics of narrow, liquid-filled pores. *J Chem Phys.* (1985) **83**:1888–901. doi: 10.1063/1.449375
5. Todd B, Evans DJ, Daivis PJ. Pressure tensor for inhomogeneous fluids. *Phys Rev E.* (1995) **52**:1627. doi: 10.1103/PhysRevE.52.1627
6. Ikeshoji T, Hafskjold B, Furuholt H. Molecular-level calculation scheme for pressure in inhomogeneous systems of flat and spherical layers. *Mol Simulat.* (2003) **29**:101–9. doi: 10.1080/10286620210000 2518a
7. Hafskjold B, Ikeshoji T. Microscopic pressure tensor for hard-sphere fluids. *Phys Rev E.* (2002) **66**:1–4. doi: 10.1103/PhysRevE.66.0 11203
8. Hassanizadeh SM, Gray WG. Mechanics and thermodynamics of multiphase flow in porous media including interphase boundaries. *Adv Water Resour.* (1990) **13**:169–86. doi: 10.1016/0309-1708(90)90040-B
9. Gray WG, Hassanizadeh SM. Macroscale continuum mechanics for multiphase porous-media flow including phases, interfaces. *Adv Water Resour.* (1998) **21**:261–81. doi: 10.1016/S0309-1708(96)0 0063-2
10. Kjelstrup S, Bedeaux D, Hansen A, Hafskjold B, Galteland O. Non-isothermal transport of multi-phase fluids in porous media. the entropy production. *Front Phys.* (2018) **6**:126. doi: 10.3389/fphy.2018.00126

11. Kjelstrup S, Bedeaux D, Hansen A, Hafskjold B, Galteland O. Non-isothermal transport of multi-phase fluids in porous media. Constitutive Equations. *Front Phys.* (2019) **6**:150. doi: 10.3389/fphy.2018.00150
12. Irving JH, Kirkwood JG. The statistical mechanical theory of transport processes. IV. The equations of hydrodynamics. *J Chem Phys*. (1950) **18**:817–29. doi: 10.1063/1.1747782
13. Tolman RC. The effect of droplet size on surface tension. *J Chem Phys*. (1949) **17**:333–7. doi: 10.1063/1.1747247
14. Helfrich W. Elastic properties of lipid bilayers: theory and possible experiments. *Zeitschrift für Naturforschung C*. (1973) **28**:693–703.
15. Li J, Liao D, Yip S. Coupling continuum to molecular-dynamics simulation: reflecting particle method and the field estimator. *Phys Rev E*. (1998) **57**:7259–67. doi: 10.1103/PhysRevE.57.7259
16. Plimpton S. Fast parallel algorithms for short - range molecular dynamics. *J Comput Phys*. (1995) **117**:1–19. doi: 10.1006/jcph.1995.1039
17. Hoover WG, Holian BL. Kinetic moments method for the canonical ensemble distribution. *Phys Lett Sect A*. (1996) **211**:253–7. doi: 10.1016/0375-9601(95)00973-6

Conflict of Interest Statement: The authors declare that the research was conducted in the absence of any commercial or financial relationships that could be construed as a potential conflict of interest.

frontiers in Physics

ORIGINAL RESEARCH
published: 07 May 2019
doi: 10.3389/fphy.2019.00065

Rheology of High-Capillary Number Two-Phase Flow in Porous Media

Santanu Sinha[1,2*], *Magnus Aa. Gjennestad*[2], *Morten Vassvik*[2], *Mathias Winkler*[2], *Alex Hansen*[2,1] *and Eirik G. Flekkøy*[3]

[1] Beijing Computational Science Research Center, Beijing, China, [2] PoreLab, Department of Physics, Norwegian University of Science and Technology (NTNU), Trondheim, Norway, [3] PoreLab, Department of Physics, University of Oslo, Oslo, Norway

Flow of immiscible fluids in porous media at high capillary numbers may be characterized by an effective viscosity. We demonstrate that the effective viscosity is well-described by the Lichtenecker-Rother equation. Depending on the pore geometry, wettability, and viscosity of the fluids, the exponent α in this equation can have different values. We find $\alpha = 1$ when fluids are well-mixed with small bubbles, $\alpha = 0.6$ in two- and 0.5 in three-dimensional systems when there is less mixing with the appearance of big bubbles, and $\alpha = -0.5$ when lubrication layers are formed along the pore walls. Our arguments are based on analytical and numerical methods.

Keywords: porous media, two-phase flow, effective viscosity, pore-network modeling, lattice-boltzman method (LBM)

OPEN ACCESS

Edited by:
Josè S. Andrade Jr., Universidade Federal do Ceará, Brazil

Reviewed by:
Wenzheng Yue, China University of Petroleum, Beijing, China
Bikas K. Chakrabarti, Saha Institute of Nuclear Physics, India

***Correspondence:**
Santanu Sinha
santanu@csrc.ac.cn

Specialty section:
This article was submitted to Interdisciplinary Physics, a section of the journal Frontiers in Physics

Received: *11 January 2019*
Accepted: *15 April 2019*
Published: *07 May 2019*

Citation:
Sinha S, Gjennestad MA, Vassvik M, Winkler M, Hansen A and Flekkøy EG (2019) Rheology of High-Capillary Number Two-Phase Flow in Porous Media. Front. Phys. 7:65. doi: 10.3389/fphy.2019.00065

1. INTRODUCTION

The hydrodynamics of real systems very often happens at small scale, such as in a porous medium [1]. This is the case in a wide variety of biological, geological, and technological systems where there are often several immiscible fluids present. The challenge of describing such systems in a unified way, however, is largely unsolved. An important reason for this is the lack of a length scale above which the system may be averaged. Such a length scale gives rise to the representative elementary volume (REV) which is the conceptual basis for conventional theories that seek to up-scale the description of flow in porous media. However, since the fluid structures in question are often fractal, the REV average of intensive quantities, such as saturations, will depend on the size of the REV.

An important and rather general exception where this is not a problem, is the case of steady state flow [2, 3]. Steady state flow is characterized by potentially strong fluctuations at the pore scale, but with steady averages at the REV scale. Steady state configurations have much in common with ensembles in equilibrium statistical mechanics. Steady state flow implicitly assumed in conventional descriptions of porous media flows that take the existence of a REV for granted.

When the flow in question contains immiscible phases that are strongly forced in the sense that viscous forces dominate capillary forces, the description of the steady state simplifies to the description of a single fluid. This is the subject of the present work, and we show how the emergent description is manifestly incompatible with the conventional theories that have been in use for more than 80 years, most notably perhaps by the petroleum industry.

2. THEORY

The first and still leading theory describing immiscible two-phase flow in porous media is that of Wyckoff and Botset [4]. They based their theory of *relative permeability* on the idea that when the porous medium is seen from the viewpoint of one of the fluids, the pore volume accessible to this

fluid would be the pore volume of the porous medium minus the pore volume occupied by the other fluid. This reduces the effective permeability seen by either fluid and the relative reduction factor is the relative permeability. In order to account for the surface tension between the immiscible fluids in the pores, the concept of capillary pressure was introduced [5]. The central equations in relative permeability theory are

$$\vec{v}_j = -\frac{K}{\mu_j}\, k_{r,j}(S_j)\, \vec{\nabla} P_j \,, \tag{1}$$

where the subscript j either refers to the wetting fluid ($j = w$) or the non-wetting fluid ($j = n$). $\vec{v}_w$ and $\vec{v}_n$ are superficial velocities of the two fluids, defined as the volumetric flow rates of each fluid entering a REV divided by the area of entry. K is the permeability of the porous medium, μ_w and μ_n are the wetting and non-wetting viscosities. $k_{r,w}(S_w)$ and $k_{r,n}(S_w)$ are the relative permeabilities and they are both functions of the wetting saturation S_w only. The corresponding non-wetting saturation is $S_n = 1 - S_w$. The wetting and non-wetting pressure fields P_w and P_n are related through the capillary pressure function $P_c(S_w) = P_n - P_w$. We define a total superficial velocity $\vec{v}$ given by,

$$\vec{v} = \vec{v}_w + \vec{v}_n \,. \tag{2}$$

$\vec{v}$ is defined as the volumetric flow rate of all fluids entering the REV divided by the area of entry.

Let us now consider the case when the flow rates are so large that the capillary pressure may be ignored. Hence, we have $P_n = P_w = P$ and we may combine the relative permeability Equation (1) with Equation (2) to find

$$\vec{v} = -K\left[\frac{k_{r,w}(S_w)}{\mu_w} + \frac{k_{r,n}(S_n)}{\mu_n}\right]\vec{\nabla} P = -\frac{K}{\mu_{\text{eff}}(S_w)}\vec{\nabla} P \,, \tag{3}$$

where we have defined an *effective viscosity* μ_{eff} as

$$\frac{1}{\mu_{\text{eff}}(S_w)} = \frac{k_{r,w}(S_w)}{\mu_w} + \frac{k_{r,n}(S_n)}{\mu_n} \,. \tag{4}$$

There have been many suggestions as to what functional form the relative permeabilities $k_{r,w}(S_w)$ and $k_{r,n}(S_w)$ take. The most common choice is to use those of Brooks and Corey assuming $k_{r,w}(S_w) = k^0_{r,w} S_w^{n_w}$ and $k_{r,n}(S_w) = S_n^{n_n}$ where $0 \le k^0_{r,w} \le 1$ and the Corey exponents n_w and n_n being typically in the range 2–6 [6, 7].

Equation (4) is problematic. When $\mu_w = \mu_n$, a dependency of μ_{eff} on the saturation is predicted when n_w and/or n_n are larger than 1 when using the Brook–Corey relative permeabilities. Other functional forms for the relative permeabilities give similar dependencies. Clearly, such behavior is not physical.

McAdams et al. [8] proposed an effective viscosity for two-phase flow by assuming a saturation-weighted *harmonic* average

$$\frac{1}{\mu_{\text{eff}}} = \frac{S_w}{\mu_w} + \frac{S_n}{\mu_n} \,. \tag{5}$$

Cicchitti et al. [9] proposed an effective viscosity based on the saturation-weighted *arithmetic* average

$$\mu_{\text{eff}} = \mu_w S_w + \mu_n S_n \,. \tag{6}$$

Both of these expressions become saturation-independent when $\mu_w = \mu_n$ as they should. There are several other proposals for the functional form of the effective viscosity μ_{eff} in the literature [10].

A one-dimensional porous medium, e.g., a capillary tube where the two fluids move as bubbles in series [11] constitutes a series coupling and the arithmetic average (6) is appropriate. If the capillary tubes forms a parallel bundle, each filled with either only the wetting or the non-wetting fluid, we have a parallel coupled system and Equation (5) is appropriate. We now consider a capillary bundle, where each capillary i in the bundle is filled with a bubble train with a corresponding wetting saturation $S_{w,i}$. The probability distribution for finding a capillary having this saturation, $S_{w,i}$, is $p(S_{w,i})$ so that

$$S_w = \int_0^1 dS\, p(S)\, S \,. \tag{7}$$

The capillary bundle is essentially a parallel combination of tubes, each filled with a series of bubbles. The effective viscosity for the capillary bundle is therefore given by,

$$\frac{1}{\mu_{\text{eff}}} = \int_0^1 \frac{p(S)\, dS}{\mu_w S + \mu_n (1 - S)} \,. \tag{8}$$

As a model for the distribution $p(S_{w,i})$, we may take a Gaussian with a narrow width σ centered around S_w: $p(S_{w,i}) = \exp[-(S_{w,i} - S_w)^2/2\sigma^2]/\sqrt{2\pi\sigma^2}$. Using this distribution for saturation we can integrate Equation (8) using a saddle point approximation and we find to order σ^2 that,

$$\mu_{\text{eff}} = \mu_w S_w + \mu_n S_n - \frac{(\mu_n - \mu_w)^2}{\mu_w S_w + \mu_n S_n}\, \sigma^2 \,. \tag{9}$$

We now consider a wide distribution of saturations in the capillaries. Considering a uniform distribution for $p(S_{w,i})$ in Equation (8) rather than a Gaussian, we find for an average wetting saturation $S_w = 1/2$,

$$\mu_{\text{eff}} = \left|\frac{\mu_w - \mu_n}{\ln\left(\frac{\mu_w}{\mu_n}\right)}\right| \,. \tag{10}$$

The functional form of the latter equation is very different from the one for the Gaussian distribution, Equation (9).

For the extreme case when the capillaries are filled completely by either the wetting or the non-wetting fluids given by $p(S_{w,i}) = S_w \delta(S_{w,i} - 1) + S_n \delta(S_{w,i})$, we find the effective viscosity according to Equation (5), as already pointed out. We may study this either-or situation in a more complex network, namely a square lattice. We assume that the wetting saturation is set to $S_w = 1/2$, which defines the bond percolation threshold and that the links are

randomly filled with either fluid. We may then use Straley's exact result [12] leading to an effective viscosity

$$\mu_{\text{eff}} = \sqrt{\mu_w \mu_n}\,. \tag{11}$$

We may calculate the effective viscosity of a regular lattice by using Kirkpatrick's mean field theory [13]. The mobility between nodes i and j is K_{ij}/μ_{ij} where K_{ij} is the permeability and μ_{ij} is the effective viscosity of the link given by $\mu_{ij} = \mu_w S_{w,ij} + \mu_n S_{n,ij}$. Here $S_{w,ij}$ and $S_{n,ij}$ are the local wetting and non-wetting saturations in the links between the nodes. This form of μ_{ij} is due to the fluids being connected in series in one link. Kirkpatrick's theory is based on the idea that the network with link mobilities K_{ij}/μ_{ij} may be replaced by a network with a uniform mobility K/μ_{eff} such that the total network mobility remains the same. In that case, the value of K/μ_{eff} is given by [13]

$$\left\langle \frac{\frac{K}{\mu_{\text{eff}}} - \frac{K_{ij}}{\mu_{ij}}}{\frac{K_{ij}}{\mu_{ij}} + \left[\left(\frac{z}{2}\right) - 1\right]\frac{K}{\mu_{\text{eff}}}} \right\rangle = 0, \tag{12}$$

where z is the coordination number of the lattice. Considering the wetting saturation distribution $p(S_{w,ij})$ fulfilling Equation (7), the ensemble average is given by, $\langle ... \rangle = \int_0^\infty dK_{ij} P(K_{ij}) \int_0^1 dS_{w,ij} p(S_{w,ij}) ...$, where $P(K_{ij})$ is the permeability distribution. We assume a square lattice so that $z = 4$. By assuming that the saturation distribution is a narrowly peaked Gaussian with width σ, we may again use the saddle point approximation to get,

$$\mu_{\text{eff}} = \mu_w S_w + \mu_n S_n + \mathcal{O}\left(|\mu_n - \mu_w|\sigma^2\right). \tag{13}$$

This is similar to that found for the parallel capillary bundle, Equation (9).

From the systems giving rise to Equations (9), (10), (11), and (13), the form of μ_{eff} is not clear. Does it depend on the details of the porous medium or is there a general form? We may generalize Equations (5) and (6) by writing them in the form

$$\mu_{\text{eff}}^{\alpha} = \mu_w^{\alpha} S_w + \mu_n^{\alpha} S_n, \tag{14}$$

where $\alpha = -1$ for parallel coupling and $\alpha = +1$ for series coupling. Equation (14) has been used for estimating the effective electrical permittivity of heterogeneous conductors and in connection with permeability homogenization in porous media and is known as the Lichtenecker–Rother equation [14–17]. The effective viscosity in (11) corresponds to $\alpha \to 0$, whereas Equations (9) and (13) suggest $\alpha = 1$. Only Equation (10) does not fit this form.

In order to test Equation (14) in case of a porous medium, we now present two numerical approaches in the following: dynamic pore-network modeling and lattice Boltzmann simulations.

3. PORE-NETWORK MODELING

The dynamic pore-network model used here has successfully explained several experimental and theoretical results for both the transient and steady-state two-phase flow in porous media over decades [18–21]. During the transients, the model shows the different regimes of two-phase flow, namely the capillary fingering, viscous fingering, and the stable displacement pattern while changing the capillary number and viscosity ratio [18]. In the steady state, the crossover from linear Darcy regime to a quadratic regime that was observed experimentally have also been studied with this pore-network model [19, 22]. The model have also shown the experimental observation of history independence in the steady-state two-phase flow at higher capillary numbers [20]. Recently, relations between steady-state seepage velocities in porous media was obtained analytically by introducing of a new velocity function, the co-moving velocity. These relations were also established numerically with this model [23].

In the model, the porous medium is represented by a network of links, connected at nodes. In the links, two immiscible fluids, separated by interfaces, are transported. We consider both two-dimensional (2D) and three-dimensional (3D) networks for our simulations. For 2D, regular square and honeycomb networks with disordered link radii are used, whereas for 3D, reconstructed pore networks extracted from real samples are used [19]. The flow rate inside a link between two neighboring nodes i and j with respective pressures p_i and p_j obeys

$$q_{ij} = -\frac{g_{ij}}{l_{ij}}\left(p_j - p_i\right), \tag{15}$$

where l_{ij} is the link length and g_{ij} is the link mobility which is inversely proportional to the link viscosity given by $\mu_{ij} = \mu_w S_{w,ij} + \mu_n S_{n,ij}$ [24, 25]. There is no contribution to the pressure from interfaces as the surface tension (γ) is zero. This sets the capillary number, defined as the ratio of viscous to capillary forces given by $\text{Ca} = u\mu_r/\gamma$, to infinity. Here u is the Darcy velocity and μ_r is the viscosity of the more viscous fluid. Simulations are performed with a constant global pressure drop ΔP across the network and the local pressures (p_i) are determined by solving the Kirchhoff equations. Flow rates q_{ij} through each link are then calculated using Equation (15) and the interfaces are moved with small time steps.

A crucial point here is how to distribute the two fluids after they mix at the nodes. Whether the system will allow high or low fragmentation of the fluids will depend on the geometry and nature of the pore space [26, 27]. This will have impact on the size of the bubbles and the number of interfaces inside a link. As small bubbles of either fluid may not necessarily imply a large number of interfaces or *vice versa*, we implemented two different algorithms for the interface dynamics. In the *bubble-controlled* algorithm, we decide the minimum size of a bubble before entering a link and in the *interface-controlled* algorithm we decide the maximum number of interfaces that can exist in a link. We considered two different possibilities for each algorithm: for the bubble-controlled case, (A) small bubbles are allowed, with minimum sizes $b_{\min} = 0.02 r_{ij}$, (B) bubbles with sizes at least equal to the respective pore radii ($b_{\min} = r_{ij}$) are allowed. For the interface-controlled algorithm, we study two cases, (C) one with

maximum four and (D) another with maximum two interfaces per link. Our model does not include lubrication layers, and the simulations therefore cannot capture the wetting film effects at the pore walls. More details of the interface algorithm is provided in the **Supplementary Material**.

4. LATTICE BOLTZMANN SIMULATIONS

We then turn to lattice Boltzmann simulations which have no explicit parameters for the bubble size or for the number of interfaces and permits arbitrary shapes of the fluid domains within the link. The lattice Boltzmann model applied here is based on the original triangular lattice and the interaction rules first introduced by Gunstensen et al. [28]. It models the Navier–Stokes equation for two immiscible fluids within a 2D pore geometry of rectangular pipes of equal width, and in the pores the fluids organize only according to the flow and geometry of the system. The two fluids are represented by different colors, here red (more viscous) and blue (less viscous), and their respective densities ρ_r and ρ_b define a local color gradient. The surface tension is introduced by the application of two steps, first a perturbation of the mass distribution that is proportional to the magnitude of the color gradient, thus increasing the mass in the directions transverse to a fluid-fluid interface, and second, a re-coloring step that sends red toward red and blue toward blue. Both steps conserve the local momentum, the first step creates the change in the stress tensor which is responsible for the surface tension, and the last step causes an anti-diffusive flux of both phases. The solid obstacles are represented by the bounce-back rule, which ensures the hydrodynamic no-slip condition and the wetting property is controlled by coloring the solid obstacles with the same saturations as in the bulk fluid. The aim is to simulate flows that are not governed by surface tension effects and this wetting rule creates a relatively neutral wetting property that does not affect the flow as much as full wetting of one phase. The model also allows for tuning of the surface tension γ, so that the capillary number given by $\mathrm{Ca} = \frac{u\mu_r}{\gamma}$, is set to high values. Here, u is the overall Darcy velocity and μ_r is the viscosity of the red fluid with higher viscosity. In all the simulations $\mathrm{Ca} > 9$. For the more viscous wetting fluid, the wetting saturation $S_w = \rho_r/(\rho_r + \rho_b)$ controls the viscosity according to the local rule

$$\mu = \left[S_w + M(1 - S_w)\right]\mu_r, \tag{16}$$

where $M = \mu_b/\mu_r$ here and the pressure gradient is implemented as a constant body force in the diagonal direction point to upper right corner of the simulation domain. The body force is introduced as a constant momentum input at every time step and at every lattice site.

Initially, the flow velocity is zero everywhere and ρ_r and ρ_b initialized according to the specified value of S_w but with a small random component added. This randomness then triggers an initial phase separation which is responsible for the subsequent distribution of bubbles. Unlike the network modeling, the wetting effects of the pore walls are included here [29]. For the neutral wetting condition and for more viscous wetting fluid, we choose a rectangular pore network to emulate the network model. For the case of complete wetting with less viscous wetting fluid, the wetting layers are important and we therefore avoid the singular sharp corners. The model is implemented on a 128×128 biperiodic lattice with the pressure gradient implemented as a constant body force in the diagonal direction pointing to the upper right corner.

5. RESULTS AND DISCUSSION

We perform simulations under constant external pressure drop ΔP and the systems are evolved to the steady state. The results here are in the high capillary number regime and therefore do not depend on the history or the initial preparation of the system [20]. In the steady state, we compare the results with $(\mu_{\mathrm{eff}}/\mu_w)^\alpha = S_w + M^\alpha S_n$ (Equation 14), where $M = \mu_n/\mu_w$. In the network model, we measure the total flow rate Q as a function of the saturations S_w. As $Q = -\frac{KA}{L\mu_{\mathrm{eff}}}\Delta P$, we measure μ_{eff}/μ_w by calculating Q_w/Q where Q_w is the total flow rate at $S_w = 1$. In the lattice Boltzmann simulations, the μ_{eff} is calculated by measuring the effective permeability, obtained by measuring the total flux Q through the system and dividing by the forcing or average pressure gradient. We chose $M = 2$, 5, and 10 here. Higher values of M increase the computational cost and do not change the conclusions of this study for the network model with $\gamma = 0$. Simulations with M and $1/M$ produce the same results due to symmetric bubble rules and the absence of film flow in the network model. Depending on the pore geometry, wettability and viscosities of the fluids, we find three flow regimes. All can be characterized by Equation (14) with three different values of α. When smaller bubbles (model A) or more interfaces (model C) are allowed in the network model, we find $\alpha = 1$ for both 2D and 3D systems as shown in **Figures 1**, **2**, respectively were the fluids are well mixed. This regime is also observed in the lattice Boltzmann simulations for neutral wetting properties, or when the wetting fluid is more viscous. This is shown in **Figure 3**, where the straight lines confirm $\alpha = 1$ in Equation (14). Here the continuous merging and break-up of droplets give rise to a flow where each pore channel contains a sequence of individual drops. The fluids effectively behave as if they are arranged in series, and on the average the life-time of the droplets does not have any impact on the up-scaled behavior.

When we allow only larger bubbles with the size of the order of the pore size (model B) or few interfaces (model D) in the network model, we find $\alpha = 0.6$ for 2D and $\alpha = 0.5$ for 3D that are consistent with Equation (14). Results are plotted in **Figures 4**, **5**, respectively. Here the steady-state fluid distribution shows less mixing and larger clusters compared to **Figure 1**. This also affects the fractional flow, making the less viscous fluid to flow with higher velocity (**Supplementary Material**). So far, we could not find a set of suitable parameters or pore geometry for the lattice Boltzmann simulations that can reproduce this regime of flow.

When the wetting fluid is made less viscous in the lattice Boltzmann simulations, it produces lubrication layers of the

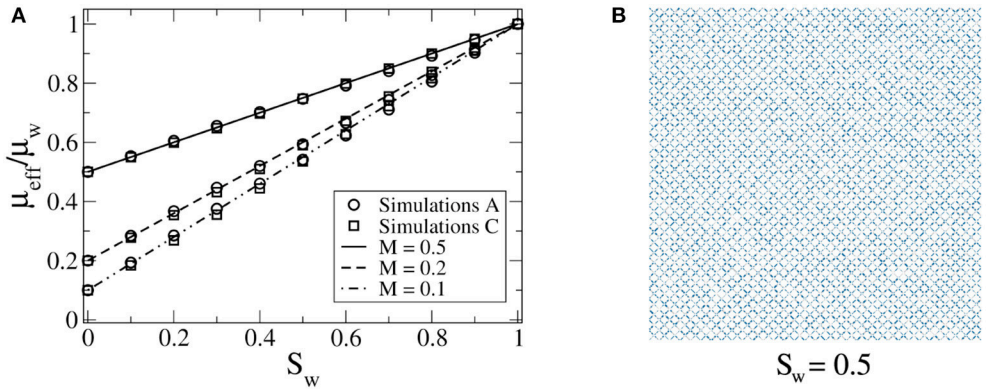

FIGURE 1 | (A) Plot of $(\mu_{eff}/\mu_w)^\alpha$ obtained from 2D network simulations (symbols) with small bubbles (A) or with many interfaces (C). Results are consistent with Equation (14) (straight lines) with $\alpha = 1$. A steady-state snapshot for model C is shown in **(B)**, where gray and blue are the wetting and non-wetting fluids respectively. Here the wetting fluid is more viscous and the results for less viscous wetting fluid are the same for the network model due to the symmetry in the interface rules and the lack of film flow mechanism in the model.

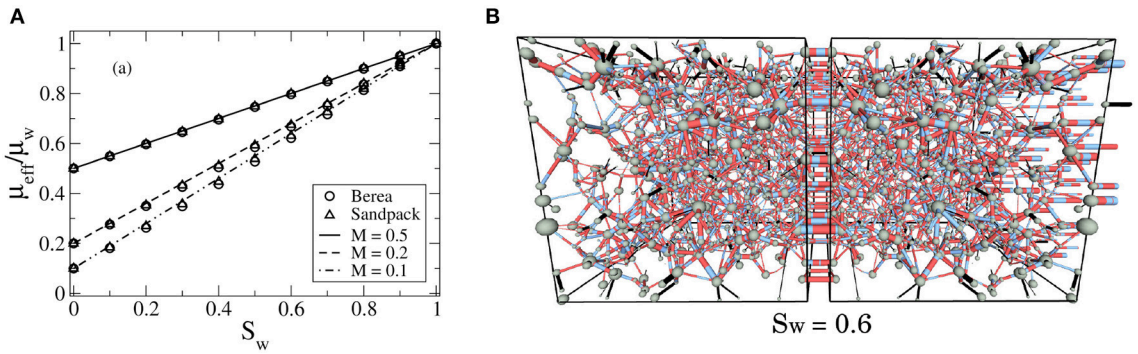

FIGURE 2 | (A) Plot of $(\mu_{eff}/\mu_w)^\alpha$ for 3D networks reconstructed from Berea sandstone and sandpack samples for the simulations with four interfaces (C). Results are consistent with Equation (14) (straight lines) with $\alpha = 1$, similar to the 2D networks. A snapshot of fluids in Berea sandstone in the steady state for model C is shown in **(B)**, where blue and red are the wetting and non-wetting fluids respectively.

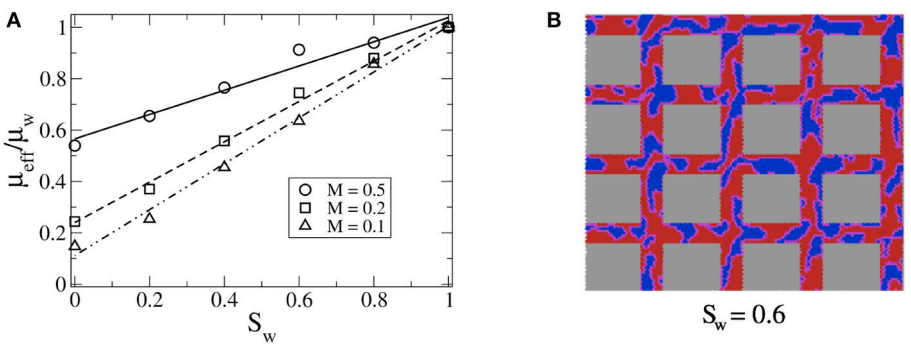

FIGURE 3 | (A) Plot of $(\mu_{eff}/\mu_w)^\alpha$ obtained from lattice Boltzmann simulations with more viscous wetting fluid which shows $\alpha = 1$ when compared with Equation (14). **(B)** Typical steady-state distribution of the fluids, where the blue and red are the more viscous (wetting) and less-viscous (non-wetting) fluids, respectively.

wetting fluid along the pore walls. This introduces a third regime with a negative value of α. The results are shown in **Figure 6** which indicate a robust $\alpha = -0.5$ behavior over a range of M values. This means that, due to the lubrication layers flow comes close to the parallel-coupling scenario, which is described by $\alpha = -1$, but there is still a significant difference. The flow paths that appear in parallel are not stationary as they would be in a parallel coupled

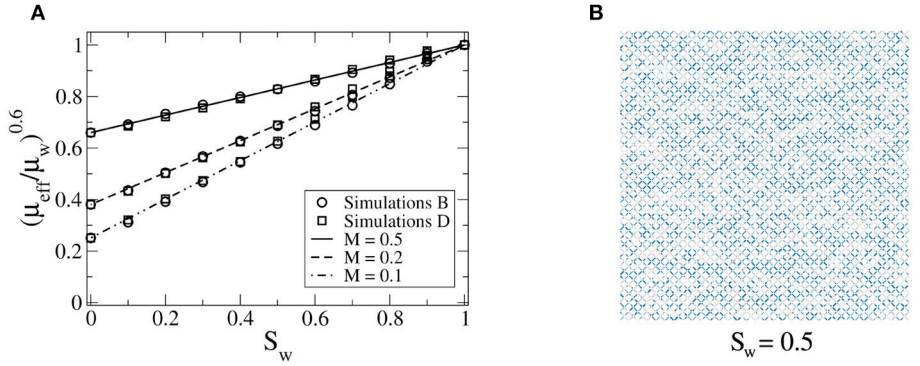

FIGURE 4 | (A) Plot of $(\mu_{\text{eff}}/\mu_{\text{w}})^{\alpha}$ obtained from network simulations with larger bubbles (B) or few interfaces (D) which shows $\alpha = 0.6$ for 2D. **(B)** Typical steady-state snapshot for model D, showing less mixing of fluids and larger clusters compared to **Figure 1B**.

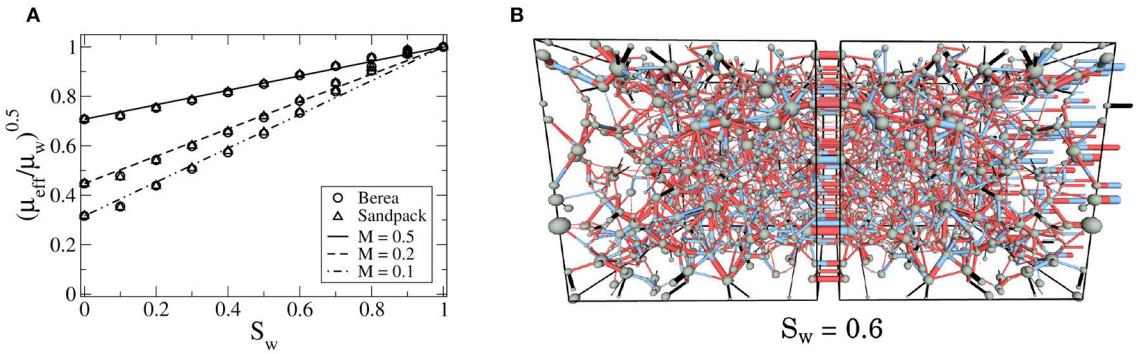

FIGURE 5 | (A) Plot of $(\mu_{\text{eff}}/\mu_{\text{w}})^{\alpha}$ for 3D networks reconstructed from Berea sandstone and sandpack samples for the simulations with two interfaces (D). Results are consistent with Equation (14) (straight lines) with $\alpha = 0.5$. A steady-state snapshot of Berea sandstone for model D is shown in **(B)**, where blue and red are the wetting and non-wetting fluids respectively.

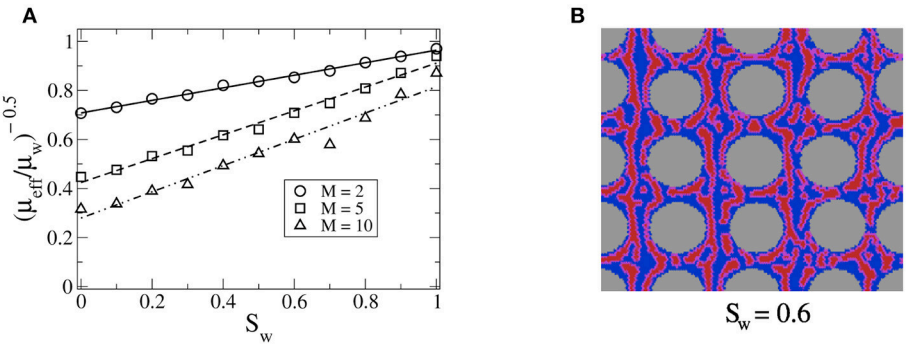

FIGURE 6 | (A) Plot of $(\mu_{\text{eff}}/\mu_{\text{w}})^{\alpha}$ from lattice Boltzmann simulations with less viscous wetting fluid where we find $\alpha = -0.5$. The steady state is dominated by lubrication layers of less viscous blue fluid as seen in **(B)**. The end points close to $S_W = 1$ fall a little below 1, which could have several explanations, one being finite Reynolds numbers, an effect that is likely to increase with increasing M the way the simulations are done.

system, they break up and merge continuously. We could not study this regime with our network model as the model does not contain film flow. It will be interesting to study this in the future with a network model that includes the film flow [30].

6. CONCLUSION

In summary, we show that immiscible two-phase flow in porous media at high capillary number limit can be characterized by measuring the effective viscosity in the steady state. We find that

the Lichtenecker–Rother Equation (14) describes the effective viscosity well for different flow configurations. We identified three flow regimes characterized by the exponent α, which depend on the organization of the two fluids in the pores. When the fluids are well mixed, we find a result which is consistent with the Kirkpatrick's mean field theory [13] with $\alpha = 1$. This is observed in both the network model and lattice Boltzmann simulations, by allowing small bubbles or more interfaces in the network model, and with the neutral wetting condition or more viscous wetting fluid in the lattice Boltzmann simulations. When only larger bubbles or fewer interfaces are allowed, we find the second regime with $\alpha = 0.6$ in 2D and $\alpha = 0.5$ in 3D with the network model. Third, when the wetting fluid is less viscous, lubrication layers are formed at the pore walls, and we find $\alpha = -0.5$ from the lattice Boltzmann simulations.

Finally, we like to point out that in the network model, we have varied the minimum bubble size over the range $0.02r_{ij}$ to $0.5r_{ij}$ finding α decreasing gradually from 1 to 0.6. Taking into account that $r_{ij} \leq 0.4\ l$, where l is the link length, this shift of α from 1 to 0.6 occurs over the narrow range from 0.008 l to 0.2 l, indicating that we see a crossover. In case of the lattice Boltzmann simulation there is no gradual transition with different wetting properties from $\alpha = 1$ to $\alpha = -0.5$. The former is observed in the neutrally wetting case or in the case when the viscous fluid is the completely wetting. The latter is observed in the case of complete wetting of the less viscous fluid.

AUTHOR CONTRIBUTIONS

MG and SS did the network model computations. EF did the Lattice Boltzmann computations. AH wrote the first draft of the manuscript. All the authors contributed in developing the theory and developing the manuscript to its final form.

ACKNOWLEDGMENTS

The authors thank Dick Bedeaux, Carl Fredrik Berg, Signe Kjelstrup, Knut Jørgen Måløy, Per Arne Slotte, and Ole Torsæter for interesting discussions. EF and AH thank the Beijing Computational Science Research Center (CSRC) and Hai-Qing Lin for hospitality. SS was supported by the National Natural Science Foundation of China under grant number 11750110430. This work was partly supported by the Research Council of Norway through its Centers of Excellence funding scheme, project number 262644.

SUPPLEMENTARY MATERIAL

The Supplementary Material for this article can be found online at: https://www.frontiersin.org/articles/10.3389/fphy.2019.00065/full#supplementary-material

REFERENCES

1. Bear J. *Dynamics of Fluids in Porous Media*. Mineola, NY: Dover (1988).
2. Tallakstad KT, Knudsen HA, Ramstad T, Løvoll G, Måløy KJ, Toussaint R, et al. Steady-state two-phase flow in porous media: statistics and transport properties. *Phys Rev Lett.* (2009) **102**:074502. doi: 10.1103/PhysRevLett.102.074502
3. Aursjø O, Erpelding M, Tallakstad KT, Flekkøy EG, Hansen A, Måløy KJ. Film flow dominated simultaneous flow of two viscous incompressible fluids through a porous medium. *Front Phys.* (2014) **2**:63. doi: 10.3389/fphy.2014.00063
4. Wyckoff RD, Botset HG. The flow of gasliquid mixtures through unconsolidated sands. *J Appl Phys.* (1936) **7**:325. doi: 10.1063/1.1745402
5. Leverett MC. Capillary behavior in porous solids. *Trans AIME.* (1941) **142**:152. doi: 10.2118/941152-G
6. Brooks RH, Corey AT. Hydraulic properties of porous media. In: Corey AT, Dils RE and Yevdjevich VM, editors. *Hydrology Papers 3*. Fort Collins, CO: Colorado State University (1964). p. 27.
7. Lake LW. *Enhanced Oil Recovery*. Englewood Cliffs, NJ: Prentice Hall (1989).
8. McAdams WH, Woods WK, Heroman LC Jr. Vaporization inside horizontal tubes-II: Benzene-oil mixtures. *Trans ASME.* (1942) **64**:193.
9. Cicchitti A, Lombardi C, Silvestri M, Soldaini G, Zavattarelli R. Two-phase cooling experiments: Pressure drop, heat transfer and burnout measurements. *Energia Nucl.* (1960) **7**:407.
10. Awad M, Muzychka YS. Effective property models for homogeneous two-phase flows. *Exp Therm Fluid Sci.* (2008) **33**:106. doi: 10.1016/j.expthermflusci.2008.07.006
11. Sinha S, Hansen A, Bedeaux D, Kjelstrup S. Effective rheology of bubbles moving in a capillary tube. *Phys Rev E.* (2013) **87**:025001. doi: 10.1103/PhysRevE.87.025001
12. Straley JP. Critical exponents for the conductivity of random resistor lattices. *Phys Rev B.* (1977) **15**:5733. doi: 10.1103/PhysRevB.15.5733
13. Kirkpatrick S. Percolation and conduction. *Rev Mod Phys.* (1973) **45**:574. doi: 10.1103/RevModPhys.45.574
14. Lichtenecker K, Rother K. Die Herleitung des logarithmischen Mischungsgesetzes aus allgemeinen Prinzipien der stationären Strömung. *Phys Z.* (1931) **32**:255.
15. Guéguen Y, Palciauskas V. *Introduction to the Physics of Rocks*. Princeton, NJ: Princeton University Press (1994).
16. Todd MG, Shi FG. Complex permittivity of composite systems: a comprehensive interphase approach. *IEEE Trans Dielectr Electr Insul.* (2005) **12**:601. doi: 10.1109/TDEI.2005.1453466
17. Brovelli A, Cassiani C. A combination of the Hashin-Shtrikman bounds aimed at modelling electrical conductivity and permittivity of variably saturated porous media. *Geophys J Int.* (2010) **180**:225. doi: 10.1111/j.1365-246X.2009.04415.x
18. Aker E, Måløy KJ, Hansen A, Batrouni GG. A two-dimensional network simulator for two-phase flow in porous media. *Transp Porous Media.* (1998) **32**:163. doi: 10.1023/A:1006510106194
19. Sinha S, Bender AT, Danczyk M, Keepseagle K, Prather CA, Bray JM, et al. Effective rheology of two-phase flow in three-dimensional porous media: Experiment and simulation. *Transp Porous Media.* (2017) **119**:77. doi: 10.1007/s11242-017-0874-4
20. Erpelding M, Sinha S, Tallakstad KT, Hansen A, Flekkøy EG, Måløy KJ. History independence of steady state in simultaneous two-phase flow through two-dimensional porous media. *Phys Rev E.* (2013) **88**:053004. doi: 10.1103/PhysRevE.88.053004
21. Gjennestad MA, Vassvik M, Kjelstrup S, Hansen A. Stable and efficient time integration of a dynamic pore network model for two-phase flow in porous media. *Front Phys.* (2018) **13**:56. doi: 10.3389/fphy.2018.00056
22. Sinha S, Hansen A. Effective rheology of immiscible two-phase flow in porous media. *Europhys Lett.* (2012) **99**:44004. doi: 10.1209/0295-5075/99/44004
23. Hansen A, Sinha S, Bedeaux D, Kjelstrup S, Gjennestad MA, Vassvik M. Relations between seepage velocities in immiscible, incompressible two-phase flow in porous media. *Transp Porous Media.* (2018) **125**:565. doi: 10.1007/s11242-018-1139-6

24. Langglois WE. *Slow Viscous Flow*. New York, NY: The Macmillan Company (1964).
25. Jia P, Dong M, Dai L, Yao J. Slow viscous flow through arbitrary triangular tubes and its application in modelling porous media flows. *Transp Porous Media*. (2008) **74**:153. doi: 10.1007/s11242-007-9187-3
26. Ody CP, Baroud CN, de Langre E. Transport of wetting liquid plugs in bifurcating microfluidic channels. *J Colloid Interface Sci*. (2007) **308**:231. doi: 10.1016/j.jcis.2006.12.018
27. Liu X, Zhang C, Yu W, Deng Z, Chen Y. Bubble breakup in a microfluidic T-junction. *Sci Bull*. (2016) **61**:811. doi: 10.1007/s11434-016-1067-1
28. Gunstensen AK, Rothman DH, Zaleski S, Zanetti G. Lattice Boltzmann model of immiscible fluids. *Phys Rev A*. (1991) **43**:4320. doi: 10.1103/PhysRevA.43.4320
29. Rothman DH, Zaleski S. *Lattice-Gas Cellular Automata: Simple Models of Complex Hydrodynamics*. Cambridge: Cambridge University Press (2004).
30. Tørå G, Øren PE, Hansen A. A dynamic network model for two-phase flow in porous media. *Transp Porous Media*. (2012) **92**:145. doi: 10.1007/s11242-011-9895-6

Conflict of Interest Statement: The authors declare that the research was conducted in the absence of any commercial or financial relationships that could be construed as a potential conflict of interest.

frontiers in Physics

ORIGINAL RESEARCH
published: 14 May 2019
doi: 10.3389/fphy.2019.00074

The Impact of Nanoparticle Adsorption on Transport and Wettability Alteration in Water-Wet Berea Sandstone: An Experimental Study

Shidong Li[1,2]*, *Ole Torsæter*[1,3], *Hon Chung Lau*[2,4], *Nanji J. Hadia*[2] *and Ludger P. Stubbs*[2]

[1] *Department of Geoscience and Petroleum, Norwegian University of Science and Technology, Trondheim, Norway,* [2] *Institute of Chemical and Engineering Sciences, Agency for Science, Technology, and Research, Singapore, Singapore,* [3] *PoreLab, Norwegian Center of Excellence, Norwegian University of Science and Technology, Trondheim, Norway,* [4] *Department of Civil and Environmental Engineering, National University of Singapore, Singapore, Singapore*

Wettability alteration was proposed as one of the enhanced oil recovery (EOR) mechanisms for nanoparticle fluid (nanofluid) flooding. The effect of nanoparticle adsorption on wettability alteration was investigated by wettability index measurement of Berea sandstone core injected with nanofluids and by contact angle measurement of a glass surface treated with nanofluids. Nanoparticle adsorption was studied by single phase coreflooding with nanofluids in Berea sandstone. The adsorption isotherm and the impact of adsorption on the effective permeability were investigated by measuring the effluent nanoparticle concentration and differential pressure across the core. Results showed that hydrophilic nanoparticles (e.g., fumed silica) made the core slightly more water wet, and hydrophobic nanoparticles (e.g., silane modified fumed silica) delayed spontaneous imbibition but could not alter the original wettability. It was found that hydrophilic nanoparticles treatment reduced contact angle between oil and water by about 10 to 20 degree for a glass surface. Results also showed that different types of nanoparticle have different adsorption and desorption behavior and different ability to impair the permeability of Berea sandstones cores.

Keywords: wettability alteration, nanoparticle, adsorption and desorption, transport, contact angle

OPEN ACCESS

Edited by:
Antonio F. Miguel,
University of Evora, Portugal

Reviewed by:
Farid B. Cortés,
Universidad Nacional de Colombia, Colombia
Antero Martins,
Universidade do Porto, Portugal

***Correspondence:**
Shidong Li
Li_Shidong@ices.a-star.edu.sg

Specialty section:
This article was submitted to Interdisciplinary Physics, a section of the journal Frontiers in Physics

Received: *20 December 2018*
Accepted: *24 April 2019*
Published: *14 May 2019*

Citation:
Li S, Torsæter O, Lau HC, Hadia NJ and Stubbs LP (2019) The Impact of Nanoparticle Adsorption on Transport and Wettability Alteration in Water-Wet Berea Sandstone: An Experimental Study. Front. Phys. 7:74. doi: 10.3389/fphy.2019.00074

INTRODUCTION

The wettability of reservoir rock plays an important role in oil field development. It controls the relative permeability, capillary pressure, and residual oil distribution. Altering wettability to a favorable status will lead to more oil production. It has been reported that oil recovery is optimum at slightly water-wet to neutral wet reservoir [1]. Traditionally, surfactant flooding was utilized to alter reservoir rock wettability to more water wet, which can enhance spontaneous imbibition and increase oil recovery during water injection [2, 3]. Hammond and Unsal [4] discussed the possible mechanisms of wettability alteration with surfactants. They include surfactant adsorption onto rock surface and surfactant complexing with contaminant molecules of crude oil that are adsorbed on the rock surface and stripping them off. Salehi et al. studied the mechanisms of wettability alteration using surfactant in naturally fractured reservoirs, they found that both ion-pair formation and

adsorption of surfactant molecules are the two main mechanisms responsible for altering the rock wettability to more water-wet, and surfactants with higher charge density on the head groups were more effective in altering wettability to a more water-wet state [2].

Recently, nanoparticles were proposed as wettability alteration agents to change the wettability of reservoir rock [5, 6]. A nanoparticle is a particle with size ranging from 1 to 100 nm. A nanoparticle suspension is called a nanofluid. It has been applied in many different disciplines including heat transfer [7], biomedicines [8], and soil remediation [9]. Besides EOR and wettability alteration, nanofluids have been proposed for applications on exploration, drilling and production, equipment manufacturing, refining and processing [10]. The EOR mechanisms of a nanofluid were discussed by Li et al. [11]. They include interfacial tension reduction, wettability alteration, pore channels plugging, disjoining pressure, and emulsification.

Miranda et al. [12] reported that silica nanoparticles have many advantages as EOR agents, such as: (1) 99.8% of silica nanoparticle is silicon dioxide, which is the main component of sandstone, thus making it an environmentally friendly material; (2) properties such as thermal conductivity, stress–strain relationship and rheology strongly depend on size and shape of the nanoparticles, which can be tailor designed during the manufacturing process; (3) the chemical behavior of nanoparticles can be controlled by changing surface coating; (4) the price of silica nanoparticle is cheaper than most of EOR chemicals.

The ability of nanoparticles to alter the wettability has been extensively studied. Contact angle measurements show that different types of nanoparticle (silicon dioxide, iron oxide, aluminum oxide and titanium dioxide) can reduce contact angle between oil and water, making surface more water wet regardless of initial surface wettability [13–16]. Microfluidic flooding experiments show that nanofluid flooding can alter wettability of glass grains. Nanoparticle adsorption on glass grains leading to wettability change from oil wet to water wet was observed in microfluidic experiments [13]. Lu et al. [17] reported imbibition of nanofluids into a capillary channel that changes wettability to strongly water wet, so the residual oil formed spherical droplets and can move freely with low resistance. Disjoining pressure is proposed as another mechanism of wettability alteration by nanofluids. Various researchers have investigated the ability of a nanofluid to displace oil from a solid surface due to disjoining pressure [18–20]. The phenomenon of nanoparticles ordering themselves into a confined wedge between an oil drop and a solid substrate is a consequence of entropy increase of the overall nanofluids by permitting greater freedom for nanoparticles in the bulk liquid. These ordered microstructures exert an excess pressure separating the two surfaces confining the nanofluids. This excess pressure is defined as a structural disjoining pressure [20]. The particles that are present in this three-phase contact region tend to form a wedge-like structure and force themselves between the discontinuous phase and the substrate. Particles present in the bulk fluid exert a pressure forcing the particles in the confined region to move forward. The energies that drive this mechanism are Brownian motion and electrostatic repulsion between the particles. The force imparted by a single particle is extremely weak, but when large amounts of small particles are present, the pressure can be upwards of 50,000 Pa at the vertex. Particle size and the associated particle charge density also affect the strength of this force. The smaller the particle size, the higher is the charge density, and the larger is the electrostatic repulsion between those particles. When this force is confined to the vertex of the discontinuous phase, displacement occurs in an attempt to regain equilibrium. As with any colloidal system, particle size, temperature, salinity and surface characteristics of the substrate affect the magnitude of the disjoining force [21].

Adsorption and transport behavior of nanoparticles inside porous media play a very critical role for wettability alteration. Normally, when hydrophilic nanoparticles are injected into

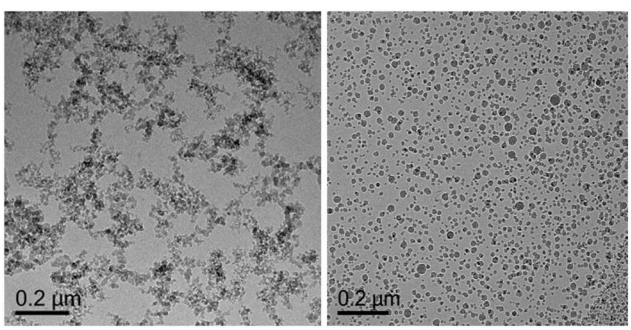

FIGURE 1 | Cryo-TEM image of nanoparticles: **Right**: FNP; **Left**: CNP.

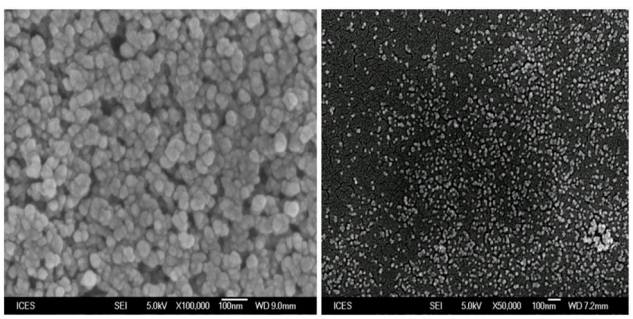

FIGURE 2 | SEM image of nanoparticles: **Right**: FNP; **Left**: CNP.

TABLE 1 | Fluid properties.

Fluid	Density*, g/cm^3	Viscosity*, cP
3 wt. % NaCl brine	1.022	1.003
0.05 wt. % FNP nanofluid	1.022	1.086
0.2 wt. % FNP nanofluid	1.022	1.155
0.5 wt. % FNP nanofluid	1.022	1.563
0.05 wt. % CNP nanofluid	1.022	1.033
0.2 wt. % CNP nanofluid	1.022	1.034
0.5 wt. % CNP nanofluid	1.022	1.037

**All properties were measured under room temperature.*

a porous medium, five phenomena can occur: adsorption, desorption, blocking, transport and aggregation of nanoparticles. Five forces dominate the interactions between nanoparticles and pore walls: the attractive potential force of van der Waals, repulsion force of electric double layers, Born repulsion, acid-base interaction, and hydrodynamics [22]. When the total force of these five forces is negative, the attraction is larger than repulsion between nanoparticles and pore walls, which leads to adsorption of nanoparticles on the pore walls. Otherwise desorption of nanoparticles from the pore walls will occur. Adsorption and desorption is a dynamic balance process controlled by the total force between nanoparticles and pore walls. Zhang et al. [23] discussed that both reversible and irreversible adsorption of nanoparticles occur during transport through porous media. Blocking will take place if the diameter of the particle or nanoparticle aggregate is larger than the size of pore throat. Aggregation of nanoparticles happens if the previous equilibrium system breaks up and nanoparticles form clusters [24].

In this paper, in order to study the effect of nanoparticles (hydrophilic and hydrophobic) adsorption on wettability alteration, several commonly used silica nanoparticles were used. Two approaches were used in wettability alteration experiments. First, overall wettability change of a core plug treated with nanoparticles was studied by measuring the wettability index. Second, the contact angle between oil and water was measured on a glass surface soaked in a nanofluid. The results from these two approaches were analyzed comprehensively. Since the nanoparticle adsorption is crucial for wettability alteration of the core, the adsorption behavior of nanoparticles inside porous media was investigated by single phase coreflooding of a nanofluid. Nanoparticles adsorption curves and differential pressure curves were plotted to analyzed nanoparticles adsorption and transport behavior inside porous media.

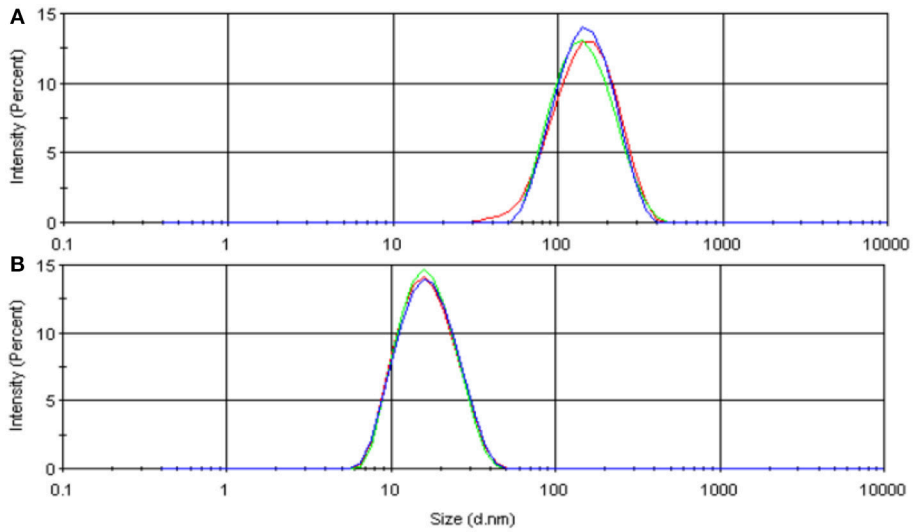

FIGURE 3 | Size distribution measured by DLS: **(A)** FNP; **(B)** CNP. The Y axis is light scattering intensity.

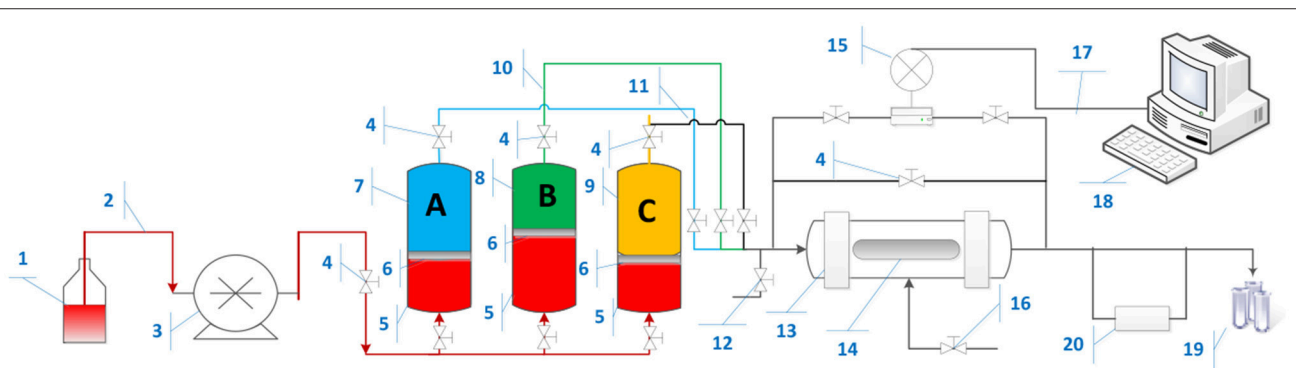

FIGURE 4 | Nanoparticles coreflooding apparatus. (1) Pump fluid (Exxol D60); (2) injection line; (3) Quzix Pump; (4) Valve; (5) Pump Fluid in reservoir; (6) Piston plate; (7) Brine; (8) Nanofluids; (9) Nanofluids; (10) Oil line; (11) Brine/Nanofluids line; (12) Bypass Valve; (13) Hassler Core Cell; (14) Core plug; (15) Pressure gauge; (16) Sleeve pressure; (17) connection cable; (18) Computer; (19) Accumulator; (20) electrical resistivity meter.

This study is novel in several aspects. First, this is the first quantitative study of the ability of nanoparticles to change the wettability of a core using the wettability index, which can provide an overall wettability state for an oil reservoir. Second, this is the first reported study of the transport of nanoparticles in Berea sandstone cores giving the transport behavior of nanoparticles in such porous medium with complex pore structures.

MATERIALS AND METHODS

Nanoparticle

Hydrophilic fumed silica nanoparticles (FNP), dimethyldichlorosilane modified hydrophobic fumed silica nanoparticles (FNP-O) and hydrophilic silica colloidal nanoparticles (CNP) were provided by Evonik Industries and employed in this study. They were supplied by Evonik Industries. FNP and FNP-O were manufactured as solid powder and CNP were provided as a highly concentrated suspension. FNP and CNP have been characterized with Cryo-Transmission Electron Microscope (Cryo-TEM) and Scanning Electron Microscopy (SEM) and images are shown in **Figures 1**, **2**, respectively. FNP has irregular shape in suspension and CNP is seen as separate spherical particles. FNP and FNP-O have an average primary particle size of 7 nm and specific surface area of 300 m^2/g. However, they may aggregate to form bigger particles in dispersion. CNP have an average single particle size of 18 nm and specific surface areas of 350 m^2/g. They do not aggregate in dispersion.

Preparation of Nanofluids

Based on the experience of previous flooding experiments [11, 25], three nanoparticle concentrations (0.05, 0.2, and 0.5 wt.%) were used in this study. A 3 wt.% Sodium chloride (NaCl) brine was used as dispersion fluid for FNP and CNP, and n-decane was used as a dispersion fluid for FNP-O. For nanofluids preparation, solid powder nanoparticles were weighed, and then were mixed with dispersing fluid with a high-speed magnetic stirrer for 5–10 min and continued agitation by using a sonicator for 20–30 min at room temperature. The CNP nanofluids were diluted from a concentrated dispersion. Fluid properties of each hydrophilic nanofluids measured at room temperature are shown in **Table 1**. Nanoparticle size distribution in suspension was measured with dynamic light scattering (DLS) and are shown in **Figure 3**. The particle size for FNP and CNP is 153.3 and 17.5 nm, respectively. The results of DLS also were used to check the homogeneity of nanoparticles suspension.

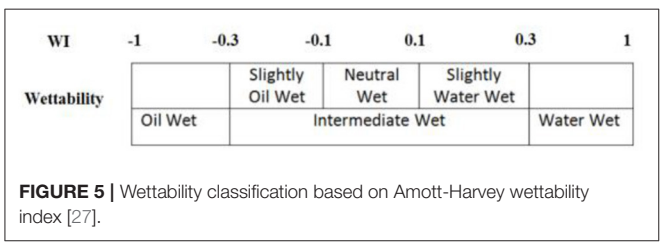

FIGURE 5 | Wettability classification based on Amott-Harvey wettability index [27].

Oil

The oil used in this experiment was n-decane and crude oil from North Sea. The density was 0.73 and 0.82 g/ml, respectively. The API gravity value of crude oil was 41.06°.

Core Plugs

Berea sandstone core plugs were used. Twenty short core plugs and six long core plugs drilled from the same block of Berea Sandstone were used for the wettability index (WI) measurement and nanoparticles transport experiments. The average porosity and permeability are 18.3% and 316 mD, respectively. The diameter was 3.83 cm and the length was 3 cm for the short cores and 8 cm for the long cores. All core plugs were cleaned with methanol before experiment.

Amott Cell and Centrifuge

Amott cells and centrifuge were used to measure WI of core.

Flooding Setup

Figure 4 shows schematic of coreflooding setup. The pump injected Exxol D-60 as pumping fluid to push the piston located inside the reservoir, which was filled with brine and nanofluids. The differential pressure across the core plug during nanoparticle transport experiments was recorded by precision pressure gauge.

Core Treatment With Nanoparticles

A total of eighteen short core plugs (designated as S3-S20) were treated with nanoparticles. Two cores (S1 and S2) were used for wettability index measurement of core without nanoparticle treatment. Three pairs of short cores (S3, S4; S5, S6 and S7, S8) were injected with three concentrations (0.05, 0.2, and 0.5 wt. %) of FNP nanofluids and another three pairs (S9, S10; S11, S12 and S13, S14) were injected with three concentrations (0.05, 0.2, and 0.5 wt. %) of CNP nanofluids. The rest of core plugs (S15, S16; S17, S18 and S19, S20) were injected with three concentrations (0.05, 0.2, and 0.5 wt. %) of FNP-O nanofluids. First, each pair of core plugs was saturated with nanofluids by using a vacuum container, and then the same nanofluids were injected into the core for 20 pore volumes (PV), inlet and outlet were exchanged at 10 PVs. Afterwards, deionized water/n-decane was injected to flush free nanoparticles out. Finally core plugs were dried in a heating cabinet and used for wettability index measurement.

Wettability Index Measurement

The wettability indexes of all core plugs were measured at room temperature (25°C). The core treated with nanoparticles was saturated with n-decane and then placed into an Amott cell surrounding with brine. Brine was allowed to imbibe into the core displacing oil out until equilibrium was reached, and the volume of water imbibed (V_{o1}) was measured. Then the remaining oil in the core was reduced to residual oil saturation by using a centrifuge. The volume of oil displaced (V_{o2}) was determined by weight measurements. The core saturated with water at residual oil saturation was returned to the Amott cell and surrounded with n-decane. Oil was allowed to imbibe into the core displacing water out of core. The volume of water displaced (V_{w1}) was measured after equilibrium was reached. The remaining water in the core was forced out by displacement in a

centrifuge. The volume of water displaced (V_{w2}) was measured. The wettability index of the core was defined and calculated by the following equation:

$$\mathrm{WI} = \frac{V_{o1}}{V_{o1} + V_{o2}} - \frac{V_{w1}}{V_{w1} + V_{w2}} \quad (1)$$

During brine imbibition process, oil production volume vs. time was measured to plot the spontaneous imbibition curve. The WI is a generally accepted quantitative measure of the wettability of a reservoir core sample. A WI of −1.0 indicates a strongly oil-wet core, whereas a WI of +1.0 indicates a strongly water-wet core.

Contact Angle Measurement

Contact angle measurements were performed under room temperature (25°C) Small glass chips cut from microscope slides were used as the solid phase in this experiment. First, glass chips were cleaned and soaked in FNP or CNP nanofluids for about 1 day, and then the captive drop method [26] was applied to measure the contact angle between 3 wt.% brine and crude oil on glass chip. Three concentrations 0.05, 0.2, and 0.5 wt.% of nanofluids were used in this experiment. For each case three measurements were performed to obtain an average value. Using glass chips as substrate provides a smooth surface for contact angle measurement, since glass is 100% silicon dioxide so it cannot mimic other minerals in Berea sandstone.

Nanoparticles Transport Experiment

Single phase nanofluids flooding was performed for nanoparticles transport experiment. Six long core plugs (8 cm length) were employed in this experiment for FNP and CNP. Different salt concentrations of brine were used as a tracer. First, core plugs were saturated with a 2.5 wt.% brine by using a vacuum pump and then injected with one PV of the same brine for measuring the absolute water permeability. Afterwards, about 4 PVs of nanofluids with 3 wt.% brine as dispersing phase were injected into the core plug to investigate the effect of nanoparticle adsorption and retention on permeability. Finally, 4 PVs of 2.5 wt.% brine were injected as a post-flush to observe the desorption of nanoparticles. A constant flow rate of 2 ml/min was used. The resistivity of the effluent was measured to determine the breakthrough time of the tracer. Differential pressure across the core was recorded during the whole injection process. Effluent fluid was collected every 4 ml (about 1/4 PV),

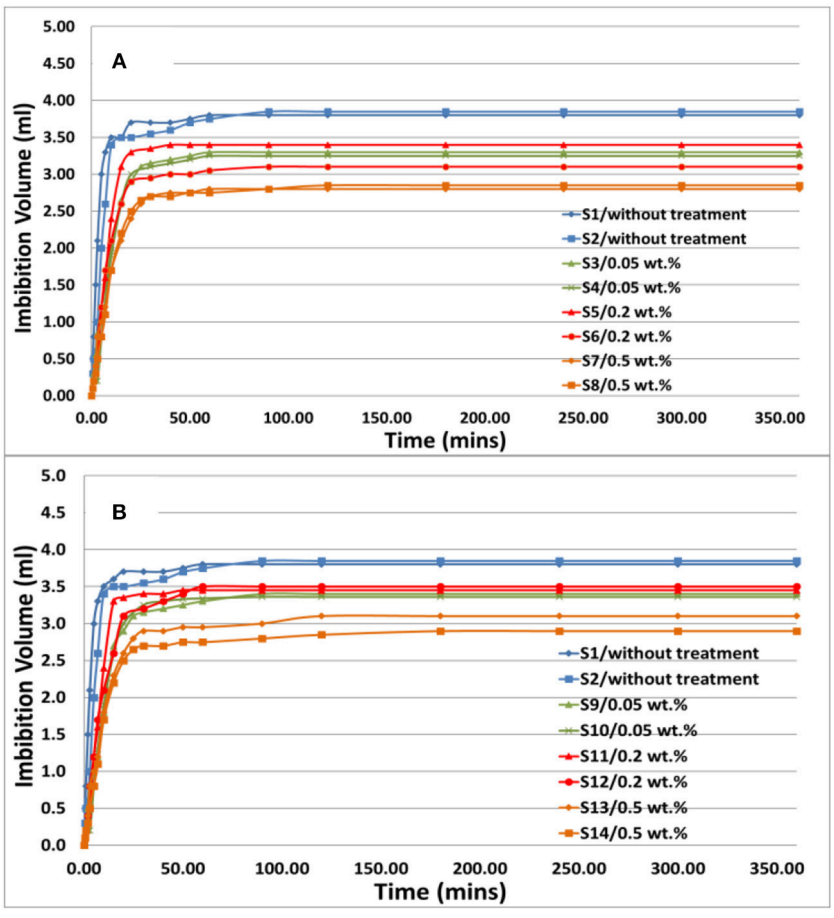

FIGURE 6 | Spontaneous imbibition curves: **(A)** core plugs treated with FNP; **(B)** core plugs treated with CNP.

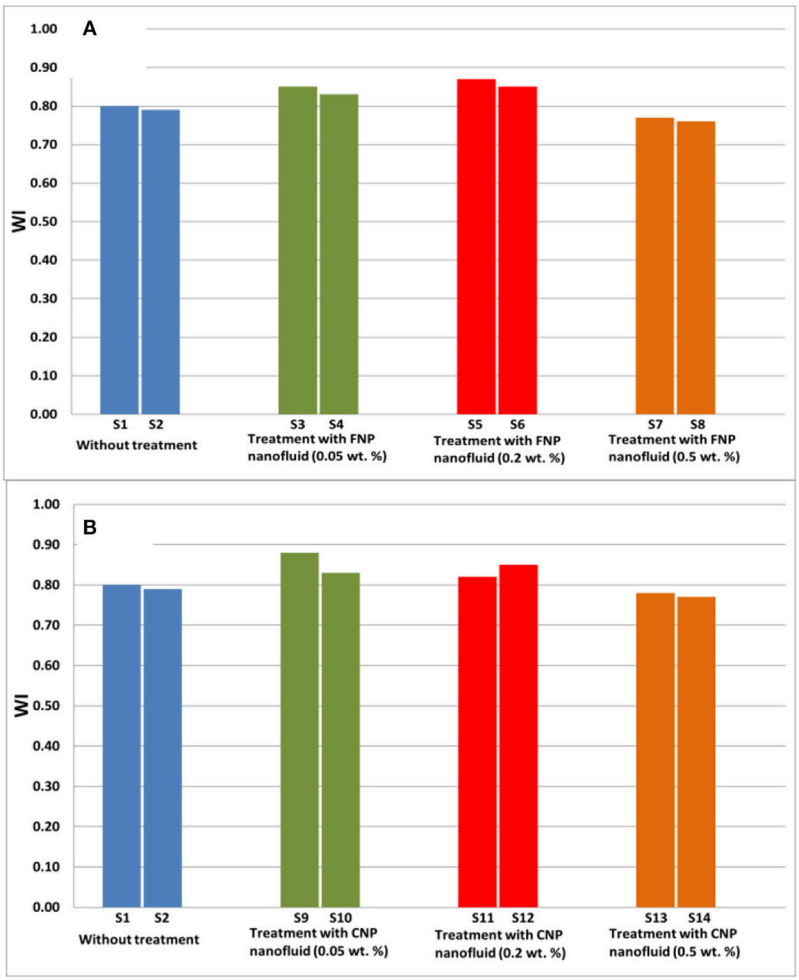

FIGURE 7 | Wettability Index: **(A)** core plugs treated with FNP; **(B)** core plugs treated with CNP.

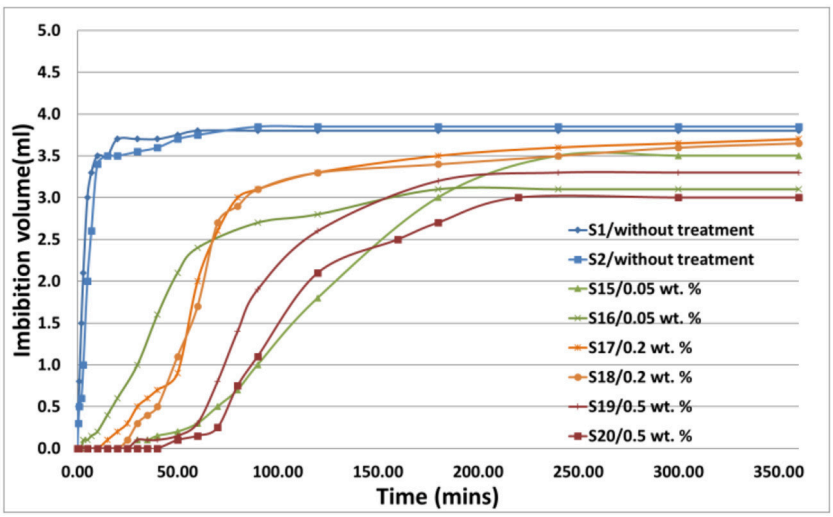

FIGURE 8 | Spontaneous imbibition curves for core plugs treated with FNP-O.

and nanoparticle concentration was measured by using a UV-VIS spectrophotometer.

RESULTS AND DISCUSSION

In this section, we first present the results of wettability alteration for core plugs treated with nanoparticles. One pair of core plugs was used for each case to test repeatability. The average wettability index for untreated core plugs (S1 and S2) was 0.795. Since all core plugs were drilled from the same block of Berea sandstone, we assumed that the original wettability index for all cores plugs before nanoparticles treatment was also 0.795. Based on wettability classification (**Figure 5**), the wettability for original core plugs was classified as water wet.

Wettability Index Measurement of Core Plugs Treated With Hydrophilic Nanoparticles (FNP and CNP)

Three pairs of core plugs (S3, S4; S5, S6 and S7, S8) were treated with injection of FNP nanofluids with concentration of 0.05, 0.2, and 0.5 wt.%, and another three pairs of core plugs (S9, S10; S11, S12, and S13, S14) were treated with injection of CNP nanofluids with concentration of 0.05, 0.2, and 0.5 wt.%. After treatment with nanoparticles, core plugs were put into an Amott cell. During spontaneous imbibition oil production volume vs. time was recorded and spontaneous imbibition curves were plotted and are shown in **Figure 6**. Both FNP and CNP have similar spontaneous imbibition performance. Most of the oil was displaced at the beginning of the spontaneous imbibition, and oil volume remained constant when it reached to maximum. This meant that core plugs treated with hydrophilic nanofluids were still strongly water wet, and the oil was produced rapidly because of capillary force. However, compare to the core plugs without treatment, the core plugs treated with both FNP and CNP had slower spontaneous imbibition rate and less final oil production volume, which might due to permeability impairment during nanofluids injection and drying process. The results of wettability index measurement are shown in **Figure 7** (detail data in **Supplementary Tables 1, 2**). There is no significant change of wettability observed for the core plugs treated with both FNP and CNP. For both 0.05 and 0.2 wt.% FNP and CNP cases, core plugs changed to slightly more water wet from original wetting state, because adsorption of hydrophilic nanoparticles on pore wall made core more water wet. For core plugs treated with 0.5 wt.% nanofluids, they should have the similar wettability index value with 0.05 and 0.2 wt.% cases, while the results showed that they were slightly less water wet than the original cores. This might be because of the permeability impairment (pore channels were plugged during drying process). Overall, there is no significant difference between the core plugs treated with hydrophilic CNP or FNP. Both have potential to alter the wettability of core plugs slightly to more water wet.

Wettability Index Measurement of Core Plugs Treated With Hydrophobic Nanoparticles (FNP-O)

The rest of the three pairs of core plugs (S15 S16, S17 S18, and S19 S20) were treated with injection of hydrophobic FNP nanofluids with concentration 0.05, 0.2, and 0.5 wt.%, respectively. Spontaneous imbibition rate was also recorded and plotted in **Figure 8**. Unlike hydrophilic nanoparticle cases, the imbibition rate of core plugs treated with hydrophobic nanoparticle was very slow at beginning. For core plugs treated with 0.5 wt.% there was no oil production during first 40 min meaning they were oil wet at beginning. After some delay oil was produced at a low rate and gave the similar ultimate oil production volume as the hydrophilic nanoparticles cases (**Figure 6**). The wettability index measurement results of core plugs treated with hydrophobic nanoparticle are shown in **Figure 9** (detail data in **Supplementary Table 3**). It can be seen

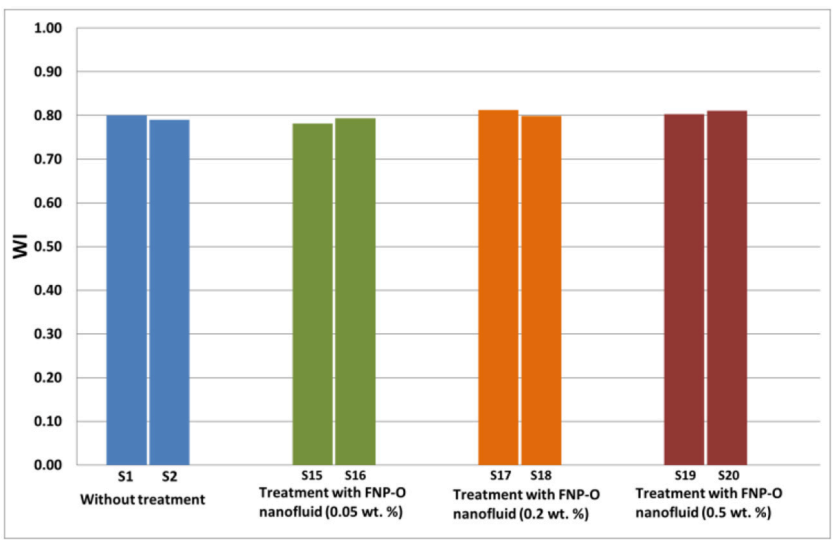

FIGURE 9 | Wettability index for core plugs treated with FNP-O.

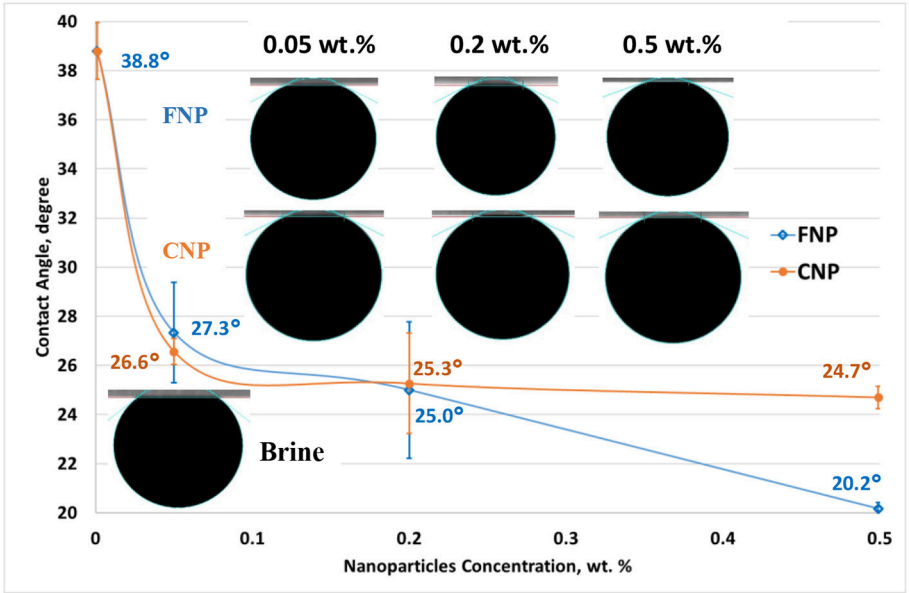

FIGURE 10 | Contact angle for a glass chip soaked in nanofluids.

that there was almost no change of wettability index after core treatment with hydrophobic nanoparticle. The reasons for this result and delay of spontaneous imbibition might be the adsorption of hydrophobic nanoparticle on water wet pore wall was weak. So some adsorbed nanoparticle desorbed and dispersed in decane, and those hydrophobic nanoparticles were transported out of core together with the oil. Thus, the wettability of core restored to what it was originally.

Contact Angle Measurements for Glass Chips Soaked in Nanofluids

The contact angle between crude oil and brine on glass chips was measured and the results are shown in **Figure 10**. Glass chips were soaked in nanofluids for about 1 day before measurement. Unlike some contact angle measurements conducted before, in this experiment 3 wt.% brine was utilized as aqueous phase rather than nanofluids, which is similar to the condition of wettability index measurement. As shown in **Figure 10**, both soaking in FNP and CNP nanofluids reduced the contact angle and change the glass surface to more water wet. For CNP nanofluids, a concentration higher than 0.1 wt.% cannot reduce contact angle anymore, while for FNP nanofluids the higher the concentration of nanoparticles, the smaller was the contact angle. We also observed that for glass chips soaked in higher concentration nanofluids, due to nanoparticles adsorption, oil was not sticky on the glass surface anymore and an oil drop can easily slip on the surface. This indicated existence of a strongly hydrophilic surface.

Both wettability index and contact angle were measured at room temperature, which gave good stability to nanoparticles suspension but cannot show the performance of nanoparticles at realistic reservoir condition, for instance, high temperature may make nanoparticle suspension less stable.

Hydrophilic Nanoparticles Transport in Porous Media

Hydrophilic nanoparticles transport experiments were conducted to study nanoparticle adsorption behavior inside core and its influence on the permeability. Differential pressure across the core plug was recorded and effluent was collected during flooding. Effluent nanoparticle concentrations were measured after flooding. Six long core plugs were used in this experiment. Three of them were injected with FNP nanofluids with concentrations of 0.05, 0.2, and 0.5 wt.%. Another three long cores were injected by CNP nanofluids with concentrations of 0.05, 0.2, and 0.5 wt.%.

Figure 11 shows the differential pressure during nanoparticles transport experiments for FNP and CNP nanofluids with different concentrations. FNP and CNP nanofluids exhibited a totally different differential pressure behavior. For all FNP nanofluids injection (**Figure 11A**) the differential pressure increased after 1 PV of nanofluids injection and the higher the concentration, the faster differential pressure climbed. At the end of nanofluids injection, the pressure was still increasing and seemed far away from reaching its ultimate value. During the post-flush brine injection, due to residual nanofluids in inlet tubing and pores, differential pressure still increased to a high value and peaked until the end of injection. This indicated that nanoparticle retention cannot be flushed out of core and the higher concentration, the higher the plateau. **Figure 11B** shows that there is no big differential pressure change between CNP nanofluids injection and post-flush injection for all injection cases, which means that CNP adsorption does not impair permeability of the core. The ratio of permeability of core before nanofluids injection to after nanofluids injection was calculated and is shown in **Table 2**. FNP injection impairs permeability

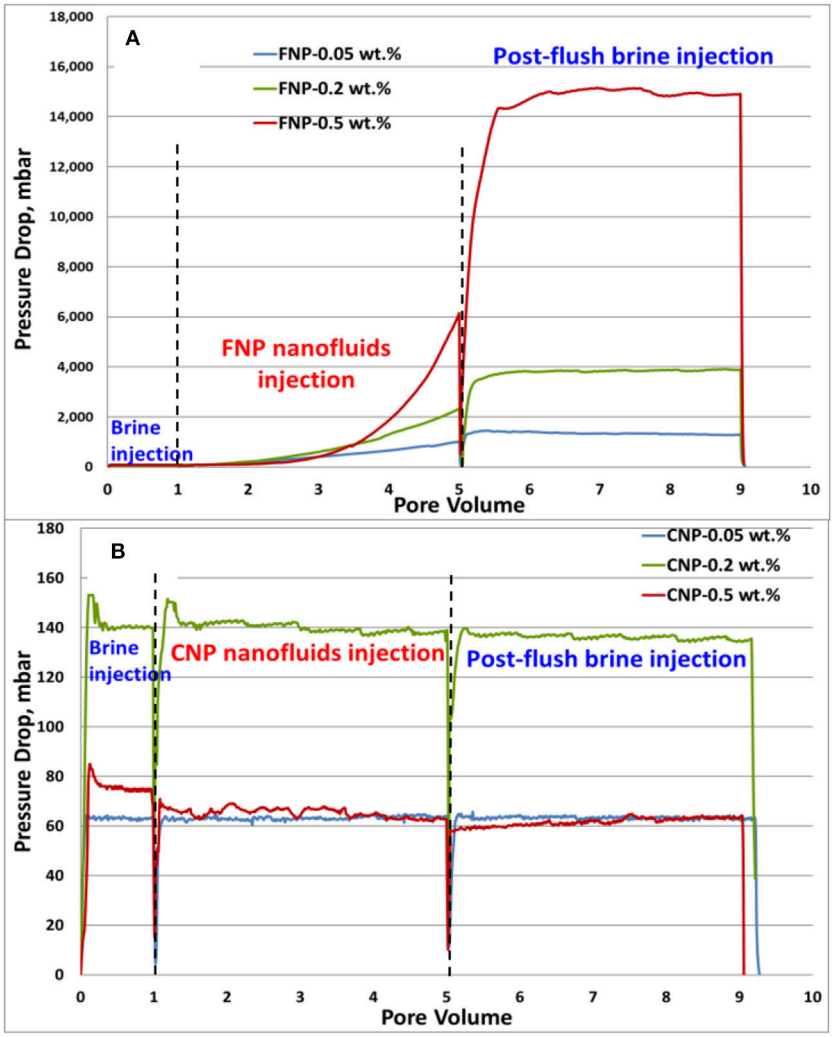

FIGURE 11 | Differential pressure curves for nanoparticles transport experiment: **(A)** core plugs treated with FNP; **(B)** core plugs treated with CNP.

TABLE 2 | Permeability of core plugs before and after nanofluids injection.

Injection scenario	K1, mD (before NP injection)	K2, mD (after NP injection)	K2/K1, %
FNP 0.05 wt.%	269.3	18.1	6.72
FNP 0.2 wt.%	463.2	5.9	1.28
FNP 0.5 wt.%	326.2	1.6	0.48
CNP 0.05 wt.%	367.6	364.8	99.25
CNP 0.2 wt.%	165.4	169.5	102.49
CNP 0.5 wt.%	308.8	313.8	101.64

significantly at all concentrations, while CNP injection has no effect on permeability.

Dimensionless effluent nanoparticles concentration curves were plotted vs. time and are shown in **Figure 12**. The dimensionless nanoparticle concentration is defined as the ratio of effluent nanoparticle concentration to the injection nanoparticle concentration. Due to very weak responded signal during UV-VIS measurement, effluent nanoparticle concentration could not be measured for 0.05 wt.% CNP case. Therefore, the adsorption curve is absent from **Figure 12B**. In **Figure 12A**, nanoparticle concentration increased later than the tracer curve indicating nanoparticles adsorption and/or retention. After reaching the peak, FNP concentration started to decrease. It might be due to the "self-adsorption" of nanoparticles, which means that the previous adsorbed nanoparticles can adsorb nanoparticles injected afterwards resulting in multilayer adsorption and/or nanoparticles aggregation. If the nanoparticle aggregates are larger than one-seventh of the pore size [28], they can be retained in the porous medium thus causing plugging. This indicates that FNP adsorption is multilayer. In **Figure 11A** rapid differential pressure increase is observed after 2 PVs FNP nanofluids injection, which is another evidence of nanoparticles retention and core plugging. FNP concentration decreased rapidly during

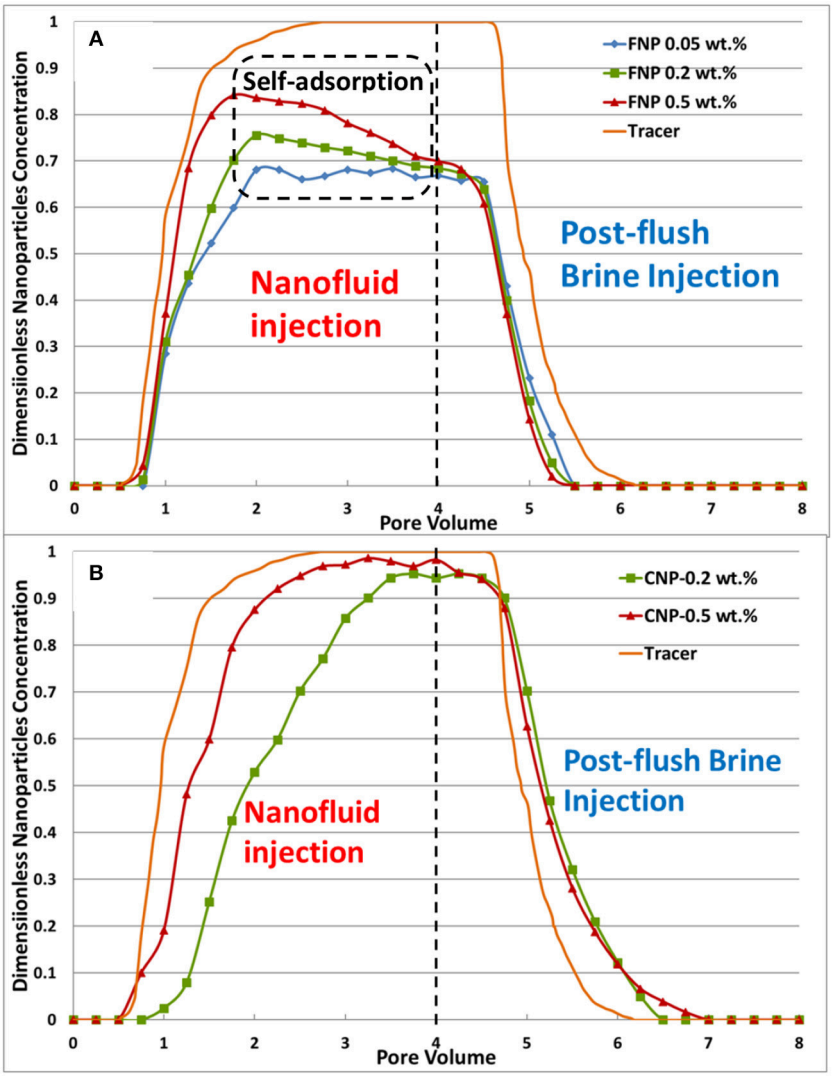

FIGURE 12 | Nanoparticles adsorption curves: **(A)** core plugs treated with FNP; **(B)** core plugs treated with CNP.

post-flush injection and earlier than the tracer curve indicating almost no desorption of nanoparticles. This is consistent with the results from differential pressure curve (no pressure decline during the post-flush in **Figure 11A**). In **Figure 12B**, CNP shows an almost ideal adsorption curve, where its concentration both increased and decreased later than tracer curve, indicating adsorption and desorption of CNP and effluent nanoparticle concentration kept at a plateau after nanoparticles adsorption on pore walls reached an equilibrium. It was observed that the 0.2 wt.% CNP curve increased and reached to plateau later than 0.5 wt.% CNP curve, which may indicate that amount of CNP adsorbed for the core plug is constant (Once pore walls of core were saturated with nanoparticles almost no nanoparticles will be adsorbed since adsorption and desorption reached a balance). So 0.2 wt.% CNP case takes a longer time to reach this amount. The CNP concentration decline curves for both concentrations are almost overlapped. Since the area between tracer and decline concentration curve indicate amount of nanoparticle desorbed, so the amount of CNP desorbed for the core plug is also constant (when adsorption and desorption reached an equilibrium).

The percentage of nanoparticles adsorbed or trapped inside core plug was calculated for both FNP and CNP and is shown in **Figure 13**. More than 25% of FNP were adsorbed and trapped during the experiment, and the lower the concentration, the higher was the percentage. However, much less CNP was adsorbed compared to FNP. The adsorbed nanoparticles percentage of 0.2 wt.% case is 2.7 times that of the 0.5 wt.% case. Since this value is close to 2.5 (concentration ratio between 0.5 and 0.2 wt.%), it proves that adsorption capacity of the core plug for CNP is nearly constant and independent of concentration.

Hydrophilic nanoparticle adsorption and/or retention inside water wet core was observed in nanoparticle transport experiment. For FNP, it was easy to observe this phenomenon both with differential pressure curve and nanoparticle adsorption

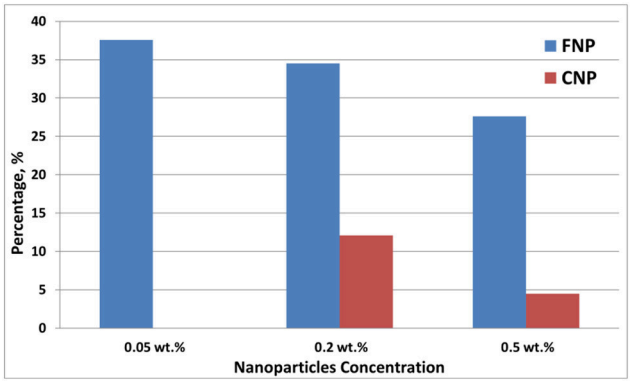

FIGURE 13 | Percentage of adsorbed nanoparticles inside core plug.

curve. However, since CNP injection did not influence differential pressure too much, so the adsorption and desorption of CNP could only be found in nanoparticle adsorption curve. This difference may indicate that two different kinds of nanoparticles have different adsorption behavior when they are injected into the core plug. This indirectly indicates that the adsorption and/or retention of FNP could be multilayer in nature whereas that of CNP is nearly monolayer.

CONCLUSIONS

In this study the effect of nanoparticle adsorption on wettability alteration was investigated by measuring wettability index of core plugs treated with nanoparticles and the contact angle between oil and brine on a glass surface treated with nanoparticles. Adsorption behavior of nanoparticle in porous media was investigated by coreflooding experiments with Berea sandstone core plugs. The results of wettability alteration experiment showed that treatment with hydrophilic nanoparticles altered wettability of sandstone slightly to more water wet and reduced the contact angle between oil and brine on a glass surface by about 10°. However, treatment with hydrophobic nanoparticles could not change wettability of core plug, but only delayed the spontaneous imbibition. For nanoparticle transport experiment, injection of FNP resulted in significant nanoparticle retention and permeability impairment, while injection of CNP had almost no influence on permeability. Nanoparticle adsorption curves indicated that FNP injection resulted in large amount of adsorption and/or retention, while no desorption was observed. However, compare to FNP cases, CNP injection only had less adsorption and significant desorption during post-flush was found. These results also suggested that FNP adsorption and/or retention inside core plug might be multilayer, while CNP adsorption is close to monolayer.

CNP has favorable injectivity into core plug compared with FNP, and it also has enough adsorption inside the core to alter wettability. FNP injection can change wettability to slightly more water wet, while a large amount of adsorption and/or retention result in unfavorable injectivity. FNP is not recommended for flooding without further surface modification. The wettability change during crude oil displacement with a nanofluid inside a core plug is interesting to investigate in the future.

AUTHOR CONTRIBUTIONS

SL: experimental work, results analysis, manuscript writing. OT: scientific advice, experimental suggestion, paper review. HL: paper review, scientific advice. NH: paper review. LS: scientific advice.

ACKNOWLEDGMENTS

The authors would like to acknowledge Science and Engineering Research Council (SERC), A*STAR, Singapore for their financial support and the Research Council of Norway for their financial support through the Centers of Excellence funding scheme, project number 262644.

SUPPLEMENTARY MATERIAL

The Supplementary Material for this article can be found online at: https://www.frontiersin.org/articles/10.3389/fphy.2019.00074/full#supplementary-material

REFERENCES

1. Norman RM. Wettability and its effect on oil recovery. *J Petroleum Technol.* (1990) **42**:P1476. doi: 10.2118/21621-PA
2. Salehi M, Johnson SJ, Liang JT. Mechanistic study of wettability alteration using surfactants with applications in naturally fractured reservoirs. *Langmuir.* (2008) **24**:14099–107. doi: 10.1021/la802464u
3. Zhang J, Nguyen QP, Flaaten AK, Pope GA. Mechanisms of enhanced natural imbibition with novel chemical. *SPE Reservoir Eval. Eng.* (2009) **12**:912–20. doi: 10.2118/113453-PA
4. Hammond PS, Unsal E. Spontaneous imbibition of surfactant solution into an oil-wet capillary: wettability restoration by surfactant contaminant complexation. *Langmuir.* (2011) **27**:4412–29. doi: 10.1021/la1048503
5. Karimi A, Fakhroueian Z, Bahramian A, Khiabani NP, Darabad JB, Azin R, et al. Wettability alteration in carbonates using zirconium oxide nanofluids: EOR implications. *Energy Fuels.* (2012) **26**:1028–36. doi: 10.1021/ef201475u
6. Li S, Kaasa AT, Hendraningrat L, Torsæter. O. Effect of Silica Nanoparticles Adsorption on the Wettability Index of Berea Sandstone. In *Presented at the International Symposium of the Society of Core Analysts* (Napa valley, CA) (2013).
7. Ghadimi A, Saidur R, Metselaar HSC. A review of nanofuid stability properties and characterization in stationary conditions. *Int J Heat Mass Transfer.* (2011) **54**:4051–68. doi: 10.1016/j.ijheatmasstransfer.2011.04.014
8. Rubilar O, Rai M, Tortella G, Diez MC, Seabra AB, Durán N. Biogenic nanoparticles: copper, copper oxides, copper sulphides, complex copper nanostructures and their applications. *Biotechnol Lett.* (2013) **35**:1365–75. doi: 10.1007/s10529-013-1239-x
9. Tungittiplakorn W, Lion LW, Cohen C, Kim J. Engineered polymeric nanoparticles for soil remediation. *Environ Sci Technol.* (2004) **38**:1605–10. doi: 10.1021/es0348997
10. Kong X, Ohadi MM. Applications of micro and nano technologies in the oil and gas industry - overview of the recent progress. In: *Paper SPE 138241-MS*

Presented at Abu Dhabi International Petroleum Exhibition and Conference. Abu Dhabi (2010).
11. Li S, Hendraningrat L, Torsæter O. Improved oil recovery by hydrophilic silica nanoparticles suspension: 2-phase flow experimental studies. In: *IPTC-16707-MS. Presented at the International Petroleum Technology Conference*. Beijing (2013).
12. Miranda CR, De Lara LS, Tonetto BX. Stability and mobility of functionalized silica nanoparticles for enhanced oil recovery application. In: *SPE 157033-MS presented* at: *SPE International Oilfield Nanotechnology Conference and Exhibition*. Noordwijk (2012).
13. Li S, Hadia NJ, Lau HC, Torsaeter O, Stubbs LP, Ng QH. Silica nanoparticles suspension for enhanced oil recovery: stability behavior and flow visualization. In: *Presented at the SPE Europec featured at the 80th EAGE Conference and Exhibition*. Copenhagen (2018).
14. Bayet AE, Junin R, Samsuri A, Piroozian A, Hokmabadi M. Impact of metal oxide nanoparticles on enhanced oil recovery from limestone media at several temperatures. *Energy Fuels*. (2014) **28**:6255–66. doi: 10.1021/ef5013616
15. Jiang R, Li K, Horne R. A mechanism study of wettability and interfacial tension for eor using silica nanoparticles. In: *Presented at the SPE Annual Technical Conference and Exhibition.* San Antonio, TX (2017). doi: 10.2118/187096-MS
16. Joonaki E, Ghanaatian S. The application of nanofluids for enhanced oil recovery: effects on interfacial tension and coreflooding process. *Petroleum Sci Technol*. (2014) **32**:2599–607. doi: 10.1080/10916466.2013.855228
17. Lu T, Li Z, Zhou Y, Zhang C. Enhanced oil recovery of low-permeability cores by SiO2 nanofluid. *Energy Fuels*. (2017) **31**:5612–21. doi: 10.1021/acs.energyfuels.7b00144
18. Wasan DT, Nikolov A. Spreading of nanofluids on solids. *J Nat.* (2003) **423**:156–9. doi: 10.1038/nature01591
19. Chengara A, Nikolov A, Wasan DT, Trokhymchuk A, Henderson D. Spreading of nanofluids driven by the structural disjoining pressure gradient. *J Colloid Interf Sci.* (2004) **280**:192–201. doi: 10.1016/j.jcis.2004.07.005
20. Wasan DT, Nikolov A, Kondiparty K. The wetting and spreading of nanofluids on solids: Role of the structural disjoining pressure. *Curr Opin Colloid Interf Sci.* (2011) **16**:344–9. doi: 10.1016/j.cocis.2011.02.001
21. McElfresh P, Holcomb D, Ector D. Application of Nanofluid Technology to Improve Recovery in Oil and Gas Wells. In *Presented at the SPE International Oilfield Nanotechnology Conference and Exhibition.* Noordwijk (2012). doi: 10.2118/154827-MS
22. Kartic KC, Fogler HS. *Migrations of Fines in Porous Media*. Dordrecht: Kluwer Academic Publishers (1998).
23. Zhang T, Murphy M, Yu H, Bagaria HG, Huh C, Bryant SL. Investigation of Nanoparticle Adsorption during Transport in Porous Media. In: *Paper was Prepared for Presentation at the SPE ATCE.* New Orleans (2013). doi: 10.2118/166346-MS
24. Ju B, Dai S, Luan Z, Zhu T, Su X, Qiu X. A study of wettability and permeability change caused by adsorption of nanometer structured polysilicon on the surface of porous media. In: *Presented at the SPE Asia Pacific Oil and Gas Conference and Exhibition*. Melbourne, VIC (2002).
25. Li S, Genys M, Wang K, Torsæter O. Experimental study of wettability alteration during nanofluid enhanced oil recovery process and its effect on oil recovery. In: *Presented at the SPE Reservoir Characterisation and Simulation Conference and Exhibition*. Abu Dhabi (2015).
26. Baek Y, Kang J, Theato P, Yoon J. Measuring hydrophilicity of RO membranes by contact angles via sessile drop and captive bubble method: a comparative study. *Desalination.* (2012) 303:23–8. doi: 10.1016/j.desal.2012.07.006
27. Anderson WG. Wettability literature survey –Part 2: Wettability measurement. *J Pet Technol.* (1986) **38**:1246–62. doi: 10.2118/13933-PA
28. Lau HC, Davis CL. Laboratory studies of plugging and clean-up of production screens in horizontal wellbores. In: *Presented at the SPE Annual Technical Conference and Exhibition*. San Antonio, TX (1997).

Conflict of Interest Statement: The authors declare that the research was conducted in the absence of any commercial or financial relationships that could be construed as a potential conflict of interest.

frontiers in Physics

ORIGINAL RESEARCH
published: 30 May 2019
doi: 10.3389/fphy.2019.00071

Determination of the Effective Viscosity of Non-newtonian Fluids Flowing Through Porous Media

Ursin Eberhard[1], Hansjoerg J. Seybold[1], Marius Floriancic[1], Pascal Bertsch[1], Joaquin Jiménez-Martínez[1,2], José S. Andrade Jr.[3] and Markus Holzner[1]*

[1] ETH Zürich, Zurich, Switzerland, [2] Eawag, Dübendorf, Switzerland, [3] Departamento de Física, Universidade Federal do Ceara, Fortaleza, Brazil

OPEN ACCESS

Edited by:
Alex Hansen,
Norwegian University of Science and Technology, Norway

Reviewed by:
Laurent Talon,
UMR7608 Fluides, Automatique et Systèmes Thermiques (FAST), France
Santanu Sinha,
Beijing Computational Science Research Center, China

***Correspondence:**
Ursin Eberhard
ursine@student.ethz.ch

Specialty section:
This article was submitted to Interdisciplinary Physics, a section of the journal Frontiers in Physics

Received: 20 December 2018
Accepted: 23 April 2019
Published: 30 May 2019

Citation:
Eberhard U, Seybold HJ, Floriancic M, Bertsch P, Jiménez-Martínez J, Andrade JS Jr and Holzner M (2019) Determination of the Effective Viscosity of Non-newtonian Fluids Flowing Through Porous Media. Front. Phys. 7:71. doi: 10.3389/fphy.2019.00071

When non-Newtonian fluids flow through porous media, the topology of the pore space leads to a broad range of flow velocities and shear rates. Consequently, the local viscosity of the fluid also varies in space with a non-linear dependence on the Darcy velocity. Therefore, an effective viscosity μ_{eff} is usually used to describe the flow at the Darcy scale. For most non-Newtonian flows the rheology of the fluid can be described by a (non linear) function of the shear rate. Current approaches estimate the effective viscosity by first calculating an effective shear rate mainly by adopting a power-law model for the rheology and including an empirical correction factor. In a second step this averaged shear rate is used together with the real rheology of the fluid to calculate μ_{eff}. In this work, we derive a semi-analytical expression for the local viscosity profile using a Carreau type fluid, which is a more broadly applicable model than the power-law model. By solving the flow equations in a circular cross section of a capillary we are able to calculate the average viscous resistance $\langle\mu\rangle$ directly as a spatial average of the local viscosity. This approach circumvents the use of classical capillary bundle models and allows to upscale the viscosity distribution in a pore with a mean pore size to the Darcy scale. Different from commonly used capillary bundle models, the presented approach does neither require tortuosity nor permeability as input parameters. Consequently, our model only uses the characteristic length scale of the porous media and does not require empirical coefficients. The comparison of the proposed model with flow cell experiments conducted in a packed bed of monodisperse spherical beads shows, that our approach performs well by only using the physical rheology of the fluid, the porosity and the estimated mean pore size, without the need to determine an effective shear rate. The good agreement of our model with flow experiments and existing models suggests that the mean viscosity $\langle\mu\rangle$ is a good estimate for the effective Darcy viscosity μ_{eff} providing physical insight into upscaling of non-Newtonian flows in porous media.

Keywords: non-newtonian fluids, porous media, flow profile, shear rate, effective viscosity

1. INTRODUCTION

Flow through porous media is ubiquitous in many natural and industrial systems. Examples include flow through biological tissues, blood vessels and bones [1–3] or through soils, sediments and rocks, with long-standing interest in hydrology [4, 5], petroleum [6], and chemical engineering [7–9]. At low Reynolds numbers (Re$\ll$1) the bulk flow of a Newtonian fluid flowing through porous media is described by Darcy's law

$$q = \frac{\kappa}{\mu}\frac{\Delta p}{L}, \tag{1}$$

where q is the mean flow rate per unit area, also called Darcy velocity and μ is the dynamic viscosity. The variable κ is the permeability and $\Delta p/L$ is the pressure drop over the distance L. The proportionality constant $K = \kappa/\mu$ is called hydraulic conductivity and can be derived from Stokes' equation assuming a linear relation between the viscous forces and the flow velocity [10].

While Darcy's law is a sound description for the bulk behavior of a fluid whose viscosity μ is constant, many relevant fluids in e.g., in food [11–13] and petroleum [14, 15] industry, show a much more complex constitutive law. For most of these so-called non-Newtonian fluids, the viscosity can be described by a nonlinear function of the stress-strain rate tensor $\mathbf{E}$ or more specifically its first principal invariant $\dot{\gamma} = \frac{1}{2}\sqrt{\mathbf{E}:\mathbf{E}}$ [16]. Due to the heterogeneity of the flow velocities in the interstitial pore space, shear rates vary considerably inside the porous media. For non-Newtonian flows the coupling of the constitutive equations with the flow field leads to a spatial variable viscous resistance. Consequently, the relation between Darcy velocity and pressure drop cannot be described by a linear function anymore as in the case of Newtonian fluids. In order to obtain a bulk equation for the flow that is linear in the pressure drop, an effective viscosity μ_{eff}—which itself depends on the flow variables—must be used in order to account for the non-linear effects i.e.,

$$q = \frac{\kappa}{\mu_{\text{eff}}}\frac{\Delta p}{L}. \tag{2}$$

Here we assumed that the permeability κ is a characteristic constant representing the complexity of the pore space alone. Several empirical and semi-empirical models have been proposed to estimate μ_{eff} [17–23]. Most of these models start from a capillary bundle representation of the different flow paths through a porous medium and estimate an effective shear rate $\dot{\gamma}_{\text{eff}}$ by comparing the flow rate of a power-law fluid with that of a Newtonian Poiseuille flow [24] (see also SI). Although analytical solutions can be derived to determine $\dot{\gamma}_{\text{eff}}$ for power-law rheologies, previous studies proposed various empirical correction factors [19, 20] to relate Darcy velocity to the effective shear rate. The effective shear rate $\dot{\gamma}_{\text{eff}}$ is then inserted into the constitutive law of the fluid of interest $\mu(\dot{\gamma})$ to obtain an effective viscosity μ_{eff}. This approach requires an empirical factor to relate q to $\dot{\gamma}_{\text{eff}}$, which can vary over several orders of magnitude [25, 26], depending on the properties of the fluid, the tortuosity and the permeability. This suggests that the above assumptions are questionable. Additionally most of these models predict a linear relationship between the effective shear rate and the Darcy velocity.

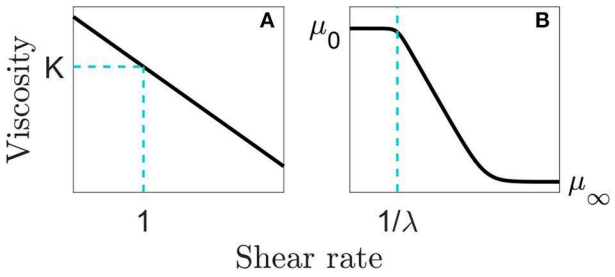

FIGURE 1 | Sketch of two shear thinning rheologies: **(A)** pure power-law model with two parameters K and n, **(B)** Carreau model with five parameters μ_0, μ_∞, λ, n and α.

In this manuscript we show that for a Carreau fluid [27], the local viscosity can be derived directly from the fluid's constitutive law and the velocity profile in a mean pore size, using a circular capillary to mimic the flow at pore scale. Contrary to commonly used capillary bundle models, our approach does neither require the knowledge of the tortuosity nor of the permeability. The capillary is only used to calculate a fully developed average flow profile. Finally, we calculate the mean viscous resistance by spatially averaging the local viscosity $\langle\mu\rangle$. Comparisons of our results with flow cell experiments and existing models show that $\langle\mu\rangle$ is a good estimate for μ_{eff}.

2. METHODOLOGY

2.1. Characterization of the Fluid

In order to model the flow of a non-Newtonian fluid, we first need to characterize its constitutive behavior. For most non-Newtonian fluids the constitutive relation between the deviatoric stress tensor $\mathbf{T}$ and the applied strain rates $\mathbf{E}$ can be described by a time independent scalar function $\mu = \mu(\dot{\gamma})$, such that $T = 2\mu(\dot{\gamma})\mathbf{E}$. Here μ is a generalized viscosity which depends only on the first principal invariant $\dot{\gamma} = \frac{1}{2}\sqrt{\mathbf{E}:\mathbf{E}}$ of the stress-strain rate tensor $\mathbf{E}$ [16]. In the case of simple shear flow $\dot{\gamma}$ reduces to the shear rate. Many functional forms for $\mu(\dot{\gamma})$ have been proposed, where the most common ones are the power-law model (**Figure 1A**), the Carreau model (**Figure 1B**), the Cross model or the Herschel-Bulkley model [18, 28].

The power-law model is described by

$$\mu(\dot{\gamma}) = K\dot{\gamma}^{n-1}, \tag{3}$$

where K is the viscosity at the shear rate $\dot{\gamma} = 1\ \text{s}^{-1}$ and n is the power-law index defining the steepness of the shear-thinning decay for $n < 1$ (see **Figure 1**). Due to its simplicity, the power-law model is the most commonly used rheology to derive analytical expressions. However, the unbounded power-law model has two drawbacks: first the model does not capture the linear shear-strain relation for very low and very high shear rates, that are prevalent in most natural systems, and second

the viscosity curve becomes singular in the limit of vanishing shear. Consequently constitutive models which "blend" a power-law regime between a Newtonian behavior at low and high shear rates—such as the Carreau model—have been proposed for real world applications. The constitutive law of a Carreau fluid is parametrized by

$$\mu(\dot{\gamma}) = (\mu_\infty + (\mu_0 - \mu_\infty)(1 + (\lambda\dot{\gamma})^\alpha)^{\frac{n-1}{\alpha}}), \tag{4}$$

where n is the power-law exponent, μ_0 and μ_∞ are the limits of the viscosity at zero and infinite shear and λ is the reciprocal of the critical shear rate, which describes the onset of the shear thinning regime. The parameter α describes how smoothly the Newtonian regime blends into the power-law.

2.2. Current Models

Most commonly applied models to estimate μ_{eff} can be derived by equating the flow rate of a Poiseuille flow [29] with the flow rate of a power-law fluid [30]

$$Q_{\text{Poiseuille}} = Q_{\text{power-law}}. \tag{5}$$

For a circular capillary with radius R one obtains

$$\frac{\pi}{8\mu}\frac{\Delta p}{L}R^4 = \frac{\pi n}{3n+1}\left(\frac{1}{2K}\right)^{\frac{1}{n}}\left(\frac{\Delta p}{L}\right)^{\frac{1}{n}}R^{\frac{3n+1}{n}}, \tag{6}$$

where we used

$$Q_{\text{power-law}} = \frac{\pi n}{3n+1}\left(\frac{1}{2K}\right)^{\frac{1}{n}}\left(\frac{\Delta p}{L}\right)^{\frac{1}{n}}R^{\frac{3n+1}{n}}, \tag{7}$$

which is also known as the Rabinowitsch equation [30] to describe the flow rate of a power-law fluid in a capillary. Solving Equation (6) for μ, a power-law viscosity $\mu_{\text{power-law}}$ can be defined as

$$\mu_{\text{power-law}} = \frac{1}{8\,(2K)^{-\frac{1}{n}}}\frac{3n+1}{n}\left(\frac{\Delta p}{L}\right)^{\frac{n-1}{n}}R^{\frac{n-1}{n}}. \tag{8}$$

Equation (8) can be simplified to

$$\mu_{\text{power-law}} = K\frac{3n+1}{4n}\left(\frac{\Delta p}{2KL}\right)^{\frac{n-1}{n}}R^{\frac{n-1}{n}}. \tag{9}$$

This power-law viscosity corresponds to the viscosity of a Newtonian fluid which would have given the same pressure drop $\Delta p/L$ along a capillary.

For a power-law constitutive relation $\mu = K\dot{\gamma}^{n-1}$ Equation (9) can be inverted to obtain an effective shear rate $\dot{\gamma}_{\text{eff}}$

$$\dot{\gamma}_{\text{eff}} = \left(\frac{3n+1}{4n}\right)^{\frac{1}{n-1}}\left(\frac{\Delta pR}{2KL}\right)^{\frac{1}{n}}. \tag{10}$$

Using the Rabinowitsch equation, we can express the term $\left(\frac{\Delta p}{KL}\right)^{\frac{1}{n}}$ as

$$\left(\frac{\Delta p}{KL}\right)^{\frac{1}{n}} = 2^{\frac{1}{n}}\frac{3n+1}{n}R^{-\frac{n+1}{n}}q_{\text{cap}}, \tag{11}$$

where q_{cap} is the mean capillary velocity defined as $Q_{\text{power-law}}/(\pi R^2)$. Furthermore, the mean capillary velocity q_{cap} can be defined as the Darcy velocity divided by the porosity, $q_{\text{cap}} = \frac{q}{\Phi}$. Following Savins [31], the radius R_{eq} can be expressed by

$$R_{\text{eq}} = \sqrt{\frac{8\kappa\zeta}{\Phi}}, \tag{12}$$

where ζ is the tortuosity, R_{eq} is the radius of a capillary in the capillary bundle model (see detailed derivation in **Supplementary Information**). Inserting R_{eq} into Equation (10) then yields

$$\dot{\gamma}_{\text{eff}} = \frac{1}{\sqrt{\zeta}}\left(\frac{3n+1}{4n}\right)^{\frac{n}{n-1}}\frac{4q}{\sqrt{8\kappa\Phi}}. \tag{13}$$

Empirically it has been found by Cannella et al. [19] that the factor $1/\sqrt{\zeta}$ does not fit realistic data and replaced the term $1/\sqrt{\zeta}$ by a constant C, i.e.,

$$\dot{\gamma}_{\text{eff}} = C\left(\frac{3n+1}{4n}\right)^{\frac{n}{n-1}}\frac{4q}{\sqrt{8\kappa\Phi}}. \tag{14}$$

Hirasaki and Pope [20] proposed to use $C = 1/\sqrt{25/12} \approx 0.69$ by using the tortuosity ζ of packed spheres, which has been widely reported to be 25/12 [32, 33]. Ignoring the tortuosity ζ, Cannella et al. [19] found a factor of $C = 6$ to be suitable to describe many flows in different settings. Additionally, Cannella et al. accounted for unsaturated and multiphase flows by correcting the permeability κ to $\kappa_{\text{r,w}}\kappa$ and the porosity Φ to $S_{\text{w}}\Phi$. Here, $\kappa_{\text{r,w}}$ is the relative permeability and S_{w} is the saturation. Consequently, the effective shear rate according to Cannella et al. [19, 26] is given by

$$\dot{\gamma}_{\text{eff}} = 6\left[\frac{3n+1}{4n}\right]^{\frac{n}{n-1}}\left[\frac{4}{\sqrt{8}}\frac{q}{\sqrt{\kappa_{\text{r,w}}\kappa S_{\text{w}}\Phi}}\right]. \tag{15}$$

Cannella et al. then used this effective shear rate together with a constitutive law $\mu(\dot{\gamma})$ to calculate an effective viscosity. For this last step, mostly the Carreau model has been used due to its ability to fit a wide range of different rheologies.

Other models, that have been developed, are using more complex rheological descriptions of the fluid. Nevertheless, they generally require to correct the analytical solution with empirical factors to achieve reasonable agreement with experimental data [17].

2.3. Average Viscosity Approach

Here we present a new approach to estimate μ_{eff} by solving directly for the viscosity profile of a fully developed Carreau flow inside a single capillary of radius R that mimics a mean pore with a mean flow rate of $\frac{q}{\Phi}$. This approach assumes that a single constitutive law can be used both on the pore as well as on Darcy scale. This assumption is supported by the observation that even at pore scale, the viscosity distribution covers the whole range of viscosities given by the Carreau model equation. Consequently a single power-law is insufficient to describe the transitional behavior at the low and high shear limits.The onset of the power-law regime occurs at a characteristic combination of the Darcy velocity and the pore size. Therefore, it is important to determine at which Darcy velocity the onset of the non-linearities of the fluid starts to matter for a given pore size.

The Carreau model allows to obtain an average viscosity profile in a pore without invoking an effective shear rate and an intermediate power-law rheology. Note that the Carreau model includes the critical shear rate $1/\lambda$, which defines the onset of the power-law regime, see **Figure 1**. To model the flow of a Carreau fluid we perform the following steps:

(*i*) We estimate the characteristic pore size in order to set the diameter of the average pore for which we examine the flow profile. This characteristic pore size can be readily obtained from an pore- or grain-size distribution. (*ii*) We then compute the velocity profile as a function of the flow rate. (*iii*) The velocity profile obtained in the previous step can subsequently be used to determine local shear rates $\dot{\gamma}(r) = \mathrm{d}u(r)/\mathrm{d}r$. (*iv*) Combining the shear and the Carreau rheology (Equation 4) we obtain the local viscosity distribution $\mu(\dot{\gamma}(r))$ in a cross section of the capillary. (*v*) Finally, we use the local viscosity, to estimate the effective viscosity μ_{eff} by averaging the viscosity profile over the cross section of the capillary.

In order to apply this concept of a mean profile in a pore, we use a capillary with a circular cross section and assume a fully developed flow profile. The steady state Navier-Stokes equation at low Reynolds numbers in a circular capillary can be written as

$$\frac{1}{r}\frac{\mathrm{d}}{\mathrm{d}r}\left(\mu\left(\frac{\mathrm{d}u}{\mathrm{d}r}\right) r\frac{\mathrm{d}u}{\mathrm{d}r}\right) = \frac{\mathrm{d}p}{\mathrm{d}x}, \tag{16}$$

where the pressure gradient along the capillary is constant $\frac{\mathrm{d}p}{\mathrm{d}x} = const$. Integrating with respect to r yields

$$\mu\left(\frac{\mathrm{d}u}{\mathrm{d}r}\right)\frac{\mathrm{d}u}{\mathrm{d}r} = \frac{r}{2}\frac{\mathrm{d}p}{\mathrm{d}x} + K_1. \tag{17}$$

Based on the symmetry of the flow profile, the velocity is maximal along the center line of the capillary at $r = 0$. By definition of a maximum, the shear rate $\dot{\gamma} = \frac{\mathrm{d}u}{\mathrm{d}r}$ vanishes, $\frac{\mathrm{d}u}{\mathrm{d}r}\Big|_{r=0} = 0$, which results in $K_1 = 0$. Thus, Equation (17) simplifies to

$$\mu(\dot{\gamma})\dot{\gamma} = \frac{r}{2}\frac{\mathrm{d}p}{\mathrm{d}x}. \tag{18}$$

Since the pressure drop $\frac{\mathrm{d}p}{\mathrm{d}x}$ along the capillary is assumed to be constant, we can replace it by a reference pressure $p_{\text{ref}} \neq 0$ divided by a reference length scale. Choosing the capillary radius R as characteristic length, we define

$$\frac{1}{2}\frac{\mathrm{d}p}{\mathrm{d}x} = \frac{p_{\text{ref}}}{R}. \tag{19}$$

Then, we insert the reference pressure from Equation (19) into Equation (18) and obtain

$$\mu(\dot{\gamma})\dot{\gamma} = \frac{r}{R}p_{\text{ref}}. \tag{20}$$

Inserting the constitutive law of a Carreau fluid (Equation 4) into (Equation 20) and solving for r yields

$$\boxed{r = \frac{R}{p_{\text{ref}}}\dot{\gamma}\left(\mu_\infty + (\mu_0 - \mu_\infty)(1 + (\lambda\dot{\gamma})^\alpha)^{\frac{n-1}{\alpha}}\right).} \tag{21}$$

This expression can be rewritten by using the boundary condition for the shear rate ($\dot{\gamma}|_{r=R} = -\dot{\gamma}_w$), where $\dot{\gamma}_w$ is the shear rate at the wall of the capillary. Consequently, the reference pressure is given by the following equation:

$$\boxed{p_{\text{ref}} = -\dot{\gamma}_w\left(\mu_\infty + (\mu_0 - \mu_\infty)(1 + (-\lambda\dot{\gamma}_w)^\alpha)^{\frac{n-1}{\alpha}}\right).} \tag{22}$$

In order to obtain an expression for the flow profile $u(r)$ and $\dot{\gamma}_w$, we integrate $r(\dot{\gamma}')$ given by Equation (21) radially with respect to $\dot{\gamma}'$. As the shear rate $\dot{\gamma}'(r)$ is an odd function, the relation $\int_0^{-\dot{\gamma}} \mathrm{d}\dot{\gamma}' = -\int_0^{\dot{\gamma}} \mathrm{d}\dot{\gamma}'$ holds for all r. Consequently, the shear rate $\dot{\gamma}$ will be our free parameter ranging from 0 to $-\dot{\gamma}_w$.

The resulting integral can be expressed as

$$\begin{aligned}
\int_0^{-\dot{\gamma}} r(\dot{\gamma}')\mathrm{d}\dot{\gamma}' &= -\int_0^{\dot{\gamma}} \frac{R}{p_{\text{ref}}}\dot{\gamma}'\mu(\dot{\gamma}')\mathrm{d}\dot{\gamma}' \\
&= -\frac{R}{p_{\text{ref}}}\left[\int_0^{\dot{\gamma}} \mu_\infty\dot{\gamma}'\mathrm{d}\dot{\gamma}' + (\mu_0 - \mu_\infty)\right. \\
&\qquad \left.\int_0^{\dot{\gamma}} \dot{\gamma}'(1 + (\lambda\dot{\gamma}')^\alpha)^{\frac{n-1}{\alpha}}\mathrm{d}\dot{\gamma}'\right] \\
&= -\frac{R}{p_{\text{ref}}}\left[\frac{1}{2}\mu_\infty\dot{\gamma}^2 + \frac{1}{2}(\mu_0 - \mu_\infty)\dot{\gamma}^2\right. \\
&\qquad \left.\times\, {}_2F_1\left(\frac{2}{\alpha}, \frac{1-n}{\alpha}; \frac{2+\alpha}{\alpha}; -(\lambda\dot{\gamma})^\alpha\right)\right] \\
&= -\frac{R\dot{\gamma}^2\mu_\infty}{2p_{\text{ref}}} - \frac{R}{p_{\text{ref}}}(\mu_0 - \mu_\infty)\frac{1}{2}\dot{\gamma}^2 \\
&\qquad \times\, {}_2F_1\left(\frac{2}{\alpha}, \frac{1-n}{\alpha}; \frac{2+\alpha}{\alpha}; -(\lambda\dot{\gamma})^\alpha\right).
\end{aligned} \tag{23}$$

Here ${}_2F_1(a, b; c; z)$ is a hypergeometric function with parameters a, b and c. Further details about the hypergeometric function can be found in the *Handbook of mathematical functions* by M. Abramowitz and I.A. Stegun [34]. Using the chain rule on $\mathrm{d}(r\dot{\gamma}')$, we can rewrite $r(\dot{\gamma}')\mathrm{d}\dot{\gamma}'$ as $\mathrm{d}(r\dot{\gamma}') - \dot{\gamma}'\mathrm{d}r$, which yields

$$r\mathrm{d}\dot{\gamma}' = \mathrm{d}(r\dot{\gamma}') - \mathrm{d}u, \tag{24}$$

where we already substituted $\dot{\gamma}'\mathrm{d}r$ with $\mathrm{d}u$. Performing now the integration with respect to $\dot{\gamma}'$ gives

$$\begin{aligned}\int_0^{-\dot{\gamma}} r(\dot{\gamma}')\mathrm{d}\dot{\gamma}' &= -\int_0^{\dot{\gamma}} \mathrm{d}(r(\dot{\gamma}')\dot{\gamma}') - \int_{u_{\max}}^{u} \mathrm{d}u \\ &= -\frac{R}{p_{\mathrm{ref}}}\dot{\gamma}^2\left(\mu_\infty + (\mu_0-\mu_\infty)(1+(\lambda\dot{\gamma})^\alpha)^{\frac{n-1}{\alpha}}\right) \\ &\quad + u_{\max} - u. \end{aligned} \tag{25}$$

Setting Equation (23) equal to Equation (25) allows to solve for the velocity u inside the capillary (Equation (26)).

$$\boxed{u = u_{\max} - \frac{R\dot{\gamma}^2\mu_\infty}{2p_{\mathrm{ref}}} - \frac{R}{p_{\mathrm{ref}}}(\mu_0-\mu_\infty)\dot{\gamma}^2\left((1+(\lambda\dot{\gamma})^\alpha)^{\frac{n-1}{\alpha}} - \frac{1}{2}{}_2F_1\left(\frac{2}{\alpha},\frac{1-n}{\alpha};\frac{2+\alpha}{\alpha};-(\lambda\dot{\gamma})^\alpha\right)\right)}. \tag{26}$$

Applying the non-slip boundary condition at the wall for velocity ($u|_{r=R} = 0$) and shear ($\dot{\gamma}|_{r=R} = -\dot{\gamma}_w$) finally yields u_{max} as defined in Equation (27).

$$\boxed{u_{\max} = \frac{R\dot{\gamma}_w^2\mu_\infty}{2p_{\mathrm{ref}}} + \frac{R}{p_{\mathrm{ref}}}(\mu_0-\mu_\infty)\dot{\gamma}_w^2\left((1+(-\lambda\dot{\gamma}_w)^\alpha)^{\frac{n-1}{\alpha}} - \frac{1}{2}{}_2F_1\left(\frac{2}{\alpha},\frac{1-n}{\alpha};\frac{2+\alpha}{\alpha};-(-\lambda\dot{\gamma}_w)^\alpha\right)\right)} \tag{27}$$

Therefore, for any given maximum velocity $u_{\max}$ at the center of a capillary, the two Equations (27) and (22) can be solved for the two unknown parameters p_{ref} and $\dot{\gamma}_w$ using a non-linear root finding algorithm. These two parameters can then be inserted into Equations (26) and (21) to obtain the velocity field u and the corresponding radial coordinate r. The remaining free parameter is the shear rate $\dot{\gamma}$, which varies between $-\dot{\gamma}_w$ and 0. Consequently, one can calculate the flow profile $u(r)$ in a capillary of radius R for any $u_{\max}$. The mean capillary velocity q_{profile} is then readily calculated by integrating $u(r)$ over the capillary cross section Ω, i.e.,

$$q_{\mathrm{profile}} = \frac{\int_\Omega u(r)\mathrm{d}A}{\int_\Omega \mathrm{d}A}. \tag{28}$$

To obtain the Darcy velocity, the mean capillary velocity q_{profile} has to be multiplied by the porosity Φ, namely, $q = q_{\mathrm{profile}}\Phi$. Further, we can determine the shear rate profile from $u(r)$ by differentiation using $\dot{\gamma}(r) = \frac{\mathrm{d}u}{\mathrm{d}r}$. In combination with the Carreau model (Equation 4), the shear rate can be used to calculate the local viscosity $\mu(r)$ in a cross section of the capillary from which we can infer the spatial average of $\langle\mu\rangle$ as

$$\langle\mu\rangle = \frac{\int_\Omega \mu(r)\mathrm{d}A}{\int_\Omega \mathrm{d}A}. \tag{29}$$

Based on this formalism, we now propose that the effective viscosity can be appropriately estimated directly from the average viscosity $\langle\mu\rangle$ without using an effective shear rate $\dot{\gamma}_{\mathrm{eff}}$. Our approach is purely based on the physical constitutive law of the fluid (here represented by a Carreau rheology) and the solution of the momentum equation of such a non-Newtonian fluid in a circular capillary.

In order to test the hypothesis that μ_{eff} is appropriately described by $\langle\mu\rangle$, we benchmark our approach with flow experiments and compare our model's prediction with that of Cannella et al. [19] and Hirasaki & Pope [20].

2.4. Experimental Setup

To measure the effective viscosity of a non-Newtonian fluid flowing through porous media we set up a Darcy experiment in a column (405 mm height; 50.3 mm diameter) of monodisperse glass beads with a diameter of 8 mm (**Figure 2**). A constant static pressure was applied using a Boyle-Mariotte bottle connected to a pressure controller (*Fluigent MFCS^{TM}-EZ*). The flow rate was determined by measuring the weight of the outflowing fluid over time, while the pressure drop was measured with two pressure sensors (*Keller, PAA-36XW*) connected to the Darcy column. The porosity of the packed bed was $\Phi = 0.4$. Before determining the effective viscosity of the non-Newtonian solution we measured the permeability κ of the porous medium using a Newtonian solution (66.7 vol% Glycerol + 33.3 vol% D.I. water) with a well specified viscosity $\mu_{\mathrm{Newt}} = 0.0266$ Pa · s [35]. We then measured the pressure drop over the length $L = 300$ mm at different flow rates, obtaining five measurements for $q(\Delta P/L)$. Fitting a straight line to the measured data yields $\kappa = 4.4 \cdot 10^{-8}\mathrm{m}^2$ (**Figure 3**).

As a non-Newtonian fluid, we used a solution of 0.05 wt% xanthan gum produced by *Sigma Aldrich*. The rheology curve of the xanthan gum solution was measured with an *Anton Paar MCR 702* rheometer with a double gap DG 26.7 geometry. **Figure 4** shows the dynamic viscosity of our solution as a function of the applied shear rate together with the fitted Carreau model with parameters $\mu_0 = 0.085$ Pa · s, $\mu_\infty = 0.001$ Pa · s, $\lambda = 2$ s, $n = 0.48$ and $\alpha = 0.8$ (Equation 4). Very high shear rates have not been measured, but literature values [36] indicate that the viscosity of xanthan gum solutions approach the viscosity of water at high shear rates.

After characterizing the non-Newtonian fluid's constitutive behavior, we perform the same Darcy experiment for the non-Newtonian solution as in the Newtonian case, measuring the pressure drop at 8 different flow rates. The effective viscosity μ_{eff} of the non-Newtonian fluid was then computed from the measured Darcy velocity q, the measured pressure drop $\Delta p/L$ and the previously measured permeability κ according to

$$\mu_{\mathrm{eff}} = \frac{\kappa}{q}\frac{\Delta p}{L}. \tag{30}$$

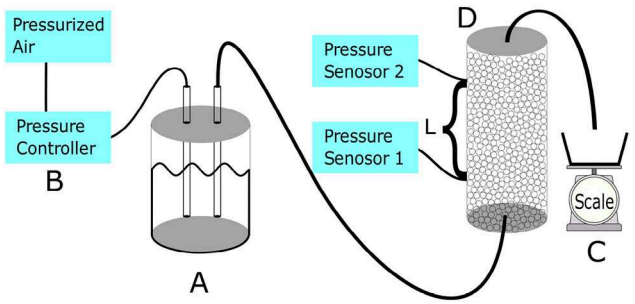

FIGURE 2 | Scheme of the Darcy column experimental setup: constant flow is imposed from the Boyle-Mariotte bottle **(A)** by compressed air from pressure controller **(B)**. We measured the outflow on a scale **(C)** and the pressure drop at the column with two sensors **(D)**, where the distance between the sensors defines L.

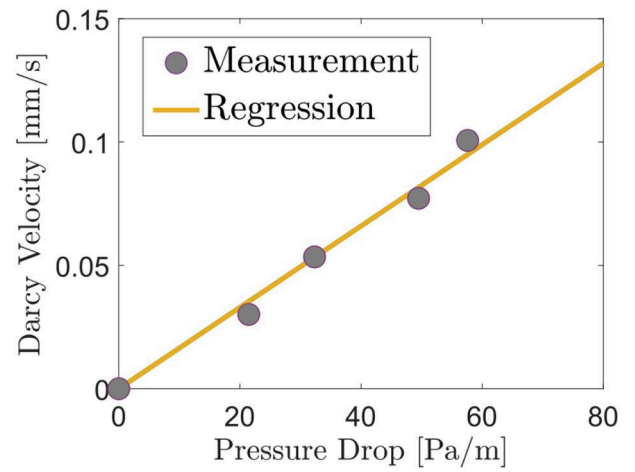

FIGURE 3 | Darcy velocity q vs. pressure drop Δp for the Newtonian fluid (66.7 vol% Glycerol + 33.3 vol% D.I. water) used in the permeability estimation, $\kappa = K\mu_{Newt} = 4.4 \cdot 10^{-8}\text{m}^2$.

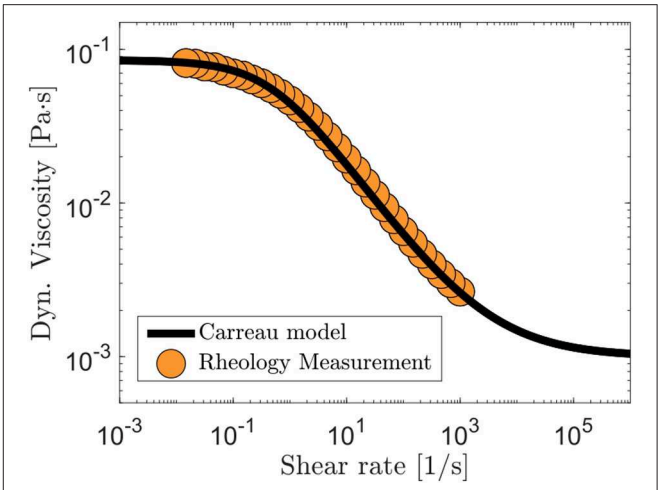

FIGURE 4 | Measured rheology of a 0.05 wt% xanthan gum solution, with the best fit of the Carreau model for the parameters: $\mu_0 = 0.085$ Pa · s, $\mu_\infty = 0.001$ Pa · s, $\lambda = 2$ s, $n = 0.48$ and $\alpha = 0.8$. Very high shear rates have not been measured. Literature values indicate that μ_∞ for xanthan gum solutions approximates water, i.e., $\mu_\infty = 0.001$ Pa s [36].

3. RESULTS AND DISCUSSION

Before discussing the upscaling of our capillary model and the averaging of the viscosity approach we analyze how the profiles of velocity, shear and ultimately viscosity behave inside a single capillary. **Figure 5** shows the velocity, the shear rate and the viscosity profiles, normalized by the respective means, for a capillary of radius 1 mm for two flow rates $q_{\text{profile}} = 0.003$ mm/s and $q_{\text{profile}} = 3.7$ mm/s. For the rheology of the fluid we use the Careau model with parameters $\mu_0 = 0.085$ Pa · s, $\mu_\infty = 0.001$ Pa · s, $\lambda = 2$ s, $n = 0.48$ and $\alpha = 0.8$. The profiles have been calculated numerically by solving Equations (22) and (27) to determine p_{ref} and $\dot{\gamma}_w$ together with Equations (21) and (26) as described above.

For the low flow rate $q_{\text{profile}} = 0.003$ mm/s, the shear rate does not exceed the critical shear rate $\dot{\gamma}_{\text{crit}} = 1/\lambda$ at any radial position in the capillary. Consequently the viscosity is almost constant at μ_0 resulting in a Newtonian flow behavior and a parabolic velocity profile. Here the shear rate increases linearly from $\dot{\gamma} = 0$ at the center of the capillary to $\dot{\gamma} = \dot{\gamma}_w$ at the wall. As soon as the flow rate exceeds a certain threshold, nonlinear effects become important and the velocity profile flattens at the center (c.f. purple line in **Figure 5A**). This nonlinear behavior can also be observed in the shear rates $\dot{\gamma} = \text{d}u/\text{d}r$, as well as in the local viscosity $\mu(r)$ which starts to develop a very distinct maximum at the center of the capillary, **Figure 5C**. As a result, first averaging the shear rate and then calculating the viscosity leads to a significantly different results than calculating the average viscosity itself, namely $\mu(\langle\dot{\gamma}\rangle) \neq \langle\mu(\dot{\gamma})\rangle$. The models of Cannella et al. and Hirasaki & Pope assume a pure power-law rheology for the calculations of the effective shear rate $\dot{\gamma}_{\text{eff}}$ at all flow rates (Equations 7, 11). This does not agree with the bahavior shown in **Figures 5A–C**, which indicates that the profile changes from a Newtonian to a nonlinear behavior depending on the applied flow rate.

After discussing the problem of averaging shear and viscosity in a single capillary, we now benchmark the average viscosity approach. We compare our model estimates with our experimental results and the predictions of the models by Cannella et al. and Hirasaki & Pope.

Figure 6 shows the measurement of the effective viscosity as a function of the Darcy velocity using Equation (30) (red diamonds). The predictions of the models by Cannella et al. ($C = 6$) and Hirasaki & Pope ($C = 0.69$) are marked in orange and green, respectively. The solid violet line represents the prediction of our average viscosity model using a pore radius $R = 0.62$ mm. The characteristic pore radius R used in **Figure 6** has been calculated from the bead diameter as the maximal radius of the void space between three beads that are in contact with each other (see **Figure 7**). Consequently we find for a bead diameter of $d = 8$ mm a capillary radius of $R = 0.62$ mm.

While Cannella et al.'s model does not capture the experimental measurements, the model of Hirasaki & Pope

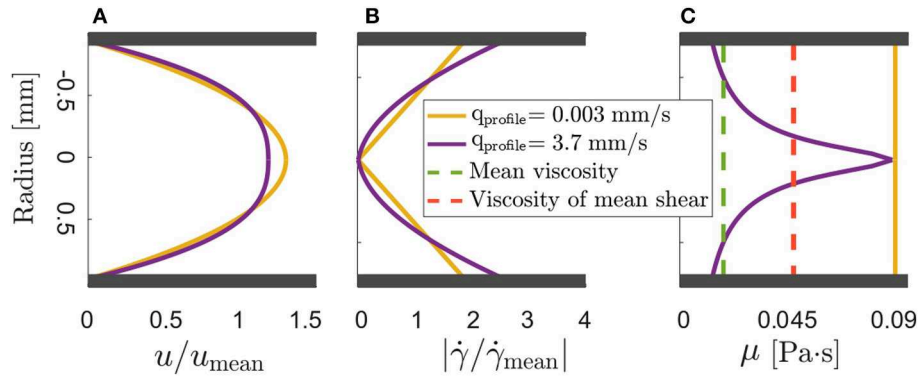

FIGURE 5 | (A) Normalized flow and **(B)** shear profile for flow in a capillary with an exemplary radius of 1 mm. The fluid is described by the Carreau model using the fitting parameters for the measured rheology. **(C)** Viscosity distribution $\mu(\dot{\gamma}(r))$, including the viscosity of the mean shear rate and the mean viscosity for a mean velocity of $q_{\mathrm{profile}} = 3.7$ mm/s.

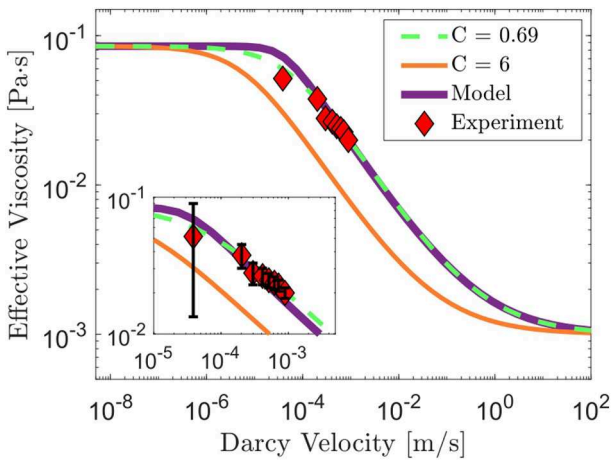

FIGURE 6 | Comparison of the experimental measurements (red diamonds) with the proposed model (purple solid line). The model is calculated for a pipe of radius $R = 0.62$ mm. Additionally, the correlations of Cannella et al. [19] ($C = 6$) and Hirasaki and Pope [20] ($C = 0.69$) are shown. The latter was defined from packed beds of monodisperse spheres.

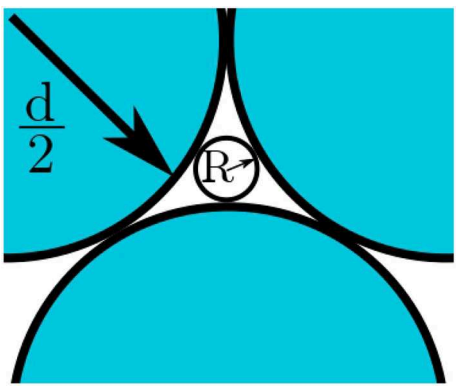

FIGURE 7 | Characteristic pore size with radius R between three glass beads with radius $d/2$ (blue circles).

fits the experimental data equally well as the average viscosity model. Nevertheless, all three models agree in terms of slope in the shear thinning power-law regime. This is consistent with the observation of Teeuw & Hesselink [22], who found that the power-law exponent of the microscopic rheology equals the exponent of the effective viscosity μ_{eff} as function of the Darcy velocity q [19]. The major difference in the behavior of our model compared to the approach of Hirasaki & Pope [20] is found at the transition from the low shear Newtonian regime to the power-law regime. Here the former model predicts a slightly smoother transition than the average viscosity formulation. However, the error bars shown in the inset of **Figure 6** reveal that this region also has the highest uncertainty due to the noise in the pressure measurements. Consequently, we cannot conclude that the proposed model, using an average viscosity, captures the transition between the low shear Newtonian regime and the power-law regime better than the previous models. Nevertheless, in favor of the proposed model, the linear relation in Equation (13) assumed for $\dot{\gamma}_{\mathrm{eff}} \sim q$ used by both Cannella et al. and Hirasaki & Pope does not reflect the non-linear behavior of the profiles shown in **Figure 5** for a single capillary.

A major challenge of models based on effective shear rates is the need of an empirical factor to compute $\dot{\gamma}_{\mathrm{eff}}$. This, so-called C-factor, can vary over several orders of magnitude [25, 26]. This problem is especially evident considering the fact that the shape factor varies for different fluids and pore geometries [26]. While the shape-factor C is used to fit the onset of the power-law regime in μ_{eff} against Darcy velocity plot, our model describes this transition intrinsically through the Carreau parameter $1/\lambda$.

Comparing the models of Cannella et al. and Hirasaki & Pope reveals that the empirical shape factor C of Cannella et al.'s model corresponds to $C = 1/\sqrt{\zeta}$ in the model of Hirasaki & Pope. Using the tortuosity of $\zeta = 25/12$ for a packed bed of uniform spheres [32, 33] Hirasaki & Pope arrive at a shape factor of $C = 0.69$. However, Cannella et al. later found empirically that this tortuosity dependence does not hold in many different settings

and proposed $C = 6$ as a generally good value. However if we calculate the tortuosity associated with this empirical value we obtain a tortuosity $\zeta = 0.03$, which is inconsistent with the geometric interpretation of ζ as the elongation of flow paths in a capillary bundle model. Another problematic point of the models of Hirasaki & Pope and Cannella et al. is that the tortuosity should not matter at all for the determination of the effective viscosity as the viscosity profile does not change along the capillary. Hence the viscosity, respectively the effective shear rate, should not change with the elongation of the flow paths contrary to Equation (13).

In contrast to most currently used capillary bundle models which try to mimic the flow paths inside porous media, our average viscosity approach uses a capillary only to calculate a fully developed flow profile in a single pore. Generally, we find good agreement with experimental measurements and with previous models, provided that the free parameters have been determined from experimental data [16, 19, 32, 33, 37–39]. Averaging the viscosity over the mean flow profile has several advantages. First of all, the model only includes the physical rheology of the fluid and does not need a singular power-law model as an intermediate step to calculate an effective shear rate $\dot{\gamma}_{\text{eff}}$. This eliminates the problem that arises from $\mu(\langle\dot{\gamma}\rangle) \neq \langle\mu(\dot{\gamma})\rangle$. Using the mean viscosity to describe the flow resistance of the fluid is physically more intuitive than using an effective quantity derived from comparisons of non-Newtonian flows with Newtonian behavior. Additionally our model only requires a characteristic geometric length factor rather than an empirical shape factor which depends on geometric properties as well as on the fluid. Our characteristic length scale is a property of the porous medium alone and can be estimated independently from permeability, porosity or tortuosity using e.g., pore or grain size distributions. Furthermore, our approach includes the parameter λ, which describes the onset of the shear thinning regime and is given by the rheology. Consequently, the average viscosity approach provides a consistent nonlinear upscaling of a flow profile in a pore with mean pore size and does not require tortuosity [40].

4. CONCLUSIONS

In summary, we presented a new approach to extend Darcy's law to Carreau fluids using the mean viscosity over a representative capillary as the effective flow resistance. The major advantage of the new model is that it does not require an intermediate effective shear rate and calculates the average viscosity directly using the microscopic constitutive law of the fluid. This approach allows us to upscale the average viscosity of a single pore with a mean pore size to a Darcy scale. This procedure also avoids an empirical shape parameter, which has been replaced by a characteristic length scale derived from the physical property of the porous medium itself. Furthermore, the proposed approach does not require commonly made capillary bundle assumptions like the elongation of a capillary by using the tortuosity and it does not require the permeability [40] to estimate an equivalent capillary diameter. Experimental measurements for a flow through a packed bed of monodisperse beads and comparison with other non-Newtonian capillary models reveal that the average viscosity provides a robust estimate for the effective Darcy viscosity μ_{eff}.

AUTHOR CONTRIBUTIONS

UE designed the research, carried out the experiment, performed the calculations, and analyzed the data. HS helped with the mathematical derivations and the analysis. MF assisted with the experimental setup and PB measured the rheology. JJ-M and JA supported by discussions and consulting. UE wrote the paper with input from all co-authors. MH supervised the research.

ACKNOWLEDGMENTS

We kindly acknowledge Prof. Roman Stocker, Ela Burmeister, and Dr. Eleonora Secchi from the Department of Civil, Environmental and Geomatic Engineering at ETH Zürich for providing access to laboratory equipment and material. Furthermore we acknowledge Patrick Rühs from the Department of Materials and Prof. Peter Fischer from the Department for Health Sciences and Technology at ETH Zürich for suggestions and discussions. Additionally we acknowledge Nicola Gruber for cross-checking the mathematical derivations and Marius M. Neamtu Halic from the Department of Civil, Environmental and Geomatic Engineering at ETH Zürich proofreading the manuscript. JA thanks the Brazilian agencies CNPq, CAPES and FUNCAP for financial support.

SUPPLEMENTARY MATERIAL

The Supplementary Material for this article can be found online at: https://www.frontiersin.org/articles/10.3389/fphy.2019.00071/full#supplementary-material

REFERENCES

1. Khaled ARA, Vafai K. The role of porous media in modeling flow and heat transfer in biological tissues. *Int J Heat Mass Tran.* (2003) **46**:4989–5003. doi: 10.1016/S0017-9310(03)00301-6
2. Rejniak KA, Estrella V, Chen T, Cohen AS, Lloyd M, Morse DL. The role of tumor tissue architecture in treatment penetration and efficacy: an integrative study. *Front Oncol.* (2013) **3**:111. doi: 10.3389/fonc.2013.00111
3. Cowin SC, Cardoso L. Blood and interstitial flow in the hierarchical pore space architecture of bone tissue. *J Biomech.* (2015) **48**:842–54. doi: 10.1016/j.jbiomech.2014.12.013
4. Mackay DM, Cherry JA. Groundwater contamination: pump-and-treat remediation. *Environ Sci Technol.* (1989) **23**:630–6. doi: 10.1021/es00064a001
5. Valdes-Abellan J, Jiménez-Martínez J, Candela L, Jacques D, Kohfahl C, Tamoh K. Reactive transport modelling to infer changes in soil hydraulic properties induced by non-conventional water irrigation. *J Hydrol.* (2017) **549**:114–24. doi: 10.1016/j.jhydrol.2017.03.061
6. Middleton RS, Carey JW, Currier RP, Hyman JD, Kang Q, Karra S, et al. Shale and non-aqueous fracturing fluids: Opportunities and challenges for supercritical CO_2. *Appl Energy.* (2015) **147**:500–9. doi: 10.1016/j.apenergy.2015.03.023

7. Britton MM, Sederman AJ, Taylor AF, Scott SK, Gladden LF. Magnetic resonance imaging of flow-distributed oscillations. *J Phys Chem A*. (2005) **109**:8306–13. doi: 10.1021/jp053063i
8. Wakao N, Kagei S. *Heat and Mass Transfer in Packed Beds*. Vol. 1. New York, NY: Taylor & Francis (1982).
9. Jackson R. *Transport in Porous Catalysts*. New York, NY: Elsevier Scientific Pub. Co., distributors for the U.S. and Canada, Elsevier North-Holland Amsterdam (1977).
10. Whitaker S. Flow in porous media I: a theoretical derivation of Darcy's law. *Transport Porous Med*. (1986) **1**:3–25. doi: 10.1007/BF01036523
11. Tagliavini G, Solari F, Montanari R. CFD Simulation of a co-rotating twin-screw extruder: validation of a rheological model for a starch-based dough for snack food. *Int J Food Eng*. (2018) **14**:32–8. doi: 10.1515/ijfe-2017-0116
12. Fischer P, Pollard M, Erni P, Marti I, Padar S. Rheological approaches to food systems. *C R Phys*. (2009) **10**:740–50. doi: 10.1016/j.crhy.2009.10.016
13. Fischer P, Windhab EJ. Rheology of food materials. *Curr Opin Colloid Interface Sci*. (2011) **16**:36–40. doi: 10.1016/j.cocis.2010.07.003
14. Sandvik EI, Maerker JM. Chapter 19. Application of xanthan gum for enhanced oil recovery. In: *ACS Symposium Series, Vol. 45*, Houston, TX: Exxon Production Research Co (1977). p. 242–264. doi: 10.1021/bk-1977-0045.ch019
15. López OV, Castillo LA, Ninago MD, Ciolino AE, Villar MA. Modified starches used as additives in enhanced oil recovery (EOR). In: Goyanes S, D'Accorso N, editors. *Industrial Applications of Renewable Biomass Products*. Cham: Springer (2017). p. 227–48.
16. Sorbie KS. *Polymer-Improved Oil Recovery*. New York, NY: Springer Science & Business Media (2013).
17. Sadowski TJ, Bird RB. Non-newtonian flow through porous media. I. theoretical. *Trans Soc Rheol*. (1965) 9:243–50. doi: 10.1122/1.549000
18. Nguyen Q, Nguyen N. Incompressible non-Newtonian fluid flows. In: *Continuum Mechanics-Progress in Fundamentals and Engineering Applications*. Rijeka: InTech (2012).
19. Cannella WJ, Huh C, Seright RS. Prediction of xanthan rheology in porous media. In: *SPE Annual Technical Conference and Exhibition*. Houston, TX: Society of Petroleum Engineers (1988).
20. Hirasaki GJ, Pope GA, et al. Analysis of factors influencing mobility and adsorption in the flow of polymer solution through porous media. *Soc Petrol Eng*. (1974) **14**:337–46. doi: 10.2118/4026-PA
21. Christopher RH, Middleman S. Power-law flow through a packed tube. *Ind Eng Chem Res*. (1965) **4**:422–6. doi: 10.1021/i160016a011
22. Teeuw D, Hesselink FT. Power-law flow and hydrodynamic behaviour of biopolymer solutions in porous media. In: *SPE Oilfield and Geothermal Chemistry Symposium*. Stanford, TX: Society of Petroleum Engineers (1980).
23. Delshad M, Kim DH, Magbagbeola OA, Huh C, Pope GA, Tarahhom F. Mechanistic Interpretation and Utilization of Viscoelastic Behavior of Polymer Solutions for Improved Polymer-Flood Efficiency. In: *SPE Symposium on Improved Oil Recovery, 20-23 April,* Tulsa, OK (2008).
24. Skauge A, Zamani N, Gausdal Jacobsen J, Shaker Shiran B, Al-Shakry B, Skauge T. Polymer flow in porous media: relevance to enhanced oil recovery. *Colloids Inter*. (2018) **2**:27. doi: 10.3390/colloids2030027
25. Wreath D, Pope GA, Sepehrnoori K. Dependence of polymer apparent viscosity on the permeable media and flow conditions. *In Situ*. (1990) 1:263–84.
26. Berg S, van Wunnik J. Shear Rate Determination from Pore-Scale Flow Fields. *Transport Porous Med*. (2017) **117**:229–46. doi: 10.1007/s11242-017-0830-3
27. Carreau PJ. Rheological equations from molecular network theories. *Trans Soc Rheol*. (1972) **16**:99–127. doi: 10.1122/1.549276
28. Bird RB. Useful non-Newtonian models. *Annu Rev Fluid Mech*. (1976) **8**:13–4. doi: 10.1146/annurev.fl.08.010176.000305
29. Batchelor GK. *An Introduction to Fluid Dynamics*. Cambridge: Cambridge University Press (2000).
30. Lenk R. The Hagen-Poiseuille equation and the Rabinowitsch correction. The pressure drop in tapered channels. In: *Polymer Rheology*. Dordrecht: Springer (1978). p. 75–85.
31. Savins JG. Non-Newtonian flow through porous media. *Ind Eng Chem*. (1969) **61**:18–47. doi: 10.1021/ie50718a005
32. Willhite GP, Uhl JT. Correlation of the flow of Flocon 4800 biopolymer with polymer concentration and rock properties in berea sandstone. In: *Water-Soluble Polymers for Petroleum Recovery*. Kansas: Springer (1988). p. 101–19.
33. Chauveteau G. Fundamental criteria in polymer flow through porous-media-and their importance in the performance differences of mobility-control buffers. *Adv Chem Ser*. (1986) **213**:227–67. doi: 10.1021/ba-1986-0213.ch014
34. Abramowitz M, Stegun IA. *Handbook of Mathematical Functions: With Formulas, Graphs, and Mathematical Tables*. Vol. 55. Washington, DC: Courier Corporation (1965).
35. Volk A, Kähler CJ. Density model for aqueous glycerol solutions. *Exp Fluids*. (2018) **59**:75. doi: 10.1007/s00348-018-2527-y
36. Sworn G. 8-Xanthan gum. In: Phillips GO, Williams PA, editors. *Handbook of Hydrocolloids*. 2nd ed. Woodhead Publishing Series in Food Science, Technology and Nutrition. Cambridge: Woodhead Publishing (2009). p. 186–203.
37. Chauveteau G. Rodlike polymer solution flow through fine pores: influence of pore size on rheological behavior. *J Rheol*. (1982) **26**:111–42. doi: 10.1122/1.549660
38. Chauveteau G, Zaitoun A. Basic rheological behavior of xanthan polysaccharide solutions in porous media: effects of pore size and polymer concentration. In: *Proceedings of the First European Symposium on Enhanced Oil Recovery, Bournemouth, England, Society of Petroleum Engineers*, Richardson, TX (1981). p. 197–12.
39. Sun Y, Saleh L, Bai B. Measurement and impact factors of polymer rheology in porous media. In: *Rheology*. Missouri: InTech (2012).
40. Dvorkin J. *Kozeny-Carman Equation Revisited*. (2009). Available online at: pangea.stanford.edu/∼jack/KC_2009_JD.pdf

Conflict of Interest Statement: The authors declare that the research was conducted in the absence of any commercial or financial relationships that could be construed as a potential conflict of interest.

frontiers in Physics

ORIGINAL RESEARCH
published: 09 July 2019
doi: 10.3389/fphy.2019.00092

Effective Rheology of Two-Phase Flow in a Capillary Fiber Bundle Model

Subhadeep Roy[1]*, *Alex Hansen*[1,2] *and Santanu Sinha*[2,1]

[1] PoreLab, Department of Physics, Norwegian University of Science and Technology (NTNU), Trondheim, Norway, [2] Beijing Computational Science Research Center, Beijing, China

We investigate the effective rheology of two-phase flow in a bundle of parallel capillary tubes carrying two immiscible fluids under an external pressure drop. The diameter of the tubes vary along the length which introduce capillary threshold pressures. We demonstrate through analytical calculations that a transition from a linear Darcy to a non-linear behavior occurs while decreasing the pressure drop ΔP, where the total flow rate $\langle Q \rangle$ varies with ΔP with an exponent 2 as $\langle Q \rangle \sim \Delta P^2$ for uniform threshold distribution. The exponent changes when a lower cut-off P_m is introduced in the threshold distribution and in the limit where ΔP approaches P_m, the flow rate scales as $\langle Q \rangle \sim (|\Delta P| - P_m)^{3/2}$. While considering threshold distribution with a power α, we find that the exponent γ for the non-linear regime vary as $\gamma = \alpha + 1$ for $P_m = 0$ and $\gamma = \alpha + 1/2$ for $P_m > 0$. We provide numerical results in support of our analytical findings.

Keywords: two-phase flow, capillary fiber bundle model, effective rheology, non-Darcy flow at low velocity, porous media

OPEN ACCESS

Edited by:
Ferenc Kun,
University of Debrecen, Hungary

Reviewed by:
Allbens Picardi Faria Atman,
Federal Center for Technological Education of Minas Gerais, Brazil
Muktish Acharyya,
Presidency University, India

***Correspondence:**
Subhadeep Roy
subhadeep.roy@ntnu.no

Specialty section:
This article was submitted to Interdisciplinary Physics, a section of the journal Frontiers in Physics

Received: *23 February 2019*
Accepted: *11 June 2019*
Published: *09 July 2019*

Citation:
Roy S, Hansen A and Sinha S (2019) Effective Rheology of Two-Phase Flow in a Capillary Fiber Bundle Model. Front. Phys. 7:92. doi: 10.3389/fphy.2019.00092

Understanding the hydrodynamic properties of simultaneous flow of two or more immiscible fluids is essential due its relevance to a wide variety of different systems in industrial, geophysical and medical sectors [1, 2]. Different applications, such as bubble generation in microfluidics, blood flow in capillary vessels, catalyst supports used in the automotive industry, transport in fuel cells, oil recovery, ground water management and CO_2 sequestration, deal with the flow of bubble trains in different types of systems, ranging from single capillaries to more complex porous media. The underlying physical mechanisms in multiphase flow are controlled by a number of factors, such as the capillary forces at the interfaces, viscosity contrast between the fluids, wettability and geometry of the system, which make the flow properties different from single phase flow. When one immiscible fluid invades a porous medium filled with another fluid, different types of transient flow patterns, namely viscous fingering [3, 4], stable displacement [5], and capillary fingering [6] are observed while tuning the physical parameters [7]. These transient flow patterns were modeled by invasion percolation [8] and diffusion limited aggregation (DLA) models [9]. When steady state sets in after the initial instabilities, the flow properties in are characterized by relations between the global quantities, such as flow rate, pressure drop and fluid saturation [10, 11]. It has been observed theoretically and experimentally that, in the regime where capillary forces compete with the viscous forces, the two-phase flow rate of Newtonian fluids in the steady state no longer obeys the linear Darcy law [12, 13] but varies as a power law with the applied pressure drop [14–17]. Tallakstad et al. [14, 15] experimentally measured the exponent of the power law to be close to two (= 1/0.54) in a two-dimensional system and followed this observation up with arguments why the exponent should be two. Rassi et al. [16] found a value for the exponent varying between 2.2 (= 1/0.45)

and 3.0 ($= 1/0.33$) in a three-dimensional system. Sinha et al. [17] considered a similar system to that which had been studied by Rassi et al. finding an exponent 2.17 ± 0.24 ($= 1/(0.46 \pm 0.05)$). The reason behind the discrepancy between the results of Rassi et al. and those of Sinha et al. is the possibility of a non-zero threshold pressure that observed in the later study, under which there would be no flow, which was assumed to be zero in the former study. The reciprocals in the brackets are provided in order to compare the exponent values reported in the literature [14–17] with those we present here in this article, as we express our results as $\langle Q \rangle$ as a power law in ΔP, whereas in the cited papers ΔP was expressed as a power law in $\langle Q \rangle$.

This power law behavior is in contrast to the assumption of linearity in the relation between flow rate and pressure drop that is generally assumed in the relative permeability approach dominating reservoir simulations [18].

For a single capillary tube with varying diameter, Sinha et al. [19] showed that the average volumetric flow rate $\overline{q}$ in the steady state has a non-linear square-root type relationship with the pressure drop ΔP as $\overline{q} \sim \sqrt{\Delta P^2 - P_c^2}$. This was shown analytically by integrating the instantaneous linear two-phase flow equation over the whole capillary tube. Here P_c is the threshold pressure difference below which there is no flow. It appears due to the capillary barriers at the interfaces at the narrow pore throats. Extending this non-linear relationship to a network of disordered pores, the relationship between the steady-state flow rate and an excess pressure drop leads to a quadratic relationship in the capillary dominated regime [20]. The quadratic relationship for the pore network, both in two and in three dimensions, was obtained analytically by mean-field calculations and numerically with pore network modeling [17, 20].

While increasing the pressure drop, the capillary forces become negligible compared to the viscous forces. This leads to a crossover from the non-linear regime to a linear Darcy regime for both the single capillary tube and for the pore network. Such non-linear quadratic relationship at low flow rate and a crossover to a linear regime at high flow rate was also observed in case of the single-phase flow of Bingham viscoplastic fluid in porous media [21, 22]. A Bingham fluid is a yield threshold fluid which behaves like a solid below the threshold and flows like a Newtonian fluid above it. The origin of the quadratic regime for the Bingham fluid flowing in a porous media can be understood intuitively in this way: the flow starts when one connected channel appears in the system just above a threshold pressure and the flow rate varies linearly with the excess pressure drop; while increasing the applied pressure drop further, more number of connected flow channels start to appear enhancing the overall flow rate more rapidly than the applied pressure drop leading to the quadratic relationship. Finally, when all possible flow paths become active, the flow become Newtonian following the linear Darcy law. Note that, in general, the rheology of the Bingham fluid is linear above the yield threshold. It is the disorder in the yield thresholds due to the porous medium that creates the quadratic regime.

The argument presented by Tallakstad et al. [14, 15] focused on the successive opening of fluid channels when the pressure drop across the system was increased. When $|\Delta P|$ is small, the flow will occur along isolated channels. The volumetric flow rate in such a channel will be proportional to $|\Delta P|/L$. Between the channels there will be fluid clusters held in place by capillary forces, say of the order p_t. There is a pressure gradient $|\Delta P|/L$ in the flow direction. A given cluster of length $l_\parallel$ will be stuck if $p_t > l_\parallel |\Delta P|/L$. The largest stuck cluster will then have a size $l_{\parallel,\max} = L p_t/|\Delta P|$. If we now assume that this length, $l_{\parallel,\max}$ is same as the distance between the channels where there is flow, $l_\perp$, then the total flow rate must be equal to the number of channels, which is proportional to $1/l_\perp$, multiplied by the flow rate in each channel. Hence, we have $Q \propto (1/l_\perp)\ |\Delta P| \propto |\Delta P|^2$. Though this argument provides the same behavior as the one based on the mean field calculation [20] for two-dimensional networks, a difference appears in three dimensions. When following the same arguments, it leads the flow rate to vary with the pressure drop with third power as long as the isolated channels remain one-dimensional strings rather than two-dimensional sheets in three dimensions.

We present in this article a capillary fiber bundle model [23, 24], which is a system of N parallel capillary tubes, disconnected from each other, each carrying an independent bubble trail of two immiscible fluids under an external pressure drop. In a porous medium, a typical pore consists of two wide pore bodies at the ends and a narrow pore throat in the middle. When an interface moves along the pore, the capillary pressure associated with the interface becomes position dependent due to the change in the radius of curvature. This introduces an overall threshold pressure that depends on the position of all the interfaces [19]. One can simplify the shape of the pore by a sinusoidal type and a long capillary tube with varying radius can be seen as a series of many pores. In the capillary bundle model, the diameter of each tube varies along the axis identically and the disorder in the threshold appear due to the different interface positions in different tubes. This model is essentially the only model for immiscible two-phase flow which is analytically tractable. We calculate the total average flow rate as a function of the applied pressure drop and study the effect of disorder in the threshold distribution. We point out that, here we do not address the question of the relation between the fluid distributions in the capillaries and the respective threshold distributions. Our aim with this model is to investigate how the range of the disorder in the threshold distribution controls the effective flow properties. This provides an insight into the non-linearities in steady-state two-phase flow. We will see that the exponent for the non-linear regime depends on the lower cut-off of the threshold distribution as well as on the behavior of the distribution near the cut-off. The possibility to study analytically for this model how the competition between viscous and capillary forces renders the Darcy relation non-linear, is a new and useful discovery.

The capillary fiber bundle model is a hydrodynamic analog of the fiber bundle model used in fracture mechanics to study mechanical failure under stress [25]. The fiber bundle model is an ideal example of a disordered system in statistical mechanics that is driven by threshold activated dynamics. It is a simple, yet very rich model to understand failure events in mechanical systems. In its simplest form it is analytically tractable. In more complex

versions of the model, analytical calculations go hand in hand with numerical simulations.

Figure 1 illustrates a bundle with $N = 5$ parallel capillaries. Each capillary tube has a length L and an average inner area a. For each capillary, the diameter varies along the long axis identically. Each capillary is filled with a bubble train of wetting and non-wetting fluids. Due to the varying diameter, the capillary forces at the interfaces vary as the bubble train moves along the tubes. We assume that the wetting fluid does not form films along the pore walls so that the fluids do not pass each other. The lengths of the wetting and non-wetting fluids in each tube is L_w and L_n, respectively such that the volume of the wetting fluid in each tube is $L_w a$ and the volume of the non-wetting fluid is $L_n a$, where a is the average cross-sectional area of the capillary tubes. Hence, the saturations are given by $S_w = L_w/L$ and $S_n = L_n/L$ for each capillary tube. The cross-sectional pore area of the capillary fiber bundle is

$$A_p = Na. \tag{1}$$

Though each tube contains the same amount of each fluid, it has its own division of the fluids into bubbles. We average over the ensemble of capillary tubes in the bundle by averaging over the fluids in each tube that pass at a given instance through an imaginary cut as shown in the figure. We will obtain the same averages if we consider a single capillary tube, averaging over a time interval the fluid passing the imaginary cut [19, 26]. This shows that the model is ergodic.

The volumetric flow rate in a capillary tube is given by [19]

$$q = -\frac{a^2}{8\pi\mu_{\rm av}L}\Theta(|\Delta P| - P_c)\left[\Delta P - P_c\right], \tag{2}$$

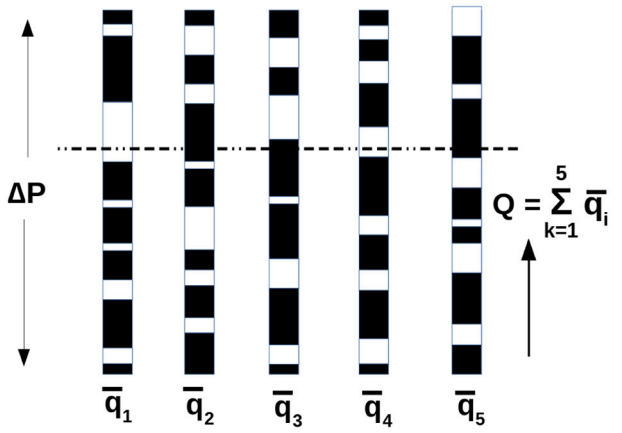

FIGURE 1 | The capillary tube model. There are $N = 5$ capillaries, each filled with a bubble train of wetting (white) and non-wetting (black) fluids moving in the direction of the arrow. The diameter along each tube vary so that the capillary force from each interface vary with its position. The variation in the diameters are not illustrated in the figure. The average diameters are the same for all tubes. The broken line illustrates an imaginary cut through the capillary fiber bundle.

where ΔP is the pressure drop across the capillary tube, P_c the sum of all the capillary forces along the capillary tube due to the interfaces and

$$\mu_{\rm av} = S_w\mu_w + S_n\mu_n, \tag{3}$$

is the effective viscosity. $\Theta(|\Delta P| - P_c)$ is the Heaviside function which is zero for negative arguments and one for positive arguments.

Sinha et al. [19] showed that the time average when the pressure difference across the tube is kept fixed is given by

$$\overline{q}(P_c) = -\frac{a^2}{8\pi\mu_{\rm av}L}\,\mathrm{sgn}(\Delta P)\Theta(|\Delta P| - P_c)\sqrt{\Delta P^2 - P_c^2}, \tag{4}$$

where the function $\mathrm{sgn}(\Delta P)$ is the sign of the argument. Suppose now that the thresholds P_c are distributed uniformly between zero and a maximum value P_M. The cumulative threshold probability is then

$$\Pi(P_c) = \begin{cases} 0 & , P_c \le 0, \\ \frac{P_c}{P_M} & , 0 < P_c \le P_M, \\ 1 & , P_c > P_M. \end{cases} \tag{5}$$

We have N capillary tubes. Using order statistics, we may order the N averaged threshold values,

$$\Pi(P_c(k)) = \frac{k}{N+1}, \tag{6}$$

where $1 \le k \le N$. Hence,

$$P_c(k) = P_M\frac{k}{N+1}. \tag{7}$$

The average volumetric flow rate through the capillary fiber bundle for $|\Delta P| > 0$ is then

$$\langle Q\rangle = \sum_{k=1}^{(N+1)\min\left(\frac{|\Delta P|}{P_M},1\right)} \overline{q}\left(P_c(k)\right) \tag{8}$$

We assume the limit $N \to \infty$ turning the sum into an integral,

$$\frac{\langle Q\rangle}{N} = -\frac{a^2 P_M\,\mathrm{sgn}(\Delta P)}{8\pi\mu_{\rm av}L}\int_0^{\min(|\Delta P|/P_M,1)} dx\sqrt{\left(\frac{|\Delta P|}{P_M}\right)^2 - x^2}\,. \tag{9}$$

This integral is doable and we find

$$\frac{\langle Q\rangle}{N} = -\frac{a^2}{32\mu_{\rm av}L}\left|\frac{\Delta P}{P_M}\right|\Delta P \tag{10}$$

when $|\Delta P| \leq P_M$ and

$$\frac{\langle Q \rangle}{N} = -\frac{a^2 P_M \mathrm{sgn}(\Delta P)}{16\pi\mu_{\mathrm{av}} L} \left[\sqrt{\left(\frac{|\Delta P|}{P_M}\right)^2 - 1} + \left(\frac{|\Delta P|}{P_M}\right)^2 \arcsin\left(\frac{P_M}{|\Delta P|}\right) \right], \quad (11)$$

when $|\Delta P| > P_M$. In the limit $|\Delta P| \gg P_M$, Equation (11) gives

$$\frac{\langle Q \rangle}{N} = -\frac{a^2}{8\pi\mu_{\mathrm{av}} L}\,\Delta P\,. \quad (12)$$

Hence, the Darcy relation for a tube is recovered.

We see that this picture is consistent with that central to the arguments of Tallakstad et al. [14, 15] leading to the quadratic dependence of Q on ΔP. From Equation (7) we deduce that a number k_c of the capillary tubes are active, where

$$k_c = \frac{|\Delta P|}{P_M}\,(N+1)\,. \quad (13)$$

The typical distance between active capillary tubes in units of the distance between the tubes is then given by

$$l_\perp = \frac{N+1}{k_c} = \frac{P_M}{|\Delta P|}\,, \quad (14)$$

in accordance with the argument of Tallakstad et al.

How stable is the square law $Q \propto |\Delta P|^2$? That is, how much does it hinge on the choice of cumulative threshold probability $\Pi(P_c)$. So far we have only considered the one given in Equation (5). Let us now generalize it to

$$\Pi(P_c) = \begin{cases} 0 & , P_c \leq 0\,, \\ \left(\frac{P_c}{P_M}\right)^\alpha & , 0 < P_c \leq P_M\,, \\ 1 & , P_c > P_M\,, \end{cases} \quad (15)$$

where $\alpha > 0$. The average ordered threshold are then given by

$$P_c(k) = P_M \left(\frac{k}{N+1}\right)^{1/\alpha}\,, \quad (16)$$

and when combined with the expression for $\langle Q \rangle$, Equation (8) in the limit $N \to \infty$, we find

$$\frac{\langle Q \rangle}{N} = -\frac{a^2 P_M \mathrm{sgn}(\Delta P)}{8\pi\mu_{\mathrm{av}} L} \int_0^{\min\left((|\Delta P|/P_M)^\alpha, 1\right)} dx \sqrt{\left(\frac{|\Delta P|}{P_M}\right)^2 - x^{2/\alpha}}\,. \quad (17)$$

Since we are interested in the behavior for $|\Delta P| \to 0$, we do this integral under the assumption that $|\Delta P| < P_M$ finding

$$\frac{\langle Q \rangle}{N} = -\frac{a^2 \alpha}{32\sqrt{\pi}\mu_{\mathrm{av}} L} \frac{\Gamma\left(\frac{\alpha}{2}\right)}{\Gamma\left(\frac{3+\alpha}{2}\right)} \left(\frac{|\Delta P|}{P_M}\right)^\alpha \Delta P\,, \quad (18)$$

where the Γ function for real positive z is defined as, $\Gamma(z) = \int_{-\infty}^{\infty} t^{z-1} e^{-t} dt$. When $\alpha = 1$, we recover Equation (10).

Equation (10) shows the behavior observed experimentally in References [14] and [15]. With Equation (18), we have just shown that $\langle Q \rangle / N \sim |\Delta P|^\gamma$ as $|\Delta P| \to 0$, where γ depends on the threshold distribution, i.e., on α in Equation (15). Does this imply that there is no universality; that the experimentally observed behavior is due to the presence of a very specific threshold distribution?

As we now argue, there is universality. We note that the threshold distribution $p(P_c) = d\Pi(P_c)/dP_c$ behaves as $p(P_c) \propto P_c^{\alpha-1}$. Hence, if $\alpha > 1$, the distribution vanishes as $P_c \to 0$, whereas it diverges for $\alpha < 1$. Thus, the behavior of the distribution is vastly different for these two cases, and this causes γ to depend on α. However, for $\alpha = 1$, the distribution reaches a constant, non-zero value for $P_c \to 0$. Any threshold distribution with this behavior for small P_c, i.e., $p(P_c)$ reaching a non-zero value and $dp(P_c)/dP_c \to 0$ in the limit $P_c \to 0$ will give rise to the square power law seen in Equation (10). Such distributions are ubiquitous, and $\gamma = 2$ is universal over this class of distributions.

We now consider $\alpha = 1$ again, but introduce a minimum threshold P_m so that the cumulative threshold probability is given by

$$\Pi(P_c) = \begin{cases} 0 & , P_c \leq P_m\,, \\ \frac{P_c - P_m}{P_M - P_m} & , P_m < P_c \leq P_M\,, \\ 1 & , P_c > P_M\,. \end{cases} \quad (19)$$

Equation (6) yields in this case the ordered threshold sequence

$$P_c(k) = P_m + (P_M - P_m)\frac{k}{N+1}\,. \quad (20)$$

Equation (8) now becomes in the limit $N \to \infty$

$$\frac{\langle Q \rangle}{N} = -\frac{a^2 (P_M - P_m) \mathrm{sgn}(\Delta P)}{8\pi\mu_{\mathrm{av}} L} \int_{\frac{P_m}{P_M - P_m}}^{\frac{|\Delta P|}{P_M - P_m}} dx \sqrt{\left(\frac{|\Delta P|}{P_M - P_m}\right)^2 - x^2}\,, \quad (21)$$

when we assume $P_m \leq |\Delta P| \leq P_M$. We find

$$\frac{\langle Q \rangle}{N} = -\frac{a^2(P_M - P_m)\mathrm{sgn}(\Delta P)}{32\pi\mu_{\mathrm{av}}L}\left(\frac{|\Delta P|}{P_M - P_m}\right)^2 \left[\pi - 4\left(\frac{P_m}{|\Delta P|}\right)^2\sqrt{\left(\frac{|\Delta P|}{P_m}\right)^2 - 1} - 2\,\mathrm{arccot}\left(\frac{2\sqrt{\left(\frac{|\Delta P|}{P_m}\right)^2 - 1}}{2 - \left(\frac{|\Delta P|}{P_m}\right)^2}\right)\right]. \tag{22}$$

We find to lowest order in $(|\Delta P| - P_m)$, that this expression behaves as

$$\frac{\langle Q \rangle}{N} = -\frac{a^2\mathrm{sgn}(\Delta P)}{3\sqrt{2}\pi\mu_{\mathrm{av}}L}\frac{\sqrt{P_m}}{(P_M - P_m)}(|\Delta P| - P_m)^{3/2}, \tag{23}$$

as $|\Delta P| \to P_m$.

We now turn to numerical simulations and observe that the numerical results are in good a agreement with the analytical findings. The numerical simulations also allow us to explore the regions which are analytically challenging. Results are shown in **Figure 2** for a bundle containing $N = 10^5$ capillary tubes and averaged over 10^4 configurations. In **Figure 2A**, we show the behavior of the volumetric flow rate $\langle Q \rangle$ as a function of increasing pressure drop ΔP for uniform threshold distributions with $P_m = 0$ and $P_m > 0$, given by Equations (5, 19), respectively. The results show that, for each threshold distribution, the relationship is linear for high ΔP obeying the Darcy law as predicted by Equation (12). For small pressure drops, $\langle Q \rangle$ follows a power law in ΔP with an exponent 2 when there is no lower cut-off in the threshold distribution, i.e., $P_m = 0$. This is predicted in Equation (10). When a lower cut-off is introduced in the threshold distribution ($P_m > 0$), this exponent shifts from 2 to

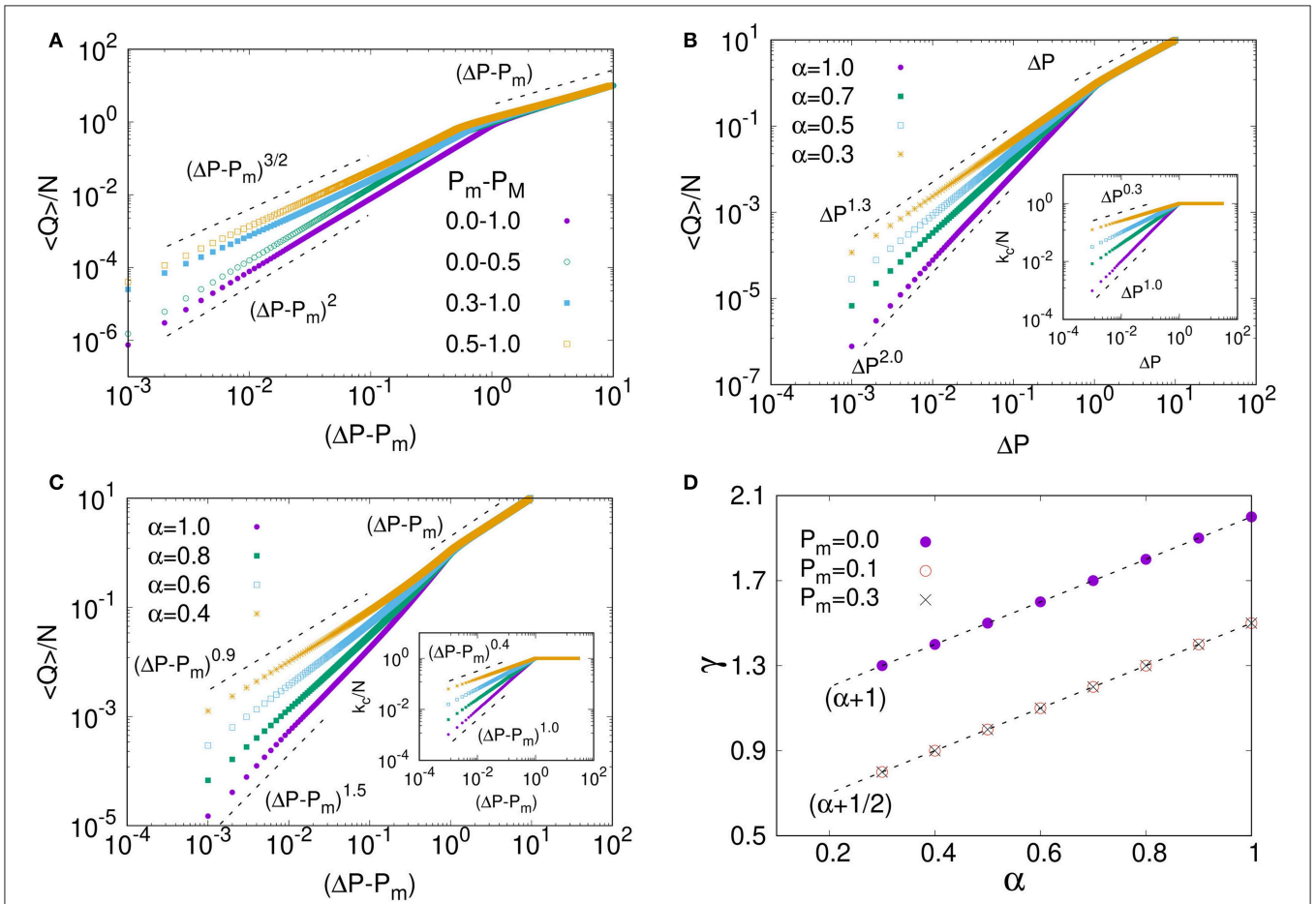

FIGURE 2 | Results from numerical simulations performed with $N = 10^5$ capillaries and averaged over 10^4 configurations. Variation of $\langle Q \rangle / N$ as a function of pressure drop ΔP for different threshold distributions are shown in **(A–C)** where non-linear to linear transitions are observed while increasing the pressure drop.
(A) Corresponds to uniform threshold distribution (Equation 5) where the power-law exponent γ for the non-linear regime has a value 2 without a lower cut-off ($P_m = 0$). With any non-zero lower cut-off ($P_m > 0$), the exponent shifts to 3/2 (Equation 23). Results for the threshold distribution with a power α (Equation 24) are shown in **(B,C)** for $P_m = 0$ and $P_m > 0$, respectively, where γ varies with α as $\gamma = \alpha + 1$ for $P_m = 0$ and as $\gamma = \alpha + 1/2$ for $P_m > 0$. These two relations are shown in **(D)** for the range of α which show two distinct straight lines for $P_m = 0$ and for $P_m > 0$. Here, the number of active capillaries (k_c) vary with ΔP as $k_c/N \sim (\Delta P - P_m)^\alpha$ as shown in the insets of **(B,C)**.

3/2 as predicted in Equation (23). These exponents in the non-linear regime are not sensitive to the span of the distribution as shown in **Figure 2A**. An insight to a more generalized picture is presented in **Figures 2B,C** for a threshold distribution given by a generalization of Equation (15) with an introduction of a lower cut-off P_m,

$$\Pi(P_c) = \begin{cases} 0 & , P_c \leq P_m \, , \\ \left(\frac{P_c - P_m}{P_M - P_m}\right)^{\alpha} & , P_m < P_c \leq P_M \, , \\ 1 & , P_c > P_M \, , \end{cases} \tag{24}$$

With this distribution of thresholds, the exponent γ in the non-linear region shows a continuous variation with α as $\gamma = \alpha + 1$ for $P_m = 0$. Such variation is given in Equation (18) and matches well with the numerical results as shown in **Figure 2D**. In presence of a lower cut-off $P_m > 0$, γ varies as $(\alpha + 1/2)$ instead of $(\alpha + 1)$ irrespective of the position of the lower cut-off. An analytical treatment for a general α value with $P_m > 0$ is rather challenging. Nevertheless, our numerical result matches with the analytical study (see Equation 23) in the limit $\alpha = 1$.

Equation (18) predicts an exponent $\gamma = \alpha + 1$. A simple argument, related to that given by Roux and Herrmann [22], goes as follows: The number of active capillary tubes is proportional to $(|\Delta P| - P_m)^{\alpha}$. This behavior is observed in the insets in **Figures 2B,C**. The flow rate in an active capillary is proportional to $(|\Delta P| - P_m)^{1/2}$. Hence, the total flow rate should be $\langle Q \rangle \propto (|\Delta P| - P_m)^{\alpha + 1/2}$. It is accidental that this argument works out for $P_m > 0$ (**Figure 2C**), as it does *not* when $P_m = 0$, where $\gamma = \alpha + 1$. For the argument to function, the distribution of active capillaries and the flow rate in each capillary should be uncorrelated. It is not.

We find the same behavior with respect to the cut-off: An exponent 3/2 for the cumulative threshold probability

$$\Pi(P_c) = \begin{cases} 0 & , P_c \leq P_m \, , \\ \frac{\log\left(\frac{P_c}{P_m}\right)}{\log\left(\frac{P_c}{P_M}\right)} & , P_m < P_c \leq P_M \, , \\ 1 & , P_c > P_M \, , \end{cases} \tag{25}$$

where $P_m = 10^{-\beta}$ and $P_M = 10^{\beta}$ and β ranging from 0.5 to 1.5. The same goes for the cumulative threshold probability

$$\Pi(P_c) = \begin{cases} 0 & , P_c \leq P_m \, , \\ 1 - e^{-P_c - P_m / P_d} & , P_m < P_c \, , \end{cases} \tag{26}$$

where we have set $P_m = 0.1$ and $P_d = 1$. In both of these cases, the probability density at $P_c = P_m$ is finite.

We have presented an analytical study supported by numerical simulations of steady-state two-phase flow in a system of parallel capillary tubes. Considering a uniform distribution for the threshold pressures for the capillaries, we have calculated the average flow rate as a function of the applied pressure drop. When the thresholds are distributed according to a uniform distribution between zero and a maximum value—or more generally, the threshold distribution approaches a non-zero value in the limit of zero thresholds—we obtain a quadratic relationship between the flow rate and the applied pressure drop when the applied pressure drop is below the maximum threshold pressure, and the linear Darcy relationship for higher pressure drops. This crossover between a quadratic non-linear and linear flow regimes is in agreement with many existing results of two-phase flow in porous media which shows that this simple model can capture effective two-phase flow properties of more complex porous media. When a lower cut-off is introduced in the threshold distribution, the quadratic relationship changes, and the flow rate varies with an excess pressure drop with an exponent 3/2 as the pressure drop approaches to the lowest threshold pressure.

The difference between the capillary fiber bundle model and a porous medium is that in the latter, the fluids meet and mix at the nodes of the pore network. This is an essential mechanism that leads to the non-linear Darcy law is a power law with an exponent two as seen in the experiments, the numerical simulations and the mean-field calculations. However, it remains a mystery how the mixing at the nodes leads to this universality.

DATA AVAILABILITY

The datasets for this manuscript are not publicly available because all data sets are included in manuscript. Requests to access the datasets should be directed to subhadeep.roy@ntnu.no.

AUTHOR CONTRIBUTIONS

AH developed the theory and performed the analytical calculations of the manuscript. AH and SS wrote the first draft of the manuscript. SR did the numerical simulations. All the authors contributed in developing the theory and writing the manuscript to its final form.

ACKNOWLEDGMENTS

The authors thank Dick Bedeaux, Carl Fredrik Berg, Eirik G. Flekkøy, Signe Kjelstrup, Knut Jørgen Måløy, Per Arne Slotte, and Ole Torsæter for interesting discussions. This work was partly supported by the Research Council of Norway through its Centres of Excellence funding scheme, project number 262644. SS was supported by the National Natural Science Foundation of China under grant number 11750110430.

REFERENCES

1. Bear J. *Dynamics of Fluids in Porous Media*. Mineola, NY: Dover (1988).
2. Dullien FAL. *Porous Media: Fluid, Transport and Pore Structure*. San Diego, CA: Academic Press (1992).
3. Chen JD, Wilkinson D. Pore-scale viscous fingering in porous media. *Phys Rev Lett*. (1985) **55**:1892–5. doi: 10.1103/PhysRevLett.55.1892
4. Måløy KJ, Feder J, Jøssang T. Viscous fingering fractals in porous media. *Phys Rev Lett*. (1985) **55**:2688–91. doi: 10.1103/PhysRevLett.55.2688

5. Lenormand R, Touboul E, Zarcone C. Numerical models and experiments on immiscible displacements in porous media. *J Fluid Mech*. (1988) **189**:165–87. doi: 10.1017/S0022112088000953
6. Lenormand R, Zarcone C. Invasion percolation in an etched network: measurement of a fractal dimension. *Phys Rev Lett*. (1985) **54**:2226–9. doi: 10.1103/PhysRevLett.54.2226
7. Løvoll G, Méheust Y, Toussaint R, Schmittbuhl J, Måløy KJ. Growth activity during fingering in a porous Hele-Shaw cell. *Phys Rev E*. (2004) **70**:026301. doi: 10.1103/PhysRevE.70.026301
8. Wilkinson D, Willemsen JF. Invasion percolation: a new form of percolation theory. *J Phys A Math Gen*. (1983) **16**:3365–76. doi: 10.1088/0305-4470/16/14/028
9. Witten TA Jr, Sander LM. Diffusion-limited aggregation, a kinetic critical phenomenon. *Phys Rev E*. (1981) **47**:1400–3. doi: 10.1103/PhysRevLett.47.1400
10. Valavanides M. Review of steady-state two-phase flow in porous media: independent variables, universal energy efficiency map, critical flow conditions, effective characterization of flow and pore network. *Transp Porous Media*. (2018) **123**:45–99. doi: 10.1007/s11242-018-1026-1
11. Hansen A, Sinha S, Bedeaux D, Kjelstrup S, Gjennestad MA, Vassvik M. Relations between seepage velocities in immiscible, incompressible two-phase flow in porous media. *Transp Porous Media*. (2018) **125**:565–87. doi: 10.1007/s11242-018-1139-6
12. Darcy H. *Les Fontaines Publiques de la Ville de Dijon: Exposition et Application des Principes à Suivre et des Formules à Employer dans les Questions de Distribution d'eau*. Paris: V. Dalamont (1856).
13. Whitaker S. Flow in porous media I: a theoretical derivation of Darcy's law. *Transp Porous Media*. (1986) **1**:3–25. doi: 10.1007/BF01036523
14. Tallakstad KT, Knudsen HA, Ramstad T, Løvoll G, Måløy KJ, Toussaint R, et al. Steady-state two-phase flow in porous media: statistics and transport properties. *Phys Rev Lett*. (2009) **102**:074502. doi: 10.1103/PhysRevLett.102.074502
15. Tallakstad KT, Løvoll G, Knudsen HA, Ramstad T, Flekkøy EG, Måløy KJ. Steady-state, simultaneous two-phase flow in porous media: an experimental study. *Phys Rev E*. (2009) **80**:036308. doi: 10.1103/PhysRevE.80.036308
16. Rassi EM, Codd SL, Seymour JD. Nuclear magnetic resonance characterization of the stationary dynamics of partially saturated media during steady-state infiltration flow. *New J Phys*. (2011) **13**:015007. doi: 10.1088/1367-2630/13/1/015007
17. Sinha S, Bender AT, Danczyk M, Keepseagle K, Prather CA, Bray JM, et al. Effective rheology of two-phase flow in three-dimensional porous media: experiment and simulation. *Transp Porous Media*. (2017) **119**:77–94. doi: 10.1007/s11242-017-0874-4
18. Wyckoff RD, Botset HG. The flow of gas-liquid mixtures through unconsolidated sands. *J Appl Phys*. (1936) **7**:325. doi: 10.1063/1.1745402
19. Sinha S, Hansen A, Bedeaux D, Kjelstrup S. Effective rheology of bubbles moving in a capillary tube. *Phys Rev E*. (2013) **87**:025001. doi: 10.1103/PhysRevE.87.025001
20. Sinha S, Hansen A. Effective rheology of immiscible two-phase flow in porous media. *Europhys Lett*. (2012) **99**:44004. doi: 10.1209/0295-5075/99/44004
21. Chevalier T, Talon L. Generalization of Darcy's law for Bingham fluids in porous media: from flow-field statistics to the flow-rate regimes. *Phys Rev E*. (2015) **91**:023011. doi: 10.1103/PhysRevE.91.023011
22. Roux S, Herrmann HJ. Disorder-induced nonlinear conductivity. *Europhys Lett*. (1987) **4**:1227. doi: 10.1209/0295-5075/4/11/003
23. Scheidegger AE. Theoretical models of porous matter. *Producers Monthly*. (1953) **17**:17.
24. Scheidegger AE. *The Physics of Flow Through Porous Media*. Toronto, ON: University of Toronto Press (1974).
25. Hansen A, Hemmer PC, Pradhan S. *The Fiber Bundle Model: Modeling Failure in Materials*. Berlin: Wiley (2015).
26. Savani I, Sinha S, Hansen A, Bedeaux D, Kjelstrup S, Vassvik M. A Monte Carlo algorithm for immiscible two-phase flow in porous media. *Transp Porous Media*. (2016) **116**:869–88. doi: 10.1007/s11242-016-0804-x

Conflict of Interest Statement: The authors declare that the research was conducted in the absence of any commercial or financial relationships that could be construed as a potential conflict of interest.

frontiers in Physics

ORIGINAL RESEARCH
published: 10 July 2019
doi: 10.3389/fphy.2019.00096

Experimental Observation of Dissolution Finger Growth in Radial Geometry

Le Xu[1]*, *Piotr Szymczak*[2], *Renaud Toussaint*[1,3], *Eirik G. Flekkøy*[1] and *Knut J. Måløy*[1]

[1] PoreLab, Department of Physics, The NJORD Center, University of Oslo, Oslo, Norway, [2] Faculty of Physics, Institute of Theoretical Physics, University of Warsaw, Warsaw, Poland, [3] Université de Strasbourg, CNRS, IPGS UMR 7516, Strasbourg, France

Reaction-infiltration instability refers to the morphological instability of a reactive fluid front flowing in a soluble porous medium. This process is important for many naturally occurring phenomena, such as the weathering and diagenesis of rocks, dissolution in salt deposits and melt extraction from the mantle. This paper is focused on experiments on dissolution finger growth in radial geometries in an analog fracture. In the experiments, pure water dissolves a plaster sample forming one of the fracture walls in a Hele-Shaw cell with controlled injection rate and aperture. The flow is directed inwards to the center, and we observe the reaction-infiltration instability developing along the relatively long perimeter of the plaster. Our experimental results show a number of features consistent with the theoretical and numerical predictions on the finger growth dynamics such as screening and selection between the fingers. Statistical properties of the dissolved part evolution with time are also investigated.

Keywords: dissolution, fracture, reaction-infiltration, fingering, Hele-Shaw cell, screening effect

OPEN ACCESS

Edited by:
Antonio F. Miguel, University of Evora, Portugal

Reviewed by:
Dominique Salin, Sorbonne Universités, France
Xiaojing (Ruby) Fu, University of California, Berkeley, United States

***Correspondence:**
Le Xu
le.xu@fys.uio.no

Specialty section:
This article was submitted to Interdisciplinary Physics, a section of the journal Frontiers in Physics

Received: *08 April 2019*
Accepted: *19 June 2019*
Published: *10 July 2019*

Citation:
Xu L, Szymczak P, Toussaint R, Flekkøy EG and Måløy KJ (2019) Experimental Observation of Dissolution Finger Growth in Radial Geometry. Front. Phys. 7:96. doi: 10.3389/fphy.2019.00096

1. INTRODUCTION

In geological systems, dissolution plays an important role in the weathering and diagenesis of Earth's rocks [1, 2], chemical erosion of salt deposits [3, 4], and melt extraction from the mantle [5]. It is also of fundamental importance in many engineering applications, including dam stability [6] and CO_2 sequestration [7]. The important applications in the oil industry include acidization of petroleum reservoirs [8] in order to enhance oil and gas production by increasing the permeability of the rock [9, 10].

Because the reaction-infiltration instability plays an important role in a variety of fields, it stimulates dissolution-related research projects, both theoretical and numerical. Linear stability analysis can be applied to characterize the initial instability in porous media dissolution [11–14], but after fingering develops, we enter a nonlinear regime, where very few theoretical tools can be applied and one needs to resort to numerical simulations [3, 8, 15–21]. Compared to the theoretical and numerical works on the subject, there are relatively few experimental studies, especially on the observation of dissolution in quasi-2D radial geometry, which is the focus of this article.

In the lab experiments, two different setups are usually used: rock core acidization in Hassler cell and quasi-2D systems in Hele-Shaw cell which are aimed to study the dissolution in quasi-2D porous media and fractures. The number of core-flooding experiments reported in the literature is significantly larger than Hele-Shaw cell studies. There are two reasons for that: First, the core-flooding is closer to the real conditions encountered in the wellbore acidization in petroleum

industry. Second, in core flooding it is easier to inject the flow into a porous matrix with negligible boundary effect. Many variables are systematically controlled in core-flooding experiments, including: injection rate [22], sample material [23], system scale [24], pH and temperature [25].

In this work, we have decided to use a 2D Hele-Shaw cell, as quasi-2D systems are easier to visualize and due to a large number of numerical work performed on these systems [18, 21, 26, 27]. On the experimental side, Daccord et al. [28, 29] investigated the water/plaster system in radial Hele-Shaw cell with central injection, and Golfier et al. [16] used a water/salt system in rectangular Hele-Shaw cells. The intention of both works was to study flow in a porous matrix, however, because of the difficulty in avoiding wall effects at boundaries, the injected water in most cases was found to flow along the difficult-to-detect aperture between the medium and the confining cell plate. This problem can be turned into advantage, if we promote it in a controlled manner instead of avoiding the wall flow. Such a controlled-aperture system can then be considered as an analog of a fracture, and the study is then directed at the investigation of how the fracture aperture evolves in time as a result of dissolution. Within this frame, Detwiler et al. [30] undertook a well-controlled dissolution study of the water/KDP system in rectangular Hele-Shaw cell and systematically measured the evolution of aperture at different flow rates. Osselin et al. [31] have performed experiments on the onset of reactive-infiltration instabilities in a fracture with a microfluidic setup using a rectangular water/plaster system. However, in many cases the relevant geometry is radial rather than rectangular, for instance, in the oil industry where the acid fluids are injected from a well, and in groundwater protection where pollutants expand with or without dissolution radially from the pollution source. Xu et al. [32] have recently studied dispersion in fractures in radial geometry with a dissolution pattern around the inlet.

The aim of this project is to study the dissolution finger growth in a fracture aperture of radial geometry. In section 2, we describe our experimental setup. In section 3, we present our experimental results discussing the screening effect and the statistical properties of the dissolved part evolution. The conclusions are drawn in section 4.

2. DESCRIPTION OF EXPERIMENTS

The experimental scheme is illustrated in **Figure 1**. A Hele-Shaw cell is formed by two circular glass plates which are separated by 1 mm aluminum spacers and held together by clamps. The bottom glass plate (diameter d_1 = 36.0 cm) is larger than the upper one (diameter d_2 = 25.0 cm) and has an external rim to hold the water surface at a fixed altitude level. There is an outlet at the center of the lower glass plate. A lightbox with a homogeneous intensity of light illuminates the system from below. A digital camera (Nikon D7100) records the sample images from the top every 5 min, and the whole dissolution process is thus recorded from the beginning of fluid withdrawing up to the dissolution channel breakthrough at the central outlet.

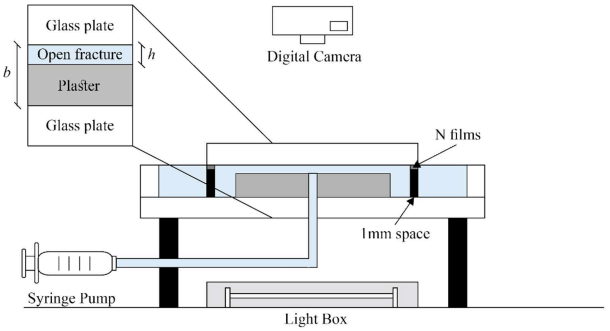

FIGURE 1 | Schematic diagram of the experimental setup. A circular Hele-Shaw cell (spacing 1 mm) contains a plaster plate with a small gap h above the plaster upper surface. The aperture is created artificially by the spacers and kept clamped. Water is withdrawn by a syringe pump from the center of the bottom glass plate (the outlet), where it flows radially inwards. The plaster plate is surrounded by freshwater. The model is illuminated from below by a light box.

The circular plaster sample between the two plates was prepared as follows: A gypsum saturated water solution was first injected into the Hele-Shaw cell. We made a plaster paste by mixing water and plaster powder with the ratio 2:3 by weight. This paste was then injected from the center of the Hele-Shaw cell. The paste displaced the plaster saturated water and formed a circular plate of radius $R_0 = 8.0cm$. The hydration of this circular plaster paste requires approximately one hour to complete. During the plaster hydration process, the plaster paste was kept in the cell surrounded by saturated water. Over time, a form of segregation called bleeding takes place, where some of the water in the plaster tends to rise to the top surface of the plaster plate [33]. This process creates a small gap $h_0 = 50\mu m$ above the upper surface of the plaster. After the completion of the hydration process, we removed the top glass plate, put several plastic films (each film thickness $h_1 = 100\mu m$) on the aluminum spacers and put back the top glass plate. The artificial aperture in our experiment h is defined as the distance between the upper glass plate and the surface of the plaster sample. The aperture created in this way is thus $h = h_0 + n \cdot h_1$ where n is the number of plastic films. In the experiments reported here, we used n = 2 films which gave $h = 250\mu m$. When the sample preparation was completed, we started the dissolution experiments.

Because the radial dissolution by injection from the center gives a very short dissolution front around a point-like inlet, it becomes difficult to analyze the evolution of the fingers and the periodic wavelength from the experimental images in such a setup. Therefore, we chose instead to withdraw the water by a syringe pump from the outlet located at the center of the bottom glass plate. In this way, the freshwater flows from the rim toward the center and dissolves the plaster sample from the outer boundary. The instability can then be observed along the external perimeter of the sample. The withdrawing flow rate Q is set as $Q = 0.18ml/min$ and the initial aperture of the artificial fracture is $h = 250\mu m$. The permeability of the porous plaster matrix is $\kappa_p = 6.0 \cdot 10^{-14}m^2$ [34] but the permeability of the fracture

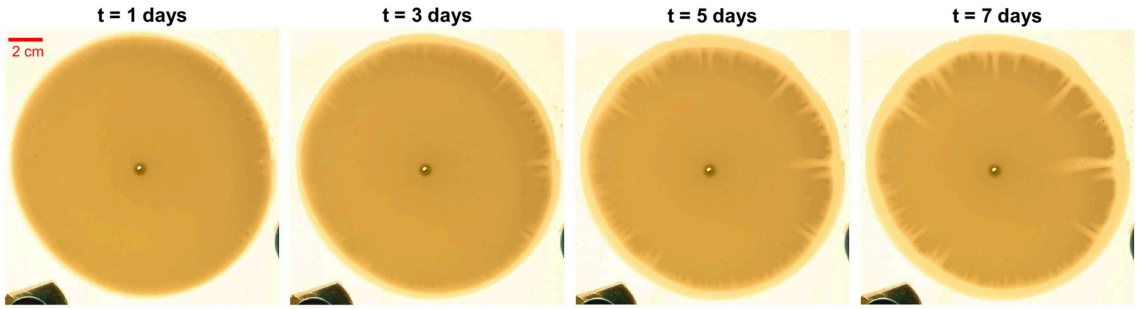

FIGURE 2 | Experimental photos of the developing fingering pattern at different moments of time. The time interval between the photos is 2 days. In the circular plaster sample, the dark yellow disk is the undissolved part of plaster and the light yellow part represents the dissolved or partially dissolved part.

calculated as $\kappa = h^2/12$ is around $5.2 \cdot 10^{-9} m^2$, thus 5 magnitudes larger than the permeability of the porous matrix of our plaster sample. Therefore almost all the freshwater flows through the fracture instead of the porous matrix. The freshwater pumped through the system is distilled water at room temperature $T = 22^{\circ}C$ with $pH = 7.17$. The molecular diffusion coefficient of plaster (gypsum) in water is $D_m = 1.0 \cdot 10^{-9} m^2/s$ [35]. One experiment lasts around 10 days. The camera records the entire dynamic evolution process from initial instabilities to fingering formation, then to dissolution finger growth, and finally to the breakthrough of the longest fingers at the outlet.

2.1. Characteristic Timescales

The initial aperture h is an important characteristic length scale in our system. A characteristic timescale for diffusion across the aperture is $t_D = h^2/Dm = 62.5s$ and the characteristic timescale for the reaction on the same length scale is $t_R = h/k = 54.3s$, where k is the chemical reaction kinetic constant ($k = 4.6 \cdot 10^{-6} m/s$) [36]. A relevant time scale for convection is the time it takes to flush the system, i.e., $t_C = \pi R_0^2 h/Q = 1,670s$. As we see, $t_C \gg t_D \approx t_R$. It means that reaction and diffusion across the aperture happen almost immediately compared with the time it takes for a fluid particle to flow through the system and we therefore expect that the calcium concentration of the water will reach the saturation concentration at the outlet. We performed density measurements to determine the concentration of the effluent solution. The concentration at the outlet is $C_{outlet} = 2.5g/L$ which is consistent with the value of the saturation concentration reported in the literature $C_{sat} = 2.53g/L$ [37].

3. EXPERIMENTAL RESULTS AND DISCUSSION

3.1. Dissolution Finger Growth With Screening Effect

As the freshwater flows from the edge of the plaster sample to the center, the plaster begins to dissolve. In this process, the water becomes saturated, thus the dissolution concentrates at the perimeter. After several days, a visible dissolution front appears and it slowly develops into many dissolution fingers as a result of the reactive-infiltration instability. The further growth of these fingers becomes nonlinear, with scarce theoretical results concerning their shapes or growth rates [38, 39]. On the other hand, numerical models give a number of predictions for the fingering which can be qualitatively compared with experiments [17, 18, 21]. In particular, one can study the screening between the fingers, with the longer ones suppressing the growth of their shorter neighbors. As a results, approximately half of the active fingers continue to grow while the other half cease to grow. The process then repeats itself, leading to the scale-free distribution of finger lengths [40, 41].

Such a hierarchical growth of the fingers is clearly observed in the experimental images. Four experimental photos are chosen to show the process of the finger growth in **Figure 2** (see also **Figure S1** and **Videos S1**, **S2**).

A dissolution front is extracted from the experimental images by using thresholding. A front position D is calculated as the distance between the point at the dissolution front and the outlet center. The front position varies with the polar angle θ and time t and we define the dissolution length as $l(\theta, t) = D(\theta, t = 0) - D(\theta, t)$, where $D(\theta, t = 0)$ is the initial front line. The initial front position $D(\theta, t = 0)$ has a small variation with the radius of the plaster sample R because in the experiments, the initial plaster sample is not perfectly circular. The dissolution length evolution with time $l(\theta, t)$ is shown in **Figure 3**. We should notice that the dissolution length function $l(\theta, t)$ is not a unique function because one polar angle θ could correspond to more than one dissolution front point, at different radial positions. This is because fingers develop along the radial direction and can also grow wider, with an orthoradial growth component.

In **Figure 3**, the competitive growth of the fingers is observed, due to the screening effect. The time interval we choose is fixed (1.0 day between neighboring curves), but the growth rate for different fingers varies significantly. One part of the fingering pattern (with θ in between 4 and 5 radians) grows more slowly than the rest over the entire time which means that the fluid flux through this part must have been significantly smaller. Such a flow inhomogeneity could be accidental, because the geometry of the system is not perfectly uniform. It leads to an initial circular symmetry breaking, where one side becomes a freshwater preferential flow path, screening off dissolution at other sides. Due to a positive feedback loop, eventually, some fingers will dominate so that most freshwater concentrates in

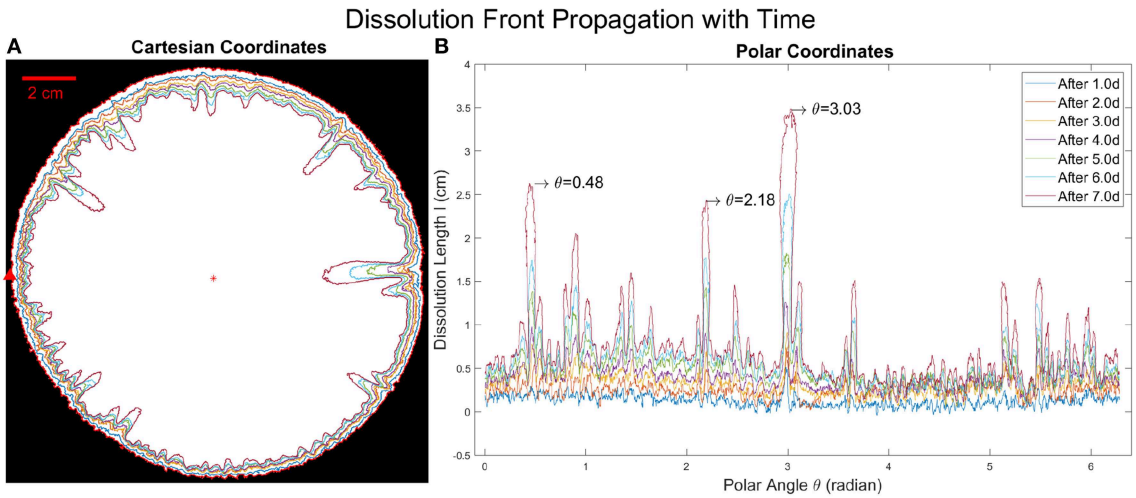

FIGURE 3 | (A) Dissolution front propagation with time in Cartesian coordinates. The outermost red circle is the initial boundary, the red star marks the origin, where the outlet is located. The red arrow shows the point where $\theta = 0$ and the direction in which the polar angle increases. Different colors of the curves show the dissolution front in different times with the time interval of 1 day between two neighboring curves. **(B)** The evolution of the dissolution length with time is shown in polar coordinates, obtained by calculating $l(\theta, t) = D(\theta, t = 0) - D(\theta, t)$ from binary experimental images. Different colors represent different times corresponding to the colors in **(A)**. The longest finger located at $\theta = 3.03$ radians and the two second longest fingers located at $\theta = 0.48$ radians and $\theta = 2.18$ radians are indicated in the plot.

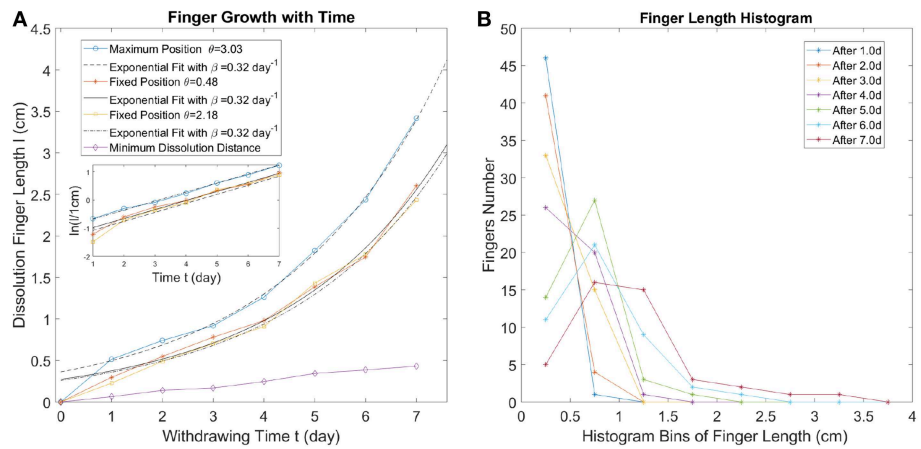

FIGURE 4 | (A) The finger length evolution with time. The longest finger and two second longest fingers growth with time are displayed. Fingers located at different angular positions (see **Figure 3B**) are represented by different colors. The finger growth with time at these positions (fixed θ) have been fitted with an exponential function $l = a \cdot e^{\beta t}$, displayed by three different black curves (solid or dashed). Minimum dissolution distance (corresponding to the point on the perimeter with the slowest dissolution speed) is shown by the purple curve. The inset shows the exponential fits for the finger length vs. time. **(B)** Dissolution finger length histograms obtained by counting the peaks in the dissolution length profiles (see **Figure 3B**). Different colors represent different times. The histogram bins cover the range 0–4.0 cm with bin size 0.5 cm.

these dissolution fingers. These long fingers then continue to grow while the short fingers grow very slowly (see **Figure 3B**). For the dissolution front propagation with time in a repeated experiment (see **Figure S2**). The longest fingers grow almost exponentially with time judging from **Figure 4A**, where we fit the finger length vs. time with an exponential function $l = a \cdot e^{\beta t}$. The exponential growth rate β is shown in the legend of **Figure 4A**. Interestingly, the values of exponential growth rates are the same for all the three different fingers $\beta = 0.32 day^{-1}$, which shows that the longest fingers grow largely independent of each other. From **Figure 3A**, the distance between these longest fingers is comparable to the length of their lengths. This is in agreement with the observation [41, 42] that the long finger screens the area of a lateral extent approximately equal to its length. For the analysis of the growth rates of other fingers (see **Figure S3A**).

In order to perform the statistical analysis of the dissolution finger growth, we find the local maxima of the curves in **Figure 3B** and define the dissolution finger length as the dissolution length corresponding to these maxima. The dissolution finger length histogram is shown in **Figure 4B**. The bins are chosen from 0 to 4.0 cm with a bin size of 0.5 cm, which divides the fingers into several types (orders). At an early

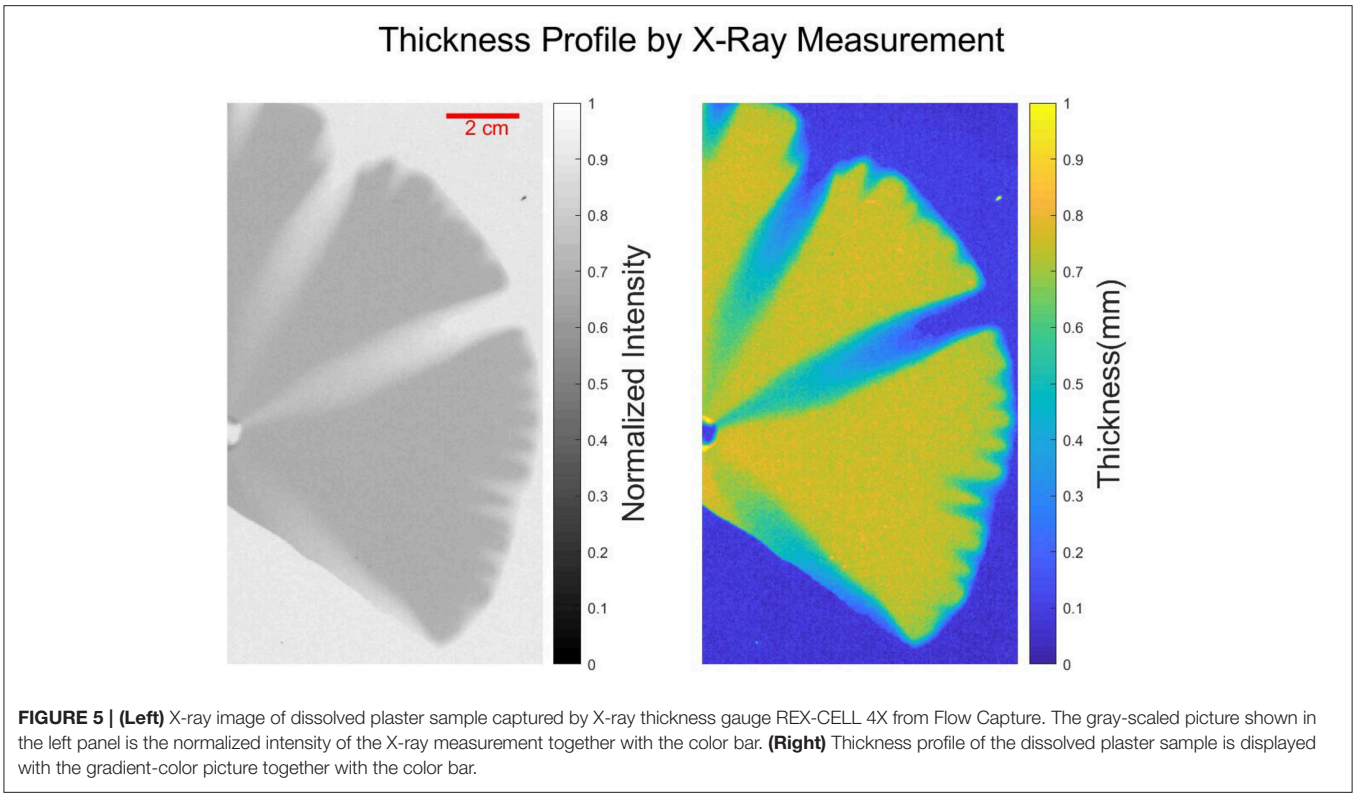

FIGURE 5 | (Left) X-ray image of dissolved plaster sample captured by X-ray thickness gauge REX-CELL 4X from Flow Capture. The gray-scaled picture shown in the left panel is the normalized intensity of the X-ray measurement together with the color bar. **(Right)** Thickness profile of the dissolved plaster sample is displayed with the gradient-color picture together with the color bar.

stage, a lot of small fingers appear, with the length below 0.5 cm; these are the first order fingers. After 3 days, 2nd order fingers become clearly visible and the distribution gets wider as time progresses. With time, the number of small fingers (finger length below 1 cm in **Figure 4B**) decreases significantly since they are absorbed by the moving dissolution front while the longest fingers (finger length above 2.5 cm in **Figure 4B**) continue to grow. For the dissolution finger length histogram of other fingers (see **Figure S3B**).

3.2. Statistical Properties of the Dissolution Patterns

We observe from **Figure 2** that the interface between the dissolved and the undissolved part is diffuse as the thickness of plaster sample at the dissolution front gradually transitions from the dissolved part to the undissolved part. Therefore, thresholding of the image, although useful for analyzing the dissolution patterns, leads inevitably to the information loss, as partially dissolved region are either interpreted as fully dissolved or as undissolved. In order to measure the aperture variation in the experimental images, a calibration between the thickness profile of the plaster sample and the intensity profile of the photos is performed by an X-ray Thickness Gauging REX-CELL 4X from Flow Capture [43–45].

The X-ray measurement for the thickness of dissolved plaster sample is displayed in **Figure 5**. The data records the photon counts at different positions of the sample by the X-ray measurement. Then the thickness profile is obtained from the intensity data by

$$d = d_s \cdot \frac{ln(I/I_0)}{ln(I_s/I_0)},$$

where d_s is the initial thickness of the undissolved plaster sample, I is the intensity at a given pixel, I_0 is the average intensity value of the background and I_s is the average intensity value of the undissolved part. This formula is derived based on the Beer-Lambert law, $I = I_0 e^{-\zeta d}$ [46] where $\zeta = 0.43mm^{-1}$ normalized by a reference intensity $I_s = I_0 e^{-\zeta d_s}$ corresponding to the undissolved sample.

The X-ray measurement and the calibration with the images illuminated by white light are shown in **Figure 6**. We compared the image illuminated by X-ray and the image illuminated by lightbox, we found a linear regression for the scatter plot of two images with $y = 0.94 \cdot x - 0.02$. The Pearson correlation coefficient [47] between the two images is 0.95, which confirms that we can calculate the thickness of the plaster based on the lightbox measurements.

This allows us to quantify the local volume of dissolved gypsum in the sample. First, we define the aperture growth at a given point as as $\delta h_t(r,\theta) = h_t(r,\theta) - h$ where $h_t(r,\theta)$ is the aperture at radial position r and polar angle θ and h is the initial aperture. Next, we calculate the dissolved volume per unit angle as $V_\theta(\theta,t) = \int_0^{R_0} \delta h_t(r) \cdot r dr$. Note that the total dissolved volume is an integral of $V_\theta(\theta,t)$ over the polar angle, $V_{diss}(t) = \int_0^{2\pi} V_\theta(\theta,t) d\theta$. Subsequently, we find it more convenient to use the arc length along the perimeter, $p = R_0\theta$, instead of θ itself,

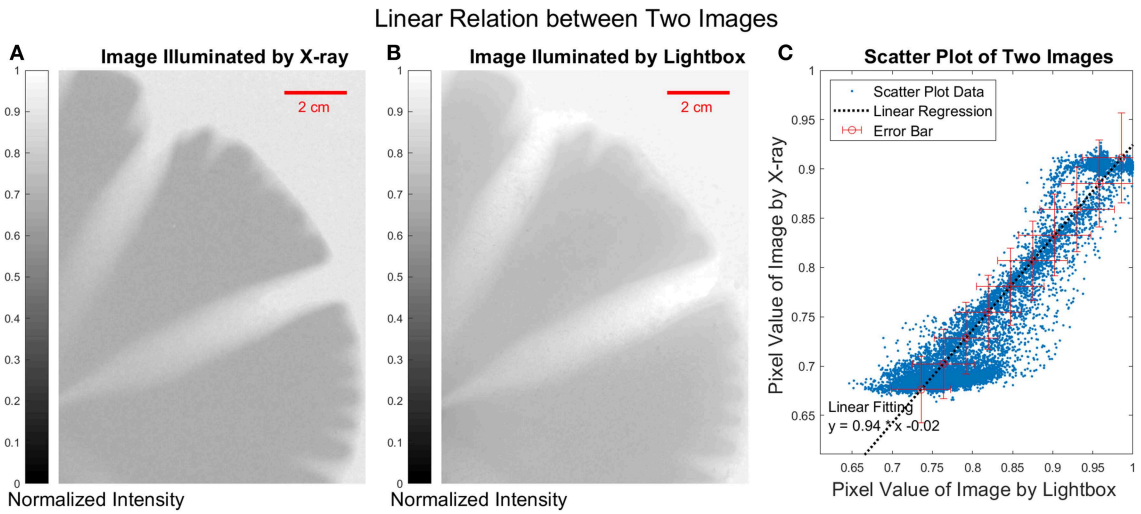

FIGURE 6 | (A) X-ray image of the plaster sample. **(B)** Image illuminated by light box of the white light. **(C)** The scatter plot, each point in the scatter plot represents a pixel at the same position in both images illuminated by X-ray and the white light. The error bars are of the order of 5% on each of the axes. The pixel value below 0.7 represents the undissolved part and the pixel value above 0.9 represents the empty area outside of the plaster sample.

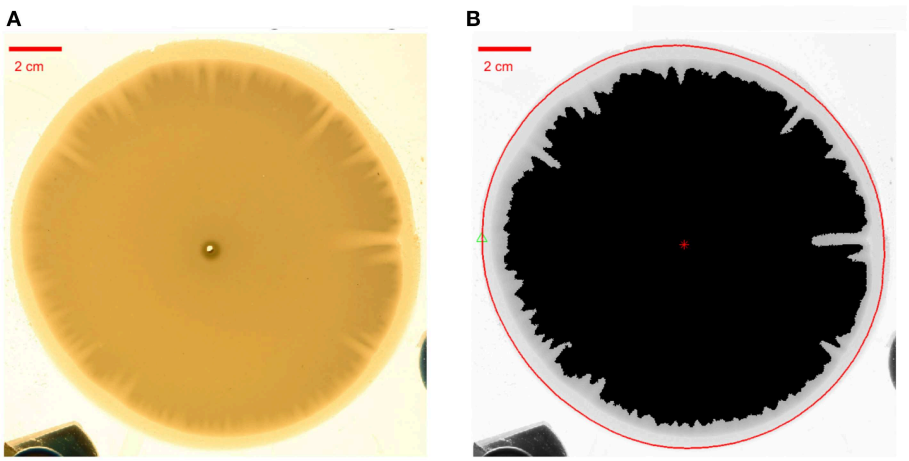

FIGURE 7 | Estimation of the local dissolved part. **(A)** An experimental photo to be processed. **(B)** The red circular line acts as the reference curve, which represents the boundary of the initial plaster sample. The black part represents the undissolved part of the plaster sample. The red star marks the center of the plaster sample. We integrate the aperture variation values along a radial line from a point on the perimeter of the red circular line to the center.

to parameterize the experimental data. Then we define a local dissolved part as $S_D(p,t) = \int_0^{R_0} \delta h_t(r) \frac{r}{R_0} dr = V_\theta(\theta,t)/R_0$. The calculation method is illustrated in **Figure 7**.

The local dissolved part $S_D(p,t)$ evolves in time as the dissolution front propagates, as illustrated in **Figure 8A**. In order to analyze this function quantitatively, a fast Fourier transform with a Blackman window [48] is applied at different times to obtain power spectrum $S(k,t)$ where k is the spatial frequency or wavenumber ($k = 1/\lambda$ where λ is the wavelength).

The data in **Figure 6A** shows another manifestation of the screening of the shorter fingers by the longer ones. The power spectrum in **Figure 8B** has two main peaks before wavenumber $k = 0.1cm^{-1}$. The first peak (Peak 1 indicated by the red circle) at $0.02\ cm^{-1}$ with wavelength $\sim 50cm$ comes from the perimeter of the plaster sample and the second peak (Peak 2 indicated by the blue circle) at $0.06\ cm^{-1}$ with a wavelength $\sim 17cm$ is connected with the deviation of the initial gypsum disk from the circular shape (see **Figures S6, S7** in Supplementary Data). We will ignore these two peaks because they come from the geometric properties of the initial plaster sample and not from the dissolution process. Beyond these two peaks, the maximum of the power spectrum is observed at $0.24cm^{-1}$ with wavelength $\sim$ $4.2cm$, indicated by the red star in **Figure 8B**. This wavelength is related to the characteristic distance between the longest fingers, which is the main contribution to the power spectrum after finger formation. From the semi-log representation in **Figure 8C**, we see that the

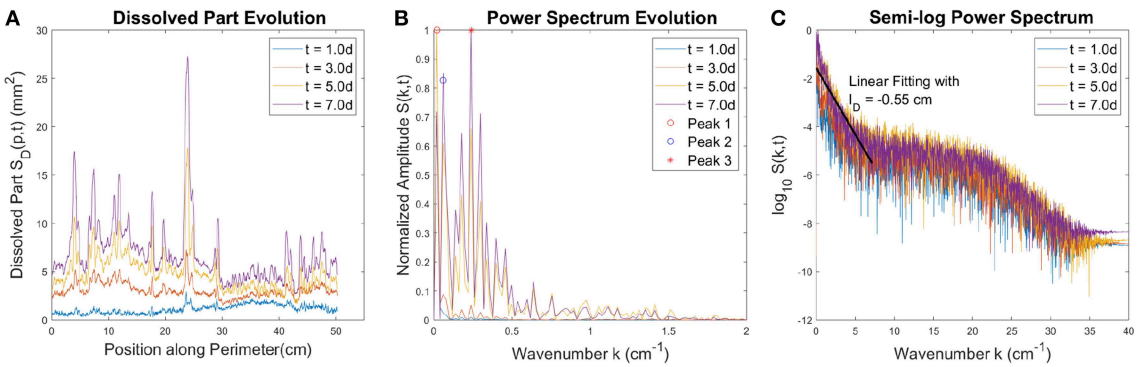

FIGURE 8 | (A) The local dissolved part $S_D(p,t)$ at different time moments. **(B)** The power spectrum of $S_D(p,t)$ profiles presented in **(A)**. Three main peaks are indicated in the plot. The first two (marked by red and blue circles) are related to the initial geometry of the plaster sample. On the other hand, the peak at 0.24 cm^{-1} with wavelength $\sim 4.2cm$ (marked by the red star) is related to the characteristic wavelength of the fingering pattern. **(C)** Semi-log plot of the power spectrum, which allows to observe power amplitude trends in a larger scope. The amplitude decays almost exponentially with wavenumber at low wavenumber (high wavelength), followed by a flat plateau at higher wavenumbers. The solid black line in **(C)** is the linear fit, the slope of which gives the characteristic decay length, $l_D = 0.55cm$.

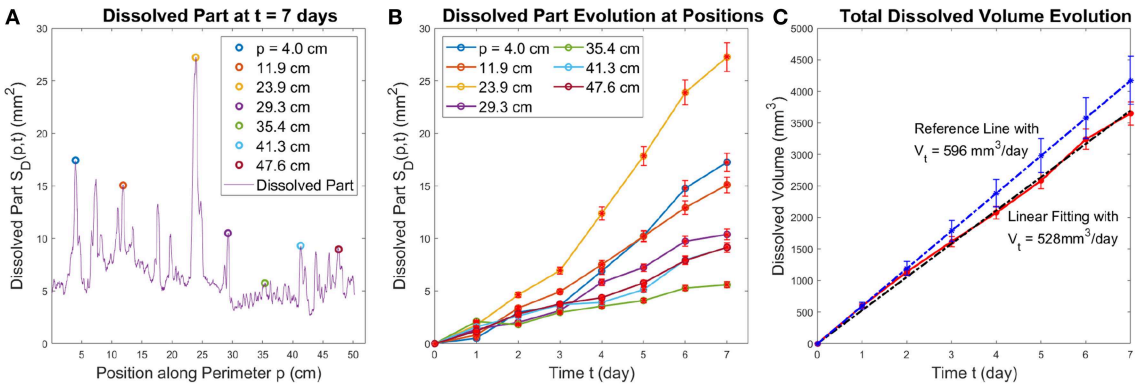

FIGURE 9 | The left panel **(A)** shows the local dissolved part along the perimeter, $S_D(p,t)$ at $t = 7$ days. The positions corresponding to the individual fingers, at $p =$ [4.0, 11.9, 23.9, 29.3, 35.4, 41.3, 47.6] cm are marked with color circles. The center panel **(B)** displays the growth of $S_D(p_i,t)$ at these positions with error bars. The right panel **(C)** shows the total dissolved volume as a function of time (red line) together with a linear fit (black line) and the theoretical estimate (blue line) with the corresponding error bars. The overlap between error bars show the experimental measurement fits well with the theoretical estimate.

amplitude decays almost exponentially with wavenumber at low wavenumbers (high wavelengths), followed by a flat plateau at higher wavenumber. The decay is exponential, $S(k,t) \propto S(0,t) \cdot e^{-l_D \cdot k}$ with the characteristic decay length $l_D = 0.55cm$ as shown in **Figure 8C**. The Fourier transform of a Lorentzian gives an exponential function [49]. The width of the Lorentzian gives the characteristic decay length of this exponential function. Since the largest fingers are of a similar shape, we expect the decay length $l_D = 0.55cm$ to correspond to their characteristic width, which is indeed the case. The amplitude of the power spectrum decays gradually after a crossover at wavenumber $k = 20cm^{-1}$ corresponding to the wavelength $\lambda = 0.5mm$. The part of the spectrum with the wavenumber larger than $k = 20cm^{-1}$ are considered as noise from the roughness of the dissolution front.

The local dissolved part increases in time, as illustrated in **Figure 9**. The uncertainty of the measurement of the thickness variation is about 5% according to **Figure 6**. In **Figure 9**, we present the evolution of $S_D(p,t)$ with error bars at several different points along the perimeter of the sample, the positions of which are marked by circles with the corresponding color in **Figure 9A**. **Figure 9B** further confirms the crucial role played in the dynamics by the competition between the fingers—the longer fingers speed up at the expense of the shorter ones.

To validate the calibration between the aperture profile and intensity profile, we have also calculated the growth of the total dissolved volume in time. The results, presented in **Figure 9C**, show that V_D increases linearly in time with the slope of $528mm^3$ per day. This is close to the theoretical estimate of the growth of the dissolved volume based on the mass balance of the reactant

$$V_D = \frac{Q \cdot c_{sat}}{\rho_b} t, \tag{1}$$

where Q is the injection rate, c_{sat} is the solubility of gypsum in pure water at 20°C and ρ_b is the bulk density of experimental

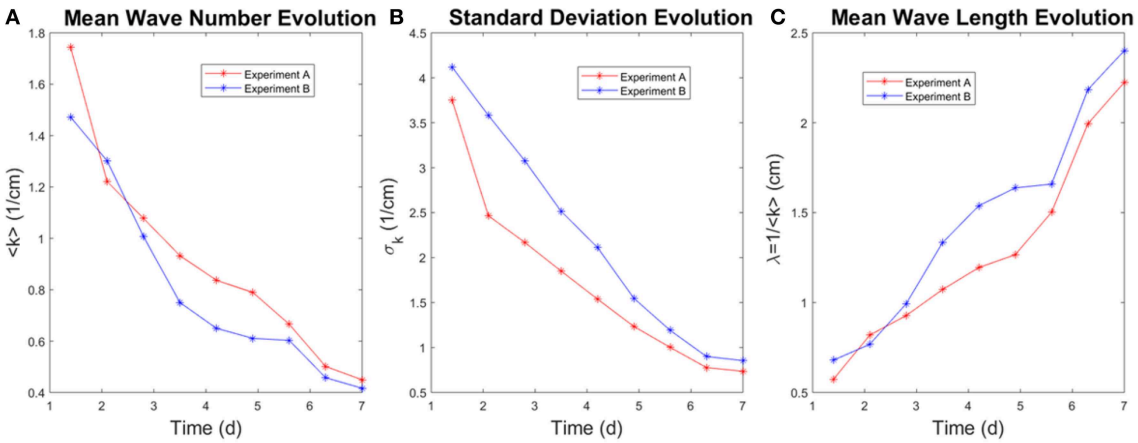

FIGURE 10 | The figure shows the mean wavenumber (for $k > 0.1cm^{-1}$), its standard deviation and the mean wavelength ($\lambda = 1/k$) evolution with time for two experiments with the same aperture $h = 250\mu m$ and the withdrawing rate $Q = 0.18ml/min$. **(A)** The average wavenumber decreases with time. **(B)** The standard deviation decreases with time. **(C)** The average fingering wavelength increases with time.

plaster sample. For $Q = 0.180ml/min$, $c_{sat} = 2.53g/l$ [37] and $\rho_b = 1.1g/ml$ we get the rate of growth of the dissolved volume of $596mm^3/day$ with an uncertainty of 9.1%, a reference line of this slope with error bars is shown in **Figure 9C**. The possible factors influencing the difference between the theoretical slope and the one measured experimentally come from inaccuracy in theH measurement of the bulk density ρ_b, measurement of the thickness variation δh and the linear fitting for $V_D(t)$ based on the image analysis. Importantly, the second run of this experiment results in similar statistical properties of the dissolved pattern (see the Supplemental Data in **Figures S4, S5**).

We now introduce a calculation method by Vinningland et al. [50] who characterized the mean wavenumber of a growing interface. We again ignore the low frequencies since they are related to the initial geometric properties of the sample and only consider the wavelength $\lambda < 10cm$ i.e., $k > 0.1cm^{-1}$. An average wavenumber $< k >$ from the power spectrum $S(k)$ for $k > 0.1cm^{-1}$ is defined as:

$$< k >= \frac{\Sigma k \cdot S(k)}{\Sigma S(k)}, \tag{2}$$

where the sum Σ is over all $k > 0.1cm^{-1}$. The standard deviation σ_f is defined as:

$$\sigma_k = \sqrt{\frac{\Sigma k^2 \cdot S(k)}{\Sigma S(k)} - < k >^2}. \tag{3}$$

We calculate the temporal evolution of $< k >$ and σ_k, shown in **Figure 10**. As observed, the average wavenumber decreases with time, i.e. the average wavelength increases. This is another manifestation of the competition between the fingers: longer fingers develop and screen off nearby shorter fingers, which leads to a larger wavelength. The average wavenumber ranges from 0.4 to 1.8 cm^{-1}, thus the average wavelength ranges from 0.6 to 2.5 cm which fits the observation of characteristic wavelength from the experimental images.

4. CONCLUSIONS

Understanding of the dissolution of fractures is important both for basic science (e.g., for studies of speleogenesis) as well as for technological applications, particularly in petroleum industry. However, the dissolution experiments in quasi-2d, radial geometry are relatively seldom performed. We dissolve a plaster disk in a Hele-Shaw cell by withdrawing water from the center, thus creating the inward flow pattern, and for the first time to our knowledge, we report the reactive-infiltration instability and finger growth along the perimeter of the circular plaster sample. The perimeter is 50.3 cm long which is sufficient to perform a statistical study of the reactive-infiltration instability and the dissolution fingers growth with time.

We observe strong competition between the growing fingers with the longest fingers growing exponentially with time in our experiments. We measure the thickness variation of the plaster sample by X-ray gauge and quantify the evolution in time of the dissolved volume. We then analyze it using statistical methods. The characteristic wavelength of the perturbations of the front is measured by a fast Fourier transform of the local dissolved volume. The power spectrum shows exponential decay with a characteristic decay length $l_D = 0.55cm$. On the other hand, the average wavelength increases linearly with time.

Our experimental setup allows us to adjust both the aperture thickness and flow rate. In the future, we will systematically control these two parameters to study a dissolution phase diagram in a radial geometry.

DATA AVAILABILITY

The raw data supporting the conclusions of this manuscript will be made available by the authors, without undue reservation, to any qualified researcher.

AUTHOR CONTRIBUTIONS

LX and KM designed the experiment. LX performed the experiments, analyzed the data, and authored the paper. PS, RT, EF, and KM assisted with the interpretation and data analysis, and editing of the manuscript.

FUNDING

This project has received funding from the European Union's Seventh Framework Programme for research, technological development and demonstration under grant agreement no 316889. We acknowledge the support of the University of Oslo and the support by the Research Council of Norway through its Centres of Excellence funding scheme, project number 262644, the INSU ALEAS program, the French-Norwegian LIA D-FFRACT, and the support by the National Science Centre (Poland) under Research Grant 2012/07/E/ST3/01734.

ACKNOWLEDGMENTS

We thank Atle Jensen, Bin Hu for technical support of X-ray measurement and Marcel Moura, Fredrik K. Eriksen, Mihailo Jankov, Monem Ayaz, Guillaume Dumazer, and Florian Osselin for useful discussions.

SUPPLEMENTARY MATERIAL

The Supplementary Material for this article can be found online at: https://www.frontiersin.org/articles/10.3389/fphy.2019.00096/full#supplementary-material

Video S1 | The video of the experiment described in the main text shows the sequence of the experimental photos of the developing fingering pattern at different moments of time.

Video S2 | The video of the experiment described in the Supplementary Material shows the sequence of the experimental photos of the developing fingering pattern at different moments of time.

REFERENCES

1. Iyer K, Jamtveit B, Mathiesen J, Malthe-Sørenssen A, Feder J. Reaction-assisted hierarchical fracturing during serpentinization. *Earth Planet Sc Lett.* (2008) **267**:503–16. doi: 10.1016/j.epsl.2007.11.060
2. Ortoleva P, Chadam J, Merino E, Sen A. Geochemical self-organization II: the reactive-infiltration instability. *Am J Sci.* (1987) **287**:1008–40. doi: 10.2475/ajs.287.10.1008
3. Bekri S, Thovert J, Adler P. Dissolution of porous media. *Chem Eng Sci.* (1995) **50**:2765–91. doi: 10.1016/0009-2509(95)00121-K
4. Steefel CI, Lasaga AC. A coupled model for transport of multiple chemical species and kinetic precipitation/dissolution reactions with application to reactive flow in single phase hydrothermal systems. *Am J Sci.* (1994) **294**:529–92. doi: 10.2475/ajs.294.5.529
5. Aharonov E, Spiegelman M, Kelemen P. Three-dimensional flow and reaction in porous media: Implications for the Earth's mantle and sedimentary basins. *J Geophys Res.* (1997) **102**:14821–14. doi: 10.1029/97JB00996
6. Romanov D, Gabrovšek F, Dreybrodt W. Dam sites in soluble rocks: a model of increasing leakage by dissolutional widening of fractures beneath a dam. *Eng Geol.* (2003) **70**:17–35. doi: 10.1016/S0013-7952(03)00073-5
7. Michael K, Golab A, Shulakova V, Ennis-King J, Allinson G, Sharma S, et al. Geological storage of CO2 in saline aquifers review of the experience from existing storage operations. *Int J Greenh Gas Con.* (2010) **4**:659–67. doi: 10.1016/j.ijggc.2009.12.011
8. Fredd CN, Fogler HS. Influence of transport and reaction on wormhole formation in porous media. *AIChE J.* (1998) **44**:1933–49. doi: 10.1002/aic.690440902
9. Lake LW, Liang X, Edgar TF, Al-Yousef A, Sayarpour M, Weber D, et al. Optimization of oil production based on a capacitance model of production and injection rates. In: *Hydrocarbon Economics and Evaluation Symposium.* Dallas, TX: Society of Petroleum Engineers (2007).
10. Sudaryanto B, Yortsos YC. Optimization of displacements in porous media using rate control. In: *SPE Annual Technical Conference and Exhibition.* New Orleans, LA: Society of Petroleum Engineers (2001).
11. Chadam J, Hoff D, Merino E, Ortoleva P, Sen A. Reactive infiltration instabilities. *IMA J Appl Math.* (1986) **36**:207–21. doi: 10.1093/imamat/36.3.207
12. Szymczak P, Ladd AJ. Instabilities in the dissolution of a porous matrix. *Geophys Res Lett.* (2011) **38**:L07403. doi: 10.1029/2011GL046720
13. Szymczak P, Ladd AJ. Reactive-infiltration instabilities in rocks. Part 2. Dissolution of a porous matrix. *J Fluid Mech.* (2014) **738**:591–630. doi: 10.1017/jfm.2013.586
14. Szymczak P, Ladd AJ. Reactive-infiltration instabilities in rocks. Fracture dissolution. *J Fluid Mech.* (2012) **702**:239–64. doi: 10.1017/jfm.2012.174
15. Budek A, Szymczak P. Network models of dissolution of porous media. *Phys Rev E.* (2012) **86**:056318. doi: 10.1103/PhysRevE.86.056318
16. Golfier F, Zarcone C, Bazin B, Lenormand R, Lasseux D, Quintard M. On the ability of a Darcy-scale model to capture wormhole formation during the dissolution of a porous medium. *J Fluid Mech.* (2002) **457**:213–54. doi: 10.1017/S0022112002007735
17. Kalia N, Balakotaiah V. Modeling and analysis of wormhole formation in reactive dissolution of carbonate rocks. *Chem Eng Sci.* (2007) **62**:919–28. doi: 10.1016/j.ces.2006.10.021
18. Panga MK, Ziauddin M, Balakotaiah V. Two-scale continuum model for simulation of wormholes in carbonate acidization. *AIChE J.* (2005) **51**:3231–48. doi: 10.1002/aic.10574
19. Zhang C, Kang Q, Wang X, Zilles JL, Muller RH, Werth CJ. Effects of pore-scale heterogeneity and transverse mixing on bacterial growth in porous media. *Environ Sci Technol.* (2010) **44**:3085–92. doi: 10.1021/es903396h
20. Zhang X, Deeks LK, Glyn Bengough A, Crawford JW, Young IM. Determination of soil hydraulic conductivity with the lattice Boltzmann method and soil thin-section technique. *J Hydrol.* (2005) **306**:59–70. doi: 10.1016/j.jhydrol.2004.08.039
21. Szymczak P, Ladd A. Wormhole formation in dissolving fractures. *J Geophys Res.* (2009) **114**:B06203. doi: 10.1029/2008JB006122
22. Daccord G, Lenormand R. Fractal patterns from chemical dissolution. *Nature.* (1987) **325**:41–3. doi: 10.1038/325041a0
23. Hoefner M, Fogler HS. Pore evolution and channel formation during flow and reaction in porous media. *AIChE J.* (1988) **34**:45–54. doi: 10.1002/aic.690340107
24. McDuff D, Shuchart CE, Jackson S, Postl D, Brown JS. Understanding wormholes in carbonates: unprecedented experimental scale and 3-D visualization. In: *SPE Annual Technical Conference and Exhibition.* Florence: Society of Petroleum Engineers (2010).

25. Wang Y, Hill A, Schechter R. The optimum injection rate for matrix acidizing of carbonate formations. In: *SPE Annual Technical Conference and Exhibition*. Houston, TX: Society of Petroleum Engineers (1993).
26. Szymczak P, Ladd A. Microscopic simulations of fracture dissolution. *Geophys Res Lett.* (2004) **31**:L23606. doi: 10.1029/2004GL021297
27. Cohen C, Ding D, Quintard M, Bazin B. From pore scale to wellbore scale: impact of geometry on wormhole growth in carbonate acidization. *Chem Eng Sci.* (2008) **63**:3088–99. doi: 10.1016/j.ces.2008.03.021
28. Daccord G, Touboul E, Lenormand R. Chemical dissolution of a porous medium: limits of the fractal behaviour. *Geoderma.* (1989) **44**:159–65. doi: 10.1016/0016-7061(89)90025-6
29. Daccord G. Chemical dissolution of a porous medium by a reactive fluid. *Phys Rev Lett.* (1987) **58**:479. doi: 10.1103/PhysRevLett.58.479
30. Detwiler RL, Glass RJ, Bourcier WL. Experimental observations of fracture dissolution: the role of Peclet number on evolving aperture variability. *Geophys Res Lett.* (2003) **30**:1648. doi: 10.1029/2003GL017396
31. Osselin F, Kondratiuk P, Budek A, Cybulski O, Garstecki P, Szymczak P. Microfluidic observation of the onset of reactive-infitration instability in an analog fracture. *Geophys Res Lett.* (2016) **43**:6907–15. doi: 10.1002/2016GL069261
32. Xu L, Marks B, Toussaint R, Flekkøy EG, Måløy KJ. Dispersion in fractures with ramified dissolution patterns. *Front Phys.* (2018) **6**:29. doi: 10.3389/fphy.2018.00029
33. Powers TC. *The Properties of Fresh Concrete*. New York, NY: John Wiley and Sons (1968).
34. Ewers OR. *Cavern Development in the Dimensions of Length and Breadth* (Open access dissertations and thesis). McMaster University, Hamilton, ON, Canada (1982).
35. Colombani J, Bert J. Holographic interferometry study of the dissolution and diffusion of gypsum in water. *Geochim Cosmochim Acta.* (2007) **71**:1913–20. doi: 10.1016/j.gca.2007.01.012
36. Colombani J. Measurement of the pure dissolution rate constant of a mineral in water. *Geochim Cosmochim Acta.* (2008) **72**:5634–40. doi: 10.1016/j.gca.2008.09.007
37. Klimchouk A. The dissolution and conversion of gypsum and anhydrite. *Int J Speleol.* (1996) **25**:2. doi: 10.5038/1827-806X.25.3.2
38. Nilson RH, Griffiths SK. Wormhole growth in soluble porous materials. *Phys Rev Lett.* (1990) **65**:1583–6. doi: 10.1103/PhysRevLett.65.1583
39. Kondratiuk P, Szymczak P. Steadily translating parabolic dissolution fingers. *SIAM J Appl Math.* (2015) **75**:2193–213. doi: 10.1137/151003751
40. Huang Y, Ouillon G, Saleur H, Sornette D. Spontaneous generation of discrete scale invariance in growth models. *Phys Rev E.* (1997) **55**:6433. doi: 10.1103/PhysRevE.55.6433
41. Budek A, Garstecki P, Samborski A, Szymczak P. Thin-finger growth and droplet pinch-off in miscible and immiscible displacements in a periodic network of microfluidic channels. *Phys Fluids.* (2015) **27**:112109. doi: 10.1063/1.4935225
42. Upadhyay VK, Szymczak P, Ladd AJ. Initial conditions or emergence: what determines dissolution patterns in rough fractures? *J Geophys Res.* (2015) **120**:6102–21. doi: 10.1002/2015JB012233
43. Gouze P, Noiriel C, Bruderer C, Loggia D, Leprovost R. X-ray tomography characterization of fracture surfaces during dissolution. *Geophys Res Lett.* (2003) **30**:1267. doi: 10.1029/2002GL016755
44. Hu B, Stewart C, Hale CP, Lawrence CJ, Hall AR, Zwiens H, et al. Development of an X-ray computed tomography (CT) system with sparse sources: application to three-phase pipe flow visualization. *Exp Fluids.* (2005) **39**:667–78. doi: 10.1007/s00348-005-1008-2
45. Smith L, Kolaas J, Jensen A, Sveen K. Investigation of surface structures in two phase wavy pipe flow by utilizing X-ray tomography. *Int J Multiphas Flow.* (2018) **107**:246–55. doi: 10.1016/j.ijmultiphaseflow.2018.06.004
46. Curry TS, Dowdey JE, Murry RC. *Christensen's Physics of Diagnostic Radiology*. Lippincott Williams & Wilkins (1990).
47. Lee Rodgers J, Nicewander WA. Thirteen ways to look at the correlation coefficient. *Am Stat.* (1988) **42**:59–66.
48. Harris FJ. On the use of windows for harmonic analysis with the discrete Fourier transform. *Proc IEEE.* (1978) **66**:51–83.
49. Bracewell RN, Bracewell RN. *The Fourier Transform and Its Applications.* Vol. 31999. New York, NY: McGraw-Hill (1986).
50. Vinningland JL, Johnsen Ø, Flekkøy EG, Toussaint R, Måløy KJ. Granular rayleigh-taylor instability: experiments and simulations. *Phys Rev Lett.* (2007) **99**:048001. doi: 10.1103/PhysRevLett.99.048001

Conflict of Interest Statement: The authors declare that the research was conducted in the absence of any commercial or financial relationships that could be construed as a potential conflict of interest.

frontiers in Physics

ORIGINAL RESEARCH
published: 09 January 2020
doi: 10.3389/fphy.2019.00225

Effective Rheology of Bi-viscous Non-newtonian Fluids in Porous Media

Laurent Talon[1]* *and Alex Hansen*[2]

[1] Laboratoire FAST, Université Paris-Sud, UPMC, CNRS, Université Paris-Saclay, Orsay, France, [2] PoreLab, Department of Physics, Norwegian University of Science and Technology, Trondheim, Norway

We model the flow of bi-viscous non-Newtonian fluids in porous media by a square lattice where the links obey a piece-wise linear constitutive equation. We find numerically that the flow regime, where the network transitions from all links behaving according to the first linear part of the constitutive equation to all links behaving according to the second linear part of the constitutive equation, is characterized by a critical point. We measure two critical exponents associated with this critical point, one of them being the correlation length exponent. We find that both critical exponents depend on the parameters of the model.

Keywords: porous media, non-newtonian fluid, percolation, critical system, non-linear Darcy law

OPEN ACCESS

Edited by:
Lev Shchur,
Landau Institute for Theoretical Physics, Russia

Reviewed by:
Allbens Picardi Faria Atman,
Federal Center for Technological Education of Minas Gerais, Brazil
Jordan Yankov Hristov,
University of Chemical Technology and Metallurgy, Bulgaria
Alexandre Lavrov,
SINTEF Industry, Norway

***Correspondence:**
Laurent Talon
talon@fast.u-psud.fr

Specialty section:
This article was submitted to Interdisciplinary Physics, a section of the journal Frontiers in Physics

Received: *09 April 2019*
Accepted: *04 December 2019*
Published: *09 January 2020*

Citation:
Talon L and Hansen A (2020) Effective Rheology of Bi-viscous Non-newtonian Fluids in Porous Media. Front. Phys. 7:225. doi: 10.3389/fphy.2019.00225

1. INTRODUCTION

The behavior of complex fluids when being inside a porous medium may be very different from that when they are not. This is a problem encountered in many biological or industrial applications ranging from impregnation of fibrous materials to immiscible multi-phase flow in porous media. Among the different types of non-Newtonian fluids, many undergo behavioral changes depending on the stress or strain applied. One can mention the Carreau rheology which is Newtonian at low shear rate but behaves as a power law fluid above a certain shear rate [1]. Other examples are yield stress fluid that responds as a solid below a critical yield threshold. Above, they behave as a power law fluid [2]. At the mesoscopic level, this rheological approach can also be extended to other situations. For example, inertial effects can be described as a rheological change from a Newtonian fluid to a power law (quadratic or cubic) for a given large Reynolds number [3]. Another possible extension is the displacement of immiscible fluids in porous media. In this case, the fluids may each be Newtonian. However, the interfacial tension between them makes them effectively behave in a non-Newtonian way inside the porous medium [4]. Indeed, a non-zero amount of stress is then required for a non-wetting phase to invade the smaller pore throats.

Non-Newtonian fluids are notoriously difficult to treat analytically and computationally. When in addition the flow is constrained by the very complex boundary conditions of a porous medium, the effective rheology of the fluid flow is not well understood. This might for example be seen in the fact that the leading theory for describing immiscible multi-phase flow in porous media is still the relative permeability theory dating from 1936 [5] a theory which has evident weaknesses.

The purpose of this manuscript is to investigate the coupling between the heterogeneity of the medium and a rheology with a change of behavior. We study a very simple model, namely a bi-viscous fluid, where the fluid is Newtonian but with a change of viscosity at one particular shear rate (or shear stress) [6, 7]. The second viscosity might be lower (shear thinning) or higher (shear thickening). As we shall see, the coupling between the disorder and such a simple rheological model is enough to generate a rich problem.

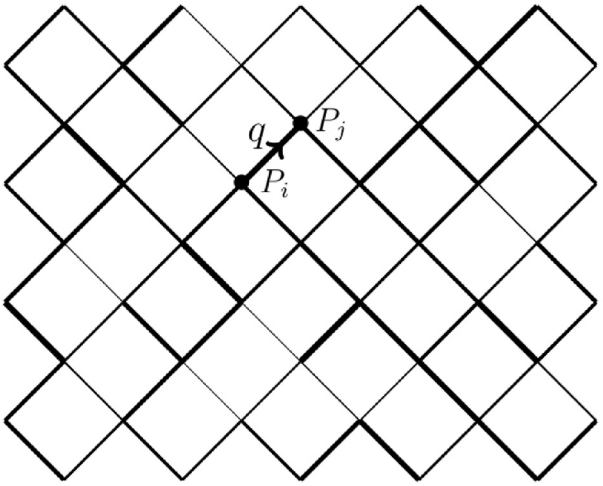

FIGURE 1 | Diamond lattice used in this work. At each node, a pressure P_i is defined. In each link, the flow rate is a function of the pressure difference $\delta P = P_i - P_j$ according to a bi-viscous model.

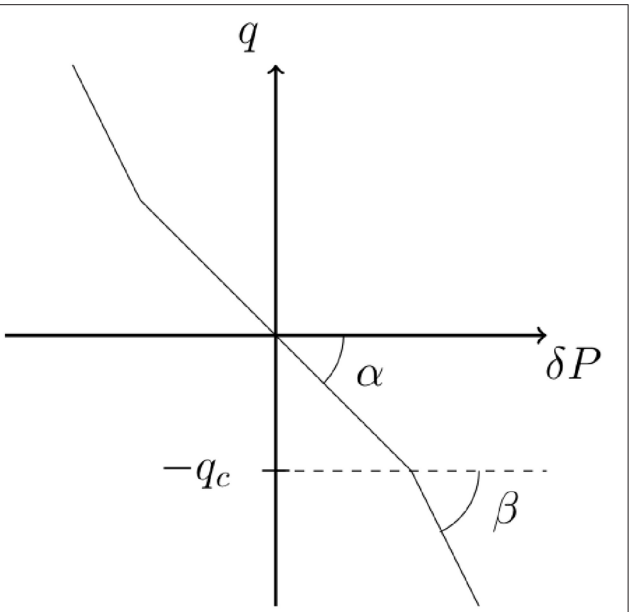

FIGURE 2 | Bi-viscous flow curve. If the absolute value of the flow rate is below a local threshold q_c, the flow is linear with a mobility α. Once the absolute value of the flow rate has reached the threshold the evolution is still linear but with different mobility β.

We also choose a simple porous medium; a square lattice oriented at 45° with respect to the average flow direction, see **Figure 1**, consisting of N_x links in the flow direction and N_y links in the direction orthogonal to the flow direction.

The constitutive equation for the fluid in a link in the lattice is given by

$$q(\nabla p) = \begin{cases} -\alpha \nabla p & : |q| \leq q_c \,, \\ -\beta \nabla p + \mathrm{sgn}(q) \left[1 - \frac{\beta}{\alpha}\right] q_c & : q_c \leq |q| \,, \end{cases} \tag{1}$$

where q is the volumetric flow rate in the link, and ∇p is the pressure drop across the link. There are three parameters, α, β and q_c. The two first parameters, α and β are the mobilities when the fluid is either in the "α-mode" or in the "β-mode." The third parameter, q_c is the flow rate at which the fluid changes from being in α-mode to β-mode. We illustrate the constitutive equation in **Figure 2**. To simplify the problem as much as possible, we let the two the α-mobilities and the β-mobilities be the same for all links in the lattice. However, each link has its own flow rate threshold q_c drawn from a distribution $p(q_c)$.

We will in the following study this system for different values of α and β and for two threshold distributions $p(q_c)$; a uniform distribution and an exponential distribution.

In section 2, we consider the symmetries inherent in the system. There are two types of symmetries. The first type is related to what happens to the volumetric flow rate through the system, Q when we scale the system parameters. Using the Euler theorem for homogeneous functions, we are able to write down the most general form of the volumetric flow rate. If we define $\langle q \rangle$ as Q/N_y, where N_y is the width of the lattice in terms of nodes, we find that $\langle q \rangle = \alpha\, \overline{q}(\nabla p, \beta/\alpha, \{q_c\}/\alpha)$, where $\{q_c\}$ refers to the set of thresholds, one for each link. The second type of symmetry is the self-duality of the square lattice leading to a mapping between the behavior of the system for a given ratio β/α and its inverse, α/β. Hence, we only need to discuss parameters for which $\beta/\alpha \geq 1$, see **Figure 3**.

We study in section 3 the lattice with $N_x = 1$, i.e., there is only one layer. The model then becomes the *capillary fiber bundle model* which is analytically tractable. We find that for the uniform threshold distribution, the flow rate behaves as $\langle q \rangle - \langle q_c \rangle \sim (\nabla p - \nabla p_c)^2$ where $(\langle q_c \rangle, \nabla p_c)$ is a point only dependent on the value of the ratio β/α and the limits of the uniform distribution $q_{\min}$ and $q_{\max}$. This is reminiscent of a *critical point*. However, it is not a critical point. There are no correlations developing in the system as ∇p approaches ∇p_c. Furthermore, the power law behavior is *not* seen when the threshold distribution is exponential.

Section 4 is devoted to the numerical algorithm we use to solve the flow patterns. Our algorithm is based on the augmented Lagrangian algorithm, which we describe in this section.

We present our results in section 5. First we note that the two limits $\beta/\alpha \to 1$ and $\beta/\alpha \to \infty$, or equivalently, $\beta/\alpha \to 0$ correspond to the *directed percolation* [8] and the *directed polymer* problems respectively [9]. This points us in the direction of there being a critical point in the problem in spite of the conclusion drawn for the capillary fiber bundle model in section 3. Indeed, this is what we find, i.e., that $\langle q \rangle - \langle q_c \rangle \sim (\nabla p - \nabla p_c)^{\mu}$ where μ depends on the ratio β/α for the same type of threshold distribution that gave a power law dependence in the capillary fiber bundle model studied in section 3. We define and measure a correlation length $L_{\max} \sim (\nabla p - \nabla p_c)^{-\nu}$. The correlation length exponent ν also depends on the ratio β/α. In the limit $\beta/\alpha \to 1$, the longitudinal directed percolation correlation length exponent $\nu_{\parallel} = 1.733847(6)$ [10] is expected and our numerical results are consistent with this. In the directed polymer limit $\beta/\alpha \to \infty$,

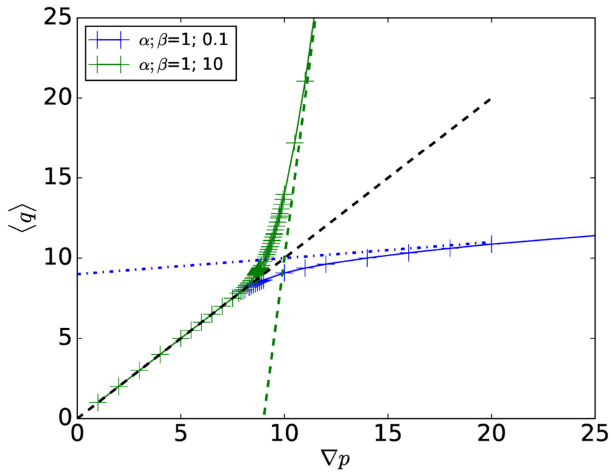

FIGURE 3 | Example of the mean flow rate $\langle q \rangle$ as function of the mean gradient ∇p for two different bi-viscous model $(\alpha, \beta) = (1, 10)$ (blue) and $(\alpha, \beta) = (1, 0.1)$ (green). As described in the text, the two cases are symmetrical through a duality mapping.

however, the corresponding correlation length exponent is *not* the usual one, $\nu_\parallel = 3/2$ [11], but rather one that describes a *correlated directed percolation problem*.

The last section 6 contains our summary and conclusions.

2. SYMMETRIES

In this section, we discuss the symmetries that lie hidden in the system we study, a diamond lattice of links obeying the constitutive (Equation 1). We consider two types of symmetry: one is based on scaling of the size and parameters of the model. Through the Euler theorem for homogeneous functions, we are able to write down the most general functional form the volumetric flow rate through the network takes. We then go on to exploring the geometrical symmetry inherent in the diamond lattice due to self-duality in the same way as first done by Straley [12]. This symmetry demonstrates that we only need to explore the part of parameter space for which $\beta/\alpha \geq 1$.

2.1. Scaling Symmetry

The volumetric flow rate Q shows a number of scaling symmetries. We combine these with the Euler theorem for homogeneous functions to deduce the functional form of $Q = Q(\Delta P, \alpha, \beta, \{q_c\}, N_x, N_y)$ [13]. Here $\{q_c\}$ is the set of thresholds, one for each link in the network. The volumetric flow rate is extensive in the width of the network, N_y. Hence,

$$\begin{aligned} &Q(\Delta P, \alpha, \beta, \{q_c\}, N_x, \lambda_y N_y) \\ &= \lambda_y Q(\Delta P, \alpha, \beta, \{q_c\}, N_x, N_y) \, . \end{aligned} \tag{2}$$

With respect to the length of the system, we find the symmetry

$$\begin{aligned} &Q(\Delta P, \alpha, \beta, \{q_c\}, N_x, N_y) \\ &= Q(\lambda_x \Delta P, \alpha, \beta, \{q_c\}, \lambda_x N_x, N_y) \, . \end{aligned} \tag{3}$$

A more subtle scaling symmetry is

$$\begin{aligned} &Q(\Delta P, \lambda_q \alpha, \lambda_q \beta, \{\lambda_q q_c\}, N_x, N_y) \\ &= \lambda_q Q(\Delta P, \alpha, \beta, \{q_c\}, N_x, N_y) \, . \end{aligned} \tag{4}$$

We also have the scaling symmetry

$$\begin{aligned} &Q\left(\Delta P, \alpha, \beta, \{q_c\}, N_x, N_y\right) \\ &= Q\left(\lambda_P \Delta P, \frac{\alpha}{\lambda_P}, \frac{\beta}{\lambda_P}, \{q_c\}, N_x, N_y\right) \, . \end{aligned} \tag{5}$$

The length N_x and width N_y of the network are discrete variables. By setting $\lambda_y = 1/N_y$ we find from Equation (2) that

$$\begin{aligned} &Q(\Delta P, \alpha, \beta, \{q_c\}, N_x, N_y) \\ &= N_y Q(\Delta P, \alpha, \beta, \{q_c\}, N_x, 1) \, . \end{aligned} \tag{6}$$

The second scaling relation, Equation (3) gives when setting $\lambda_x = 1/N_x$,

$$\begin{aligned} &Q(\Delta P, \alpha, \beta, \{q_c\}, N_x, N_y) \\ &= Q(\nabla p, \alpha, \beta, \{q_c\}, 1, N_y) \, , \end{aligned} \tag{7}$$

where we have used the definition $\nabla p = \Delta P / N_x$. We now combine (Equations 6 and 7) to get

$$\begin{aligned} &Q(\Delta P, \alpha, \beta, \{q_c\}, N_x, N_y) \\ &= N_y Q(\nabla p, \alpha, \beta, \{q_c\}, 1, 1) = \langle q \rangle \, . \end{aligned} \tag{8}$$

Hence, we define the average flow rate in the links as

$$\langle q \rangle (\nabla p, \alpha, \beta, \{q_c\}) = Q(\nabla p, \alpha, \beta, \{q_c\}, 1, 1) \, . \tag{9}$$

This is thus an intensive variable with respect to the width and the length of the network.

The two remaining scaling relations (4) and (5) involve continuous variables and we may thus make use of Euler's theorem for homogeneous functions. The Euler theorem is easy to implement for each of these four scaling symmetries: we take the derivative with respect to the scaling variable λ in each expression and set the variable equal to one.

The scaling relation (4) gives

$$\begin{aligned} &Q(\Delta P, \alpha, \beta, \{q_c\}, N_x, N_y) \\ &= \left(\frac{\partial Q}{\partial \alpha}\right) \alpha + \left(\frac{\partial Q}{\partial \beta}\right) \beta + \sum_{\text{links}} \left(\frac{\partial Q}{\partial q_c}\right) q_c \, , \end{aligned} \tag{10}$$

or in terms of the intensive variable

$$\begin{aligned} &\langle q \rangle (\nabla P, \alpha, \beta, \{q_c\}) \\ &= \left(\frac{\partial \langle q \rangle}{\partial \alpha}\right) \alpha + \left(\frac{\partial \langle q \rangle}{\partial \beta}\right) \beta + \sum_{\text{links}} \left(\frac{\partial \langle q \rangle}{\partial q_c}\right) q_c \, . \end{aligned} \tag{11}$$

We define the functions

$$A = -\left(\frac{\partial \langle q \rangle}{\partial \alpha}\right) \, , \tag{12}$$

$$B = -\left(\frac{\partial \langle q \rangle}{\partial \beta}\right) , \tag{13}$$

and,

$$\{c\} = \left\{\left(\frac{\partial \langle q \rangle}{\partial q_c}\right)\right\} . \tag{14}$$

There is one function c for each link in the network.

Whereas $\langle q \rangle$ is homogeneous of order one[1] in the variables α, β and $\{q_c\}$, the functions A, B and $\{c\}$ are homogeneous of order zero in these variables. This means that the parameters α, β and $\{q_c\}$ only appear as ratios in these functions,

$$A = A\left(\nabla p, \frac{\beta}{\alpha}, \frac{\{q_c\}}{\alpha}\right) , \tag{15}$$

$$B = B\left(\nabla p, \frac{\beta}{\alpha}, \frac{\{q_c\}}{\alpha}\right) , \tag{16}$$

and

$$\{c\} = \left\{c\left(\nabla p, \frac{\beta}{\alpha}, \frac{\{q_c\}}{\alpha}\right)\right\} . \tag{17}$$

Equation (10) may thus be written

$$\begin{aligned} \langle q \rangle(\nabla P, \alpha, \beta, \{q_c\}) = \\ -A\left(\nabla p, \frac{\beta}{\alpha}, \frac{\{q_c\}}{\alpha}\right)\alpha - B\left(\nabla p, \frac{\beta}{\alpha}, \frac{\{q_c\}}{\alpha}\right)\beta \\ + \sum_{\text{links}} c\left(\nabla p, \frac{\beta}{\alpha}, \frac{\{q_c\}}{\alpha}\right) q_c . \end{aligned} \tag{18}$$

Scaling Equation (5) combined with the Euler theorem gives

$$\left(\frac{\partial Q}{\partial \Delta P}\right)\Delta P = \left(\frac{\partial Q}{\partial \alpha}\right)\alpha + \left(\frac{\partial Q}{\partial \beta}\right)\beta , \tag{19}$$

In terms of $\langle q \rangle$ and Equation (17), we may rewrite this Equation

$$\begin{aligned} m\left(\nabla p, \frac{\beta}{\alpha}, \frac{\{q_c\}}{\alpha}\right)\nabla p \\ = A\left(\nabla p, \frac{\beta}{\alpha}, \frac{\{q_c\}}{\alpha}\right)\alpha \\ + B\left(\nabla p, \frac{\beta}{\alpha}, \frac{\{q_c\}}{\alpha}\right)\beta , \end{aligned} \tag{20}$$

where we have defined the mobility

$$m = -\left(\frac{\partial \langle q \rangle}{\partial \nabla p}\right) . \tag{21}$$

From Equations (10) and (19), we deduce that

$$\langle q \rangle = \left(\frac{\partial \langle q \rangle}{\partial \nabla p}\right)\nabla p + \sum_{\text{links}} c\, q_c = -m\nabla p + \sum_{\text{links}} c\, q_c , \tag{22}$$

[1]A homogeneous function $f(x, y)$ of order n in variables x and y fulfills the scaling relation $\lambda^n f(x, y) = f(\lambda x, \lambda y)$.

and with the help of Equation (20) we find

$$\begin{aligned} \langle q \rangle = -a\left(\nabla p, \frac{\beta}{\alpha}, \frac{\{q_c\}}{\alpha}\right)\alpha\nabla p \\ - b\left(\nabla p, \frac{\beta}{\alpha}, \frac{\{q_c\}}{\alpha}\right)\beta\nabla p \\ + \sum_{\text{links}} c\left(\nabla p, \frac{\beta}{\alpha}, \frac{\{q_c\}}{\alpha}\right) q_c , \end{aligned} \tag{23}$$

where we have defined

$$a\left(\nabla p, \frac{\beta}{\alpha}, \frac{\{q_c\}}{\alpha}\right)\nabla p = A\left(\nabla p, \frac{\beta}{\alpha}, \frac{\{q_c\}}{\alpha}\right) , \tag{24}$$

and,

$$b\left(\nabla p, \frac{\beta}{\alpha}, \frac{\{q_c\}}{\alpha}\right)\nabla p = B\left(\nabla p, \frac{\beta}{\alpha}, \frac{\{q_c\}}{\alpha}\right) . \tag{25}$$

We may take Equation (23) one step further by dividing out the parameter α,

$$\frac{\langle q \rangle}{\alpha} = \overline{q}\left(\nabla p, \frac{\beta}{\alpha}, \frac{\{q_c\}}{\alpha}\right) , \tag{26}$$

where,

$$\begin{aligned} \overline{q}\left(\nabla p, \frac{\beta}{\alpha}, \frac{\{q_c\}}{\alpha}\right) = \\ - a\left(\nabla p, \frac{\beta}{\alpha}, \frac{\{q_c\}}{\alpha}\right)\nabla p \\ - b\left(\nabla p, \frac{\beta}{\alpha}, \frac{\{q_c\}}{\alpha}\right)\frac{\beta}{\alpha}\nabla p \\ + \sum_{\text{links}} c\left(\nabla p, \frac{\beta}{\alpha}, \frac{\{q_c\}}{\alpha}\right)\frac{q_c}{\alpha} . \end{aligned} \tag{27}$$

We may as a check, compare Equation (23)—our main result in this section—with the constitutive Equation (1) in the case when there is no disorder, i.e., when all q_c are equal. In this case, $\langle q \rangle$ should be equal to the constitutive equation. Hence, in this case we find,

$$a\left(\nabla p, \frac{\beta}{\alpha}\right) = \Theta(q_c - |q|) , \tag{28}$$

$$b\left(\nabla p, \frac{\beta}{\alpha}\right) = \Theta(|q| - q_c) , \tag{29}$$

and

$$c\left(\nabla p, \frac{\beta}{\alpha}\right) = \Theta(|q| - q_c)\,\text{sign}(q)\left(1 - \frac{\beta}{\alpha}\right) . \tag{30}$$

Here Θ is the Heaviside step function which is one for positive arguments and zero for negative arguments. We note that if $|q| < q_{\min}$, then Equations (28–30) are correct as the disorder is not "noticeable" in this flow regime.

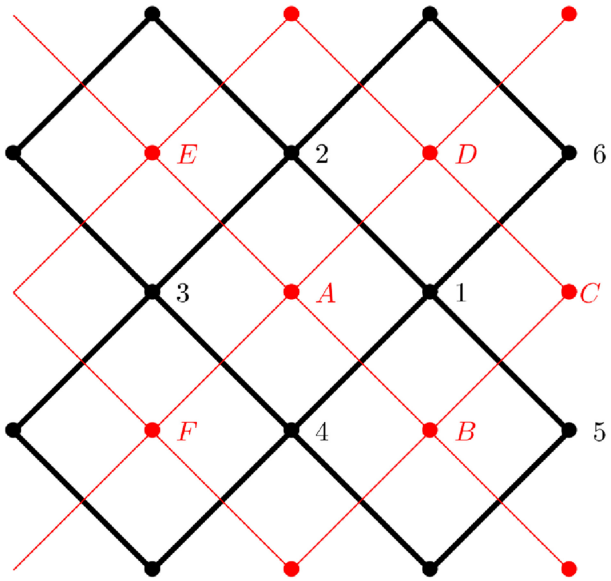

FIGURE 4 | Sketch of the dual network construction. From the original network (black), one can construct a dual one (red), where the nodes are located at the center of the original cells. At each link of the dual network we associate a "dual" flow rate obtained from the pressure difference of the original network. At each node we associate a "dual" pressure based on the original flow rate. See the text for details.

2.2. Self-Duality of the Square Lattice

We define a dual network as sketched in **Figure 4**. A node is located at the center of each cell and there is a link connecting each adjacent cell. On each link, a "dual" current is defined from the pressure difference between pressure by the crossed link (from the original network),

$$\begin{aligned} j_{A\to B} &= P_1 - P_4 \,, \\ j_{A\to D} &= P_2 - P_1 \,, \\ j_{F\to A} &= P_3 - P_4 \,, \\ j_{E\to A} &= P_2 - P_3 \,. \end{aligned} \tag{31}$$

The current in the dual lattice satisfies the conservation of mass at each node (e.g., the Kirchhoff condition) since $j_{A\to B} + j_{A\to D} - j_{F\to A} - j_{E\to A} = 0$.

Moreover, one can define a pressure field W on the dual lattice defined from this gradient,

$$\begin{aligned} W_A - W_B &= q_{1\to 4} \,, \\ W_B - W_C &= q_{1\to 5} \,, \\ W_C - W_D &= q_{1\to 6} \,, \\ W_D - W_A &= q_{1\to 2} \,. \end{aligned} \tag{32}$$

The definition is consistent once W is defined at a single point since the sum over a closed loop (and thus any) is equal to zero, $(W_A - W_B) + (W_B - W_C) + (W_C - W_D) + (W_D - W_A) = q_{1\to 4} + q_{1\to 5} + q_{1\to 6} + q_{1\to 2} = 0$.

Hence, the "dual" pressure gradient and current follow the constitutive equation,

$$W_A - W_B = q_{1\to 4} = q(P_A - P_B) = q(j_{A\to B}) \,, \tag{33}$$

so that,

$$j_{A\to B} = q^{-1}(W_A - W_B) \,. \tag{34}$$

Hence, the dual pressure and flow rate field satisfy the same kind of equation but with a local law which is inverted. It is important to note that the mean flow in the dual lattice is perpendicular to the original one.

3. CAPILLARY FIBER BUNDLE MODEL

We now consider an analytically solvable model for the flow. Let us assume that the network consists of a set of parallel links placed between two fluid reservoirs kept at pressure $p = 0$ and $p = \nabla p < 0$, i.e., we are describing the *capillary fiber bundle model* [14–16]. The constitutive equation for the fiber bundle is then given by

$$\begin{aligned} Q = \sum_{i=1}^{N_y} \Big[& -\Theta(q_i - \alpha|\nabla p|)\alpha\nabla p \\ & - \Theta(\alpha|\nabla p| - q_i)\beta\nabla p \\ & + \Theta(\alpha|\nabla p| - q_i)\left(1 - \frac{\beta}{\alpha}\right) q_i \Big] \,, \end{aligned} \tag{35}$$

where we have labeled the links according to their position, $i = 1, \cdots, N_y$ and q_i is the threshold of the ith link.

Let us now relabel the links in ascending order with respect to their thresholds: $q_{(1)} \le q_{(2)} \le \cdots \le q_{(N_y)}$. Equation (35) then becomes

$$\begin{aligned} Q = \sum_{k=1}^{N_y} \Big[& -\Theta(q_{(k)} - \alpha|\nabla p|)\alpha\nabla p \\ & - \Theta(\alpha|\nabla p| - q_{(k)})\beta\nabla p \\ & + \Theta(\alpha|\nabla p| - q_{(k)})\left(1 - \frac{\beta}{\alpha}\right) q_{(k)} \Big] \,. \end{aligned} \tag{36}$$

The thresholds are distributed according to the probability distribution $p(q_c)$, with a corresponding *cumulative probability* given by

$$P(q_c) = \int_0^{q_c} p(q) dq \,. \tag{37}$$

According to order statistics, the mean value of kth largest threshold—mean value in the sense of averaging over an ensemble of networks—is given by

$$P(\overline{q}_{(k)}) = \frac{k}{N_y + 1} \approx \frac{k}{N_y} \,. \tag{38}$$

Thus, the ensemble averages of the three types of sums in Equation (36) are then

$$\sum_{k=1}^{N_y} \Theta(\overline{q}_{(k)} - \alpha|\nabla p|) = N_y[1 - P(\alpha|\nabla p|)] \,, \tag{39}$$

$$\sum_{k=1}^{N_y} \Theta(\alpha|\nabla p| - \overline{q}_{(k)}) = N_y P(\alpha|\nabla p|) \,, \tag{40}$$

and

$$\sum_{k=1}^{N_y} \Theta(\alpha|\nabla p| - \overline{q}_{(k)})\overline{q}_{(k)} = N_y \int_0^{\alpha\nabla p} p(q) q \, dq \,. \tag{41}$$

Inserted into Equation (36), these averages give

$$\begin{aligned} \langle q \rangle \; &= \; -[1 - P(\alpha|\nabla p|)]\alpha\nabla p - P(\alpha|\nabla p|)\beta\nabla p \\ &+ \left[1 - \frac{\beta}{\alpha}\right] \int_0^{\alpha|\nabla p|} p(q) q \, dq \,, \end{aligned} \tag{42}$$

where $\langle q \rangle = Q/N_y$.

3.1. Uniform Threshold Distribution

We now consider the concrete threshold distribution we will also employ in our numerical simulations on the square lattice: a uniform distribution on the interval $(q_{\min}, q_{\max})$. Hence,

$$p(q_c) = \begin{cases} 0 & : q_c \le q_{\min} \,, \\ (q_{\max} - q_{\min})^{-1} & : q_{\min} < q_c < q_{\max} \,, \\ 0 & : q_{\max} \le q_c \,. \end{cases} \tag{43}$$

We define

$$\nabla p_{\min} = -\frac{q_{\min}}{\alpha}, \tag{44}$$

and

$$\nabla p_{\max} = -\frac{q_{\max}}{\alpha}. \tag{45}$$

We also define

$$\nabla p_0 = \frac{1}{2}\left[\nabla p_{\min} + \nabla p_{\max}\right] \,. \tag{46}$$

Inserting these expressions into Equation (42) gives

$$\langle q \rangle = \begin{cases} -\alpha\nabla p & : |\nabla p| \le |\nabla p_{\min}| \,, \\ \frac{(\alpha-\beta)(\nabla p - \nabla p_c)^2}{2(\nabla p_{\max} - \nabla p_{\min})} & \\ -\frac{\alpha(\alpha\nabla p_0 - \beta\nabla p_{\min})}{\alpha-\beta} & : |\nabla p_{\min}| < |\nabla p| \\ & : |\nabla p| < |\nabla p_{\max}| \,, \\ -\beta\nabla p - (\alpha-\beta)\nabla p_0 & : |\nabla p_{\max}| \le |\nabla p| \,. \end{cases} \tag{47}$$

We have here defined

$$\nabla p_c = \frac{\alpha\nabla p_{\max} - \beta\nabla p_{\min}}{\alpha - \beta} \,. \tag{48}$$

If we now define

$$\langle q_c \rangle = \frac{\alpha(\beta\nabla p_{\min} - \alpha\nabla p_0)}{\alpha - \beta} \,, \tag{49}$$

we may cast the middle regime where $|\nabla p_{\min}| < |\nabla p| < |\nabla p_{\max}|$ in the form

$$\langle q \rangle = \langle q_c \rangle + \frac{(\alpha - \beta)}{2(\nabla p_{\min} - \nabla p_{\max})} (\nabla p - \nabla p_c)^2 \,. \tag{50}$$

It straight forward but somewhat tedious to rewrite the average flow rate $\langle q \rangle$, Equation (47) in the general form (26) and (27) resulting from the scaling relations (2) to (5).

3.2. Exponential Threshold Distribution

Let us now consider the exponential threshold distribution

$$p(q_c) = \frac{e^{-q_c/q_0}}{q_0} \,, \tag{51}$$

for $0 \le q_c < \infty$. The corresponding cumulative distribution is

$$P(q_c) = 1 - e^{-q_c/q_0} \,. \tag{52}$$

Inserted into Equation (42), this gives

$$\begin{aligned} \langle q \rangle \; &= \; -e^{\alpha\nabla p/q_0}\alpha\nabla p \\ &- \left(1 - e^{\alpha\nabla p/q_0}\right)\beta\nabla p \\ &+ \left[1 - \frac{\beta}{\alpha}\right]\left[q_0 - e^{\alpha\nabla p/q_0}\left(q_0 - \alpha\nabla p\right)\right] \,, \end{aligned} \tag{53}$$

where we are still assuming $\nabla p < 0$. Let us set $q_0 = -\alpha\nabla p$. We then have the limits

$$\langle q \rangle = \begin{cases} -\alpha\nabla p & : |\nabla p| \ll q_0/\alpha \,, \\ -\beta\nabla p + (\alpha - \beta/)\nabla p_0 & : q_0/\alpha \ll |\nabla p| \,. \end{cases} \tag{54}$$

In contrast to the uniform distribution discussed in section 3.1, there is *not* a transitional regime between the two limits of Equation (54) which is on the form (50).

Hence, the uniform distribution on an interval, (43) results in $\langle q \rangle$ following a power law in $\langle q \rangle - \langle q_c \rangle$ vs. $\nabla p - \nabla p_c$, Equation (50), whereas the exponential distribution (51) does not. From the simple capillary fiber bundle model we may conclude that the power law behavior seen in Equation (50) is incidental and due to the uniform threshold distribution, which in itself is a power law (with exponent zero).

We study a two-dimensional network mode in section 5. Surprisingly, we find that also in this case, only the uniform distribution leads to a flow dependency on the pressure drop of the form

$$\langle q \rangle - \langle q_c \rangle \sim (\nabla p - \nabla p_c)^{\mu} \,. \tag{55}$$

In this case, however, the exponent μ depends on the parameter ratio β/α.

4. NUMERICAL METHOD: AUGMENTED LAGRANGIAN

For completeness, this section describes the numerical method used to solve the non-linear Kirchhoff equations. This section is not required to understand the results that follow.

The method used is based on the Augmented Lagrangian method commonly used to solve the Stokes Equation for yield stress fluids [17, 18]. It is based on a variational approach. We start by rewriting the local Equation (1), introducing the function $f(q)$ as

$$\delta p(q) = -f(q) = \begin{cases} -\frac{1}{\alpha} q & : |q| < q_c \\ -\frac{1}{\beta}\left[q - \frac{q}{|q|}(1-\frac{\beta}{\alpha})\right] & : |q| > q_c \, . \end{cases} \tag{56}$$

We define a function $\phi(q) = \int_0^q f(q')dq'$. The flow field $\{q_l\}$ solution of Equation (1), with the constraints of imposed inlet and outlet pressures at the boundaries p_{in} and p_{out}, can be written as the saddle point of the functional

$$\begin{aligned} &\max_{\{\lambda_n\}} \min_{\{q_l\}} \Phi[\{q_l\},\{\lambda_n\}] \\ &= \sum_{l\in\mathcal{L}} \left[\phi(q_n) - \delta_{l,in} p_{in} q_l + \delta_{l,out} p_{out} q_l\right] \\ &+ \sum_{n\in\mathcal{N}} \lambda_n \sum_{l'\in\mathcal{V}(n)} q_{l'}, \end{aligned} \tag{57}$$

where $\mathcal{L}$ represents the ensemble of links, $\mathcal{N}$ the ensemble of nodes and $\mathcal{V}(n)$ the ensemble of links connected to node n. The symbol $\delta_{l,in}$ (resp. $\delta_{l,out}$) is equal to 1 if the link is connected to the inlet (resp. outlet) node and to 0 otherwise. The $\{\lambda_n\}$ field is a set of Lagrangian multipliers which imposes the conservation of mass at each node (and it may thus be associated to a pressure field).

The main idea of the Augmented Lagrangian method is to introduce a secondary set of velocities $\{j_l\}$ to decouple the non-linear rheology from the Kirchhoff Equation. Another constraint is then added $\{j_l\} = \{q_l\}$ via the Lagrangian method.

Hence, the velocity field is the solution of the equation

$$\begin{aligned} &\max_{\{\lambda_n\},\{\mu_n\}} \min_{\{q_l\},\{j_l\}} \Psi[\{q_l\},\{j_l\},\{\lambda_n\},\{\mu_l\}] \\ &= \sum_{l\in\mathcal{L}} \Big[\phi(q_n) - \delta_{l,in} p_{in} j_l + \delta_{l,out} p_{out} j_l \\ &+ \mu(j_l - q_l) + \frac{\epsilon}{2}|q_l - j_l|^2\Big] \\ &+ \sum_{n\in\mathcal{N}} \lambda_n \sum_{l'\in\mathcal{V}(n)} j_{l'} \, , \end{aligned} \tag{58}$$

where $\{\mu_l\}$ is a set of Lagrangian multipliers. The quadratic term is an additional penalty term which characterizes the augmented Lagrangian approach. Here ϵ is a parameter determining its strength.

The methods consists now in implementing an iterative algorithm to reach the saddle point starting from an initial guess $\{q_l^0\}$, $\{j_l^0\}$, $\{\lambda_n^0\}$ and $\{\mu_l^0\}$.

Knowing $\{q_l^n\}$, $\{j_l^n\}$, $\{\lambda_n^n\}$ and $\{\mu_n^n\}$, the algorithm is decomposed in the following steps.

Determination of $\{j_l^{n+1}\}$ and $\{\lambda_n^{n+1}\}$:
For this step we solve

$$\begin{aligned} &\forall l \in \mathcal{L}, \frac{\partial}{\partial j_l}\Psi[\{q_l^n\},\{j_l\},\{\lambda_n\},\{\mu_l^n\}] = 0 \, , \\ &\forall n \in \mathcal{N}, \frac{\partial}{\partial \lambda_n}\Psi[\{q_l^n\},\{j_l\},\{\lambda_n\},\{\mu_l^n\}] = 0 \, , \end{aligned} \tag{59}$$

which reads

$$\forall l \in \mathcal{L}, j^{n+1} = -\frac{1}{\epsilon}(\lambda_{l+}^{n+1} - \lambda_{l-}^{n+1} + \mu_l^n - \epsilon q_l^n) \tag{60}$$

$$\forall n \in \mathcal{N}, \sum_{l'\in\mathcal{V}(n)} j_{l'}^{n+1} = 0, \tag{61}$$

where λ_{l+}^{n+1} and λ_{l-}^{n+1} are the Lagrangian multipliers of the two nodes adjacent to link l. For nodes adjacent to the outlet (resp. inlet), λ_+ (resp. λ_-) has to be replaced with p_{out} (resp. p_{in}).

The most important point of this set of equations is that it is equivalent to solving the standard linear Kirchhoff equations with a constant permeability $1/\epsilon$ but with an additional source term $\mu_l^n - \epsilon q_l^n$. Hence, it may be solved by standard linear methods (uch as Cholesky, LU decomposition, etc.).

Determination of q_l^{n+1}:
We solve

$$\forall l \in \mathcal{L}, \frac{\partial}{\partial q_l}\Psi[\{q_l\},\{j_l^{n+1}\},\{\lambda_n^{n+1}\},\{\mu_l^n\}] = 0, \tag{62}$$

which the local, but implicit equation

$$\forall l \in \mathcal{L}, \phi'(q_l^{n+1}) + \epsilon q_l^{n+1} = \mu + \epsilon j_l^{n+1}; \, . \tag{63}$$

Noting that $y = \mu + \epsilon j_l^{n+1}$, the solution is given by

$$q_l^{n+1} = \begin{cases} \frac{1}{1/\alpha+\epsilon} y & : |y| < \epsilon i_c + \frac{i_c}{\alpha} \, , \\ \frac{1}{1/\beta+\epsilon}\left[|y| + (1/\beta - 1/\alpha) i_c\right] \text{sign(y)} & : |y| > \epsilon i_c + \frac{i_c}{\alpha} \, . \end{cases} \tag{64}$$

Determination of μ_l^{n+1}:
For this step, we update in the direction of the gradient (Newton method)

$$\mu_l^{n+1} = \mu_l^{n+1} + \gamma(j_l^{n+1} - q_l^{n+1}) \, , \tag{65}$$

where γ is a parameter set to $\gamma = \epsilon$ for simplicity.

In practice, this algorithm is iterated until the relative variation of the total flow rate between two step is below 10^{-5}%. The computational time and the number of steps are strongly varying depending on β but also on the applied pressure.

5. RESULTS

We now our numerical model based on the network show in **Figure 1** and the algorithm described in section 4. We use the link threshold distribution (43) with $q_{\min} = 7.5$ and $q_{\max} = 12.5$ in the following.

5.1. Criticality

As noted above, due to the distribution of thresholds, the links will reach their thresholds at different macroscopic pressures. A link l will be defined as being in β-mode if $q_l > q_c$ and in α-mode otherwise. Similar to the percolation problem, a macroscopic change in flow regime is expected once there are percolation pathways of β-mode links. However, it is important to note a major difference with the percolation problem: the mode of a link influences the neighboring links. Indeed, in the case of $\beta > \alpha$, once a link switches to β-mode, the flow will be easier through it. This will tend to concentrate the flow toward it. It will therefore increase the flow in the upstream and downstream neighboring links and as a consequence push these links toward the β-mode. In the opposite case, for $\beta < \alpha$, the β-mode has a lower conductivity once entering this mode compared to what it would have in α-mode. Flow will therefore tend to go around it, increasing the flow in the other lateral links. Consequently β-mode links will tend to correlate in the stream-wise (or lateral) direction for $\beta > \alpha$ and orthogonally to the stream-wise direction for $\beta < \alpha$ [19].

The intermediate case $\beta = \alpha$ is interesting as the mode of a link has no influence on its neighbors. Since the mobility are the same for every link, the flow rate and the pressure gradient become homogeneous and equal to the mean flow rate and mean gradient. The problem is therefore identical to the *directed percolation problem* [8].

The other limit $\beta/\alpha \gg 1$, the problem becomes identical to that of a yield stress fluid in a porous medium [9, 20, 21]. The critical path is then related to the directed polymer problem [9, 22–24], as it corresponds to the path that minimizes the sum of local pressure threshold $\Delta P_c = \min \sum(q_c/\alpha)$.

5.2. Pathscape Method

To quantify this phenomenon and to determine the percolation pressure, we determine the longest directed path of the β-mode links. This quantity is essentially the longitudinal correlation length in directed percolation [10]. We map the length of all paths by invoking a pathscape approach as described in Talon et al. [24] for yield-stress fluids.

We introduce the node field L_n representing the longest upstream directed path ending at n. L_n can be determined from a transfer matrix algorithm propagating from left to right (stream direction). If we note, at a given node n, l_1 and l_2 the two upstream neighbor links and n_1 and n_2 the corresponding nodes. We associate binary variables m_1 and m_2 with the two links l_1 and l_2. If link l_1 is in β-mode, then $m_1 = 1$, otherwise $m_1 = 0$ — and likewise for the link l_2. We then have that

$$L_n = \max\left[(L_{n_1} + 1)m_1, (L_{n_2} + 1)m_2\right] . \tag{66}$$

We proceed by constructing the node field R_n containing the longest directed path ending at n but propagating in the downstream direction. This algorithm is identical to the previous one but it propagates in the upstream direction from the rightmost column.

Once both fields have been determined, we sum the two to obtain the pathscape $T_n = L_n + R_n$, which contains the length of longest directed percolating path passing by the node n. From this pathscape, we can then identify the longest directed path $L_{max} = \max(T_n)$. In **Figure 5**, we present two examples of such a pathscape at two different imposed pressure. We see here the longest cluster path in dark blue. At low applied pressure, the longest cluster is quite low $L_{\max} = 7$, whereas at higher pressure, $L_{\max}$ is closer to the system size.

It is important to note that the pathscape we have defined here is *not* the landscape of minimal paths [24]. In the limit $\beta \to \alpha$ the pathscape reflects the clusters in directed percolation as noted in section 5.1. However, when $\beta \neq \alpha$, the paths we identify correspond to directed percolation clusters. However, the directed percolation is now *correlated.*

5.3. Evolution of the Correlation Length $L_{\max}$

In **Figure 6**, we investigate the evolution of $L_{\max}$ as function of the applied pressure. As it can be seen, the correlation length increases with pressure until it reaches the system length N_x. Similarly to percolation, one can see in **Figure 6B** that the correlation length diverges as a power law close to a critical pressure gradient ∇p_c,

$$L_{\max} \propto (\nabla p_c - \nabla p)^{-\nu} . \tag{67}$$

We note in this figure that the exponent ν seems to vary with β. In **Figure 7**, we display the evolution of ν and the critical pressure gradient ∇p_c against the parameter β. As we can see, ν and ∇p_c decrease significantly with β. Where the limit $\beta \to 1$ is consistent with the results found in the literature on directed percolation, $\nu = \nu_{\parallel} = 1.733847(6)$ [10]. Our best estimate of the threshold pressure is $\nabla p_c \approx 10.72$.

At the end of section 5.2 we noted that the pathscape we have identified is *not* related to the pathscape spanned by minimal paths in the limit $\beta/\alpha \to \infty$. If that were the case, we would have expected ν to approach the value $\nu_{\parallel} = 3/2$ [11]. Rather, we are identifying directed percolation clusters in a correlated landscape, and this directed percolation ν is approaching the value 1 in this limit.

5.4. Flow Curve

We now investigate the flow curve. **Figure 8** displays the evolution of the mean flow rate as function of the pressure gradient and for different β. In the lower figure, we show that, close to the critical pressure, the flow rate also follows a power-law which can be written on the form

$$\langle q \rangle - \langle q \rangle_c \propto (\nabla p - \nabla p_c)^{\mu} , \tag{68}$$

where q_c is a constant obtained by interpolating the data at the critical pressure. We note here that the exponent μ varies with the coefficient β. In **Figure 9**, we report the evolution of this exponent as a function of $1/\log(\beta)$. For $\beta = \alpha = 1$ we have the obvious limiting value $\mu = 1$. As β increases, so does the value of μ. By plotting μ against $1/\log(\beta)$ we estimate the limiting value for $\beta \to \infty$, which is consistent with the value $\mu = 2$; the value suggested by Roux and Herrmann in 1987 [25].

We note that the functional form $\langle q \rangle$, Equation (68), based on the uniform threshold distribution (43), gives a behavior closely

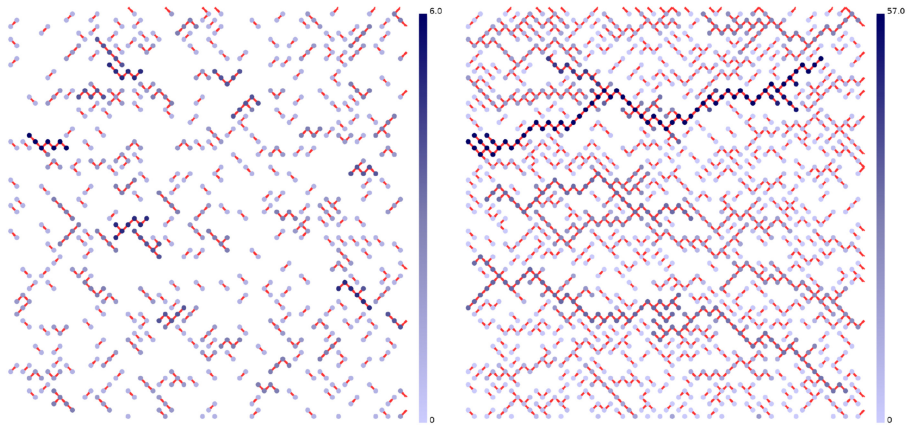

FIGURE 5 | Pathscapes in the network at pressure differences $\nabla p = 8$ **(Left)** and $\nabla p = 8.6$ **(Right)**. The links in α-mode are not shown. Each link in β-mode have been assigned a color. The color reflects the length of the path to which the link in β-mode belongs, according to the bar to the right of each network. The shortest paths are light blue, the longest are dark blue.

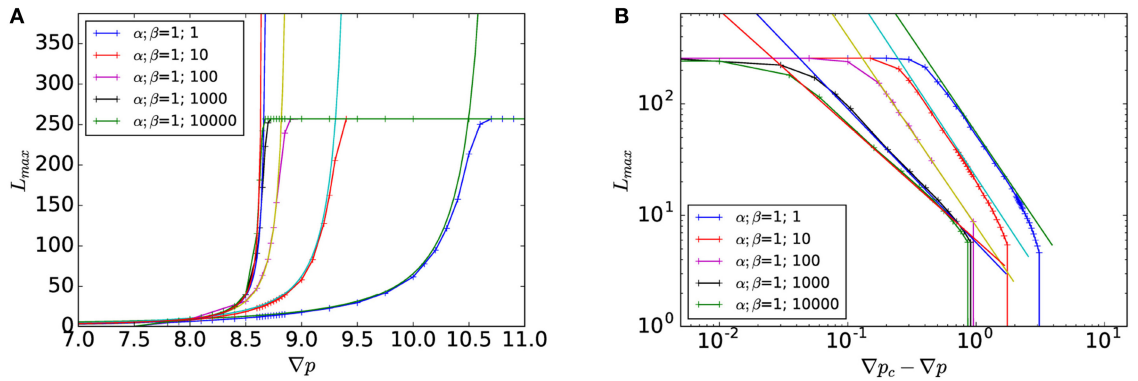

FIGURE 6 | Correlation length $L_{\max}$ as function of the gradient of pressure ∇p **(A)** or of the distance to the critical pressure $|\nabla p - \nabla p_c|$ **(B)** for different value of β. The solid line correspond to the power law fit given by Equation (67). The system size is 256×256.

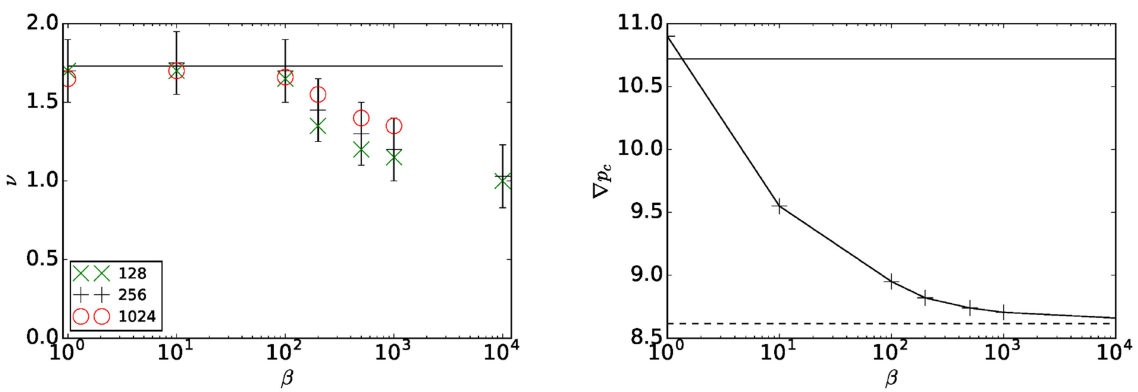

FIGURE 7 | (Left) ν as function of β for system sizes 128×128, 256×256 and $1,024 \times 1,024$. The data set for $L = 128, 256$, and $1,024$ are respectively based on 200, 200 and 10 realizations for each value of β. The horizontal line corresponds to the directed percolation exponent $\nu \approx 1.72$. **(Right)** Critical gradient of pressure $\nabla P_c(\beta)$ as function of β for the system size 256×256. The upper line corresponds to directed percolation ($p_c = 0.644700185(5)$ [10]). The line below (dashed) corresponds to the average of the directed polymer algorithm.

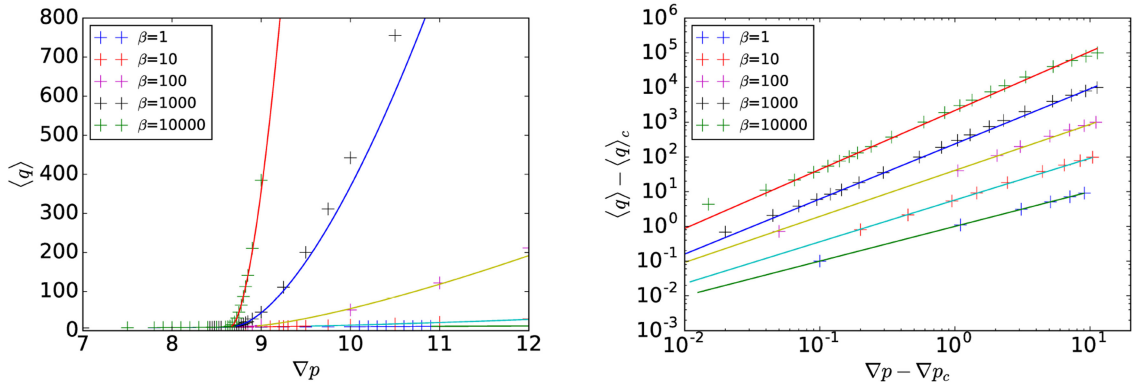

FIGURE 8 | Mean flow rate $\langle q \rangle$ as function of the mean pressure gradient **(Left)** and of the distance to the critical pressure gradient $\nabla p - \nabla p_c$ **(Right)** for different β. The solid lines correspond the power law fit given by Equation (68). The system size is 256 × 256.

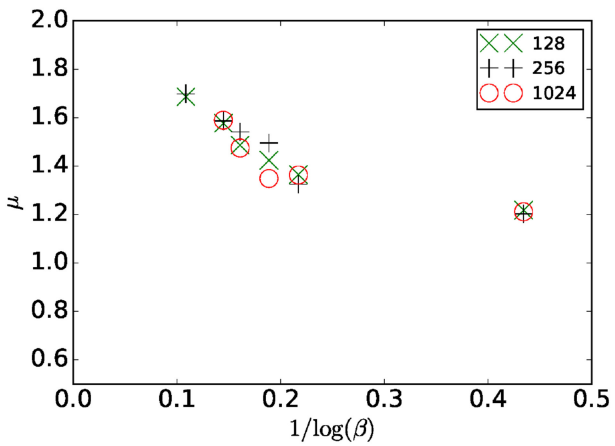

FIGURE 9 | Flow exponent μ as function of $1/\log(\beta)$ for a system sizes $L = 128 \times 128$, 256×256, and $1,024 \times 1,024$. The dependence of the exponent with system size is smaller than the error bars.

related to the one found for the capillary fiber bundle model with the same type of threshold distribution, see Equation (50), but with $\mu = 2$. The correlation length exponent ν cannot be defined in the capillary fiber bundle model.

In section 3.2, we studied the capillary fiber bundle model with an exponential threshold distribution (51). We have used the same distribution for the network model considered here. As in the capillary fiber bundle model, we do not find a power law of the type (68) in this case, nor do we find a power law for the correlation length (67).

6. SUMMARY AND CONCLUSIONS

We have explored the behavior of a bi-viscous fluid moving in a diamond lattice subject to the constitutive Equation (1) for each link. This system contains a critical point which leads to the behavior $\langle q \rangle - \langle q_c \rangle \sim (\nabla p - \nabla p_c)^{\mu}$ for the volumetric flow rate and $L_{\max} \sim (\nabla p - \nabla p_c)^{-\nu}$ for the correlation length when a uniform threshold distribution is used. However, the two limits of the ratio between the two parameters representing the mobilities, $\beta/\alpha \to 1$ and $\beta/\alpha \to \infty$, or equivalently, $\beta/\alpha \to 0$ correspond to the *percolation* and the *directed polymer* problems respectively. These *are* problems containing critical points.

There are still a number of open questions concerning this system. We list them as follows:

- We have only considered $\nabla p \geq \nabla p_c$. What happens on the other side of the critical point?
- The critical exponents μ and ν are functions of the parameter ratio β/α. Is this a crossover or are we dealing with non-universal exponents?
- We have only dealt with $\beta \geq 0$. What happens for $\beta < 0$? The limit $\beta \to -\infty$ turns the model into the fuse model. What happens when β is barely negative? Our numerical algorithm is not capable of handling this problem.
- It would be more realistic, but also more challenging to consider a power-law type characteristic for the constitutive Equation for $q \geq q_c$. How will this change our conclusions?
- Why do we not see critical behavior for the exponential threshold distribution in the network model?

DATA AVAILABILITY STATEMENT

All datasets generated for this study are included in the article/supplementary material.

AUTHOR CONTRIBUTIONS

LT did the numerical computations. AH did the theoretical part. Both authors wrote the paper.

ACKNOWLEDGMENTS

We thank the Research Council of Norway through its Centers of Excellence funding scheme, project number 262644. AH thanks the Université de Paris-Sud for funding through a visiting professorship.

REFERENCES

1. Carreau PJ. Rheological equations from molecular network theories. *Trans Soc Rheol.* (1972) **16**:99. doi: 10.1122/1.549276
2. Herschel WH, Bulkley R. Konsistenzmessungen von Gummi-Benzollösungen. *Kolloid Zeitschrift*. (1926) **39**:291–300. doi: 10.1007/BF01432034
3. Whitaker S. The forchheimer equation: a theoretical development. *Transp Porous Med.* (1996) **25**:27–61. doi: 10.1007/BF00141261
4. Sinha S, Hansen A. Effective rheology of immiscible two-phase flow in porous media. *EPL.* (2012) **99**: 44004. doi: 10.1209/0295-5075/99/44004
5. Wyckoff RD, Botset HG. The flow of gas-liquid mixtures through unconsolidated sands. *J Appl Phys.* (1936) **7**:325. doi: 10.1063/1.1745402
6. Roux S, Hansen A, Guyon E. Criticality in non-linear transport properties of heterogeneous materials. *J Phys France.* (1987) **48**:2125–30. doi: 10.1051/jphys:0198700480120212500
7. Hinrichsen EL, Roux S, Hansen A. The conductor-superconductor transition in disordered superconducting materials. *Physica C.* (1990) **167**:433–55. doi: 10.1016/0921-4534(90)90364-K
8. Hinrichsen H. Non-equilibrium critical phenomena and phase transitions into absorbing states. *Adv Phys.* (2000) **49**:815. doi: 10.1080/00018730050198152
9. Hansen A, Hinrichsen EL, Roux S. Roughness of crack interfaces. *Phys Rev Lett.* (1991) **66**:2476. doi: 10.1103/PhysRevLett.66.2476
10. Jensen I. Low-density series expansions for directed percolation: I. A new efficient algorithm with applications to the square lattice. *J Phys A.* (1999) **32**:5233. doi: 10.1088/0305-4470/32/28/304
11. Roux S, Hansen A, Hinrichsen EL. A direct mapping between Eden growth model and directed polymers in random media. *J Phys A Math Gen.* (1991) **24**:L295. doi: 10.1088/0305-4470/24/6/008
12. Straley JP. Critical exponents for the conductivity of random resistor lattices. *Phys Rev B.* (1977) **15**:5733. doi: 10.1103/PhysRevB.15.5733
13. Hansen A, Sinha S, Bedeaux D, Kjelstrup S, Aa Gjennestad M, Vassvik M. Relations between seepage velocities in immiscible, incompressible two-phase flow in porous media. *Transp Por Med*. (2018) **125**:565–87. doi: 10.1007/s11242-018-1139-6
14. Scheidegger AE. Theoretical models of porous matter. *Producers Monthly*. 10: 17 (1953).
15. Scheidegger AE. *The Physics of Flow Through Porous Media*. Toronto: University of Toronto Press (1974).
16. Roy S, Hansen A, Sinha S. Effective rheology of two-phase flow in a capillary fiber bundle model. *Front Phys.* (2013) **7**:92. doi: 10.3389/fphy.2019.00092
17. Duvaut G, Lions JL. *Inequalities in Mechanics and Physics*. Berlin: Springer Verlag (1976).
18. Glowinski R, Le Tallec P. *Augmented Lagrangian and Operator-Splitting Methods in Nonlinear Mechanics*. Philadelphia, PA: SIAM (1989).
19. Wennberg KE, Batrouni GG, Hansen A, Horsrud P. Band formation in deposition of fines in porous media. *Transp Porous Med*. (1996) **25**:247–73. doi: 10.1007/BF00140983
20. Guyon E, Roux S, Hansen A, Bideau D, Troadec JP Crapo H. Non-local and non-linear problems in the mechanics of disordered systems: application to granular media and rigidity problems. *Rep Prog Phys*. (1990) **53**:373. doi: 10.1088/0034-4885/53/4/001
21. Talon L, Bauer D. On the determination of a generalized Darcy Equation for yield-stress fluid in porous media using a Lattice-Boltzmann TRT scheme. *Eur Phys J E.* (2013) **36**:139. doi: 10.1140/epje/i2013-13139-3
22. Kardar M, Zhang YC. Scaling of directed polymers in random media. *Phys Rev Lett*. (1987) **58**:2087. doi: 10.1103/PhysRevLett.58.2087
23. Barabasi AL, Stanley HE. *Fractal Concepts in Surface Growth.* Cambridge: Cambridge University Press (1995).
24. Talon L, Auradou H, Pessel M, Hansen A. Geometry of optimal path hierarchies. *EPL.* (2013) **103**:30003. doi: 10.1209/0295-5075/103/30003
25. Roux S, Herrmann HJ. Disorder-induced nonlinear conductivity. *EPL.* (1987) **4**:1227. doi: 10.1209/0295-5075/4/11/003

Conflict of Interest: The authors declare that the research was conducted in the absence of any commercial or financial relationships that could be construed as a potential conflict of interest.

Advantages of publishing in Frontiers

OPEN ACCESS
Articles are free to read for greatest visibility and readership

FAST PUBLICATION
Around 90 days from submission to decision

HIGH QUALITY PEER-REVIEW
Rigorous, collaborative, and constructive peer-review

TRANSPARENT PEER-REVIEW
Editors and reviewers acknowledged by name on published articles

Frontiers
Avenue du Tribunal-Fédéral 34
1005 Lausanne | Switzerland

Visit us: www.frontiersin.org
Contact us: info@frontiersin.org | +41 21 510 17 00

REPRODUCIBILITY OF RESEARCH
Support open data and methods to enhance research reproducibility

DIGITAL PUBLISHING
Articles designed for optimal readership across devices

FOLLOW US
@frontiersin

IMPACT METRICS
Advanced article metrics track visibility across digital media

EXTENSIVE PROMOTION
Marketing and promotion of impactful research

LOOP RESEARCH NETWORK
Our network increases your article's readership